Springer Series in Materials Science 248

Vladimir G. Plekhanov

Introduction to Isotopic Materials Science

Springer

Springer Series in Materials Science

Volume 248

Series editors

Robert Hull, Troy, USA
Chennupati Jagadish, Canberra, Australia
Yoshiyuki Kawazoe, Sendai, Japan
Richard M. Osgood, New York, USA
Jürgen Parisi, Oldenburg, Germany
Udo W. Pohl, Berlin, Germany
Tae-Yeon Seong, Seoul, Republic of Korea (South Korea)
Shin-ichi Uchida, Tokyo, Japan
Zhiming M. Wang, Chengdu, China

The Springer Series in Materials Science covers the complete spectrum of materials physics, including fundamental principles, physical properties, materials theory and design. Recognizing the increasing importance of materials science in future device technologies, the book titles in this series reflect the state-of-the-art in understanding and controlling the structure and properties of all important classes of materials.

More information about this series at http://www.springer.com/series/856

Vladimir G. Plekhanov

Introduction to Isotopic Materials Science

Springer

Vladimir G. Plekhanov
Mathematics and Physics Department
Computer Science College
Tallinn, Estonia

ISSN 0933-033X ISSN 2196-2812 (electronic)
Springer Series in Materials Science
ISBN 978-3-319-42260-2 ISBN 978-3-319-42261-9 (eBook)
https://doi.org/10.1007/978-3-319-42261-9

Library of Congress Control Number: 2016960025

© Springer Nature Switzerland AG 2018
This work is subject to copyright. All rights are reserved by the Publisher, whether the whole or part of the material is concerned, specifically the rights of translation, reprinting, reuse of illustrations, recitation, broadcasting, reproduction on microfilms or in any other physical way, and transmission or information storage and retrieval, electronic adaptation, computer software, or by similar or dissimilar methodology now known or hereafter developed.
The use of general descriptive names, registered names, trademarks, service marks, etc. in this publication does not imply, even in the absence of a specific statement, that such names are exempt from the relevant protective laws and regulations and therefore free for general use.
The publisher, the authors and the editors are safe to assume that the advice and information in this book are believed to be true and accurate at the date of publication. Neither the publisher nor the authors or the editors give a warranty, express or implied, with respect to the material contained herein or for any errors or omissions that may have been made. The publisher remains neutral with regard to jurisdictional claims in published maps and institutional affiliations.

This Springer imprint is published by the registered company Springer Nature Switzerland AG
The registered company address is: Gewerbestrasse 11, 6330 Cham, Switzerland

Preface

This book describes new trends in the nanoscience of isotopic materials science. Assuming a background in graduate condensed matter physics and covering the fundamental aspects of isotopic materials science from the very beginning, it equips readers to engage in high-level professional research in this area. The book's main objective is to share in the question of why solids are the way they are, either because of how their atoms are bonded with one another, because of defects in their structure, or because of how they are produced or processed. Accordingly, it explores the science of how atoms interact, connects the results to real materials properties, and demonstrates the engineering concepts that can be used to produce or improve semiconductors by design. In addition, it shows how the concepts discussed are applied in the laboratory.

The book addresses the needs of researchers, graduate students, and senior undergraduate students alike. Although primarily written for a materials science audience, it will be equally useful to those teaching electrical engineering, materials science, or even chemical engineering or physics curricula. In order to maintain the focus on materials concepts, the details of many of the derivations and equations are left out of the book. Similarly, the author does not delve into the details of electrical engineering topics in as much detail as an electrical engineer might wish. It is assumed that readers have a basic command of these topics.

Tallinn, Estonia Vladimir G. Plekhanov

Acknowledgements

The list of acknowledgements has to be necessarily long since the author has received a great amount of help from many person. I owe all of them a great deal and I would like to express my sincere grateful to each one. Most of them appear explicitly as authors in the references. Nevertheless, first of all I would like to acknowledge Prof. F. F. Gavrilov, who first introduced the author in the physics of isotopes. Thank you very much Prof. G. I. Pilipenko for a very long and warm collaboration. I deeply thank the authors and publishers who have kindly permitted us to reproduce figures and tables from their papers and books. In a few cases I have been unable to contact the authors, and I would be grateful if they would nevertheless retrospectively give me the necessary permission. Again it is a pleasure to thank the staff of Springer, in particular Dr. C. Ascheron and Elke Sauer, for continued excellent cooperation. Many thanks are due to Prof. D. Reder for carefully reading my manuscript. I also would like to acknowledge Dr. D. Jonson for his help in improving the English style of the my manuscript and Mr. R. Ermakov for technical assistants. It is very pity that Estonia State has never supported my scientific investigations. I wish to express my deep gratitude kids and grandchildren for their patience during the time preparation of this book.

Tallinn, Estonia Vladimir G. Plekhanov

Contents

1 Introduction 1
References 3

2 Energy Band Structure 5
2.1 Electronic Band Structure of Bulk Samples 5
2.1.1 General Remarks 5
2.1.2 Energy Band Structure 7
2.2 Density of States 12
2.3 Effective Mass 15
2.4 Optical Properties of Isotope-Mixed Substances 16
2.4.1 Isotope Renormalization of the Fundamental Gap's Energy 16
2.4.2 Exciton Emission Spectra 23
2.5 Electron Excitations in Low-Dimensional Structures 28
2.5.1 Wavelike Properties of Electrons 28
2.5.2 Dimensionality and Density of States 32
2.5.3 Electron in Quantum Dot 35
2.6 Excitons in Nanostructures 37
2.6.1 Excitons in Quantum Wells 38
2.7 Biexcitons in Quantum Dots 43
References 47

3 Phonon States in Bulk and Low-Dimensional Structures 53
3.1 Hamiltonian of Perfect Crystals 53
3.2 The Adiabatic and Harmonic Approximations 55
3.3 The Anharmonic Crystal 58
3.4 Disordered Crystals 64
3.4.1 Model of Virtual Crystal Approximation 65
3.4.2 Model of Coherent Potential Approximation 66
3.5 The Dispersion Relation 68

3.6 Measurement of Phonon Dispersion by the Method of Inelastic Neutron Scattering . . . 74
3.6.1 Background . . . 74
3.6.2 Experimental Results . . . 77
3.7 Raman Spectra of Isotope-Mixed Crystals . . . 84
3.8 Disorder Shift and Broadening of the Line in the Raman Spectra . . . 94
3.9 Vibrations in Low-Dimensional Structures . . . 99
3.9.1 General Remarks . . . 99
3.9.2 Elastic Continuum Model of Phonons . . . 101
3.9.3 Dielectric Continuum Model of Phonons . . . 103
3.10 Optical and Acoustic Phonons in Nanostructures . . . 105
3.11 Experimental Manifestation of Phonons in Low-Dimensional Structures of Different Kinds . . . 107
3.11.1 Electron–Phonon Interaction in Low-Dimensional Structures . . . 115
3.11.2 Exciton–Phonon Interaction in Low-Dimensional Systems . . . 123
References . . . 130

4 Application of Isotopic Materials Science in Bulk and Low-Dimensional Structures . . . 139
4.1 General Considerations . . . 139
4.2 Nonlinear Excitons in Bulk Isotope-Mixed Materials . . . 142
4.2.1 General Remarks . . . 142
4.2.2 Free-Exciton Emission from Diamond at Room Temperature . . . 143
4.2.3 UV Emission from a Diamond p–n Junction . . . 146
4.3 Exciton Lasing in LiH_xD_{1-x} Crystals . . . 149
4.4 Phonon-Related Isotope Effects . . . 156
4.4.1 Isotope Dependence of the Thermal Expansion Coefficient . . . 156
4.4.2 Effect of the Isotope Composition of a Crystal Lattice on the Specific Heat . . . 165
4.4.3 Dependence of Thermal Conductivity on the Isotope Composition of Materials . . . 172
4.4.4 Influence of the Isotope Composition Materials on the Lattice Constant . . . 179
4.4.5 Isotopic Fiber Optics . . . 189
4.5 Isotope-Mixed Graphene and Its Application . . . 194
4.6 Chemical Mechanisms Bandgap Engineering in Graphene . . . 205

4.7 Low-Dimensional Devices 215
4.7.1 Background 215
4.7.2 Resonant-Tunneling Diodes 217
4.7.3 Field-Effect Transistor 219
4.7.4 Single-Electron Transistor 221
4.7.5 Graphene Quantum Dots Electronics 226
4.7.6 Light-Emitting Diodes and Lasers 229
4.7.7 Radiation Detectors 235
4.8 Isotope-Based Quantum Computers 239
4.8.1 General Remarks 239
4.8.2 Current Status: The Di Vincenzo Criteria 240
4.8.3 Elementary Gates for Quantum Computation 242
4.8.4 A Physical Models for a Quantum Computer 251
References 266

Index 279

Symbols and Abbreviations

Symbols

α	Polarizability
α	Spring constant
Δ	Splitting value
$\delta(x)$	Dirac's delta function
ε	Dielectric constant of medium
ε_0	Permittivity of free space
θ	Polar angle
θ	Debye's temperature
λ	Wavelength
μ	Electron mobility
μ	Reduced mass
$\boldsymbol{\Phi}$	Thermodynamical potential
ϕ	Polar angle
ρ	Three-dimensional density
σ	Cross section
σ	Conductivity
ξ	Dimensional coordinate
τ	Scattering rate
a	Lattice constant
A	Amplitude of wave
$\boldsymbol{a}_1$, $\boldsymbol{a}_2$, $\boldsymbol{a}_3$	Basis vectors
$\boldsymbol{B}$	Magnetic field
C	Capacitance
C_p	Specific heat at constant pressure
C_v	Specific heat at constant volume
c	Velocity of light
D	Diffusion coefficient
d	Dimension
e	Electron charge

E	Energy of system
E_b	Binding energy
E_g	Band-to-band transition energy
E_F	Fermi level
E_{th}	Energy threshold
$\boldsymbol{F}$	Electric field
$\boldsymbol{f}$	Vector of force
f	Frequency
G	Conductance
h	Planck's constant
$\boldsymbol{H}$	Magnetic field
$\boldsymbol{H}$	Vector of reciprocal lattice
$\widehat{\mathrm{H}}$	Hamiltonian operator
H_{exc}	Exciton Hamiltonian
$\hbar\omega$	Phonon energy
I	Current
I_T	Tunnel current
J	Current density
$\boldsymbol{k}$	Wave vector
k_B	Boltzmann's constant
k_F	Fermi's wave vector
k_x, k_y, k_z	Components of the wave vector
l	Orbital quantum number
L	Inductance
L_T	Thermal diffusion length
$\boldsymbol{M}$	Magnetic dipole moment
m^*	Effective electron's mass
m_e	Mass of the electron
m_i	Mass of ith electron
M_j	Mass of the jth nucleus
M_p	Proton's mass
$N(E)$	Number of electrons with energy E
P_j	The momentum operators of the nucleus
$P(\xi)$	Hermite polynomial
p_i	The momentum operators of the electron
Q	Quality factor
$\boldsymbol{r}$	Coordinate vector
R	Radius of quantum dot
R	Reflection coefficient
r_i	The position of the ith electron
R_j	The position of the jth nucleus
R_T	Quantum resistance
s	Spin
s_z	Projection of the spin of electron

T	Ambient temperature
T	Time period
T_e	Electron kinetic energy
T_e	Electron's temperature
T_i	Ion kinetic energy
U	Process
U_m	Potential energy
U_0	Zero-point vibration energy
V	Potential energy
V	Volume
$V(R_i–R_j)$	Potential depending on the distance between ions
W	Crystalline potential
x	Concentration
z	Atomic number of the nucleus

Abbreviations

1D	One-dimensional system
2D	Two-dimensional system
AFM	Atomic force microscope
APD	Avalanche photodiode
FET	Field effect transistor
HENT	High electron mobility transistor
HES	Highly excited semiconductors
IR	Infrared
LA	Longitudinal acoustic
LED	Light-emitting diode
LO	Longitudinal optical
LT	Longitudinal transversal
MBE	Molecular beam epitaxy
MFM	Magnetic force microscope
MISFET	Metal–insulator–semiconductor–FET
MOCVD	Metal-organic chemical vapor deposition
MODFET	Modulation-doped FET
NDR	Negative differential resistance
OD	Zero-dimensional system
PIN	Positive intrinsic negative photodiode
QDs	Quantum dots
QWl	Quantum wells
QWr	Quantum wire
RTD	Resonant-tunneling diode
RTT	Resonant-tunneling transistor
SED	Single-electron devices
SET	Single-electron transistor
SNOM	Scanning near-field optical microscope

STM	Scanning tunnel microscope
TA	Transverse acoustic
TO	Transverse optic
UV	Ultraviolet

Chapter 1
Introduction

Abstract In this introductory chapter, we recall some facts about low-dimensional structures of isotope-based compounds which is the main subject of isotopic materials science. Modern physics distinguishes three fundamental properties of nuclei: mass, spin (and related magnetic moment), and volume (surrounding field strength), which are the essence of the isotope effect. It is underlined that stable and radioactive isotopes have a wide application in biology, medicine, optoelectronics as well as quantum processors.

As is well known, nanoscience and nanotechnology refer to the comprehensive interdisciplinary body of knowledge on the nanometer-size scale involving the sciences—physics, chemistry, biology, and materials science—and engineering—electronics, computer, mechanical, chemical construction, environment, etc.—fields. The modern world had witnessed the exceptionally rapid development of both our theoretical understanding and technological advancement of nanoelectronic devices. These new fabrication technologies have made it possible to reduce device dimensions to the point, where quantum size effects play a significant role in any realistic description of device operation and are required to reliably predict their performance in electronic and optical applications. Today's electronic and optical communications and information technology is still silicon based and can, thus far, meet the current needs by either increasing the production rate or by developing new production technologies and materials. In this connection, we should rememeber that the elemental semiconductors C (diamond), Ge, and Si in their natural form consist of a mixture of two or more stable isotopes and almost all compound materials consist of similar constituent elements. The availability of isotopically enriched materials which can be used to grow different crystals and epitaxial layers having modified isotopic compositions had led to many recent studies on the effects of isotopic composition on the vibrational, thermal, and electronic properties of different materials, as summarized in several comprehensive reviews [1–4] and monographs [5–8].

In the past four decades, the development of techniques capable of producing semiconducting structures [9] made from layers whose thickness can be as small as

© Springer International Publishing AG, part of Springer Nature 2018

V. G. Plekhanov, *Introduction to Isotopic Materials Science*,
Springer Series in Materials Science 248, https://doi.org/10.1007/978-3-319-42261-9_1

a nanometer has stimulated a wealth of new physics and led to the production of a wide range of electronic and optoelectronic devices [10]. Further advances have been made using techniques such as molecular-beam epitaxy (MBE) and metalorganic chemical vapor deposition (MOCVD) (see, e.g. [11]) that allow these two-dimensional (2D) systems to be formed into quantum wires, one-dimensional (1D) systems, in which electronic motion is essentially restricted to one direction, and quantum dots, zero-dimensional (0D) systems, which can be thought of as artificial atoms. The last one is very close to the essence of isotopic materials science. This is a very simple and not an expensive method for the creation of new low-dimensional structures. Indeed, neutron radiation of the matter can create the quantum dots of different sizes [12]. We should underline that the subject of this book—isotopic materials science is the new field of the nanoscience. The choice of topics in this book is influenced by several factors. Most of the heavier emphasis on isotopic materials science reflects the expertise of the author. One feature that sets this book apart from others on the market is that the isotopic materials science is given a more important role.

The present book is a comprehensive introduction to the main ideas and techniques of the field of isotopic materials science. The present book was written with a desire to satisfy three types of possible readers: first, of course, students of physics and chemistry who desire to learn some details new branch of nanoscience—isotope physics—that has a general use; second, experimental physicists and chemists and engineers as well as material scientists with mathematical learning who are interested in keeping an eye on the field of isotope-condensed matter physics that is of possible value to them; third, theoretical physicists at various stages of development who are interested in the present status of isotope solid-state physics and isotopic materials science. This book tells us how the excitations and very simple imperfections (isotopes) of real solids can be understood with simple models, whose power and scope are now firmly established. The subject matter supports a probable interplay of experiment, theory, and application (traditional and modern). This book is underlining that the isotopic technology is a next step in the nanotechnology. I hope to give sufficient references to published work so that the interested reader can easily find the primary literature sources to this rapidly expanding field of solid-state physics. The present book is devoted to a description of the fundamentals and different applications of the isotopic materials science.

Modern physics distinguishes three fundamental properties of atomic nuclei: mass, spin (and related magnetic moment), volume (surrounding field strength), which are the source of isotope effect (see, e.g., [13]). The stable elementary particles (electrons, protons, and neutrons) have intrinsic properties. Some of these properties such as mass and electrical charge are the same for macroscopic objects. Some are purely quantum mechanical and have no macroscopic analog [14]. Spin is an intrinsic angular momentum associated with elementary particles. The spin angular moment of an electron, measured along any particular direction, can only take on the values $\hbar/2$ or $-\hbar/2$. The nuclear magnetic moment associates with nuclear spin and produces the magnetic interaction with its environment [7, 8, 15]. The ability to manipulate and control electron and/or nucleus spin in semiconductor devices provides a new route to expand the capabilities of inorganic semiconductor-based

electronics and to design innovative devices with potential application in quantum computing. One of the major challenges toward these objectives is to develop semiconductor- based systems and architectures in which the spatial distribution of spins and their properties can be controlled. For instance, to eliminate electron spin decoherence resulting from hyperfine interaction due to nuclear spin background, isotopically controlled nuclear-spin-depleted devices are needed. The control of the spatial distribution of isotope with nuclear spins is a prerequisite to implement the quantum bits or qubits. Therefore, stable semiconductor isotopes are important elements in the development of solid-state quantum information. At the present time spintronics refer to spin electronics, the phenomena of spin-polarized transport in metals and semiconductors. The study of spin phenomena in solids characterize electrical (field-effect transistor), optical and magnetic properties of solids due to the presence of equilibrium and nonequilibrium spin populations, as well as spin dynamics. These fundamental aspects of spintronics give us as important insights about the nature of spin interaction, hyperfine, or spin exchange couplings—in solids (for details, see e.g., [16]).

My intention has been to write an introductory book on isotopic materials science that starts with the physics of isotope low - dimensional materials and quantum heterostructures would build up to the treatment of those new electronic, transport, and optical properties which arise as a consequence of both energy quantization of electrons and phonons in potential wells and the reduced dimensionality (2D, 1D, and 0D) of nanostructures. Once the basic concepts of quantum nanostructures are presented in a unified scheme, the last chapter of my textbook deals with the applications of isotopic materials science in nanoelectronic and optoelectronics.

With numerous illustrations, this book will be of great interest to undergraduate and graduate students taking courses in mesoscopic physics or nanoelectronic as well as quantum information, and academic and industrial researches working in this field. The references I cite are those with which I am most familiar with and which have helped us understand the subject as presented here. While there has been no attempt to give credit to each contributor, I primarily selected those reviews and monographs which contain extensive references in isotopic materials science.

References

1. A.A. Berezin, A.M. Ibrahim, Effects of the diversity of stable isotopes on properties of materials. Mater. Chem. Phys. **19**, 407–430 (1988)
2. E.E. Haller, Isotopically engineered semiconductors. J. Appl. Phys. **77**, 2857–2878 (1995)
3. M. Cardona, M.L.W. Theawalt, Isotope effects on the optical spectra of semiconductors. Rev. Mod. Phys. **77**, 1173–1224 (2005)
4. V.G. Plekhanov, Elementary excitations in isotope-mixed crystals. Phys. Rep. **410**, 1–235 (2005)
5. V.G. Plekhanov, *Isotope Effects in Solids* (Academic Press, San Diego, 2001)
6. V.G. Plekhanov, *Isotopes in Condensed Matters* (Springer, Berlin, 2013)
7. M. Wolfsberg, W.A. Hook, P. Paneth, *Isotope Effect in Chemical, Geological and Bio Sciences* (Springer, Heidelberg, 2010)

8. A. Vertis, S. Nagu (eds.), *Nuclear Chemistry* (Springer, Berlin, 2001)
9. ZhI Alferov, The history and future of semiconductor heterostructures. Phys. Tech. Semicond. **32**, 3–18 (1998). (in Russian)
10. K. Goser, P. Glösekötter, J. Dienstuhl, *Nanoelectronics and Nanosystems* (Spinger, Berlin, 2004)
11. V.G. Plekhanov, *Isotope Low-Dimensional Structures* (Springer, Berlin, 2012)
12. V.G. Plekhanov, *Isotope Effect - Macroscopic Maniestation of the Strong Interaction* (Lambert Academic Publishing, Saarbrücken, 2017). (in Russian)
13. V.G. Plekhanov, V.F. Myshkin, V.A. Khan, D.A. Izhoikin, Manifestation of the spin on the isotope effects. Adv. Mat. Res. **1084**, 147–151 (2015)
14. P.A.M. Dirac, *The Principles of Quantum Mechanics* (Clarendon Press, Oxford, 1958)
15. J.R. Gould, N.J. Turro, M.B. Zimmt, Magnetic field and magnetic isotope effects on the product of organic reactions, in *Advances in Physical Organic Chemistry*, vol. 20, eds. by V. Gold, D. Bethell (Academic Press, San Diego), pp. 19840
16. J. Fabian, A. Matos, Abiague, C. Ertler et al., Semiconductor spintronics. Acta Phys. Slovaca **57**, 565–907 (2007)

Chapter 2
Energy Band Structure

Abstract Optical probing and manipulation of electron quantum states in isotope-mixed compounds at the nanoscale are key to developing future nanophotonic devices, which are capable of ultrafast and low-power operation. Before beginning a general discussion on the application of isotopic materials science, it is helpful to have the knowledge of the electronic band structure used in materials. The modern view of solid-state physics is based on the presentation of elementary excitations having mass, quasi-impulse, and electrical charge. The base of such view of solid is ideal gas, which described the behavior of the system, e.g., noninteracting electrons. Such an approach to model of elementary excitations as a suitable model for the application of the quantum mechanics for the solution of solid-state physics task. In this chapter, some peculiarities of isotopic materials science will be considered by taking into account the dependence of the properties of elementary excitations on the isotope effect. It is illustrated when the dimensions of a solid are reduced to the size of the characteristic length of electrons in the isotope-mixed materials (de Broglie wavelength, localization length), new physical properties due to quantum effects become apparent. Our intention has been to physics of low-dimensional isotope-based compounds and quantum devices would built up to the treatment of those new electronic, transport and optical properties.

2.1 Electronic Band Structure of Bulk Samples

2.1.1 General Remarks

Before a general discussion on isotope materials science, it is helpful to have an idea of the electronic structure of bulk materials. As it is well known, the nature of materials is determined by the interaction of their valence electrons with their charged nuclei and core electrons. This determines how elements react with each other, what structure the solid prefers, its optoelectronic properties, and all other aspects of the

© Springer International Publishing AG, part of Springer Nature 2018

V. G. Plekhanov, *Introduction to Isotopic Materials Science*,
Springer Series in Materials Science 248, https://doi.org/10.1007/978-3-319-42261-9_2

material. The present paragraph describes the general method for understanding and modeling the energy bands of electronic states in solids.

The modern view of solid-state physics is based on the presentation of elementary excitations, having mass, quasi-impulse, electrical charge, and so on (see, e.g., [1]). According to this presentation, the elementary excitations of the nonmetallic materials are electrons (holes), excitons (polaritons [2]), and phonons [3]. The last one is the elementary excitations of the crystal lattice, the dynamics of which is described in harmonic approximation (see, e.g., [4]). The theory discussed below forms the basis for the modern theory of electrons in solids [5–8]. It arises from the consideration of the periodicity of the crystal structure. This periodicity leads to the formation of energy bands. An underlying assumption is that the entire electron–electron interaction can be taken into account via the independent electron approximation [7–9]. At room temperature and normal pressure, the elements from group IV in Mendeleev's table takes up the same structure as carbon in its diamond form. The cubic lattice constants are 0.543095 nm for Si, 0.56533 nm for GaAs, and 0.56611 nm or AlAs. In each case, the atoms are tetrahedrally coordinated [10].

The Schrödinger equation for the many-ion many-electron problem of a solid is exceedingly complex, but there is well- established knowledge for simplifying such an equation (see, e.g., [10, 11]). The ions are regarded as rigidly fixed at their lattice sites, and any one of the valence electrons is considered to move in a potential formed by the ions and all the other electrons, this is one-electron approximation. The effective one-electron potential $V(\boldsymbol{r})$ is periodic sharing the periodicity of the underlying lattice. If the potential has zero value everywhere in a large volume V (and infinity outside), the Schrödinger equation is

$$(-\hbar^2/2m)\nabla^2\Psi(\boldsymbol{r}) = E\Psi(\boldsymbol{r}), \tag{2.1}$$

where $\hbar = h/2\pi$ is the reduced Planck constant and m is the electron mass, with plane wave solutions

$$\Psi(\boldsymbol{r}) = \exp(i\boldsymbol{k}\boldsymbol{r})/\sqrt{\mathrm{V}} \tag{2.2}$$

and energy

$$E(\boldsymbol{k}) = \hbar^2\boldsymbol{k}^2/2m. \tag{2.3}$$

It follows that $\hbar\boldsymbol{k}$ has a dimension of momentum.

Bloch theorem [10] for a periodic one-electron potential $V(\boldsymbol{r})$ states that the eigenfunctions (Bloch functions) $\Psi_n(\boldsymbol{r})$ of the one-electron Schrödinger equation

$$\left[-(\hbar^2/2m*)\nabla^2 + V(\boldsymbol{r})\right]\Psi_n(\boldsymbol{r}) = E_n(\boldsymbol{k})\Psi_n(\boldsymbol{r}) \tag{2.4}$$

are of the form of the same plane waves exp $(i\boldsymbol{k}\boldsymbol{r})$ multiplied by another function $u_n(\boldsymbol{k},\boldsymbol{r})$ sharing the same underlying periodicity as the potential

$$\Psi_n(\boldsymbol{r}) = \exp(i\boldsymbol{k}\boldsymbol{r})u_n(\boldsymbol{k},\boldsymbol{r}), \tag{2.5}$$

where it is assumed that the function $u_n(\boldsymbol{k}, \boldsymbol{r})$ is normalized over the volume V. The relation between $\boldsymbol{k}$, a crystal momentum represented by a point in the energy first Brillouin zone, and the associated energy $E_n(\boldsymbol{k})$ is known as the energy band structure, or just the band structure, and is the starting point or describing most of the electrical and optical properties of solids.

2.1.2 Energy Band Structure

The importance of the electronic theory of solids as embodied in band theory is that it provides us with clear means of understanding how solids may be insulators, semiconductors, or metals. This depends upon whether or not it is a Fermi surface. The existence of a Fermi surface produces metallic behavior, whereas at 0 K, if the filled electron levels are separated from vacant ones, we have insulating properties. If the separation is large, say $\geq$5 eV, the substance remains an insulator at a temperature above 0K, whereas semiconducting properties arise if the filled and empty levels lie within 0–2 eV of one another. As was mentioned above, the detailed study of the electronic band structure is the key to understand the behavior of the electrons in solids, as well as their interaction with the lattice vibrations (phonons). The properties of a solid containing of the order of 10^{23} atoms/cm^3 are very complicated to predict. Several approaches to solve this problem were followed in the past providing a great amount of work in this field [7, 8]. For example, calculations of the band structure were performed using methods as $\boldsymbol{k} \cdot \boldsymbol{p}$, tight binding or LCAO, pseudopotentials, etc. (for details, see [7–10]).

Below a simple basic frame to understand the electronic properties of crystal will be presented. It is not the author's purpose to give a detailed derivation of the fundamental equations governing the band structure, but to present the main ideas to understand the physical origin of the electronic band structure, phonon dispersion relations and electron–phonon interactions, responsible, for instance, for the Raman effect (see also [4]).

Semiconductors may be pure elements like Si (Ge), but may also be compounds (like insulator LiH), for example, ZnS, CdS, SiC, Cu_2O, and GaAs. Their properties are strongly affected by the presence of impurities, defects, or departures from exact stoichiometry. The properties of a perfect crystal of a pure element or perfectly stoichiometric compound are called intrinsic properties, whereas the influences of added impurities or defects give rise to extrinsic properties.

The electronic configuration of a Si atom is $1s^2 2s^2 2p^6 3s^2 3p^2$ (see, e.g., [8]). When Si atoms form a crystal, it can divide their electrons into core electrons and valence electrons as pointed in different textbooks [9–11]. In crystalline Si 1s, 2s, and 2p orbitals are completely occupied and form the core shells. The outer 3s and 3p shells are only partially filled. Electrons in these shells are called valence electrons because they are involved in bonding with neighboring Si atoms. The crystal structure of Si at ambient pressure is similar to that of diamond. The tetrahedral arrangement of bonds between Si atoms (see, e.g., Fig. 4.18 in [10]) and its four nearest neighbors

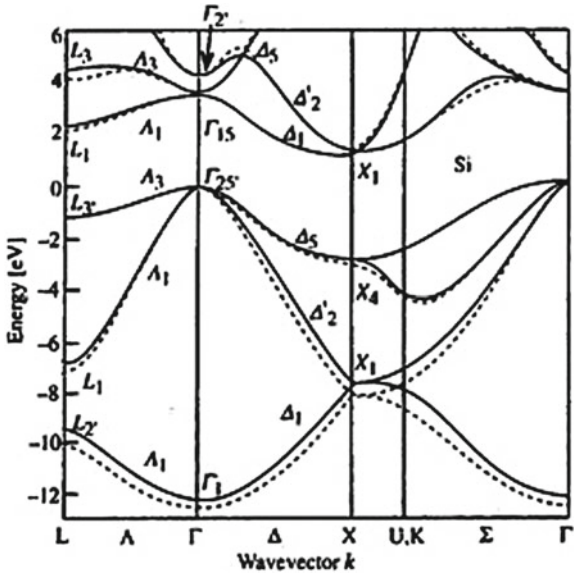

Fig. 2.1 Electronic band structure of Si calculated by pseudopotential technique. The solid and the dotted lines represent calculations with a nonlocal and a local pseudopotential, respectively (after [11])

can be understood if one of the electrons in the 3s shell is promoted to the 3p shell so that the four valence electrons form hybridized sp^3 orbitals. It is these valence electrons in the outermost shells of a Si atom that are nearly free. These electrons are not affected by the full nuclear charge as a result of screening of the nucleus by the filled core shells. In the core region, the valence electron wave functions must be orthogonal to those of the core [12–14].

Figure 2.1 shows the calculated band structure for Si in some highly symmetric directions of the Brillouin zone. As observed in this figure, the band structure of Si is indirect since the minimum transition energy is not at the zone center but in the $\Gamma \longrightarrow X$. This transition is known as an indirect gap, resulting in $\simeq$1.1 eV [11].

As we know, the crystal structure of Ge is the same as that of Si. The electronic energy band structure of Ge is, thus, essentially the same as that of Si. Ge is a very important semiconducting material used as a transistor element and also for optoelectronic device applications including extremely sensitive IR photodetectors (see, e.g., [15]). Figure 2.2 shows the electronic energy band structure of Ge obtained by Empirical Nonlocal Pseudopotential Method with including spin–orbit coupling [16]. As a result of this coupling, the irreducible representation of the electron wave function must include the effects of symmetry operations on the spin wave function. For example, a rotation by 2π will change the sign of the wave function of a spin-1/2 particle. The notation used in Fig. 2.2, including this feature, are known as the double group notations [14] and indicated in Fig. 2.3. The crystal structure of Ge is the same as that of Si. The electronic energy band structure of Ge is thus essentially the same as that of Si. However, the conduction band ordering at the Γ point of Ge Brillouin zone (BZ) is quite different from that of Si. In Si the lowest lying Γ conduction band

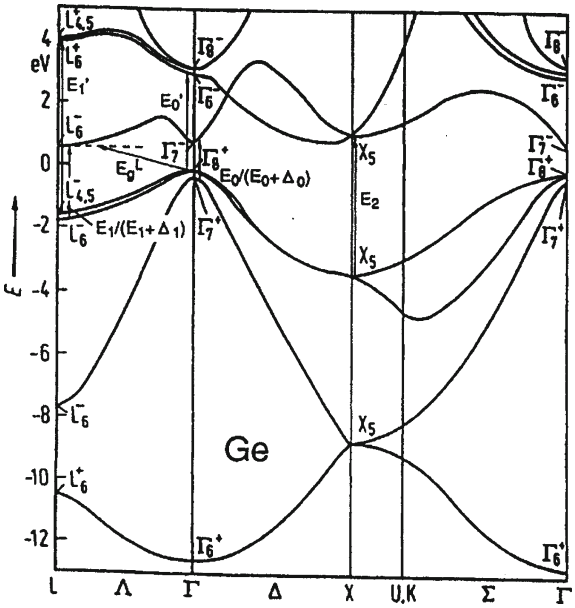

Fig. 2.2 Electronic energy band structure of Ge obtained by an ENPM by including SO interaction [16]. The locations of several interband transitions are included by the vertical arrows

is p-like Γ_{15} (Γ_6^-, Γ_8^-); however, in Ge the s-like Γ_7^- band is the lowest conduction band. Such conduction band ordering in Ge is the same as that in III-V and II-VI, zinc-blende semiconductors (i.e., these zinc-blende-type semiconductors have the s-like lowest lying and p-like second lowest lying conduction bands [11, 16]).

Considering the series of Ge, Si, GaAs, ZnSe, CuBr, for example, the 3d states of the first constituent play an increasing role in determining the band structure. In Ge, these states can be considered as localized core states (atomic energy level ≈ -30 eV). Already, however, in GaAs they have moved up in energy by 10 eV, and their hybridization with the top of the valence band affects the gap (see, e.g., [18, 19]). Proceeding further in the series, this effect becomes more important, and in CuBr and CuCl 3d states even overlap in energy with halogen p- states, with which they strongly hybridize. Therefore, we cannot exclude that the main reason for the opposite sign of the isotope effect in these compounds (see below) may be connected to the different characters of the d-electron–phonon interactions (Chap. 3) in these semiconductors.

Returning to the Ge, we should indicate that the fundamental absorption edge of Ge corresponds to the indirect transition from the highest valence band at the Γ point to the lowest conduction band at or near L (i.e., $\Gamma_8^+ \longrightarrow \mathrm{L}_6^-$ [or Λ_6^-]). As in the zinc-blende semiconductors, the lowest direct-gap transitions in Ge occur at the center of the BZ, $\Gamma_8^+ \longrightarrow \Gamma_7^-$ (E_0) and $\Gamma_7^+ \longrightarrow \Gamma_7^-$ ($E_0 + \Delta_0$). The E_1 and $E_1 + \Delta_1$ structures result from transition in the $\Lambda(L)$ direction of the BZ. The next prominent structure, $E_{2'}$, is attributed to an accidental coincidence of an M_1 saddle point at X and an M_2 saddle point in the Σ directions [11, 18]. All indicated structures are clearly

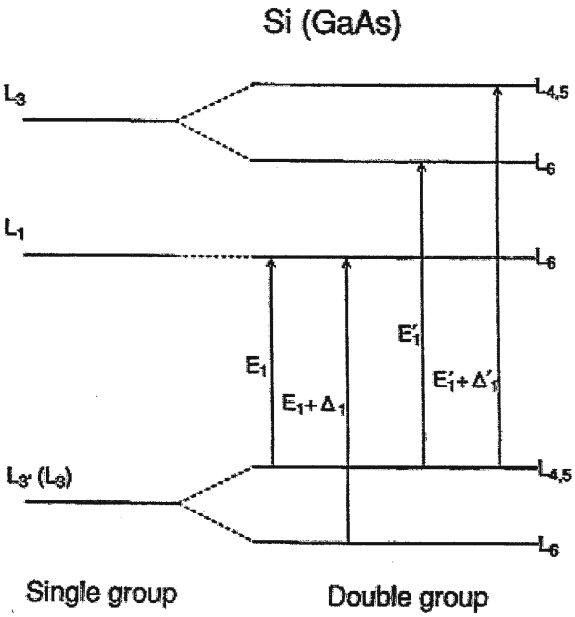

Fig. 2.3 Single and double group notations. Δ-spin –orbit coupling equals 0.035, 0.28, and 0.06 eV respectively, for Si, Ge, and C (after [17])

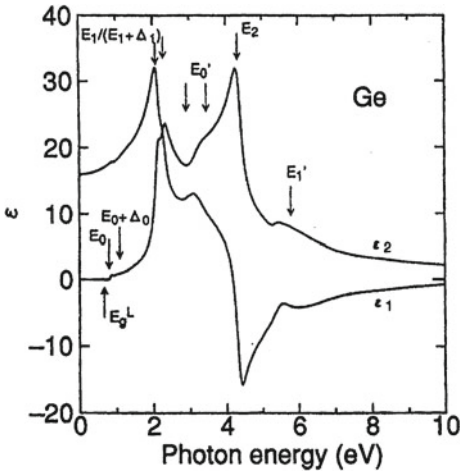

Fig. 2.4 $\varepsilon_1(E)$ and $\varepsilon_2(E)$ spectra for Ge at 300 K

shown in Fig. 2.4. The Δ_0 and Δ_1 splitting in Ge are considerably larger than those of Si, and thus their related transitions have been clearly observed experimentally. Table 2.1 summarizes the CP energies and indirect bandgap energy in Ge.

Diamond is one of the simplest and most important systems, especially in isotope effect of condensed matter. It has considerable mechanical strength; also it has high thermal conductivity and chemical stability even at several hundreds of degrees Celsius [17, 20]. Diamond has, perhaps, the simplest and most basic covalent band

Table 2.1 Energies of the indirect bandgap (E_g^L) and CPs in Ge at 300 K (after [18])

E_g^L, CPs	eV
E_g^L	0.67
E_o	0.80
$E_o + \Delta_o$	1.09
E_I	2.11
$E_I + \Delta_1$	2.30
$E_{o'}$ region	2.8–3.47
E_2	4.35
$E_{1'}$	5.8

structure. Figure 2.5 shows the electronic energy band along several lines of high symmetry from the center (Γ) to the boundary of the first BZ as calculated with modified LCAO method in paper [21]. The electronic states are labeled using the notation for the single group of the diamond structure. The location of several interband transitions is included by the vertical arrows. The fundamental absorption edge of diamond corresponds to indirect transitions from highest valence band at the Γ point to the lowest conduction band in the Δ direction (X point) (i.e., $\Gamma_{25'} \longrightarrow \Delta_1$ [X_1]). The theoretical indirect gap energy E_g^{ID} lays between 5.05 and 5.6 eV [22], which is in reasonable agreement with the experimental data: $E_g^{ID} = 5.470 \pm 0.005$ eV [20]. Like in Si, the lowest lying conduction band at Γ point of BZ in diamond, Γ_{15} is p-like, however, as we can see in Ge the s-like $\Gamma_{2'}$ band is the lowest conduction band. As mentioned in the literature (see, e.g., [20] and references therein), one common characteristic of all published spectra in the UV region of diamond is the presence of two major peaks at ~7.02–7.4 eV and ~12.2–12.7 eV. The first peak may originate from $\Gamma_{25'} \longrightarrow \Gamma_{15}$ transition (E_0') and the second one from $X_4 \longrightarrow X_1$ and $\Sigma_2 \longrightarrow \Sigma_3$ transitions (E_2) (for more detail see [20]).

The dependence of the bandgap energy on isotopic composition has already been observed for insulators and lowest (indirect–direct) gap of different semiconductors [23, 24]. It has been shown to result primarily from the effect of the average isotopic mass on the electron–phonon interaction (for details see below), with a smaller contribution from the change in lattice constant. This simplest approximation in which crystals of mixed isotopic composition are treated as crystals of identical atoms having the average isotopic mass is referred to as virtual crystal approximation (VCA). Going beyond the VCA, in isotopically mixed crystals one would also expect local fluctuations in the bandgap energy from statistical fluctuations in local isotopic composition within some effective volume, such as that of an exciton. Figure 2.6 shows the concentration dependence of the energy of interband transition E_g in isotope-mixed crystals LiH_xD_{1-x}. As can be seen from this figure, the VCA method cannot describe observed experimental results. By now, the change in E_g caused by isotopic substitution has been observed for many broad-gap and narrow-gap compounds (see

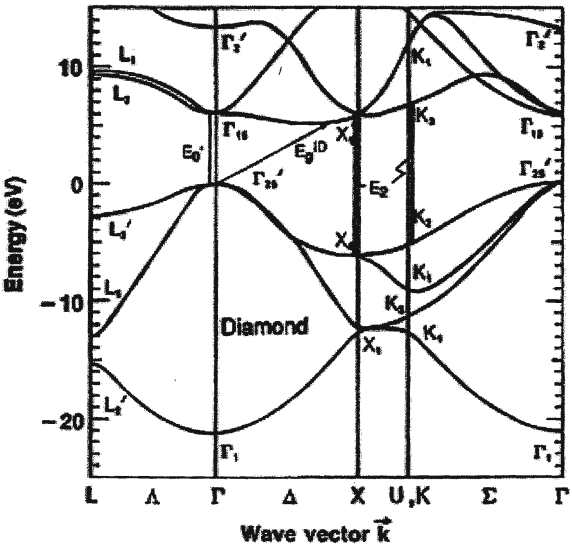

Fig. 2.5 Electronic energy band structure of diamond along several lines of high symmetry from the center (r) to the boundary of the first BZ as calculated with a modified LCAO method [21]. The locations of several interband transitions are included by the vertical arrows

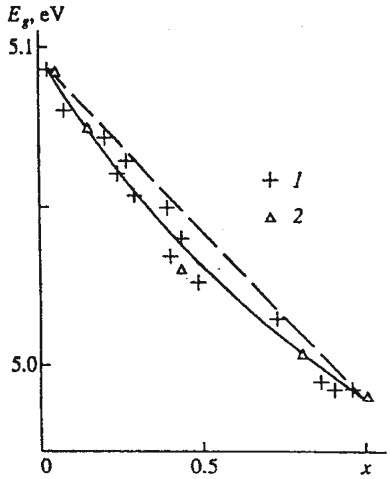

Fig. 2.6 Dependence of the interband transition energy E_g in mixed crystals LiH_xD_{1-x} on the concentration x. The straight dashed line is the linear dependence $E_g = f(x)$ in the virtual crystal model. The solid line corresponds to calculations using the polynomial of second degree. Points derived from the reflection spectra are indicated by crosses, and those from luminescence spectra are by triangles (after [25])

Table 2.2). In Table 2.2, the variation of E_g and $\partial E_g/\partial M$ are shown at the isotopic effect. We should highlight here that the most prominent isotope effect is observed in LiH crystal (see also [23]).

2.2 Density of States

One of the most fundamental properties of a material, which determines many of its properties, is its density of states. This refers to the number of states per unit energy

Table 2.2 Values of the coefficients $\partial E_g/\partial M$ (meV) and energies of the band-to-band transitions E_g (eV) (after [23])

Substance	$\partial E_g/\partial M$ (meV)	E_g (eV)
$^{13}C \longrightarrow {}^{12}C$	14.6	5.4125
$^{7}LiH \longrightarrow {}^{7}LiD$	103	4.992 $\longrightarrow$ 5.095
$^{7}LiH \longrightarrow {}^{6}LiH$	12	4.980
$CsH \longrightarrow CsD$	60	4.440
$^{30}Si \longrightarrow {}^{28}Si$	2	3.652
$^{30}Si \longrightarrow {}^{28}Si$	2.09	1.166
$^{68}ZnO \rightarrow {}^{64}ZnO$	0.372	3.400
$Zn^{18}O \rightarrow Zn^{16}O$	3.533	3.400
$^{68}ZnO \rightarrow {}^{64}ZnO$	0.40	3.400
$Zn^{18}O \rightarrow Zn^{16}O$	3.20	3.400
$^{69}GaP \longrightarrow {}^{71}GaP$	0.19	2.400
$^{65}CuCl \rightarrow {}^{63}CuCl$	−0.076	3.220
$Cu^{37}Cl \rightarrow Cu^{35}Cl$	0.364	3.220
$Cd^{34}S \rightarrow Cd^{32}S$	0.370	2.580
$^{110}CdS \rightarrow {}^{116}CdS$	0.040 ÷ 0.068	2.580
$Cu_2^{18}O \rightarrow Cu_2^{16}O$	1.116	2.151
$^{71}GaAs \rightarrow {}^{69}GaAs$	0.39	1.53
$^{76}Ge \rightarrow {}^{72}Ge$	0.225	0.74
$^{76} \rightarrow {}^{73} \rightarrow {}^{70}Ge$	0.37	0.74

in the band structure. To put this in more visual terms, if one takes a thin horizontal slice through an energy band structure diagram such as those shown in Fig. 2.7. The density of states for a complex band structure can be computed and is normally developed as part of calculations describing a different material (semiconductors, metals, and insulators). Below we will have to be content with derivation of the density of states for a model of free electron. In this case, in three dimensions, the energy is given by

$$E = \frac{\hbar^2}{2m^*}\boldsymbol{k}^2 = \frac{\hbar^2}{2m^*}(k_x^2 + k_y^2 + k_z^2), \tag{2.6}$$

where k_x, k_y, and k_z are the components of the wave vector $\boldsymbol{k}$ along the three coordinate directions and m^* is the effective electron mass. If one thinks of wave vectors as resonant states of the crystal, the longest wavelength or lowest energy state would be a half wavelength across the entire width of the crystal, L. Higher energy modes are integer multiples of this state. Therefore, the separation of states along any given direction, i, is π/L_i and the wave vector is then $k_i = n_i\pi/L_i$. For such situation, the energy can be rewritten as

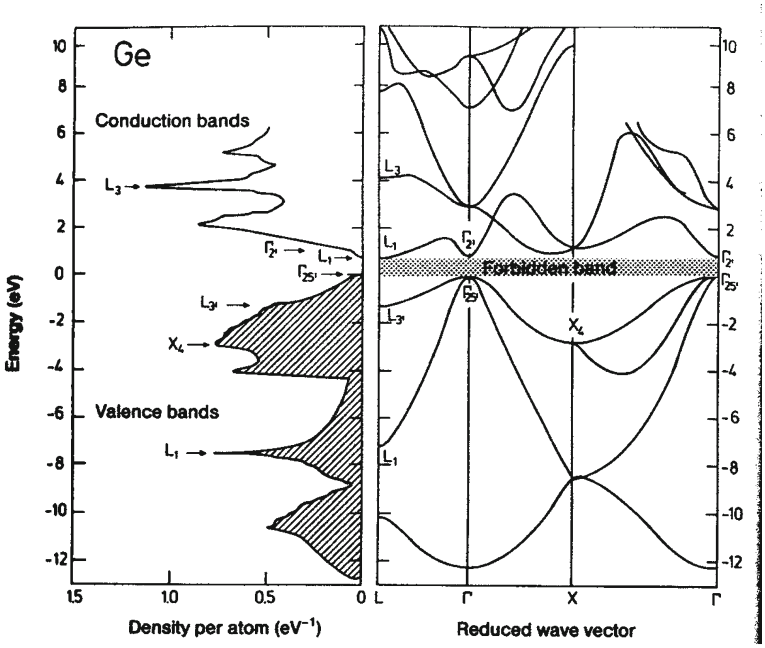

Fig. 2.7 Theoretically derived band structure $E(\boldsymbol{k})$ for germanium along the direction of high symmetry (right), and the corresponding electronic density of states (left) (after [18])

$$E = \frac{h^2}{8m^* L^2}(n_x^2 + n_y^2 + n_z^2) = k_F^2 E_0, \tag{2.7}$$

here n_x, n_y, and n_z are the indexes of the reciprocal lattice inside a sphere of radius $k_F = \sqrt{n_x^2 + n_y^2 + n_z^2}$. $E_0 = \frac{h^2}{8m^* L^2}$ is the lowest energy state of the system. The number of electrons that can be accommodated in states with energy E or less is (see, e.g., [10]):

$$N(E) = 2\left(\frac{1}{8}\right)\left(\frac{4\pi}{3}k_F^3\right) = \frac{\pi}{3}\left(\frac{E}{E_0}\right)^{3/2}. \tag{2.8}$$

In the last equation, the factor of 2 is because each state has two possible electron spins and 1/8 is because we must take only positive values of n_x, n_y, and n_z. The density of these states $g(E)$ per unit volume of reciprocal space in an energy interval dE is given by (1/V) (dN/dE), where $V = L^3$ is the crystal volume (for a cube-shaped solid), or

$$g(E) = \frac{1}{V}\frac{\mathrm{d}N}{\mathrm{d}E} = \frac{\pi}{2L^3}E_0^{-3/2}E^{1/2} = \frac{\pi}{2}\left(\frac{8\mathrm{m}^*}{h^2}\right)^{3/2} E^{1/2}. \tag{2.9}$$

This density of states will apply to any band extremum where the band can be approximated at least locally with quadratic dependence of energy on momentum

(free-electron-like model). Since all band edges will have this general behavior equation, (2.9) provides an approximate picture of the number of states per unit energy near a band edge. The importance of the density of states may be found in the calculation of the rate of any process in a solid, from scattering of an electron off a defect or another electron to absorption and emission of light. The rate of such a process is given in its most general form by Fermi Golden Rule [18]. Mathematically, the rate of a process ($\boldsymbol{H}$) moving an electron from state Ψ_i to state Ψ_f may be written in symbols as follows:

$$r_{i\longrightarrow \mathrm{f}} = \int [g(E_\mathrm{i})f(E_\mathrm{i})]\,[g(E_\mathrm{i})(1-f(E_\mathrm{i}))]\,\langle\Psi_\mathrm{i} \mid \boldsymbol{H} \mid \Psi_\mathrm{f}\rangle\delta(E_\mathrm{i}-E_\mathrm{f}+\Delta E)\mathrm{d}E_\mathrm{i}, \tag{2.10}$$

where E_i and E_f are the initial and final state energies, ΔE is the change in energy of the process, $\mathrm{g_i}$ and $\mathrm{g_f}$ are the density of states at energies E_i and E_f, $f(E_\mathrm{i})$ and $f(E_\mathrm{f})$ are the corresponding Fermi functions, and $\delta\,(E_\mathrm{i}-E_\mathrm{f}+\Delta E)$ is a Kronecker delta function which enforces conservation of energy. The expression $\langle\Psi_\mathrm{i}\,|\boldsymbol{H}|\,\Psi_\mathrm{f}\rangle$ is a mathematical function, which enforces the conservation of momentum of the electrons and other quantum mechanical selection rules in process $\boldsymbol{H}$ [26].

2.3 Effective Mass

The nearly free-electron model of solids shows that electrons are strongly affected by the lattice in which they move (the more detail see below). The interaction of the electron with a solid modified the relationship between energy and momentum. Recall that the total energy of an electron is given by the sum of kinetic and potential energies. Because the interactions of an electron with the lattice potential and the lattice spacing along a given direction vary from material to material, the change in kinetic energy with wavelength changes from one material to another. In some materials, the energy gain is small for a given momentum increase. In others, it is larger for the same added momentum. Given the classical relationship between energy and momentum, $E = \boldsymbol{p}^2/2\mathrm{m}$, the change in the proportionality constant between energy and momentum appears as a change in the effective mass of the electron. The exact form of this relationship can be developed from the above energy band relationship as follows. The energy of a free electron Bloch wave is related to the wave vector as [10]

$$E = \frac{\hbar^2\boldsymbol{k}^2}{2m^*} \tag{2.11}$$

Differentiating both sides with respect to $\boldsymbol{k}$, we have

$$\frac{\boldsymbol{k}}{m^*} = \frac{1}{\hbar^2}\frac{\mathrm{d}E}{\mathrm{d}\boldsymbol{k}} \tag{2.12}$$

and differentiating a second time,

$$\frac{1}{m^*} = \frac{1}{\hbar^2}\frac{\mathrm{d}^2 E}{\mathrm{d}\boldsymbol{k}^2}. \tag{2.13}$$

In other words, the effective mass of an electron Bloch wave is inversely related to the curvature of the $E(\boldsymbol{k})$ diagram. Strong curvatures mean small effective masses and vice versa. The effective mass is generally expressed in units of electron rest mass in a vacuum, i.e., m^*/m. Usually, the effective mass concept is only defined near a band maximum or minimum where the energy can be approximated as a quadratic function of wave vector, $\boldsymbol{k}$. Note that near minimum in energy bands, the $E(\boldsymbol{k})$ function is concave up and $1/m^* > 0$ while near a maximum, $1/m^* < 0$.

2.4 Optical Properties of Isotope-Mixed Substances

Isotopic substitution only affects the wavefunction of phonons; therefore, the energy values of electron levels in the Schrödinger equation ought to have remained the same. This, however, is not so, since isotopic substitution modifies not only the phonon spectrum, but also the constant of electron–phonon interaction (see above). It is for this reason that the energy values of purely electron transition in molecules of hydride and deuteride are found to be different [27]. This effect is even more prominent when we are dealing with a solid [28]. Intercomparison of absorption spectra for thin films of LiH and LiD at room temperature revealed that the long-wave maximum (as we know now, the exciton peak [29]) moves 64.5 meV toward the shorter wavelengths when H is replaced with D. For obvious reasons, this fundamental result could not then receive consistent and comprehensive interpretation, which does not be little its importance even today. As will be shown below, this effect becomes even more pronounced at low temperatures (see also [23]).

2.4.1 Isotope Renormalization of the Fundamental Gap's Energy

The mirror reflection spectra of mixed and pure LiD crystals cleaved in liquid helium are presented in Fig. 2.8. For comparison, in the same diagram, we have also plotted the reflection spectrum of LiH crystals with a clean surface. All spectra have been measured with the same apparatus under the same conditions. As the deuterium concentration increases, the long-wave maximum broadens and shifts toward the shorter wavelengths. As can clearly be seen in Fig. 2.8, all spectra exhibit a similar long-wave structure. This circumstance allows us to attribute this structure to the excitation of the ground (Is) and the first excited (2s) exciton states. The energy values of exciton maxima for pure and mixed crystals at 2 K are presented in Table 2.3. The binding energies of excitons E_b, calculated by the hydrogenlike formula, and the energies of interband transitions E_g are also given in Table 2.3.

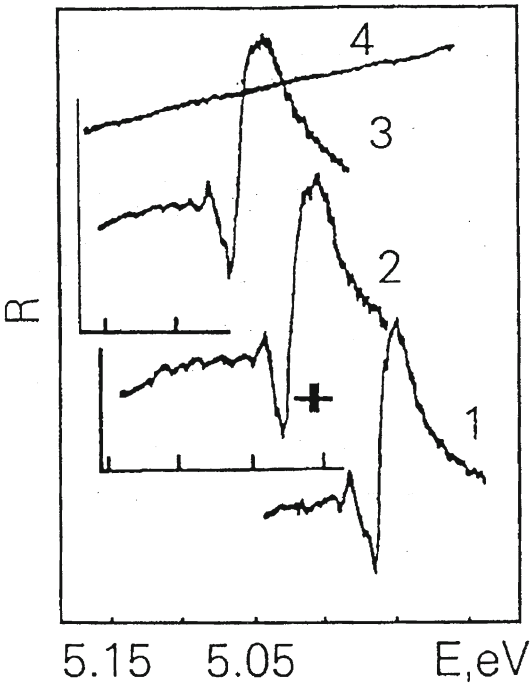

Fig. 2.8 Mirror reflection spectra of crystals: 1 - LiH; 2 - LiH_xD_{1-x}; 3 - LiD; at 4.2 K. 4 - source of light without crystal. Spectral resolution of the instrument is indicated on the diagram (after [25])

Table 2.3 Values of the energy of maxima (in meV) in exciton reflection spectra of pure and mixed crystals at 2 K, and energies of exciton binding E_b, band-to-band transitions E_g (after [30])

Energy, meV	LiH	$LiH_{0.82}D_{0.18}$	$LiH_{0.40}D_{0.60}$	LiD	^{6}LiH (78 K)
E_{1s}	4950	4967	5003	5043	4939
E_{2s}	4982	5001	5039	5082	4970
E_b	42	45	48	52	41
E_g	4992	5012	5051	5095	4980

Going back to Fig. 2.8, it is hard to miss the growth of Δ_{12}, [25], which in the hydrogenlike model causes an increase of the exciton Rydberg with the replacement of isotopes (see Fig. 90 in [23]). When hydrogen is completely replaced with deuterium, the exciton Rydberg (in the Wannier–Mott model) increases by 20% from 40 to 50 meV, whereas E_g exhibits a 2% increase, and at $2 \div 4.2$ K is $\Delta E_g = 103$ meV. This quantity depends on the temperature, and at room temperature is 73 meV, which agrees well enough with $\Delta E_g = 64.5$ meV as found in the paper of Kapustinsky et al. [29]. Isotopic substitution of the light isotope (^{32}S) by the heavy one (^{34}S) in CdS crystals [31] reduces the exciton Rydberg, which was attributed to the tentative contribution from the adjacent electron bands (see also [6, 32] and references therein),

which, however, are not present in LiH. The single-mode nature of exciton reflection spectra of mixed crystals LiH_xD_{1-x} agrees qualitatively with the results obtained with the virtual crystal model (see, e.g., Elliott et al. [33]; Onodera and Toyozawa [34]), being at the same time its extreme realization, since the difference between ionization potentials ($\Delta\zeta$) for this compound is zero (see also [35]). According to the virtual crystal model, $\Delta\zeta = 0$ implies that $\Delta E_g = 0$, which is in contradiction with the experimental results for LiH_xD_{1-x} crystals. The change in E_g caused by isotopic substitution has been observed for many broad-gap and narrow-gap semiconductor compounds (see Table 2.2). All of these results are documented in Table 2.3, where the variations of E_g, E_b are shown at the isotope affecting LiH crystals. We should highlight here that the most prominent isotope effect is observed in LiH crystals, where the dependence of $E_b = f(C_H)$ is also observed and investigated. To end this section, let us note that E_g decreases by 97 cm^{-1} when ^7Li is replaced with ^6Li.

Further, we will briefly discuss the variation of the electronic gap (E_g) of semiconducting crystals with its isotopic composition. In the last time the whole raw of semiconducting crystals were grown with isotope substitution. These crystals are diamond, copper halides, germanium, silicon, CdS, and GaAs. All numerated crystals show the dependence of the electronic gap on the isotope masses (see reviews [23, 24]).

Before we complete the analysis of these results, we should note that before these investigations, studies were carried out on the isotopic effect on exciton states for a whole range of crystals by Kreingold and coworkers (see also [36, 37]). First, the following are the classic crystals Cu_2O [37, 38] with the substitution $^{16}O \rightarrow {}^{18}O$ and $^{63}Cu \rightarrow {}^{65}Cu$. Moreover, there have been some detailed investigations of the isotopic effect on ZnO crystals, where E_g was seen to increase by 55 cm^{-1} ($^{16}O \rightarrow {}^{18}O$) and 12 cm^{-1} (at $^{64}Zn \rightarrow {}^{68}Zn$) [39, 40].

More detailed investigations of the exciton reflectance spectrum in CdS crystals were done by Zhang et al. [41]. Zhang et al. studied only the effects of Cd substitutions, and were able to explain the observed shifts in the bandgap energies, together with the overall temperature dependence of the bandgap energies in terms of a two-oscillator model provided that they interpreted the energy shifts of the bound excitons and $n = 1$ polaritons as a function of average S mass reported as was noted above, earlier by Kreingold et al. [31] as shifts in the band gap energies. However, Kreingold et al. [31] had interpreted these shifts as resulting from isotopic shifts of the free-exciton binding energies (see also [25]), and not the bandgap energies, based on their observation of different energy shifts of features which they identified as the $n = 2$ free-exciton states (for details see [31]). The observations and interpretations, according to Meyer at al. [42], presented by Kreingold et al. [31] are difficult to understand, since on the one hand a significant bandgap shift as a function of the S mass is expected [41], whereas it is difficult to understand the origin of the relatively huge change in the free-exciton binding energies which they claimed. Very recently Meyer et al. [42] reexamined the optical spectra of CdS as a function of average S mass, using samples grown with natural Cd and either natural S (~95% ^{32}S), or highly enriched (99% ^{34}S). These author observed shifts of the bound excitons and the $n = 1$ free-exciton edges consistent with those reported by Kreingold et al. [31], but, contrary to their results, Meyer et al. observed essentially identical shifts of the

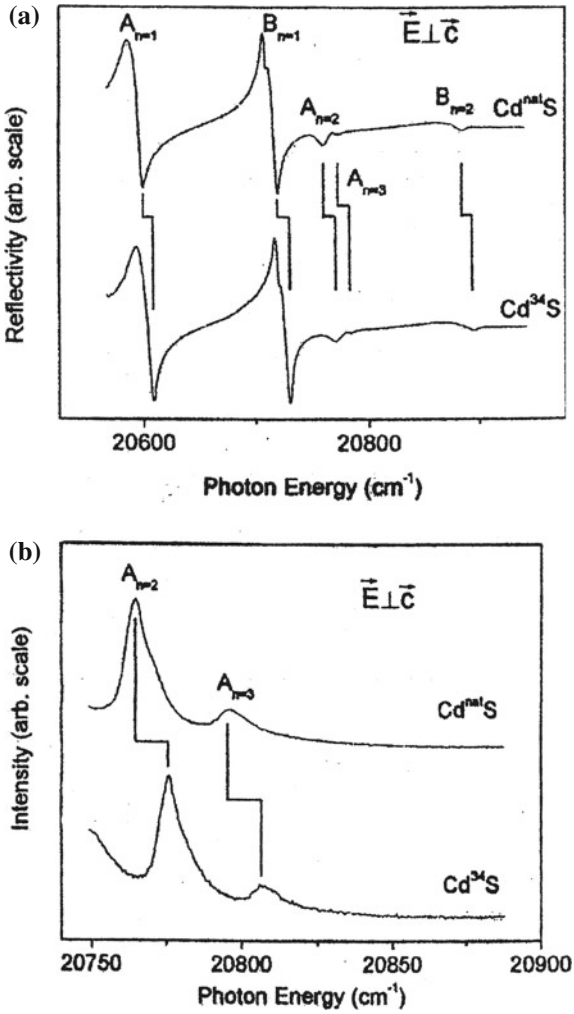

Fig. 2.9 **a** Reflection spectra in the *A* and *B* excitonic polaritons region of $Cd^{nat}S$ and $Cd^{34}S$ at 1.3K with incident light in the $\boldsymbol{E} \perp \boldsymbol{C}$. The broken vertical lines connecting peaks indicate measured energy shifts reported in Table 2.4. In this polarization, the $n = 2$ and three excited states of the *A* exciton, and the $n = 2$ excited state of the *B* exciton can be observed. **b** Polarized photoluminescence spectra in the region of the $A_{n=2}$ and $A_{n=3}$ free-exciton recombination lines of $Cd^{nat}S$ and $Cd^{34}S$ are taken at 1.3 K with the $\boldsymbol{E} \perp \boldsymbol{C}$. The broken vertical lines connecting peaks indicate measured energy shifts reported in Table 2.4 (after [42])

free-exciton-excited states, as seen in both reflection and luminescence spectroscopy. The reflectivity and photoluminescence spectra in polarized light ($\boldsymbol{E}\perp\boldsymbol{C}$) over the A and B exciton energy regions for the two samples is depicted in Fig. 2.9. For the $\boldsymbol{E}\perp\boldsymbol{C}$ polarization used in Fig. 2.9 both A and B excitons have allowed transitions, and therefore reflectivity signatures. Figure 2.9 also reveals both reflectivity signatures of the $n = 2$ and 3 states of the *A* exciton as well that of the $n = 2$ state of the B exciton.

Meyer et al. summarized the energy differences $\Delta E = E$ ($Cd^{34}S$) - E ($Cd^{nat}S$), of a large number of bound exciton and free-exciton transitions, measured using photoluminescence, absorption, and reflectivity spectroscopy, in CdS made from natural S ($Cd^{nat}S$, 95% ^{32}S) and from highly isotopically enriched ^{34}S ($Cd^{34}S$, 99% ^{34}S)

Table 2.4 The energy shifts of all of the transitions studied in [42] are given in terms of the $Cd^{34}S$ minus the $Cd^{nat}S$ energy, ΔE

Transition	Method	ΔE (cm^{-1})
I_2	PL	10.6 ± 0.1
I_2^z	PL	11.1 ± 0.1
I_2^a	PL	10.6 ± 0.1
$A_{n=1}$ (Γ_6)	A$\parallel$	10.8 ± 0.2
$A_{n=1}$ (Γ_5^L)	PL	11.0 ± 0.2
$A_{n=1}$ (Γ_5^L)	R$\perp$	10.9 ± 0.2
$A_{n=2}$	PL$\parallel$	11.3 ± 0.4
$A_{n=2}$	PL$\perp$	11.1 ± 0.4
$A_{n=2}$	R$\perp$	10.2 ± 0.5
$A_{n=3}$	PL$\parallel$	11.8 ± 1.1
$A_{n=3}$	PL$\perp$	10.9 ± 0.6
$A_{n=3}$	R$\perp$	10.7 ± 0.6
$B_{n=1}$ (Γ_1)	R$\parallel$	10.9 ± 0.3
$B_{n=1}$ ($\Gamma_5^L + \Gamma_5^T$)	R$\perp$	10.6 ± 0.4
$B_{n=2}$	R$\parallel$	9.4 ± 1.2
$B_{n=2}$	R$\perp$	9.8 ± 1.2
$C_{n=1}$ (Γ_1)	R$\parallel$	15 ± 6
$C_{n=1}$ (Γ_5)	R$\perp$	14 ± 5

(see Table 2.4). As we can see, all of the observed shifts are consistent with a single value, $10.8 \pm 0.2\,cm^{-1}$. Several of the donor bound exciton photoluminescence transitions, which in paper [42] can be measured with high accuracy, reveal shifts which differ from each other by more than the relevant uncertainties, although all agree with the $10.8 \pm 0.2\,cm^{-1}$ average shift. These small differences in the shift energies for donor bound exciton transitions may reflect a small isotopic dependence of the donor binding energy in CdS. This value of $10.8 \pm 0.2\,cm^{-1}$ shift agrees well with the value of $11.8\,cm^{-1}$ reported early by Kreingold et al. [31] for the $B_{n=1}$ transition, particularly when one takes into account the fact that enriched ^{32}S was used in that earlier study, whereas Meyer et al. have used natural S in place of an isotopically enriched $Cd^{32}S$.

The authors [42] conclude that all of the observed shifts (see Table 2.4) arise predominantly from an isotopic dependence of the bandgap energies, and that the contribution from any isotopic dependence of the free-exciton binding energies is much smaller. On the basis of the observed temperature dependencies of the excitonic transitions energies, together with a simple two-oscillator model, Zhang et al. [41] earlier calculated such a difference, predicting a shift with the S isotopic mass of 950 μeV/amu for the A exciton and 724 μeV/amu for the B exciton. Reflectivity and photoluminescence study of $^{nat}Cd^{32}S$ and $^{nat}Cd^{34}S$ performed by Kreingold et al. [31] shows that for anion isotope substitution the ground state ($n = 1$) energies of both A

and B excitons have a positive energy shifts with rate of $\partial E/\partial M_S = 740\,\mu$eV/amu. Results of Meyer et al. [42] are consistent with a shift of $\sim$710 μeV/amu for both A and B excitons. Finally, it is interesting to note that the shift of the exciton energies with Cd mass is 56 μeV/amu [41], an order of magnitude less than found for the S mass.

The present knowledge of the electronic band structure of Si stems from experimental observation of electronic transitions in transmission, reflectivity, or cyclotron resonance, on the one hand, and theoretical calculations, e.g., those based on pseudopotential or $\boldsymbol{k} \cdot \boldsymbol{p}$ methods (for details see [43–48] and references therein). In this manner, it has been established that the fundamental, indirect bandgap of Si occurs between the Γ_8^+ valence band maximum and the Δ_0 conduction band minima along (100) (see Fig. 2.1).

Recently, Lastras-Martinez et al. [44] performed ellipsometric measurements on isotopically enriched ^{28}Si and ^{30}Si and deduced the isotopic dependence of E_1 from the analysis of the data in reciprocal (Fourier inverse) space. However, these measurements did not resolve the nearly degenerate E'_0 and E_1 transitions and the isotopic shift was assigned solely to the stronger E_1 transitions (see, however, Fig. 2.10). We should add that in papers [46, 47] very recently the dependence of indirect bandgap in Si on the isotopic mass was studied. Photoluminescence and wavelength-modulated transmission spectra displaying phonon-assisted indirect excitonic transitions in isotopically enriched ^{28}Si, ^{29}Si, ^{30}Si as well as in natural Si have yielded the isotopic gap E_{gx} which equals 1213.8 ± 1.2 meV. This is purely an electronic value in the absence of electron–phonon interaction and volume changes associated with anharmonicity (for details see [47] and below).

Returning to Fig. 2.10, we can see that the spectrum contains two characteristic signatures, attributed to the excitonic transitions across the E'_0 and E_1 gaps. Isotopic dependence of the E'_0 and E_1 is displayed in Fig. 2.10, where the photomodulated reflectivity spectra of ^{28}Si, ^{29}Si, and ^{30}Si are shown for the spectral range $3.3 \leq E \leq 3.58$ eV. The E'_0 and E_1 excitonic bandgaps determined in paper [44] from the line-shape analysis. Linear least squares fit yielded the corresponding isotopic dependences $E'_0 = (3.4468 - 0.3378M^{-1/2})$ eV and $E_1 = (3.6120 - 0.6821M^{-1/2})$ eV. In conclusion, we should note that the spin–orbit interaction depends on Ge in contrast to that on Si [44].

As is well known, the fundamental energy gap in silicon, germanium, and diamond is indirect (see, e.g., [49] and Fig. 2.1). While the conduction band minima in Si and diamond are located at the Δ point along $\langle 100 \rangle$, with Δ_6 symmetry, those of germanium with L_6^+ symmetry occur at the $\langle 111 \rangle$ zone boundaries [18]. The onset of the absorption edge corresponds to optical transition from the Γ_8^+ valence band maximum to the L_6^+ conduction band minima in Ge, and the Δ_6 in Si and diamond; for wave vector conservation, these indirect transitions require the emission or absorption of the relevant phonons. In Si and C, transverse acoustic (TA), longitudinal acoustic (LA), transverse optic (TO), or longitudinal optic (LO) phonons of Δ symmetry must be simultaneously emitted or absorbed. In Ge (see also above), the wave vector conserving phonons are TA, LA, TO, or LO phonons with L symmetry. At low temperatures, these indirect transitions are assisted by phonon emission.

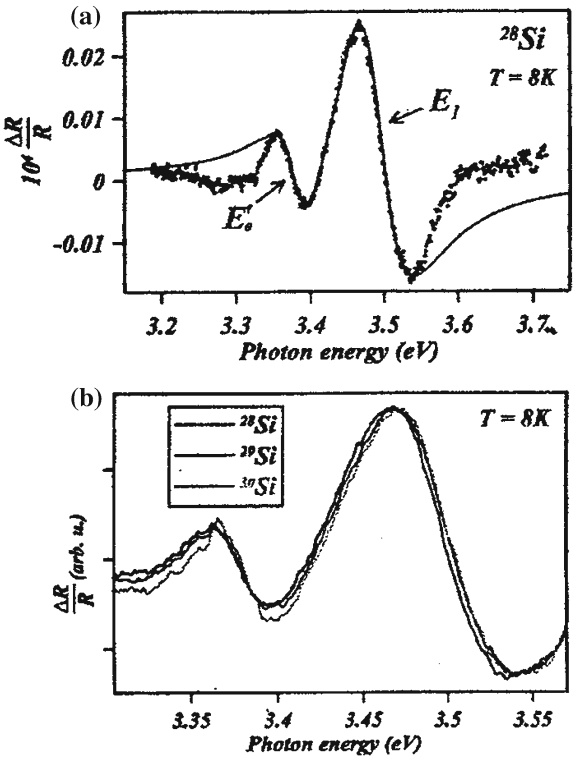

Fig. 2.10 **a** Signatures of the E_0' and E_1 excitonic bandgaps of ^{28}Si observed (dots) in photomodulated reflectivity. The solid line is a theoretical fit using the excitonic line shape. **b** Photomodulated reflectivity spectra of isotopically enriched Si exhibiting isotopic shifts of the E_0' and E_1 gaps (after [44])

In this case, we should expect at low temperatures four excitonic derivative signatures at photon energies $E_{gx} + \hbar\omega_{q,j}$ in modulated transmission experiments and in photoluminescence at the photon energies $E_{gx} - \hbar\omega_{q,j}$. Here, E_{gx} is the excitonic bandgap and j corresponds to a wave vector preserving phonon. In Fig. 2.11a, the photoluminescence and wavelength-modulated spectra of ^{30}Si (M = 2.81 amu) are displayed; the labels $n = 1$ and 2 designate the ground and the first excited states of the indirect TA and TO excitons. From the energies of the photoluminescence and wavelength-modulated excitonic signatures in all isotopic specimens (see [46]) the cited authors deduce E_{gx} as well as the energies of the participating TO, LO, and TA phonons, shown in Fig. 2.11b as a function of $M^{-1/2}$. The excitonic band gap data are fitted well with expression $E_{gx}(M) = E_{gx}(\infty) - CM^{-1/2}$, yielding $E_{gx}(\infty) = (1213.8 \pm 1.2)$ meV and $C = (313.7 \pm 5.3)$ meV/amu. A linear fit in M can be made over a small range of available masses (see Fig. 2.11b) with a slope $(\partial E_{gx}/\partial M)_{P,T} 1.01 \pm 0.04$ meV/amu, which agrees with the results of bound exciton photoluminescence of Karaiskaj et al. [45]. The experiments in papers [46, 47] also indicate that separation of the $n = 2$ and $n = 1$ excitons is isotope mass independent, implying, according to these authors, the excitonic binding energy is independent of isotope mass within the experimental error. In concluding this part, we should note that recent high-resolution spectroscopic studies of excitonic and impurity transition

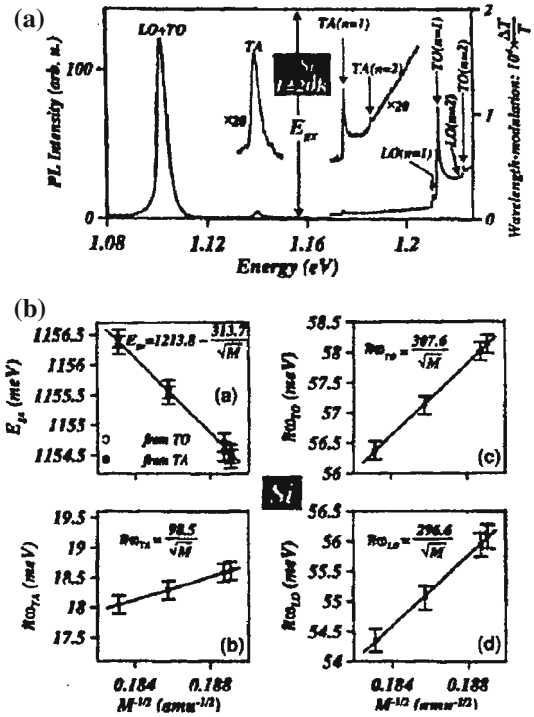

Fig. 2.11 a Photoluminescence (PL) and wavelength-modulated transmission (WMT) spectra of isotopically enriched ^{30}Si recorded at 20 K; **b** The excitonic indirect bandgap and the associated phonon energies as a function of M (after [46])

in high-quality samples of isotopically enriched Si have discovered the broadening of bound exciton emission (absorption) lines connected with isotope-induced disorder as well as the dependence of their binding energy on the isotope mass [44, 49]. The last effect was observed early on the bound excitons in diamond [45, 46], and earlier on the free excitons [50] in LiH_xD_{1-x} mixed crystals (see also [51] and references therein).

2.4.2 Exciton Emission Spectra

Because of the low intensity of scattered light, and thanks to the high resolution of modern spectroscopic instruments, the development of highly sensitive techniques for the detection of weak optical signals (photon counting mode, optical multichannel analyzers, optical linear arrays, and other specialized systems), the luminescence method has become one of the most common and useful techniques for studying excitons dynamics in dielectrics and semiconductors. While the structure of spectra of fundamental reflection (absorption) depends on the internal degrees of freedom of Wannier–Mott excitons, the structure and shape of the luminescence spectrum are determined primarily by its external degrees of freedom. The latter are associated with the translational motion of large-radius excitons as a whole, with translational

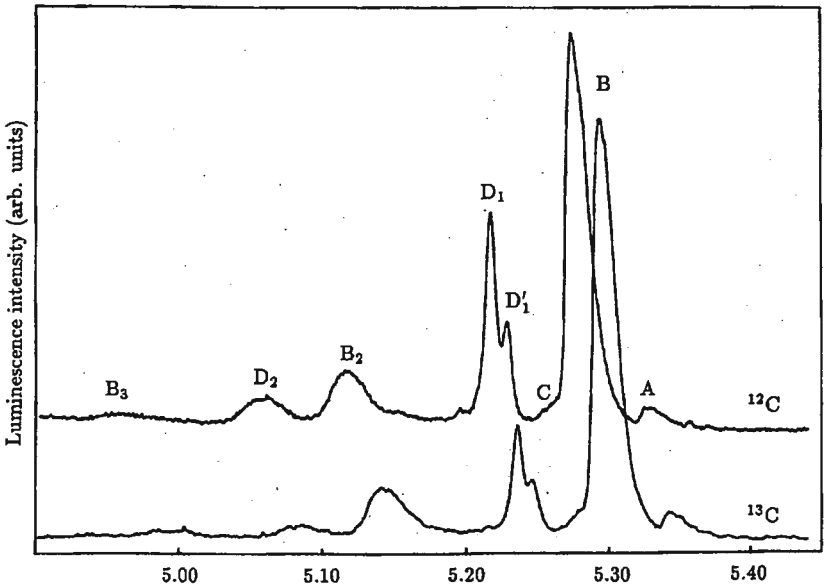

Fig. 2.12 Spectra measured at 77 K of the phonon-assisted free-exciton cathodoluminescence feature (A, B, and C) and the phonon-assisted bound exciton features (D) from a natural semiconducting ^{12}C diamond and a ^{13}C synthetic diamond (after [53])

mass $m = m_c + m_v$ [52]. There have been several studies indicating large isotope effects and/or bandgap renormalization of diamond [23, 53–56]. Pioneering research focusing on isotope composition-controlled diamond was performed by Collins et al. in 1990 [53]. In the next part, we will follow their paper. The change of the indirect gap of diamond between pure ^{12}C and ^{13}C has been determined by Collins et al. [53], using for this purpose the luminescence spectra of diamond. The luminescence spectra of the natural (^{12}C) and synthetic (^{13}C) diamond were investigated by many authors at the present time. Figure 2.12 compares the edge luminescence for a natural diamond with that for a synthetic diamond. The peaks labeled A, B, and C are due, respectively, to the recombination of a free exciton with the emission of transverse acoustic, transverse optic, and longitudinal optic phonons having wavevector $\pm k_{\min}$ (see Fig. 2.5) and quanta (in ^{12}C diamond) [57, 58]:

$$\hbar\omega_{TA} = 87 \pm 2, \quad \hbar\omega_{TO} = 141 \pm 2, \quad \hbar\omega_{LO} = 163 \pm 1\,\text{meV}. \tag{2.14}$$

Features B_2 and B_3 are further free-exciton processes involving the above TO phonon with one and two zone-center optic phonons, respectively (see also [59]).

Boron forms an effective masslike acceptor in diamond, and both the specimens used in Fig. 2.12 are slightly semiconducting with uncompensated boron concentrations around $5 \cdot 10^{16}\,\text{cm}^{-3}$ in the natural diamond and $3 \cdot 10^{16}\,\text{cm}^{-3}$ in the synthetic diamond. Peaks labeled D are associated with the decay of excitons bound to the

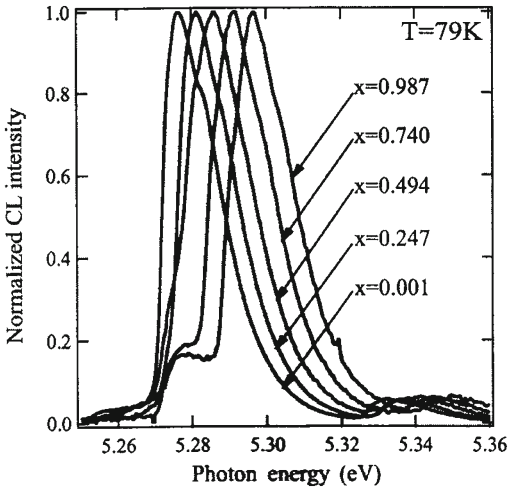

Fig. 2.13 Luminescence spectra of free excitons in homoepitaxial diamond films grown from a mixture of methane in hydrogen by means of a microwave plasma-assisted CVD. The spectra illustrate the effects of isotope composition $^{12}C^{13}_{1-x}C_x$ ($x = 0.001, 0.247, 0.494, 0.740$, and 0.987) mixed in the CVD gas phase. All spectra are normalized to the same height (after [56])

boron acceptors (for details see [53]). Comparison of the data from the two diamonds shows that the zero-phonon lines D_0 and D_0^t are 14 ± 0.7 meV higher for ^{13}C than for ^{12}C diamond, and that the LO and TO phonon energies are lower by a factor of 0.96, equal within experimental error to the factor $(12/13)^{1/2}$ expected for first order when the lattice is changed from ^{12}C to ^{13}C. The low-energy thresholds of the free-exciton peaks A, B and C are given by [57]

$$E_{\mathrm{th}}(A) = E_{\mathrm{gx}} - \hbar\omega_{\mathrm{TA}}; \quad E_{\mathrm{th}}(B) = E_{\mathrm{gx}} - \hbar\omega_{\mathrm{TO}} \quad \text{and} \quad E_{\mathrm{th}}(C) = E_{\mathrm{gx}} - \hbar\omega_{\mathrm{LO}}. \tag{2.15}$$

As was shown by Collins et al., the predicted thresholds are entirely consistent with the experimental data. From the results of Collins et al., it was concluded that the dominant contribution arises from electron–phonon coupling, and that there is a smaller contribution due to a change in the volume of the unit cell produced by changing the isotope. These two terms were calculated as 13.5 ± 2.0 and 3.0 ± 1.3 meV, respectively. The more detailed and quantitative investigations of $E_g \sim f(x)$, where x is the isotope concentration, were done by Watanabe et al. [56], where five samples of very pure diamond with different concentrations was studied x (Fig. 2.13). From these data, Ruf et al. determined the linear variation of $E_g \sim f(x)$ for diamond. Linear fits the experimental data of Watanabe et al., (solid line in Fig. 2.14) yield a slope of 15.4 ± 0.5 meV/amu, close to the theoretical predictions and earlier observation [23, 36].

In semiconductor applications [60], superlattice architectures (periodic layers of materials with different bandgap) play an important role in creating quantum wells. These low-dimensional structures can exhibit high electron and hole mobilities, and they can be used to tune the emission properties of light-emitting diodes and lasers, to realize optical gratings for dielectric resonator structures, or simply to confine electrons and holes in well-defined heterojunction devices [55]. In 2009, diamond

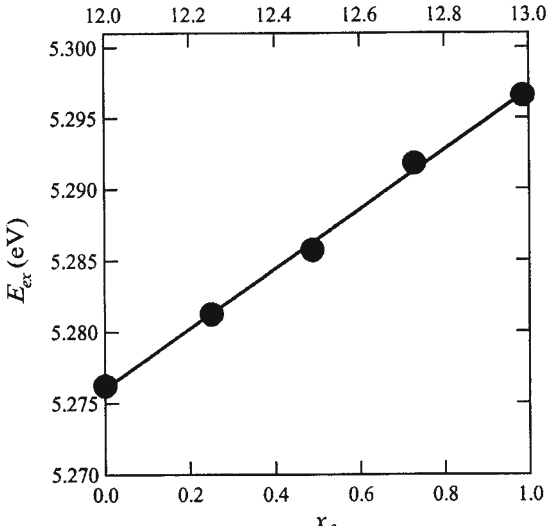

Fig. 2.14 Excitonic bandgap energy E_{ex} obtained for the CL peak energies in Fig. 2.13 as a function of the ^{13}C concentration of the films (x_f). The actual ^{13}C content of the films was calculated from the peak position of the first-order Raman spectrum. The solid line is a linear regression fit of the data (after [56])

superlattice structures composed of isotopically pure ^{12}C and ^{13}C layers were synthesized for the first time and confirmed to exhibit carrier confinement due to the isotope effect on the bandgap of diamond [61]. These isotope-based superlattice structures offer entirely new directions in diamond research, including use for realizing a high-mobility two-dimensional carrier gas, for exciton confinement (see also [62]), for folding of phonon dispersion branches, and for spatially controlling nuclear spins, which should be of great importance in quantum computing applications [63]. For the application of an isotope diamond superlattice through electronic bandgap engineering, an important factor to be clarified is the total amount of change in bandgap energy due to isotope effect (for details see, please, the chapter devoted the low-dimensional devices).

The results on the luminescence of LiH_xD_{1-x} ($0 \leq x \leq$) crystals presented below were obtained from the clean surface of crystals cleaved directly under superfluid helium [64] in the cell of an optical cryostat. The effects of surface states on optical spectra (including the luminescence spectra) of excitons in hygroscopic LiH and LiD crystals were briefly described in paper [65].

As demonstrated earlier [66], most low-energy electron excitations in LiH crystals are the large-radius excitons. Exciton luminescence is observed when LiH crystals are excited in the midst of fundamental absorption. The spectrum of exciton photoluminescence of crystals of lithium hydride cleaved in liquid helium consists of a narrow (in the best crystals, its half-width is $E \leq 10$ meV [64]) phononless emission line and its broader phonon repetitions, which arise due to radiative annihilation of excitons with the production of 1–5 longitudinal phonons (LO) (Fig. 2.15). The phononless emission line coincides in an almost resonant way with the reflection line of the exciton ground state [30], which is another indication of direct electron transition. The lines of phonon replicas form an equidistant series biased toward the lower

energies from the resonance emission line of excitons. The energy difference between these lines, as in [67] is about 140 meV, which is close to the calculated energy of LO phonon in the middle of the Brillouin zone [68] and measured in the paper by Plekhanov [28]. The most important distinctions between the exciton luminescence spectrum shown in Fig. 2.15 and those measured earlier ([23] and references therein) are the following: (a) the presence of a second series of LO repetitions counted from the level of the $n = 2s$ exciton state; (b) comparable intensities of the phononless emission line and its 2LO replica, (c) noticeable narrowing of the observed lines [65]. Here, we also ought to mention an overall increase in the intensity over the entire luminescence spectrum. Evidently, the intensity of phononless emission line of free excitons increases because the rate of emissionless recombination on the pure surface Fig. 2.15 decreases. This seems natural for the surface of specimen cleaved in liquid helium because the surface states (as a rule, of extrinsic origin [66]) and their electric fields (recall that the value of the exciton Rydberg is relatively low, $E_b = 40$ meV) (see above) lead not only to broadening of the luminescence lines, but also to quenching of their intensity, and first of all, quenching of the intensity of the zero-phonon line. Figure 2.16 shows the luminescence spectra of LiH and LiD crystals, cleaved and measured at 2 K. A more or less pronounced short-wave singularity of the phononless line is displayed by practically all crystals with clean surface [23]. The luminescence spectrum of LiD crystals shown in Fig. 2.16 is much more similar to the spectrum of intrinsic luminescence of LiH crystals (see Fig. 2.15). There are, however, some distinctions: one is related to the unequal intensities of the phononless line (or, more precisely, of its long-wave component) and its 2LO repetition, whereas these intensities in LiH are practically the same. Another distinction is the clearly visible double nature of the phononless emission line of free excitons in LiD crystals even at a low temperature. On top of that, the magnitude of longitudinal-transverse splitting for LiD is greater than for LiH, and constitutes 25 ± 2 meV. A pronounced doublet structure of the phononless emission line with magnitude of $\Delta_{LT} = 18 \pm 2$ meV for LiH crystal is observed at an elevated temperature (Fig. 2.15). This value of Δ_{LT} is somewhat larger than the magnitude of splitting observed early with LiH crystal cleaved in a jet of hot air. This behavior of Δ_{LT} also agrees with the results of Lester et al. [69], where the surface quality was demonstrated to dramatically affect not only the structure but also the intensity of polariton luminescence. The measured value of $\Delta_{LT} = 18$ meV for LiH crystals fit well with the magnitude of splitting observed in the reflection (see above). The doublet structure of the phononless emission line under consideration can be interpreted with the aid of the polariton dispersion curve (for more details see [23]). We see that the experimental material presented in this section gives convincing evidence of manifestation of the isotope effect on the exciton luminescence spectra of LiH_xD_{1-z} crystals (see also [66]). The more detailed investigation of the low- temperature optical spectra (luminescence and light scattering) of LiH and LiD crystals [32] allow to conclude that the origin of the isotope effect is carried out by the strong (nuclear) interaction.

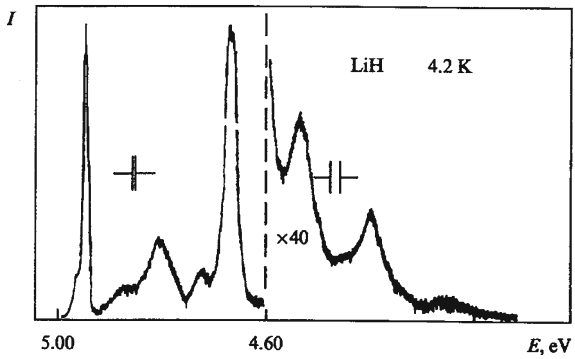

Fig. 2.15 Emission spectra of free excitons at 2 K in LiH crystals cleaved in liquid helium. Spectral resolution of instrument indicated in diagram (after [25])

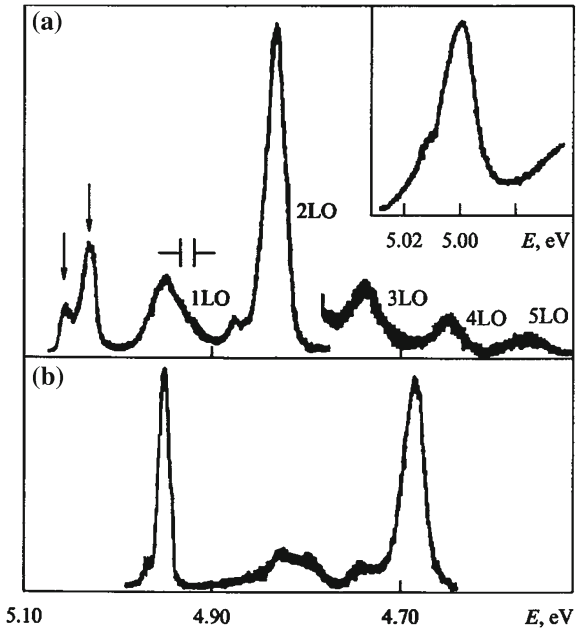

Fig. 2.16 Luminescence spectra of (1) LiH and (2) LiD crystals cleaved and measured at 2 K. The insets show the zero-phonon emission line of free excitons in a mixed crystal at 78 K (after [25])

2.5 Electron Excitations in Low-Dimensional Structures

2.5.1 Wavelike Properties of Electrons

In classical physics, we deal with two kinds of entities: particles, such as a small mass which obeys Newtonian's equations, and waves as, for example, electromagnetic waves which behave according to Maxwell's equations. Moreover, classical physical models assume the continuity of quantities and involve no restrictions concerning very small physical structures. The quantum theory shows, however, that values of some measurable variables of a system, can attain only certain discrete meanings.

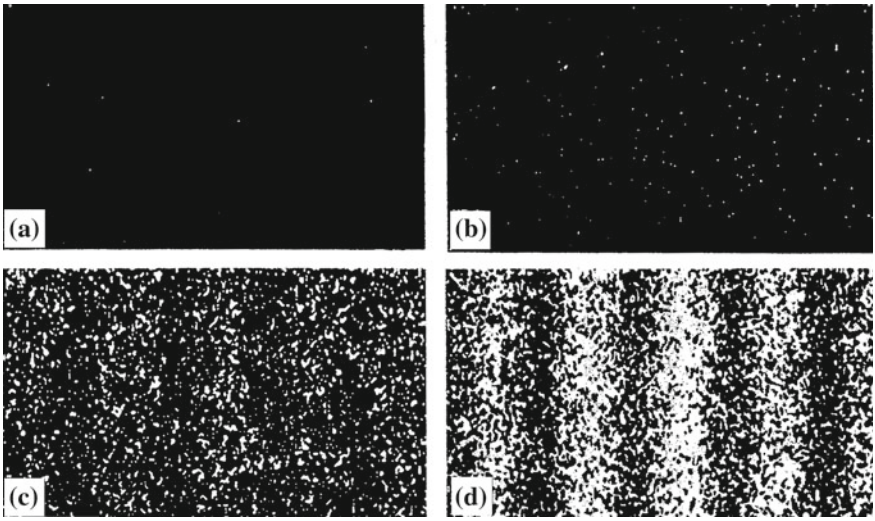

Fig. 2.17 Observing the wavelike properties of the electrons in the double-slit experiment (after [70]). The pictures **a**–**c** have been taken at various times: pictures on the monitor after **a** 10 electrons, **b** 200 electrons, **c** 6,000 electrons, and **d** 140,000 electrons. Electrons were emitted at a rate of 10 per second. (after A. Tonomura, 2006, Double-slit experiment (http://hqrd.hitachi.co.jp/globaldoubleslit.cfm))

Therefore, in dealing with very small objects, like atoms, the above classification (particles and waves) is not enough to describe their behavior, and we have to turn to quantum mechanics, and to the dual concept of wave particle. For instance, if light interacts with a material, it is better to think of it as being constituted by particles called photons instead of waves. On the other hand, electrons which have the primary concept of particle, behave like waves, when they move inside a solid of nanometric dimensions.

The electron's waves were described in more detail in paper [70]. The beautiful photograph in Fig. 2.17 clearly shows the wave–particle dualism of the electron by means of the accumulation of many single shots, corresponding to independent electrons, in an interferometry experiment performed by A. Tonomura (for details see [70]).

We start with a well-known optical example, which will help us to overcome the gap between classical waves extending over space and discrete particles having certain coordinates. Visible light behaves as an electromagnetic wave exhibiting interference, diffraction, etc. (see, e.g., [20]). On the other hand, we often see light as a light ray, which can propagate, be reflected, and be deflected. The trajectory of such a light ray is very similar to a particle trajectory. The class of optical effects or which light can be described in terms of rays constitutes the discipline of geometrical optics. The transition from wave optics to geometrical optics is justified if the wavelength of light λ is much smaller than the characteristic scales of the problem being considered:

$\lambda \ll L$, where L can be a distance of light propagation, the size of an illuminated object, a scale of inhomogeneity of the medium, etc. Traveling wave can be presented in the following form:

$$\boldsymbol{F} = Ae^{\mathrm{i}\phi}. \tag{2.16}$$

or for monochromatic light (light of a single frequency) we can write

$$\phi = \phi_0 - \omega t. \tag{2.17}$$

Here, ϕ_0 depends on $\boldsymbol{r}$. Further, we can introduce the wavevector in the form $\boldsymbol{q} = \partial\phi/\partial\boldsymbol{r} = \partial\phi_0/\partial\boldsymbol{r}$. In inhomogeneous medium, the wavevector and the wave amplitude depend on the coordinate $\boldsymbol{r} : \boldsymbol{q} = \boldsymbol{q}(\boldsymbol{r})$; $A = A(\boldsymbol{r})$. On the substituting the chosen waveform (2.16) into wave equation, we obtain

$$-\omega^2 Ae^{\mathrm{i}\phi} - \frac{c^2}{\varepsilon(\boldsymbol{r})}\left(\frac{\partial^2 A}{\partial x^2}e^{\mathrm{i}\phi} + 2i\frac{\partial A}{\partial x}\frac{\partial\phi_0}{\partial x}e^{\mathrm{i}\phi} - A\left[\frac{\partial\phi_0}{\partial x}\right]^2 e^{\mathrm{i}\phi} + \cdots\right) = 0, \tag{2.18}$$

where $c \longrightarrow c/\sqrt{\varepsilon}$ and ε is the dielectric constant of the medium. In (2.18), for simplicity, we have written only the derivatives with respect to the x-coordinate. Within the geometrical-optics approximation, both contributions to the phase are large: ωt, $|\phi_0| \gg 1$. After small algebra, we obtain an equation for ϕ_0 as follows:

$$\left(\frac{\partial\phi_0}{\partial x}\right)^2 = \omega^2\frac{\varepsilon(\boldsymbol{r})}{c^2}. \tag{2.19}$$

In the simplest case of a homogeneous medium, where ε does not depend on the coordinate, we obtain a trivial result: $\boldsymbol{q} =$ constant, i.e., the ray propagate along a straight path.

Further, we consider briefly basic concepts related to wave fields. According to quantum mechanics, electromagnetic waves interacting with matter can be emitted and absorbed in discrete energy portions (quanta [72–74]—photons). The energy of a photon, E, is proportional to the frequency of the wave

$$E = \hbar\omega, \tag{2.20}$$

where $\hbar = 1.06 \cdot 10^{-34}$ Js is the so-called reduced Planck constant. Each photon, like particle, has a momentum

$$\boldsymbol{p} = \hbar\boldsymbol{q}, \tag{2.21}$$

where $\boldsymbol{q}$ is the wavevector. Equation (2.21) is formulated for photons in free space. Apparently, the direction of the momentum vector $\boldsymbol{p}$ coincides with the direction of propagation of the wave. Equation (2.20), which represents the energy of a quantum of light, may be readily generalized or electromagnetic waves in a dielectric medium with dielectric constant ε:

$$\hbar\omega = \frac{\hbar c}{\sqrt{\varepsilon}} q. \tag{2.22}$$

It is very important that different quanta of an electromagnetic field do not interact with each other, as is reflected by the linear character of the field in free space. An interaction between these modes is possible only in special media—nonlinear optical media.

Our discussion about the relationship between electromagnetic waves and the photons provides an example of the wave–particle duality that is ubiquitous in quantum physics [72–74]. The other example of the wave–particle duality is an electron.

In 1924 deBroglie assumed, to every particle of momentum p, a wave of wavelength

$$\lambda = \frac{\hbar}{p}, \tag{2.23}$$

where as usually $\hbar$ is a Planck's constant ($\hbar = \frac{h}{2\pi}$) and

$$p = \frac{\hbar}{\lambda} = \frac{h}{2\pi} \cdot \frac{2\pi}{\lambda} = \hbar k. \tag{2.24}$$

In (2.24), k is the so-called wave number. According quantum mechanics, the electron is described by successive quantum-mechanical states, which represent a certain probability that the particle may be located in a specific spatial region [62].

Another important relation in quantum mechanics [72–74] that derives heuristically from the model described above is Heisenberg's uncertainty principle: in any experiment, the products of the uncertainties, of the particle momentum Δp_x and its coordinate Δx must be larger than $\hbar/2$, i.e.,

$$\Delta p_x \cdot \Delta x \geq \hbar/2. \tag{2.25}$$

There are, of course, corresponding relations for $\Delta p_y \cdot \Delta y$, and $\Delta p_z \cdot \Delta z$. It is important to remark that this indeterminacy principle is inherent to nature, and has nothing to do with errors in instruments that would measure p_x and x simultaneously. The second part of this principle is related to the accuracy in the measurement of the energy and the time interval Δt required for the measurement, establishing

$$\Delta E \Delta t \geq \hbar/2. \tag{2.26}$$

So, uncertainty principle denotes that the location or the momentum of a particle, and its energy or its time of observation can only be determined imprecisely. This statement is very important as we are considering nanoelectronic applications, because the dimensions of such devices are so small that we can use the uncertainty principle to roughly estimate the relevant nanoelectronic effects, for example, the tunneling effect. In the following sections some important nanoelectronic structures will be discussed. Thereby, it is inevitable to apply the wave model of matter to describe

the behavior of the electrons involved. The upcoming example of the potential well shows that is not possible to correctly determine the behavior of an electron in such configuration by using the classical particle model. Present-day interpretation of the wave function in quantum mechanics suggests the introduction of the term information. The information delivered by a measuring process is inversely proportional to the probability of localizing a particle in the observation space [70, 75]. Although this relation to information theory is interesting, the concept was not generally adopted by physicists.

2.5.2 Dimensionality and Density of States

As everyone knows from solid-state physics, most physical properties significantly depend on the density of states(DOS) function S. The DOS function, at a given value E of energy, is defined such that S(E) ΔE is equal to the number of states (i.e., solution of Schrödinger equation) in the interval energy ΔE around E (see, e.g., [76]). We also all know that if the dimensions of L_{i} ($i = x, y, z$) are macroscopic and if proper boundary condition is chosen, the energy levels can be treated as a quasi- continuous [23]. On the other hand, in the case where any dimensions of L_{i} gets small enough, the DOS function becomes discontinuous. Let us next obtain the DOS function for several low-dimensional solids (see also [76, 77]). Quantum effects arise in systems which confine electrons to regions comparable to their de Broglie wavelength. When such confinement is in one dimension only (say, by a restriction on the motion of the electronic the z-direction), with free motion in the x- and y-directions, a "two-dimensional electron gas" (2 DEG) is created. Confinement in two directions (y- and z-, say), with free motion in x-direction, gives a "one-dimensional electron gas" (1 DEG) and confinement of its x-, y -, and z-motions at once gives a "zero-dimensional electron gas" (0 DEG). In this paragraph, we consider the description of ideal electron gases in these cases, i.e., electron gases in which there is no motion in the confining direction and where we neglect interactions between the electrons.

Every textbook on the quantum mechanics considers that an unconfined electron in free space is described by the Schrödinger equation [77–81]

$$-\frac{\hbar^2}{2m}\nabla^2\varphi = -\frac{\hbar^2}{2m}\left(\frac{\partial^2\varphi}{\partial x^2} + \frac{\partial^2\varphi}{\partial y^2} + \frac{\partial^2\varphi}{\partial z^2}\right) = E\varphi, \tag{2.27}$$

where m is the free-electron mass. The solutions of this equation [72, 76]

$$\varphi_{\mathrm{k}}(\boldsymbol{r}) = \frac{1}{(2\pi)^3}e^{\mathrm{i}\boldsymbol{k}\boldsymbol{r}} \tag{2.28}$$

are plane waves labeled by the wavevector

$$\boldsymbol{k} = \left(k_x, k_y, k_z\right) \tag{2.29}$$

and correspond to the energy

$$E = \frac{\hbar^2 k^2}{2m} = \frac{\hbar^2}{2m}\left(k_x^2 + k_y^2 + k_z^2\right). \tag{2.30}$$

The vector components of $\boldsymbol{k}$ are the quantum numbers for the free motion of the electron, one for each of the classical degree of freedom.

The number of states in a volume $\mathrm{d}\boldsymbol{k} = (\mathrm{d}k_x \cdot \mathrm{d}k_y \cdot \mathrm{d}k_z)$ of $\boldsymbol{k}$-space is

$$g\left(\boldsymbol{k}\right) d\boldsymbol{k} = \frac{2}{(2\pi)^3} d\boldsymbol{k} \tag{2.31}$$

with the factor of 2 accounting for the spin degeneracy of the electrons. To express this density of states in terms of energy states, we use the act that the energy dispersion (2.30) depends only on the magnitude of $\boldsymbol{k}$. Thus, by using spherical polar coordinates (see, e.g., [8]) in $\boldsymbol{k}$-space,

$$\mathrm{d}\boldsymbol{k} = \boldsymbol{k}^2 \sin\theta dk d\theta d\phi, \tag{2.32}$$

where the variables have their usual ranges ($0 \leq \boldsymbol{k} \leq \infty$, $0 \leq \phi \leq 2\pi$, and $0 \leq \theta \leq \pi$) and integrating over the polar and azimutal angles, we are let with an expression that depends only on the magnitude $\boldsymbol{k}$:

$$g(\boldsymbol{k})\mathrm{d}\boldsymbol{k} = \frac{2}{(2\pi)^3}\mathrm{d}\boldsymbol{k} = \frac{1}{\pi^2}\boldsymbol{k}^2\mathrm{d}\boldsymbol{k}. \tag{2.33}$$

By invoking (2.30), we can perform a change of variables to cast the right-hand side of this equation into a form involving the differential of the energy:

$$\frac{1}{\pi^2}\boldsymbol{k}^2\mathrm{d}\boldsymbol{k} = \frac{1}{\pi^2}\left(\frac{2mE}{\hbar^2}\right)\frac{\mathrm{d}\boldsymbol{k}}{\mathrm{d}E}\mathrm{d}E = \frac{1}{\pi^2}\left(\frac{2m}{\hbar^2}\right)^{3/2}\sqrt{E}\mathrm{d}E. \tag{2.34}$$

From this equation, we deduce the well-known density of states $g(E)$ of a free-electron gas in three dimensions

$$g(E) = \frac{1}{2\pi^2}\left(\frac{2m}{\hbar^2}\right)^{3/2}\sqrt{E}. \tag{2.35}$$

Notice the characteristic square-root dependence on the energy (see Fig. 2.18). This results from the fact that, in three dimensions, the surfaces of constant energy in $\boldsymbol{k}$ space are spheres of radius $\sqrt{2mE}/\hbar$.

An ideal 2DEG differs from free electrons in three dimensions in that the electrons have unrestricted movement in only two dimensions (x and y) with complete confinement in the z-direction, i.e., there is no freedom of movement at all in this

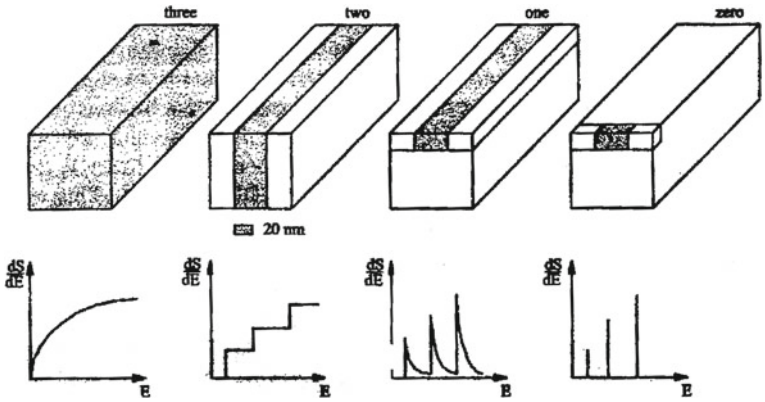

Fig. 2.18 Density of states for an ideal electron gas in one, two, and three dimensions

direction. The energy of an electron in a 2DEG is, therefore,

$$E = \frac{\hbar^2 \boldsymbol{k}^2}{2m} = \frac{\hbar^2}{2m}\left(k_x^2 + k_y^2\right) \tag{2.36}$$

as usually shown in the parabolic dispersion relation. The number of states within an area in $\boldsymbol{k}$-space box of $\mathrm{d}\boldsymbol{k} = (dk_x \cdot dk_y)$ is

$$g(E) = \frac{2}{(2\pi)^2} \tag{2.37}$$

with the factor of 2 again inserted for the spend degeneracy of the electrons. Taking into account small algebra, we obtain the density of states $g(E)$ of a 2DEG is, therefore, given by

$$g(E) = \frac{m}{\pi\hbar^2}. \tag{2.38}$$

Thus, for a 2DEG the density of states is a constant, i.e., independent of the energy (see Fig. 2.18). This is one of the fundamental features of electrons in planar heterostructures which make such structures useful for applications.

When an electron is allowed only in one-dimensional motion (along, say the x direction), the energy is given by

$$E = \frac{\hbar^2 k^2}{2m} = \frac{\hbar^2}{2m} k_x^2. \tag{2.39}$$

A procedure analogous to that used in the preceding consideration, then yields for the density of states the expression

$$g(E) = \frac{1}{2\pi^2}\left(\frac{2m}{\hbar^2}\right)^{1/2}\sqrt{E}. \tag{2.40}$$

This shows that the density of states of a one-dimensional electron gas (1DEG) has a square-root singularity at the origin (see Fig. 2.18).

An ideal zero-dimensional electron is the one that exists in a single state of fixed energy E_0. The density of states is then given by the next relation

$$g(E) = \delta(E - E_0), \tag{2.41}$$

where $\delta(x)$ is the Dirac delta function (see also Fig. 3.2 in [62]).

2.5.3 Electron in Quantum Dot

If electron motion is quantized in all three possible directions, we obtain a new physical object, a macroatom. Questions concerning the usefulness of such objects for applications naturally arise from the point of view of their electronic applications. A fundamental question is the following: what is the current through a macroatom? A valid answer is that there exists the possibility of passing an electric current through an artificial atom due to tunneling of electrons through quantum levels of the macroatom (see, e.g., [82, 83]). The field of single electron tunneling (SET) comprises of a phenomenon where the tunneling of a microscopic charge, usually carried by an electron or a Cooper pair, leads to microscopically observable effects (see also [84–86]). The basic principles for governing single charge tunneling through QD are briefly outlined in this paragraph.

Quantum dots (QDs) are often nanocrystals with all three dimensions in the nanometer range (L_x, L_y, L_z). In this case, there is no continuous DOS function, since there is quantization in three spatial directions [62]. To consider the energy spectrum of a zero-dimensional system, we have to study the Schrödinger equation [74] with a confining potential that is a function of all three directions. The simplest case is the quantum box in the form of a parallelepiped with impenetrable wells. The corresponding potential, $V(x, y, z)$ is

$$V(x, y, z) = \left\{\begin{array}{l} 0, \text{ inside of the box,} \\ +\infty, \text{ outside of the box} \end{array}\right\}, \tag{2.42}$$

where the box is restricted by the conditions $0 \le x \le L_x$, $0 \le y \le L_y$, $0 \le z \le L_z$. Using the results of the above analysis discussed previously (see also [80]), one can write down the solutions of the Schrödinger equation for a box as follows:

$$E_{n_1,n_2,n_3} = \frac{\hbar^2\pi^2}{2m*}\left(\frac{n_1^2}{L_x^2} + \frac{n_2^2}{L_y^2} + \frac{n_z^2}{L_z^2}\right), \quad n_1, n_2, n_3 = 1, 2, 3, \ldots \tag{2.43}$$

$$\Psi_{n_1,n_2,n_3}(x, y, z) = \sqrt{\frac{8}{L_x L_y L_z}} \sin\left(\frac{\pi x n_1}{L_x}\right) \sin\left(\frac{\pi y n_2}{L_y}\right) \sin\left(\frac{\pi z n_3}{L_z}\right). \tag{2.44}$$

Of fundamental importance is the fact that E_{n_1,n_2,n_3} is the total electron energy, in contrast to the previous cases, where the solution for the bound states in a quantum well and quantum wire gave us only the energy spectrum associated with the transverse confinement, see (2.35) and (2.37). Another unique feature is the presence of three discrete quantum numbers n_1, n_2, n_3 resulting straightforwardly from the existence of three directions of quantization. Thus, we obtain threefold discrete energy levels and wave functions localized in all three directions of the quantum box. In a quantum dot of a parallelepiped shape, we have three quantum numbers n_1, n_2, n_3 that substitute for the three components of the wavevector $\boldsymbol{k}$: k_x, k_y, k_z. The discrete spectrum in a quantum box and the lack of free propagation of a particle in any direction are the main features distinguishing quantum dots from quantum wells and quantum wires. As is well known, these features are typical for atomic systems as well [26, 73, 74].

Since in the case of quantum dots the electrons are totally confined, the energy spectrum is totally discrete and the DOS function is formed by a set of peaks (see Fig. 2.18) in theory with no width and with infinite height. In practice, the peaks should have a finite width, as a consequence, for instance, of the interaction of electrons with lattice phonons and impurities.

The optical control of the electric current flowing through a QD can be explained with help of a device that can be called a single-quantum dot photodiode [87–90]. In Fig. 2.19, we present the experimental results obtained [86] from excitation of the ground exciton state ($n_1 = n_2 = n_3 = n'_1 = n'_2 = n'_3$) of a single self-assembled $In_{0.5}Ga_{0.5}As$ QD embedded into a 360-nm-thick intrinsic GaAs layer. Since E_g (InGaAs) ⟨E_g (GaAs), the only optical part is the single $In_{0.5}Ga_{0.5}As$ QD. In the paper [86], the experiments were carried out at 4.2 K. In Fig. 2.19, the photocurrent is plotted as a function of the electric bias for various wavelengths of illuminating light. The wavelengths are indicated on the photocurrent curves. One can see that photocurrent–voltage dependences have, in fact, a pronounced resonant character. This is explained [90] by the fact the quantized electron and hole energies are shorted under an applied electric field, as expected from the so-called Stark effect observable for atoms and molecules. When these energies are such that wavelength corresponds to the illuminating light, the light excites electrons and holes inside the quantum well, which produces the measured photocurrent. As the applied bias increases, the energies are shifted to a smaller value and the resonance wavelength increases. In Fig. 2.19, spectra for excitation of the same ground exciton state of the dot for different biases are shown. The observed photocurrent spectra are very narrow because a single dot is involved [79]. Spectral broadening becomes visible at high biases when

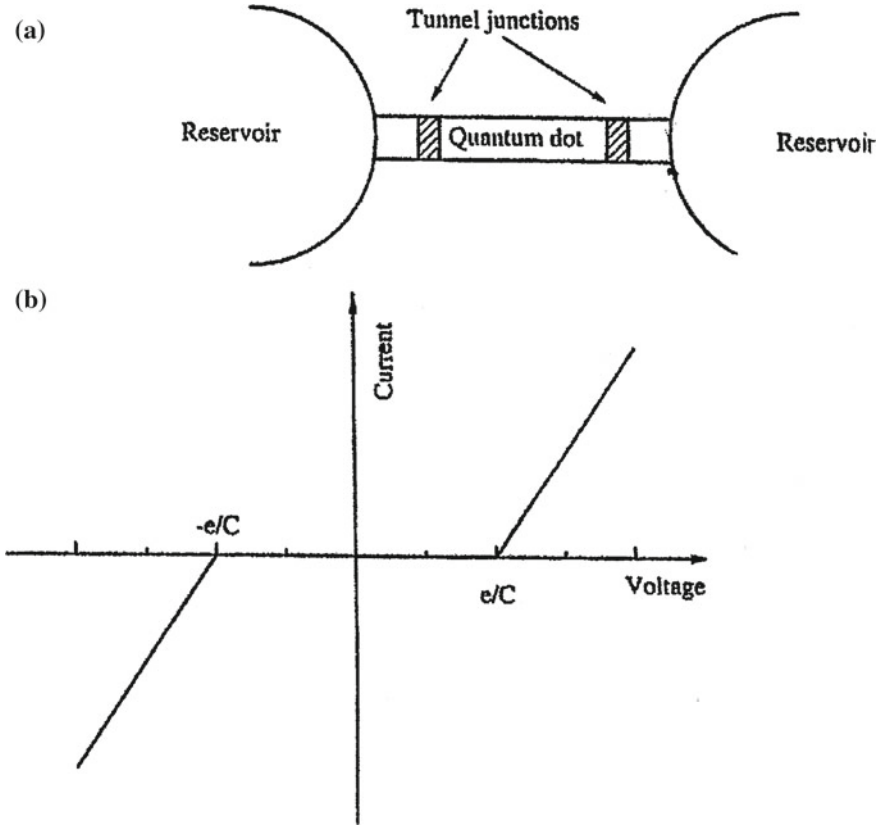

Fig. 2.19 (**a**) Scheme of a quantum system to observe Coulomb blockade effects; (**b**) I - V characteristics in a quantum dot showing the Coulomb blockade effect (after [3])

the electron and hole energy levels decay as a result of the increased rate of tunneling from the dot (for details see [90]).

In conclusion, we should underline that a very interesting challenge of future nanoelectronics is the control of the switching device by just one electron (see also below).

2.6 Excitons in Nanostructures

As is well known in a direct bandgap semiconductor (as well as an insulator an abrupt change in composition from wide to narrow band gap results in a discontinuity in the conduction and valence band profiles in the growth direction [77]. The heterointerface

so formed as Type I or Type II, depending on the bandgap alignments, determined by the conduction band offset (Fig. 2.20).

In the case of confined systems for electrons and holes, such as quantum wells (QWs), quantum wires (QWRs) and quantum dots (QDs), the excitonic effects are much more important than in bulk solids. In effect, as will be shown below, the binding energy of the electron–hole systems forming an exciton is much higher in quantum-confined systems than in the case of solids, and, therefore, the excitonic transitions can be observed even at temperatures close to room temperature, as close to the bulk case for which low temperatures are needed. This makes the role played by excitons in many optoelectronic devices of nanoscale very important (see also [76–78, 80, 90–96]). Exciton represents the Coulombic binding between the conduction electron and the isotropic part of the Γ_8 hole. Qualitatively, it is easy to understand the reason by which the binding energies of excitons E_B in quantum-confined systems are much higher than in the bulk [72]. To the zeroth approximation in Q, L, M the exciton states formed between the Γ_6 electron and the Γ_8 hole [90] are fourfold degenerate and can be calculated like the exciton states in idealized bulk material (see, e.g., [52, 91]). A quantum well (QW) is made by growing a thin layer—typically a few nanometers or 10 s of nm—of narrower gap material within a wide-gap semiconductor, where the inserted layer is thin enough to cause quantum confinement of the carriers. QWs are similarly classified as Type I or Type II in direct-gap materials (see Fig. 2.21).

2.6.1 Excitons in Quantum Wells

In a quantum well, the analysis is immediately complicated by the loss of symmetry and approximate methods must be used [97–107]. Some insight is gained from the case of a perfectly two- dimensional system, where a two-dimensional hydrogenic effective mass equation is recovered for E_{exc} [72]. This is exactly soluble and yields bound states of energy

$$E_B^{2D} = \frac{R*}{(n-1/2)^2}, \quad n = 1, 2, 3 \cdots \tag{2.45}$$

and oscillator strength

$$f_{\text{osc}} \sim \frac{1}{(n-1/2)^3}. \tag{2.46}$$

The two-dimensional ground state exciton is thus eight times as strong and four times as well bound [72] as in corresponding bulk material [52], which suggests that excitonic effects will be important in quasi-two- dimensional systems such as QWs. This would be expected intuitively since quantum confinement would impede excitonic ionization, at least through motion in the z-direction. If we decouple the in-plane and z -motion of the individual carriers to define an effective Coulomb potential $V(\rho)$,

$$V(\rho) = \frac{e^2}{4\pi\varepsilon_r\varepsilon_0} \iint \frac{|F_e(z_e)|^2 |F_h(z_h)|^2}{\sqrt{\rho^2 + (z_e - z_h)^2}} \tag{2.47}$$

we obtain an effective mass equation for F_{exc} as a function of the in-plane separation ρ:

$$\left[\frac{\hbar^2}{2\mu^*}\nabla^2 - V(\rho)\right] F_{exc}(\rho) = E_B F_{exc}(\rho). \tag{2.48}$$

Here, μ^* is the reduced in-plane electron–hole effective mass, and $F_e(z_e)$ and $F_h(z_h)$ are envelope functions for the electron and hole in their respective subbands. The interaction potential is reduced relative to the perfect two-dimensional value by the delocalization, or smearing, of the electron and hole across the QW width, and hence smaller binding energies might be expected. Equation (2.48) may be solved variationally for E_B with a trial wave function such as

$$F(\rho) = \left(\frac{2}{\pi\lambda}\right)^{1/2} e^{-\rho/\lambda}, \tag{2.49}$$

which works fairly well as a first approximation. Better estimates of the binding energy may be obtained by integrating (2.48) numerically. Either method produces binding energies of typically ≈10 meV and a strong QW width dependence.

The heavy-hole exciton is indeed heavy along z but light in the layer plane and vice versa [72]. Thus, in GaAs–$Ga_{1-x}Al_xAs$ quantum well, the curves which represent the binding energies versus the GaAs slab thickness of the two kinds of excitons should cross. For large wells, the light- and heavy-hole confinement (governed by m_{lh} and m_{hh}, respectively) are almost complete and the light hole exciton is more tightly bound because its effective bulk Rydberg is larger than that of the heavy holes. On the other hand, for narrow GaAs wells, the light holes are less confined than the heavy holes. The Coulombic interaction between the electron and the hole in the light-hole exciton is thus weaker than the one in the heavy-hole exciton. Consequently, the light-hole exciton is less bound than the heavy-hole exciton. Figure 2.20 shows Bajaj [92] results concerning the ground-bound exciton states in GaAs–$Ga_{1-x}Al_xAs$ quantum wells for two aluminum mole fractions $x = 0.15$ and $x = 0.3$. In these curves, the Dingle's rule [106] which states that the conduction band shares (85%) of the total bandgap difference between GaAs and $Ga_{1-x}Al_xAs$ has been used. Otherwise, the overall shapes of these curves look familiar: the exciton binding energies admit a maximum value versus the GaAs well thickness, whose location and amplitude depend on V_e, V_h and μ_{hh} and μ_{lh}.

To summarize, the Coulombic bound states in heterostructures are qualitatively well understood [80]. The effect of off-diagonal terms in the exciton Hamiltonian, however, an issue for quantitative understanding. We should remember that the 2D can only be approached hypothetically in an infinitely quantum well. Figure 2.21 illustrates the results of calculations of the exciton binding energy as a function of the width of an infinitely deep CdTe quantum well [82]. As is well known, the

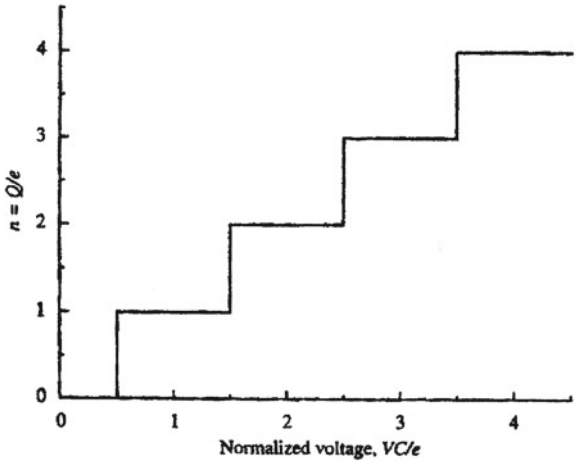

Fig. 2.20 Charging of a quantum dot capacitor as a function of voltage (in normalized coordinates)

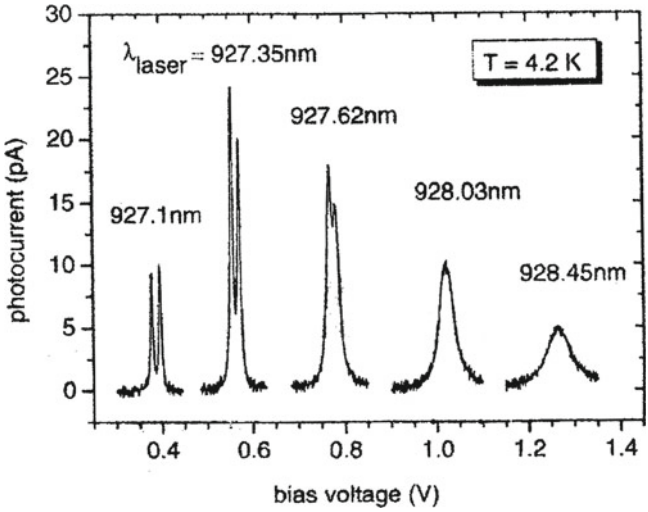

Fig. 2.21 Photocurrent resonance for various excitation wavelengths bias voltage. At low bias the fine structure splitting is fully resolved, at higher bias the linewidth is increased due to fast tunneling (after [83])

magnitude of the bulk exciton binding energy for CdTe is 10.1 meV (see, e.g., [95]). The negative values on the graph of Fig. 2.22 illustrate that it is indeed a bound state. From Fig. 2.23, it can be seen that two-dimensional exciton binding energy is equal to four meaning of bulk exciton binding energy. Figure 2.22 displays the corresponding Bohr radii r_{ex} for the energies of Fig. 2.22. Remembering that the the Bohr radius in bulk, $r_{ex}(3D) = 67$ Å, then the 2D limit, i.e.,

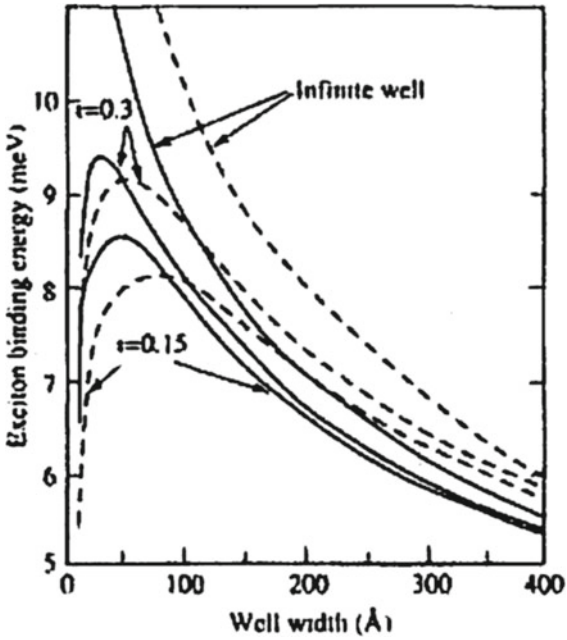

Fig. 2.22 Variation of the binding energy of the ground state E_{1s} of the heavy-hole exciton (solid lines) and the light-hole (dashed lines) as a function of the GaAs quantum well size (L) for aluminium concentration $x = 0.15$ and $x = 0.3$ and for infinite potential wells (after [92])

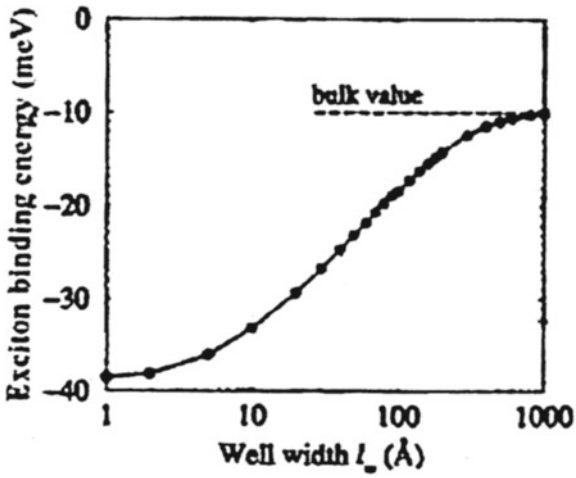

Fig. 2.23 Exciton binding energy in an infinitely deep CdTe quantum well (after [80])

$$Lim r_{ex}(2D) = \frac{r_{ex}(3D)}{2}, \quad l_w \longrightarrow 0 \tag{2.50}$$

is satisfied. The 3D limit is obeyed, although the data on the graph show a slight scatter around the bulk radii 67 Å (Fig. 2.24). According to [80], the source of this discrepancy is numerical accuracy. At the lager well widths, the wave function needs to be known at many points in order to calculate the binding energy to be of very high tolerance (according to [80] thus leading to long computational times).

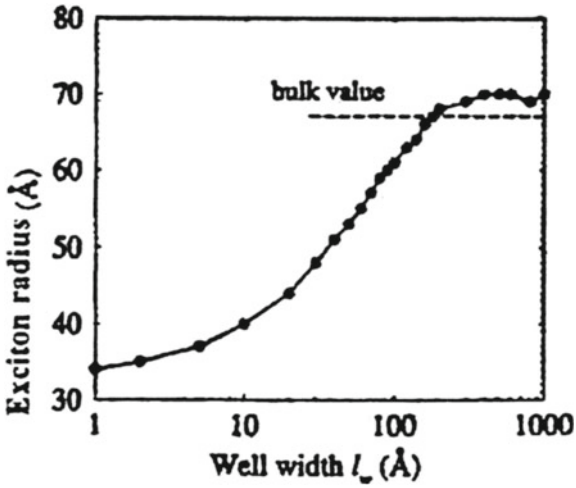

Fig. 2.24 Bohr radius of two - dimensional exciton in an infinitely deep CdTe quantum well (after [83])

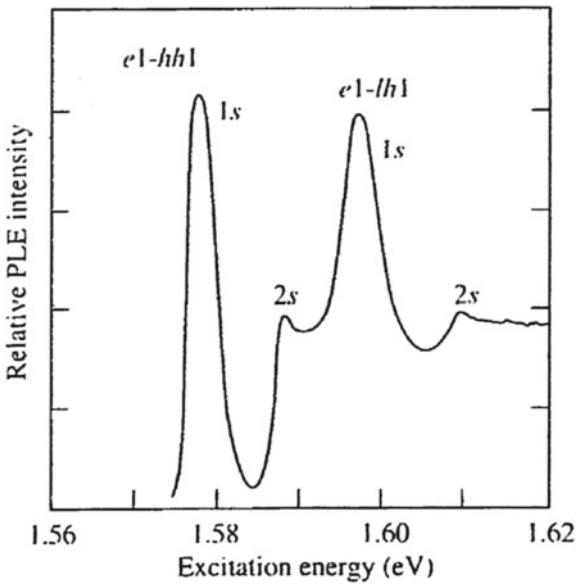

Fig. 2.25 Photoluminescence excitation spectrum of $GaAs/Al_{0.33}Ga_{0.67}As$ multi-quantum well showing the 1s and 2s excitons for the first electron-heavy-hole and electron-light-hole transitions (after [108])

To conclude this paragraph we should note that the Coulombic interaction produces an excitonic series at every subband [77]. In practice, the most important effect of the Coulomb interaction on QW band structure is the appearance of strong, sharp spectral resonances just below the band edge for the first electron-heavy-hole and electron-light -hole transitions. In real QWs, the excitons are broadened by processes such as phonon interactions, well-width fluctuation, variations in impurity levels and electric field effects. Nonetheless, in good material, the peaks are quite distinct at room temperature (Fig. 2.25) and by deliberate tuning of the peak position, for example, through an applied bias, can act as effective optical switches.

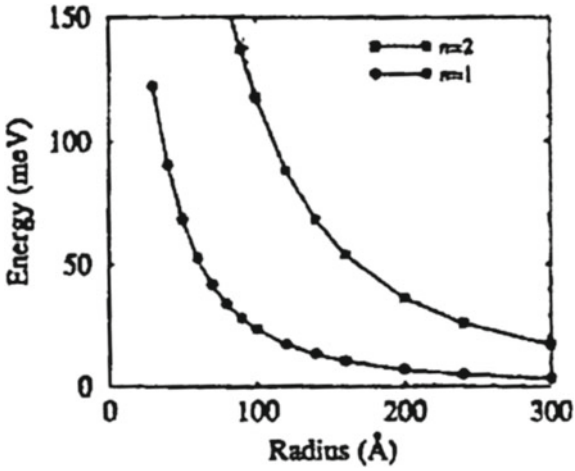

Fig. 2.26 The confinement energy in a finite barrier circular cross - section quantum wire (after [83])

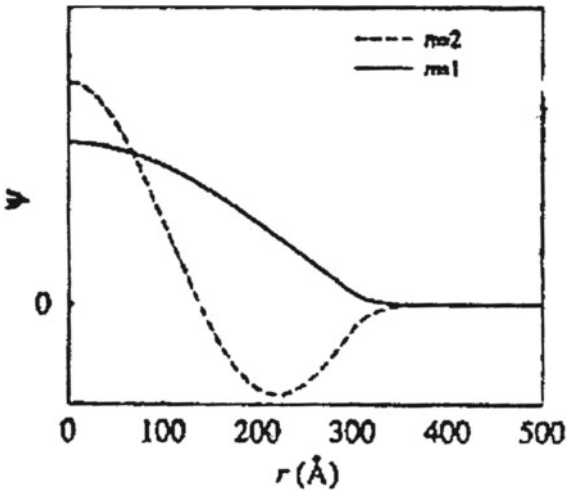

Fig. 2.27 The radial component of the wave function Ψ (r) for the lowest two eigenstates in a finite - barrier quantum wire with radius 300 Å of circular cross - section (after [83])

The relative positions of the excitons peak (Fig. 2.26) offer a very good guide to the actual exciton binding energy (Fig. 2.27) (see also [108]).

2.7 Biexcitons in Quantum Dots

In 1958, different authors [109, 110] suggested that in crystals besides excitons more complex electronic quasi-particles might exist, made up of three or four carriers (Fig. 2.28). As was shown in these papers the latter one, consisting of two electrons and two holes is well known as biexcitons or excitonic molecules [111]. As the density of excitons is increased, biexcitons are formed by increasing the light intensity.

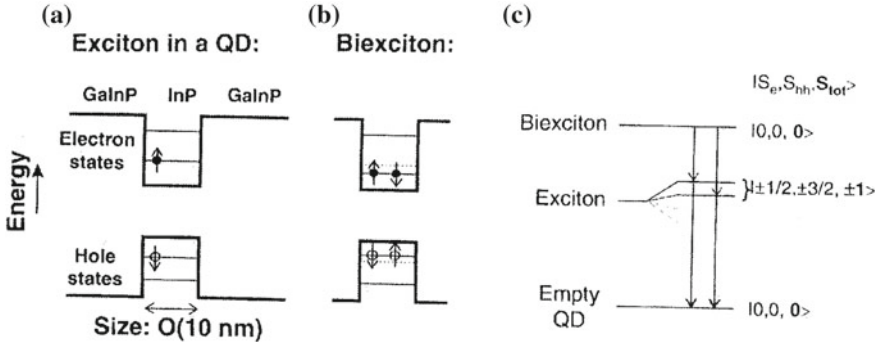

Fig. 2.28 Schematic picture of exciton and biexciton in quantum dot

Biexcitons can be generated either through ordinary excitation of the crystal or by two-photon absorption each photon having an energy

$$h\nu = E_{\mathrm{B}} - \frac{E_{\mathrm{B_{xx}}}}{2}, \tag{2.51}$$

where $E_{\mathrm{B_{xx}}}$ is the biexciton binding energy and E_{B} is the exciton energy

$$E_{\mathrm{B}} = E_{\mathrm{g}} - E_{\mathrm{B_x}} + \frac{\hbar^2 k^2}{2m_{\mathrm{x}}}. \tag{2.52}$$

In the last relation, E_{g} is the bandgap energy, $E_{\mathrm{B_x}}$ is the exciton binding energy and $\frac{\hbar^2 k^2}{2m_{\mathrm{x}}}$ is the kinetic energy with which an exciton moves through the crystal (see also [112]).

Compared to the bulk material, an increased stability of biexcitons due to the two-dimensional carrier confinement is observed for typical III-V structures like GaAs/AlGaAs QWs [100, 113] (see Fig. 2.29) or for wide bandgap II-VI materials like CdZnSe/ZnSe [114, 115]. As a consequence of the enhanced biexciton binding energy, a variety of optical properties, like, e.g., the photoluminescence (PL) spectrum, the optical gain or the four- wave mixing signal especially in wide bandgap II-VI QWs are strongly influenced by biexcitons (see [115] and references therein).

In this section, we briefly describe some results obtained from optical spectroscopy on epitaxially grown single SQDs based on II-VI and II-N compounds. As indicated above, the biexciton (XX or X_2 is a four- particle state. In its lowest energy state configuration, two electrons and two holes with antiparallel spins occupy the first quantized state of the conduction and the valence band in the SQDs, respectively (see, e.g., [115]). We should add that the QDs in the material systems described here are quite small with diameters in the order of 10 nm and heights of a few nm. The biexciton state is, therefore, a singlet state with a total spin of $J = 0$. Thus, the exciton state X represents the final state for the biexciton recombination (see also [115]). In II-

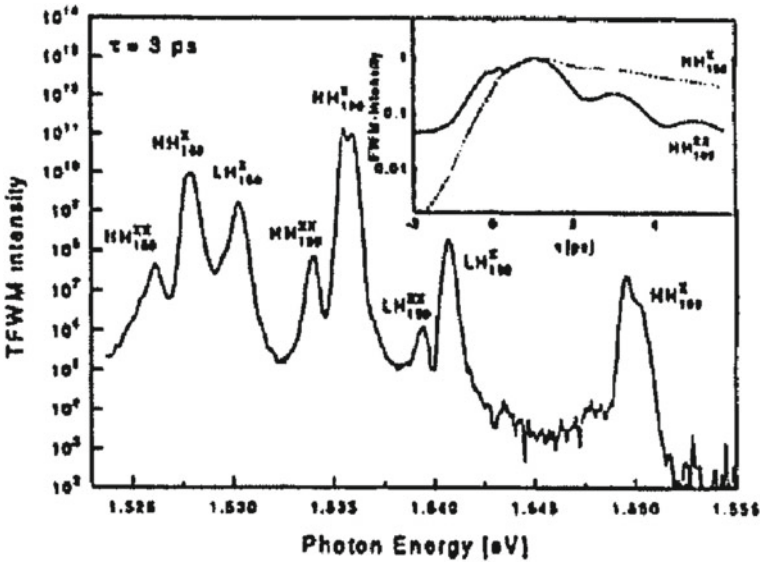

Fig. 2.29 Spectrally resolved four-wave mixing at $\tau = 3$ ps showing the heavy hole and light hole biexcitons. Insert shows the four-wave mixing intensity of the heavy hole exciton and biexciton as a function of delay (after [113])

VI semiconductors, as in III-V materials with a zinc-blende crystal lattice, Coulomb interaction leads to positive biexciton binding energies, see (2.52), i.e., the energetic distance between XX (X_2) and X is smaller than the energy difference between the first exciton state and the ground state. A typical optical fingerprint for the X_2 is, therefore, an additional PL line at the low-energy side of the exciton emission X that exhibits a strong (quadratic) dependence on the excitation power [112]. This behavior is clearly visible in left panel of Fig. 2.30. At low excitation density, the PL spectrum of CdSe/ZnSe SQDs consists of emission peaks stemming from exciton recombination of two individual QDs. With rising excitation density additional lines emerge, red shifted by about 24 meV with respect to the excitonic emission X, and rapidly increasing in intensity, which can be attributed to biexciton emission X_2. The biexciton binding energy is obviously much larger than in III-As-based QDs, where typical values of a few meV ($\sim$2 meV [113]) have been determined (see also [112–118]). When having a closer look on the PL spectra presented in Fig. 2.26, some more information can be extracted. One should have in mind that in QDs, the light-hole level is shifted to higher energies due to strain and confinement and thus, excitons are formed between electrons and heavy holes. The ground state of a heavy-hole exciton in an SQD is a spin quadruplet, which can be by the z-component (= component, according [114] in growth direction) of the total exciton spin J_z. If the z- component of the electron spin, $s_z = \pm 1/2$, and the z -component of the total angular momentum of the heavy hole $j_z = \pm 3/2$, are antiparallel, in such case, we get $J_z =_z + j_z = \pm 2$ (the dark exciton states [116]).

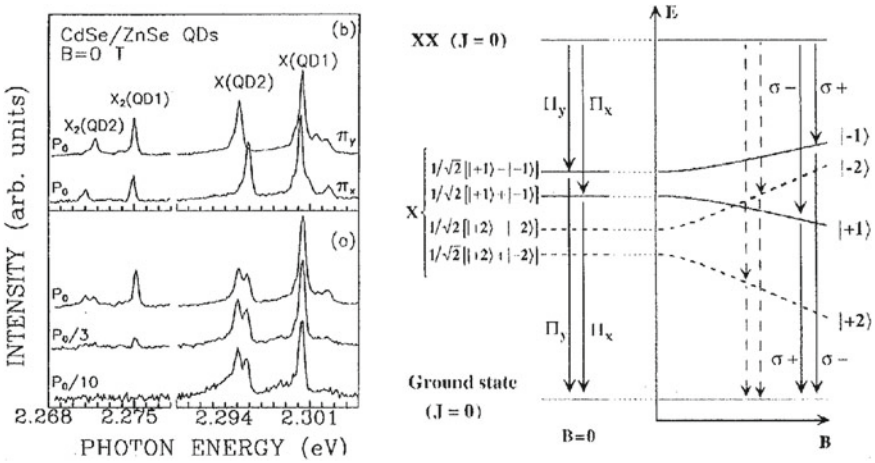

Fig. 2.30 *Left side*: Excitonic (X) and biexcitonic (X_2) emission from two individual CdSe/ZnSe SQDs for different excitation powers. The PL spectra shown in the lower panel are unpolarized, the data presented in the upper panel represent linearly polarized PL spectra (π_x and π_y, respectively). *Right side*: Energy level scheme for the biexciton - exciton cascade in a QD (after [114])

In II-VI QDs, the energy difference Δ_0 between bright and dark exciton states that is given by the isotropic electron–hole interaction energy amounts to about 1 meV and more which is nearly an order of magnitude larger than in InAs/GaAs QDs [79]. As can be seen in Fig. 2.25, the exciton fine structure is reflected both in the exciton and in the biexciton recombination: SQD1 does not show a significant splitting of the exciton PL signal, while SQD2 exhibits a doublet with an energy separation of almost 1 meV indicating a reduced QD symmetry. Exactly the same behavior is observed in the corresponding biexciton lines. Moreover, the high energy component of the X emission in SQD2 (π_x polarized) corresponds to the low-energy component of the X_2 emission and vice versa, in agreement with energy level scheme (see Fig. 2.26). All these effects are easily accessible in wide bandgap II-VI QDs, because the characteristic energy splitting are significantly enhanced with respect to III-As semiconductor QDs. We may expect a more significant value of the exchange splitting for exciton and biexciton states in QD of isotope-mixed crystals (see also [23, 118]). Thanks to the large biexciton binding energy, II -VI QDs were the first, where the biexciton–exciton cascade could be traced directly in the time domain on SQD level [115–121]. Figure 2.31 depicts transient PL spectra (left) of both emission lines and the time-dependent intensity of the exciton and the biexciton signal (right panel). The biexciton emission shows a monoexponential decay with a time constant of 310 ps. The exciton reveals a more complex behavior: the onset of the exciton line is delayed, resulting in "plateaulike" characteristics of the exciton decay curve. The excitation density according to the authors of this experiment was set to a value where an average number of two electron–hole pairs per excitation pulse in the SQD was generated. Model calculations taking into account the biexciton state, the bright and

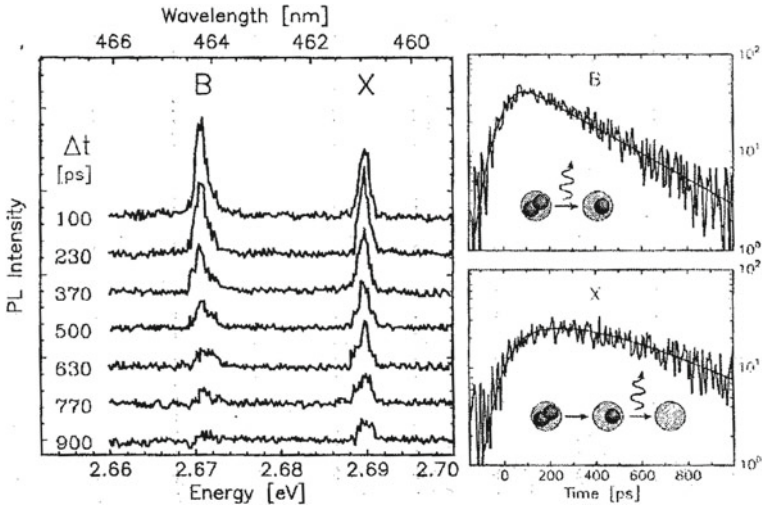

Fig. 2.31 *Left panel*: Transient PL spectra from a single CdSe/ZnSe QD showing the single exciton X and the biexciton transition (here denoted by $B = X_2$). *Right panel*: Decay curves for the exciton and the biexciton PL signal (for details see text) (after [114])

the dark exciton states and the "empty" QD (corresponding to a QD population with 2, 1, and 0 excitons, respectively), confirm that the exciton state is fed by the biexciton recombination causing the delayed onset and the "plateaulike" characteristics of the exciton emission dynamics (for details see [79] and references therein).

References

1. D. Pines, *Elementary Excitations in Solids* (W.A. Benjamin Inc., New York, 1963)
2. S.I. Pekar, *Crystaloptics and Addition Waves* (Naukova Dumka, Kiev, 1982). (in Russian)
3. G.P. Srivastava, *The Physics of Phonons* (Hilger, Bristol, 1990)
4. V.G. Plekhanov, *Isotope - Mixed Crystals: Fundamentals and Applications* (unpublished, 2011)
5. V.G. Plekhanov, Manifestation and Origin of the Isotope Effect (2009), arXiv:0907.2024
6. V.G. PLekhanov, *Giant Isotope Effect in Solids* (Stefan - University Press, La Jola, 2004)
7. J. Callaway, *Energy Band Structure* (Academic Press, New York, 1964)
8. R.M. Martin, *Electronic Structure - Basic Theory and Practical Methods* (Cambridge University Press, Cambridge, 2004)
9. J.M. Ziman, *Electrons and Phonons* (Oxford University Press, London, 1963)
10. N.W. Aschcroft, N.D. Mermin, *Solid State Physics* (Holt Reinhart and Winston, New York, 1975)
11. M.L. Cohen, J. Chelikowsky, *Electronic Properties and Optical Properties of Semiconductors*, vol. 75, 2nd edn., Springer Series Solid State Sci (Springer, Berlin, 1989)
12. V.G. Plekhanov, *Isotope Effect - Macroscopic Maniestation of the Strong Interaction* (LAMBERT Academic Publishing, Saarbrücken, 2017). (in Russian)
13. J.C. Slater, *Electronic Structure of Molecules*, vol. 1 (McCraw - Hill Company Inc., New York, 1963)

14. J.L. Birman, Space Group Symmetry, in Handbuch für Physik, vol. 25/26 (Berlin - New York, 1974)
15. A.I. Lebedev, *Physics of Semiconducting Devices* (Fizmatlit, Moscow, 2001). (in Russian)
16. J.R. Chelikowsky, M.L. Cohen, Nonlocal pseudopotential calculations for the electronic structure of eleven diamond and zinc - blende semiconductors. Phys. Rev. B **14**, 556–582 (1976)
17. V.C. Vavilov, A.A. Gippius, E.A. Konorova, *Electron and Optical Processes in Diamond* (Science, Moscow, 1985) (in Russian)
18. P.Y. Yu, M. Cardona, *Fundamentals of Semiconductors* (Springer, Berlin, 1996)
19. V.G. Plekhanov, Isotope effects in solid state physics, in *Semiconductor and Semimetals*, vol. 68, ed. by R.K. Willardson, E. Weber (Academic Press, San Diego, 2001)
20. R.P. Mildren, Intrinsic optical properties of diamond, in *Optical Engineering of Diamond*, ed. by R.P. Mildren, J.R. Ratenau (Wiley - VCH Verlag GmbH, 2013)
21. J.R. Chelikowsky, S.G. Louie, First - principles linear combination of atomic orbitals method for the cohesive and structural properties of solids: application to diamond. Phys. Rev. B **29**, 3470–3482 (1984)
22. M.S. Hybertsen, S.G. Louie, Electron correlation in semiconductors and insulators: band gaps and quasiparticle energies. Phys. Rev. B **34**, 5390–5413 (1986)
23. V.G. Plekhanov, Elementary excitations in isotope - mixed crystals, Phys. Rep. **410**(1–3), 1–235 (2005)
24. M. Cardona, Renormalization of the optical response of semiconductors by electron - phonon interaction, phys. st. sol. (a) **188**, 1209–1232 (2001)
25. V.G. Plekhanov, Wannier - Mott excitons in isotope - disordered crystals. Rep. Prog. Phys. **61**, 1045–1095 (1998)
26. P.A.M. Dirac, *The Principles of Quantum Mechanics* (Oxford University Press, Oxford, 1958)
27. G. Herzberg, *Molecular Spectra and Molecular Structure* (D. van Nostrand, New York, 1951)
28. V.G. Plekhanov, Experimental evidence of strong phonon scattering in isotopical disordered systems: the case $LiH_x D_{1-x}$. Phys. Rev. B **51**, 8874–8878 (1995)
29. A.F. Kapustinsky, L.M. Shamovsky, K.S. Bayushkina, Thermochemistry of isotopes. Acta Physicochim. (USSR) **7**, 799–810 (1937)
30. V.G. Plekhanov, Isotopic and disorder effects in large radius exciton spectroscopy. Physics - Uspekhi (moscow) **40**, 533–579 (1997)
31. F.I. Kreingold, K.F. Lider, M.B. Shabaeva, Influence of isotope substitution sulfur on the exciton spectrum in CdS crystal, Fiz. Tverd. Tela (St. Petersburg) **26**, 3940–3941 (1984) (in Russian)
32. V.G. Plekhanov, Renormalization the energy of elementary excitations in solids by the strong (nuclear) interaction. Universal J. Phys. Appl. **11**, 6–12 (2017)
33. R.J. Elliott, J.A. Krumhansl, P.L. Leath, The theory and properties of randomly disordered crystals and physical systems. Rev. Mod. Phys. **46**, 465–542 (1974)
34. Y. Onodera, Y. Toyozawa, Persistence and amalgamation types in the electronic structure of mixed crystals. J. Phys. Soc. Japan **24**, 341–355 (1968)
35. Y. Toyozawa, *Optical Processes in Solids* (Cambridge University Press, Cambridge, 2003)
36. M. Cardona, M.L.W. Thewalt, Isotope effect on the optical spectra of semiconductors. Rev. Mod. Phys. **77**, 1173–1224 (2005)
37. F.I. Kreingold, K.F. Lider, K.I. Solov'ev, Isotope shift of exciton line in absorption spectrum Cu_2O. JETP Lett. (Moscow) **23**, 679–681 (1976). (in Russian)
38. F.I. Kreingold, K.F. Lider, V.F. Sapega, Influence of isotope substitution on the exciton spectrum in Cu_2O crystal, Fiz. Tverd. Tela (St. Petersburg) **19**, 3158–3160 (1977) (in Russian)
39. F.I. Kreingold, B.S. Kulinkin, Influence of isotope substitution on the forbidden gap of ZnO crystals, ibid, **28**, 3164–3166 (1986) (in Russian)
40. F.I. Kreingold, Dependence of band gap ZnO on zero - point energy, ibid, **20**, 3138–3140 (1978) (in Russian)
41. J.M. Zhang, T. Ruf, R. Lauck et al., Sulfur isotope effect on the excitonic spectra of CdS. Phys. Rev. B **57**, 9716–9722 (1998)
42. T.A. Meyer, M.L.W. Thewalt, R. Lauck et al., Sulfur isotope effect on the excitonic spectra of CdS. Phys. Rev. B **69**, 115214–5 (2004)

43. G.L. Bir, G.E. Picus, *Symmetry and Deformation in Semiconductors* (Science, Moscow, 1972) (in Russian)
44. L.F. Lastras - Martinez, T. Ruf, M. Konuma et al., Isotopic effect on the dielectric response of Si around the E_1 gap. Phys. Rev. B **61**, 12946–12951 (2000)
45. D. Karaskaja, M.L.W. Thewalt, T. Ruf, Photoluminescence studies of isotopically - enriched silicon: isotopic effects on indirect electronic band gap and phonon energies. Solid State Commun. **123**, 87–92 (2003)
46. S. Tsoi, H. Alowadhi, X. Lu, Electron - phonon renormalization of electronic band gaps of semiconductors: isotopically enriched silicon. Phys. Rev. B **70**, 193201–4 (2004)
47. A.K. Ramdas, S. Rodriguez, S. Tsoi et al., Electronic band gap of semiconductors as influenced by their isotopic composition. Solid State Commun. **133**, 709–714 (2005)
48. S. Tsoi, S. Rodriguez, A.K. Ramdas et al., Isotopic dependence of the E_0 and E_1 direct gaps in the electronic band structure of Si. Phys. Rev. B **72**, 153203–4 (2005)
49. D.G. Thomas (ed.), *II -VI Semiconducting Comounds* (Benjamin, New York, 1967)
50. A.A. Klochikhin, V.G. Plekhanov, Isotope effect on the Wannier - Mott exciton levels. Sov. Phys. Solid state **22**, 342–344 (1980)
51. V.G. Plekhanov, Direct observation of the effect of isotope - induced - disorder on exciton binding energy in LiH_xD_{1-x} mixed crystals. J. Phys. Condens. Matter **19**, 086221–9 (2007)
52. R.S. Knox, *Theory of Excitons* (Academic Press, New York, 1963)
53. A.T. Collins, S.C. Lawson, G. Davies, H. Kanda, Indirect energy gap of ^{13}C diamond. Phys. Rev. Lett. **65**, 891–894 (1990)
54. H. Watanabe, S. Shikata, Superlattice structures from diamond. Diam. Relat. Mat. **20**, 980–982 (2011)
55. J. Barjon, F. Jomard, A. Tallaire et al., Determination of exciton diffusion lengths in isotopically engineered diamond junctions. Appl. Phys. Lett. **100**, 122107–4 (2012)
56. H. Watanabe, T. Koretsune, S. Nakashima et al., Isotope composition dependence of the band - gap energy in diamond. Phys. Rev. B **88**, 205420–5 (2013)
57. C.D. Clark, P.J. Dean, P.V. Harris, Intrinsic edge absorption in diamond. Proc. R. Soc. (London) **A277**, 312–319 (1964)
58. P.J. Dean, Inter-impurity recombinations in semiconductors. Prog. Solid State Chem. **8**, 1–126 (1973)
59. A.T. Collins, Band structure (Chap. 1), in *Handbook of Industrial Diamond and Diamond Films*, ed. by M.A. Prelas, G. Popovici, L.K. Bigelow (Marcel Dekker Inc., New York, 1998), p. 1
60. Zh.I. Alferov, The history and future of semiconductor heterostructures, Fiz. i Tech. Poluprovod. (Phys. Tech. Semicond) **32**, 3–18 (1998) (in Russian)
61. H. Watanabe, C.E. Nebel, S. Shikata, Isotopic homojunction band engineering from diamond. Science **324**, 1425–1428 (2009)
62. V.G. Plekhanov, *Isotope Low - Dimensional Structures* (Springer, Heidelberg, 2012)
63. V.G. Plekhanov, *Isotope - Based Quantum Information* (Springer, Heidelberg, 2012)
64. V.G. Plekhanov, A.V. Emel'yanenko, A.U. Grinfelds, Excitonic structure of Nai and LiH crystals cleaved in liquid helium. Phys. Lett. A **101**, 291–294 (1984)
65. V.G. Plekhanov, The influence of the surface state on the manifestation of exciton states in the wide - gap insulators. Opt. Spectr. **62**, 1300–1309 (1987). (in Russian)
66. V.G. Plekhanov, Comparative study of isotope and chemical effects on the exciton states in LiH crystals. Prog. Solid State Chem. **29**, 71–177 (2001)
67. V.G. Plekhanov, Resonant secondary emission spectra, in *Proceedings International Conference on LASERS'80* (STS Press, VA, USA, 1981), pp. 94–99
68. J.L. Verble, J.L. Warren, J.L. Yarnell, Lattice dynamics of lithium hydride. Phys. Rev. **168**, 980–989 (1968)
69. S.D. Lester, T.S. Kim, B.G. Streetman, Distortion of band - edge luminescence in InP due to self - absorption. J. Appl. Phys. **63**, 853–861 (1988)
70. M. Namiki, S. Pascazio, Quantum theory of measuremen based on the many-Hilbert-space approach. Phys. Reports **232**, 301–411 (1993)

71. N. Gerasimenko, Ju. Parhomenko, S*ilicon–Material of Nanoelectronics* (Technosphera, Moscow, 2007) (in Russian)
72. G. Bastard, *Wave Mechanics Applied to Semiconductor Heterostructures* (Halsted Press, New York, 1988)
73. R.P. Feynman, R.P. Leighton, M. Sands, *The Feynman Lecture in Physics*, vol. 3 (Reading, Addison - Wesley, 1965)
74. L.D. Landau, E.M. Lifshitz, *Quantum Mechanics (Nonrelativistic Theory)* (Pergamon Press, New York, 1977)
75. B.B. Kadomtsev, *Dynamics and Information* (UFN, Moscow, 1997). (in Russian)
76. K. Goser, P. Glösekötter, J. Dienstuhl, *Nanoelectronics and Nanosystems* (Springer, Berlin, 2004)
77. K. Barnham, D. Vvedensky, *Low - Dimensional Semicoonductor Structures* (Cambridge University Press, Cambridge, 2009)
78. M.J. Kelly, *Low - Dimensional Semiconductors* (Clarendon Press, Oxford, 1995)
79. P. Michler (ed.), *Single Semiconductor Quantum Dots* (Springer, Berlin, 2009)
80. P. Harrison, *Quantum Wells, Wires and Dots* (Wiley, New York, 2001)
81. A.M. Fox, Optoelectronics in quantum well structures. Contemp. Phys. **37**, 11–125 (1996)
82. H. Grabert (ed.), Special Issue on Single Charge Tunneling, Zs. Physik **85**, Suppl 3 (1991)
83. H. Grabert, M.H. Devored (eds.), *Single Charge Tunneling: Coulomb Blockade Phenomena in Nanostructures*, vol. 294, NATO ASI Series B (Plenum, New York, 1992)
84. S. Washburn, R.A. Webb, Quantum transport in small disordered samples from the diffuse to the ballistic regime. Rep. Prog. Phys. **55**, 131–1383 (1992)
85. D.V. Averin, A.N. Korotkov, K.K. Likharev, Theory of single electron charging of quantum wells and dots. Phys. Rev. **44**, 6199–6211 (1991)
86. J. Bylander, T. Duty, P. Delsing, Current measurement by real-time counting of single electrons. Nature **434**, 361–364 (2005)
87. D. Bimberg, M. Grundman, N.N. Ledentsov, *Quantum Dot Heterostructure* (Wiley, Chichester, 1999)
88. L. Jacak, P. Hawrylak, A. Wojs, *Quantum Dots* (Springer, Berlin, 1998)
89. G.W. Bryant, G.S. Solomon (eds.), *Optics of Quantum Dots and Wires* (Artech House Inc., London, 2005)
90. H.J. Krenner, S. Stufler, M. Sabathil et al., Recent advances in exciton-based quantum information processing in quantum dot nanostructures. New J. Phys. **7**, 185–187 (2005)
91. R.J. Nelson, Excitons (Chap. 8), in *Excitons in Semiconductor Alloys*, ed. by E.I. Rashba, M.D. Sturge (North–Holland Publ. Co., Amsterdam, 1982), pp. 319–348
92. K.K. Bajaj, Use of excitons in material characterization of semiconductor system, Mater. Sci. Eng. R. **24**, 59–120 (2001)
93. J.M. Luttinger, W. Kohn, Motion of electrons and holes in perturbed periodic fields. Phys. Rev. **97**, 869–883 (1955)
94. J.M. Luttinger, Quantum theory of cyclotron resonance in semiconductors: general theory. Phys. Rev. **102**, 1030–1041 (1956)
95. K. Seeger, *Semiconductor Physics* (Springer, New York, 1973)
96. A. Baldareschi, N.O. Lipari, Energy levels of direct excitons in semiconductors with degenerate bands. Phys. Rev. B **3**, 439–451 (1971)
97. G. Bastard, E.E. Mendez, L.L. Chang, L. Esaki, Exciton binding energy in quantum wells. Phys. Rev. B **26**, 1974–1979 (1982)
98. L.V. Keldysh, Excitons in semiconductor–dielectric nanostructures, Phys. Stat. Solidi (a) **164**, 3–12 (1997)
99. V.G. Plekhanov, *Isotope Effect: Physics and Applications* (Palmarium Academic Publishing, Saarbrücken, 2014)
100. R.C. Miller, D.A. Kleinman, W.T. Tsang, Observation of the excited level of excitons in GaAs quantum wells. Phys. Rev. B**2**, 1134–1136 (1981); Phys. Stat. Solidi A **B25**, 6545–6549 (1982)
101. R.L. Greene, K.K. Bajaj, D.E. Phelps, Energy levels of Wannier excitons in GaAs–$Ga_{1-x}Al_x$ As quantum–well structures. Phys. Stat. Solidi A **B29**, 1807–1812 (1984)

102. R.L. Greene, K.K. Bajaj, Binding energies of Wannier excitons in GaAs-$Ga_{1-x}Al_xAs$ quantum-well structures. Solid State Commun. **88**, 955–959 (1993)
103. M. Altarelli, Electronic structure and semiconductor-semimetal transitions. Phys. Rev. B **28**, 842–845 (1983)
104. M. Altarelli, Electronic structures of two-dimensional systems. J. Luminesc. **30**, 472–487 (1985)
105. A. Fasolino, M. Altarelli, in *Two-Dimensional Systems, Heterostructures and Superlattices*, vol. 43, Springer Series in Solid State Sci, ed. by G. Bauer, F. Kucher, H. Heinrich (1984), pp. 176–212
106. R. Dingle, in Festkörperprobleme, vol. 15 of Advances in Solid State Phys., ed. by H.J. Quesser (Pergamon/Vieweg, Braunschweig, 1975), p. 21
107. J. Hegarty, M.D. Sturge, Studies of exciton localization in quantum-well structures by non - linear techniques. JOSA B **2**, 1143–1154 (1985)
108. P. Dawson, K.J. Moore, G. Duggan et al., Unambiguous observation of the 2S state of the light - and heavy - hole excitons in GaAs - (AlGa)As MQW structures. Phys. Rev. B **34**, 6007–6010 (1986)
109. S.A. Moskalenko, Towards to theory of Mott excitons in alkali halides crystals. Opt. Spectr. **5**, 147–155 (1958)
110. M.A. Lampert, Mobile and immobile effective-mass-particle complexes in nonmetallic solids. Phys. Rev. Lett. **1**, 450–453 (1958)
111. V.G. Plekhanov, Fundamentals and applications of isotope effect in solids. Prog. Mat. Sci. **51**, 287–426 (2006)
112. B. Hönerlage, R. Levy, J.B. Grun et al., The dispersion of excitons, polaritons and biexcitons in direct - gap semiconductors. Phys. Reports **124**, 163–253 (1985)
113. D. Birkedal, J. Singh, V.G. Lyssenko et al., Binding of quasi-two-dimensional biexcitons. Phys. Rev. Lett. **76**, 672–675 (1996)
114. G. Bacher, T. Kömmel, Optical properties of epitaxially grown wide bandgap single quantum dots, in *Single Semiconductor Quantum Dots*, ed. by P. Michler (Berlin, Springer, 2009)
115. G. Chen, T.H. Stievater, E.T. Batteh et al., Biexciton quantum coherence in a single quantum dot. Phys. Rev. Lett. **88**, 117901–117904 (2002)
116. Special issue on high excitation and short pulse phenomena. J. Luminesc. **30**(1–4) (1985)
117. K. Herz, T. Kümmel, G. Bacher et al., Biexcitons in low-dimensional CdZnSe/ZnSe structures. Phys. Stat. Solidi (a) **164**, 205–208 (1997)
118. B. Jusserand, M. Cardona, Raman spectroscopy in light scattering of vibrations in superlattice, in *Light Scattering in Solids*, ed. by M. Cardona, G. Güntherodt (Springer, Berlin, 1989), pp. 49–152
119. F. Herman, R.L. Kortum, C.D. Kuglin et al., in *II - VI Semiconducting Compounds*, ed. by D.G. Thomas (Benjamin, New York, 1967)
120. H. Kim, S. Rodriguez, T.R. Anthony, Electronic transitions of holes bound to boron acceptors in isotopically controlled diamond. Solid State Commun. **102**, 861–865 (1997)
121. M. Cardona, Dependence of the excitation energies of boron in diamond on isotopic mass. Solid State Commun. **121**, 7–8 (2002)

Chapter 3
Phonon States in Bulk and Low-Dimensional Structures

Abstract The accumulated voluminous theoretical and experimental data suggest that the isotope composition of a crystal lattice exerts some influence on the thermal, elastic, and vibrational properties of solids. Since the vast majority of compounds derived from elements has more than one stable isotope, it is clear that phonon–phonon interactions lead to finite phonon lifetimes and additionally renormalization, including anharmonic interactions and elastic scattering. It is commonplace that two processes cannot be predicted easy. However, isotope enrichment allows to discriminate these processes. This chapter is devoted to the lattice dynamics of the bulk and low-dimensional isotope-mixed compounds. The results of this chapter are found in broad fields of applications.

3.1 Hamiltonian of Perfect Crystals

Much progress has been made during the last four decades in the theoretical understanding and its experimental verification of dynamic properties of solids, especially of disordered and anharmonic solids. Among the problems of lattice dynamics having attracted particular in recent years are dynamic properties of isotope-disordered solids (including localization of vibrational states, breakdown of quasi-momentum selection rules, role of short - range potential and anharmonic properties of isotope-mixed systems) (see, e.g., reviews [1, 2]).

As we all know, many phenomena in solid-state physics can be understood on the basis of a static lattice model. In this model [3], the atoms of the solid are taken to constitute a fixed, rigid, and immobile periodic array. Within this framework, it is, for example, possible to account for a wealth of equilibrium properties of metals [4] dominated by the behavior of the conduction electron. To some extent, it is also possible to account for the equilibrium properties of ionic and molecular insulators. The static lattice model is, of course, an approximation to the actual ionic (atomic) configuration, because the atoms or ions are not fixed to their equilibrium positions, but rather oscillate about them with an energy which is governed by the temperature

© Springer International Publishing AG, part of Springer Nature 2018

V. G. Plekhanov, *Introduction to Isotopic Materials Science*,
Springer Series in Materials Science 248, https://doi.org/10.1007/978-3-319-42261-9_3

of the solid. The reason for these oscillations is due to the fact that the atoms (ions) are not infinitely massive and are not held in place by infinitely strong forces. In classical limit of the theory, the static lattice model can, therefore, be valid only at zero temperatures. At nonzero temperatures, each ion (atom) must have some thermal energy, and therefore there is a certain amount of motion in the vicinity of its equilibrium position. In quantum theory (see below), even at zero temperature, the static lattice model is incorrect, because according to the uncertainty principle localized ions possess some nonvanishing mean square momentum.

On the other hand, the dynamics of atoms in solids are responsible for many phenomena which cannot be explained within the static lattice model. Examples are the specific heat of solids, thermal expansion, thermal conductivity, displaced ferroelectric phase transition [5], piezoelectricity, melting, transmission of sound, certain optical and dielectric properties and certain aspects of the interaction of X-rays, and neutron radiation with solids [6–13].

The classical and quantum theories of the vibrational properties of perfect crystals have been described in comprehensive and good book [13–19]. In both theoretical descriptions, we make use of the following approximation and assumptions, which greatly reduce the complexity of the many-body problem given as follows:

1. Adiabatic approximation.
2. Harmonic approximation.
3. Translational invariance.

As we all know, the solutions of the classical equations are the normal modes which are regarded as plane waves, whereas the quantum mechanical solutions are quasi-particles called as Tamm phonons [20]. The starting point for a theoretical description of the lattice dynamics is the formulation of the crystal Hamiltonian. A crystal represents a highly ordered arrangement of atoms (ions) which is stabilized by Coulomb forces among and between the appositively charged electrons and nuclei. The crystal Hamiltonian is decomposed into the individual Hamiltonians for the electrons $\mathrm{H_e}$, the ions $\mathrm{H_{ion}}$, and the electron–ion interaction $\mathrm{H_{e-ion}}$ [16].

$$\mathrm{H} = \mathrm{H_e} + \mathrm{H_{ion}} + \mathrm{H_{e-ion}}. \tag{3.1}$$

The corresponding Schrodinger equation for lattice dynamics reads

$$\mathrm{H}\Psi = \mathrm{E}\Psi, \tag{3.2}$$

where E and Ψ denote, respectively, the energy and wavefunction of the total vibrational system consisting of electrons and ions. The electronic (ionic) Hamiltonian $\mathrm{H_e}$ ($\mathrm{H_{ion}}$) is the sum of the kinetic energy T_e (T_ion) and the potential energy W_e (W_ion), which arises from electron–electron (ion–ion) interactions, whereas $\mathrm{H_{e-ion}}$ is the total potential generated by all electron–ion interactions given as

$$\mathrm{H_e} = T_\mathrm{e} + W_\mathrm{e-e}, \tag{3.3}$$

$$\mathrm{H_{ion}} = T_\mathrm{ion} + W_\mathrm{ion-ion}, \tag{3.4}$$

$$\mathrm{H_{e-ion}} = \sum_{k,i} W(\boldsymbol{r}_k, \quad \boldsymbol{R}_i), \tag{3.5}$$

where $\boldsymbol{r}_k$ and $\boldsymbol{R}_i$ label the coordinates of the electrons of index k and ions of index i, respectively.

The nucleus and the corresponding core electrons, which are tightly bound in closed shells are regarded as one rigid unit called "ion". The valence electrons interact with each other ($W_\mathrm{e-e}$) and with ions ($\mathrm{W_{e-ion}}$), and contribute to the chemical bonding. Consequently, the ions and the valence electrons are considered as independent constituents of the solid and the mathematical formalism is based on this model assumption. For solid noble gases, it is sufficient to consider only two-body interactions, but the theoretical treatment of crystals, generally, must be viewed as a many-body problem. In ionic crystals, it is difficult to find a proper description for the long-range Coulomb potentials. In covalent crystals, problems arise from the fact that the electronic and ionic motions are coupled with each other since the displacement of an ion from its equilibrium position affects the surrounding electronic wavefunctions of the covalent bonds. However, the motion of ions and electrons is separable due to the fact that the ion masses are much larger than the electron masses[1)]. This is the essence of the adiabatic approximation (Born–Oppenheimer approximation [21]). It neglects the coupling between the electronic and ionic motion, an approximation which reduces the mathematical problem encountered. If we assume that the electrons follow the motion of the ions in an instantaneous manner (adiabatically), the ions are in equilibrium position with respect to the electrons at any time and exposed to a potential field generated by the average motion of the electrons.

As we can see below, the frequencies of ionic vibrations in solids are typically less than 10^{13} s^{-1} (see, e.g., [14]). To estimate the electron time, we note that the energy required to excite electrons in a semiconductor is given by its fundamental band gap, which, in most semiconductors, is of the order of 1–3 eV [15]. Therefore, the frequencies of electronic motion in semiconductors are of the order of 10^{15} s^{-1}. As a result, electrons can respond to ionic motion almost instantaneously, or, in other words, to the electrons, the ions are essentially stationary.

3.2 The Adiabatic and Harmonic Approximations

Below, we briefly reconsider some formal expressions of the main results of the adiabatic approximation. For a detailed discussion of this topic the reader is referred to [14–19]. We start as early with the total Hamiltonian for the crystal using r as a collective symbol for the coordinates of the valence electrons and R similarly for the ionic coordinates. In such case, we have (see also [22])

$$\mathrm{H} = T_{\mathrm{e}} + T_i + \Phi_{\mathrm{ii}}(R) + \Phi_{\mathrm{ee}}(\boldsymbol{r}) + \Phi_{\mathrm{ie}}(\boldsymbol{r}, R), \tag{3.6}$$

where the subscripts i and e denoting ions and valence electrons $T_{\mathrm{e}} = \sum_i \frac{p_i^2}{2m_i}$ and $\mathrm{T}_i = \sum_j \frac{P_j^2}{2M_j}$ are the kinetic energy of the electrons and ions, $\Phi_{\mathrm{ee}}(\boldsymbol{r})=\frac{1}{2}\sum_{i,j}' \frac{\mathrm{e}^2}{|r_i - r_j|}$ and $\Phi_{\mathrm{ii}}(\mathrm{R}) = \frac{1}{2}\sum_{j,j}'' \frac{Z_j Z_{j'} \mathrm{e}^2}{|R_j - R_{j'}|}$ are the electron–electron and ion–ion interactions, respectively, while $\Phi_{\mathrm{ie}}(\boldsymbol{r},R) = -\sum_{j,i} \frac{Z_j \mathrm{e}^2}{|r_i - R_j|}$ is the electron–ion interaction. In all these formulas $\sum'$ means that the summation is only over pairs of indices which are not identical. Let $\mathrm{F}(\vec{\mathrm{r}}, \vec{\mathrm{R}})$ be the eigenfunction of the Hamiltonian (3.6), so that

$$HF(\boldsymbol{r},) = EF(\boldsymbol{r}, R), \tag{3.7}$$

here E is the total energy of the entire system. In the adiabatic approximation, we imagine the ions to be fixed in some configuration and for this particular R we construct the Schrödinger equation for the electrons

$$[T_{\mathrm{e}} + \Phi_{\mathrm{ee}}(r) + \Phi_{\mathrm{ie}}(\boldsymbol{r}, R)]\Xi_{\mathrm{R}}(\boldsymbol{r}) = E_{\mathrm{e}}(R)\Xi_{\mathrm{R}}(\boldsymbol{r}), \tag{3.8}$$

where $\Xi_{\mathrm{R}}(\boldsymbol{r})$ is a wavefunction for the entire system of electrons. We should note also that Ξ_{R} $(\boldsymbol{r})$ is a function of all variables represented by $\boldsymbol{r}$ and contains the ionic coordinates R as parameters. Likewise, the electronic energy $E_{\mathrm{e}}(R)$ depends on the ionic coordinates. We note also that $E_{\mathrm{e}}(R)$ is not just a potential energy, it includes not only the electron–electron and ion–electron interactions but also the kinetic energy of the electronic motion which automatically changes as the coordinates R are changed. Further, we put

$$F(\boldsymbol{r}, R) = \Xi_{\mathrm{R}}(\boldsymbol{r})\Psi(R). \tag{3.9}$$

Substituting (3.9) in (3.7) and making use (3.8), we see that (3.9) is indeed a solution of (3.7). In this procedure, we neglect the terms

$$-\sum_i \frac{\hbar^2}{2M_i}(\Psi_{\mathrm{ion}}\nabla_i^2\Psi_{\mathrm{e}} + 2\nabla_i\Psi_{\mathrm{ion}}\nabla_{\mathrm{i}}\Psi_{\mathrm{e}})$$

(here, M_{i} is the ion mass) connected with kinetic energy of ions, so called the non-adiabatic contribution, which represents the electron–phonon interaction [23, 24]. In this approximation, the ionic wavefunction $\Psi(R)$ is chosen to satisfy

$$[T_{\mathrm{i}} + \Phi_{\mathrm{ii}}(R) + E_{\mathrm{e}}(R)]\Psi(R) = E\Psi(R). \tag{3.10}$$

An elementary discussion of the neglected terms can be found in [17]. Equation (3.10) is an equation for a wave function of the ions alone. The essential point is that

for the ionic motion, an effective potential energy function (see, e.g., [18]).

$$\Phi(R) = \Phi_{\mathrm{ii}}(R) + E_{\mathrm{e}}(R) \tag{3.11}$$

has been introduced to which the electrons contribute through $E_{\mathrm{e}}(R)$. $\Phi(R)$ can be used as a potential energy for discussing the motion of the ions.

The validity of the adiabatic approximation for lattice dynamics has been discussed by several authors [16, 17, 23]. The main result is that the approximation is valid for the lattice dynamics of insulators as well as semiconductors and metals [4, 13, 15].

For simplicity, in further discussion, we restrict ourselves to two-body interactions, which depend on the interatomic distance. We should remember that above conclusion does not automatically follow from the adiabatic approximation, thus implying an additional assumption. As is well known, the crystal energy for a static lattice model, in which each atom (ion) remains fixed at the equilibrium position $\boldsymbol{R}_0$, simply results from the sum of the individual pair potentials $\Phi(\boldsymbol{R}_0 - \boldsymbol{R}_0')$ [1, 13].

$$V = \frac{1}{2} \sum_{\boldsymbol{R}_0, \boldsymbol{R}_0'} \Phi\left(\boldsymbol{R}_0 - \boldsymbol{R}_0'\right). \tag{3.12}$$

Effectively, the crystal potential is a superposition of potentials that arise from attractive and respulsive Coulomb forces (see also [19]). The dynamics of the system is introduced by allowing for small displacements $\mathrm{u}(\boldsymbol{R}_0)$ around the equilibrium sites $\boldsymbol{R}_0$

$$V = \frac{1}{2} \sum_{\boldsymbol{R}_0, \boldsymbol{R}_0'} \Phi\left(\boldsymbol{R}_0 - \boldsymbol{R}_0' + u(\boldsymbol{R}_0) - u(\boldsymbol{R}_0')\right). \tag{3.13}$$

The potential V has a minimum at the equilibrium vector $\widetilde{R_0} = \boldsymbol{R}_0 - \boldsymbol{R}_0'$. If the elongations of the ions remain small against the interatomic distances, the pair potentials can be expanded in a Taylor series around $\widetilde{R_0}$ in powers of the relative displacements $\widetilde{u} = u(\boldsymbol{R}_0) - u(\boldsymbol{R}_0')$ as

$$\Phi(\widetilde{R_0} + \widetilde{u}) = \Phi(\widetilde{R_0}) + \widetilde{u}\nabla\Phi(\widetilde{R_0}) + \frac{1}{2}(\widetilde{u}\nabla)^2\Phi(\widetilde{R_0}) + \frac{1}{3!}(\widetilde{u}\nabla)^3\Phi(\widetilde{R_0}) + \ldots \tag{3.14}$$

The summation over all pair potentials finally leads to the crystal potential as

$$\begin{aligned} V &= \frac{N}{2} \sum_{\boldsymbol{R}_0} \Phi(\widetilde{R_0}) + \frac{1}{2} \sum_{\boldsymbol{R}_0, \boldsymbol{R}_0'} \widetilde{u}\nabla\Phi(\widetilde{R_0}) + \frac{1}{4} \sum_{\boldsymbol{R}_0, \boldsymbol{R}_0'} (\widetilde{u}\nabla)^2\Phi(\widetilde{R_0}) + \ldots \\ &= V_0 + V_1 + V_2 + V_3 \ldots \end{aligned} \tag{3.15}$$

The first term of (3.15) is a constant which represents the binding energy of the crystal. It does not affect the dynamics and can be set equal to zero. The second

term of (3.15) vanishes because restoring forces at the equilibrium positions are zero. In the harmonic approximation, the force on atom is strictly proportional to its displacement relative to its neighbors (we keep the harmonic term, which is quadratic in the displacements), which is nothing other than Hook's law. Further corrections to V, especially the cubic and higher order terms are known as anharmonic terms. The theory of lattice dynamics is much more complicated if anharmonic effects are considered. The additional (cubic and high-order terms) terms can often be treated as a perturbation and are essential for discussion of such properties as thermal expansion and other thermal effects (heat capacity and thermal conductivity). Anharmonicity leads to interactions between different normal modes; the particle picture of this leads to collision between phonons [16]. Thus, we see that the harmonic approximation is a special case of the adiabatic approximation.

3.3 The Anharmonic Crystal

When anharmonicity is present, vibrational excitations of a crystal can no longer be described by noninteracting quasi-particles or phonons [20, 24]. However, provided that the anharmonicity is not too strong, the anharmonicity may be accounted for by perturbation theory, taking the harmonic Hamiltonian for the unperturbed system. Anharmonicity gives rise to the phenomenon of thermal expansion and to interactions between phonons. The latter interactions open up channels for the decay of phonons and lead to an energy shift and damping of phonons. The most important consequences of the harmonic approximations are

1. There is no thermal expansion;
2. The force constants and hence the elastic constants are independent of temperature and pressure;
3. The heat capacity becomes constant at high temperatures;
4. The specific heats measured at constant pressure and constant volume are equal: $c_p = c_v$;
5. Since there are no collisions between phonons, their mean free paths and lifetimes are infinite;
6. As a consequence of (5), a perfectly harmonic crystal would have an infinite thermal conductivity; and
7. The linewidths of the infrared absorption peaks and of the Raman, Mandelstam–Brillouin, and inelastic neutron-scattering peaks are zero for perfectly ordered harmonic crystals.

In real crystals, none of these consequences is satisfied accurately. The theoretical understanding of anharmonic processes in diamond structure of crystals has been discussed by Cowley [25], Klemens [26], Hart et al. [27], Menendez and Cardona [28], and Balkanski et al. [29] from a phenomenological point of view. The theory of Maradudin and Califano [30] takes into account both the harmonic and anharmonic processes including isotope disorder. Ab initio calculations of vibrational properties,

based on the electronic band structure, have been performed by Debernardi [31–33], Lang et al. [34], Steininger et al. [35], and Vast and Baroni [36]. Within the harmonic approximation, the basic mass dependence of a phonon frequency reads $\omega(\boldsymbol{q}, j) \propto \mu^{-1/2}$ [2], where μ is a reduced mass. In weak isotopically disordered systems, the anharmonic processes for localization [37–39] generally not fulfilled, unlike in strong isotopically disordered system like Li_xD_{1-x} [39, 40]. The relative mass difference between isotopes of silicon $\Delta m/\overline{m} \approx 7\%$ [2] is too small to activate local modes, for which case ≈20% is necessary. In LiH_xD_{1-x}, similar estimates as shown in paper [39] is fulfilled and local vibration is directly observed in the Raman spectra of this system (see below).

The line shape of the Raman spectrum of a phonon is an important property directly related to the way that phonon interacts with others through anharmonic coupling, while the harmonic or quasi-harmonic (i.e., including thermal expansion) theory of phonons has provided a good description of phonon branches, and there is a class of phenomena, e.g., the phonon linewidths, that can be explained only by taking into account the anharmonicity of the crystal potential. The thermal shift of a phonon peak in a Raman spectrum, i.e., the change in its frequency when the temperature is raised, is entirely due to anharmonic effects [13], among others the thermal expansion. The anharmonic terms in the phonon Hamiltonian (see below), directly related to the phonon–phonon interaction, lead to the complex self-energies of phonons. A theoretical computation of these self-energies is an essential ingredient for the interpretation of the mechanisms which is determined by asymmetry and linewidths of Raman peaks and their dependence on pressure and temperature [41]. In spite of some attempts to compute anharmonic properties of Raman lines by means of models [25, 26, 31], realistic ab initio calculations have become available only recently [31–34]. The magnitude of twice the imaginary part of the phonon self-energy (2Γ) represents the inverse of the phonon lifetime and is usually responsible for the linewidths of the Raman peak. As shown in papers [31–34], calculations of this quantity by first principles are, in general, in good agreement with experimental data. The real part of the phonon self-energy Δ yields the shift of the Raman peak observed when varying the temperature.

A number of theoretical papers dealing with the anharmonic shift and broadening of Raman lines, as abovementioned, have been published (see also [25]). Our discussion is based on an anharmonic contribution to the Hamiltonian, which can be written as [32]

$$H_{\mathrm{A}} = \sum_{\boldsymbol{q}_1,\boldsymbol{q}_2,\boldsymbol{q}_3} \sum_{j_1,j_2,j_3} V \begin{bmatrix} \boldsymbol{q}_1\boldsymbol{q}_2\boldsymbol{q}_3 \\ j_1 j_2 j_3 \end{bmatrix} A(\boldsymbol{q}_1, j_1) A(\boldsymbol{q}_2, j_2) A(\boldsymbol{q}_3, j_3) \tag{3.16}$$
$$+ \sum_{\boldsymbol{q}_1,\boldsymbol{q}_2,\boldsymbol{q}_3,\boldsymbol{q}_4} \sum_{j_1,j_2,j_3,j_4} V \begin{bmatrix} \boldsymbol{q}_1\boldsymbol{q}_2\boldsymbol{q}_3\boldsymbol{q}_4 \\ j_1 j_2 j_3 j_4 \end{bmatrix} A(\boldsymbol{q}_1, j_1) A(\boldsymbol{q}_2, j_2) A(\boldsymbol{q}_3, j_3) A(\boldsymbol{q}_4, j_4),$$

where the phonon displacement operator A can be written , as usual, in terms of

$$A(\boldsymbol{q}, j) = a^{+}_{-\boldsymbol{q},j} + a_{\boldsymbol{q},j}$$

phonon creation and annihilation operators a^{+} and a, respectively. The anharmonic interaction alter the self-energies of the normal modes. The three lowest order diagrams are shown in Fig. 3.1, and their effect on the optic mode of vibration is to make its frequency and lifetime dependent upon both the temperature and the applied frequency (Ω). The effect of these anharmonic interactions on the Raman allowed optical mode is to change its harmonic frequency $\omega(\mathbf{0}, j)$ to a damped frequency $\omega(\mathbf{0}, j; \Omega)$ given by

$$\omega^2(\mathbf{0}, j; \Omega) = \omega^2(\mathbf{0}, j) + 2\omega(\mathbf{0}, j)\left[\Delta(\mathbf{0}, j; \Omega) + i\Gamma(\mathbf{0}, j; \Omega)\right]. \tag{3.17}$$

The index j labels the three degenerate $\boldsymbol{q} = \mathbf{0}$ phonons. For our crystals, the real and imaginary parts of the self-energy, $\Delta(\mathbf{0}, j; \Omega)$ and $\Gamma(\mathbf{0}, j; \Omega)$, are much smaller than $\omega(\mathbf{0}, j)$ and (3.17) can be rewritten as

$$\omega(\mathbf{0}, j; \Omega) = \omega(\mathbf{0}, j) + \Delta(\mathbf{0}, j; \Omega) + i\Gamma(\mathbf{0}, j; \Omega). \tag{3.18}$$

Thus, the line shape of the Stokes–Raman line becomes

$$I_{\mathrm{s}}(\mathbf{0}, j; \Omega) \infty \frac{\Gamma(\mathbf{0}, j; \Omega)}{\left[\Delta(\mathbf{0}, j) + i\Gamma(\mathbf{0}, j; \Omega) - \Omega\right]^2 + \Gamma^2(\mathbf{0}, j; \Omega)} \cdot \left[n(\Omega) + 1\right], \tag{3.19}$$

where the thermal occupation number is

$$n(\Omega) = \frac{1}{\exp(\hbar\Omega/kT) - 1}. \tag{3.20}$$

The function $\Delta(\mathbf{0}, j; \Omega)$ gives the shift of the peak position. The three lowest order contributions to the diagrammatic expansion of the self-energy yield [25]

$$\Delta(\mathbf{0}, j; \Omega) = \Delta^{(0)} + \frac{12}{\hbar}\sum_{\boldsymbol{q},j'} V\begin{bmatrix}\mathbf{0}\mathbf{0}\boldsymbol{q} - \boldsymbol{q}\\ jjj'j'\end{bmatrix}\left[2n(\boldsymbol{q}, j') + 1\right] - \frac{18\pi}{\hbar^2}\sum_{\boldsymbol{q},\mathrm{j}_1\mathrm{j}_2}\left|V\begin{bmatrix}\mathbf{0}\boldsymbol{q} - \boldsymbol{q}\\ jj_1j_2\end{bmatrix}\right|^2$$
$$\times\left[n(\boldsymbol{q}, j_1) + n(-\boldsymbol{q}, j_2) + 1\right]\cdot x\left[\frac{1}{\omega(\boldsymbol{q}, j_1) + \omega(\boldsymbol{q}, j_2) - \Omega}\right]_{\mathrm{P}}, \tag{3.21}$$

with $\mathrm{n}(\boldsymbol{q}, j) = n(\omega(\boldsymbol{q}, j))$ given in (3.20).

The first term in (3.21) is the thermal expansion contribution to the line shift. It may be written as (see also [42])

$$\Delta^{(0)} = \omega(\mathbf{0}, j)\exp\left[-3\gamma(\mathbf{0}, j)\int_0^{\mathrm{T}}\alpha(T')\mathrm{d}T'\right], \tag{3.22}$$

where $\alpha(T)$ is the coefficient of linear thermal expansion and $\gamma(\mathbf{0}, j)$ is the Grüneisen parameter for the optical phonon mode. This term as well as the fourth-order

Fig. 3.1 Feynman diagrams of the leading order terms in the real part of the phonon self-energy; **a** the contribution of the thermal expansion $\Delta^{(0)}$; **b** the third-order contribution $\Delta^{(3)}$; **c** the fourth-order contribution $\Delta^{(4)}$ (after [1])

contribution to $\Delta(\mathbf{0}, j; \Omega)$ (the second term in (3.21)) does not depend on Ω. The broadening of the Raman line is given by

$$\Gamma(\mathbf{0}, j; \Omega) = \frac{18\pi}{\hbar^2} \sum_{\boldsymbol{q} j_1 j_2} \left| V \begin{bmatrix} \mathbf{0}\boldsymbol{q} - \boldsymbol{q} \\ j j_1 j_2 \end{bmatrix} \right|^2 \times \left[n(\boldsymbol{q}, j_1) + n(-\boldsymbol{q}, j_2) + 1 \right] \delta(\omega(\boldsymbol{q}, j_1) + \omega(-\boldsymbol{q}, j_2) - \Omega). \tag{3.23}$$

The last terms in (3.21) and (3.23) are the third-order contributions to the shift and width, respectively. They are related by a Kramers–Kronig relation (see, e.g., [43] and references therein). The physical meaning of (3.23) is quite transparent and owing to the anharmonic interactions, the optical Raman phonon decays in a combination of two phonons $\omega(\boldsymbol{q}, j_1)$ and $\omega(-vecq, j_2)$ satisfying $\omega(\boldsymbol{q}, j_1) + \omega(-\boldsymbol{q}, j_2) = \Omega$. If the matrix elements in (3.23) are assumed to be constant, one obtains, for $\Gamma(\Omega)$, a value proportional to the two-phonon density of states when $T \to 0$,

$$\Gamma(\Omega) \propto \frac{1}{V} \sum_{\boldsymbol{q}, j_1 j_2} \delta(\omega(\boldsymbol{q}, j_1) + \omega(-\boldsymbol{q}, j_2) - \Omega) \equiv \rho^2(\Omega). \tag{3.24}$$

The last equation implies that one should expect a large $\Gamma(\Omega)$ whenever the frequency ω_0 of the optical mode happens to coincide with a peak in the two-phonon density of states. The matrix elements which determine the width $\Gamma(\Omega)$ are actually given by

$$V \begin{bmatrix} \mathbf{0}\boldsymbol{q} - \boldsymbol{q} \\ j j_1 j_2 \end{bmatrix} = \frac{1}{6} \left[\frac{\hbar^3}{8NM^3 \omega_0 \omega(\boldsymbol{q}, j_1) \omega(-\boldsymbol{q}, j_2)} \right]^{1/2} x \cdot \sum_{l', l^{prime'}} \sum_{k, k', k''} \sum_{\alpha\beta\gamma} \phi_{\alpha\beta\gamma} \begin{bmatrix} 0 l' l'' \\ k k' k'' \end{bmatrix} \times e_\alpha(k \mid \mathbf{0}, j) e_\beta(k' \mid \boldsymbol{q}, j_1) e_\gamma(k'' \mid -\boldsymbol{q}, j_2) e^{\mathrm{i}} \boldsymbol{q} [\boldsymbol{R}(\mathrm{l}') - \boldsymbol{R}(\mathrm{l}'')], \tag{3.25}$$

where

$$\Phi_{\alpha\beta\gamma} \begin{bmatrix} 0 l' l'' \\ k k' k'' \end{bmatrix}$$

is the third derivative of the interatomic potential with respect to displacements along directions of the Cartesian coordinates α, β, and γ of the ions

$$\begin{bmatrix} 0 \\ k \end{bmatrix} ts, \quad \begin{bmatrix} l' \\ k' \end{bmatrix}, \quad \begin{bmatrix} l'' \\ k'' \end{bmatrix},$$

respectively. The index l labels the primitive cells, while k labels the position of the two atoms (ions) within primitive cell. The vectors $e(k \mid \boldsymbol{q}, j)$ are the eigenvectors of the harmonic approximation problem. M is the atomic mass and N is the number of cells in the crystal. Taking into account (3.25) and (3.23) one can obtain (see also [28])

$$\Gamma(\Omega) \propto 1/Ma^2. \tag{3.26}$$

Below we follow very close to the result of papers by Debernardi [31–33]. If we assume as above that Δ and Γ are small compared with the harmonic frequency ω_0(0 = LO, TO), the position of the Raman peak Ω is given by [25]

$$\Omega = \omega_0 + \Delta_0(\Omega), \tag{3.27}$$

which can be solved self-consistently. In the following, to lighten the notation, we will drop the branch index 0 in the real and imaginary parts of the phonon self-energy where there is no possibility of confusion. Debernardi deals only with the self-energies of phonons at the Γ-point, since phonons at other points of the Brillouin zone are not optically active. To the lowest nonvanishing order in the cubic and quartic anharmonic force constants, the real part of the phonon self-energy is given by three contributions as

$$\Delta(\omega) = \Delta^{(0)} + \Delta^{(3)}(\omega) + \Delta^{(4)}. \tag{3.28}$$

The Feynman diagrams (Fig. 3.1) corresponding to these terms are the same as in Cowley [25]. The first term on the right-hand side(rhs) of (3.28) represents the change in frequency due to the thermal expansion of the lattice [42] given by

$$\Delta^{(0)} = \omega_0 \left\{ \exp\left[-3\gamma_0 \int_0^T \alpha(T')\mathrm{d}T' \right] - 1 \right\}, \tag{3.29}$$

where γ_0 is the mode Grüneisen parameter and $\alpha(T)$ is the linear thermal expansion coefficient at temperature T. The last term in the rhs of (3.28) can be expressed by

$$\Delta^{(4)} = \frac{12}{\hbar N} \sum_{\boldsymbol{q}\mathrm{j}} \frac{\partial^4 E_{\mathrm{tot}}}{\partial u_0^2(0)\partial u_{\mathrm{j}}(\boldsymbol{q})\partial u_{\mathrm{j}}(-\boldsymbol{q})} u_0^2(0) u_{\mathrm{j}}(\boldsymbol{q}) u_{\mathrm{j}}(-\boldsymbol{q})(2n_{\mathrm{j}} + 1), \tag{3.30}$$

where N is the number of unit cells in crystal, $u_{\mathrm{j}}(\boldsymbol{q})$ are the atomic displacements pertaining to a phonon in the j-branch of wave vector $\boldsymbol{q}$ and the $\mathrm{n_j}$'s are the thermal

occupation numbers of the phonon modes with frequencies $\omega_{\mathrm{j}}(\boldsymbol{q})$. $\Delta^{(4)}$ represents the process of scattering of a zone center (Γ - point) O-phonon by a phonon of wave vector $\boldsymbol{q}$. The second term in the rhs in (3.28) can be obtained through the Hilbert transform of $\Gamma_0(\omega)$,

$$\Delta^{(3)}(\omega) = -\frac{2}{\pi} P \int_0^\infty \frac{\omega' \Gamma(\omega')}{(\omega'^2 - \omega^2)} \mathrm{d}\omega', \tag{3.31}$$

where P means the Cauchy principal part of the integral. In the following, we will refer to $\Delta^{(3)}$ as the third term.

To the leading order in the expansion versus phonon displacement, the imaginary part of the self-energy zone-center optical modes reads

$$\begin{aligned}\Gamma_0(\omega) = \frac{\pi}{2\hbar^2} \sum_{\boldsymbol{q},\mathrm{j}_1 \mathrm{j}_2} & \left| \frac{\partial^3 E_{\mathrm{tot}}}{\partial u_0(0) \partial u_{\mathrm{j}_1}(\boldsymbol{q}) \partial u_{\mathrm{j}_2}(-\boldsymbol{q})} u_0(0) u_{\mathrm{j}_1}(\boldsymbol{q}) u_{\mathrm{j}_2}(-\boldsymbol{q}) \right| \\ & \times \left[(n_{\mathrm{j}_1} + n_{\mathrm{j}_2} + 1) \delta(\omega - \omega_{\mathrm{j}_1}(\boldsymbol{q}) - \omega_{\mathrm{j}_2}(-\boldsymbol{q})) \right. \\ & \left. + 2(n_{\mathrm{j}_1} + n_{\mathrm{j}_2}) \delta(\omega + \omega_{\mathrm{j}_1}(\boldsymbol{q}) - \omega_{\mathrm{j}_2}(\boldsymbol{q})) \right].\end{aligned} \tag{3.32}$$

At zero temperature, $\Gamma(\omega)$ represents the process of decay of the optical phonon at the zone center into two phonons (of opposite $\boldsymbol{q}$ for wave vector conservation) whose frequencies sum up to ω, whereas at finite temperature also other three phonon processes can contribute to $\Gamma(\omega)$ [32]. The central ingredient to determine this quantity is the square modulus of the third derivative of the total energy with respect to the phonon displacement (details see [38]). If the Raman peak is symmetric, the Raman line shape [36] can be assumed to be Lorentzian and its full width at half maximum(FWHM) equals $2\Gamma(\Omega)$ (Fig. 3.2).

Figure 41 of [1] have displayed the Debernardi results [33] on the temperature dependence of $\Delta(\Omega)$ for the TO and LO phonons in GaAs. In the upper part of figure there are present the temperature dependence of different contributions to $\Delta(\Omega)$, while in the lower part the total shift Δ is compared with available experimental data [22]. Good agreement with experiment is found.

According to Lang et al. [34], the width due to spontaneous decay at zero temperature have been found to be 0.97 cm^{-1} for C, 1.44 cm^{-1} for Si, and 0.69 cm^{-1} for Ge, while the corresponding values of [31] are 1.01 cm^{-1}, 1.48 cm^{-1}, and 0.67 cm^{-1}, respectively. In Fig. 42 of [1] the results of Lang et al. [34] for the temperature dependence of the Raman linewidths of diamond, silicon, and germanium are compared with experimental data (for details see [1] and references therein). Except for diamond, where the experimental data shows a large scatter and are consistently larger than the theoretical ones, the agreement between theory and experiment is quite satisfactory. As will be shown below, anharmonic decay is the main contribution to the linewidth of Raman-active modes once isotopic and other inhomogeneous broadening contributions are subtracted [44].

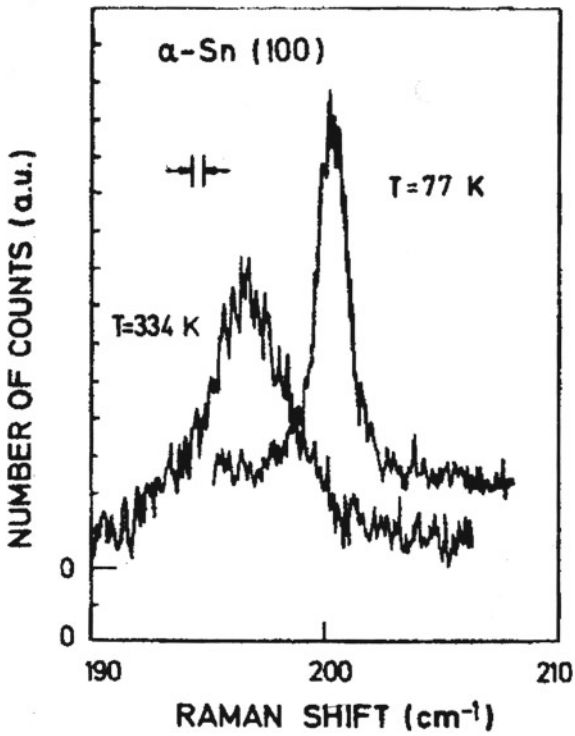

Fig. 3.2 Two typical first-order Raman spectra for α-Sn at different temperatures (after[28])

Thus, the influence of anharmonicity is in general, the greater the weaker the binding of the atoms to the crystal and the smaller their masses. The ratio of the cohesive energy [45] to zero-point energy might be regarded as a characteristic quantity [7].

3.4 Disordered Crystals

As is well known, two sets of quantities determine the phonon properties, namely, the masses of the atoms and the force constants which are describing the attractive and repulsive Coulomb forces between the atoms. It is insightful that only a perfect elemental, i.e., monoatomic crystal that is isotopically pure represents the ideal ordered case. We should remind that the structural defects such as impurity atoms, interstitials, dislocation, and others are neglected in our approximation. It is clear that a disordered crystal is characterized either by fluctuations of the masses or by the force constants or both. Much attention has been paid in the past investigations to alloys which represent mixed crystals whose lattice or sublattices is/are varied with respect to the stoichiometric composition of the corresponding elements (see, e.g.,

[46, 47]. For example, in systems of $Si_{1-x}Ge_x$, $CdS_{1-x}Se_x$, etc. disorder is present with respect to the masses and force constant (see also [48]). In isotope-mixed crystals [1, 2], the isotopic abundance are varied rather than the concentration of chemical elements as in the case of alloys. Many natural elements consist of several stable isotopes (see, e.g., [49]. The type of disorder inherent in the isotopically disordered crystals is qualitatively different from that of alloys of chemical elements due to the following reasons: (1) The variation of the ion masses represents the only type of disorder in isotopically substituted crystals isotopic mass disorder [50]. (2)There is almost no electronic disorder since the number of core and valence electrons is equal and thus the chemical bonds are nearly identical between various isotopes [45]. (3) The magnitude of isotopic mass disorder is small in the case of the elements of semiconductor crystals and large in the case of insulators [39, 40]. In last case, it has a direct experimental evidence [39]. Indicated facts make the isotopically controlled crystals ideal for test systems for theories treating substitutional isotope disorder. The structure of systems with substitutional disorder such as isotopically disordered crystals/alloys is known, but still the actual distribution of isotopes in the system is not known. The lattice site is assumed to be occupied randomly (for details see also [51]). Modern theories have been developed that find a configurational average of a disordered system, allowing predictions of physical observables. As well known, the method of Green's functions represents a mathematical tool which can be applied to calculate macroscopic properties in crystals (see, e.g., [52]). To first approximation, a disordered crystal can be described by the model of virtual crystal, which is conceived as a perfect crystal consisting of atoms, whose masses represent the average value of the constituents. The virtual crystal approximation(VCA) represents a crude approximation, which cannot describe isotope disorder effects. In order to describe isotope-disorder-induced effects in semiconductors, weak disorder, it usually uses the CPA [2, 53].

3.4.1 Model of Virtual Crystal Approximation

As we all know, only four elements of the periodic table of Mendelejev have just one stable isotope [49] (^{27}Al, ^{31}P, ^{75}I, and ^{127}As). All others elements have at least two stable isotopes and occur as isotopic mixtures with naturally fixed composition. Based on the assumption that the isotopes are distributed at random, it is plausible to consider a virtual crystal, whose constituents reflect the weighted average of all atoms. Therefore, the VCA uses the average of the masses and force constants [46]

$$\langle m \rangle = \boldsymbol{m} \sum_i c_i m_i, \tag{3.33}$$

$$\langle \Phi \rangle = \sum_i c_i c_j \Phi_{ij}, \tag{3.34}$$

where c_i and m_i describe the concentration and mass of the isotope i, respectively, and c_i, c_j and Φ_{ij} the concentration and force constants, respectively (see also [53]). It is convenient to use the average virtual crystal as the unperturbated crystal when applying perturbation theory. Within VCA, the first-order perturbation terms vanish. The lowest order nonvanishing terms are of second order (for details see [46, 53]).

3.4.2 Model of Coherent Potential Approximation

The coherent potential approximation(CPA) has been developed as a mean-field theory for the calculation of macroscopic properties of disordered systems [54, 55]. Its applicability to problems related to electronic and vibrionic properties of materials with substitutional disorder has been investigated in many papers (see, e.g., [56–58]), whereas mostly electronic properties have been addressed in these publications, the formulation for phonons, which was developed by Taylor in 1967 [55, 56], and has been applied in several studies [53, 59–62]. The basic idea of the CPA is that the crystal Hamiltonian, though an a prior unknown function, can be approximated in a self-consistent fashion. The assumption that the isotopes are distributed randomly requires, in principle, averaging over a large number of possible configurations. Alternatively, an effective medium is conceived, represented by an effective Hamiltonian whose properties are assumed to be similar to that of configuration average if the CPA Hamiltonian is to be meaningful. The perturbation relevant to a given configuration is determined by the mass fluctuations relative to a reference mass of the effective medium that we choose to be the mass $\overline{m}$ of the virtual crystal. In contrast to the VCA, the CPA considers the interaction of a single impurity with its vicinity. From this it is clear that isotopic mass disorder acts as an appropriate test system for the CPA since it represents the simplest form of substitutional disorder (see also [51]). Due to the assumption that the force constants (i.e., the interatomic potentials) are not modified in semiconductors by isotopic substitution, the relative task is solved very simple (see, however, [63]).

In tetrahedrally coordinated semiconductors, the second-order vibrational Raman spectrum for parallel incident and scattered photon polarization follows closely the phonon overtone density of states. Therefore, the first approach is to evaluate the effects of isotopic disorder on the overtone density of states by means of the coherent potential approximation (CPA) [55, 64] and compare the results of this calculations directly with the second-order Raman spectra. Using CPA, as was indicated above, the usual approximations inherent in this method are made, mainly that only the effects of differences in isotopic masses are taken into account (not force constant changes), and the isotopes are randomly distributed on the lattice (not clustered). It should be noted that Fuchs and coworkers [61] found that self-energy corrections due to isotopic disorder for certain phonon may be quite large, thus a multiple scattering formalism such as the CPA is expected to provide a more accurate estimation of such corrections than lowest order perturbation theory. Hass and others [53], Fuchs and coworkers [61] treat scattering in the CPA with respect to the virtual crystal

approximation (VCA), defined to be a perfect diamond-structured crystal with each site occupied by an atom of atomic mass equal to the concentration-weighted average isotopic mass. In the VCA, the phonon frequencies are given by $\omega_{\boldsymbol{q},\mathrm{j}}$, where $\boldsymbol{q}$ is the wave vector and j is the branch index. Scattering is treated by considering an effective medium characterized by the dimensionless "self-energy" $\tilde{\varepsilon}(\omega)$ with respect to the VCA. In this condition, the VCA DOS is equal (normalized to unity)

$$g_{\mathrm{VCA}}(\omega) = (6N)^{-1} \sum_{\boldsymbol{q},\mathrm{j}} \delta(\omega - \omega_{\boldsymbol{q}\mathrm{j}}), \tag{3.35}$$

where N is the number of unit cells in a normalized volume. As mentioned above, this medium is characterized by a dimensionless self-energy $\tilde{\varepsilon}(\omega)$, which represents a complex "mass defect" relative to $\bar{\mathrm{M}}$ (in the case of diamond $\bar{\mathrm{M}} = 12 + \mathrm{x}$) at frequency ω. Self-consistency is imposed by the condition that the average scattering from a single site in the effective medium vanishes and it is convenient to express this condition as [64]

$$\bar{M}\tilde{\varepsilon}(\omega) = \frac{x(1-x)(\Delta M)^2\omega^2 \boldsymbol{F}(\omega^2)}{1 + \omega^2\left[(1-2x)\Delta M + \boldsymbol{M}\tilde{\varepsilon}(\omega)\right] F(\omega^2)}, \tag{3.36}$$

where ΔM is the 1-amu mass difference (between ^{12}C and ^{13}C) and $\boldsymbol{F}(\omega^2)$ is the site Green's function (see [52]) given as

$$\boldsymbol{F}(\omega^2) = (6N\bar{M})^{-1} \sum_{\boldsymbol{q},\mathrm{j}} G_{\mathrm{j}}(\boldsymbol{q},\omega) = \frac{1}{\bar{M}} \int_0^\infty \frac{g_{\mathrm{VCA}}(\eta)\mathrm{d}\eta}{\omega^2\left[1 - \tilde{\varepsilon}(\omega)\right] - \eta^2}. \tag{3.37}$$

The second term of (3.37) follows from the definition of the $\boldsymbol{q}$-space Green's function as

$$G_{\mathrm{j}}(\boldsymbol{q},\omega^2) = \frac{1}{\omega^2\left[1 - \tilde{\varepsilon}(\omega)\right] - (\omega_{\boldsymbol{q}\mathrm{j}})^2}, \tag{3.38}$$

whose negative imaginary part defines the CPA spectral function. As mentioned above, with matrix element effects neglected this spectral function is proportional to the Raman- and neutron-scattering cross section [46]. In absence of disorder, -$\mathrm{Im}G_{\mathrm{j}}(\boldsymbol{q},\omega^2)$ reduces to a δ-function at $\omega_{\boldsymbol{q}\mathrm{j}}$. To a good approximation [61], the real and imaginary parts of $\tilde{\varepsilon}(\omega)$ describe shift the spectral peak to a frequency $\tilde{\omega}_{\boldsymbol{q}\mathrm{j}} = \omega_{\boldsymbol{q}\mathrm{j}}[1 - Re\tilde{\varepsilon}(\omega_{\boldsymbol{q}\mathrm{j}})]^{-1/2}$ and broaden it to a full width at half maximum (FWHM) of $-\tilde{\omega}_{\boldsymbol{q}\mathrm{j}}\mathrm{Im}\tilde{\varepsilon}(\tilde{\omega}_{\boldsymbol{q}\mathrm{j}})$. The shift and broadening are related by the Kramers–Kronig relation as

$$\mathrm{Re}\,\tilde{\varepsilon}(\omega) = \frac{2}{\pi} \int_0^\infty \frac{\eta \mathrm{Im}[\tilde{\varepsilon}(\eta)]\mathrm{d}\eta}{\eta^2 - \omega^2}. \tag{3.39}$$

The normalized one-phonon CPA DOS is given by [55, 61]

$$g(\omega) = -\frac{2}{\pi\omega}\int_0^\infty g_{\mathrm{VCA}}(\eta)\mathrm{d}\eta \mathrm{Im}\left[\frac{\eta^2}{\omega^2[1-\tilde{\varepsilon}(\omega)]-\eta^2}\right]. \tag{3.40}$$

The CPA self-energy $\tilde{\varepsilon}(\omega)$ is formally independent of $\boldsymbol{q}$. An implicit $\boldsymbol{q}$ dependence does arise, however, through (3.38). The lack of an explicit $\boldsymbol{q}-$ dependence is a consequence of the single-site nature of the CPA. In the limits of weak scattering ($\Delta M/\bar{M} \ll 1$) and/or dilute concentrations, the CPA self-energy becomes exact and the $\boldsymbol{q}$ independence is rigorous [64]. In other regimes, the CPA is a highly successful interpolation scheme and $\boldsymbol{q}$- dependent corrections should only appear at a relatively high order in the scattering strength.

Equation (3.36) in the weak scattering reduces to

$$\bar{M}\tilde{\varepsilon}(\omega) = x(1-x)(\Delta M)^2\omega^2 F_{\mathrm{VCA}}(\omega^2), \tag{3.41}$$

where $\boldsymbol{F}_{\mathrm{VCA}}(\omega^2)$ is the VCA site Green's function obtained by setting $\tilde{\varepsilon}(\omega) = 0$ in (3.37). Using the fact that -Im$\mathrm{F}_{\mathrm{VCA}}(\omega^2) = \pi g_{\mathrm{VCA}}(\omega)/(2\bar{M}\omega)$, we obtain the perturbative "golden-rule" expression for the FWHM broadening as

$$-\,\omega\,\mathrm{Im}\,\tilde{\varepsilon}(\omega) = \frac{\pi}{2}x(1-x)\left[\frac{\Delta M}{\boldsymbol{M}}\right]^2\omega^2 g_{\mathrm{VCA}}(\omega). \tag{3.42}$$

The full CPA (3.36) and (3.37) are easily solved numerically by an iterative process beginning with VCA DOS (for details see Hass et al. [53]).

3.5 The Dispersion Relation

Certain bulk properties of a crystal, such as the specific heat (see also above), are determined by an average over the whole phonon spectrum [14]. This means that while the specific heat can be predicted when the $\omega_{\mathrm{j}}(\boldsymbol{q})$ relation is known, the converse does not hold. Generally, it is through the interaction of radiation with the crystal that its dynamical properties can be most effectively investigated. If we wish to obtain detailed information about lattice vibrations for which the value of $\boldsymbol{q}$ is anywhere in the Brillouin zone, we must study their interaction with radiation of wavelength comparable with interatomic distances and having an energy quantum $\hbar\omega$ comparable with phonon energies. X-rays satisfy the first of these conditions, but not the second since $\hbar\omega \sim 10^4\,\mathrm{eV}$ for X-rays while $\hbar\omega_{\mathrm{j}}(\boldsymbol{q}) \sim 0.01\,\mathrm{eV}$ for phonons. However, a beam of neutrons having a velocity $\mathrm{v_n} = 2\,\mathrm{kms}^{-1}$ has a wave vector $\boldsymbol{k} = \mathrm{m}_n\boldsymbol{v}_n/\hbar$ or wavelength $2\pi/k = 2.0\,\text{Å}$ and the energy quantum is $\frac{1}{2}\mathrm{m}_n\mathrm{v}_n^2 = 0.02\,\mathrm{eV}$ (see, e.g., [16]). The scattering of a beam of monoenergetic neutrons of about this wavelength provides the most powerful method of studying lattice vibrations and measuring phonon energies. Such experiments are experiments in neutron spectroscopy [1, 65] rather than in neutron diffraction since they involve the measurement of the change

in wavelength (or energy, or velocity) of the scattered neutrons and not merely the intensity of scattering in a particular direction.

As is well known, when certain approximations are made, the dynamics of a three-dimensional crystal is not a particularly difficult subject, but it is a very algebraic one with a profusion of indices and suffices and it is easy to lose one's way among them. Many of the essential features can be brought out by considering a one-dimensional crystal or linear chain (see, e.g., [14, 16, 50]). The simplest type of one-dimensional vibrating system with many degrees of freedom is a stretched wire with fixed ends. The normal modes of vibration of this system (constrained to move in a plane) are standing waves with an integral number of half waves fitted into the length of the wire. The amplitude of each such standing wave is a normal coordinate of the system and the total energy of the vibrating system is the sum of the energies of the different modes of vibrations simultaneously present. The frequency of each mode of vibration is inversely proportional to the corresponding wavelength, i.e., proportional to wave number. We begin with the simplest type of crystal, one which contains only one atom of mass m in a unit cell of dimension a (Fig. 3.23). We assume further that forces between the atoms extend only to nearest neighbors, and that the crystal is harmonic in the sense mentioned above, so we represent the interaction between nearest neighbors by a spring of force constant f (see Fig. 3.3). We take the vibrations to be longitudinal, that is the displacement of an atom is along the length of the chain. Each atom is identified by an index l so that its equilibrium position measured from some convenient origin is $r_l = la$, and l can assume the values 0, 1, 2, ..., N-1. Taking the displacement of the l's atom to be u_l, its equation of motion is

$$m\frac{\partial^2 u_l}{\partial t^2} = f(u_{l+1} - u_l + u_{l-1} - u_l). \tag{3.43}$$

Guided by the result which applies for a vibrating wire, we assume that there is a solution of the form

$$u_l = (Nm)^{-1/2}|B(q)|\cos[qr_l - \omega(q)t + \alpha(q)]. \tag{3.44}$$

The factor $(Nm)^{-1/2}$ is convenient for normalizing purposes. We shall sometimes ignore its presence in referring to $|B(q)|$ as the amplitude of the wave. Correspondingly, q, $\omega(q)$, and $\alpha(q)$ are obviously the wave number (wave vector), (angular) frequency, and initial phase of a wave traveling to the right. $|B(q)|$ and $\alpha(q)$ will be determined by the initial conditions. It is often convenient (see [44]) to introduce a complex amplitude

$$B(q) = |B(q)|\exp[i\alpha(q)]. \tag{3.45}$$

On substituting (3.44) in (3.43), one finds that the equation is satisfied provided that

$$m\omega^2(q) = 2f(1 - \cos qa) = 4f\sin^2\left(\frac{qa}{2}\right). \tag{3.46}$$

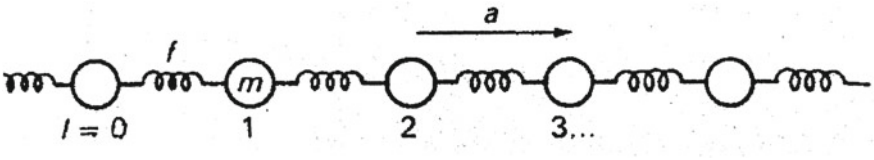

Fig. 3.3 A one-dimensional crystal or linear chain (after [1])

This relation between ω and q is called the dispersion relation or dispersion curve. For modes of vibration of long wavelength, i.e., small value of q, the result reduces to

$$\omega(q) = qa(f/m)^{1/2}, \tag{3.47}$$

which is the same result as for a wire with tension fa and linear density m/a (see, for example, [1] and references therein). Since the wavelength is large compared with the lattice spacing in this limit, a disturbance of this sort must clearly propagate like a longitudinal compressional wave in a continuum and the velocity defined by the initial slope dω/dq is thus the velocity of sound. The dispersion relation is not linear for larger values of q. The frequency rises to a maximum of $2(f/m)^{1/2}$ at $q = \pi/a$ and falls to zero at $q = 2\pi/a$, in fact $\omega(q)$ is periodic with periodicity 2π/a, which we recognize as the dimension of the one-dimensional reciprocal lattice [16, 18].

Further, we suppose that our sample has a structure based on two different kinds of atom, e.g., NaCl. The crystallographic unit cell now contains two different atoms. In the model of linear lattice this can be represented by two different masses, for example, M_1 and M_2 and $M_1 \rangle M_2$. Now, we must assume different displacements for different atom types, and we have next equations (nearest-neighbor interaction) given as

$$\begin{aligned} M_1 H u_{\mathrm{s}} &= C_1 \left(v_{\mathrm{s}+1/2} + v_{\mathrm{s}-1/2} - 2u_{\mathrm{s}}\right), \\ M_2 v_{\mathrm{s}+1/2} &= C_1 \left(u_{\mathrm{s}+1} + u_{\mathrm{s}} - 2v_{\mathrm{s}+1/2}\right). \end{aligned} \tag{3.48}$$

If we assume as before u_{s} = ue^i (ksa − ωt) and

$$v_{\mathrm{s}+1/2} = ve^i \left[\mathrm{k(s+1/2)a} - \omega\mathrm{t}\right], \tag{3.49}$$

then we obtain the following dispersion relation with nearest - neighbor interaction:

$$M_1 M_2 \omega^4 - 2C_1(M_1 + M_2)\omega^2 + 4C_1^2 \sin^2 \frac{1}{2} ka = 0. \tag{3.50}$$

The latter is readily solved to give

$$\omega^2 = C_1\left(\frac{M_1+M_2}{M_1M_2}\right) \pm \left[C_1^2\left(\frac{M_1+M_2}{M_1M_2}\right)^2 - \frac{4C_1}{M_1M_2}\sin^2\frac{1}{2}ka\right]^{1/2},$$

$$\text{or} \quad \omega^2 = A \pm \left(A^2 - B\sin^2\frac{1}{2}ka\right)^{1/2}. \tag{3.51}$$

In (3.49) and (3.51), a is lattice constant. There are now two solutions for ω^2, providing two distinctly separate groups of vibrational modes. The first group, associated with ω_-^2, contains the acoustic modes (see Fig. 3.4). The second group arises with ω_+^2 and contains the optical modes; these correspond to the movement of the different atom sorts in opposite directions, it is a contra - motion, whereas the acoustic behavior is motion in unison. The name optical modes arises because in ionic crystals like NaCl, they cause an electric polarization and can, therefore, be excited by light, which is a result strongly absorbed. However, these optical modes occur in all structures with two or more different atoms. For small ka from (3.51), we have

$$\omega^2 \simeq 2C_1\left(\frac{M_1+M_2}{M_1M_2}\right) \tag{3.52}$$

$$\text{and} \quad \omega^2 \simeq \frac{C_1}{2(M_1+M_2)}k^2a^2. \tag{3.53}$$

Taking into account that $k_{max} = \pm\pi/a$, where a is a period of the crystal lattice, i.e., k_{max} respond the border of the fist Brillouin zone (see also Fig. 3.4), we get

$$\omega^2 = \frac{2C_1}{M_1} \quad \text{and} \quad \omega^2 = \frac{2C_1}{M_2}. \tag{3.54}$$

We repeat that formula (3.52) that describes the optical branch of vibrations, whereas (3.53)-acoustical branch of vibrations. Usually, the last formula is written in this way

$$\omega = \sqrt{\frac{\alpha}{M}}, \tag{3.55}$$

where α is the so-called force constant. From the preceding relation, it is clear that in solids the isotope effect manifests in vibration spectrum, which naturally depends on the symmetry of vibrations.

When a thermal neutron impinges on a solid material, it may either be absorbed or scattered in various ways, or, more usually, it may pass through the solid without change. The cross section for neutron absorption varies very considerably from one element to another (see, for example, [66]), from 2.4×10^5 barn for ^{157}Gd to less than 2×10^{-4} barn for ^{16}O (1 barn = 10^{-24} cm^2; these cross sections are appropriate for neutrons of energy 0.025 eV, or de Broglie wavelength 1.8 Å) [65]. Elements with high absorption cross sections are more difficult, perhaps impossible in some cases, to study by neutron scattering techniques, but this is an experimental restriction for only a few isotopes of relatively few elements. From the present viewpoint, of course,

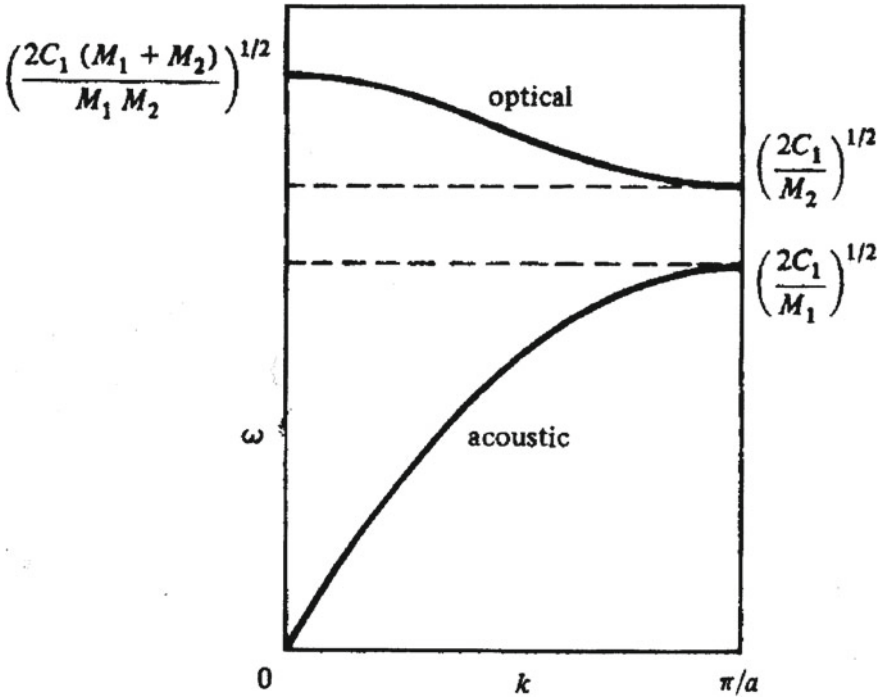

Fig. 3.4 Optical and acoustic modes. The optical modes lie at higher frequencies and show less dispersion than the acoustic modes (for details see text)

the scattering processes are of prime importance, and we shall now consider these a little more closely. The essential features of the calculation of the cross section are as follows [22]:

1. Since the de Broglie wavelength of a thermal neutron is much greater (approximately $\sim 10^5$) than the size of the nucleus, only s-wave scattering from the nucleus is important [67], and this is isotropic and independent of neutron energy.
2. The interaction between the neutron and the ith nucleus is represented by the Fermi pseudopotential, which is a δ-function given as

$$t_{\mathrm{i}}(\boldsymbol{r}) = (2\pi\hbar^2 b_{\mathrm{i}}/m)\delta(\boldsymbol{r} - \boldsymbol{r}_{\mathrm{i}}), \tag{3.56}$$

   where m is the neutron mass and b_i is the so-called bound atom scattering length. The possibility of expressing the potential in this simple form depends upon the assumption that the scattering by a single nucleus is very weak.
3. The scattering from the entire assembly of nuclei in the solid is then obtained by summing over the scattering from individual nuclei with due regard to the relative phases of these scattered waves. In general, this will clearly depend on a

complicated correlation function describing the relative positions of all nuclei as a function of time [44].

4. The scattering length b_i may not be the same for all nuclei of the same element, since different isotopes will scatter differently, and also, if the nuclear spin is nonzero, the scattering amplitude will depend on whether the neutron and nuclear spins are parallel or antiparallel (for details see [68]). Normally, these nuclei having different scattering length will be distributed randomly throughout the crystal, and in this case, it is convenient to split up the total scattering cross section σ_t into two parts, a *coherent* σ_{coh} and an *incoherent* σ_{inc} part. The precise definitions of these cross sections are given in detail in [65, 67], but the essential points may be understood from the following simple discussion. Let us refer to the very complicated motions of the nuclei in the crystal by a symbolic wave function Ψ. Then, the total scattering cross section may be written as

$$\sigma_t = \Psi \langle b_i b_j \rangle, \tag{3.57}$$

where $\langle ... \rangle$ denotes an average overall pairs of nuclei i, j. If we denote those terms in which $i = j$ by the subscript s (self, or single nucleus) and terms $i \neq j$ by subscript d (interference, or distinct nuclei), then

$$\sigma_t = \Psi_s \langle b_i^2 \rangle + \Psi_d \langle b_i \rangle^2 = \Psi_s \left\{ \langle b_i^2 \rangle - \langle b_i \rangle^2 \right\} + \{\Psi_s + \Psi_d\} \langle b_i \rangle^2 = \sigma_{inc} + \sigma_{coh}. \tag{3.58}$$

We note that the coherent cross section depends on the square of the mean scattering length, and contains interference and self components of our symbolic wave function. The incoherent cross section, on the other hand, depends only on the scattering from individual nuclei (no interference effects), and is zero if all the b_i are equal. The importance of this division of σ_t lies in the fact that Ψ contains two delta functions.

$$\delta \left[E_0 - E_1 \mp \sum_l h\nu_j(q_l) \right] \delta \left[\boldsymbol{k}_0 - \boldsymbol{k}_1 - \boldsymbol{Q} \right], \tag{3.59}$$

where

$$\boldsymbol{Q} = \sum_l \boldsymbol{q}_l + 2\pi \boldsymbol{\tau}. \tag{3.60}$$

The summation over l indicates that the scattering process may involve the creation and/or annihilation of l phonons of wave vectors $\boldsymbol{q}_l$. $\boldsymbol{\tau}$ is any vector of the reciprocal lattice of the crystal, and $\boldsymbol{Q}$ is called the momentum transfer vector, since $\hbar \boldsymbol{Q}$ is in fact the momentum change suffered by the neutron during the scattering process. $E_0(E_1)$ and $\boldsymbol{k}_0(\boldsymbol{k}_1)$ are the incident (scattered) neutron energies and wave vectors, respectively ($E_0 = \hbar^2 |\boldsymbol{k}_0|^2/2m$).

The first δ-function, which expresses conservation of energy, appears in both Ψ_s and Ψ_d, but the second one, conservation of pseudo- or crystal-momentum, appears only in Ψ_d. Thus, the incoherent scattering cross section contains no information

about the relative positions of different nuclei in the crystal: measurement of σ_{inc} can only give information on the energies or energy distributions of phonons and other excitations in crystal. Measurements of the coherent scattering, however, can be used to obtain information about the crystal structure and about the phonon dispersion relation $\omega = \omega_{\text{j}}(\boldsymbol{q})$. If $l = 0$, in (3.59), we have elastic coherent, or Bragg, scattering, for which $\text{E}_0 = E_1$ and the scattering is confined in wave vector space to a set of reciprocal lattice points $\boldsymbol{\tau}$, from which the crystal structure in real space may be deduced. If $l = 1$, we have one-phonon coherent inelastic scattering [69], which is the scattering process of most interest to us in the present context. Multiphonon processes ($l \geq 2$) are usually to be regarded as a nuisance, contributing to unwanted background scattering which makes the observation of the coherent one-phonon scattering more difficult. Of similar nuisance value are all incoherent scattering processes, except in a certain class of experiments, mainly concerned with hydrogenous materials in which one deliberately measures the incoherent one-phonon scattering. In these experiments, which are possible because the scattering cross section of hydrogen is mainly incoherent, one is interested in measurements of energy levels or energy distributions: efforts are made to minimize any coherent scattering effects in such case (for details see [65, 70, 71]).

3.6 Measurement of Phonon Dispersion by the Method of Inelastic Neutron Scattering

3.6.1 Background

Experiments with thermal neutrons as mentioned above are most useful in the study of lattice vibrations. The advantage stems from the basic nature of the neutrons: the de Broglie wavelength of a thermal neutron is of the same order of magnitude as the interatomic distances in crystals, and the energy of a thermal neutron is of the same order as the energy of a lattice excitation. Table 1 of [1] gives some characteristical values and physical constants of thermal neutrons. In a scattering process (see, for example, [65–71]), the neutron matches the lattice vibrations with respect to energy and wave vector (Fig. 3.5), and there exist pronounced interference phenomena. Coherent neutron scattering allows direct measurement of the dispersion relation, i.e., of the frequencies for distinctive polarizations and wave vectors in the Brillouin zone, and hence gives the best proof for the existence of phonons [16]. The neutron interacts with the target via nuclear forces, and there are no restrictions with respect to the type of interatomic binding forces: metallic-, ionic-, covalent-, molecular-, and hydrogen-bonded crystals can be investigated. The neutron probes directly the motion of the nucleus, whereas in optical measurements the nuclear motions are observed through the coupling of the photon with the electrons or ions. The neutron is uncharged, it penetrates deeply into the target and allows the study of bulk properties: there are no limitations due to surface effects [72]. One disadvantage of neutron

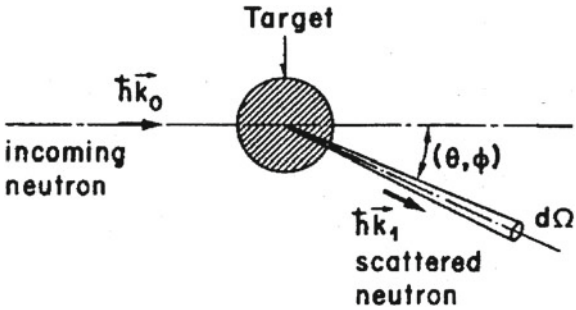

Fig. 3.5 Neutron-scattering process

scattering is the relatively poor energy and wave vector resolution, in the order of 1% for a normal experiment [65], due to the low intensity of available neutron beams. The necessity of having a large experimental facility, a nuclear reactor or a spallation source, makes this method somewhat exclusive (for details see [73]).

Further, suppose that a beam of monoenergetic thermal neutrons is incident on a crystalline sample, as shown in Fig. 3.5. The neutrons may either be scattered, be absorbed, or pass without interaction [1]. The incident and the scattered neutrons are characterized by the momentum vectors $\hbar\boldsymbol{k}_0$ and $\hbar\boldsymbol{k}_1$, respectively, where $k = 2\pi/\lambda$ and λ is the neutron wavelength. Every nucleus in the sample is a center of scattering, and the scattered neutrons will interfere and combine to a total field. If the field neutrons are found with their momentum changed by

$$\hbar\boldsymbol{Q} = \hbar(\boldsymbol{k}_0 - \boldsymbol{k}_1), \tag{3.61}$$

and their energy changed by (see also above)

$$\hbar\omega_{\mathrm{j}}(\boldsymbol{q}) = \frac{\hbar^2}{2m_{\mathrm{n}}}(k_0^2 - k_1^2) = E_0 - E_1, \tag{3.62}$$

then the crystalline sample must be able to change its dynamic properties by the same quantities. In these equations, as early, m_n is the neutron mass and $\boldsymbol{Q}$ is the scattering vector.

As already mentioned, the process of scattering is characterized by the cross section. It tells us how likely a neutron is scattered as a function of energy or momentum transfer. The angular distribution of the scattered neutrons is given by the differential cross section, defined by

$$\frac{\mathrm{d}\sigma}{\mathrm{d}\Omega} = \frac{\text{number of neutrons scattered per second in d}\Omega(\theta, \phi)}{\text{incident flux}}. \tag{3.63}$$

In the process of scattering, the neutron has changed its momentum; if the scattering was not elastic, the energy of the neutron is changed too. The scattered intensity is then described by the partial differential cross section

$$\frac{\mathrm{d}^2\sigma}{\mathrm{d}\Omega\mathrm{d}E_1} = \frac{\begin{array}{l}\text{number of neutrons scattered per second into } \mathrm{d}\Omega(\theta,\phi)\\ \text{with energy between } E_1 \text{ and } E_1+\mathrm{d}E_1\end{array}}{\text{incident flux}}, \tag{3.64}$$

which gives the most detailed information of the scattering process. In a neutron-scattering experiment, we essentially determine the differential cross section, and the basic problem is to derive a theoretical expression for this quantity. Quantum mechanically, the cross section is evaluated in the Born approximation (see, for example, [74]). The incoming neutrons are represented by plane wave functions $|\mathrm{k}_0\rangle$, and they are incident on the sample in the state $|\,i\rangle$. In the scattering process, the neutron changes to the state $|\mathrm{k}_1\rangle$ and leaves the sample in state $|\,f\rangle$. The transition probability is given by Fermi's golden rule as

$$W(\boldsymbol{k}_0, i \longrightarrow \boldsymbol{k}_1, f) \cong |\langle \boldsymbol{k}_1, f \mid V \mid \boldsymbol{k}_0, i\rangle|^2\, \delta(E_\mathrm{i} - E_\mathrm{f} + \hbar\omega), \tag{3.65}$$

where the δ-function represents the conservation of energy in the neutron-target system during the scattering process and V is the interaction potential. The cross section

$$\mathrm{d}\sigma = \frac{W(\boldsymbol{k}_0, i \longrightarrow \boldsymbol{k}_1, f)}{\text{incident flux}}; \tag{3.66}$$

together with (3.65), and by considering the density of final scattering states, we get

$$\left(\frac{\mathrm{d}^2\sigma}{\mathrm{d}\Omega\mathrm{d}E_1}\right)_{\boldsymbol{k}_0, i \longrightarrow \boldsymbol{k}_1, f)} = \frac{k_1}{k_0}\left(\frac{m_\mathrm{n}}{2\pi\hbar^2}\right)^2 \times |\langle \boldsymbol{k}_1, f \mid V \mid \boldsymbol{k}_0, i\rangle|^2\, \delta(E_\mathrm{i} - E_\mathrm{f} + \hbar\omega). \tag{3.67}$$

As already mentioned, the scattering length b depends on the isotope and the combined neutron–nucleus spin, and generally it is not the same for all nuclei even in a single elemental scattering system. Nuclei having different scattering lengths will statistically be distributed in the crystal, and therefore the neutron "sees" a crystal in which the scattering length varies from one point to other. The cross section contains products of pairs of scattering length, which can be written as the sum of a correlated part and an uncorrelated part. Only the system with average length can give interference effects; this coherent scattering is proportional to the average value $\overline{b}$. Incoherent scattering arises from the random distribution of the deviations from $\overline{b}$ and shows no interference effects (the example of Si cross section see in Fig. 25 in [75]).

The cross section can be split in a coherent part, given by the average system

$$\left(\frac{\mathrm{d}^2\sigma}{\mathrm{d}\Omega\mathrm{d}E_1}\right)_\mathrm{coh} \cong \overline{b}^2 \frac{k_1}{k_0} \sum_{\mathrm{ll}'} \langle \exp[-i\,\boldsymbol{Q}\cdot\boldsymbol{R}_{\mathrm{l}'}(0)] \times \exp[\boldsymbol{Q}\cdot\boldsymbol{R}_\mathrm{l}(t)]\rangle \exp(-i\omega t)\mathrm{d}t, \tag{3.68}$$

and an incoherent part

$$\left(\frac{\mathrm{d}^2\sigma}{\mathrm{d}\Omega\mathrm{d}E_1}\right)_{\mathrm{inc}} \cong \left(\overline{b^2} - \overline{b}^2\right)\frac{k_1}{k_0}\sum_{1}\int_{-\infty}^{\infty}\langle\exp[-i\,\boldsymbol{Q}\cdot\boldsymbol{R}_1(0)]\times\exp[i\,\boldsymbol{Q}\cdot\boldsymbol{R}_1(t)]\rangle \times\exp(-i\omega t)\mathrm{d}t. \tag{3.69}$$

These equations show that the coherent scattering (3.68) is determined by the correlation between the positions of the same atom at different times and by the correlation between the positions of different atoms at different times. Coherent scattering from crystals arises only if the geometrical conditions (translational symmetry) are satisfied. The incoherent or single-atom scattering (3.69) depends only on the correlation between the positions of the same nucleus at different times.

Inelastic neutron scattering enables the direct measurement of a phonon frequency for a distinctive wave vector. The intensity of experimentally observed "neutron group" of the one-phonon peak is plotted versus the energy transfer. The peak position determines the phonon frequency, and the linewidth and the integrated intensity of the peak contain information on the lifetime and the eigenvectors of the observed phonon mode, respectively. With a series of scans of this type, the dispersion curves can experimentally be determined along any desired crystallographic direction (for details see [65, 70, 71]).

3.6.2 Experimental Results

The frequency of phonon involved in scattering is found from (3.62) by measuring neutron velocities before and after the interaction. If the scattering angle is also measured, the phonon wave vector $\boldsymbol{q}$ can be found from (3.61). Thus, the dispersion law in a point of the Brillouin zone is totally determined. What actually happens is that the situation is complicated by the presence of several frequency values for each $\boldsymbol{q}$; in other words, for each value of the transmitted momentum $\boldsymbol{Q}$, there are several groups of neutrons scattered by each branch [19]. In the case of incoherent scattering, only the law of conservation of energy (3.62) is fulfilled, so that the scattering spectrum proves to be continuous within $\mathrm{E}_i \pm \hbar\omega_{\max}$. The scattering cross section is proportional to the frequency distribution function $(g\omega)$ (see above) and also contains a frequency factor, which depends on the polarization vectors of phonons $\boldsymbol{e}^{\mathrm{s}}(\boldsymbol{q})$ [73–75]. For this reason, function $(g\omega)$, reconstructed from experiments, reflects to some degree, the model that was used for determining polarization vectors. In the case of lithium hydride crystals, neutron scattering strongly depends on the isotopic composition. The nonzero spin of the hydrogen nucleus results in a very strong incoherent scattering. For this reason, in lithium hydride, only the frequency distribution function can be measured, but not the dispersion law. In contrast, in LiD (containing 100% D), only coherent scattering takes place. However, an addition of a small amount of hydrogen allows one to observe incoherent scattering as well. Scattering of thermal neutrons by LiH(LiD) crystals was investigated in papers of Zemlianov

Table 3.1 Comparison of calculated and measured parameters of LiD (after [1])

	c_{11},GPa	c_{12},GPa	c_{44}GPa	$\hbar\omega_{LO}$, cm^{-1}	ε_∞	e_s^*/e
Theory	69.3	3.0	47.1	819	2.89	0.51
Experiment	67.7	14.8	47.0	880	3.61	0.56

et al. [76] and Verble et al. [77]. Zemlianov et al. studied the incoherent scattering (see also below). Figure 3.5 presents dispersion curves for lithium deuteride, measured by Veble et al. The accuracy of these data, according to the authors, is 3–4%. Despite great efforts, Verble et al. failed to observe scattering by longitudinal-optical phonons. They explained this fact by the very short lifetime of LO phonons (see also [1, 78]). Verble et al. described their experimental results by means of the shell model with seven parameters: constants A_{+-} and B_{+-} of the short-range potential for the interaction between nearest neighbors, constants A_{--} and B_{--} of the same potential for the interaction between nearest anions, the effective charge Z, and electrical and "mechanical" polarizabilities, α and d, respectively, of the deuterium ion (cations were assumed to be nonpolarizable). All the above parameters were found from the best fit with experimental data. They are presented in Table 4 of paper by Plekhanov [50].

Figure 3.6 shows the dispersion curves of LiD calculated with these parameters. One can see that the greatest discrepancy, as expected, is observed in the vicinity of the L-point of the Brillouin zone. The values of parameters obtained can be used for calculating elastic and dielectric constants, which can be compared with experimental data. The latter represents the average values of data presented earlier. One can see from Table 3.1 that calculated values agree satisfactorily with experimental data except for the c_{12} and ε_∞ constants. As for the first constant, it is not surprising if one bears in mind that noncentral forces are treated incorrectly in the shell model, as was noted above. Note also that the ionicity $Z = 0.88e$ obtained in the shell model is in good agreement with the above estimates. As mentioned above, the dispersion curves for LiH crystals cannot be measured. However, it is reasonable to suggest by Verble et al. that all parameters of the model are, with good accuracy, the same for LiH and LiD crystals except, of course, for the anion mass. The dispersion curves calculated by Verble et al. under this assumption are presented in Fig. 3.7. The shell model correctly predicts frequencies of not only TO and LO phonons shown in Fig. 3.7 but also of other phonons found from absorption spectra of color centers in LiH crystals [71, 79].

Very accurate experiments of the dispersion relation were performed for diamond (Fig. 3.8) by Warren et al. [80], for silicon (Fig. 3.9) by Dolling and Cowley [81], and for germanium by Nilsson and Nelin [82]. The numerous calculations [73, 83–85] of the dispersion relation for these semiconductors are shown rather good accordance with the experimental ones (see also Dolling and Cowley [81]), excluding diamond.

Diamond has unusual static properties when compared to other groups 1 V tetrahedral semiconductors characterized by a small lattice parameter, a large bulk modulus,

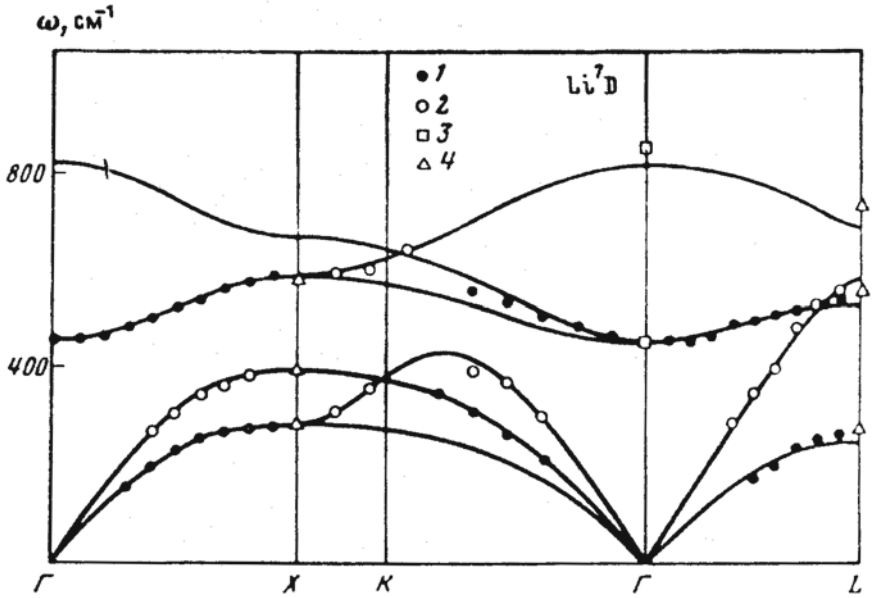

Fig. 3.6 Dispersion of phonons in a ^{7}LiD crystal. (1) and (2) measurements of inelastic neutron scattering by TO and LO phonons, respectively (after [77]); (3) IR measurements [86]; and (4) data on Raman scattering [44, 87]. Solid lines correspond to calculations according to the shell model of Verble et al. [77]

and a large cohesive energy [80]. Lattice dynamic characteristics such as phonon dispersion and thermal expansion are also distinctive. Additionally, the occurrence of a maximum in the phonon dispersion of the most energetic phonons away from the Brillouin zone center is peculiar to diamond. A necessary condition to have such an overbending is to have sufficiently large second-order nearest-neighbor force constants [88–90]. Interest in the lattice dynamics of diamond has been especially strong since the report of a sharp peak in the second-order Raman spectrum at a frequency slightly higher than twice the largest single-phonon frequency, i.e., at $\omega_2 - 2\omega_0 = 2\,\mathrm{cm}^{-1}$ (0.25 meV) at room temperature ($\omega_0 = E(\Gamma)$, Solin and Ramdas [91] and reference therein). This situation is unlike that of Si [92], and a first explanation invoked the occurrence of phonon–phonon interactions to produce a two-phonon bound state [93]. However, later theoretical work led to the conclusion that anharmonic coupling constants have the wrong sign to allow formation of a bound state [91, 92]. An alternate explanation was suggested involving an unusual LO phonon dispersion with an energy maximum away from the Brillouin zone center [53, 94–96]. The occurrence of this overbending for the Δ branch was supported by the valence force field model [83, 89]. They obtained a sharp peak in the overtone density of states (see below) at $2\omega_0$ (i.e., without a shift) due to a van Hove singularity at Γ. Later, Hass et al. [53] reported that the model used by Tubino and Birman [89] does not yield the peak in the overtone density of states (DOS). However, their

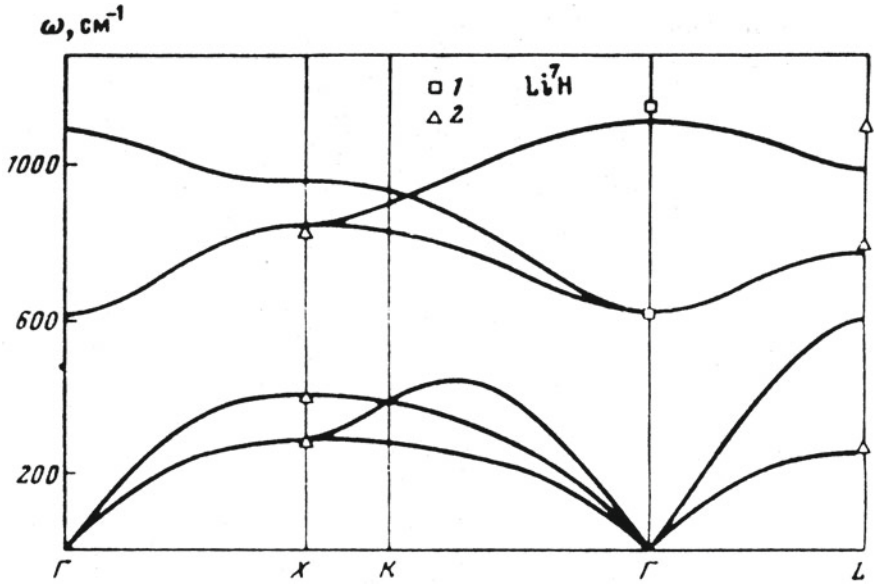

Fig. 3.7 Dispersion of phonons in a ^{7}LiH crystal (1) IR measurements and (2) data on Raman scattering [78, 79, 87]. Solid lines correspond to calculations according to the shell model of Verble et al. [77]

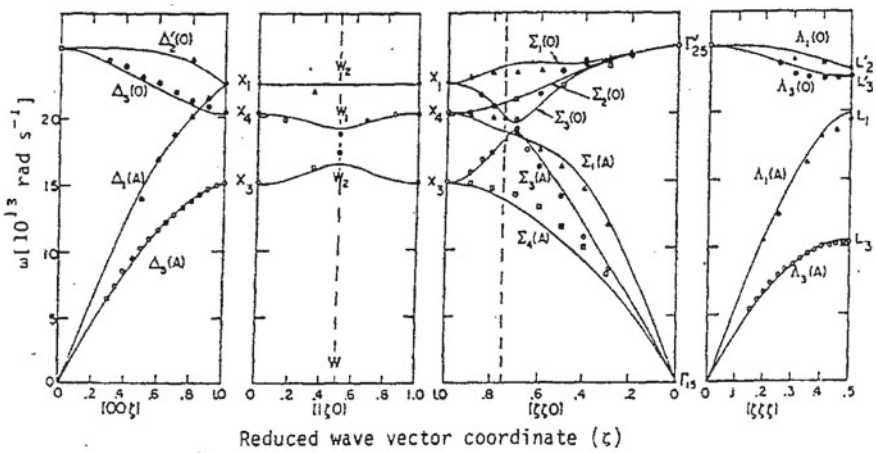

Fig. 3.8 The dispersion relation for the normal modes of vibration of diamond in the principal symmetry directions at 296 K [80]. The full curves represent a shell-model fit to the data points (after Bilz and Kress [73])

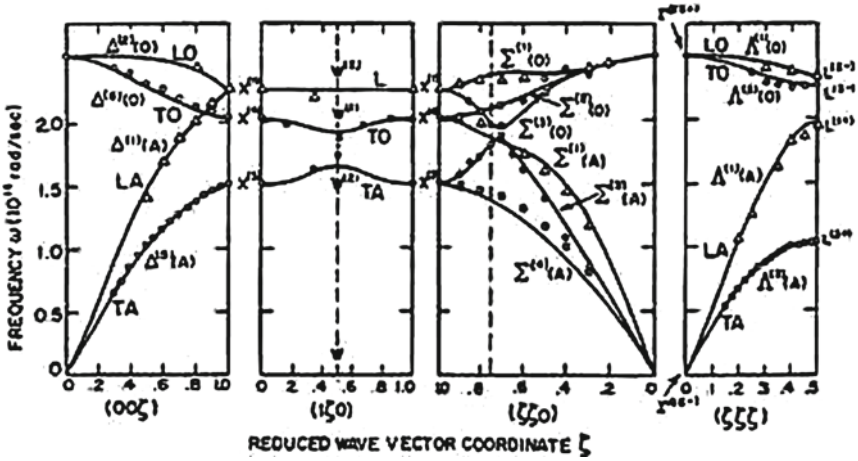

Fig. 3.9 Single-phonon dispersion curves of Si deduced from neutron spectroscopic data at RT (after [73, 81])

Raman scattering studies performed on various isotopic compositions of diamond support the occurrence of such peak (see also below). Hass et al. added ad hoc a peak to the DOS to achieve agreement with their two-phonon Raman spectra.

The first ab initio calculations by Vanderbilt and coworkers [95] found overbending along Δ. More recently Windl and coworkers [97] have obtained such dispersion in ab initio calculation along all three directions for diamond having a natural isotopic abundance. However, they obtained a two-phonon shift of $25\,\mathrm{cm}^{-1}$ (3 meV), an order of magnitude larger than the observed value. Although the measurements obtained for diamond dispersion by inelastic neutron scattering 30 years ago were not focused on subtle features in LO phonon dispersion [85], overbending along Δ has been reported for recent neutron scattering measurements [98]. The results of Schwoerer-Bohning and coworkers [99] of phonon dispersion of diamond measured by inelastic X-ray scattering are depicted on Fig. 3.10. Their data agree quite well with the raw data from Kulda et al. Although the data of Schwoerer-Bohning et al. deviate from the neutron results toward the zone boundary, they show the same magnitude and position of the maximum in the phonon dispersion. The maximum obtained by Schwoerer-Bohning et al. is 1.2 meV above ω_0 and appears at the phonon wave vector $\boldsymbol{q} = 0.4(2\pi/\mathrm{a})$ which is closer to the results of Kulda et al. (maximum at 1.5 meV above ω_0 and $\boldsymbol{q} = 0.35(2\pi/\mathrm{a})$). However, this in contradiction to the ab initio calculation presented in the paper of Kulda et al., which predicts a different magnitude (3 meV) and position $[0.48(2\pi/a)]$ (see also [44, 100]). So, the momentum-resolved inelastic X-ray scattering experiment yields directly the dispersion of optical phonons. The Schwoerer-Bohning results demonstrate overbending along Δ, and possible along $\sum$ directions (for details see [99]).

In Fig. 3.11, we show the LO and TO optical phonon branches from Γ to X obtained for a ^{76}Ge enriched crystal and natural one according to the results of Etchegoin

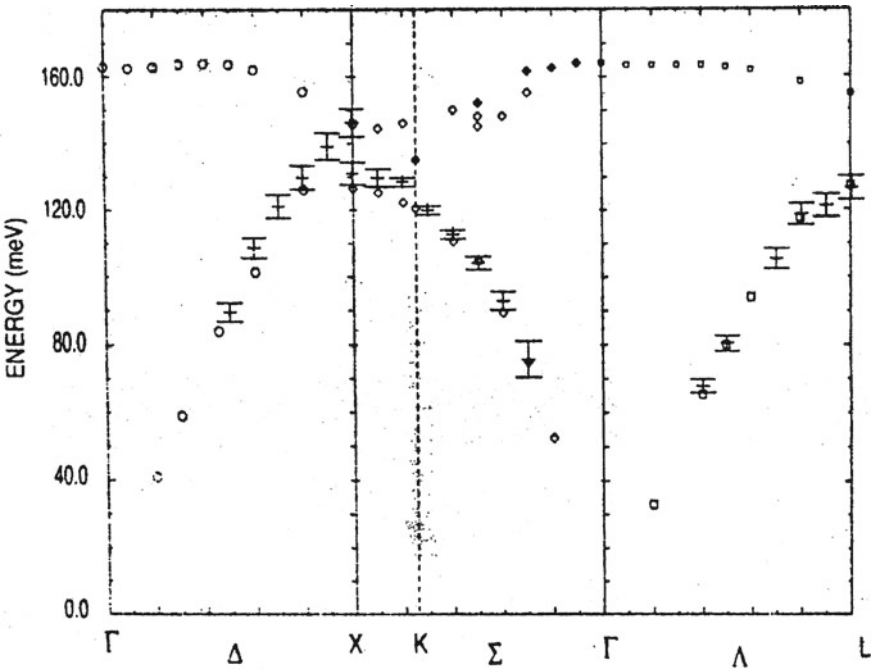

Fig. 3.10 Dispersion of the high-energy branches as obtained by HRIXS (data points) together with ab initio results (lines) from Windl and coworkers [97, 98]. The error of the data is their symbol size (except along $\sum$). The horizontal lines indicate the phonon energy at the zone center Γ (after Schwoerer-Bohning et al. [99])

and coworkers [101]. Measurements of the TO branch are shown in Fig. 3.11b. The latter include the mapping of the branches along two different lines in the reciprocal space with a different orientation of the resolution ellipsoid with respect to the dispersion (focusing and defocusing conditions). The frequencies of the ^{76}Ge crystal have been multiplied by 1.0208, thus eliminating the trivial proportionality to $1/\sqrt{\bar{m}}$ (where $\bar{m}$ is the average atom mass). The differences that are left should be solely due to disorder (see below). Although these differences are small, it is possible to discern systematic deviations between the experimental values of the enriched and natural samples. The change in the broadening of the peaks can also be evaluated. The numerical values for the energy shift of the TO phonons at the critical points are summarized in Table X1 of paper [44]. These results show that the shift of the LO phonons is more larger that TO phonons and LO phonons (as will be shown below) do not have an isotopical broadening in Ge crystal (see also [102]).

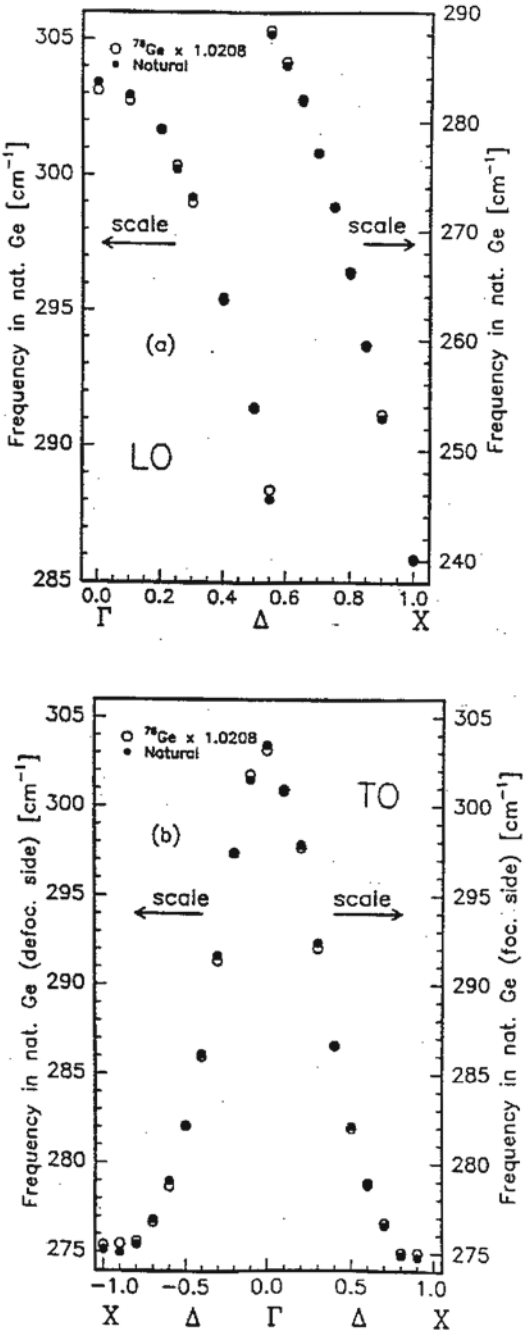

Fig. 3.11 Inelastic neutron scattering results, in **a** the LO phonon branch is displayed. The frequencies of the isotopically enriched sample ^{76}Ge were multiplied by 1.0208 so as to eliminate the trivial mass dependence of the phonon frequencies. Differences between the two measurements are due to isotopic disorder. In **b** results for the TO phonon branch are shown. Two sets of measurements are displayed, for an incident focused or defocused neutron beam (after Etchegoin et al. [101])

3.7 Raman Spectra of Isotope-Mixed Crystals

As is well known, the evaluation of the incoherent part of the scattering cross section is similar to the procedure used for the coherent scattering (see, for example, [1, 3, 68, 73]). The basic equation is (3.69). We again consider a Braves crystal; and for the partial cross section, we have

$$\left(\frac{\mathrm{d}^2\sigma}{\mathrm{d}\Omega\mathrm{d}E_1}\right)_{\mathrm{inc}} \cong \sigma_{\mathrm{inc}}\frac{k_1}{k_0}e^{-2\mathrm{W}}\int_{-\infty}^{\infty}\exp\left[\langle \boldsymbol{Q}\cdot\boldsymbol{u}_0(0)\,\boldsymbol{Q}\cdot\boldsymbol{u}_0(t)\rangle\right]\exp(-i\omega t)\mathrm{d}t, \quad (3.70)$$

with the incoherent cross section

$$\sigma_{\mathrm{inc}} = 4\pi(\overline{b^2} - \overline{b}^2). \quad (3.71)$$

As usually can be expanded in a power series, the nth term corresponding to the n-phonon process. For the elastic scattering, we get [44]

$$\left(\frac{\mathrm{d}\sigma}{\mathrm{d}\Omega}\right)_{\mathrm{inc}}^{\mathrm{el}} \cong \sigma_{\mathrm{inc}}\mathrm{e}^{-2\mathrm{W}}, \quad (3.72)$$

ith is a dependence of the scattered intensity on temperature and momentum transfer through the Debye–Waller factor $\exp[-2W(Q,T)]$.

The one-phonon term is given by

$$\left(\frac{\mathrm{d}^2\sigma}{\mathrm{d}\Omega\mathrm{d}E_1}\right)_{\mathrm{inc}}^{1} \cong \sigma_{\mathrm{inc}}\frac{\boldsymbol{k}_1}{\boldsymbol{k}_0}\mathrm{e}^{-2\mathrm{W}}\sum_{\boldsymbol{q},j}\frac{\left|\boldsymbol{Q}\cdot\boldsymbol{e}\left(\begin{smallmatrix}\boldsymbol{q}\\ j\end{smallmatrix}\right)\right|^2}{\omega_{\mathrm{j}}}\left\langle n_{\mathrm{j}} + \frac{1}{2} \pm \frac{1}{2}\right\rangle\delta(\omega \mp \omega_{\mathrm{j}}), \quad (3.73)$$

where the upper and lower sign refer to phonon creation and annihilation, respectively (see also [22]). As compared to the coherent cross section (see above), the δ-function for crystal-momentum conservation no longer appears, and there is only the δ-function for energy conservation. Hence, a measurement of the incoherent scattering gives only information on the number of phonon modes as function of energy, but not on the dispersion relations. The cross section can further be simplified for a cubic Braves crystal. The summation over all modes $(\boldsymbol{q}, j)$ can be replaced by an integral over all frequencies by introducing the phonon density of states $\mathrm{g}(\omega)$. The polarization vector contribution can be averaged and we obtain

$$\left(\frac{\mathrm{d}^2\sigma}{\mathrm{d}\Omega\mathrm{d}E_1}\right)_{\mathrm{inc}}^{1} \cong \sigma_{\mathrm{inc}}\frac{\boldsymbol{k}_1}{\boldsymbol{k}_0}\mathrm{e}^{-2\mathrm{W}}\frac{g(\omega)}{\omega}\left\langle n + \frac{1}{2} \pm \frac{1}{2}\right\rangle. \quad (3.74)$$

The phonon density of states (DOS) is proportional to the one-phonon cross section and can, in principle, directly be measured. The method is best suited for predominantly incoherent scatters, but the condition "cubic Braves crystal" is very restrictive for a practical application. Some values of σ_{inc} and σ_{coh} for some elements are given in Table 3 of [1]. As we can see hydrogen is by far the best incoherent scatterer, almost an order of magnitude stronger than deuterium and the other elements.

Figure 3.12 shows frequency distribution functions $g(\omega)$ calculated in the shell model for lithium hydride and lithium deuteride crystals (see, e.g., Plekhanov [50]). One can see that spectral distributions of phonons in LiH and LiD are virtually identical in the region of acoustic vibrations ($\leq 450\,\text{cm}^{-1}$). At the same time, the optical band in LiH is broader by the factor $\sqrt{2}$ than in LiD. This is explained by the fact that in a crystal lattice containing ions with substantially different masses, heavy ions primarily take part in acoustic vibrations, and light ions are involved in optical vibrations. In addition, there is a narrow gap in $g(\omega)$ between 583 and 608 cm^{-1} in LiH crystals, whereas in LiD, such a gap is absent. Note also that the frequency of a transverse optical phonon in LiH lies at the band boundary, where the density of states is very low. Figure 3.13 compares the frequency distribution function $g(\omega)$ calculated within the framework of the shell model [68, 73] with the function obtained in experiments on incoherent neutron scattering (Zemlianov et al. [76]). Note several interesting facts that follow from this comparison. For LiD crystals, the agreement is

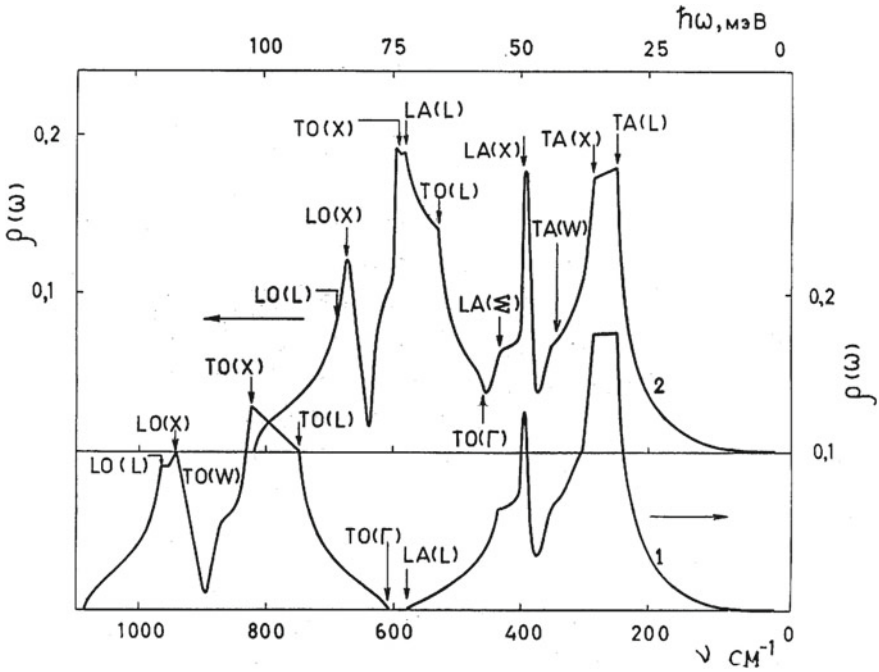

Fig. 3.12 Density of phonon states in (1) LiH and (2) LiD crystals (after [45])

good, except for the region of LO phonons. However, in LiH, there is a great discrepancy between the theory and experimental data (see also Fig. 3.14). This can be due to several reasons. First, in the determination of the frequency distribution function by Verble et al. for some polarization vectors, a rough model of rigid ions was used, which took into account the interaction between nearest neighbors. Second, incoherent scattering in LiH can contain a considerable contribution from multiphonon processes, which can severely distort the true frequency distribution function. This is obviously the main reason for the strong overstating of the phonon frequency in LiH crystals, especially in the region of LO phonons (see also [40, 44]). Further, we will discuss briefly the Raman light scattering by isotope -mixed crystals.

The phonon density of states g(ω) of a crystalline solid is defined as follows. The function g(ω)dω signifies the fraction of the total number of phonon states in the frequency interval (ω, ω+dω) if $\int g(\omega)\mathrm{d}\omega$ is normalized to 1. Knowledge of g(ω) is essential for understanding of the thermodynamic properties (see below) as well as for extraction of the electron–phonon coupling, etc. It is difficult to make good direct measurements of the density of states, and few spectra have been actually (e.g., LiH) studied. Usually, measurements of incoherent scattering of neutrons reveal only the main peaks. Theoreticians have produced mathematically accurate $g(\omega)$ functions for lattice models in about four decades, and one of the most striking results of these calculations are the existence of kinks in $g(\omega)$ or discontinues in dg/dω.

A direct comparison between Raman spectra and overtone density of states cannot be done with great precision because the Raman scattering efficiency is the combination and overtone phonon density of states is weighted by electron–phonon matrix elements and energy denominators (see, e.g., [1]). For tetrahedrally coordinated semiconductors these matrix elements in the second-order spectra involving phonon overtones dominate the scattering efficiency and, away from resonance, vary weakly with Raman frequency shift, thus second-order spectra are in good measure of the overtone density of states. It must be kept in mind, however, that resonant intermediate states will be in general distort shape of Raman spectra away from the density of states [44].

As said above, from the appropriate models for different materials, it is relatively straightforward to compare the frequency distribution function $g(\omega)$ for the normal modes of vibrations. As we can see below (Figs. 3.15 and 3.16), the curves clearly display sharp critical points arising from regions of the dispersion curves having zero gradient. Many of these can be correlated with features of $\omega(\boldsymbol{q})$ for wave vectors along the principal symmetry directions, although some must owe from non-symmetry direction modes. The two-phonon absorption spectra (Raman spectra) of semiconducting crystals (C, Ge, Si, and α-Sn) were compared with the density of the combined vibrational states in the paper of Tubino and coworkers (Tubino et al. [83]). In this paper, it was shown that the comparison holds only in what concerns the peak position and not the intensity ratios, since the "joint density of states" has not been modified by the thermal factor and the frequency dependence of the coupling Hamiltonian has not been taken into account because of the intrinsic difficulty of "a priory" knowledge of the second-order dipole moment (see also Lax and Burstein [104]).

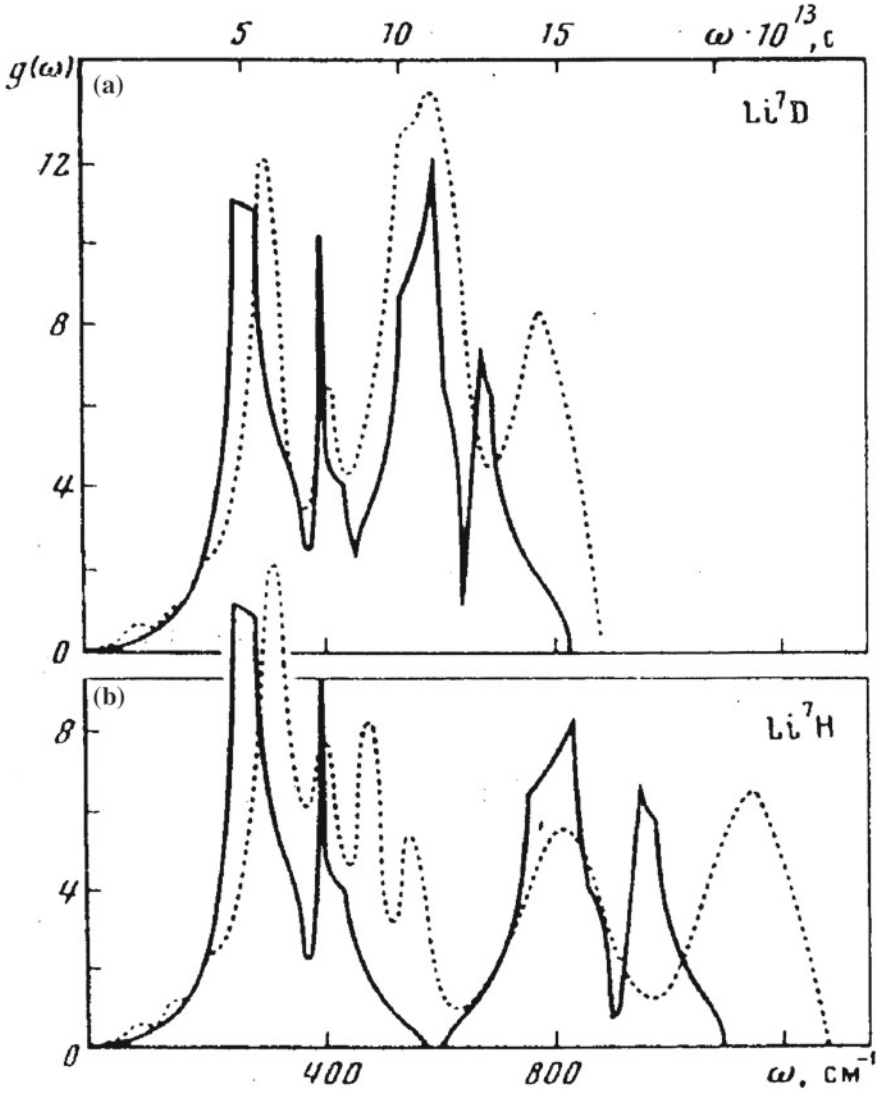

Fig. 3.13 Density of phonon states in **a** LiH and **b** LiD crystals. Dashed curves correspond to data on incoherent scattering of thermal neutrons (after Zemlianov et al. [76])

In study, the Raman scattering due to phonons is concerned with the changes in the electronic polarizability of the crystal due to the lattice vibrations (Loudon [105]). For small oscillations, the polarizability tensor can be expanded in terms of the ionic displacement about the equilibrium position of the ions. Since a cubic crystal (with NaCl structure; e.g. LiH) has inversion symmetry about every ion, the first-order terms in the polarizability expansion are zero, and hence this crystal

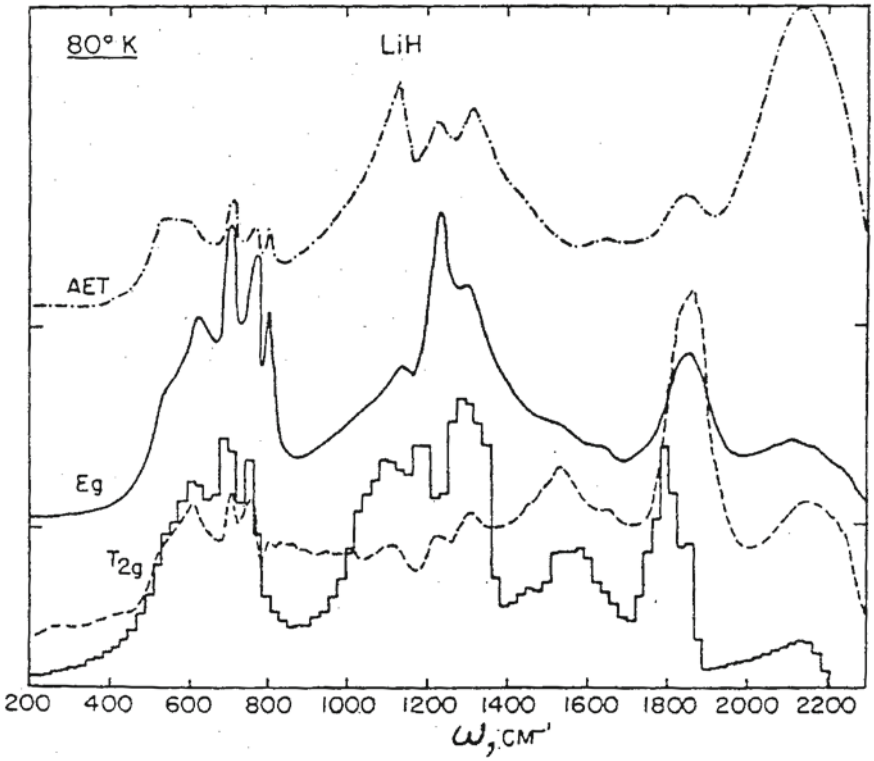

Fig. 3.14 Raman spectra (A_{1g}, E_g, T_{2g}, and AET) at 78 K and a histogram of temperature-weighted density of two-phonon states of a LiH crystal (after Jaswal et al. [103])

does not produce any one-phonon Raman scattering. It should be noted that the diamondlike crystals (C, Si, Ge, etc.) does not have inversion symmetry and possess the first-order Raman scattering. The second-order terms in the expansion give rise to the continuous two-phonon Raman scattering due to all phonons pairs with wave vectors $+\boldsymbol{q}$ and $-\boldsymbol{q}$ allowed by the symmetry of the crystal.

The intensity of the Raman scattered light from system of phonons is given by (Born and Huang, [14])

$$I(\omega_f) = \frac{\omega_i^4}{2\pi c^3} \sum_{\boldsymbol{k}=1}^{2} \sum_{\alpha\beta\gamma\delta} \boldsymbol{n}_\alpha^k \boldsymbol{n}_\beta^k i_{\alpha\beta\gamma\delta}(\omega) E_\gamma^- E_\lambda^+ \tag{3.75}$$

with

$$i_{\alpha\beta\gamma\delta}(\omega) = \sum_{v'} \left\{ \langle v'|\boldsymbol{P}_{\alpha\gamma}|v\rangle \langle v|\boldsymbol{P}_{\beta\delta}|v'\rangle \right\}_{Av}, \tag{3.76}$$

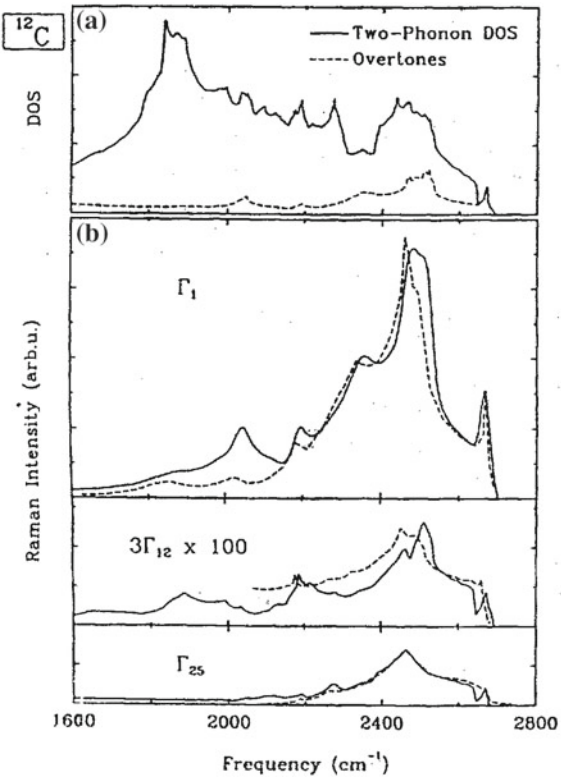

Fig. 3.15 **a** Two-phonon and overtone density of states of diamond ^{12}C. **b** Second-order Raman spectrum of diamond ^{12}C in the high-frequency region (after [91])

where $\omega = \omega_i - \omega_f$, with ω_i and ω_f being the frequencies of incident and scattered light, respectively, $\boldsymbol{n}^1$ and $\boldsymbol{n}^2$ are two mutually perpendicular unit vectors in a plane perpendicular to the direction of scattering; E_γ^- and E_λ^+ are the components of the amplitudes of the incident electric field; v and v', respectively, refer to the initial and final vibrational states of system; c is the velocity of light; $\{\}_{Av}$ means thermal average over the initial states; $\boldsymbol{P}_{\alpha\beta}$ is the electronic polarizability tensor; the subscripts α, β, etc. refer to the three axes of our coordinate system; and ε_v is the vibrational energy of the state v of the system. In (3.76), ω_i actually should be ω_f but the small change in ω_i corresponding to the change in the vibrational energy of the system is negligible. By choosing polarization of the exciting light parallel to one of the axes (x, y, and z), one can avoid the summation in (3.76). Then, the intensity of the scattered light is essentially determined by $i_{\alpha\beta\gamma\delta}(\omega)$.

The polarizability tensor is expanded in terms of the displacement of the ions about their equilibrium positions. The zeroth-order term gives rise to the Raleigh scattering and the first term is zero because of the inversion symmetry about every ion (excluding the crystals with diamondlike structure). When the displacements are Fourier analyzed in terms of the normal coordinates, the second-order term in the polarizability expansion becomes

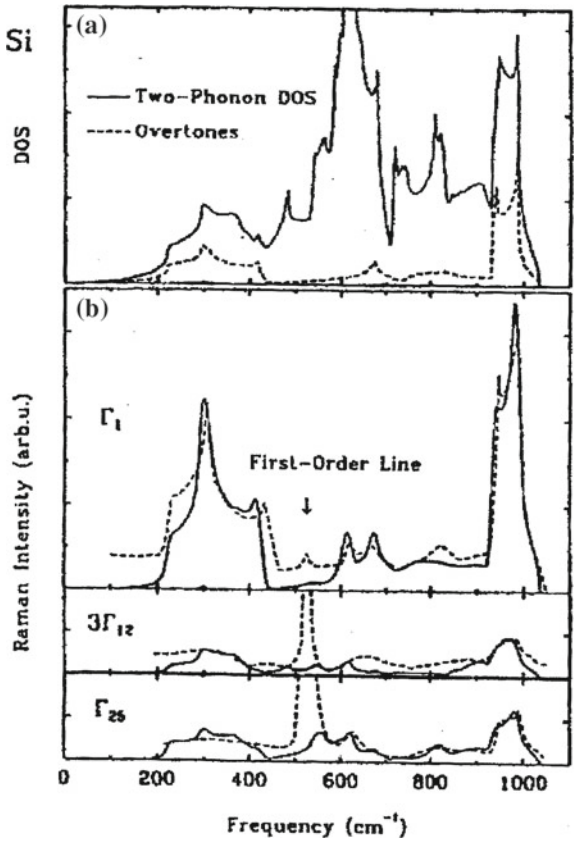

Fig. 3.16 **a** Two-phonon and overtone density of states of silicon. **b** Second-order Raman spectrum of silicon. The solid lines represent calculated spectra; the dashed lines are experimental ones from Temple and Hathaway [106] (after Windl et al. [97])

$$\boldsymbol{P}^{(2)}_{\alpha\beta} = \frac{1}{2}\sum_{gjj'} P_{\alpha\beta}\left(\begin{smallmatrix}-\boldsymbol{q}\boldsymbol{q}\\ j'j\end{smallmatrix}\right) Q\left(\begin{smallmatrix}\boldsymbol{q}\\ j\end{smallmatrix}\right) Q\left(\begin{smallmatrix}-\boldsymbol{q}\\ j'\end{smallmatrix}\right) \tag{3.77}$$

with

$$\begin{aligned}&\boldsymbol{P}_{\alpha\beta}\left(\begin{smallmatrix}-\boldsymbol{q}\mathrm{q}\\ j'j\end{smallmatrix}\right) \\ &= \sum_{l'kk'} \boldsymbol{P}_{\alpha\beta\gamma\delta}\left(\begin{smallmatrix}-l'\\ k'k'\end{smallmatrix}\right)\cdot\sigma_\gamma(k \mid \boldsymbol{q}\,j)\sigma(k' \mid -\boldsymbol{q}\,j')(M_k M_{k'})^{-1/2}\exp\left[2\pi i\boldsymbol{q}\boldsymbol{a}\left(\begin{smallmatrix}l-l'\\ kk'\end{smallmatrix}\right)\right],\end{aligned} \tag{3.78}$$

where $Q(\begin{smallmatrix}\boldsymbol{q}\\ j\end{smallmatrix})$ is the normal coordinate corresponding to wave vector $\boldsymbol{q}$ and branch j of the phonon dispersion curves and

$$P_{\alpha\beta\gamma\delta}\left(\begin{smallmatrix}l-l'\\ kk'\end{smallmatrix}\right) = \frac{\partial^2 \boldsymbol{P}_{\alpha\beta}}{\partial \boldsymbol{u}_\gamma(lk)\partial \boldsymbol{u}_\delta(l'k')\mid_0} \tag{3.79}$$

is the coefficient of the second-order term in the polarizability expansion with $u_\alpha(^l_k)$ being the α-component of the kth ion in the lth cell, $\boldsymbol{\sigma}(k \mid \boldsymbol{q}\, j)$ is the eigenvector, M_k is the mass of the kth type of ion, and $\boldsymbol{a}(^{l-l'}_{kk'})$ is the position vector of ion $(l'k')$ with respect to ion (lk). When (3.77) is substituted in (3.76) and thermal average is taken, one gets

$$i_{\alpha\beta\gamma\delta}(\omega) = \left(\frac{\hbar^2}{8}\right) \sum_{\boldsymbol{q}jj'} \left[\omega_j(\boldsymbol{q})\omega_{j'}(-\boldsymbol{q})\right]^{-1} \cdot \boldsymbol{P}_{\alpha\gamma}\left(^{-\boldsymbol{q}\boldsymbol{q}}_{j'j}\right) \boldsymbol{P}_{\beta\delta}\left(^{-\boldsymbol{q}\boldsymbol{q}}_{j'j}\right)$$
$$\times f(\omega_j(\boldsymbol{q})) \cdot f(\omega_{j'}(-\boldsymbol{q}))\delta\left\{\omega \pm \omega_j(\boldsymbol{q}) \pm \omega_{j'}(-\boldsymbol{q})\right\}, \qquad (3.80)$$

where $\omega_j(\boldsymbol{q})$ is the phonon frequency,

$$f(\omega_j(\boldsymbol{q})) = n(\omega_j(\boldsymbol{q})) + 1$$

for the creation of a phonon and

$$f(\omega_j(\boldsymbol{q})) = n(\omega_j(\boldsymbol{q}))$$

when a phonon is destroyed with

$$n(\omega_j(\boldsymbol{q})) = \left[\exp\{\hbar\omega_j(\boldsymbol{q})/kT\} - 1\right]^{-1}$$

being the usual Bose factor, + and − signs in the δ-function correspond to the destruction and creation of a phonon, respectively. One can see from (3.80) that the second-order Raman spectrum is a weighted two-phonon DOS. For positive and negative values of ω, the spectra are called Stokes and anti-Stokes, respectively. In this paper, we consider only the Stokes spectra.

If we assume the polarizability tensor to be symmetric, then the tensor $i_{\alpha\beta\gamma\delta}(\omega)$ has the same transformation properties as the elastic constant tensor (see below). Cubic LiH (LiD) crystals possess three different components of scattering tensor $i_{11} = i_{1111}$, $i_{12} = i_{1212}$, and $i_{44} = i_{1122}$. It is known from the group theory (see, e.g., Birman [107]) that components $\boldsymbol{P}_{\alpha\beta}$ of the second-rank tensor are transformed over three irreducible representations A_{1g}, E_g, and T_{2g} of the O_h^5 group. In nonpolarized scattering, all three components are present with certain weights. However, by choosing an experimental geometry of scattering in a proper way, one can separate E_g and T_{2g} components of the scattering tensor. The intensities of these components are described by the expressions (see also review of [50])

$$I(A_{1g}) \sim \left(\frac{A_{xx} + A_{yy} + A_{zz}}{\sqrt{3}}\right)^2;$$
$$I(E_g) \sim \left[\left(\frac{A_{xx} + A_{yy} - 2A_{zz}}{\sqrt{6}}\right)^2 + \left(\frac{A_{xx} + A_{yy}}{\sqrt{2}}\right)^2\right];$$

$$I(T_{2g}) \sim \left(A_{xy}^2 + A_{yz}^2 + A_{zx}^2\right)/3. \tag{3.81}$$

In this case,

$$\begin{aligned} i_{1111}(\omega) &= \left[I(A_{1g}) + I(E_g)/4 + 3I(T_{2g})\right]/3 = AET, \\ i_{1212}(\omega) &= I(E_g)/4 = E_g, \\ i_{1313}(\omega) &= I(T_{2g}) = T_{2g}, \\ i_{3333}(\omega) &= \left[I(A_{1g}) + I(E_g)\right]/3 = AE. \end{aligned} \tag{3.82}$$

One can see from (3.82) that the theoretical calculation of the Raman spectrum consists of the calculation [108] of three tensor components i_{11}, i_{12}, and i_{44}. Such calculations were done in the paper of Jaswal et al. [103]. In cited paper, the lattice dynamic model used for LiD and LiH was a deformation dipole model. This model is based on the neutron scattering data for ^{7}LiD (Verble et al. [77]) and the experimental second-order Raman spectra of LiD. Jaswal and coworkers [103] showed that if the contributions to polarizability from nearest and next-to-nearest neighbor are taken into account, one can select the values of tensor components $\boldsymbol{P}_{\alpha\gamma}$ that allow one to reproduce Raman spectra with good accuracy for different polarizations (see also Laplaze [109]). Figure 3.14 shows a comparison of experimental Raman spectra (A_{1g}, T_{2g}, E_g and AET) recorded at liquid nitrogen temperature(LNT) with a histogram of the density of two-phonon states of a LiH crystal, obtained by Jaswal et al. To improve agreement between the theory and experimental data, the interaction between next-to-nearest neighbors was taken into account. In order to obtain agreement with experimental data, 6 and 13 parameters were introduced for the T_{2g} and E_g (or A_{1g}) components, respectively. It was also noted [110] that high polarization of hydrogen (deuterium) ions requires the consideration of the $+-+$ interaction between next-to-nearest neighbors. Similar conclusions were made later by (Dick and Jex [111]), where good agreement was achieved between experimental Raman spectra and spectra calculated based on the model of deformable dipoles [3] with 13 parameters. However, although agreement between theory and experimental data in the region of 2LO(Γ) phonons (see also [50]) obtained by Dick and Jex is better than in paper of Jaswal et al., the values of frequencies at the L-point calculated by Dick and Jex are nevertheless in poor agreement with experimental values. Laplaze [86] managed to substantially improve agreement between calculated and experimental elastic constants, but he failed to obtain agreement with experimental data in the region of the TO + LO and LO(Γ) phonons in Raman spectra of LiH crystals (for details, see Plekhanov [44]).

The DOS of diamond and Si was calculated in papers of Pavone et al. [88] and Windl et al. [97]. The eigenvectors and eigenvalues that are necessary to evaluate $\boldsymbol{P}_{\alpha\beta}$ (3.78) have been calculated in cited papers using the local-density-approximation(LDA) plane-wave pseudopotential method. The results for the second-order Raman spectra for diamond ^{12}C and silicon are shown together with experimental curves in Figs. 3.15 and 3.16. As shown in Table 3.2 and Fig. 3.15, for diamond ^{12}C Pavone et al. found especially in comparison to previous works by Cowley [112]

Table 3.2 Critical-point analysis of the second-order Raman spectra of diamond ^{12}C (after Windl et al. [97])

Overtones and combinations	Active in	Theory, cm^{-1}	Experiment, cm^{-1}
"sharp peak"	Γ_1^+; Γ_{12}^+; Γ_{25}^+	2671	2670
$2O(\Gamma)$	Γ_1^+; Γ_{12}^+; Γ_{25}^+	2646	2667
2L(X)	Γ_1^+; Γ_{12}^+; Γ_{25}^+	2453	2370
2TO(X)	Γ_1^+; Γ_{12}^+; Γ_{25}^+	2186	2138
2TA(X)	Γ_1^+; Γ_{12}^+; Γ_{25}^+	1596	1614
L(X) + TA(X)	Γ_{25}^+	2024	1992
L(X) + TO(X)	Γ_{25}^+	2319	2254
TO(X) + TA(X)	Γ_{12}^+	1891	1864
$2O_2(W) = 2A_2(W)$	Γ_1^+; Γ_{12}^+; Γ_{25}^+	2035	1998
$2O_1(W)$	Γ_1^+; Γ_{12}^+; Γ_{25}^+	2375	2358
$2A_1(W)$	Γ_1^+; Γ_{12}^+; Γ_{25}^+	1864	1817
$O_2(W) + O_1(W)$	Γ_{12}^+; Γ_{25}^+	2205	2177
$A_2(W) + A_1(W)$	Γ_{12}^+; Γ_{25}^+	1949	1907
$O_1(W) + A_1(W)$	Γ_1^+; Γ_{12}^+; Γ_{25}^+	2119	2178
2LO(L)	Γ_1^+; Γ_{25}^+	2548	2504
2TO(L)	Γ_1^+; Γ_{12}^+; Γ_{25}^+	2459	2422
2LA(L)	Γ_1^+; Γ_{25}^+	2147	2011
2TA(L)	Γ_1^+; Γ_{12}^+; Γ_{25}^+	1117	1126
LO(L) + TO(L)	Γ_{12}^+; Γ_{25}^+	2503	2458
LA(L) + TA(L)	Γ_{12}^+; Γ_{25}^+	1632	1569

and Go and Cardona [113] shows very good agreement between calculation and experiment (peaks position deviate by generally less than 2%). From Fig. 3.15, it can also be seen that within harmonic approximation, which was done by Pavone et al., the sharp peak at the frequency cutoff in all representations is well reproduced as it should be from symmetry considerations [107, 114]. The origin of this sharp peak is connected with the overbending of the LO branch dispersion (see above). The detailed analysis [99] of the force constants shows that an overbending of the LO branch in the phonon dispersion can be obtained only for significantly large values of the force constants between second neighbors (see also [115]).

In order to show that the origin of the sharp peak at the high-frequency cutoff is not an effect of the matrix elements Windl et al. also fitted the second-order Raman spectrum in its three representations for silicon. The results of these calculations are shown in Fig. 3.16. Again Windl et al. found a good agreement between calculation and experiment for all representations. The positions of the calculated peaks with experimental values within generally less than 2% (see also Table 5 of [1]). As expected from phonon dispersion (see Fig. 3.9) and the high-frequency density of

states there is no sharp peak at the high-frequency cutoff. So, these results give a strong evidence that the long-standing controversy seems to be resolved.

3.8 Disorder Shift and Broadening of the Line in the Raman Spectra

In this section, we compare the theoretical predictions on the disorder shit and broadening of the line in the Raman spectra with experimental observations for the elemental semiconductors as well as insulator LiH_xD_{1-x}. The coherent potential approximation (CPA) [54–56] has been employed for diamond and Si, while ab intio electronic-structure- based calculations have been performed for diamond and Ge [36]. As it was described in preceding sections, the isotopically enriched samples of Ge show a frequency inversely proportional to the square root of the average mass (see Fig. 20 of [44]), and a linewidth inversely proportional to the mass (Fig. 3.17), in agreement with the harmonic approximation and Fermi's golden rule, respectively. However, in natural Ge and $^{70/76}$Ge alloy isotope, there is a disorder of Gaussian additional shift of the phonon frequency and a broadening of the linewidth. This additional shift is $0.34 \pm 0.04\,\mathrm{cm}^{-1}$ in natural Ge, and $1.06 \pm 0.4\,\mathrm{cm}^{-1}$ in the $^{70/76}$Ge alloy sample, which has nearly the maximum isotopic disorder possible with natural isotopes. Recent single-site CPA calculations [2, 116], based on the density of states obtained within the harmonic approximation, predict that the disorder-induced frequency shift of the Γ-point optical phonon amounts to $(0.4 \pm 0.1)\,\mathrm{cm}^{-1}$ for natural Ge, and $(1.2 \pm 0.1)\,\mathrm{cm}^{-1}$ for the alloy sample, depending on the lattice-dynamical model used to obtain the phonon density of states. A simple estimate from second-order perturbation theory can also provide a reasonable prediction of these disorder-induced frequency shifts [117]. The disorder-induced shift is given by

$$\Delta\omega = g_2 \frac{\omega^2}{12} \int_0^\infty \frac{1}{\omega^2 - \omega_\mathrm{i}^2} N_\mathrm{d}(\omega_i)\mathrm{d}\omega_i \tag{3.83}$$

with the phonon density of states [118] are normalized through $\int_0^\infty N_\mathrm{d}(\omega_i)\mathrm{d}\omega_i = 6$. The mass fluctuation parameter g_2 is given by

$$g_2 = \sum_i x_i \left(1 - \frac{M_i}{\bar{M}}\right)^2, \tag{3.84}$$

where x_i is the fraction of isotope i, M_i its mass, and $\bar{M}$ is the average mass. This equation yields $g_2 = 5.87 \cdot 10^{-4}$ for natural Ge and $g_2 = 1.53 \cdot 10^{-3}$ for the alloy, respectively. Using (3.83), Zhang et al. [119] obtained a disorder-induced frequency shift of $0.41\,\mathrm{cm}^{-1}$ for the natural sample and $1.07\,\mathrm{cm}^{-1}$ for the $^{70/76}$Ge alloy sample, respectively.

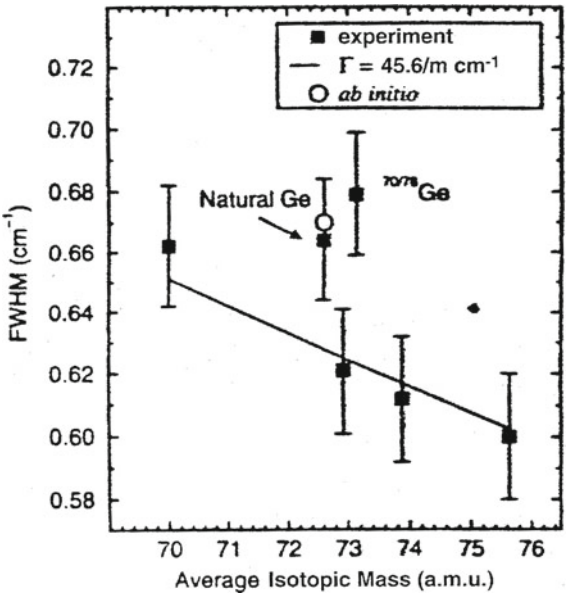

Fig. 3.17 Intrinsic phonon linewidth of isotopic Ge vs average mass, measured at 10 K an excitation of 6471 Å (after [120])

An additional broadening $[(0.03 \pm 0.03)\,\mathrm{cm}^{-1}$ for natural Ge and $(0.06 \pm 0.03)\,\mathrm{cm}^{-1}$ for the alloy sample] is clearly seen (see Fig. 3.17) in the two isotopically mixed samples. Their linewidth lie significantly above those expected from the inverse-average-mass rule. This can be attributed to a combination of disorder-induced scattering and anharmonic decay . Including the anharmonic broadening in the phonon density of states $N_{\mathrm{d}}(\omega)$, yields a nonvanishing scattering probability on the mass defects. One can thus estimate the mass disorder broadening of the optical phonon with the expression (see [2] and references therein).

$$\Gamma_{\mathrm{isotope}} = g_2 \frac{\pi\omega^2}{12} N_{\mathrm{d}}(\omega). \tag{3.85}$$

This calculation gives an additional broadening of $0.017\,\mathrm{cm}^{-1}$ for natural Ge and $0.046\,\mathrm{cm}^{-1}$ for the $^{70}\mathrm{Ge}_{0.5}^{76}\mathrm{Ge}_{0.5}$ alloy in agreement with the measured data.

Turning to the second-order spectra, Table 3.3 summarizes the observed shifts of peak positions. Agreement with the calculated shifts within framework of CPA is good. From above results, it can be concluded that the maximal shift possess LO(Γ) phonons, but broadening acoustic and optical phonons with $\boldsymbol{q} \neq 0$.

Figure 3.18 compares the composition of the Raman frequency in the VCA and CPA according to Hass et al. [53] and Spitzer et al. [122]. The present Raman data in Fig. 3.18a are in excellent agreement with those of Chrenko [123] and Hanzawa et al. [124]. Both sets of data exhibit a pronounced bowing (nonlinearity) relative to the VCA that is described very well by CPA. Hass et al. concluded that the bowing is a direct consequence of the scattering due to isotopic disorder. Similar nonlinearities

Table 3.3 Observed peaks in the second-order Raman spectra of isotopically enriched ^{70}Ge and natural Ge, with frequency shifts compared to coherent potential approximation (CPA) calculations (after [121])

Identification	Phonon energies, cm^{-1}			Relat. shift of phon. energy, %	
	in ^{70}Ge	in natural Ge	in natural Ge		
	Expt.	Expt.	CPA	Expt.	CPA
2TA(X)	165.1	162.5	161.8	1.6	2.0
2TA(W-K,L-W)	235.9	231.2	231.5	2.0	2.0
O(Γ)	309.4	304.5	304.8	1.6	1.4
TO(X) + TA(X)	361.1	354.6	354.0	1.7	1.9
2LA(K-L)	389.8	382.3	382.1	1.9	2.0
2TO(X)	554.8	546.0	542.5	1.6	2.2
2TO(W)	562.8	553.6	553.9	1.7	1.6
2TO(L)	586.7	577.5	575.2	1.6	2.0
2O(Γ)	618.8	609.0	609.6	1.6	1.4

are observed in many other properties of alloy systems (e.g., the bandgaps of semiconductor alloys and isotope-mixed crystals [45]. The deviation from linearity is approximately 5 cm^{-1}near the middle of the composition range. This is much larger than the experimental uncertainties (about the size of the data points) and should certainly be considered if the Raman frequency is to be used as a measure of isotopic composition [115].

The measured Raman linewidth (Fig. 3.18b) is larger near the center of the composition range than near the end points. The variation is not symmetric in x and $(1-x)$ and the maximum width occurs at approximately 70 at% ^{13}C. The CPA curves represent intrinsic contributions to the Raman linewidth due to the disorder-induced broadening of the zone-center optic mode. The observed widths, according to Hass and coworkers [115] contain additional contributions due to instrumental resolution ($\sim 1.8\,\text{cm}^{-1}$) and anharmonic decay [1, 50]. The anharmonic broadening of the Raman line has been calculated for diamond by Wang et al. [96] to be on the order of 1 cm^{-1} at 300 K. Contributions other than disorder thus account well for the observed widths near $x = 0$ and 1. Assuming that such contributions are reasonably constant across the entire composition range, we see that both CPA calculations account very well for the qualitative trend in the data, including the peak near $x = 0.7$. The pure valence force field model [82] underestimates the magnitude of the variation, however, by about a factor of 2 (for details see [115, 122]).

Detailed calculations of the self-energy and the first-order Raman line shape were performed by Spitzer and coworkers [122]. They have obtained a qualitative agreement with experimental results. Comparing the Raman line shape of Ge and C, it should be noted that the presence of a large isotopic broadening for diamond has been observed, contrary to the small broadening observed for Ge. The reason lies in the fact that $\boldsymbol{k} = 0$ is not the highest point of the phonon dispersion relation in

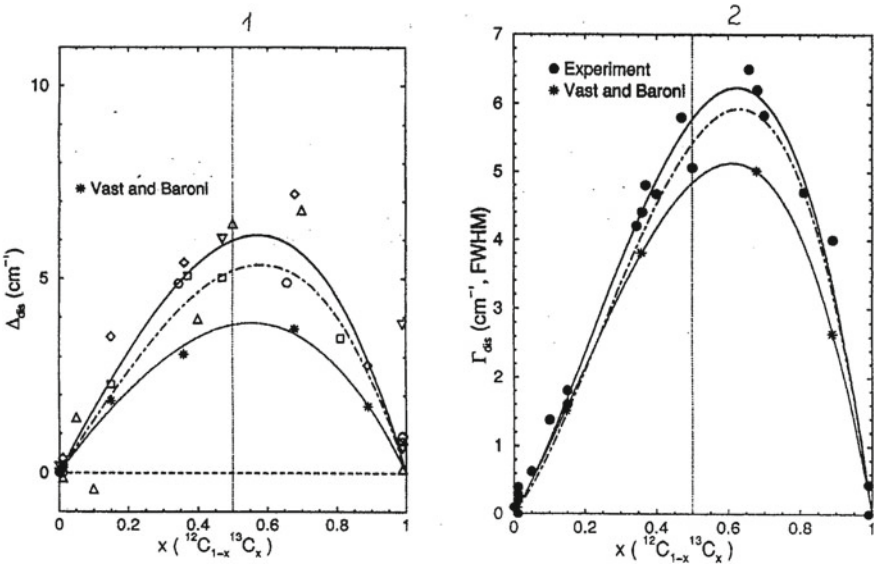

Fig. 3.18 (1) Disorder-induced shift of the Raman phonon of diamond as a function of the ^{13}C concentration. The open symbols are Raman experimental data, whereas the asterisks correspond to **ab initio** calculations. The solid line is a theoretical fit [1]. The dotted and dot-dashed lines represent the fits to theoretical values obtained from ab initio and CPA calculations, respectively (after [115]); (2) Disorder-induced broadening of the Raman phonon of diamond as a function of the ^{13}C concentration. The filled circles have been obtained from the Raman data by taking into account the corresponding instrumental resolutions and subtracting the anharmonic broadening $\Gamma_{\text{anh}} \approx 2\,\text{cm}^{-1}$ (FWHM). The solid line is a theoretical fit [1]. The dotted and dot-dashed lines are the corresponding fits to the values obtained from ab initio and CPA calculations, respectively (after [115])

the case of diamond [99]. This maximum lies somewhat off $\boldsymbol{k} = 0$, resulting in a nonvanishing density of states at ω_0, considerably larger than that found from relation $N_{\text{d}} \sim \text{Re}(\omega_0 - \omega + i\,\frac{\Delta\omega_0}{2})^{1/2}$ [2]. This density of states is strongly asymmetric about ω_0, a fact which yields an asymmetric phonon line shape. This asymmetry also results in a lopsided dependence of the linewidth vs concentration (Fig. 3.18), which disagrees with the symmetric dependence expected from the proportionality to g (3.84).

As already mentioned, because of the isotopic disorder not only $\boldsymbol{k} = 0$ phonons should contribute to the first-order Raman spectrum but also all others, with maximum contributions for ω in the regions where the density of states has a maximum, especially for the TO phonon branches. The experimental results for Ge are shown in Fig. 3.19, where the vertical scale has been normalized to be one at the peak of the Raman peak. The disorder-induced contribution is rather weak (less than 0.4% of the peak) but clearly identifiable since it increases from natural Ge to $^{70}\text{Ge}_{0.5}$ $^{76}\text{Ge}_{0.5}$ and is absent for ^{70}Ge [121]. The two structures observed (at 275 and 290 cm^{-1}) correspond to maxima in the density of TO phonons. The disorder-induced

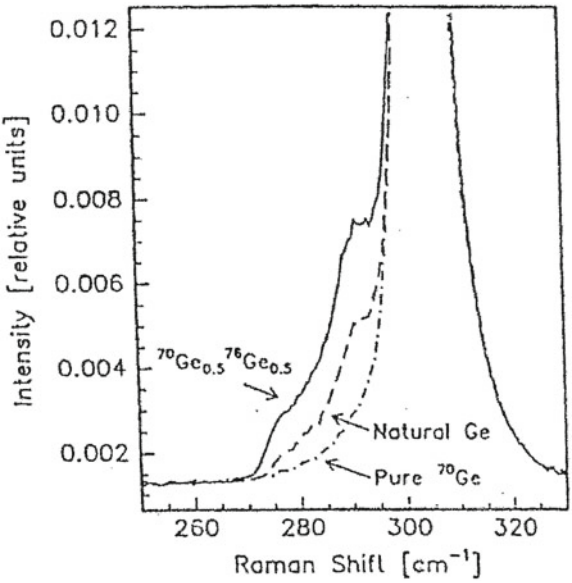

Fig. 3.19 Vertically expanded first-order Raman line of Ge with different amounts of isotopic disorder, exhibiting the disorder-induced scattering (after [2])

contribution of Fig. 3.19 can be theoretically calculated using CPA techniques. Fuchs and coworkers found two different contributions: a "coherent" one, due to the structure in the imaginary part of the self-energy of the $\boldsymbol{k} = 0$ phonon, plus an "incoherent" part due to nonconservation of $\boldsymbol{k}$ [111]. The two contributions, together with their sum, are compared with the experimental results in Fig. 3.20. The agreement is excellent. This effect has also been observed for diamond, α-Sn, as well as for LiH_xD_{1-x} (see also below Fig. 3.21). Effects of the isotopic disorder observed in Raman spectra of LiH_xD_{1-x} crystals are similar, but have some important differences [18]. In contrast to germanium and diamond, whose first-order Raman spectra exhibit the one-mode behavior of LO phonons over entire range of concentrations, Raman spectra of LiH_xD_{1-x} crystals show the one-and- two-mode behavior of LO(Γ) phonons and the localized mode at low x [45]. Figure 3.21 shows the dependence of the half width of the 2LO(Γ) phonon line in the Raman spectrum on the isotope concentration. As the excitation wavelength increases, the LO phonon line slightly broadens both in pure and mixed crystals [45], which was earlier observed by Klochikhin et al. 1973 [6]. However, the half width of this line (Fig. 3.20) strongly depends on the isotope concentration. Because the width of optical bands of pure LiH and LiD crystals are comparable, it is reasonable to assume as was done by Plekhanov [45] that the broadening of LO(Γ) phonon lines in Raman spectra of LiH_xD_{1-x}crystals is partially caused by the isotopic disorder of a crystal lattice. This assumption is consistent with a nonlinear dependence of the half width of LO(Γ) phonon lines in the second-order Raman spectra of LiH_xD_{1-x}crystals (Fig. 3.21) as well as with additive structure in the resonant Raman spectra of these crystals [48]. It is not improbable that the shift and the broadening of LO(Γ) phonon lines in Raman

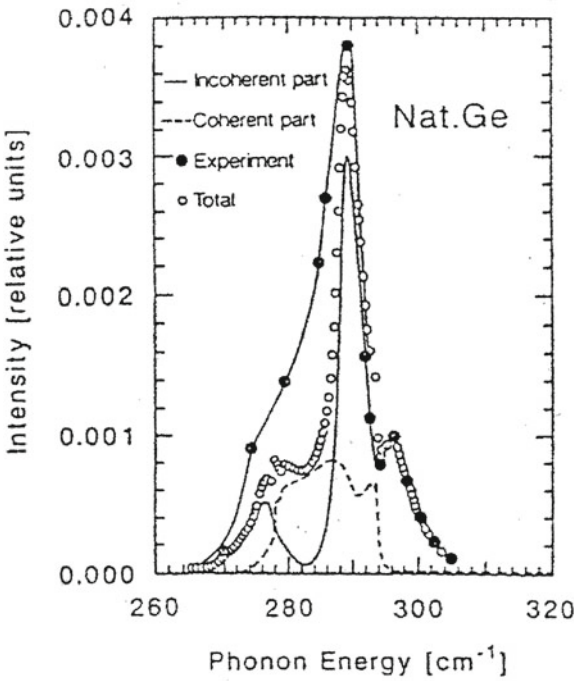

Fig. 3.20 Coherent and incoherent components of the disorder-induced Raman scattering of natural Ge calculated with the CPA (after [2])

spectra of LiH_xD_{1-x}crystals also can be described within the framework of CPA in the anharmonic approximation.

Returning to the Raman spectra of GaN crystals the following should be noted. The calculations of CPA are more complicated in polyatomic crystals since mass fluctuations can exist at different atomic sites where the atoms have different eigenvectors. In addition, the phonon density of states of GaN with wurtzite structure, whose accuracy should be as high as possible when it is used in a CPA calculation, is not available at present. Zhang et al. performed a rough estimate of the disorder-induced frequency shifts from second-order perturbation theory (for details see [125]). Thus, if the impurity concentration in a crystal is high enough that the interaction between impurity atoms (ions) plays an important role, such a system is called a mixed crystal with various degrees of disorder (for details see [50]).

3.9 Vibrations in Low-Dimensional Structures

3.9.1 General Remarks

Forming quantum wells or superlattices clearly changes the electronic energy of a crystal from what they are in an infinite bulk crystal (see, e.g., [9, 10]). In fact, all of the crystal properties are changed to a greater or lesser extent. Phonon

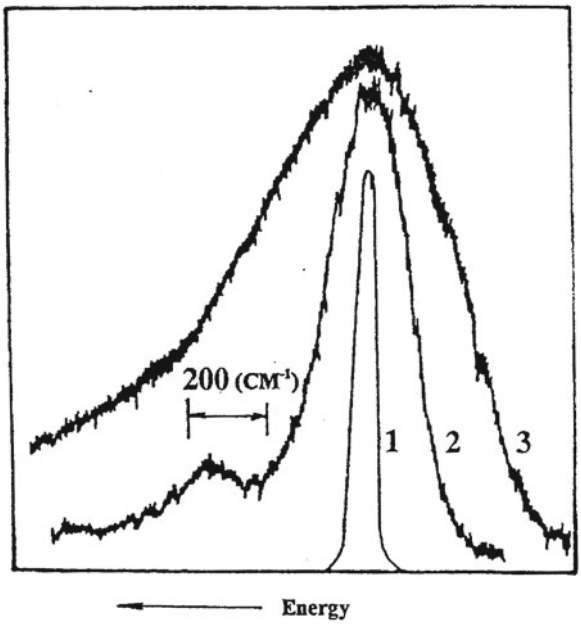

Fig. 3.21 Line shape of the excited light (1) 2LO(Γ) line scattering at 4.2 K in LiH (2) mixed crystals LiH_xD_{1-x} (3) excited at $\lambda = 253.7$ nm (after [45])

interaction has been altered unavoidably by the effects of dimensional confinement on the phonon modes in nanostructures. As shown in detail in well-known books [8, 9], the dimensional confinement of phonons resulted in restriction in the phase space of the phonon wave vector $\boldsymbol{q}$. Indeed, as shown in paper [126] that the wave vectors of the optical phonons in a dielectric layer of thickness L_z are given by $q_z = n\pi/L_z$ in analogy to the case of an electron in an infinitely deep quantum well. Later, Fasol et al. [127] used Raman scattering techniques to show that the wave vectors $q_z = n\pi/L_z$ of optical phonons confined in a ten-monolayer-thick AlAs/GaAs/AlAs quantum well are so sensive to changes in L_z that a one-monolayer change in the thickness of the quantum well is readily detectable as a change in q_z. These early experiments demonstrated not only that phonons are confined in nanostructures but also that the measured phonon wave vectors are well described by relative simple continuum model of phonon confinement.

The most elaborate superlattice linear chain model [128] is based on ab initio local density calculations of the effective interplanar forces in GaAs [129, 130]. In these papers, both longitudinal and transverse dispersion curves are obtained by taking into account all significant interactions, including long-range Coulomb forces, through a few short-range effective forces (see also [131]).The problem of transferability of the bulk forces is circumvented in this description of GaAs/AlAs superlattices: the difference between the vibrational properties of GaAs and AlAs is mainly attributed to the mass difference between gallium and aluminum. Some corrections in the Coulomb long-range interactions are introduced to better describe the longitudinal transverse splitting of AlAs. These corrections are obtained by introducing an additional term

involving a Coulomb interaction between effective charges in a rigid ion model and calculating the extra charge needed to accurately describe the splitting. This somewhat artificial correction preserves the main advantage of the method: the modulated quantities (masses, effective charges) are local and thus are directly transferable to the dynamic matrix of the superlattice. The only exception is the effective charge of As interfacial atom which is different in GaAs and AlAs and must be interpolated. This model is particularly well adapted to obtaining realistic dispersion curves with a minimum of arbitrary assumptions. Other fitting procedures which describe the bulk dispersion curves with intermediate range forces, different in both compounds, indeed involve rather questionable interpolation schemes to generate the superlattice interactions.

The so-called dielectric and elastic continuum models of phonons in nanostructures (see below) lead to modes which are confined to the individual semiconductor layers—confined modes—while some propagate along boundaries between the layers—the so-called interface modes [132, 133].

3.9.2 Elastic Continuum Model of Phonons

A precise knowledge of the phonon deformation potentials, i.e., the derivative of the optical phonon frequency with respect to an elastic deformation of the lattice is crucial for an effective use of Raman scattering as powerful strain-characterization tool in compound semiconductor nanostructures [15]. As will become clear, the elastic continuum model of acoustic phonons provides an adequate description of acoustic phonons for nanostructures having confined dimensions of about two atomic monolayers (see, e.g., [134]). The case of a longitudinal acoustic mode propagating in quasi-one -dimensional structure provides an illuminating application of elastic continuum model [135]. Consider an element dx on a quasi-one-dimensional slab located between x and $x + \mathrm{d}x$. Let us take a longitudinal displacement as an example. The stress F(x), which is the force per unit area in this structure of area A, is given following from Hook's law:

$$F = Kg \tag{3.86}$$

where $g = \mathrm{d}u/\mathrm{d}x$ is the strain, $u(x, t)$ describes the uniform longitudinal displacement of the element dx, and $\boldsymbol{K}$ is a proportionality constant known as Young's modulus (see, e.g., [13]). In such a case, Newton's second law is

$$\rho(x) A \mathrm{d}x \frac{\partial^2 u(x,t)}{\partial t^2} = [T(x + \mathrm{d}x) - T(x)]\, A, \tag{3.87}$$

describing the dynamics of the element dx and $\frac{\partial^2 u(x,t)}{\partial t^2}$. Using Hook's law

$$T(x+\mathrm{d}x)-T(x)=\left(\frac{\partial t}{\partial x}\right)=\left(K\frac{\partial g}{\partial x}\right)\mathrm{d}x=\left(K\frac{\partial^2 u}{\partial x^2}\right)\mathrm{d}x, \tag{3.88}$$

and from (3.87), we have

$$\frac{\partial^2 u}{\partial t^2}=\left(\frac{\rho(x)}{K}\right)\frac{\partial^2 u}{\partial t^2}, \tag{3.89}$$

which is recognized as the one-dimensional wave equation, also known as the classical Helmholtz equation (see, e.g., [136]).

Seeking solution of this one-dimensional wave equation $u(x)=\xi \mathrm{e}^{\mathrm{i}(\mathrm{qx}-!\mathrm{t})}$, where $q=2\pi/\lambda$ and ω is the angular frequency of the wave. From this model, it follows that the dispersion relation for the longitudinal acoustic (LA) mode is $\rho\omega^2=\mathrm{Kq}^2$ or $\omega=\mathrm{v_l q}$, where $\mathrm{v_l}=\sqrt{K/\rho}$. The longitudinal sound speed, $\mathrm{v_l}$, has typical values of (3–5) x $10^5\,\mathrm{cms}^{-1}$ and $\rho=4\,\mathrm{gcm}^{-3}$. It follows that $\boldsymbol{K}$ must have an order of magnitude of $10^{12}\,\mathrm{gcms}^{-2}$.

In physical acoustics, the solutions of the displacement fields are frequently specified in terms of two potentials functions, a scalar potential ϕ and a vector potential $\boldsymbol{\Psi}=(\Psi_x,\Psi_y,\Psi_z)$, through [137]

$$\begin{aligned} u&=\frac{\partial\phi}{\partial x}+\frac{\partial\Psi_x}{\partial y}-\frac{\partial\Psi_y}{\partial z},\\ v&=\frac{\partial\phi}{\partial y}+\frac{\partial\Psi_x}{\partial z}-\frac{\partial\Psi_z}{\partial x},\\ w&=\frac{\partial\phi}{\partial z}+\frac{\partial\Psi_y}{\partial x}-\frac{\partial\Psi_x}{\partial y}, \end{aligned} \tag{3.90}$$

where ϕ and Ψ_i, $i=x,y,z$ satisfy

$$\begin{aligned} \nabla^2\phi&=\frac{1}{c_\mathrm{l}^2}\frac{\partial^2\phi}{\partial t^2},\quad c_\mathrm{l}^2=\frac{\lambda+2\mu}{\rho},\\ \nabla^2\Psi_\mathrm{i}&=\frac{1}{c_\mathrm{t}^2}\frac{\partial^2\Psi_i}{\partial t^2},\quad i=x,y,z,\quad c_\mathrm{t}^2=\frac{\lambda}{\rho}. \end{aligned} \tag{3.91}$$

The scalar potential ϕ corresponds to the irrotational part of the solution and the vector potential corresponds to any remaining rotational fields. In the scientific literature, the irrotational solutions are also referred to as the longitudinal, compressional, or dilatation solutions. Moreover, seismologists frequently refer to these solutions as P waves [138]. Likewise, the rotational vector potential solutions based on Ψ_i are identified as transverse, shear, distortial, or equivoluminal solutions. In seismology, these solutions are commonly identified as S waves.

Herein, the irrotational solutions will generally be referred to as longitudinal modes and the corresponding sound speed will be denoted by $\mathrm{c_l}$. Likewise, the rotational fields will be denoted as transverse modes and the associated sound speed will be denoted by $\mathrm{c_t}$. The principal interest in this chapter is on using the

longitudinal and transverse solutions of the elastic continuum model to describe the longitudinal acoustic (LA) and transverse acoustic (TA) phonons in nanostructures (see also [139]).

3.9.3 Dielectric Continuum Model of Phonons

This macroscopic model was first invoked by Zucker et al. [140] to explain the anomalous selection rules observed in right-angle Raman scattering from GaAs–AlGaAs structures (see also [139]). It is well known that the long-wavelength optical vibrations in ionic crystals with two atoms per unit cell can be characterized by two coupled (Born–Huang [14]) equanions that lead to dielectric functions of the form [131] given as

$$\varepsilon(\Omega) = \varepsilon_\infty \frac{\Omega^2 - \Omega_{\mathrm{LO}}^2}{\Omega^2 - \Omega_{\mathrm{TO}}^2}, \tag{3.92}$$

where Ω_{TO} and Ω_{LO} are the transverse (TO) and longitudinal-optical (LO) phonon frequencies, respectively, and ε_∞ is the purely electronic contribution. These vibrations are associated with a macroscopic potential that satisfies the Laplace equation [136] given by

$$\varepsilon \nabla^2 \phi = 0. \tag{3.93}$$

If we consider a superlattice as a stacking of layers of two different ionic media, (3.93) has to be solved in the two layers that form the unit cell of the system. These solutions must be matched, corresponding to the different dielectric functions of the two media. These solutions must be matched at the interfaces by requiring that the potential and the perpendicular component of the electric displacement be continuous. The potential function is also required to satisfy Bloch's theorem [13].

Below, we apply the above to a GaAs–AlAs superlattice. We will use $\varepsilon^{\mathrm{G}}(\Omega)$ for the dielectric function of GaAs and $\varepsilon^{\mathrm{A}}(\Omega)$ for the dielectric function of AlAs. If z is the superlattice growth axis, the solution will be characterized by a superlattice wave vector $(k_z, k_\parallel)$ in the superlattice Brillouin zone. A solution to (3.93) is [141]

$$\Phi = e^{\mathrm{i}k_\parallel \mathrm{x}} \boldsymbol{f}(z). \tag{3.94}$$

The function $f(z)$ satisfies the Bloch condition

$$f(z + d) = e^{\mathrm{i}k_\perp \mathrm{d}} \boldsymbol{f}(z), \tag{3.95}$$

where $\mathrm{d} = N_0 d_0$ is the superlattice period. Let us first consider solutions with $\varepsilon^{\mathrm{G}}(\Omega) = 0$, which correspond to the bulk LO-mode in GaAs. With this condition, (3.93) is atomically fulfilled in the GaAs layers. For the AlAs layers, (3.93) becomes

$$\frac{\mathrm{d}^2 \boldsymbol{f}(z)}{\mathrm{d}z^2} = k_\parallel^2 \boldsymbol{f}(z). \tag{3.96}$$

We, therefore, further propose the following set of solutions, choosing $z = 0$ at the center of the GaAs-slab:

$$\boldsymbol{f}(z) = A_\mathrm{G} \sin k_1 z + B_\mathrm{G} \cos k_1 z \quad \text{on GaAs}, \tag{3.97a}$$

$$\boldsymbol{f}(z) = A_\mathrm{A} \sin k_\parallel z + B_\mathrm{A} \cos k_\parallel z \text{on AlAs}. \tag{3.97b}$$

Applying the boundary conditions, we obtain $A_\mathrm{A} = B_\mathrm{A} = 0$, and

$$A_\mathrm{G} = 0, \quad k_1 = \frac{m\pi}{N_0 d_0} \quad \text{for} \quad m = 1, 3, 5, ...\text{or} \tag{3.98a}$$

$$B_\mathrm{G} = 0, \quad k_1 = \frac{m\pi}{N_0 d_0} \quad \text{for} \quad m = 2, 4, 6, ... \tag{3.98b}$$

Therefore, the modes are confined to GaAs. Similar solutions, confined to AlAs, are obtained for $\varepsilon^\mathrm{A} = 0$. The phonon displacement u for LO-modes can be obtained by noting that the displacement is proportional to the polarization, which in turn is proportional to the electric field given as

$$u \propto \boldsymbol{P} = -4\pi \boldsymbol{E} = 4\pi \nabla \phi. \tag{3.99}$$

For $m = 1, 3, 5, ...$ for instance, we obtain the following for the normalized displacement w:

$$w_\mathrm{LO}(, z) = \sqrt{\frac{2}{N_0 d_0}} \frac{1}{\sqrt{(k_1^2 + k_\parallel^2)}} \mathrm{e}^{\mathrm{i}k_\parallel \mathrm{x}} \left[i k_\parallel \cos(k_1 z) \boldsymbol{e}_\mathrm{x} + k_1 \sin(k_1 z) \boldsymbol{e}_\mathrm{z} \right], \tag{3.100}$$

where $\boldsymbol{e}_x$ and $\boldsymbol{e}_z$ are unit vectors in the x and z directions, respectively. Equation (3.100) has a number of interesting features as follows:

1. The modes do not depend on k_z, reflecting their perfect confinement within this model.
2. In the macroscopic model, all confined modes have the same bulk LO-frequency determined by the condition $\varepsilon^\mathrm{GA}(\Omega) = 0$. This is also to be expected, because the underlying bulk model represented by (3.92) neglects phonon dispersion.
3. For $k_z \ll k_\parallel \ll k_1$, the modes have essentially TO character but LO-frequencies. This is because k_1 can be regarded as an effective wave vector along the growth direction, which is bigger than the actual phonon wave vector $(k_\parallel, k_z)$, determines its LO or TO character. Precisely this feature was invoked by Zucker et al. [140] to explain the observation of modes with LO-frequency but with Raman selection rule characteristic of TO phonons (see also [142]).
4. A consequence of (3.100) is the fact that, while ϕ goes to zero at the GaAs–AlAs interface ($z = N_0 d_0/2$), the displacements, which are proportional to $\nabla\phi$, have

maxima at these points and drop abruptly to zero. This discontinuity is a rather unphysical result in contradiction with microscopic model where displacement is continuous [141].

The assertion that the mth mode from (3.98a)–(3.100) corresponds to the $m+1$ mode from microscopic models implies that the fundamental mode is missing in the macroscopic approach. In fact, one always expects a modeless mode to appear [141] which is clearly not the case with the solutions of (3.100). A detailed analysis of the completeness of the solution set in (3.100) shows indeed that some solutions are missing [142]. To understand this, let us remember that we imposed $\varepsilon^{\mathrm{G}} = 0$ to derive (3.100). An analogous set of confined AlAs modes is obtained for $\varepsilon^{\mathrm{A}} = 0$. The additional solutions must represent the case in which neither condition $\varepsilon^{\mathrm{G}} = 0$ nor $\varepsilon^{\mathrm{A}} = 0$ have been imposed from the outset. In this case, the solutions in both layers are of the form (3.97b). Applying the boundary conditions, the following equation is obtained [142]:

$$\cos(k_z d) = \frac{\eta^2 + 1}{2\eta} \sinh(k_\parallel d_1) \sinh(k_\parallel d_2) + \cosh(k_\parallel d_1) \cos(k_\parallel d_2), \tag{3.101}$$

where $\eta = \frac{\varepsilon^{\mathrm{G}}}{\varepsilon^{\mathrm{A}}}$ and $d_1 = N_1 d_0, \mathrm{d}_2 = N_2 d_0$. Since the functions ε^{G} and ε^{A} are quadratic in Ω, (3.101) is a fourth-order equation which gives four solution for each wave vector value: two AlAs-like and two GaAs-like modes. One observes a band of modes with frequencies between the TO- and LO-bulk values (the more details see [132, 141, 143]).

3.10 Optical and Acoustic Phonons in Nanostructures

During the last two decades, there has been a steady effort to understand the optical and acoustic phonons in nanostructures such as the semiconductor superlattice, quantum wires, and quantum dots (see, e.g., [135, 144]). As a preliminary to describing relations and mode structures for optical and acoustic phonons in nanostructures, phonon amplitudes are quantized in terms of the harmonic approximation, and anharmonic effects leading to phonon decay in terms of the dominant phonon decay channels (e.g., Klemen's channel [145] and Ridley channel [132]) as shown in many papers (see, e.g., [135]). These dielectric and elastic continuum models are applied to describe the deformation potential, Fröhlich and piezoelectric interactions in a variety of nanostructures including quantum wells, quantum wires, and quantum dots. We should stress that the dimensional confinement of phonons in nanostructures leads to modifications in the electronic, optical, acoustic, and superconducting properties of modern devices.

A close look at Fig. 3.22 shows a qualitative similarity between the phonon spectra of GaAs and AlAs. In layered superlattice, we have a reduced Brillouin zone for the phonons. The description for superlattices is nicely encapsulated in a 1D chain model

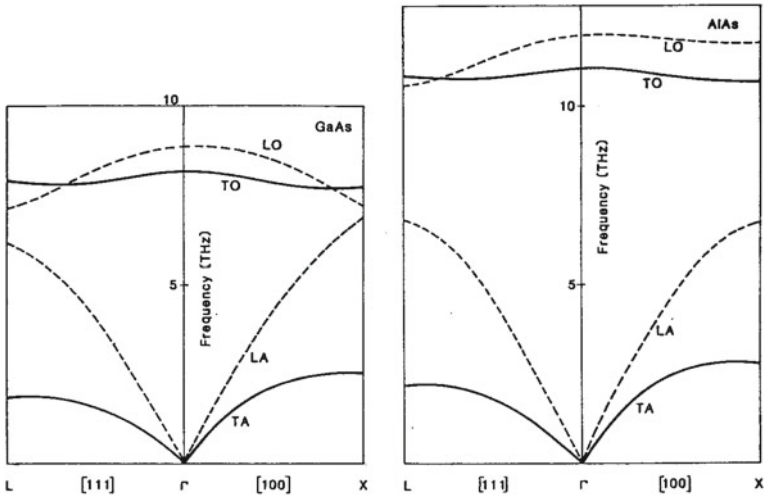

Fig. 3.22 The phonon spectra of GaAs and AlAs. Note that similarity of the latter follows from scaling the effects of the different masses of Ga and al with respect to As (after [141])

in Fig. 3.23. In this picture, a line of alternating atoms was taken corresponding to five unit cells of GaAs followed by four unit cells of AlAs , which employed a single spring constant between adjacent atoms, and considered only longitudinal displacements. We can see, at lower energies, the folding back of the acoustic branch gives many low-lying branches having optic mode behavior as viewed within the superlattice unit cell and which are, therefore, detectable in optical experiments (see below). At intermediate energies, there are modes closely associated with GaAs optic modes. Above these there is a gap to the optic modes associated with AlAs. Note that we are strictly dealing with normal modes of the entire superlattice, but in practice the amplitudes of the different modes can be greatly enhanced in one or another section of the superlattice unit cell, particularly for the optic modes. The 3D version of the essence of Fig. 3.23 is more complex, with the extra polarizations and the 3D geometry, but the physics can be obtained directly from a combination of the phonon spectra of GaAs and AlAs and the superlattice concept. One important feature missing from this simple model is the possibility of modes that are localized at the interface [135]. These modes are particular solutions of the dynamic equations of motion [131], which are not free to propagate in a direction normal to the interface, and they have an exponentially decaying amplitude away from the interface in each normal direction. As shown [135], the existence of such modes depends in a subtle manner on the quantitative details of the force constants and mass differences. The interests are in the vibrational properties of microstructure parallels that of electron states in the same microstructures [9], namely, finite size effects and the discrete separation in energy of the normal modes of vibrations [146]. The densities of phonon modes in 1D, 2D, 3D, Q1D, and Q2D systems are given in Fig. 3.24. The difference with

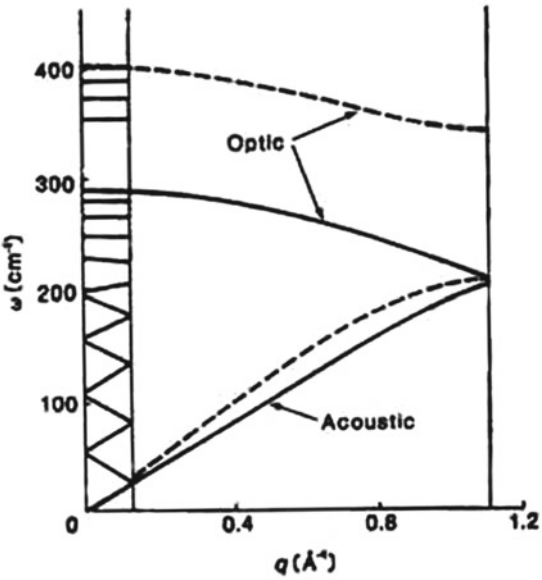

Fig. 3.23 A 1D schematic diagram of superlattice phonon modes. The phonon spectra for GaAs (solid curves) and AlAs (broken curves) are plotted in the large Brillouin zone, and the modes for a superlattice consisting of five layers of GaAs and four layers of AlAs are given in the small Brillouin zone (after [147])

electronic picture is due to the quadratic versus linear dispersion of energy with wave vector for electrons and acoustic phonon, respectively.

3.11 Experimental Manifestation of Phonons in Low-Dimensional Structures of Different Kinds

Below, we present briefly some experimental manifestations of phonons in low-dimensional structures of different kinds. In this part of our book, selected Raman measurements of optical and acoustic modes in dimensionally confined semiconductors and insulators are discussed, since these measurements illuminate the properties of such modes. We show in Fig. 3.25 obtained [141] in four scattering configurations which correspond to different combinations of irreducible symmetry components A_1 (also called Γ_1), $E(\Gamma_{12})$, and $T_2(\Gamma_{15})$ (see also [107]). The four bands of phonons mentioned above are also observed in these spectra although they would be forbidden in the perfectly ordered single crystal constituents (GaAs and AlAs). They are thus activated by the chemical disorder of the Ga and Al atoms (disorder activated ≡ DA, DATA, DALA, DATO, and DALO bands). Analogous picture of Raman spectra for isotope-disorder crystals $LiH_{1-x}D_x$ (Fig. 3.26) were observed in paper [148].

In Fig. 3.27, we present some Raman spectra of folded acoustic phonons obtained for several typical superlattices. Figure 3.28 depicts Raman spectra taken at 15 K $GaAs_N/AlAs_N$ quantum well heterostructures with thickness of $N = 10 \pm 1$ monolayers, for three different laser energies: (a) $E_L = 1.933$ eV, (b) $E_L = 1.973$ eV, and

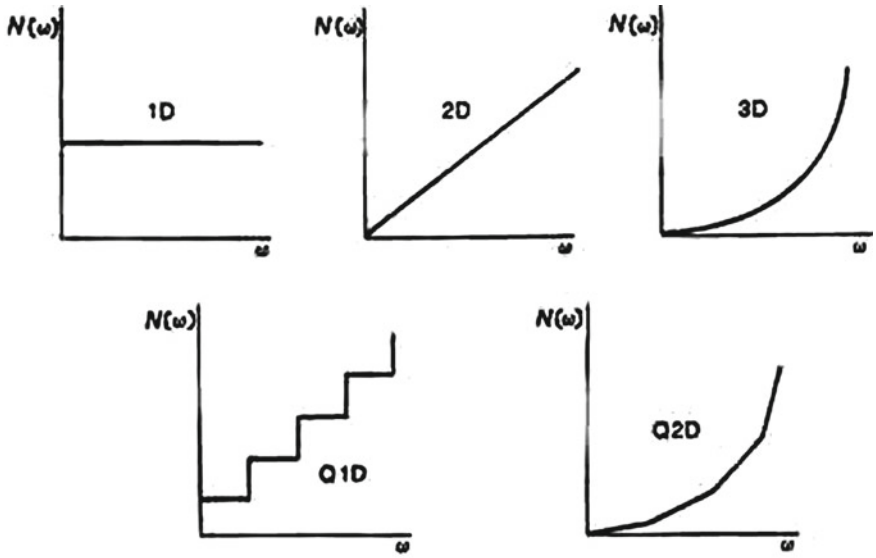

Fig. 3.24 Densities of states of acoustic-phonon modes in1D, 2D, 3D, Q1D, and Q2D systems (after [33])

(c) $E_L = 2.410\,eV$ [127]. In cases (a) and (b), the measurements were made in the $z(xx)\bar{z}$ polarization configuration and for case (c) the polarization configuration was $z(xy)\bar{z}$. The peaks on the various spectra are denoted by 10_N, 8_N, 6_N, 6_{N-1}, 5_N, 5_{N-1}, 4_N, 4_{N-1}, 3_N, 2_N, and 1_N. This notation is used to identify the LO_4 mode— confined mode with $n = 4$—in quantum well with N monolayers as the 4_N peak. Likewise, the peak associated with the LO_4 mode in a quantum well with N−1 monolayers is identified by 4_{N-1}. A remarkable feature of Fig. 3.28 is that the confined phonon wave vectors, $q_z = n\pi/L_z$, for $n = 4$, 5, and 6 are sensitive to even a one-monolayer fluctuation in the thickness of the GaAs quantum well. Moreover, Fasol et al. [127] showed that the change in q_z from monolayers to nine monolayers. These observations indicate that the phonons in AlAs/GaAs/AlAs quantum well heterostructures are confined very strongly at the heterointerfaces.

The layers of the classical superlattices are composed of different chemical constituents with their physical and chemical properties. At the interface, these different properties have to be matched, which sets limits on the growth of the superlattice structures (e.g., strain due to different lattice constants, dislocations due to strain relaxation, etc.). Moreover, for the theoretical description of these superlattices, often simplified models or assumptions about the properties at the interface have to be employed which complicates the comparison between theory and experiment. Below, we describe the vibrational properties and the corresponding Raman spectra of a new type of superlattice: the isotopic germanium and silicon superlattices where only the mass of the atoms changes at the interface, but neither the lattice constant

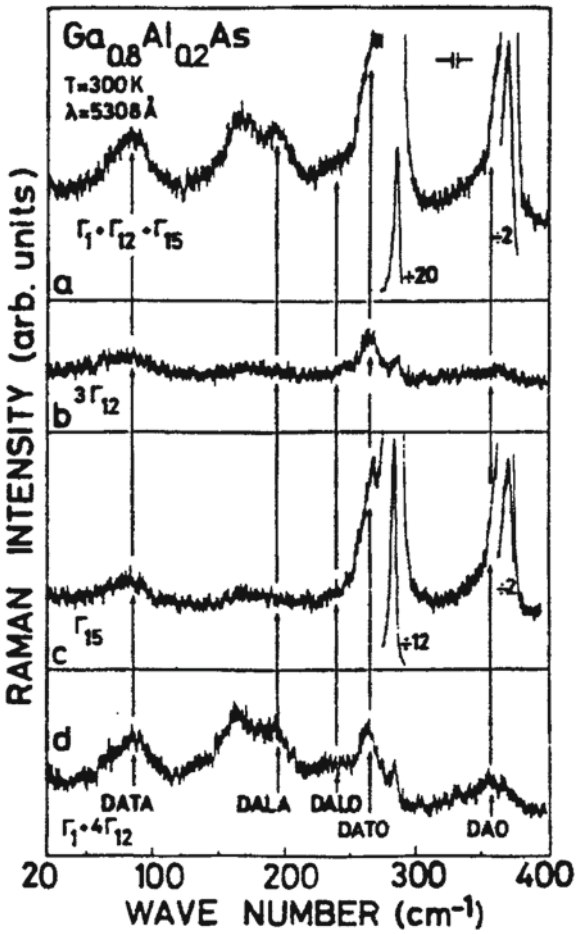

Fig. 3.25 Raman spectra of $Ga_{0.8}Al_{0.2}As$ in several scattering configurations at room temperature showing the disorder-activated DATA, DALA, DATO, and DALO bands (after [141])

nor the electronic properties. The change of the value E_g at the isotopic substitution of Si and Ge equals 1 meV and less than 0.36 meV, respectively [1, 2]. Isotopic superlattices are ideal structure for phonon studies because the electronic band structure of these semiconductors is not significantly affected by the isotope effect, i.e., the indicated materials look bulklike for electrons throughout the crystal layers. Isotopic superlattices have been proposed as waveguides for light by Berezin [149] and later Haller suggested [150] the use of neutron transmutation doping to selectively dope the layers of isotopic Ge superlattices (see also [151]). The motivation for vibrational studies of isotopic superlattices lies in their one-dimensional character which should make localization possible, regardless of the magnitude of the mass difference. A plane of ^{70}Ge embedded in bulk ^{74}Ge, for instance, should always lead to a localization vibrational mode above the Raman frequency of ^{74}Ge (compare LiH_xD_{1-x} [1]). Since it is difficult to see experimentally just one plane, the authors of [122]

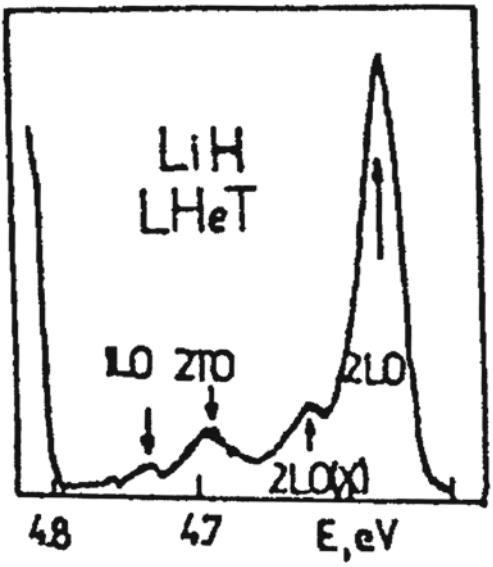

Fig. 3.26 Resonant Raman scattering spectrum of a LiD crystal at 4.2 K ($E_{excit} = 4.992$ eV). The arrow 1S indicates the energy position of the ground exciton state. Additional structure are the disorder-activated TO and LO phonons [148]

consider the possibility of a periodic superlattice with the repeat unit consisting of several planes of ^{70}Ge followed by several planes of ^{74}Ge. Thus far, such structures have been grown along [1] direction, with periods ^{70}Ge^{74}Ge ranging from $n = 2$ till $n = 32$ [122]. The results of this paper are shown in Fig. 3.29. In this figure, we can see the Raman spectra obtained for a series of these superlattices with n ranging from 2 till 32. The agreement between theory and experiment is rather good. The shortest periods studied consisted of two atomic layers each and produce a single Raman line corresponding to the Brillouin zone center optical phonon in an age crystal with isotope mass A = 72, the arithmetic average of the two masses. The $n = 4$ superlattice shows the Raman line predicted at $\sim$290 cm^{-1} though at a slightly lower intensity. In the $n = 12$ superlattice, one observes at least three strong Raman lines. For $n = 32$, the Raman spectra begin to approach the structure one would expect for two isotopically pure bulk crystals, one made up of ^{70}Ge, the other of ^{74}Ge (the more detail see [122]). Nakajima et al. [152] used Ge isotope superlattices for dynamic pump-and-probe phonon studies. These authors recorded the oscillatory reflectivity generated by high-order coherent confined phonons (see Fig. 3.30), while these oscillations monotonically decay in natural Ge, the isotope superlattices show a beating in the oscillation amplitude. Fourier transformation of the reflection oscillations shows directly the frequencies of the longitudinal- optical (LO) phonons confined to the ^{70}Ge and ^{74}Ge layers. The experimental findings are in good agreement with calculation based on a planar force constant model and a bound polarizability (see [2, 141] and references therein).

After paper of Spitzer et al. [122] the whole row of papers were devoted to isotopic low-dimensional structure [151–159]. Below, we have used the results of the paper by Kojima et al. [156]. As is well known, naturally available silicon (^{nat}Si) is

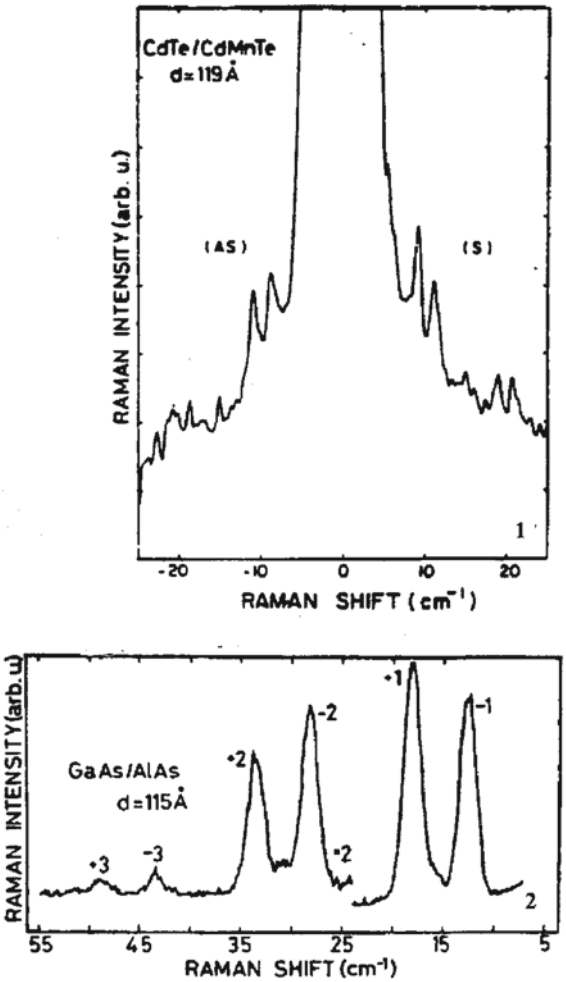

Fig. 3.27 Some typical Raman spectra exhibiting folded acoustic lines on: **1** a CdTe/CdMnTe superlattice and **2** a GaAs/AlAs superlattice [141]

always composed of three stable isotopes in fixed proportions: ^{28}Si (92.9 at.%), ^{29}Si (4.7 at.%), and ^{30}Si (3.1 at.%). The mass difference of ~7% between ^{28}Si and ^{30}Si isotopes may be an important determinant of the properties of silicon nanostructures. Besides electron and vibrational properties, the Si superlattices can control the nuclear spin properties through manipulation of Si isotopes since ^{28}Si and ^{30}Si isotopes have no nuclear spin moment while ^{29}Si has a moment of I = 1/2 [1]. Kojima et al. have grown three kinds of isotope superlattices ($^{28}Si_n/^{30}Si_n$ with $n = 8$, 12, and 24) using the solid-source MBE technique (Fig. 3.31). Here, n denotes the thickness of each isotope layer in atomic monolayers, each 0.136 nm thick. The periodicity, i.e., the number of ^{28}Si/^{30}Si pair layers stacked vertically are 80, 50, and 30 for $n = 8$, 12, and 24 samples, respectively. The resulting total thicknesses of the superlattices are 160–200 nm.

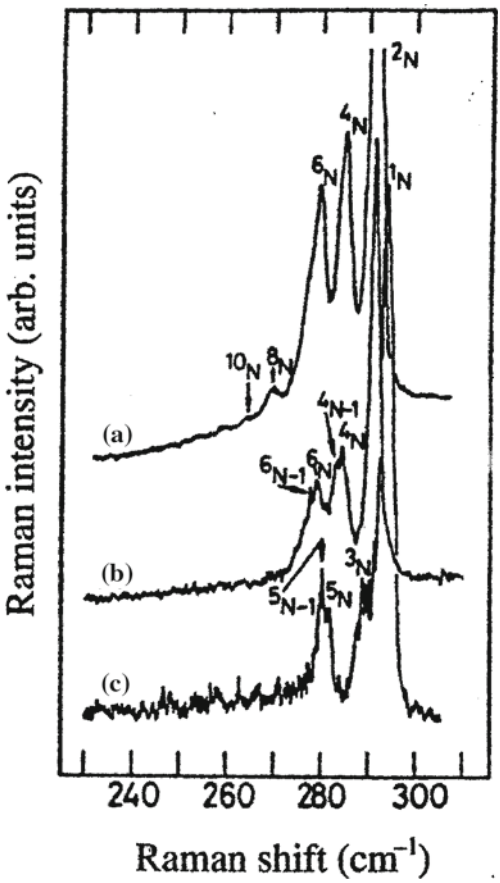

Fig. 3.28 Raman spectra taken at 15 K for $GaAs_N/AlAs_N$ quantum well heterostructures with thickness of N=10 ± 1 monolayers for three different laser energies **a**, **b**, and **c**—for detail see text (after [127])

Raman spectroscopy has been performed in order to show that it is indeed possible to manipulate phonon properties through nanoscale thickness control of the isotopic layers, and that the $^{28}Si/^{30}Si$ interfaces in isotope superlattices are abrupt. Figure 3.32 shows the Raman spectra of the Si superlattices. As expected, many peaks are observed on the shoulders of the large ^{nat}Si substrate LO peak around 523.5 cm^{-1} [2]. The wave numbers of the identified peaks are indicated in Fig. 3.32 for comparison with theoretical prediction. In parallel, phonon frequencies expected for each superlattice have been calculated theoretically using the planar bond-charge model [141] for Si. According to the authors of cited paper [156], agreement between theoretical and experimental Raman spectra is rather good.

In diamond, a wide bandgap semiconductor ($E_g = 5.48$ eV [158]) superlattice structure has not been realized yet, because diamond cannot be alloyed with other elements (admixtures to the diamond lattice cause defect formation [152]. However, bond-charge model can alter the electronic structure through electron–phonon coupling and through the change of volume with isotopic mass [1]. These effects have

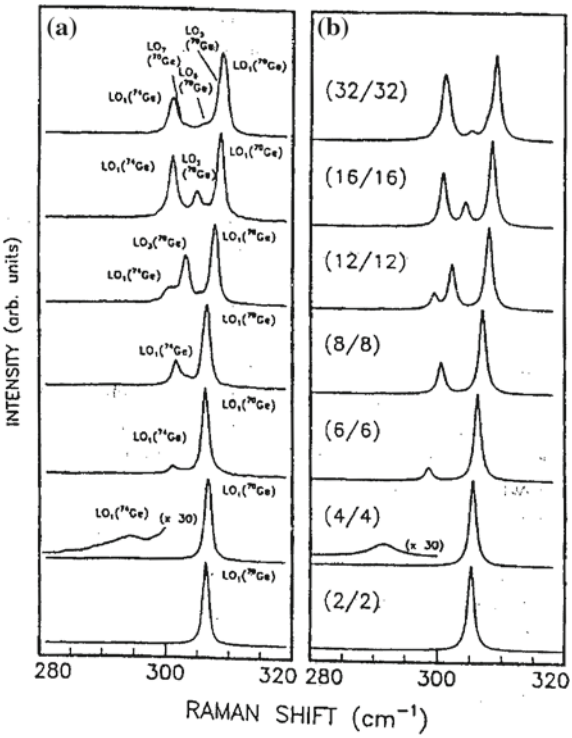

Fig. 3.29 **a** Measured and **b** calculated Raman spectra of a series isotopic $^{70}Ge_n^{74}Ge_n$ superlattices showing various confined modes of ^{70}Ge and ^{74}Ge layers. The measurements were performed with the 514.5 nm line of an Ar^+ laser at a temperature of 10 K (after [122])

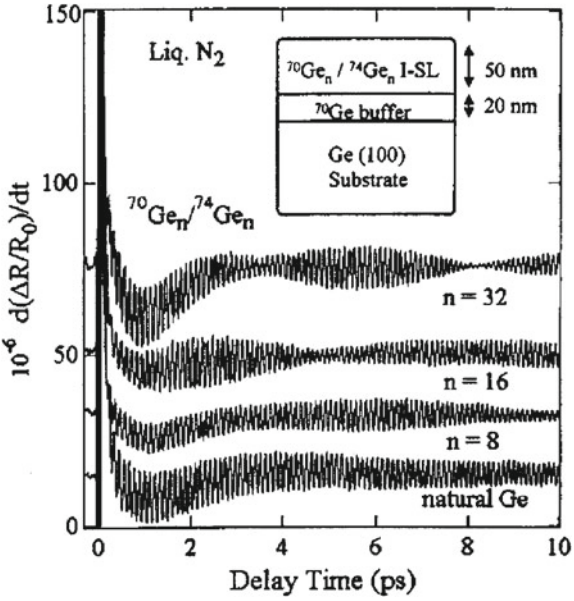

Fig. 3.30 Oscillatory component of the time-domain signals in $^{70}Ge_n/^{74}Ge_n$ isotope superlattices with various layer thicknesses and in natural Ge. Insert shows the structure of $^{70}Ge_n/^{74}Ge_n$ isotope superlattices (the number of monolayers $n = 8$, 16, and 32) (after [152])

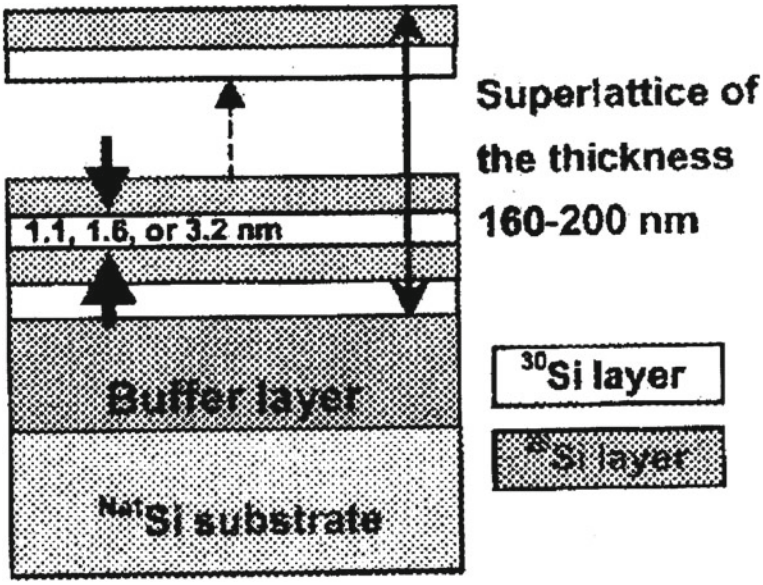

Fig. 3.31 Schematics of Si isotope superlattices grown in [156]. Thicknesses of each isotope layer are 1.1, 1.6, and 3.2 nm for $^{28}Si_8/^{30}Si_8$, $^{28}Si_{12}/^{30}Si_{12}$, and $^{28}Si_{24}/^{30}Si_{24}$ samples, respectively (after [156])

applied to realize low-dimensional superlattices from diamond [159]. According to cited paper, the excitonic bandgap of diamond as a function of mass decreases from ^{13}C to ^{12}C by 19 meV, which is about one order greater than for the heavier elements Si and Ge [2] but less one order than in Li_xD_{1-x} [1]. This relatively strong variation E_g in diamond have used to create a type of superlattice, based on isotope variations that allowed fabrication of two-dimensional electronic devices as high-electron-mobility transistors from diamond. In paper [159], diamond superlattice structures have been realized by homoepitaxial growth on single-crystalline diamond substrates with alternating layers of ^{13}C and ^{12}C (Fig. 3.33). These authors used the free-exciton emission properties to investigate the cathodoluminescence signal at 80 K from above- described structure. Figure 3.34 shows cathodoluminescence spectra taken at 80 K from diamond superlattices. As shown in Fig. 3.34a, a single peak is observed at 5.281 eV. This emission spectrum has been explained by cited authors as the free-exciton emission from the ^{12}C diamond with transverse optical phonons. No peak was detected for ^{13}C. In contrast, in Fig. 3.34C and D, this spectrum consists of two components with peaks at 5.280 and 5.297 eV, respectively, with the expected energy difference of 17 meV. In the case A and B of Fig. 3.34, excitonic emission is not observed from the higher energy bandgap of ^{13}C, but it was observed from the ^{12}C layer, which is lower in energy. The carriers that form in the ^{13}C layer migrate by carrier diffusion into the lower energy ^{12}C layers. This result

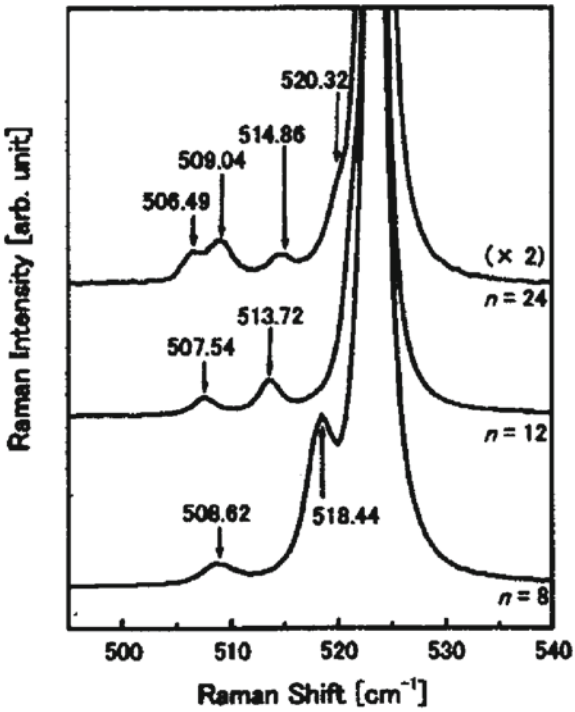

Fig. 3.32 Raman spectra of the $^{28}Si_n/^{30}Si_n$ samples with $n = 8$, 12, and 24 (after [156])

suggests that carrier confinement is possible for diamond by means of potential set up by layers of different (see Fig. 3.35).

Thus, the isotopic superlattices provide a novel and outstanding system for the study of electronic vibrational properties of superlattices: the modulation of the isotopic mass imposes no restrictions on the growth of the superlattice and the calculations of the optical spectra do not require crude assumptions about the electronic properties such as the bond polarizability (for details see [122, 152, 153]). In concluding this part, we should note that in papers [151, 155] described such low-dimensional structures as quantum wells, quantum wires, and quantum dots in isotope-mixed crystals.

3.11.1 Electron–Phonon Interaction in Low-Dimensional Structures

Taking into account the significance of the electron–phonon interaction in the low-dimensional structures we should briefly repeat our early consideration of this subject (see also [24]). One of the central themes of this part is how to reduce the size of semiconductor structures down to mesoscopic and smaller scales bringing the quantum

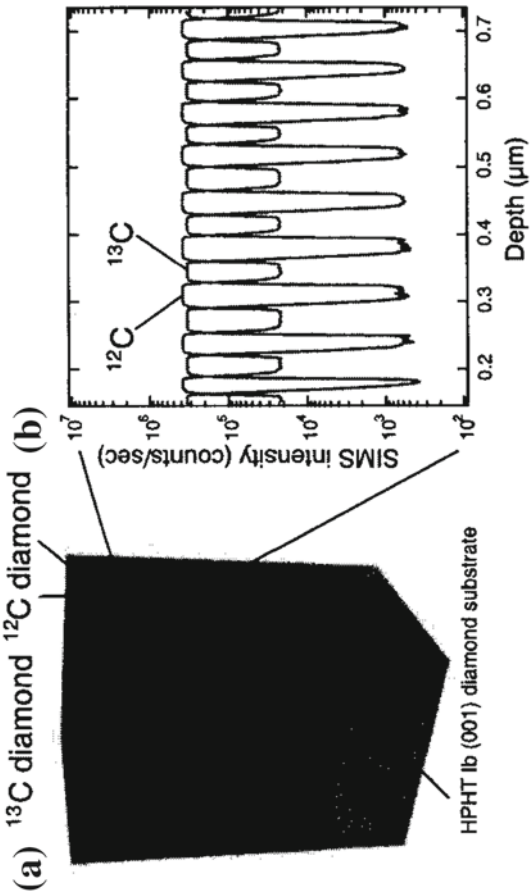

Fig. 3.33 **a** Schematic sketch of the periodic-layered structures of isotopically enriched diamond films grown in paper [159], **b** Depth profiles measured by SIMS in cited paper

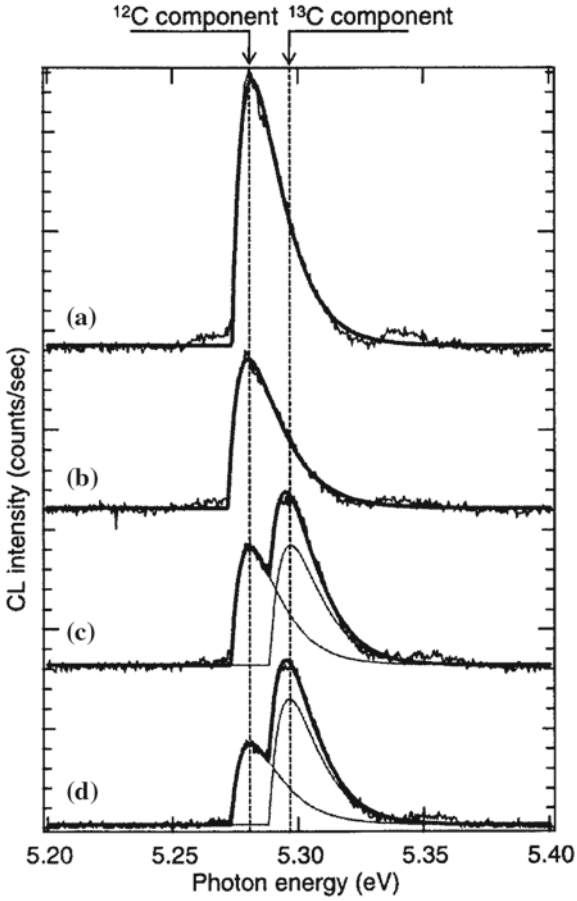

Fig. 3.34 a–d Spectra correspond respectively to layered structures. The thick line shows one fitting of an experimental spectrum (after [159])

wave nature of electrons into play, resulting in electronic and optical properties which are markedly different from those of bulk structures. Many references [11, 144, 160] describe how these properties can be exploited in device applications. But one of the key challenges facing physicists and engineers is how to make devices operate at room temperature. The main obstacle to achieving this goal is unavoidable presence of phonons, the quantum vibration of atoms (ions) making up a solid, and their ability to scatter electrons. As is well known, the room temperature mobility of 2D (1D, 0D) electron gas is limited by phonon scattering and phonons provide the principal channel of energy exchange between confined electrons and their surroundings. Over the last three decades, this topic has been the focus of intensive experimental and theoretical investigation, the progress of which has been charted specifically through two series of International Conferences: Phonon Scattering in Condensed Matter and Hot Carriers in Semiconductors (see, e.g., [132, 141, 161]). Although most of the basic concepts of electron–phonon interaction are the same as for 2D carrier– phonon

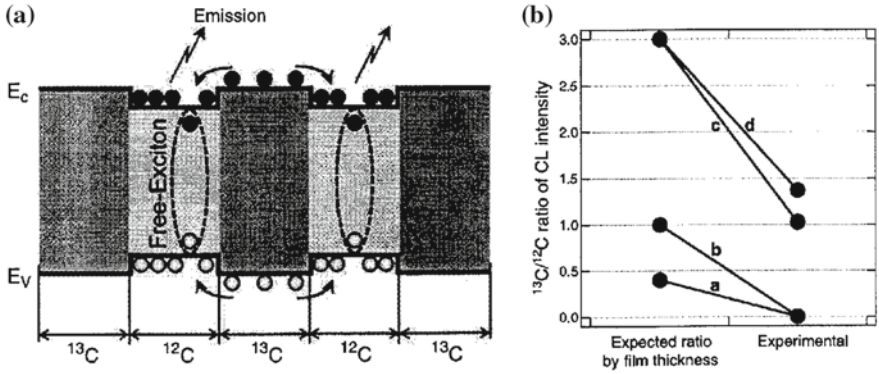

Fig. 3.35 **a** Energy band diagram. Simplified schematic diagram of arrangements of the confinement of electrons and holes in the periodic-layered structures of isotopically enriched diamond films (Fig. 3.34a, b) showing the observed excitonic spectra. E_c and E_v are conduction band edge and valence band edge, respectively. **b** Changes in $^{13}C/^{12}C$ ratio of cthodoluminescence-integrated luminescence intensity. The behaviors of "a" to "d" correspond, respectively, to the **a–d** spectra results shown in Fig. 3.34 (after [159])

interactions [162–167], the additional carrier confinement gives rise to some interesting differences. The most notable of these is the so-called phonon bottleneck [168–171]. Reducing the dimensionality of the carrier system has the effect of reducing the phase space for carrier scattering. Corresponding to each new direction of carrier confinement, a form factor arises in the electron–phonon scattering rate. This imposes a restriction on the magnitude of the momentum component in that given direction of a phonon that can be emitted or absorbed. To illustrate this effect, we consider the simple picture of an infinite rectangular confinement potential of width W. The maximum phonon wave vector component in the confinement direction is given by $q_{max} \sim \pi/W$. Additionally, the confinement breaks up the carrier energy spectrum into a set of discrete levels (see Fig. 3.2 in [24]) $E_n = \pi^2\hbar^2/2m^*W^2$. We can see that, for interlevel transitions, as W is reduced, the energy $\hbar\omega = E_{N'}\text{-}E_N$ of the emitted phonon increases as W^{-2}, while the momentum cutoff increases more slowly, as W^{-1}. Since, for acoustic phonons, $sq = \omega$, it becomes increasingly difficult for a phonon to be emitted or absorbed as W gets smaller. For optic phonons, the momentum cutoff does not present a problem, but the narrow energy dispersion means that the carrier-level spacing must lie very close to the optic phonon energy for emission or absorption to take place. This could have very serious consequence for carrier relaxation in QDs (for detail see below Fig. 3.37). However, in QWRs, the continuous carrier energy spectrum along the wire direction lifts the restriction a little (for details, see also [135, 172]).

As we have indicated above, theoretical investigations [170] have found that in heterostructures, the electron–phonon scattering rate with correct phonon mode solutions taken into account does not differ significantly from the rate assuming bulk phonon modes (see, however, [171]). For example, the electron –phonon scattering

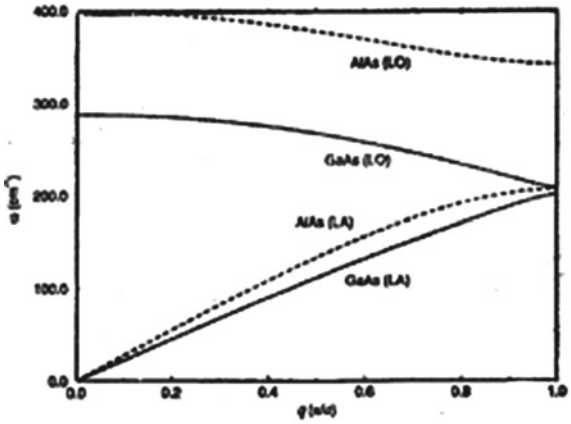

Fig. 3.36 Longitudinal [1] acoustic (LA) and optical (LO) phonon dispersion curves for GaAs (solid line) and AlAs (dotted line)

rate for AlAs–GaAs–AlAs quantum well will be somewhere in between the rates for bulk GaAs and AlAs phonons, approaching the rate for bulk GaAs (AlAs) phonons as the well width increases (decreases) [173]. Only in free-standing structures, when the confined electrons and phonons are both of lower dimension, are the rates expected to be qualitatively different from those assuming bulk phonons [174, 175]. In the following, we shall restrict ourselves to quantum wells and wires embedded in a substrate and make the simplifying approximation of bulk phonons (see also [132]). The qualitative differences in the electron–phonon rates between low- dimensional and bulk semiconductors are then a consequence of the reduced dimensionality of the electron only.

At 100 K, the dominant phonon energy $3k_BT \simeq 26\,\text{meV} = 210\,\text{cm}^{-1}$, that is, mostly acoustic phonons will be present (see Fig. 3.36). On this reason, for the first, we should consider the lower temperature range where the effect of optical phonons on electron–phonon rate can be neglected. As is well known (see, e.g., [132]), acoustic phonons give rise to a perturbing potential in two different ways. In the first, small changes in the relative positions of the atoms perturb the electrostatic potential experienced by the electrons, resulting in a change in the electron energy. In the second way, changes in the relative position of oppositely charged ions Ga and As produce an electric polarization, and hence long-range electric field which again affects the electron energy. The perturbing potentials known, respectively, as the deformation and piezoelastic potentials (see, e.g., [101, 118]) have the following form [137]:

$$V_{\boldsymbol{q}}^{\text{DP}}(\boldsymbol{r}) \approx C^{\text{DP}} q^{1/2} e^{-\boldsymbol{q}\boldsymbol{r}}, \tag{3.102}$$

$$V_{\boldsymbol{q}}^{\text{PE}}(\boldsymbol{r}) \approx C^{\text{PE}} q^{1/2} e^{-\boldsymbol{q}\boldsymbol{r}}. \tag{3.103}$$

Here, C^{DP} and C^{PE} are the coupling strength constants and $\boldsymbol{q}$ is the phonon wave vector. In this relations, we have neglected the screening due to the reduced electron–phonon interaction strength (see also [173]). Below, we have also neglected the

dependence on longitudinal/transverse mode type and have approximated the atomic lattice as an elastically isotropic continuum (see, however, [135]). For the considered temperature range, the dominant phonon wavelength is much larger than the interatomic spacing, justifying our use of the continuum approximation which replaces the discrete atomic lattice vector with continuous position vector $\boldsymbol{r}$. For the perturbing potentials (3.102) and (3.103) and electron states in the case of a quantum well with thickness d and infinite well-plane dimensions

$$\Psi_{\boldsymbol{k}}(\boldsymbol{r}) = Ce^{\mathrm{i}(\mathrm{k_x x}+\mathrm{k_y y})}\sin(\pi z/d) \tag{3.104}$$

and for quantum wire with width w, thickness d, and infinite length along the x-direction, we have

$$\Psi_{\boldsymbol{k}}(\boldsymbol{r}) = Ce^{\mathrm{ik_x x}}\sin(\pi y/w)\sin(\pi z/d) \tag{3.105}$$

the quantum well matrix elements are

$$\begin{aligned} &|\langle\Psi_{\mathrm{k}'}\mid\widehat{V}(q)\mid\Psi_{\mathrm{k}}\rangle|^2 \\ &\sim(|C^{\mathrm{DP}}|^2 q+|C^{\mathrm{PE}}|^2 q^{-1})q_{\mathrm{z}}^{-2}\left[(2\pi/d)^2-q_{\mathrm{z}}^2\right]^{-2}\sin^2(q_{\mathrm{z}}d/2)\delta_{\mathrm{k}'_{\mathrm{x}},\mathrm{k}_{\mathrm{x}\pm\mathrm{qx}}},\delta_{\mathrm{k}'_{\mathrm{y}},}\delta_{\mathrm{k}_{\mathrm{y}\pm\mathrm{qy}}} \end{aligned} \tag{3.106}$$

and the quantum wire matrix elements are

$$\begin{aligned} &|\langle\Psi_{\mathrm{k}'}\mid\widehat{V}(q)\mid\Psi_{\mathrm{k}}\rangle|^2 \\ &\sim(|C^{\mathrm{DP}}|^2 q+|C^{\mathrm{PE}}|^2 q^{-1})q_{\mathrm{y}}^{-2}\left[(2\pi/w)^2-q_{\mathrm{y}}^2\right]^{-2} \\ &\times\sin^2(q_{\mathrm{y}}w/2)q_{\mathrm{z}}^{-2}\left[(2\pi/d)^2-q_{\mathrm{z}}^2\right]^{-2}\sin^2(q_{\mathrm{z}}d/2)\delta_{\mathrm{k}',\mathrm{k}_{\pm\mathrm{q}}} \end{aligned} \tag{3.107}$$

where C is a normalization constant, m* is the effective electron mass, for wire we usually have $w > d$, and k and k' are the electron wave vectors before and after scattering, respectively. In addition to energy being conserved during a scattering event, we can see that the momentum components parallel to the QW plane and wire length are also conserved. On the other hand, the momentum components normal to the well plane and wire length are not conserved. Furthermore, the matrix elements are suppressed for normal momentum components exceeding the inverse well and wire thickness. Let us restrict ourselves to the case where the electrons and phonons are in thermal equilibrium at a common temperature T (hot electrons see [132]). Taking into account the relation between Fermi energy and areal electron density, $\mathrm{E_F} = \mathrm{n}\pi\hbar^2/\mathrm{m}^*$, we find that an AlAs/GaAs quantum well with n $5\cdot10^{11}\,\mathrm{cm}^{-2}$ has Fermi energy in units of temperature, $\mathrm{E_F/k_B} \simeq 200\,\mathrm{K}$, here $\mathrm{m}^* = 0.067\,\mathrm{m_0}$ for GaAs [176]. A split-gate AlAs/GaAs quantum wire with a Fermi wave vector of the order $\mathrm{k_F} \approx \pi/\mathrm{w} = 6\cdot10^9\,\mathrm{cm}^{-1}$ for width $w = 500\,\text{Å}$ has a Fermi energy $\mathrm{E_F/k_B} \simeq 30\,\mathrm{K}$. Such numbers are representative of those for actual structures, and therefore we typically find for QWs that electron scattering is approximately elastic in the acoustic-phonon-dominated temperature regime, while for QWRs temperatures must be somewhat lower to have approximate elastic scattering (for details see [173]). We should

add that the electron–phonon interaction due to optical modes has been reviewed in [135].

Below, we will briefly consider carrier–phonon interactions in QDs. The discussion will focus on carrier relaxation processes [176, 177] and, in particular, the predicted phonon bottleneck effects [178, 179]. In higher dimensional, e.g., QWs [132, 135], the dominant relaxation process is longitudinal-optical (LO) phonon emission via Fröhlich interaction, with subpicosecond relaxation time. In a QD, however, this process is forbidden due to the very discrete nature of the levels, unless the level separation equals the LO phonon energy $\hbar\omega_{\mathrm{LO}}$. Inoshita and Sakaki [177] considered five (LO, LA, LO ± LA and 2LA) kind of phonons for description of electron relaxation in a QD. According to the results of the authors of paper [177], a first-order contribution (LO and LA emission) was given supply by a golden rule as

$$1/\tau = \frac{2\pi}{\hbar}\sum_{\boldsymbol{q}} \mid M_{\boldsymbol{q}}^{\mathrm{if}} \mid^2 \mid N_{\mathrm{q}} + 1 \mid \delta(E_0 - \hbar\omega_{\mathrm{q}}), \tag{3.108}$$

where $\mathrm{N_q}$ is the Bose distribution function $\frac{1}{(e^{\hbar\omega_{\mathrm{q}}}/k_{\mathrm{B}}T-1)}$. The matrix element $\mathrm{M}_{\boldsymbol{q}}^{\mathrm{if}}$ can be written as

$$M_{\boldsymbol{q}}^{\mathrm{if}} = a_{\boldsymbol{q}}\langle i \mid e^{\mathrm{i}\boldsymbol{qr}} \mid f\rangle \tag{3.109}$$

with

$$a_{\boldsymbol{q}} = D\sqrt{\hbar q/2\rho c\Omega} \quad \text{(LA mode)} \tag{3.110}$$

$$a_{\boldsymbol{q}} = g_{\mathrm{f}}/q\sqrt{\Omega} \quad \text{(LO mode).} \tag{3.111}$$

Here, Ω is the system volume, the deformation potential D = 6.8 eV, density $\rho = 5.36\,\mathrm{g/cm^3}$, and the sound velocity $c = 5.15 \cdot 10^5$ cm/s (see, e.g., [176, 180]). The Fröhlich coupling constant $\mathrm{g_f} = [2\pi \mathrm{e}^2\hbar\omega_{\mathrm{LO}}(\frac{1}{\varepsilon_\infty} - \frac{1}{\varepsilon_0})]$ with $\hbar\omega_{\mathrm{LO}} = 35.9$ meV, $\varepsilon_\infty = 10.9$ and $\varepsilon_0 = 12.9$ (GaAs QD). The mode indices to $\mathrm{M}_{\boldsymbol{q}}^{\mathrm{if}}$, $\mathrm{N_q}$, and ω_{q} are suppressed to avoid unnecessary complication. By converting the summation into an integral, (3.108) can be reduced to an analytic form (see also [181]). Figure 3.37a shows the relaxation rate $1/\tau$ at T = 0 calculated in [177] as a function of $\mathrm{E_0} \simeq \hbar\omega_{\mathrm{LO}} = 35.9$ meV. The LO (one- phonon) contribution has a sharp peak immediately below $\hbar\omega_{\mathrm{LO}}$. This peak decreases exponentially on the low-energy side, while it drops more steeply (but continuously) in the high-energy side and vanishes for $\mathrm{E_0} \geq \hbar\omega_{\mathrm{LO}}$. Although the peak value exceeds $10^{15}s^{-1}$, a slight detuning of $\mathrm{E_0}$ from peak dramatically reduces $1/\tau$. (For instance, $1/\tau$ is only $10^8\,\mathrm{s}^{-1}$ for detuning $\Delta\mathrm{E_0} = -0.05$ meV). This indicates that taking advantage of the LO process requires extremely precise tuning of $\mathrm{E_0}$ to $\hbar\omega_{\mathrm{LO}}$, for more precise than it is possible with current microfabrication technology. The inclusion of the second-order LO + LA process significantly alters the situation. It gives rise to a rather broad peak on the high-energy side of $\hbar\omega_{\mathrm{LO}}$ with a peak value exceeding $\simeq 10^{11}\,\mathrm{s}^{-1}$. This peak value (corresponding to $\tau = 10$ ps), of course, is much smaller than that of the one- phonon

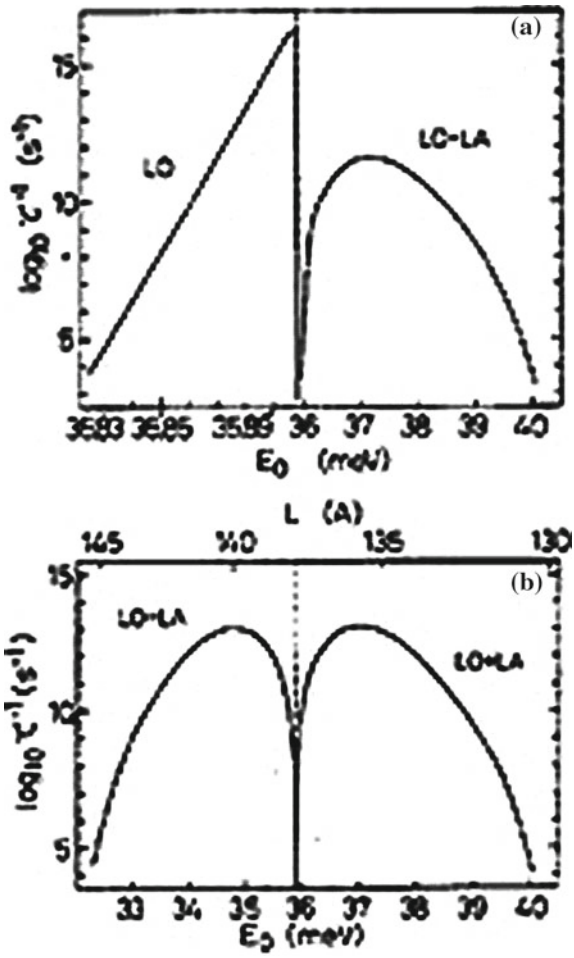

Fig. 3.37 Calculated electron relaxation rate $1/\tau$ for E_0 in the vicinity of $\hbar\omega_{LO}$. **a** $T = 0$ K, **b** $T = 300$ K. The LO peak is not shown in **b**, since it is nearly the same as in **a**, in this logarithmic scale. In **a**, the scale in abscissa is different above and below $\hbar\omega_{LO}$, which is indicated by the vertical dashed line. Dot diameter L corresponding to E_0 is shown cross the upper part (after [177])

peak, but it is still large enough for our purpose of having efficient light emission. Figure 3.37b shows $1/\tau$ at $T = 300$ K. Now, it is seen that LO–LA process, which is absent at $T = 0$ K, gives rise to another broad peak on the low-energy side of $\hbar\omega_{LO}$. The peak structure is nearly the mirror image of the LO + LA peak with respect to $\hbar\omega_{LO}$. By comparing Fig. 3.37a, b, it is seen that the LO + LA peak is enhanced by a factor of 10^2 by the temperature increase. This reflects the enhanced Bose functions of LA phonons. In Fig. 3.37b, dot diameter L is shown across the top.

To summarize the results of paper [177], it should be noted that for interval spacing $E_0 > 0.2$ meV (or dot diameter $L > 2000$ Å), multiphonon processes are generally found to provide the dominant relaxation path, with exception of the narrow energy range $\hbar\omega_{LO} - 0.3\,\text{meV} < E_0 < \hbar\omega_{LO}$. This range is so narrow that it would be hopelessly difficult to tune the interval spacing to this energy. An alternative and more

realistic way to achieve rapid relaxation is the use of the LO ± LA processes, which are in a wider range of E_0 near $\hbar\omega_{LO}$. In this paper [177], was shown that the relaxation time < 1 ns can be achieved for E_0 within the window $|E_0 - \hbar\omega_{LO}| < 3$ meV (at 300 K). This suggests that efficient photoluminescence and lasing from a QD will be possible if a dot can be designed to have a nearly harmonic (equal-spaced) level structure, where the level spacings fall into the above-indicated window (see also [178, 182]).

3.11.2 Exciton–Phonon Interaction in Low-Dimensional Systems

With main difficulty with excitons in the hybrid statistics which they obey. Diluted excitons can be treated as bosons to a first approximation, essentially because they arise from the pairing of two fermions, the electron and the hole. Excitons retain an increasing fermion nature when their density increases to the point where the concept of bound electron–hole pairs fades away to be replaced by that of an electron–hole fluid, i.e., interacting fermion systems (see also [173]). We should stress that one of the dominant features of the optical properties of GaAs–GaAlAs quantum wells are the strong intensity of the free-exciton luminescence at low temperature with respect to the intensity of the lines involving impurities. This is opposite of what is usually GaAs. This is remarkable but has not been satisfactorily explained, at least at present time. Possibly, this may be related to the very small effective volume in which the carriers and the electromagnetic wave interact in the case of quantum wells (or details, see [183]).

In the present paragraph, we are aiming to give an introduction rather than comprehensive review of all properties of 2D, 1D, and 0D excitons and exciton–phonon interactions (see, for example, [184–188]). The exciton envelope function in a state of QW with wave vector $\boldsymbol{k}$ can be written as [184]

$$\Psi_k(\boldsymbol{r}_e, \boldsymbol{r}_h) = \exp(i\boldsymbol{k}\boldsymbol{R}_\parallel) F(\rho)\varphi_e(z_e)\varphi_h(z_h), \tag{3.112}$$

where $\boldsymbol{r}_e$, $\boldsymbol{r}_h$ are the electron and hole positions, $\boldsymbol{R}_\parallel$ is the position of the exciton center of mass, $\rho = (\boldsymbol{r}_e - \boldsymbol{r}_h)_\parallel$, where $\parallel$ indicates the vector component in the QW plane, $F(\rho)$ is a function describing the relative electron–hole motion [189], z is the growth direction of the structure, and $\varphi_e(z_e)$ and $\varphi_h(z_h)$ are the electron and hole wave functions for the first size-quantized level. In the simple variational approach (see also [183, 184])

$$F(\rho) = \sqrt{\frac{2}{\pi a_B^2}} \exp\left(-\frac{\rho}{a_B}\right). \tag{3.113}$$

In last relation, a_0 is the Bohr exciton radius. In 10 nm GaAs/$Al_{0.4}Ga_{0.6}As$ QWs, a_B has a value of 12 nm and is increased to 15 nm in 20 nm QWs [144]. Below, (3.112)

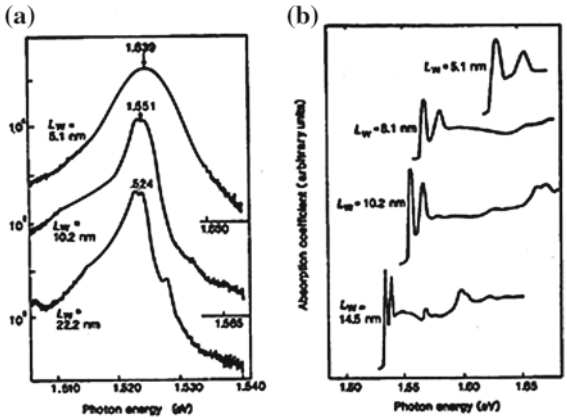

Fig. 3.38 **a** PL spectra for wells of different thickness and **b** the PLE spectra from GaAs quantum wells (after [183])

and (3.113) are used in analysis of the exciton– phonon interaction. In reality, the 2D exciton spectrum is much more complicated than suggested by these expression and includes excited exciton states (see [184, 185, 187]).

The main experimental method used to study 2D excitons is optical spectroscopy, in particular, photoluminescence (PL) and photoluminescence excitation (PLE) techniques. Optical transitions involving exciton states in QWs are governed by selection rules [184]. For example, the requirement that momentum is conserved in interactions between photons and excitons leads to the important conclusion that only excitons with $k \simeq 0$ are optically active. The result of this is that an optical spectrum usually consists of narrow lines at the energies corresponding to the minima of the exciton bands. We should indicate the absence of polariton effects in single QWs. The polariton effects, which are commonly seen in 3D exciton spectra (see, e.g., [189–191]), are due to the strong exciton– photon interaction and important when the wavelength of the coupled exciton–photon interaction (polariton [191]) is bigger than the thickness of the medium in which the polariton is propagating. In the 2D case, the thickness of a QW is so small that polariton effects may be neglected.

Typical exciton PL and PLE data for a range of thin layers of GaAs between thicker AlGaAs layers is shown in Fig. 3.38. An increase in phonon density induces an increase in the population of excited exciton states and can also lead to quenching of the PL in narrow QWs [183]. Phonons also affect the transport properties of excitons, particularly at elevated temperatures when the exciton–phonon scattering rate becomes greater than the scattering rate due to impurities and defects [179]. The basic approach used in analyzing the 2D exciton–phonon interaction is similar to that used for electrons and holes [148]. The main differences arise from the next facts as given below:

1. Excitons are Bose particles so that Bose–Einstein or frequently Boltzmann statistics are used to describe their equilibrium distribution;
2. Since their density is usually low ($n_{ex} < 10^{10}\,cm^{-2}$); therefore, it does not take into account exciton–exciton interaction;

3. excitons have a finite lifetime; and
4. exciton interaction with optical phonons results in both scattering and in their dissociation into uncoupled electron–hole pairs.

The two mechanisms responsible for the exciton–phonon interaction are those responsible for acoustic-phonon interaction with free carriers: (DP) and piezoelectric(PE) coupling, which in detail was considered in [24]. Below, we briefly report some experimental results. In polar semiconductors like GaAs, excitons are coupled to optic phonons [1, 141] through the Fröhlich interaction [189, 192] and the resulting matrix elements are approximately greater than those for acoustic phonons. However, because of their high energy ($\hbar\omega_{\mathrm{LO}} = 33.9\,\mathrm{meV}$, see above), the role of optic phonons in exciton dynamics is relatively unimportant at low temperatures, since the exciton binding energy $\mathrm{E_B} \ll \hbar\omega_{\mathrm{LO}}$ (for GaAs [139]), very few excitons exist at high temperatures ($\mathrm{k_B T} \cong \hbar\omega_{\mathrm{LO}}$) where the optic phonon population is much greater. But there is an interval of intermediate temperatures ($100\,\mathrm{K} < T < 200\,\mathrm{K}$) in which excitons can still be observed in GaAs QWs and the population of optic phonons is sufficient to influence their dynamics [191, 193].

The influence of optic phonons on the luminescence linewidths of GaAs QWs was studied by Lee et al. [191] both experimentally and theoretically. Because the optical phonon energy, $\hbar\omega_{\mathrm{LO}}$, is larger than the binding energy of an exciton,$_{\mathrm{B}}$(L), after collision of an exciton with an optical phonon, the exciton either ionized or the optical phonon energy is transferred into kinetic energy of the center of mass with elevation of the exciton to an excited state. In the former case, for the phonon absorption, these authors obtained for the transition rate

$$W_+(0)\frac{32e^2\omega_0\beta^4 m_{\mathrm{e}} N_{\mathrm{q}}}{\pi\hbar^2 L^2}\left[\frac{1}{\varepsilon_\infty}-\frac{1}{\varepsilon_0}\right]$$
$$\int_0^{\mathrm{K_{max}}} \mathrm{d}k_{\mathrm{h}} k_{\mathrm{h}} \int_0^{2\pi} \mathrm{d}\theta I(k,q)\left[(4k_{\mathrm{h}}^2+\beta^2)^{-3/2}-(4k_0^2+\beta^2)^{-3/2}\right]^2 \tag{3.114}$$

with

$$K_0 = \left[\frac{2m_{\mathrm{e}}}{\hbar^2}\right]^{1/2}\left[-E_{\mathrm{ex}}+\hbar\omega_{\mathrm{LO}}-\frac{\hbar^2 k_{\mathrm{h}}^2}{2m_{\mathrm{h}}}\right]^{1/2}, \tag{3.115}$$

$$K_{\max} = \left[\frac{2m_{\mathrm{e}}}{\hbar^2}\right]^{1/2}\left[-E_{\mathrm{ex}}+\hbar\omega_{\mathrm{LO}}\right]^{1/2}, \tag{3.116}$$

$$q^2 = k_{\mathrm{h}} + k_0 + 2k_0 K_{\mathrm{h}}\cos\theta, \tag{3.117}$$

where $\mathrm{N_q}$ is optical phonon population, $\varepsilon_\infty(\varepsilon_0)$ is the high-frequency (static) dielectric constant, k_{h} is the wave vector for the free hole, and I(k,q) has been defined in following relation:

$$I(k,q) = \frac{\pi}{2q^2(k^2+q)^2}\left[\frac{(2k^2+3q^2)\pi}{k} - \frac{k^4(1-\mathrm{e}^{-2\beta q/k})}{q(k^2+q^2)}\right]. \tag{3.118}$$

In the latter case, the exciton is in an excited state and the center of mass moving after the phonon energy has been absorbed. Their calculations show that for heavy-hole excitons, the contribution to the PL width from optical phonons becomes equal to that from acoustic phonons at $T = 200\,\mathrm{K}$. For light-hole excitons, this happens at even higher temperature. The effect of optic phonons on the exciton diffusion was analyzed by Hillmer et al. [194] who showed that it was greatest in wide QWs. Thus, in 15 nm QWs, the exciton mobility from optic phonon scattering becomes equal to that from acoustic-phonon scattering at $T \approx 150\,\mathrm{K}$, while in 4 nm QWs this does not happen until $T \approx 200\,\mathrm{K}$. So, quantum confinement produces a relative decrease in optic phonon scattering, or, in other words, acoustic phonons are more dominant in exciton scattering in QWs than in bulk material.

Optic phonons can, however, play important role in the relaxation of hot excitons at all temperatures. Peaks are often seen in excitation spectra of exciton luminescence of photon energies equal to $E(k=0)+\mathrm{n}\hbar\omega_{\mathrm{LO}}$ [190], where $E(k=0)$ is the energy at the bottom of the exciton band and n is an integer. This indicates the formation of hot excitons with kinetic energy much larger than $\mathrm{E_B}$ (up to 10 times [190]) which relax rapidly by emitting LO phonons and this relaxation process essentially determines the lifetime of hot excitons [146]. The creation of hot excitons and their relaxation by LO phonon emission in confined structure was first demonstrated in II–VI QWs (see, e.g., [195] and references therein), but has not been seen in GaAs QWs (see also [196, 197]).

The quantum dot structure has been developed and investigated in the last two decades [198, 198–200]. There is large interest in this development because there is the goal of fabricating useful and reasonable emission under low- threshold and under high-temperature operation compared to that of a QW heterostructure laser (see also [201–205]). Below, we briefly consider three effects in QDs:

1. As was shown above, the phonon bottleneck is an extremely debated issue in QDs research. The relaxation between the discrete states of QDs as well as between different exciton states in QD [206] will be slower than in QW, because the coupling of phonons is expected to be less efficient in a QD;
2. Exciton relaxation in QDs, which is crucial for high-speed devices performance [207]; and
3. Nitride material systems which include AlN, GaN, InN, and their alloys are widely used as light-emitting diodes (LEDs), laser diodes (LDs), and high-electron-mobility transistors (see, e.g., [208, 209]).

Sakaki and coworkers [210] have reported the exciton dynamics (see, however, [211–213]) in InAs/GaInP self- assembled QDs, grown by MBE technique, where the electron and hole are confined strongly. Due to the large bandgap in the barrier layer, the thermal escape of carriers from QDS to the wetting layer and to the matrix is prevented, which allows this sample to photoluminescence (PL) at room temperature. The PL spectra for the studied sample in paper [206] are shown in Fig. 3.36. The

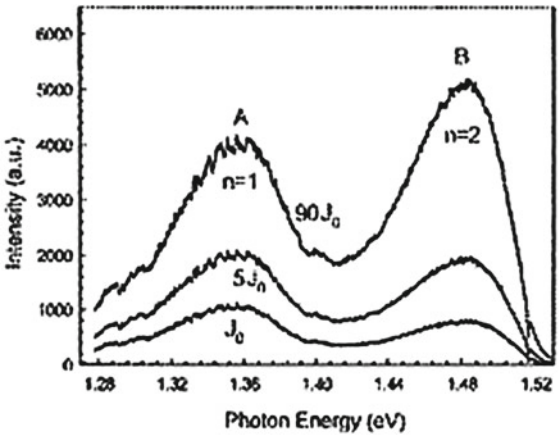

Fig. 3.39 PL spectrum of InAs/GaInP with varying excitation energy (after [206])

excitation energy is 1.590 eV (780 nm) and the temperature is 5 K. At the maximum intensity of 90 J_0, where $J_0 = 10\,J/cm^2$, the two peaks, labeled A and B, are at 1.362 and 1.484 eV, respectively. At a low intensity of J_0 to $5J_0$, the peak A is larger than B; however, as the intensity becomes stronger, the peak B dominates the entire spectra. This shows that when relatively few carriers are excited with an excitation intensity of J_0, these carriers are in the discrete energy level (A). As the intensity of excitation beam is increased, the carries are distributed over two exciton levels. From here on, the authors [206] have referred to the A peak, which is the lowest exciton level, as $n = 1$, and the B peak as $n = 2$ or the second-lowest exciton state. The time-resolved PL of the $n = 1$ and $n = 2$ exciton levels show a difference in their temporal evolution. Specifically, the rise time for the $n = 1$ data is $\sim$ 500 ps, slower than that of $n = 2$. According to the results of paper [206] there is a physical phenomenon that affects the relaxation probability that occurs between the exciton levels $n = 1$ and 2. The temperature dependence (5–200 K) of the time progression is shown that there is involvement of phonons that affect the relaxation process. Obtained results is allowed by authors of the paper [206] concluded that there is the phonon bottleneck in InAs/GaInP QDs between $n = 1$ and $n = 2$ exciton states (Fig. 3.39).

Heitz et al. have reported the optical studies of relaxation process in self-organized InAs/GaAs QDs, which were grown by the MBE method (see also [214]). The results of PLE obtained in paper [207] are depicted on the Fig. 3.40. The solid line in Fig. 3.40a presents the excitation spectrum detected at the maximum (1.11 eV) of the QD luminescence revealing excitation via absorption in the InAs WL and the GaAs barrier. Figure 3.40b compares PLE spectra recorded for different QD luminescence energies (indicated by arrows in Fig. 3.40a) displayed with respect to the detection energy.

The shape of the excitation spectra is almost independent of the detection energy showing only slight variations in the relative intensities of lines A–D. The ladder A–D not being equidistant is attributed to the finite experimental resolution of only 6 meV in the PLE measurement. Figure 3.41 shows a better-resolved luminescence spectrum

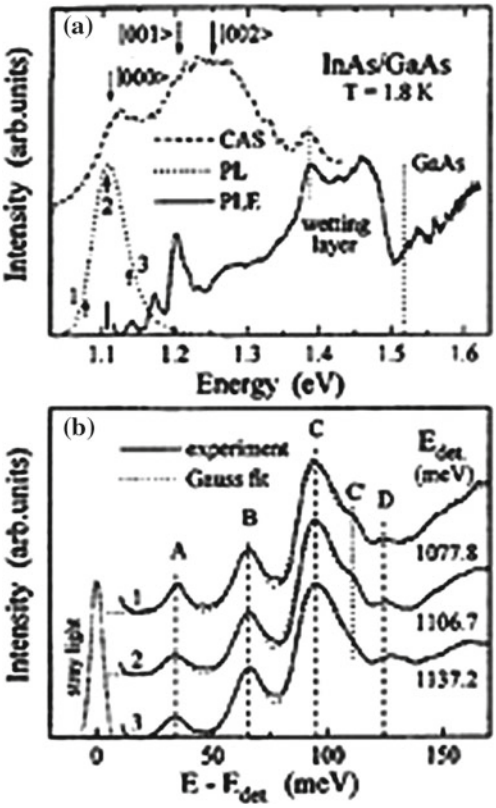

Fig. 3.40 **a** Luminescence (excited at 1.959 eV), CAS (calorimetrically absorption spectrum) and PLE (detected at the luminescence maximum) spectra of the QD structure; **b** excitation spectra of different parts of the QD luminescence [indicated by arrows in **a**] given with respect to the detection energy (after [207])

excited selectively at the high-energy onset of the QD luminescence using an Nd:YAG laser (solid line) that decomposes into three bands in the energy range of 1, 2, and 3 LO phonon replica, respectively. Four different phonon modes with energies of 29.6 meV ($InAs_{WL}$), 31.9 (InA_{QD}), 35.0 (IF), and 36.6 meV (GaAs) account for the fine structure that is not resolved in PLE spectra. In strained nanostructures, the InAs LO phonon energy of 29.9 meV is altered by both strain and phonon confinement [141]. Both effects, according to authors [207] almost perfectly compensate for each other. Thus, the phonon mode with an energy of 29.6 meV is attributed to InAs WL ($InAs_{WL}$). For the three-dimensional InAS QDs, the energy shift due to phonon confinement can be neglected. The calculated QD LO phonon energy 32.1 meV that is in excellent agreement with $InAs_{QD}$ mode energy of 31.9 meV is determined from Fig. 3.41. The mode interface (IF) with an energy of 35.0 meV is tentatively assigned to an interface phonon in the QD structure. Obtained results in paper [207] to allow the authors concluded that scattering of LO phonons from different regions of the QD structure due to the extended QD wavefunctions, together with acoustical phonon broadening, circumvents the phonon bottleneck [178, 182] effect, thus allowing exciton relaxation and carrier capture necessary for device performance.

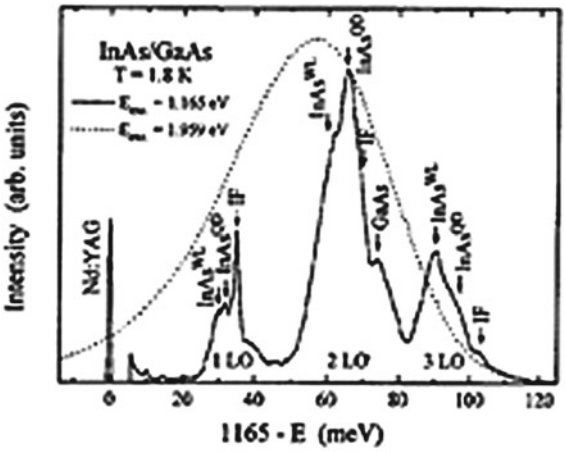

Fig. 3.41 Luminescence spectra of the QD structure excited selectively at 1.165 eV (solid line) and via the GaAs barrier (dotted line) (after [207])

The room temperature PL spectra corresponding to GaN and GaInN QDs of different sizes are displayed in Fig. 3.42. As can be seen, the PL energy is redshifted when the QD size increases. The important point to be noted is that for each kind of QDs, the PL is in the visible spectrum range. This could be quite surprising for GaN material for which the bandgap corresponds to ultraviolet luminescence. In fact, the very large built-in electrical field in GaN/AlN structures strongly decreases the transition energy. For GaN QDs in AlN matrix, a 5.5 MV/cm electrical field has been experimentally determined [208]. This very high value of the internal electrical field leads to transitions energies in GaN QDs comparable with those in GaInN QDs, although the GaInN bandgap (2.7 eV for 20% In-content) is much lower than the GaN one (3.4 eV). This is a proof of the major influence of the electrical field on the optical transitions in group III nitride materials. The comparison with QW equivalent structures indicates that QDs have higher luminescence efficiency. Moreover, the wavelength emission of QDs can be tuned from blue to orange simply by varying QD size. These results open a new route for the fabrication of efficient visible high-emitting devices.

Thus, in present paragraph, we have described some fundamental aspects of the properties of excitons in QWs and the important role that the exciton–phonon interaction plays in their dynamics. The exciton–acoustic-phonon scattering rate is surprisingly sensitive to the 2D confinement of the exciton states in nanometer layers given the 3D character of the acoustic phonons. As shown above, an important feature of this confinement is the resulting anisotropy of the matrix element for the exciton–phonon interacton. Studies of excitons and of exciton–phonon dynamics are not only of fundamental interest but also shed light on the structural and other properties of nanostructures. The position and width of the exciton resonances provide information on the quantum well layers and the quality of the material and the interfaces since exciton scattering arises from impurities and interface defects as well as from phonons and free carriers. These latter intrinsic processes are likely to be

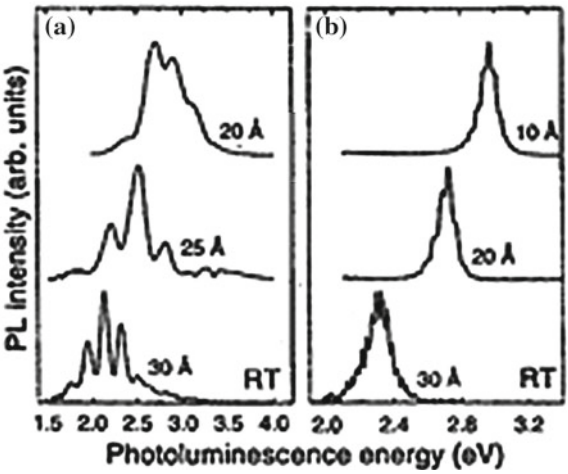

Fig. 3.42 Room temperature PL spectra of: **a** GaN QDs in AlN matrix grown on Si (111) substrate, and **b** $Ga_{0.8}In_{0.2}N$ QDs in GaN matrix grown on sapphire substrate (the 2D equivalent thickness of the QD layer corresponding to each sample is indicated) (after [208])

of increasing importance as device quality (see Chap. 4) improves and so an understanding of exciton–phonon scattering is an important aspect in the characterization of nanostructures and their technology.

References

1. V.G. Plekhanov, Elementary excitations in isotope-mixed crystals. Phys. Rep. **410**(N 1 – 3), 1–235 (2005)
2. M. Cardona, M.L.W. Thewalt, Isotope effect on the optical spectra of semiconductors. Rev. Mod. Phys. **77**, 1173–1224 (2005). October
3. J.R. Hardy, A.M. Karo, *The Lattice Dynamics and Statics of Alkali halide Crystals* (Plenum, New York, 1979)
4. A.A. Abrikosov (ed.) The Achievement of the Electron Theory of Metals (Mir, Moscow, 1984). (in Russian)
5. J.F. Scott, Soft-mode spectroscopy: experimental studies of structural phase transition. Rev. Mod. Phys. **46**(N 1), 83–128 (1974)
6. V.G. Plekhanov, *Isotope Effect in Solid State Physics* (Acdemic, San Diego, 2001)
7. G. Leibfried, W. Ludwig, Theory of anharmonic effects in crystals, in *Solid State Physics*, ed. by F. Seitz, D. Turnbull (Academic, New York, 1961), pp. 275–445
8. M.J. Kelly, *Low-Dimensional Semiconductors: Materials, Physics, Technology, Devices* (Clarendon, Oxford, 1995)
9. J.H. Davies, *The Physics of Low-Dimensional Semiconductors* (Cambridge University Press, Cmbridge, 1998)
10. J.M. Martinez-Duart, R.J. Martin-Palma, F. Aguello-Rueda, *Nanotechnology for Microelectronics and Optoelectronics* (Elsevier, Amsterdam, 2006)
11. K. Goser, P. Glösekőtter, J. Dienstuhl, *Nanoelectronics and Nanosystems* (Springer, Berlin, 2004)
12. W.A. Harrison, *Electronic Structure and the Properties of Solids* (CA, Freeman, San Francisco, 1980)

13. N.W. Aschcroft, N. David Mermin, *Solid State Physics* (Harcourt Brace College Publishers, New York, 1975)
14. M. Born, K. Huang, *Dynamical Theory of Crystal Lattice* (Oxford University Press, Oxford, 1988)
15. J. Pankove, *Optical Processes in Semiconductors* (Prentice-Hall, Englewood Cliffs, 1971)
16. G.P. Srivastawa, *The Physics of Phonons* (Hilger, Bristol, 1990)
17. J.M. Ziman, *Principles of the Theory of Solids* (Cambridge University Press, Cambridge, 1964)
18. H. Böttger, *Principles of the Theory of Lattice Dynamics* (Physik-Verlag, Weinheim, 1983)
19. P. Bruesch, *Phonons: Theory and Experiments II* (Springer, Berlin, 1986)
20. I.E. Tamm, Eine Bemerkung zur Diracschen Theorie der Lichterstroung und Dispersion. Zs. Phys. **62**(N 9), 705–708 (1930)
21. M. Born, J. Oppenheimer, Zur Quantheorie der Molekulen. Ann. Phys. **389**(N 20), 457–484 (1927)
22. V.G. Plekhanov, Lattice dynamics of isotope-mixed crystals (2010), arXiv:cond-mat/1007.5125
23. S.I. Pekar, *Untersuchungen uber die Elektronentheorie der Kristalle* (Academic, Berlin, 1954). (in German)
24. V.G. Plekhanov, *Isotope Low-Dimensional Structures* (Springer, Heidelberg, 2012)
25. R.A. Cowley, Anharmonic crystals. Rep. Prog. Phys. **31**(N 2), 123–166 (1968)
26. P.G. Klemens, Anharmonic decay of optical phonons. Phys. Rev. **148**(N 2), 845–848 (1966)
27. T.R. Hart, R.L. Aggarval, B. Lax, Temperature dependence Raman scattering in silicon. ibid **B1**(N1), 638–642 (1970)
28. J. Menendez, M. Cardona, Temperature dependence of the first-order Raman scattering by phonons in Si, Ge and α-Sn: anharmonic effect. ibid **B29**(N 4), 2051–2059 (1984)
29. M. Balkanski, R.F. Wallis, E. Harro, Theory of anharmonic damping and shift of the Raman mode in silicon. ibid **B34**(N 8), 5358–5367 (1986)
30. A.A. Maradudin, S. Califano, Theory of anharmonic processes in crystals with isotopic impurities. ibid **B48**(N 17), 12628–12636 (1993)
31. A. Debernardi, S. Baroni, E. Molinari, Anharmonic phonon lifetimes in semiconductors from density-functional perturbation theory. Phys. Rev. Lett. **75**(N 9), 1819–1822 (1995)
32. A. Debernardi, Phonon linewidth in III-V semiconductors from density-functional perturbation theory. Phys. Rev. **B57**(N 20), 12847–12858 (1998)
33. A. Debernardi, Anharmonic effect in the phonons of III-V semiconductors: first principles calculations. Solid State Commun. **113**(N1), 1–10 (2000)
34. G. Lang, K. Karch, M. Schmitt et al., Anharmonic line shift and linewidth of the Raman mode in covalent semiconductors. ibid **B59**(N 9), 6182–6188 (1999)
35. B. Steininger, P. Pavone, D. Strauch, Raman spectra of isotopic-disordered group IV semiconductors: a first principles approach. Phys. Stat. Sol. (b) **215**(N 1), 127–130 (1999)
36. N. Vast, S. Baroni, Effect of disorder on the Raman spectra of crystals: theory and ab initio calculations for diamond and germanium. Phys. Rev. **B61**(N 14), 9387–9391 (2000)
37. P.W. Anderson, Absence of diffusion in certain random lattices. Phys. Rev. **109**(N 5), 1492–1505 (1955); Solid State Phys. **2**(N1), 193–243 (1970)
38. J.M. Ziman, *Models of Disorder* (Cambridge University Press, Cambridge, 1979)
39. V.G. Plekhanov, Experimental evidence of strong phonon scattering in isotopical disordered systems: the case LiH_xD_{1-x}. Phys. Rev. B **51**(N14), 8874–8878 (1995)
40. V.G. Plekhanov, Isotope effect in lattice dynamics. Phys.-Uspekhi (Moscow) **46**(N7), 689–715 (2003)
41. B.A. Weinstein, R. Zallen, in: M. Cardona, G. Guntherodt, (eds.), Light Scattering in Solids, Vol. 4, (Berlin, Springer, 1984)
42. W.J. Borer, S.S. Mitra, K.W. Namjoshi, Line shape and temperature dependence of the first-order Raman spectrum of diamond. Solid State Commun. **9**(N16), 1377–1381 (1971)
43. W. Cochran, R.A. Cowley, Phonons in perfect crystals, *Handbuch der Physik*, vol. 25/2a (Springer, Berlin, 1967), pp. 59–156

44. V.G. Plekhanov, Isotope effect on the lattice dynamics of crystals. Mater. Sci. Eng. **R35**(N 4–6) , 139–237 (2001)
45. V.G. Plekhanov, *Giant Isotope Effect in Solids* (Stefan University Press, La Jolla, 2004)
46. R.J. Elliott, A.J. Krumhansl, P.L. Leath, The theory and properties of randomly disordered crystals and related physical systems. Rev. Mod. Phys. **46**(N 3), 465–542 (1974)
47. W. Mason, R. Thurston (eds.), *Physical Acoustics: Principles and Methods*, vol. 1–3 (Academic, New York, 1968–1970)
48. R.J. Elliott, I.P. Ipatova (eds.), *Optical Properties of Mixed Crystals* (North-Holland, Amsterdam, 1988)
49. J. Emsley, *The Elements* (Clarendon, Oxford, 1998)
50. V.G. Plekhanov, Lattice dynamics of isotopically mixed crystals. Opt. Spectr. **82**, 95–122 (1997)
51. I.M. Lifshitz, *Selected Works* (Science, Moscow, 1987). (in Russian)
52. E.N. Economou, *Green's Functions in Quantum Physics* (Springer, Heidelberg, 1983)
53. K.C. Hass, M.A. Tamor, T.R. Anthony, W.F. Banholzer, Lattice dynamics and Raman spectra of isotopically mixed diamond. Phys. Rev. **B45**(N 13), 7171–7182 (1992)
54. P. Soven, Coherent-potential model for substitutional disordered alloys. Phys. Rev. **156**, 809–817 (1967)
55. D.W. Taylor, Vibrational theory of imperfect crystals with large defect concentration. ibid, **156**, 1017–1024 (1967)
56. S.E. Gűncer, D.K. Ferry, Momentum-dependent CPA approach to disorder-induced intervalley scattering in $Al_xGa_{1-x}As$. Phys. Rev. B **48**, 17072–17079 (1993)
57. I.A. Abrikosov, B. Johansson, Applicability of the CPA in the theory of random alloys. ibid, **B57**, 14164–14169 (1998)
58. K. Koepernik, B. Velicky, R. Hayn, Analytic properties and accuracy of the generalized Blackman-Esterling-Berk coherent-potential-approximation. ibid, **B58**, 6944–6951 (1998)
59. K.C. Hass, M.A. Tamor, T.R. Anthony, W.F. Banholzer, Effect of isotopic disorder on the phonon spectrum of diamond. ibid, **B44**, 12046–12053 (1991)
60. J. Spitzer, P. Etchegoin, T.R. Anthony, Isotopic-disorder induced Raman scattering in diamond. Solid State Commun. **88**, 509–513 (1983)
61. H.D. Fuchs, G.H. Grein, C. Thomsen, Comparison of the phonon spectra of ^{70}Ge and ^{nat}Ge crystals: effects of isotopic disorder. Phys. Rev. B **43**, 483–491 (1991)
62. D.T. Wang, A. Gobel, J. Zegenhagen et al., Raman scattering on α-Sn: dependence on isotopic composition. ibid, **B56**, 13167–13171 (1997)
63. V.G. Plekhanov, Fundamentals and applications of isotope effect in modern technology, J. Nucl. Sci. Technol. (Japan) **43**(4) 375–381 (2006)
64. H. Ehrenreich, W. Schwartz, The electronic structure of alloys, *Solid State Physics*, vol. 31 (Academic, New York, 1976), pp. 149–286
65. B. Dorner, *Inelastic Neutron Scattering in Lattice Dynamics*, vol. 93, Springer Tracts in Modern Physics (Springer, Berlin, 1982)
66. V.G. Plekhanov, *Applications of the Isotopic Effect in Solids* (Springer, Berlin, 2004)
67. M.A. Krivoglaz, *Theory of scattering X-Rays and Thermal Neutrons by Real Crystals* (Science, Moscow, 1967). (in Russian)
68. W. Cochran, *The Dynamics of Atoms in Crystals* (Arnold, London, 1973)
69. A.C. Anderson, J.P. Wolfe (eds.), *Phonon Scattering in Condensed Matter* (Springer, Berlin, 1986)
70. G. Dolling, Neutron spectroscopy and lattice dynamics, in *Dynamical Properties of Solids*, vol. 1, ed. by G.K. Horton, A.A. Maradudin (North-Holland, Amsterdam, 1974), pp. 543–629
71. G. Dolling, A.D.B. Woods, Thermal vibrations crystal lattice, in *Thermal Neutron Scattering*, ed. by P.A. Egelstaff (Academic, New York, 1965), pp. 178–262
72. E.B. Wilson, J.C. Decius, P.C. Gross, *Molecular Vibrations* (McGraw-Hill, New York, 1955)
73. H. Bilz, W. Kress, *Phonon Dispersion Relations in Insulators* (Springer, Berlin, 1979)
74. L.D. Landau, E.M. Lifshitz, *Quantum Mechanics: Non-relativistic Theory* (Pergamon, Oxford, 1977)

75. V.G. Plekhanov, Application of isotope effects in solids. J. Mater. Sci. **38**, 3341–3429 (2003)
76. M.G. Zemlianov, E.G. Brovman, N.A. Chernoplekov, N.A. Shitikov, Study of dynamics of LiH and LiD by inelastic scattering of cold neutrons, *Inelastic Scattering of Neutrons*, vol. 2 (International Atomic Energy Agency, Vienna., 1965), pp. 431–439
77. J.L. Verble, J.L. Warren, J.L. Yarnell, Lattice dynamics of lithium hydride. Phys. Rev. **168**(N 3), 989 (1968)
78. V.G. Plekhanov, The influence of the surface state on the testifation of exciton states in the wide-gap insulators. Opt. Spectr. **62**(N 8), 1300–1307 (1987). (in Russian)
79. G.I. Pilipenko, O.I. Tyutyunnik, F.F. Gavrilov, D.V. Oparin, Luminescence of colour centres in LiHJ. Appl. Spectr (USSR)**42**(N 4), 657–662 (1985). (in Russian)
80. J.L. Warren, J.L. Yarnell, G. Dolling, R.A. Cowley, Lattice dynamics of diamond. Phys. Rev. **158**(N 3), 805–808 (1967)
81. G. Dolling, R.A. Cowley, The thermodynamic and optical properties of germanium, silicon, diamond and gallium arsenide. Proc. Phys. Soc. **88**(N2), 463–494 (1966)
82. V.I. Tyutyunnik, O.I. Tyutyunnik, Phonon structure of Raman scattering spectra of LiH crystals. Phys. Stat. Sol. (b) **162**(N2), 597–604 (1990)
83. R. Tubino, L. Piseri, G. Zerbi, Lattice dynamics and spectroscopic properties by a valence force potential of diamolike crystals: C, Si, Ge and α-Sn. J. Chem. Phys. **56**(N3), 1022–1039 (1972)
84. S. Baroni, S. de Girancoli, A. Dal Corso, P. Gianozzi, Phonons and related crystal properties from density-functional perturbation theory. Rev. Mod. Phys. **73**, 515–562 (2001). August
85. J. Reissland, *The Physics of Phonons* (Benjamin/Cummings, London, 1973)
86. D. Laplaze, Lattice dynamics of LiH and LiD:effect of long-range three-body forces. J. Phys. C: Solid State Phys. **10**(N18), 3519–3499 (1977)
87. A. Anderson, F. Lüty, Raman scattering, defect luminescence and phonon spectra of ^{7}LiH, ^{6}LiH and ^{7}LiD crystals. Phys. Rev. **B28**(N 6), 3415–3421 (1983)
88. P. Pavone, K. Karch, O. Schutt, et al., Ab initio lattice dynamics of diamond. Phys. Rev. **B48**(N5), 3156–3163 (1993)
89. R. Tubino, J.L. Birman, Two - phonon spectrum of diamond. Phys. Rev. Lett. **35**(14), 670–672 (1975)
90. C.A. Klein, T.M. Hartnet, C.J. Robinson, Critical point phonon frquencies of diamond. Phys. Rev. B **45**, 12854 (1992)
91. S.A. Solin, A.K. Ramdas, Raman spectrum of diamond. Phys. Rev. B **1**(N4), 1687–1699 (1970)
92. K. Uchinokuka, T. Sekina, E. Matsuuro, Critical point analysis of the two-phonon spectrum of silicon. J. Phys. Chem. Solids **35**(N1), 171–180 (1974)
93. M.H. Cohen, J. Ruvalds, Phonon dispersion of diamond measured by inelastic X-ray scattering. Phys. Rev. Let. **23**(24), 1378–1381 (1969)
94. D.C. Hurley, R.S. Gilmore, W.F. Banholzer, Ultrasounic phase velocity and elastic modulus in isotopically enriched manufactured diamond. J. Appl. Phys. **76**(N12), 7726–7730 (1994)
95. D. Vanderbilt, S.G. Louie, M.L. Cohen, Calculation of phonon-phonon interactions and the absence of phonon bound states in diamond. Phys. Rev. Lett. **53**(N15), 1477–1480 (1984)
96. C.Z. Wang, C.T. Chang, K.M. Ho, Two-phonon spectrum of diamond: a moleculen dynamics approach. Solid State Commun. **76**(N4), 483–486 (1990)
97. W. Windl, P. Pavone, K. Karch, O. Schutt, Second-order Raman spectra of diamond from ab initio phonon calculations. Phys. Rev. **B48**(N5), 3164–3170 (1993)
98. J. Kulda, B. Doner, K. Karch, P. Pavone, A neutron scattering study of overbending of the [100] LO phonon mode in diamond. Solid State Commun. **99**(N 11), 799–802 (1996)
99. M. Schwoerer-Bohning, A.T. Macrander, D.A. Arms, Phys. Rev. Lett. **80**, 5572 (1998)
100. T. Ruf, M. Cardona, P. Pavone, Catodoluminescence investigation of isotope effect in diamond. Solid State Commun. **105**(N5), 311–316 (1998)
101. P. Etchegoin, H.D. Fuchs, J. Weber, et al., Phonons in isotopically disordered Ge. Phys. Rev. **B48**(N17), 12661–12671 (1993)

102. V.F. Agekyan, V.M. Asnin, A.M. Kryukov, et al., Isotope effect in germany, Fiz. Tverd. Tela (Leningrad) **31**(N12), 101–104 (1989). (in Russian)
103. S.S. Jaswal, G. Wolfram, T.R. Sharma, Two-phonon Raman spectra of LiH and LiD crystals. J. Phys. Chem. Solids **35**(N4), 571–579 (1974)
104. M. Lax, E. Burstein, Infrared lattice absorption in ionic and homopolar crystals. Phys. Rev. **97**(N1), 39–52 (1955)
105. R. Loudon, The Raman effect in crystals. Adv. Phys. **13**(N2), 423–488 (1964)
106. P.A. Temple, C.E. Hathaway, Multiphonon Raman spectrum of silicon. Phys. Rev. **B7**(N8), 3685–3697 (1973)
107. J.I. Birman, Space group symmetry, *Handbuch der Physik*, vol. 25/26 (Springer, Berlin, 1974)
108. M. Klein, Vibrational Raman scattering from crystals, in [10], vol. 6, chapter 5 (1995), pp. 67–D127
109. D. Laplaze, Second-order Raman spectra of LiH. Phys. Stat. Sol. (b) **91**(N1), 59–69 (1979)
110. V.S. Kogan, Isotope effect in structuring properties. Sov. Phys. Uspekhi **5**(N4), 579–618 (1963)
111. W. Dyck, H. Jex, Lattice dynamics of alkali hydrides and deuterides with NaCl type structure. J. Phys. C: Solid State Phys. **14**(N29) 4193–4215 (1981)
112. R.A. Cowley, Anharmonicity. J. Phys. (Paris) **26**(N 3), 659–664 (1965)
113. S. Go, M. Cardona, Bond, charge, bond polarizibility, and phonon spectra in semiconductors. Phys. Rev. Lett. **34**(N10), 580–583 (1975)
114. A.K. Ramdas, S. Rodriguez, Lattice vibrations and electronic excitations in isotopically controlled diamonds. Phys. Stat. Sol. (b) **215**(N1), 71–80 (1999)
115. K. Karch, T. Dietrich, W. Windl et al., Contribution of quantum and thermal fluctuations to the elastice moduli in covalent semiconductors. Phys. Rev. B **53**(N11), 7259–7266 (1996)
116. H.D. Fuchs, S.H. Grein, M. Cardona, et al., Comparison of the phonon spectra ^{70}Ge and natural Ge crystals: effect of isotopic disorder. Phys. Rev. **B43**(N6), 4835–4841 (1991)
117. J. Menendez, J.B. Page, S. Guha, Vibrational spectroscopy of C_{60}, in *Light Scattering in Solids VIII*, ed. by M. Cardona, G. Güntherodt (Springer, Berlin, 2001)
118. P. Yu, M. Cardona, *Fundamentals of Semiconductors* (Springer, Heidelberg, 1996)
119. J.M. Zhang, M. Giehler, A. Gobel et al., Optical phonons in isotopic Ge studied by Raman scattering. Phys. Rev. **B57**(N16), 1348–1351 (1998)
120. J.M. Zhang, M. Giehler, A. Gobel et al., Isotope effects on exciton energies in CdS. Phys. Rev. **B57**(N16), 9716–9722 (1998)
121. H.D. Fuchs, S.H. Grein, R.I. Devlen et al., Anharmonic decay time, isotopic scattering time, and inhomogeneous line broadening optical phonons in ^{70}Ge, ^{76}Ge and natural Ge crystals. ibid, **B44**(N16), 8633–8642 (1991)
122. J. Spitzer, T. Ruf, W. Dondl et al., Raman scarttering by optical phonons in isotopic $^{70}(Ge)_n$, $^{74}(Ge)_n$ superlattices. Phys. Rev. Lett. **72**(N10), 1565–1568 (1994)
123. R.M. Chrenko, ^{13}C-doped diamond: Raman spectra. J. Appl. Phys. **63**(N12), 5873–5875 (1988)
124. H. Hanzawa, N. Umemura, Y. Nisida, H. Kanda, Disorder effect of nitrogen impurities, irradiation-induced defects and ^{13}C isotope composition on the Raman spectrum in synthetic I^b diamond. Phys. Rev. **B54**(N6), 3793–3799 (1996)
125. J.M. Zhang, T. Ruf, M. Stutzman, Raman spectra of isotopic GaN. Phys. Rev. B **56**(N22), 14399–14406 (1997)
126. R. Fuchs, K.L. Kliewer, Optical modes of vibration in an ionic crystal slab. Phys. Rev. **140**, A2076–A2088 (1965)
127. G. Fasol, M. Tanaka, H. Sakaki, Y. Horikoshi, Interface roughness and the dispersion of confined LO phonons in GaAs/AlAs quantum wells. Phys. Rev. **B38**(9), 6056–6065 (1988)
128. E. Molinari, C. Bungaro, M. Gulia, Electron-phonon interaction in two-dimensional systems: a microscopic approach. Semicond. Sci. Technol. **7**, B67–72 (1992)
129. K. Kunc, R. Martin, Ab initio force constants of GaAs: a new approach to calculation of phonons and dielectric properties. Phys. Rev. Let. **48**(2), 406–409 (1982)

130. C. Falter, A unifying approach to lattice dynamical and electronic properties of solids. Phys. Rep. **164**(1–2) 1–117 (1988)
131. K.J. Nash, Electron-phonon interactions and lattice dynamics of optic phonons in semiconductor heterostructures. Phys. Rev. B **46**, 7723–7744 (1992)
132. B.K. Ridley, *Electrons and Phonons in Semiconductor Multilayers* (Cambridge University Press, Cambridge, 1997)
133. P. Harrison, *Quantum Wells, Wires and Dots* (Wiley, New York, 2000)
134. S. Yip and Y.- C. Chang, Theory of phonon dispersion relations in semiconductor superlattices. Phys. Rev. B **30**, 7037–7059 (1984)
135. M.A. Stroscio, M. Dutta, *Phonons in Nanostructures* (Cambridge University Press, Cambridge, 2005)
136. H. Goldstein, *Classical Mechanics* (Addison-Wesley, Cambridge, 1950)
137. L. Landau, E.M. Lifshitz, *Theory of Elasticity* (Pergamon, Oxford, 1986)
138. S.M. Rytov, Acoustic properties of a tinly laminated medium. Sov. Phys. Acoust. **2**, 68–80 (1956)
139. Z. Wang, K. Reinhardt, M. Dutta et al., Phonons in bulk and low-dimensional systems, in *Length-Scale Dependent Phonon Interactions*, vol. 128, Topics in Applied Physics, ed. by S.L. Shinde, G.P. Srivastava (Springer, New York, 2014)
140. J.E. Zucker, A. Pinczuk, D.S. Chemla, Optical vibration modes and electron-phonon interaction in GaAs quantum wells. Phys. Rev. Lett. **53**, 1280–1283 (1984)
141. B. Jusserand, M. Cardona, Raman spectroscopy of vibrations in superlattices, in *Light Scattering in Solids*, ed. by V.M. Cardona, G. Güntherodt (Springer, Heidelberg, 1991)
142. J. Menendez, Phonons in GaAs - $Al_xGa_{1-x}As$ superlattices. J. lumin. **44**, 285–314 (1989)
143. E. Richter, D. Strauch, Lattice dynamics of GaAs-AlAs superlattices. Solid State Commun. **64**, 867–870 (1987)
144. G.W. Bryant, G.S. Solomon, *Optics of Quantum Dots and Wires* (Artech House, Boston, 2005)
145. P.G. Klemens, Anharmonic decay of optical phonons. Phys. Rev. **148**, 845–848 (1966)
146. C.M. Sottomar-Torres, Spectroscopy of nanostructures, in *Physics of Nanostructures*, ed. by J.H. Davies, A.R. Long (IOP, Bristol, 1992)
147. M.V. Klein, Phonons in semiconductor supelattices. IEEE J. Q. Electron. **QE–18**, 1760–1770 (1986)
148. V.G. Plekhanov, V.I. Altukhov, Light scattering in LiH crystals with LO phonon emission. J. Raman Spectrosc. **16**(6), 358–365 (1985)
149. A.A. Berezin, Isotope superlattices and isotopically ordered structures. Solid State Commun. **65**, (8), 819 (1988)
150. E.E. Haller, Isotope heterostructures selectively doped by neutron transmutation. Semicond. Sci. Technol. **5**, (4) 319 (1990)
151. L.M. Zhuravleva, V.G. Plekhanov, Nanotechnology of optical devices information transformation and processing on the base of isotope-mixed materials, in *Proceedings of the 8 All-Russian Conference* (Vladimir, 2009), pp. 4–7. (in Russian)
152. M. Nakajima, H. Harima, K. Morita et al., Coherent confined LO phonons in $^{70}Ge/^{74}Ge$ isotope superlattices generated by ultrafast laser pulses. Phys. Rev. **B63**, 161304 (R) (2001)
153. V.G. Plekhanov, Isotope-based materials science. Univer. J. Math. Sci. **1**, 87–147 (2013)
154. E. Silveira, W. Dondl, G. Abstreiter, Ge self-diffusion in isotopic $^{70}(Ge)_n^{74}(Ge)_m$ superlattices: a Raman study. Phys. Rev. B **56**, 2062–2069 (1997)
155. A.V. Kolobov, K. Morita, K.M. Itoh, A Raman scattering study of self-assembled pure isotope Ge/Si (100) quantum dots. Appl. Phys. Lett. **81**, 3855–3857 (2002)
156. T. Kojima, R. Nebashi, Y. Shiraki et al., Growth and characterization of $^{28}Si/^{30}Si$ isotope superlattices. Appl. Phys. Lett. **83**(12), 2318–2320 (2003)
157. V.G. Plekhanov, *Isotope Effect: Origin and Application* (Palmarium Academic Publishing, Saarbrücken, 2014). (in Russian)
158. H. Watanabe, T. Koretsume, S. Nakashima, Isotope compotion dependence of the band-gap energy in diamond. Phys. Rev. B **88**, 205420–5 (2013)

159. H. Watanabe, C.E. Nebel, S. Shikata, Isotopic homojunction band engineering from diamond. Science **324**, 1425–1428 (2009)
160. K. Barnham, D. Vvedensky, *Low-Dimensional Semiconductor Structures* (Cambridge University Press, Cambridge, 2009)
161. N. Balkan (ed.), *Hot Electrons in Semiconductors* (Oxford University Press, Oxford, 1998)
162. P. Ballewt, J. B. Smathers, H. Yang et al., Control of size and density of InAs/(Al, Ga)as self-organized islands. J. Appl. Phys. **90**(1), 481–487 (2001)
163. E.G. Britton, K.B. Alexander, W.M. Strobs, The atomic scale characterization of multilayer semiconductor structures using TEM. GEO. J. Res. **5**, 31–39 (1987)
164. W.M. Strobs, Recently developed TEM approach for the characterization heterostructures and interfaces, in *The Physics and Fabrication of Microstructures and Microdevices*, ed. by M.S. Kelly, C. Weisbuch (Springer, Berlin, 1986), pp. 136–149
165. D.M. Bruls, P.M. Koenrad, H.W.M. Salemink et al., Stacked long-growth-rate InAs quantum dots studied at the atomic level by cross-sectional STM. Appl. Phys. Lett. **82**(21), 3752–3755 (2003)
166. B. Grandidier, Y.M. Niquet, J.P. Nys et al., Imaging the wave–function amplitudes in cleaved semiconductor quantum boxes. Phys. Rev. Lett. **85**(5), 1068–1071 (2000)
167. S. Kret, T. Benabbes, C. Delamarre et al., High resolution electron microscope analysis of lattice distortions and In segregation in highly strained $In_{0.35}Ga_{0.65}As$ coherent islands grown on GaAs (001). J. Appl. Phys. **86**(4), 1988–1993 (1999)
168. M. Babiker, Coupling of polar optical phonons to electrons in superlattice and isolated quantum wells. Semicond. Sci. Technol. **7**, B52–B59 (1992)
169. S. Das Sarma, V.B. Campos, M.A. Stroscio, Confined phonon modes and hot-electron energy relaxation in semiconductor microstructures. Semicond. Sci. Technol. **7**, B60–B66 (1992)
170. E. Molinari, C. Bungaro, M. Gulia et al., Electron-phonon interactions in two-dimensional systems: A microscopic approach. Semicond. Sci. Technol. **7**, B67–B72 (1992)
171. T. Tchuchiya, T. Ando, Electron-phonon interaction in semiconductor superlattice. Semicond. Sci. Technol. **7**, B73–B76 (1992)
172. S. Kiravittaya, A. Rastelli, O.G. Schmidt, Advanced quantum dot configurations. Rep. Prog. Phys. **72**, 046502 (2009)
173. L. Challis (ed.), *Electron-Phonon Interaction in Low-Dimensional Structures* (Oxford University Press, Oxford, 2003)
174. N. Bannov, V. Mitin, M. Stroscio Confined acoustic phonons in semiconductor slabs and their interaction with electrons. Phys. Stat. Sol. (b) **183**(1), 131–138 (1994)
175. G. Yu, K.W. Kim, M.A. Stroscio et al., Electron-phonon scattering rates in rectangular quantum wires. Phys. Rev. B **50**, 1733–1738 (1994)
176. J.S. Blakemore, Semiconducting and other major properties of gallium arsenide. J. Appl. Phys. **53**, R123–R181 (1982)
177. T. Inoshita, H. Sakaki, Electron relaxation in a quantum dot: significance of multiphonon processes. Phys. Rev. B **46**, 7260–7263 (1992)
178. U. Bockelman, G. Bastard, Phonon scattering and energy relaxation in two -, one -, and zero-dimensional electron gases. Phys. Rev. B **42**, 8947–8951 (1990)
179. U. Bockelman, Phonon scattering and relaxation properties of lower dimensional electron gases, *Intersubband Transitions in Quantum Wells*, vol. 288, NATO ASI Series B: Physics (Plenum, New York, 1993), pp. 105–118
180. J.I. Pankove, *Optical Processes in Semiconductors* (Prentice Hall, Englewood Cliffs, 1971)
181. M.P. Blencowe, Phonons in Low Dimensional Semiconductor Structures, in: Low-Dimensional Semiconductor Structures: Fundamentals and Device Applications, K. Barnham, D. Vvedensky (eds.) (Cambridge, Cambridge University Press, 2001), pp. 123 – 148
182. H. Bensity, C.M. Sotomayor-Torres, C. Weisbuch, Intrinsic mechanism for the poor luminescence properties of quantum-box systems. Phys. Rev. B **44**, 10945–10948 (1991)
183. C. Weisbuch, B. Vinter, *Quantum Semiconductor Structures* (Academic, San Diego, 1991)
184. G. Bastard, *Wave Mechanics Applied to Semiconductor Heterostructures* (Halsted, New York, 1988)

185. L.V. Keldysh, Excitons in semiconductor–dielectric nanostructures. Phys. Stat. Solidi (a) **164**, 3–12 (1997)
186. V.I. Pipa, V.V. Mitin, M. Stroscio, Acoustic phonon bottleneck in quantum dots: role of deformation variation of electron effective mass. Solid State Commun. **117**, 713–717 (2001)
187. F. Rossi, G. Goldoni, E. Molinari, Theory of excitonic confinement in semiconductor quantum wires. J. Phys. Condens. Matter **11**, 5969–5988 (1999)
188. A.V. Akimov, Exciton–phonon interaction in quantum wires, in *Electron-Phonon Interactions in Low-Dimensional Structures*, ed. by L. Challis (Oxford University Press, Oxford, 2010), pp. 239–267
189. R.S. Knox, *Theory of Excitons, Solid State Physics, Suppl 3* (Academic, New York, 1963)
190. V.G. Plekhanov, Wannier–Mott excitons in isotope—disordered crystals. Rep. Prog. Phys. **61**(8), 1045–1095 (1998)
191. J. Lee, E.S. Koteles, M.O. Vassel, Luminescence linewidths of excitons in GaAs quantum wells below 150 K. Phys. Rev. B **33**, 5512–5516 (1986)
192. R.J. Nelson, Excitons in semiconductor alloys, in *Excitons*, Ch. 8, ed. by E.I. Rashba, M.D. Sturge (North–Holland, Amsterdam, 1982), pp. 319–348
193. R. Cingolani, K. Ploog, Frequency and density dependent radiative recombination processes in III-V quantum wells and superlattice. Adv. Phys. **40**, 535–623 (1991)
194. H. Hillmer, A. Forschel, S. Hausman, Optical investigations on the mobility of two-dimensional excitons in GaAs/$Ga_{1-x}Al_xAs$ quantum wells. Phys. Rev. B **39**, 10901–10912 (1989)
195. R. Tsu, *Superlattice to Nanoelectronics* (Elsevier Science, Amsterdam, 2005)
196. J.H. Collet, H. Kalt, Le.Si. Dang et al., Relaxation of excitons in coherently strained CdTe/ZnTe quantum wells. Phys. Rev. B **43**, 6843–6846 (1991)
197. R.P. Stanley, J. Hegarty, R. Fischer, Hot-exciton relaxation in $Cd_xZn_{1-x}Te$/ZnTe multiple quantum wells. Phys. Rev. Lett. **67**, 128–131 (1991)
198. D. Bimberg, M. Grundman, N.N. Ledentsov, *Quantum Dot Heterostructure* (Wiley, Chichester, 1999)
199. L. Jacak, P. Hawrylak, A. Wojs, *Quantum Dots* (Springer, Berlin, 1998)
200. G.W. Bryant, G.S. Solomon (eds.), *Optics of Quantum Dots and Wires* (Artech House, London, 2005)
201. H.C. Casey, M.B. Panish, *Heterostructure Lasers* (Academic, New York, 1978)
202. P.S. Zoty, *Quantum Well Lasers* (Academic, Boston, 1993)
203. Y. Arakawa, Semiconductor nano–structure lasers: fundamentals and applications, in *Confined Electrons and Photons: New Physics and Applications*, vol. 340, NATO Series B: Physics, ed. by E. Burstein, C. Weisbuch (Plenum, New York, 1995), pp. 647–673
204. L.A. Colderen, S.W. Corzine, *Diode Lasers and Photonic Integrated Cicuits* (Wiley, New York, 1995)
205. V.M. Ustinov, A.E. Zukov, AYu. Egorov, N.A. Maleen, *Quantum Dot Lasers* (Oxford University Press, Oxford, 2003)
206. K. Ikeda, H. Seguchi, F. Minami et al., Phonon bottleneck effects in InAs/GaInP quantum dots. J. Luminesc. **108**, 273–276 (2004)
207. R. Heitz, M. Grundman, N.N. Ledentsov, Multiphonon-relaxation processes in self-organized InAs/GaAs quantum dots. Appl. Phys. Lett. **68**, 361–363 (1996)
208. B. Damilano, N. Grandejan, J. Massies et al., Gan and GaInN quantum dots: an efficient way to get luminescence in the visible spectrum range. Appl. Surf. Sci. **164**, 241–245 (2000)
209. Y. Kuwahara, Y. Fujiyama, M. Iwaya et al., Nitrides based light–emitting solar cell. Phys. Stat. Sol. (c) **7**, 1807–1809 (2010)
210. V.G. Plekhanov, *Isotopes in Condensed Matter* (Springer, Heidelberg, 2013)
211. P.A.M. Dirac, *The Principles of Quantum Mechanics* (Oxford University Press, Oxford, 1958)
212. R.P. Feynman, R.P. Leighton, M. Sands, *The Feynman Lecture in Physics*, vol. 3 (Addison-Wesley, Reading, 1965)
213. L.D. Landau, E.M. Lifshitz, *Quantum Mechanics (Nonrelativistic Theory)* (Pergamon Press, New York, 1977)

214. K. Kuroda, T. Kuroda, K. Watanabe et al., Distribution of exciton emission linewidth observed for GaAs quantum dots grown by droplet epitaxy. J. Luminesc. **130**, 2390–2393 (2010)
215. D.W. Taylor, Phonon response theory and the infrared and Raman experiments, in [48], Chapter 2, pp. 35–132
216. G.L. Bir, G.E. Picus, *Symmetry and Deformation in Semiconductors* (Science, Moscow, 1972). (in Russian)
217. S.I. Pekar, *Crystaloptics and Addition Waves* (Naukova Dumka, Kiev, 1982). (in Russian)
218. N.N. Ledentsov, V.M. Ustinov, V.A. Shchukin et al., Quantum dot heterostructures: fabrication, properties, lasers. Fiz. Teh. Polup. (Physics and Technics of Semicond.) **32**(4), 385–410 (1998). (in Russian)

Chapter 4
Application of Isotopic Materials Science in Bulk and Low-Dimensional Structures

Abstract This chapter reviews the application of isotopic materials science in different fields of nanotechnology and nanoscience. The application of stable isotopes is very briefly described: in first step nonlinear excitons in bulk isotope-mixed materials as well as phonon-related isotope effect: thermal expansion, thermal conductivity, and lattice constants. Part of this chapter is devoted to very interesting results connecting with isotope-mixed graphene and its application in nanoelectronics as well as nano-optics. Semiconducting graphene is based on the electronic excitation energy renormalization by the strong (nuclear) interaction. It was shown very useful for quantum processors that have used the low-dimensional structures (quantum wells, wires, and dots) in isotope-mixed compounds including graphene. The materials of this chapter stress very perspective of the new field of nanotechnology—isotopic materials science.

4.1 General Considerations

It is commonplace in physics and chemistry where the most chemical elements have two or more isotopes (see, e.g., [1]). A number of major areas of science and technology take advantage of this fact. Various effects stemming from isotopic diversity serve as key ingredients for a broad range of fundamental research directions as providing a basis for numerous applications. Some of them were discussed under the umbrella term of Isotopic engineering [2–6], while a broad variety of topics and numerous applications were suggested and discussed in this context (see, e.g., [5, 7] and references therein). Isotopic engineering as such is still an incipient research and technological direction rather than a full-fledged area of massive effort. At the same time, as will be described in this chapter, its potential for future electronic and optics applications shows promise along several major lines of human knowledge.

Among the prime premises of quantum physics is the principle of indistinguishability of elementary particles [8]. All electrons are by definition "the same" and hence, after two (or more) electrons interact, it is possible to say "who is who". The same applies to other elementary particles and even identical atoms (e.g., two ^{70}Ge atoms are indistinguishable). Not so for isotopes. Due to their mass difference,

© Springer International Publishing AG, part of Springer Nature 2018

V. G. Plekhanov, *Introduction to Isotopic Materials Science*,
Springer Series in Materials Science 248, https://doi.org/10.1007/978-3-319-42261-9_4

various isotopes of the same chemical element (e.g., ^{70}Ge and ^{76}Ge) are classical distinguishable particles. Within the framework of statistical thermodynamics, this classical distinguishability of isotopes renders isotopic mixtures a prime illustrative tool for a discussion of the Gibbs paradox [9]. The latter refers to the (alleged) discontinuity of entropy upon the mixture of two slightly different species.

The continuing progress in the fabrication of semiconductors nanostructures with lower dimensional features has led to devices with enhanced functionality and even to novel devices with new operating principles. The critical role of phonon effect in such low-dimensional devices is well known (see, e.g., [5–8]). There is therefore a pressing need for a greater awareness and understanding of confined phonon effects. As will be shown below, phonon spectra are derived from theories of varying complexity, in an attempt to reproduce experimental in great detail, but a simple model involving bond-stretching and bond-bending forces is sufficient to generate a semiquantitative understanding [9, 10]. In our chapter, we can use such model to describe the lattice vibrations of a superlattice, low-dimensional structures, and the various acoustic, optic, and interface phonon modes that can arise. In our review, we stress an important role the interactions between electrons and phonons in such confined systems.

The experience of the past shows that throughout constant technology improvement electronics (optoelectronics) has become more reliable, faster, more powerful, and less expensive by reducing the dimensions of integrated circuits. These advantages will lead to the development of modern microelectronics. The long-term goal of this development will lead to nonelectronics. Advancing to the nanoscale is not just a step toward miniaturization, but requires the introduction and consideration of many additional phenomena. At the nanoscale, most phenomena and processes are dominated, as said above, by quantum physics and they exhibit unique behavior. Nanotechnology includes the integration of man-made nanostructures into larger material components and systems (see, e.g., [10–13]). Importantly, within these larger scale systems, the active elements of the system will remain at nanoscale. Low-dimensional structures have become one of the most active research not only in nanoscience and nanotechnology but also isotopetronics [14]. Quantum wells, quantum wires, and quantum dots structures produced in the main by epitaxial growth techniques (mainly molecular beam epitaxy (MBE) and metal-organic chemical vapor deposition (MOCVD) and their various variations such as chemical beam epitaxy (CBE), atomic layer epitaxy (ALE), etc. (see, e.g., [15–20]). MBE and MOCVD are of considerable technological interest since they are used as active components in modern devices. These devices are high-electron-mobility transistors, diodes and lasers, as well as quantum dots from quantum computations and communications perspectives. The seminal works of Esaki and Tsu [21] and others on the semiconductor superlattice stimulated a vast international research effort to understand the fabrication and electronic properties of superlattice, quantum wells, quantum wires, and quantum dots (see, for example, [10–13]). The dimensional scale of such samples between 10 and 100 nm which are the subject of nanoscience—is a broad and interdisciplinary field of emerging research and development. Nanoscience and nanotechnology are concerned with materials, structures, and systems whose components exhibit novel and significantly modified physical, chemical properties due to their nanoscale sizes. The

new direction of nanoscience is isotope-engineered materials, which is studied the more low-dimensional in size, as a rule the sizes of the sample of isotope-engineered materials are compare with the atomic size. Nuclear technology–neutron irradiation [22] is a very useful method for preparing low-dimensional structure: quantum wells, quantum wires, and quantum dots [23]. A principal goal of isotope-engineered materials as new directions of the nanotechnology is to control and exploit their new properties in structures and devices at atomic, three molecular, and supramolecular levels. The miniaturization required by modern electronics is one of the driving forces for isotope-engineered materials (isotopic materials science)—new direction of nanotechnology (see also [24]). Modern nanoscience and nanotechnology is a fertile ground for teaching, as it brings together the quantum theory of materials (see, e.g., [8]), novel physics in the electronic and optical properties of solids, the engineering of small structures, and the design of high-performance electronic, photonic, and optoelectronic systems. The treatments attempt to be introductory, comprehensive, and phenomenological in the main. The new physics described in this chapter comes from one important consideration—length scale (see also [10, 11, 25, 26]) especially in mesoscopic physics. As we all know, mesoscopic physics deals with structures which have a size between the macroscopic and the microscopic or atomic one. These structures are also called mesoscopic systems, or nanostructures [12] in a more colloquial way since their size usually ranges from a few nanometers to about 100 nm. The electrons in such mesoscopic systems show their wavelike properties [25, 26], and therefore, their behavior is markedly dependent on the geometry of the samples. In this case, the states of the electrons are wavelike and somewhat similar to electromagnetic waves (see, e.g., [26]). As mentioned above for the description of the behavior of electrons in solids, it is very convenient to define a series of characteristic lengths. If the dimension of the solids in which the electron embedded is of the order of, or smaller than these characteristic lengths (λ_B de Broglie wavelength, or a_{ex}—exciton radius, etc.) the material might show new properties, which in general are more interesting than the corresponding ones in macroscopic materials. On the contrary, a mesoscopic system approaches its macroscopic limit if its size is several times its characteristic length. As mentioned above, when the dimensions of the solid get reduced to a size comparable with, or smaller λ_B, then the particles behave wavelike and quantum mechanics should be used. Let us suppose that we have an electron confined within a box of dimensions L_x, L_y, L_z. If the characteristic length is l, we can have the following situations:

1. $l < L_x, L_y, L_z$. In this case, the electron behaves as in regular 3D bulk semiconductor (insulator).
2. $l > L_x$ and $L_x \ll L_y, L_z$. In this situation, we have a 2D semiconductor perpendicular to the x-axis. This mesoscopic system is also called a quantum well (for details see [14]).
3. $l > L_x, L_y$ and $L_x, L_y \ll L_z$. This case corresponds to a 1D semiconductor or quantum wire, located along the z-axis.
4. $l \gg L_x, L_y, L_z$. In this case, it is said that we have a 0D or a quantum dot [10, 11].

In general, we say in mesoscopic physics that a solid, very often a crystal, is of reduced dimensionality if at least one of its dimensions L_i is smaller than the characteristic length. For instance, if L_x and L_y are smaller than l we have a crystal of dimensionality equal to one. We could also have the case that l is comparable, or a little larger, than one of the dimensions of the solid but much smaller than the other two. Then, we have a quasi-2D system, which in practice is a very thin film, but not thin enough to show quantum size effect (for details see, e.g., [13]).

4.2 Nonlinear Excitons in Bulk Isotope-Mixed Materials

4.2.1 General Remarks

In order to observe highly excited semiconductors (insulators) (HES) effects, it is necessary that the electronic excitations interact with each other at a sufficiently high rate. The short lifetime and diffusion path in direct gap materials necessitate a rather high-density n of bound (excitons) or unbound electronic excitations. A value of $n = 10^{17}\,\mathrm{cm}^{-3}$ is a reasonable average [27], though the onset of highly excited semiconductors effects depends strongly on the compounds under investigation, on the quality of the individual sample and on the special conditions of the experiment (see, e.g., [28]). The lifetime of excitons in direct gap materials is about 1 ns at low densities. It is reduced at high densities by quadratic recombination processes and stimulated emission to values around 0.1 ns ([27] and references therein). The generation rate G, which is needed to obtain a stationary concentration of $n = 10^{17}\,\mathrm{cm}^{-3}$ e–h pairs with a lifetime of 10^{-10} s is at least G $\simeq 10^{27}\,\mathrm{cm}^{-3}\mathrm{s}^{-1}$. G has now to be connected with the excitation intensity I_{exc}, where $I_{\mathrm{exc}}$is the energy per units of area and time impinging on the sample. Some authors prefer to give the photon flux density I_{Ph} instead of I_{exc} in the case of optical excitation. They are connected by I_{exc}=$I_{\mathrm{Ph}} \cdot \hbar\omega$. Thus, $I_{\mathrm{exc}} \simeq 10^6\,\mathrm{Wcm}^{-2}$ with N_2 laser ($\hbar\omega_{\mathrm{exc}} = 3.78\,\mathrm{eV}$) corresponds to $I_{\mathrm{Ph}} = 1.7 \cdot 10^{24}\,\mathrm{cm}^{-2}\mathrm{s}^{-1}$.

In the case of nonresonant two-photon band-to-band excitation of semiconductors for which the absorption edge E_g fulfills the inequality $2\hbar\omega_{\mathrm{exc}} > E_g > \hbar\omega_{\mathrm{exc}}$, the relation between G and I_{exc} reads

$$I_{\mathrm{exc}} = \left(\frac{G 2\hbar\omega_{\mathrm{exc}}}{K_2}\right)^{1/2}, \tag{4.1}$$

where K_2 is the two-photon absorption coefficient. Since K_2 is of the order of $10^{-7}\mathrm{W}^{-1}\,\mathrm{cm}$ for many direct materials (see, e.g., [29]), I_{exc} has to be about $2 \cdot 10^7\,\mathrm{Wcm}^{-2}$ in order to observe highly excited semiconductors effects. In real experiments on semiconductors, I_{exc} is varied from 10^5 to $10^8\,\mathrm{Wcm}^{-2}$, where the upper limit is given by the threshold for destroying the sample surface. The excitation by two-photon absorption is especially useful if a homogeneous bulk excitation

of rather thick samples is desired. With a standard Q-switched ruby laser, volumes of several mm^3 can be pumped. In the case of one-photon excitation in the exciton or band-to-band region, an equation like

$$I_{\mathrm{exc}} = G\hbar\omega_{\mathrm{exc}}/K_1 \tag{4.2}$$

does not hold. The values of the one-photon absorption coefficient K_1 are of the order of $10^5\,\mathrm{cm}^{-1}$ or even higher. However, the created e–h pairs do not remain confined in a surface layer of a thickness of $K_1^{-1} \leq 0.1\,\mu\mathrm{m}$ but rapidly spread out into the volume of the crystal, driven by the gradient of the chemical potential. The effective penetration depth $\mathrm{d}_{\mathrm{eff}}$ is generally assumed to be one or a few micrometers [28]. A value of this order of magnitude has been found in CdS, where a thin platelet (above $4\,\mu\mathrm{m}$ thick) was excited by a N_2 laser from one side, and the change of the excitonic reflection spectra with I_{exc} was investigated on both sides of the sample (see, e.g., [27] and references therein). Therefore, (4.2) should rather be replaced by

$$I_{\mathrm{exc}} = G\hbar\omega_{\mathrm{exc}} \cdot \mathrm{d}_{\mathrm{eff}}. \tag{4.3}$$

In the experiments I_{exc} is typically varied from 10^3 up to $5 \cdot 10^6\,\mathrm{Wcm}^{-2}$; the upper limit is again given by the damage threshold of the sample surface. With one-photon excitation, it is generally possible to reach higher G values. Because of the high diffraction losses of the thin excited layers, it is possible to suppress the optical stimulation of recombination processes, especially if small diameters D of the excitation spot are used ($\mathrm{D} < 100\,\mu\mathrm{m}$) [30]. It should be pointed out that the excitation conditions for indirect gap semiconductors are quite different from those described above. In these materials, the lifetime is several orders of magnitude larger than in direct gap materials. Therefore, excitation sources with much lower values of Iexc and even conventional incandescent lamps may be used, either pulsed or in a continuously working mode.

4.2.2 Free-Exciton Emission from Diamond at Room Temperature

As was shown above, diamond has an indirect band structure similar to silicon, with six equivalent conduction band minima located on the $\langle 100 \rangle$ axes at $0.76k_{\mathrm{max}}$. Quantitatively, however, diamond is different from all standard cubic semiconductors [31] including silicon in that the valence band spin–orbit interaction Δ_0 at $k = 0$ is very much smaller than the excitonic interactions important in optical experiments. The latter are the exciton binding energy $E_{\mathrm{B}} = 80\,\mathrm{meV}$ and the localization energy $E_{\mathrm{loc}} = 51\,\mathrm{meV}$ of excitons to the acceptor in p-type semiconducting diamonds [30, 31]. Substitutional boron is the only shallow impurity in diamond with an ionization energy $E_{\mathrm{i}} = 370\,\mathrm{meV}$. The spin–orbit splitting between the fourfold degenerate Γ_8^+

band and the twofold Γ_7^+ band amounts to $\Delta_0 = 6\,\text{meV}$ experimentally or to $\Delta_0 = 13\,\text{meV}$ theoretically in linear muffin-tin orbital and $k \cdot p$ calculations (see Chap. 2 and references therein). In all other standard cubic semiconductors, this ordering of the interaction energies is inverse, yielding $\Delta_0 \gg E_B$ and E_{loc}. In silicon, e.g., $\Delta_0 = 44\,\text{meV}$, $E_B = 14.7\,\text{meV}$ and $E_{\text{loc}} \approx 0.1\,E_i$ according to Haynes' rule, with E_i ranging from ≈45 meV for the shallow donor phosphorus and the shallow acceptor boron up to ≈155 meV for the relatively deep acceptor indium [31].

As was shown above, the diamond having a wide bandgap can emit the intense ultraviolet (UV) radiation due to recombination of the indirect free exciton (see, e.g., [32]). At last time, there were grown very pure diamond crystals [33]. Below we will follow in the main results of the indicated paper. We should stress that diamond is widely recognized as a material with a high potential for application for realizing UV light-emitting device due to the fact that its bandgap energy (5.47 eV) is much larger than other semiconductors [31]. Several groups have reported UV emission from natural diamond, high-pressure synthesized diamonds, and diamonds prepared by chemical vapor deposition; however, according to the authors of paper [33], the observed emission is defect induced rather than intrinsic. In the paper [33], the authors have reported on the observation of free-exciton recombination emission at room temperature from current injection device composed of high-quality semiconductor diamond synthesized by the high-temperature, high-pressure method. Importantly, the free-exciton emission is expected to be relatively efficient despite the indirect band structure of the crystal. As-grown octahedral crystals are polished into a boar shape ($2 \times 3 \times 0.5\,\text{mm}^3$) where the largest plane {100} in the normal direction. The polished samples are treated in a heated chromic acid mixture for 20 s to clean surface. This process also prevents the surface current of the B-doped sample, and hence, the bulk p-type current dominates the electroluminescence emission from this sample. On the nondoped crystal surface, H-terminated conduction layer is formed by treating the sample in a microwave CVD apparatus at a pressure of 40 Torr with H_2 flow of $500\,\text{cv}^3/\text{min}$ at a temperature 800 °C for 5 min. Cr electrodes (50 μm square, 200 μm pitched) with Au, as shown in Fig. 4.1 are fabricated on the surface of the samples by photolithography. The insets in Fig. 4.1 show the photoluminescence spectra of nondoped and B-doped samples at room temperature under the excitation of the 5th harmonic pulses of a mode-locked YAG laser. The spectrum of the nondoped crystal shows a peak at 5.277 eV (235 nm), which has been assigned to the TO phonon-assisted free-exciton recombination emission (FE_{TO}). A broad emission band in the visible region is referred to as A-band, which is associated with the lattice dislocations in diamond crystal [31]. The presence of FE_{TO} emission in the photoluminescence spectrum at room temperature confirms the high quality of the samples. In the B-doped crystal, the intensity ratio of band-A emission to the FE_{TO} emission is about three times higher than that of the nondoped sample, indicating the increase in the dislocation concentration with doping. Although the band-A emission increases, the photoluminescence spectrum of the B-doped diamond is dominated by FE_{TO} and does not show the impurity-related line. Thus, the B-doped crystal still retains high quality for application in UV emission devices.

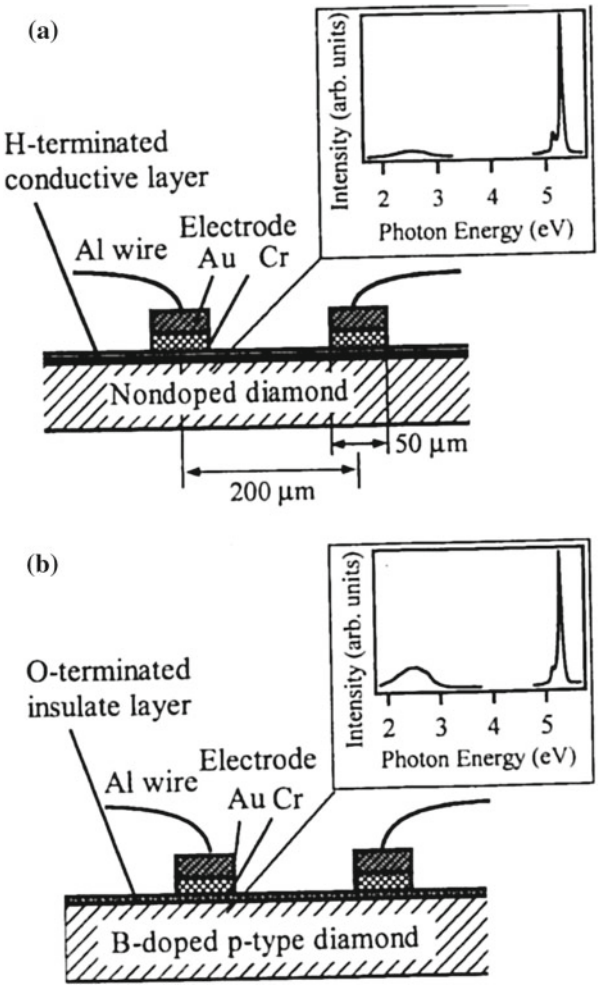

Fig. 4.1 Schematic of the fabricated diamond light-emitting device; **a** surface conduction device using the nondoped crystal, **b** p-type device using the B-doped crystal. The insets show the photoluminescence spectra of the corresponding devices measured at room temperature using the fifth harmonics of the YAG laser (after [33])

Moreover, UV and visible light emissions are observed in both devices by current injection. Figure 4.2 shows the electroluminescence of the surface conduction device at 100 mA, 80 V and the p-device at 100 mA, 50 V. Both the spectra show a UV emission centered at 5.277 eV and a broad emission between 2 and 3 eV. The inset of Fig. 4.2a shows the image of the surface conduction device, taken using a CCD camera with and without (insets 1 and 2, respectively) the UV band-pass filter. The UV emission as well as the visible emission is observed under the cathode. It is necessary to stress that the dominance of the free-exciton emission at room

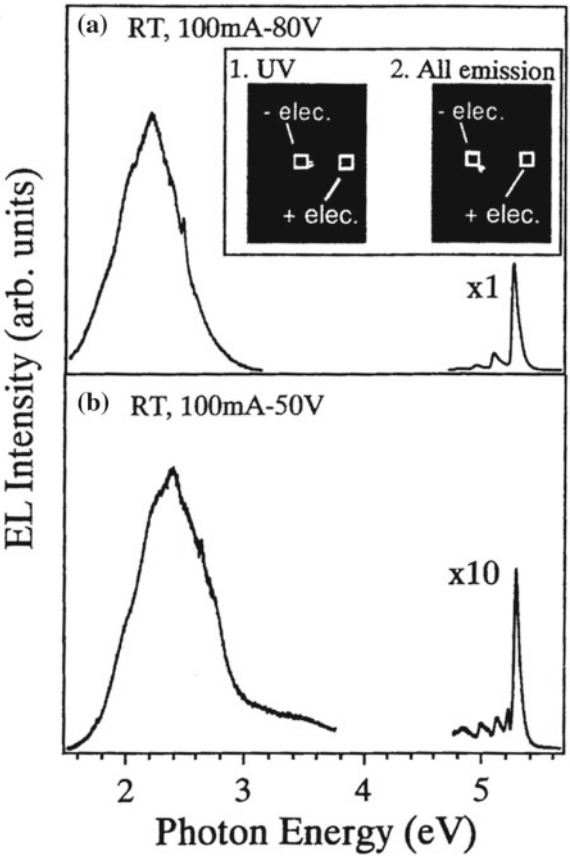

Fig. 4.2 Electroluminescence spectra at room temperature; **a** surface conduction device, **b** p-type device. The inset is the image of the surface conduction device taken with a CCD camera with and without (insets 1 and 2, respectively) the UV band-pass filter (after [33])

temperature, which is normally absent in most semiconductors, is the major feature of luminescence spectra of diamond. Further reduction of the operating voltage and increase in the emission efficiency is possible by improving the electrical properties of the semiconducting diamond crystal and using a carrier confinement structure such as the p–n junction diode structure (the more detail see [33]).

4.2.3 UV Emission from a Diamond p–n Junction

Present paragraph devotes the UV emission from a diamond p–n junction at low temperature [34, 35]. First of all, we are describing the creation p–n junction of diamond which is prepared from B-doped and P-doped diamond. Concerning the impurity doping of diamond, doping with boron atoms (B doping) leads to p-type semiconducting diamond, which also exists in nature and can be reproducibly obtained by

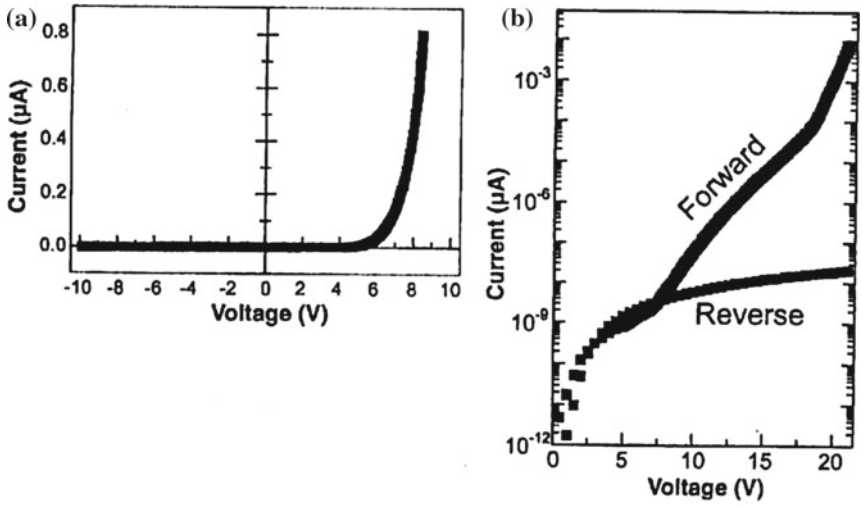

Fig. 4.3 Representative I–V characteristics of diamond p–n junction. In the linear plot (**a**), the voltage shows the applied voltage to p-type diamond. In the semilogarithmic plot (**b**), the forward direction corresponds to the case when the negative voltage was applied to n-type diamond (after [34])

either CVD or high-pressure growth techniques. Although n-type diamond does not exist in nature, thin films of n-type diamond have been grown by CVD process with phosphorus (P) doping [35]. Koizumi et al. successfully grew both B- and P-doped diamond thin films on {111} surfaces of diamond with high crystalline perfection. From these substances, they have prepared of a p–n junction diode along with the optical emission characteristics of the diode [34].

Current–voltage (I–V) characteristics of the p–n junction show clear rectifying property (see Fig. 4.3a). The rectification ratio was about three orders of magnitude when forward (n-type negative) and reverse (n-type positive) voltage applied at ± 15 V (Fig. 4.3b). The reverse current is rather high (about 10^{-8}A at -20 V) due to the imperfection of the junction at specific portions of the sample. Due to the large reverse current, the turn-on voltage (6–7 V) is observed at a higher than expected value (4–5 V). A strong deviation of the I–V profile from the exponential relation over an applied voltage of 10 V is due to the high series resistance of the sample (mainly of the P-doped layer) of more than 10^6ohms. When the forward current exceeds 10^{-4}A, the temperature of the sample rises by spontaneous resistive heating, and, as a result, the I–V profile becomes steeper. The capacitance–voltage characteristic shows an increase of capacitance according to the increase of the voltage in a reverse voltage region, confirming the existence of a depletion layer and its narrowing according to the voltage increase.

For forward currents exceeding 0.1 mA, light emission was observed. According to authors [34], in the used structure of the samples, light emission was observed around the electrode of the sample because the p–n junction and the light-emitting

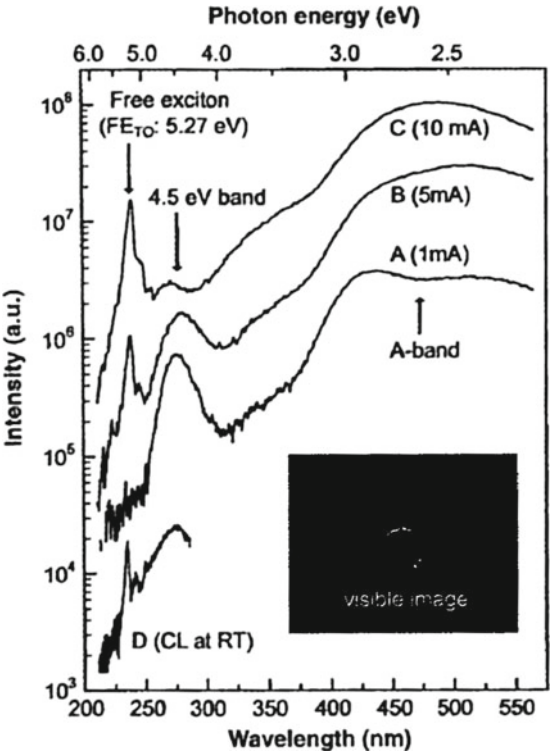

Fig. 4.4 Optical emission spectra of the p–n junction operated with forward current of (**a**) 1, (**b**) 5, and (**c**) 10 mA. A representative cathodoluminescence spectrum of P-doped diamond thin film taken at room temperature is shown in (**d**). The inset is a representative optical image of the diamond LED with light emission. The circular-shaped electrodes (diameter 150 μm are formed by separating each other by 150 μm. Light emission can be seen around the electrode located at center of the image (after [34])

area exist behind the electrode and because the driving voltage was applied perpendicular to the sample surface (see Fig. 4.4 inset). The driving voltages were 20 V for 1 mA, 21.5 V for 5 mA, and 23 V for 10 mA. For the used sample, over 5 mA, the indicated authors saw a sharp emission peak located at 235 nm (5.27 eV), which is attributed to free-exciton recombination luminescence coupled with TO phonon (FE_{TO} (Fig. 4.4 a and c). The small peak (shoulder) located at around 243 nm (5.10 eV) is attributed to the phonon replica of FE_{TO} peak. The band emission in the visible region is attributed to A-band emission that is often observed by cathodoluminescence and photoluminescence from CVD diamond thin films [33, 35]. The intensity ratio of the free-exciton peak against the A-band was 1:7 for a forward current of 10 mA (Fig. 4.4c). The appearance of the free exciton and the 4.5 eV band emissions are very consistent with room-temperature cathodoluminescence spectrum from P-doped diamond thin film (Fig. 4.4d). This result supports the high crystalline perfection of the P-doped layer prepared in [34]. The results of the paper [34] have demonstrated the appearance of a diamond light-emitting diode (LED) that emits monochromatic UV light of 235 nm. Isotopic high-electron mobility transistor was described in the paper [36] where isotopic superlattice was used.

4.3 Exciton Lasing in LiH_xD_{1-x} Crystals

With increasing excitation intensity, frequently laser action is observed in the excitonic luminescence. However, the direct recombination of an exciton can never give rise to laser action, because the coupled exciton–photon system corresponds in the resonant approximation to two linearly coupled harmonic oscillators. The equations of motion of this system do not contain the nonlinearity which is necessary to describe laser action (see, however, [37]). The participation of the third field is required in order to introduce the possibility of laser action [28], i.e., the laser action in exciton systems has to be a parametric process in which a pump field, a signal field, and an idler field participate. Below we describe a scheme for lasing action involving excitons in a pure crystal (see Fig. 4.5). In [38, 39] a general theory of various spontaneous and stimulated exciton recombination processes has been developed. In our analysis, we assume a two-band model for the crystal. Atoms at lattice sites interact with each other and an electromagnetic field. The analysis is addressed to tight-binding excitons in the first step. According to [39], the weak-binding case of Wannier–Mott excitons follows a similar description but is more involved. In the next section, we follow very closely the results of paper [38]. As is well understand now, in the recombination process in dense excitonic systems only parts of the energy of the recombining exciton leave the crystal as a photon (see Fig. 4.5), while the remaining energy is transferred to other excitations, such as free carriers, excitons, or phonons. These processes have first been introduced in 1968 by authors [40]. For

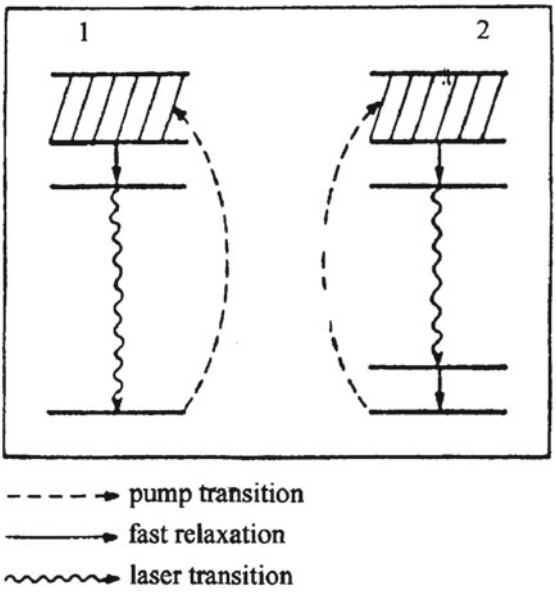

Fig. 4.5 Schematic representation of pump-relaxation and laser transition for (1) a three-level system and (2) a four-level system (after [30])

theoretical treatments of these processes, see [38]. Following [38] we shortly discuss the next optical processes:

exc–e recombination,
exc–h recombination,
exc–exc recombination,
exc–MLO recombination,
m_l recombination, and
m_t recombination.

In the exc–e process, a polariton is scattered from the exciton like part of its dispersion curve to the photonlike part, whereas a free carrier is scattered into a state with higher energy, so that in the total process energy and momentum are conserved (see Fig. 72 in [30]). The photonlike polariton can leave the crystal as a luminescence photon. The approximately thermal distribution of electrons and polaritons in their bands gives rise to a certain width of the emission band. In the exc–exc recombination, the second quasi-particle is an excitonic polariton, too, which is transferred into a state with higher energy. Mentioned above authors include in the discussion also exc–MLO process, i.e., the recombination of an exciton under simultaneous emission of MLO phonons (M = 1, 2, ...), though this is not an HES effect in the sense of our above definition, since the corresponding emissions bands may be observed even at the lowest excitation intensities. On the other hand, the exc–MLO process also gives rise to optical gain [38], especially if large crystal volumes are pumped homogeneously by two-photon excitation [28, 41]. Under this condition, exc–MLO recombination can dominate the luminescence spectra up to the highest I_{exc}. In the m_l or m_t processes a molecule decays into a photonlike polariton and into a longitudinal exciton or into an excitonlike polariton on the lower branch, respectively. As is known, the gain spectra and the spectra of the spontaneous recombination for all these processes can be obtained most directly from a laser theory [38, 41] which makes use of the polariton concept (see also [39]). In the framework of this theory, one formulates rate equations for the polaritons and all the other excitations which are involved in the considered recombination process [42]. The quantum-mechanical derivation of these rate equations has been described in detail in [28, 38, 39]. As will be shown by these authors, the derivation contains the following steps (see also [43]):

1. Construct an effective Hamiltonian for the system of interacting free carriers, excitons, excitonic molecules, and photons from the basic two-band Hamiltonian.
2. Eliminate from this Hamiltonian transverse excitons and photons by a Hopfield transformation and thereby introduce the polaritons (see also [44]).
3. Calculate the equations of motion for the creation and annihilation operators of free carriers, longitudinal excitons, polaritons, and biexcitons.
4. Include damping terms due to excitation, spontaneous emission, and other losses, and introduce the corresponding quantum noise operators. By these means, one obtains the quantum-mechanical Langevin equations.
5. Derive rate equations from the Langevin equation by an adiabatic elimination of the transition operators.

6. The resulting rate equations for the polaritons are decoupled into a rate equation for the photonlike polaritons and one for the excitonlike polaritons. Quasi-equilibrium assumptions are made for all excitations in the crystal. Furthermore, these authors take into account that only the photon component of the polaritons below the bottle-neck can leave the crystal.

The mean rate equation of the laser photons is of the form [27]

$$\mathrm{d}N/\mathrm{d}t = -2kN + \sum \frac{2\pi}{\hbar}\delta(\Delta E)|W|^2 Q. \tag{4.4}$$

N is the number of photons in the active laser mode and 2k is the damping coefficient of this mode. W is the effective transition matrix element for the considered scattering process, $\delta(\Delta E)$ symbolizes the energy conservation in the scattering process and Q stands for the statistical factor, which describes the population of the initial and final states. The summation is carried out over the moments of the scattered particles by taking into account the momentum conservation. For the exciton recombination processes, $|W|^2$ is given by [38]

$$|W|^2 = \hbar^2|U|^2 C_{11}^2|C_{12} - C_{14}|^2, \tag{4.5}$$

where U is the scattering matrix element for the exc–e, exc–h, exc–exc, and exc–LO scattering, respectively. The Hopfield coefficients $|C_{12}\text{-}C_{14}|^2$ stem from the transformation from interacting excitons to polaritons [44], while the factor C_{11}^2 originates from a transformation of the polaritons (below the bottleneck [45]) back to photons. This last transformation is necessary as only the photonlike part of the polariton can leave the crystal. For the biexciton recombination processes, $|W|^2$ is derived from the interaction matrix element U, which describes the decay of a biexciton in a photon and an exciton. For the m_l process, $|W|^2$ is given by [38]

$$|W_l|^2 = \hbar^2|C_{11}^2||C_{11} - C_{13}|^2|U|^2 \tag{4.6}$$

and for the m_t process by

$$|W_t|^2 = \hbar^2|C_{11}^2||(C_{11} - C_{13})(C_{12} - C_{14})U + \{\boldsymbol{k} \rightleftharpoons 0\}|^2. \tag{4.7}$$

Here, the expression $\{\boldsymbol{k} \rightleftharpoons 0\}$ has the form of the preceding term, but the two final polariton states with momentum k and 0, respectively, are interchanged.

Haug and co-authors list the conserved energies ΔE and the population factors Q for all excitonic recombination processes:
exc–i with i = e, h:

$$\begin{aligned} \Delta E &= E_{\mathrm{exc},\boldsymbol{k},1} + E_{i,\boldsymbol{k}'} - E_{i,\boldsymbol{k}+\boldsymbol{k}'} - \hbar\Omega, \\ Q &= n_{\boldsymbol{k},1}^{\mathrm{exc}} n_{\boldsymbol{k}'}^{\mathrm{i}}(1 - n_{\boldsymbol{k}+\boldsymbol{k}'}^{\mathrm{i}})(1 + N) - N n_{\boldsymbol{k}+\boldsymbol{k}'}^{\mathrm{i}}(1 - n_{\boldsymbol{k}'}^{\mathrm{i}})(1 + n_{\boldsymbol{k},1}^{\mathrm{exc}}). \end{aligned} \tag{4.8}$$

Here, is the laser frequency, $E_{\mathrm{exc,k},1}$ is the energy of the exciton in the 1s state, $n^{\mathrm{exc}}_{\boldsymbol{k},1}$ and $n^{\mathrm{i}}_{\boldsymbol{k}+\boldsymbol{k}'}$ are the thermal population functions of the excitons and the free carriers in the different states and, finally, N is the number of photons in the laser mode.

exc–exc:

Here, we only consider scatterings into the $n = 2$ exciton level. This is the so-called [38] P_2line;

$$\begin{aligned} \Delta E &= E_{\mathrm{exc},\boldsymbol{k},1} + E_{\mathrm{exc,k}',1} - E_{\mathrm{exc},\boldsymbol{k}+\boldsymbol{k}',2} - \hbar\Omega, \\ Q &= n^{\mathrm{exc}}_{\boldsymbol{k},1} n_{\mathrm{exc}\boldsymbol{k}',1}(1 - n_{\mathrm{exc}\boldsymbol{k}+\boldsymbol{k}',2})(1+N) - N n^{\mathrm{i}}_{\boldsymbol{k}+\boldsymbol{k}'}(1 - n^{\mathrm{i}}_{\boldsymbol{k}'})(1 + n^{\mathrm{exc}}_{\boldsymbol{k},1}). \end{aligned} \tag{4.9}$$

exc–LO:

$$\begin{aligned} \Delta E &= E_{\mathrm{exc},\boldsymbol{k},1} - \hbar\omega^{\mathrm{LO}}_{\boldsymbol{k}} - \hbar\Omega, \\ Q &= n^{\mathrm{exc}}_{\boldsymbol{k},1}(1+N)(1 + n^{\mathrm{LO}}_{\boldsymbol{k}}) - n^{\mathrm{LO}}_{\boldsymbol{k}} N(1 + n^{\mathrm{exc}}_{\boldsymbol{k},1}). \end{aligned} \tag{4.10}$$

m_{j} with j = 1 or j = t:

$$\begin{aligned} \Delta E &= E_{\mathrm{m},\boldsymbol{k}} - E_{\mathrm{excj}-\boldsymbol{k}} - \hbar\Omega, \\ Q &= n^{\mathrm{m}}_{\boldsymbol{k}}(1 + n^{\mathrm{excj}-\boldsymbol{k}}(1+N) - N n^{\mathrm{excj}-\boldsymbol{k}}(1 + n^{\mathrm{m}}_{\boldsymbol{k}}). \end{aligned} \tag{4.11}$$

The term $\sum(2\pi/\hbar)\delta(\Delta E)|W|^2 Q$ in the photon rate equation (4.4) is now split into two parts: one is proportional to the number N of already available photons and the second one is the rate of spontaneous emission into the laser mode. This last term is obtained by setting $N = 0$. These two expressions give us the gain per unit time and the rate of spontaneous emission, respectively. The gain is the probability per unit time for an induced emission minus the corresponding probability for absorption of a photon. This quantity is directly related to the experimentally determined gain per unit length. The two functions only differ by a factor equal to the velocity of the light in the crystal. For all considered recombination processes, the method of obtaining a positive gain is the same: one has to suppress the absorption probability by lowering the temperature so that the thermal population of the final states of the emission process (which are the initial states for the absorption process) is sufficiently small (the detail see [30]).

The possibility of using indirect transitions for obtaining light generation in semiconductors was probably due to Basov et al. [46]. The stimulating emission on the LO replicas (see Fig. 4.5) of a zero-phonon line free-exciton emission in CdS under two-photon excitation was first obtained by Kulevsky and Prokhorov [47]. As was shown by Liu and Liboff [39] taking into account the mixed crystals lattice potential relief the possibility on the zero-phonon line emission could not be excluded absolutely (see also [37]). The detection of LO phonon replicas of free-exciton luminescence in wide-gap insulator attracted considerable attention to these crystals (see, e.g., [48, 49]). At the same time, it allowed one to pose a question about the possibility of obtaining stimulated emission in UV (VUV) region (4–6 eV) of the spectrum, where no solid-state sources for coherent radiation exist yet. In the first

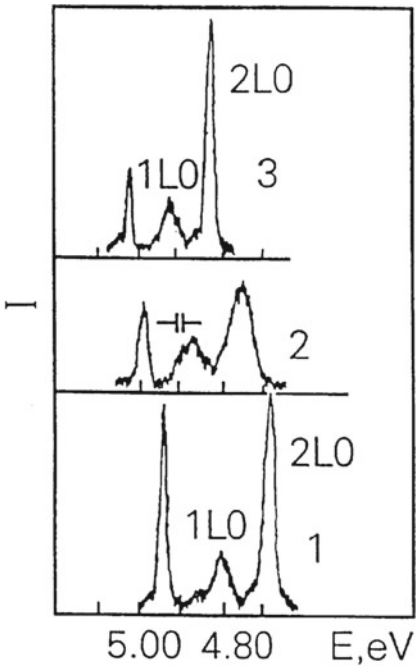

Fig. 4.6 Photoluminescence spectra of free excitons at 4.2 K: (1) LiH; (2) LiH_xD_{1-x} and (3) LiD crystals (after [50])

place, this related to the emitters working on the transitions of the intrinsic electronic excitation. The last one provides the high energetically yield of the coherent emission per unit volume of the substance. The results obtained on solidified xenon and argon under electron-beam excitation with following excimer molecules emission form an exception [49].

In this part, we will discuss the investigation results of the influence of the excitation light density on the free excitons emission spectra in the wide-gap insulator LiH (LiH–LiF) crystals. As was shown above (see Chap. 1), the cubic LiH crystals are typical wide-gap ionic insulators with relatively weak exciton–phonon interaction; however, $E_B/\hbar\omega_{LO} = 0.29$, where E_B and $\hbar\omega_{LO}$ are exciton binding energy and longitudinal optical phonon's energy, respectively. Besides, it might be pointed out that the analogous relation for CdS, diamond, and NaI is 0.73, 0.45, and 12.7, respectively (see, e.g., [30, 48] and references therein).

Despite the identical structure of all free excitons luminescence spectra (Fig. 4.6), it is necessary to note a rather big variation of the luminescence intensity of the crystals from the different batches observed in the experiment. Therefore, crystals possessing the maximum value of the free-exciton luminescence quantum yield were chosen for measurements of the density effects. As was shown earlier the exciton luminescence is observed in LiH crystals, Fig. 4.6, excited by the energy photons from the depth of the fundamental absorption. As an example, the 1LO- and 2LO-assisted luminescence lines at the low excitation density are shown in Fig. 4.7

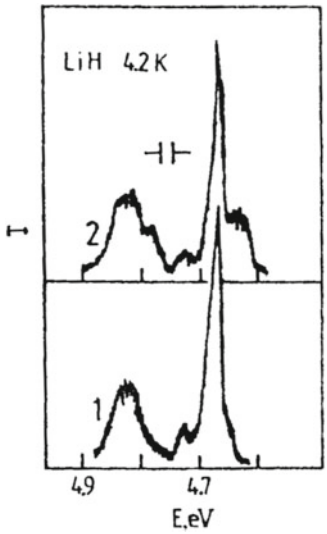

Fig. 4.7 An example of free-exciton luminescence spectra in the region of the 1 LO and 2 LO replicas in LiH crystals at 4.2 K and under low (1) and high (2) density of the photons with excitation energy 4.99 eV. The scales of the different curves are different (after [51])

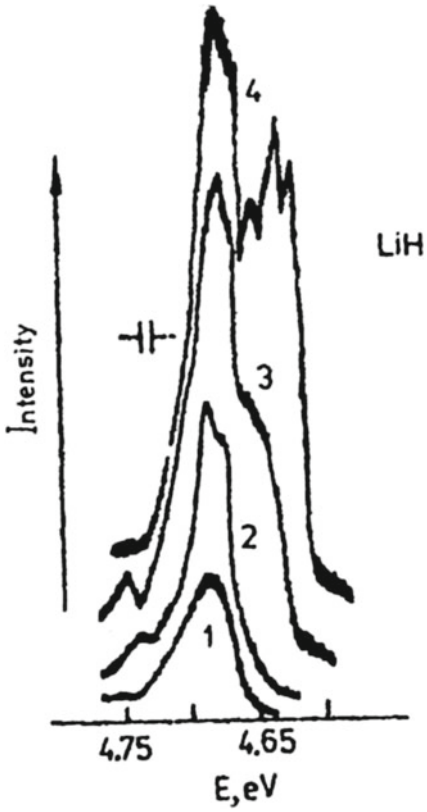

Fig. 4.8 Dependence of the line shape of the 2 LO replica at 4.2 K on the excitation light intensity I0:1—0.03; 2—0.09; 3—0.40; and 4—1 (after [51])

(curve 1). With the increase in the excitation density, an additional emission appears on the long-wavelength side of both lines (curve 2, Fig. 4.7). These results show that the increase in the excitation density of the luminescence intensity of this new feature rises more quickly in the vicinity of the 1 LO replicas than in the vicinity of the 2 LO replicas. This is common regularity. At the same time, it is necessary to note that to obtain the spectrum demonstrated in Fig. 4.7 (curve 2) the excitation light intensity was varied from three to twenty times depending on the crystal origin (see also [52]). In more detail and with better resolution, the influence of the excitation light intensity on the shape and line intensity of 2LO replicas was investigated [48]. The maximum sensitivity of the experimental equipment at the maximum spectral resolution in these experiments was achieved by the sharp focusing on not only excitation but also on the registered channel. Results presented in Fig. 4.8 witness that with the growth of the excitation light intensity a little narrowing can be observed at the beginning which is followed by an ignition of the luminescence intensity on the long-wavelength side of 2 LO replicas line, as it is repeatedly observed for other ionic semiconducting compounds (for details see also [29]). Simultaneously with this, the appearance of a characteristic probable mode structure (see curves 2 and 3, Fig. 4.8) is observed; the width of which is determined by power surpassing the threshold. The divergence angle of the generation emission is simply connected with it and for different semiconductors lies in the interval 2–25° (see, e.g., [29]). As is known, at moderate excitation levels a linear dependence of luminescence intensity on the excitation density is observed (see, e.g., [53]). Such dependence is also observed in LiH crystals and at more substantial excitation light intensities (Fig. 4.9, curve 1). Such linear coupling is usually considered to be unequivocal and testifying about exciton formation only as a result of an indirect light absorption process [52]. At the same time, the measurements of the respective dependence on the long-wavelength side of 2LO replica line (Fig. 4.9, curve 2) shows that the coupling between the luminescence and excitation intensities is not only linear but, in fact, of a threshold character as in case of other crystals (see, e.g., Klingshirn and Haug [29]). Going to the interpretation of the results presented in Figs. 4.8, 4.9 it is necessary to note that in the effective mass approximation the small parameter E_B/E_{exc} for LiH equals 0.008 that is smaller than that for CdS (0.015), where the large radius exciton model "works" excellently. These crystals possess close values to exciton–phonon interaction constant ($g_{\mathrm{F}} = 0.37$ and 0.53, respectively; [50]). We should point out a great difference of the LO phonons energies of these crystals which are 140 and 38 meV for LiH and CdS, respectively. Taking into account what is given above it seems natural that the interpretation of the densities effects in LiH presented bellows completely based on the analogy with semiconducting ionic crystals like CdS and ZnO [41]. Due to the investigation of these crystals [38] it is well known that under two-photon excitation mechanism is dependent on the quality and length of the resonator; the lowest threshold of the generation emission possesses the exciton phonon one (on the LO phonons—see also Fig. 4.5). In the different papers, values of the threshold excitation intensity for CdS crystals are advanced but the majority of them fall into concentration region $5 \cdot 10^{14}$–$10^{16}\,\mathrm{cm}^{-3}$. In the supposed exciton–phonon mechanism of generation of the light the estimation of threshold excitation density in LiH

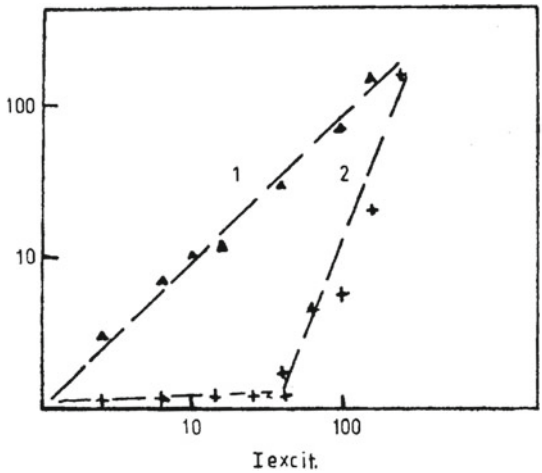

Fig. 4.9 The dependence of the intensity in the maximum (1) and on the long-wavelength side (2) of 2 LO replica emission line of LiH crystals on the excitation light intensity at 4.2 K (after [51])

gives the value of about 10^{15} cm_{-3} (for details see [49, 51]). This is a reasonable value, if the high quality of the resonator mirror, the crystal cleavage "in situ", is taken into account. The benefit of this relatively low value indicates the great valence band anisotropy in these crystals [30] as well as close energy values of direct X_1–X_4 and indirect $W - X_4$ electron transition. As an additional argument that reported above serves also the low value of an important parameter $E_{exc}/\hbar\omega_{LO}$ in the generation light theory which in LiH equals 35. In comparison, we indicate that this parameter for CdS crystals is 64. This generation mechanism must be promoted by the value of the LO phonon energy in LiH crystal also. Owing to this emission transitions realize in the spectral region with a small value of the absorption coefficient and thus with little losses. This fact has a principal significance essentially in the case of the longitudinal pump (see also [49]).

4.4 Phonon-Related Isotope Effects

4.4.1 Isotope Dependence of the Thermal Expansion Coefficient

It is well known that in real solids the forces between atoms are not truly harmonic. The higher the temperature, the more the phonons that are excited and the more pronounced the effects of anharmonicity (see, e.g., [7]. This leads to changes in the equilibrium separation of the atoms. The lattice therefore expands. Thermal expansion arises as a direct result of the asymmetrical dependence of potential energy on atomic separation, i.e., anharmonicity (see, e.g., [54, 55]). It is therefore not so surprising that the variation of the coefficient of thermal expansion with temperature

parallels that of the heat capacity (details see below). When discussing the thermal behavior of solids, it is important to remember that the energy content of the lattice resides in the phonons and not in particular atoms [56]. This may seem paradoxical, but the point is that we cannot convey thermal energy to a particular atom (we exclude the case of isolated impurity atoms). We cannot cause an atom to vibrate without exiting a collective oscillation, a phonon [57]. In a pure crystal, and within the harmonic approximation, two or more phonons may pass through one another without interaction. At the surface of the sample, these phonons would be reflected and continue to exist in unchanged form. But in real solids, we find imperfections and anharmonicity, which cause phonons to interact, to be scattered and to decay. Phonons therefore have a finite lifetime and we must think of phonon wave packets with particlelike properties. These phonons behave very much like particles in a gas: they constantly interact (collide) and in a kinetic equilibrium at a given temperature. That this is the case is particularly evident in the thermal conductivity (see below). In insulators and semiconductors (nonmetals), heat is conducted solely by the phonons and one might expect thermal energy to be transported at a speed corresponding roughly to that of sound. This may be the case in nearly perfect single crystals at very low temperatures [58–60]. However, the mutual interactions of phonons lead to mean free paths of order 100 Å, and the phonon gas therefore conducts heat in a similar manner to an ordinary gas. The energy diffuses through the gas and this is a slow process. We should remind that Debye, long before the concept of the phonon was developed, applied the results of simple kinetic gas theory to solids with remarkable qualitative success [61].

The change of crystal volume V with changing temperature is caused by the temperature dependence of the interatomic forces, and therefore atomic potential energy, leading to changes in the lattice spacing (see, e.g., Landau and Lifshitz [61]). This is why one has to take into account the terms with higher orders of x in the decomposition of potential energy of atomic interactions, $U(x)$, by their displacement from equilibrium position $x = r - r_0$. I one limits the decomposition to the third degree of x, then

$$U(x) = \frac{1}{2}ax^2 - \frac{1}{3}bx^3 \tag{4.12}$$

and the force, applied to the oscillating atom, will be

$$F = -\mathrm{d}U/\mathrm{d}x = -ax + bx^2. \tag{4.13}$$

The second term in this expression describes the anharmonicity of oscillations, and increases as the atomic displacement grows larger. The average value of force acting on atom equals zero. Consequently, the mean atom displacement is

$$\overline{x} = b\overline{x}^2/a. \tag{4.14}$$

In the harmonic approach, ($b = 0$) the mean potential energy $\overline{U}(x) = a\overline{x}^2/2$ and equals the energy of thermal vibrations $kT/2$. Then, $\overline{x} = bkT/a^2$. Thus, the mean displacement of oscillating atom relative to the equilibrium position at $b \neq 0$ changes with temperature. Its sign depends on the sign of the anharmonicity coefficient b, and its value depends both on the value b and a. usually the force of repulsion increases more quickly with atoms approaching each other than the force of attraction with their separation, so the coefficient b is positive and the mean distance between oscillating atoms, $\overline{\overline{r}} = r_0 + \overline{x}$, and consequently, the volume V increases along with temperature. However, there may be some cases U(r) is such that in a determined interval of temperatures, the mean distance between atoms and the volume V reduce with the growth of temperature. The change of volume with the change of temperature is characterized by the isobaric volume coefficient of thermal expansion

$$\beta = \frac{1}{V}\frac{\mathrm{d}V}{\mathrm{d}T}. \tag{4.15}$$

For cubic crystal [54] $\beta = 3\alpha$, where

$$\alpha = \frac{1}{l}\frac{\mathrm{d}l}{\mathrm{d}T} \tag{4.16}$$

is the linear coefficient of thermal expansion, not depending on crystallographic direction [58, 62]. From these relations, connecting thermodynamic functions and also assuming Debye approach [60] on calculations of free and internal energy, one gets the Grunaisen relation [63, 64]

$$\beta = \gamma C_{\mathrm{v}} B/V. \tag{4.17}$$

where C_v and V are the heat capacity and the volume of the body, and B is the isothermal compressibility. The value

$$\gamma = -\frac{\partial ln\theta}{\partial lnV} \tag{4.18}$$

is the Grunaisen parameter, characterizing the change of the Debye temperature θ with the change of volume (see also [65, 66]).

$$\gamma = -\frac{\partial ln\theta}{\partial lnV}. \tag{4.19}$$

Differentiating expression of the dependence of the pressure systems on the T at the $V =$ const we will have [61]

$$\left(\frac{\partial P}{\partial T}\right)_{\mathrm{V}} V = \gamma C_{\mathrm{V}}. \tag{4.20}$$

From (4.20) and using the thermodynamical relations, we have

$$\left(\frac{\partial P}{\partial T}\right)_{\mathrm{V}} = -\frac{\left(\frac{\partial V}{\partial T}\right)_{\mathrm{P}}}{\left(\frac{\partial V}{\partial P}\right)_{\mathrm{T}}} \tag{4.21}$$

and in the final form, we obtain

$$\frac{1}{V}\left(\frac{\partial V}{\partial T}\right)_{\mathrm{P}} = \gamma\frac{C_{\mathrm{V}}}{V}\left[-\frac{1}{V}\left(\frac{\partial V}{\partial P}\right)_{\mathrm{T}}\right] \quad \text{or} \quad \beta = \gamma\frac{C_{\mathrm{V}}}{V}\chi_{\mathrm{T}}. \tag{4.22}$$

The expression (4.22) is named the relation of Grüneisen and links the thermal expansion coefficient (β) with Grüneisen parameter (γ) and others thermodynamical meanings (here V is a molecular volume).

The temperature dependence of the thermal expansion coefficient may be established from relation (4.22). Since γ (its meaning vibrates in the range $1 \div 3$) in the Grüneisen approximation from the temperature does not dependent and χ_T and V are the weak temperature functions, the temperature pace of the thermal expansion coefficient will be determined, the temperature's pace of the specific heat. It is mean that at $T = 0\,\mathrm{K}$ β aspires to zero also. At high temperature, β aspires to constant value.

According Landau and Lifshitz [61], the thermodynamical potential at low temperature is expressed:

$$\Phi = \Phi_0(P) - \frac{\pi^2 T^4 V_0(P)}{30(\hbar\bar{v})^3}, \tag{4.23}$$

where $\Phi_0(P)$ does not dependent from the temperature part of the thermodynamical potential, $\bar{v} = \bar{v}(P)$ is the velocity of the sound. Expressing through volume the thermodynamical potential

$$V = \frac{\partial\Phi}{\partial P} = V_0(P) - \frac{\pi^2 T^4}{30\hbar^3}\frac{\partial}{\partial P}\left(\frac{V_0}{\bar{v}^3}\right) \tag{4.24}$$

we will obtain the following expression for the thermal expansion coefficient:

$$\beta = -\frac{2\pi^2 T^3}{15\hbar^3 V_0}\frac{\mathrm{d}}{\mathrm{d}p}\left(\frac{V_0}{\bar{v}^3}\right). \tag{4.25}$$

From this relation is following that at the low temperatures, the coefficient of the thermal expansion is proportionally the cube of absolute temperature.

At the high temperatures, the thermodynamical potential has next form

$$\Phi = \Phi_0(P) - C_V T lnT + C_V T ln\hbar\bar{v}(P), \tag{4.26}$$

and analogous for preceding one for the β, we have

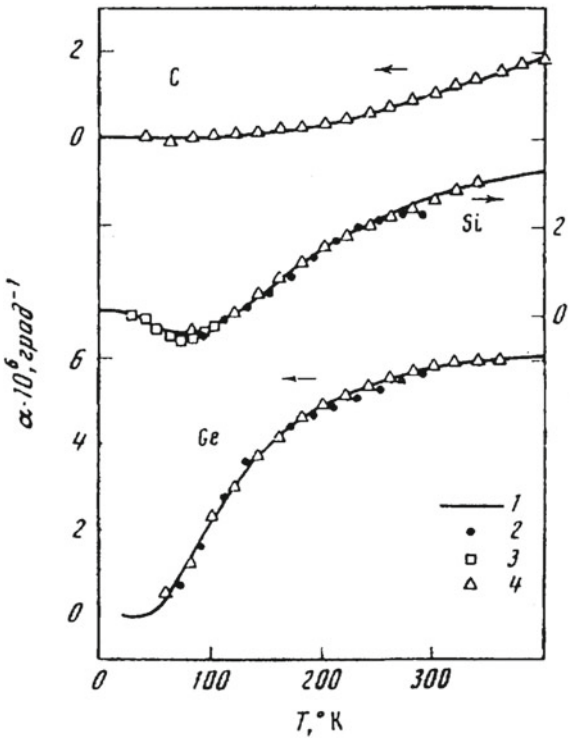

Fig. 4.10 Comparison the experimental results with calculation one for C, Si, and Ge. 1—theory [66]; 2–4—experimental results according to 2—[69]; 3—[70]; and 4—[70] (after [70])

$$\beta = \frac{C_V}{V_0 \bar{v}} \frac{\mathrm{d}\bar{v}}{\mathrm{d}P}. \tag{4.27}$$

From the last relation, it can be seen that the sign of β will be determined by the sign of $\frac{\mathrm{d}\bar{v}}{\mathrm{d}P}$.

As an example in Fig. 4.10, it displays the temperature dependence of the β for the well-known semiconductors C, Ge, and Si. From this picture, one can see a good agreement between the theory and experiment, although as a rule, that does not observe (see also [23]). The experimental data on the temperature dependence of the thermal expansion coefficient in the wide temperature range are shown that in low-temperature range, the β is decreased more quickly at the decreasing temperature than this is following from the Grüneisen low and in the high-temperature range is continuing slow growth (see, e.g., [67, 68]).

As an example of abovementioned, α linear coefficient is essentially linear with T at higher temperature. These calculated quantities are represented by the continuous curves in Fig. 4.11 and are shown together with some experimental thermal expansions values [71]. The more precisely and in more temperature range thermal expansion of LiH was investigated by Jex [72]. His results are displayed in Fig. 4.12, where we can see that the experimental results agree very well with calculations ones. The mean Grüneisen constant of ^{7}LiD and ^{7}LiH is depicted in Fig. 4.13. It can

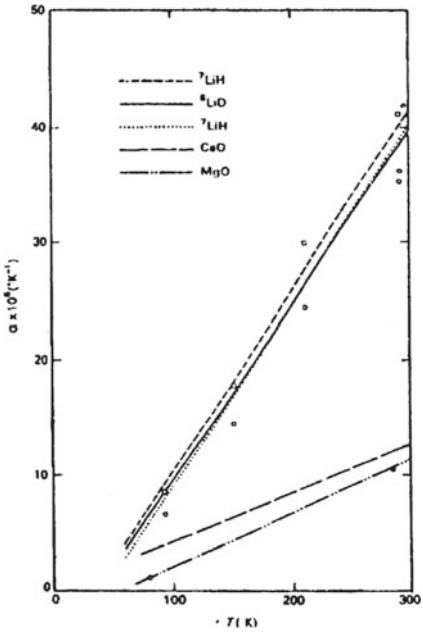

Fig. 4.11 Calculated linear coefficient of thermal expansion for several isotopic varieties of LiH and LiD (after [71])

be seen that in the wide temperature range, the value of γ is almost constant, that is, one more to indicate on the weak dependence γ from temperature, but $\gamma_{\mathrm{LiH}} > \gamma_{\mathrm{LiD}}$ in the temperature range $100 \leq T \leq 300\,\mathrm{K}$ (see also [73]).

The pressure and temperature derivatives of the elastic moduli of single-crystal LiH have been determined at room temperature by Gerlich and Smith [74]. Figure 4.14 presents the Gerlich and Smith's results of the variation the natural velocity with pressure, for sound waves propagating in the [75] direction. The dots are the experimental data points, while the straight lines are a linear least square fit to them. From the slopes of the lines, $(\rho_0 v^2)^{\mathrm{l}}_{\mathrm{P}=0}$ may be evaluated, where v is the natural velocity, P the pressure, ρ_0 zero pressure density, and $^{\prime}$ designates differentiation with respect to pressure. The values of $(\rho_0 v^2)^{\mathrm{l}}_{\mathrm{P}=0}$ thus determined are shown in Table 4.1. Sine the specimen with [76] parallel faces much longer than the one with [75] faces, and as the echo pattern for the former was much superior to the one with the [75] faces, the latter being quite poor, only the [76] propagation data were used for evaluating the pressure and temperature derivatives of the elastic moduli. The results of the pressure derivatives of $C^{\prime}_{11}$, $C^{\prime}$ and C_{44} corrected for the misalignment in the propagation direction (Fontanella and Schuele [77]), together with their associated errors, are shown in Table 4.2. It is interesting to note that pressure derivative of the bulk modulus, $\partial B^{\mathrm{S}}/\partial P$, is relatively small, some magnitude as in AHC [13, 20]. Hence under high compressive stress, LiH will not stiffer up too much, making it more susceptible to fusion. Table 4.3 presents the values of the temperature derivatives of the above elastic moduli, as well as results of Haussuhl and Skorczyk [78], and Table 4.3 presents the thermal 0 K values of the elastic moduli.

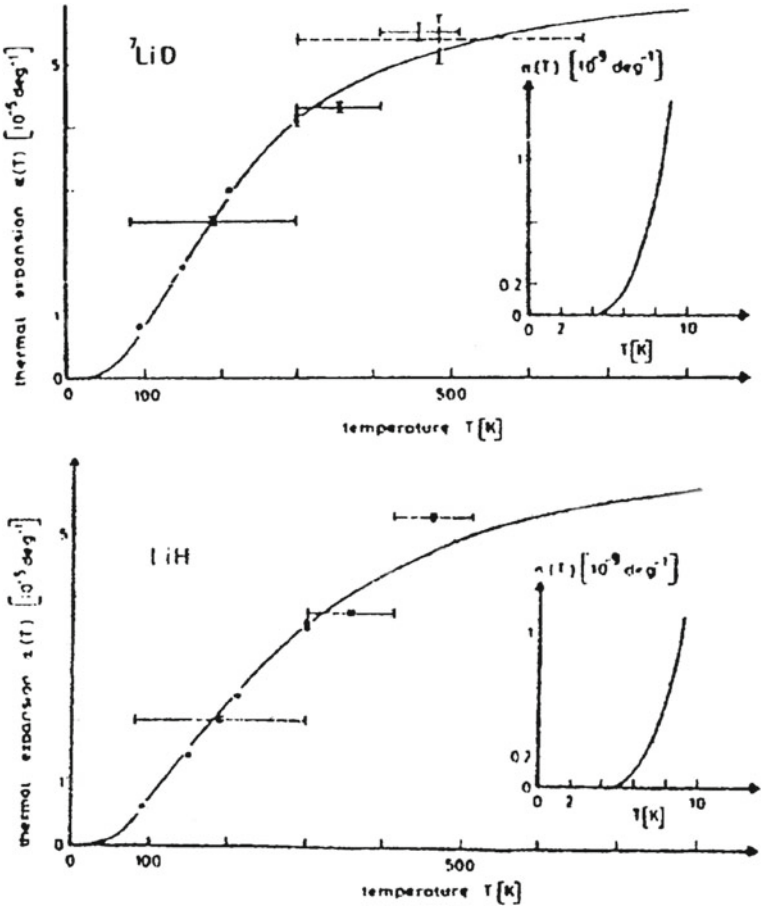

Fig. 4.12 Linear thermal expansion of LiH(^{7}LiD) (after [72])

From the pressure derivatives of the elastic moduli, and the room and low-temperature values of the latter, the mode Grüneisen parameters in any crystalline direction, as well as the low- and high-temperature limiting values of the Grüneisen constant γ_L and γ_H may be evaluated. The mode Grüneisen parameters for some crystalline directions of high symmetry are shown in Fig. 4.15. Here, 1 denotes the longitudinal mode, and 2 and 3 the fast and slow shear modes, respectively. The values of all three mode Grüneisen parameters vary strongly with crystalline direction, due to the fact that the reciprocal of the elastic stiffness and the pressure derivatives of the latter vary in opposite sense. The values of γ_L and γ_H, together with the values of the room temperature Grüneisen constant, obtained from thermal expansion data, are shown in Table 4.4. As can be seen, γ_{L} and γ_{H} are quite close in magnitude and agree well with thermal data.

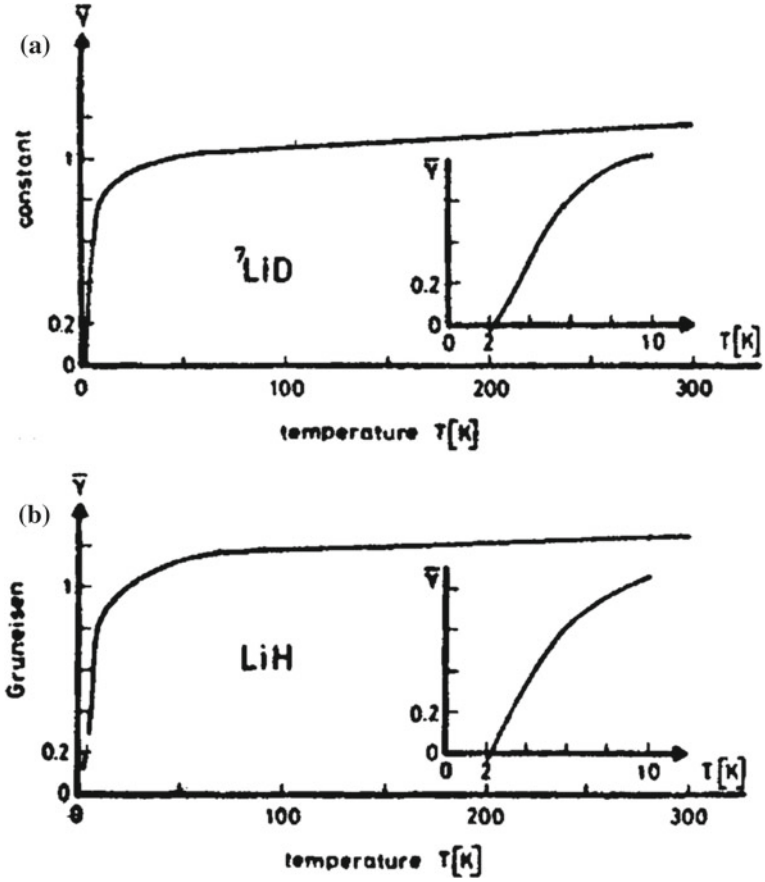

Fig. 4.13 Mean Grüneisen constant of **a** ^{7}LiD and **b** ^{7}LiH (after [72])

Ubbelohde [79] pointed out in 1936 that the substitution of one isotope for another, in a solid chemical compound, will lead to differences in the rotational and vibrational frequencies of the molecules, without producing any significant change in the structure of the potential energy of the solid [77, 80]. These substitutions cause changes in the lattice constant, a, and in the coefficient of thermal expansion, α, of the solid. The influence of isotopic composition on the thermodynamic properties of substances is usually considered to be manifestation of the quantum nature of matter. At high temperatures in the classical limit, any mass effect on thermodynamic quantities disappears and hence any quantum isotopic effect vanishes (see also Landau and Lifshitz [61]).

The dependence of the thermal expansion coefficient α from the temperature T in many cases is dictated by the temperature behavior of the specific heat (see below). It is explained that usually the integral coefficient of Grüneisen γ is weak dependence

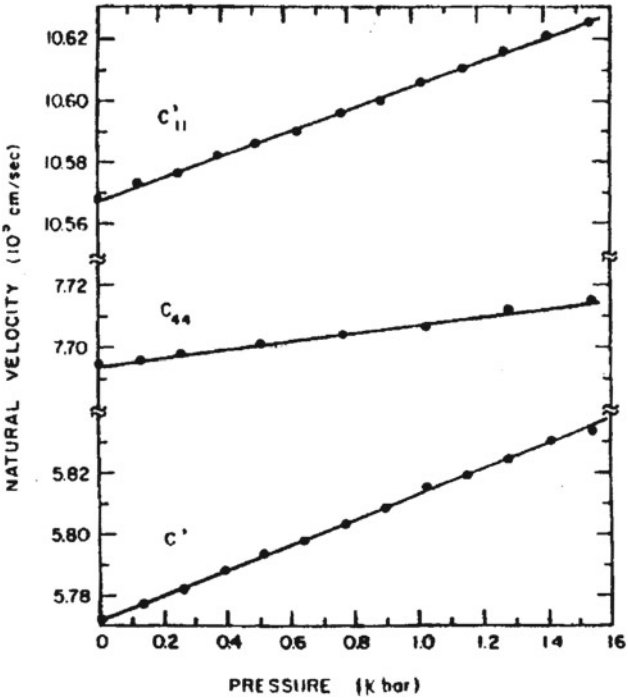

Fig. 4.14 Natural velocity as a function of the pressure for the ⟨110⟩ propagation direction (after [74])

from T. There have been several investigations of the isotope effect on the lithium hydride [72, 81]), KCN [82] and Ge [30, 31]. Table 4.5 lists the measured coefficient of thermal expansion over the temperature ranges −190°–240 °C [81]. Here, contrary to the effect found with lattice constants (for more details see below) the heavier isotopes have the larger coefficient of thermal expansion. Table 4.6 lists the ratios of the α's for these same temperature intervals. Several points should be emphasized about Tables 4.5 and 4.6. There is a definite discrepancy in α for ^{6}LiH compared to α for ^{7}LiH in the −190° to 25 °C range. There is no reasonable explanation for the higher value of ^{6}LiH over ^{7}LiH (see also Tyutyunnik [83]). It would be expected that the difference would be small due to the closeness of the reduced masses (μ) of ^{6}LiH and ^{7}LiH; however, the reversal appears to be anomalous. Table 16 in [30] shows that for any given combination, the ratio $\alpha_{\text{light}}/\alpha_{\text{heavy}}$approaches 1 as the temperature is increased. Again, all ratios should be exactly one if no isotope effect were present. The greater the relative mass differences between isotopes under study, the lower the ratio $\alpha_{\text{light}}/\alpha_{\text{heavy}}$. This is especially noticeable in comparing the data for ^{6}Li and ^{7}Li it is seen the ratios are all close to one, indicating very little effect. Theoretical estimation the ratio $\alpha_{\text{LiH}}/\alpha_{\text{LiD}}$ at 298 K is 0.80 and experimentally, the value $\alpha_{\text{LiH}}/\alpha_{\text{LiD}}$ for the −190–25 °C was 0.81. This value approaches 1.0 at the

Table 4.1 Values of $(\rho_0 W^2)'_{P=0}$ for the three propagation modes in the ⟨110⟩ direction (after Gerlich and Smith [74])

Mode	C'_{11}	C'	C_{44}
$(\rho_0 W^2)'_{P=0}$	6.21 ± 0.07	3.65 ± 0.04	1.57 ± 0.07

Table 4.2 Pressure derivatives of the second-order elastic moduli (after Gerlich and Smith [74])

$\frac{\partial C'_{11}}{\partial P}$	$\frac{\partial C'}{\partial P}$	$\frac{\partial C_{44}}{\partial P}$	$\frac{\partial C_{11}}{\partial P}$	$\frac{\partial C_{12}}{\partial P}$	$\frac{\partial B^s}{\partial P}$
7.17 ± 0.07	3.94 ± 0.04	2.06 ± 0.07	9.05 ± 0.18	1.17 ± 0.18	3.80 ± 0.15

Table 4.3 Athermaly extrapolated 0 K values of the elastic moduli. (Units 10^{11} dyn/cm^2) (after Gerlich and Smith [74])

C'_{11}	C'	C_{44}	C_{11}	C_{12}
9.630	3.338	5.093	7.875	1.199

higher temperatures. The Debye theory predicts a larger heat capacity for the heavier element ($C_{heavy} > C_{light}$) then the Grüneisen relation $\alpha = \gamma C_V / 3\chi_T V$; it is expected that $\alpha_{heavy} > \alpha_{light}$. This difference in physical properties resulting from isotopic substitution becomes much less pronounced as the temperature is increased, and should eventually become negligible (see also Kogan [84]). These results are shown in Fig. 4.12.

For comparison, in Fig. 4.16, it is shown the results of measurements of the linear thermal expansion coefficients for two samples Ge: ^{nat}Ge and ^{70}Ge (99.99%) [85]. It can be seen from this figure that the difference $\Delta\alpha$ for two samples Ge is one order less than $\Delta\alpha$ in case of LiH and LiD. In conclusion of this part, we should mention once more the results of measurements of $\Delta\alpha$ for KCN of different isotopic compositions. The precise measurements are shown no evidence of influence of isotopic composition on the thermal expansion coefficient or the compression isotherms were found [82].

4.4.2 Effect of the Isotope Composition of a Crystal Lattice on the Specific Heat

According to the classical physics, the specific heat data are probably the oldest source of information about phonons in crystal lattices and are, in fact, one of the sources of the original paradoxes that led to the development of modern quantum theory. The non-constancy of the specific heats of crystals as a function of temperature was not explicable by classical theory [89]. The term specific heat is customarily used as a synonym for heat capacity per gram. In most theoretical calculations, the heat

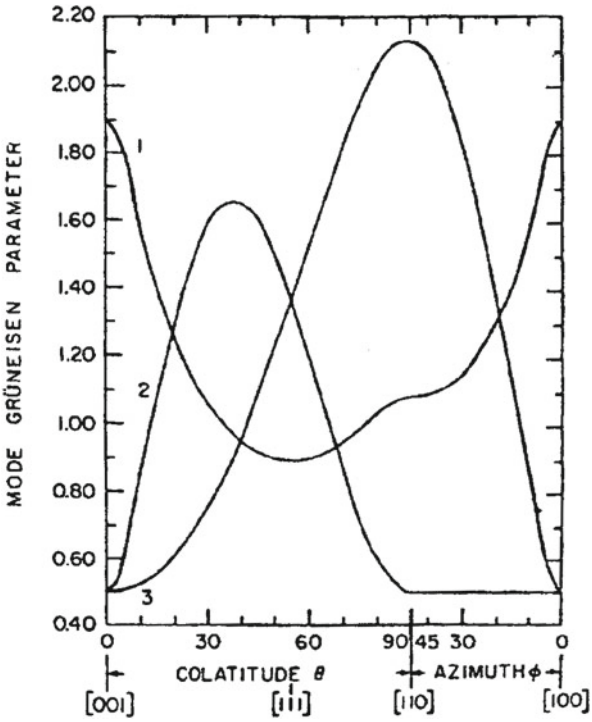

Fig. 4.15 Mode Grüneisen parameters for some crystalline directions of high symmetry (after Gerlich and Smith [74])

Table 4.4 Elastic and thermal Grüneisen constants (after Gerlich and Smith [74])

	γ_L	γ_H
Elastic data	1.21	1.12
Thermal data		1.28 (300 K)

Table 4.5 α,s·10^6 for isotopic LiH (after Anderson et al. [81])

Isotopic composition	−190–25 °C	25–140 °C	140–240 °C
^{6}LiH	21.0 ± 0.3	34.4 ± 0.8	50.0 ± 1.0
^{7}LiH	19.8 ± 0.4	37.4 ± 0.4	53.3 ± 0.6
^{6}LiD	24.0 ± 1.0	38.4 ± 1.8	54.3 ± 1.0
^{7}LiD	24.8 ± 0.4	42.9 ± 1.0	55.0 ± 1.4
^{7}LiT	26.4 ± −0.5		

capacity per gram molecule is the natural quantity to calculate, since this then refers to the properties of a fixed number of particles.

The heat capacity of a solid is measured as $C_p = (\frac{\Delta Q}{\Delta T})_p$ where ΔQ is the heat input, ΔT the change in temperature, and p is the pressure, which is constant. The heat

Table 4.6 Comparison of the effect of isotopic scattering on the thermal conductivity of natural Ge, Si, and diamond at 300 K. The % increase in k is the increase of the thermal conductivity of the nearly isotopically pure sample compared to the natural sample. The isotope is defined as $g = \sum_i f_i (\frac{\Delta M_i}{M})^2$ (after [86–88])

	% increase in k	θ	$\Gamma \cdot 10^{-4}$
Ge	30	376	5.80
Si	60	658	2.01
Diamond	50	1860	0.76

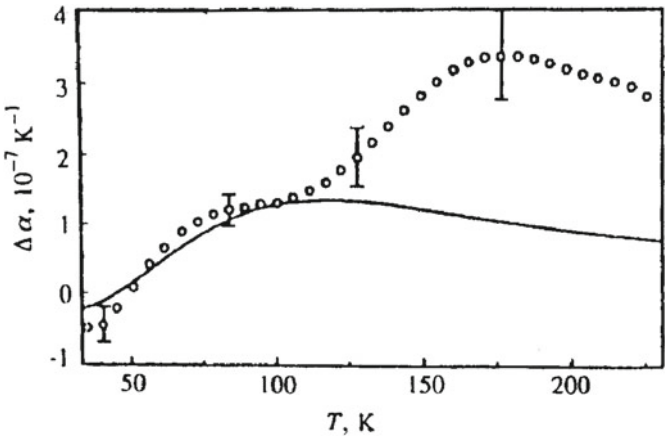

Fig. 4.16 The temperature dependence of the factor $\Delta\alpha = \alpha_c(M_{c1}) - \alpha_c(M_{c2})$, where $M_{c1} = 72.59(^{nat}Ge)$ and $M_{c2} = 70(^{70}Ge)$. The full line is the theory, and dots are experiments (after [85])

capacity which is obtained from most theoretical calculations is C_v that is pertaining to constant volume, which is equal to $(\frac{\partial E}{\partial T})_v$ where E is the internal energy and V the volume. The assumption is made here that the internal energy is a function of two parameters only, in this case T and V, though the concept of heat capacity can be generalized to include other parameters. Heat capacity depends not only on the initial and final states (in particular, the body temperature) but also on the path of the transition between them. In dielectric crystals, the heat capacity is determined by the heat capacity of the crystal lattice. At a constant volume, heat is spent only on the change of vibrational energy of the crystal lattice, and the body heat capacity C_v coincides with the phonon heat capacity [58]. If one imagines the crystal lattice as a multitude of independent harmonic oscillators with frequencies corresponding to the normal vibrations of the lattice, then it is possible to calculate the energy of the system using the methods quantum statistics. Differentiation of the energy with respect to the temperature gives an expression for heat capacity of a monoatomic crystal lattice:

$$C_v = 3nk \int \frac{(\hbar\omega/kT)^2 e^{\hbar\omega}/\mathrm{kT}}{\left(e^{\hbar\omega}/\mathrm{kT} - 1\right)^2} D(\omega)\mathrm{d}\omega, \tag{4.28}$$

where n is the number of atoms per unit volume, ω is the frequency of normal vibrations of the crystal lattice (i.e., phonons), $D(\omega)$ is the spectral density of lattice vibrations, and k and $\hbar$ are the Bolzman and Planck constants, respectively.

Since heat capacity is an integral quantity, the exact form of the function $D(\omega)$ is not great importance and Debye theory [65] gives suitable results. According to this theory, one takes into account only the acoustic vibrations of the lattice. At the same time, one assumes that independently of the polarization, the phonons are characterized by the same speed of spreading s (the velocity of sound) and by the linear dispersion dependence, $\omega_q = sq$, where q is the wave number. The condition is actually fulfilled only at low temperatures. In addition, in Brillouin zone, where there are allowed values of the vector q, a Debye sphere of the same volume is substituted in inverted space. From this condition, one can imagine that there is a maximum wave number, $\mathrm{q_D}$, and a corresponding maximum frequency of normal vibrations (phonons), ω_D, which is called Debye frequency [58]. If one uses [90] and takes into account that the full number of normal vibrations is equal to the number of atoms in the volume, corresponding to the chosen boundary conditions, then

$$q_D = (6\pi^2 n)^{1/3} \tag{4.29}$$

$$\text{and} \quad \omega_D = s(6\pi^2 n)^{1/3}. \tag{4.30}$$

The spectral density according to the Debye approximation is given by

$$D(\omega)\mathrm{d}\omega = 3\omega^2/\omega_D^3. \tag{4.31}$$

Then, (4.28) has the next form

$$C_v = 9nk \int_0^{\omega_\mathrm{D}} \frac{(\hbar\omega/kT)^2 e^{\hbar!/\mathrm{kT}}}{(e^{\hbar!/\mathrm{kT}} - 1)^2} \frac{\omega^2}{\omega^3}\mathrm{d}\omega = 9nk(T/\theta)^3 \int_0^{\omega_\mathrm{D}} \frac{x^4 e^{\mathrm{x}}}{(e^{\mathrm{x}} - 1)}\mathrm{d}x. \tag{4.32}$$

Here, $x = \hbar\omega/kT$, $\theta = \hbar\omega_D/k$, the Debye temperature. At low temperature ($T \ll \theta$), one gets from (4.32) with good accuracy

$$C_v = (12\pi^4/5)nk(T/\theta)^3. \tag{4.33}$$

That is, the heat capacity is proportional to T^3 (Debye relation of T^3 dependence). At high temperatures ($T \gg \theta$), we get

$$C_v \approx 3nk. \tag{4.34}$$

That is, the heat capacity does not depend on the temperature—the Dulong and Petit's law [56].

The expression (4.32) is exact at low temperatures, and it adequately describes the temperature dependence of energy. In this case, the heat capacity $C_v = \gamma T^3$. This dependence well agrees with experimental data within the narrow temperature range (near 0 K). Microscopic calculation based on the phonon formalism also gives (4.42) [56]. Therefore, one can conclude that the concept of phonons permits the use of mathematical ideas and procedures applicable to common real particles (for details see [91]).

The definition of a θ_D value is that it is equal to $\hbar\omega/k_B$, where ω is either a characteristic frequency or some average frequency [90]. A great deal of confusion has been caused by the assumption that θ_D values derived from different physical properties of a solid should be equal. Such an assumption may have been justified in the early stages of specific heat theory, but it has long outlived its usefulness. It would seem advisable to restrict the term θ_D to the representation of specific heat data only, since θ_D is not a constant, it is worthwhile on occasion to indicate the temperature or temperature range. In all other cases, θ_D values should be labeled in such a way that their origin is made evident. The simplest case is that of θ_D (elastic—see [7]), i.e., the θ_D value derived from the elastic constants of a solid. This is equal to θ_D if both are measured at sufficiently low temperatures. Otherwise, they are not in general equal, though it may be possible to derive a relation between them at other temperatures for a theoretical lattice model (see also [92]).

The early low-temperature specific heat was measured by Gūnther from room temperature down to 74 K (see, e.g., [64]. First detailed measurements of the specific heat of lithium hydride in a wide temperature range from 3.7 to 295 were performed by Kostryukov in 1961 [91]. In this paper, the unusual behavior of specific heat was observed between 10 and 20 K. As is shown above, at low temperatures, the heat capacity at a constant volume is $C_v \sim \gamma T^3$. Kostryukov observed strong deviations from the T^3 law, which were dependent on the sample prehistory, and explained them by the presence of free molecular hydrogen in lithium hydride. However, by using a special experimental procedure, Kostryukov managed to obtain more reproducible results that only slightly deviated from the T^3 dependence. Based on these results, cited author estimated the Debye temperature of lithium hydride to be $\theta_D = 860$ K (see Table 2 in review of Plekhanov [93]). Later, Yates et al. [94] carefully studied the low-temperature ($5 < T < 320$ K) specific heat of lithium hydride. In this paper, the effect of the isotopic substitution ($H \rightarrow D$) on the specific heat was studied for the first time (see Fig. 4.17). Yattes et al. investigated the high-purity and high-stoichiometric samples (the total content of impurities <2 x IO^{-5}). The C_p(T) dependence measured by Yates et al. at $T > 30$ was used for calculating the Debye temperature from the relation C_v =const. $(T/\theta_D)^3$. The value of θ determined in this way, as was shown above, depends on the temperature. It is known that this dependence is explained by the deviation of the postulated Debye spectrum from a real phonon spectrum. The values of θ_D found from the extrapolation of θ_D(T) to $T = 0$ (Fig. 4.17) are equal to $\theta_D(\mathrm{LiH}) = 1190 \pm 80$ and θ_D (LiD) $= 1030 \pm 50$ K. One can see that the value of the Debye temperature for LiH obtained by Yates et al. is higher than that obtained by Kostryukov. In addition, data on the Debye temperature show that this temperature decreases with increasing isotope mass in accordance with the theory. Comparison of

Debye temperatures calculated from elastic constants($\theta_D = 1083$–1135 K at 300 K) [74, 95] and calorimetric data ($\theta_D = 1190 \pm 80$ K at 0 K) [94] shows that they are in agreement, especially for LiH crystals. Note the strong temperature dependence of the Debye temperature of LiD crystals, which has not yet been adequately explained. It is likely that the Debye temperature of diamond also strongly depends on temperature (for details see also [96, 97]). Figure 4.18 displays interesting features in the results below 25 K. Associating the term anomaly with a situation in which the heat capacity rises with diminishing temperatures, the results for ^{7}LiH and ^{7}LiD will each be seen to contain anomalies, having peaks at temperatures of 11.1 ± 0.2 K and 12.8 ± 0.2 K, respectively. The results of Fig. 4.8 can be little doubt that the peaks observed in the specific heats of the two compounds at low temperatures do not arise from spurious origins, and that they are truly characteristic of the compounds. When they occur in dielectric crystals, anomalies of this type are most commonly caused by movements of atoms, and in this case it seems likely that such a rearrangement takes place in the region of 11.1 K in the case of ^{7}LiH and in the region of 12.8 K in the case of ^{7}LiD. The authors of [94] observed λ-type anomaly of the heat capacity and concluded that this anomaly in the temperature dependence of C_p(T) is related to some phase transition. Indeed, Schumacher in the early 1960s had already predicted [98] that lithium hydride should undergo a phase transition in the pressure range between 3 and 4 kilobar. Later, Berggren [75], by using a simple qualitative model, found that the binding energy in LiH with the structure of CsCl type is higher than with the NaCl structure. Based on these results, the authors [94] assumed that anomalies observed in LiH are related to the polymorphic transition from NaCl structure to CsCl structure. However, attempts to find this transitions, which were made in several papers [75, 95, 99, 100] by using an external pressure of up to 330 kilobar [101], failed. Note here that the CsCl$\longrightarrow$NaCl phase transition was also not found in a recent paper [101], where the effect of the external pressure on CsH was investigated. Note also that numerous experimental studies on reflection spectra in *exciton* region and Mandelstam–Landsberg–Raman spectra [96, 97] in these crystals did not reveal noticeable anomalies in the above temperature range (for details see [30]).

In recent years, analogous investigations were performed on semiconducting crystals (see, e.g., [102, 103]). Figure 4.19 displays the molar heat capacity of the three investigated Ge isotope samples, again in a plot of $C_p(T)/T^3$ against T (Fig. 4.19, lower panel), as well as in the representation of the corresponding calculated Debye temperature θ_D as a function of temperature T (upper panel). Molar heat capacity and Debye temperature show the characteristic low-temperature behavior known from Ge and other solids (see [103] and references therein). Most typical is the strong minimum of $\theta_D(T)$ around 20 K, as a typical for diamond structure, due to the serious departure from the Debye approximation. Anharmonic effects become important only for $T > \theta_D(0)/3$, where $\theta_D(T)$ saturates and starts to decrease with increasing T [103]. Calculations for the difference $\Delta C_{\text{isotope}}$ between the values of molar heat capacity of the isotopes show that $\Delta C_{\text{isotope}}$ increases with temperature since C_p(T) increases most strongly for the material with the greatest molar mass (compare, please with LiH data). $\Delta C_{\text{isotope}}$ reaches a maximum around $\theta_D(0)/4$ ($\approx$90 K for Ge) and at the limit of high temperatures, it approaches zero [97, 104].

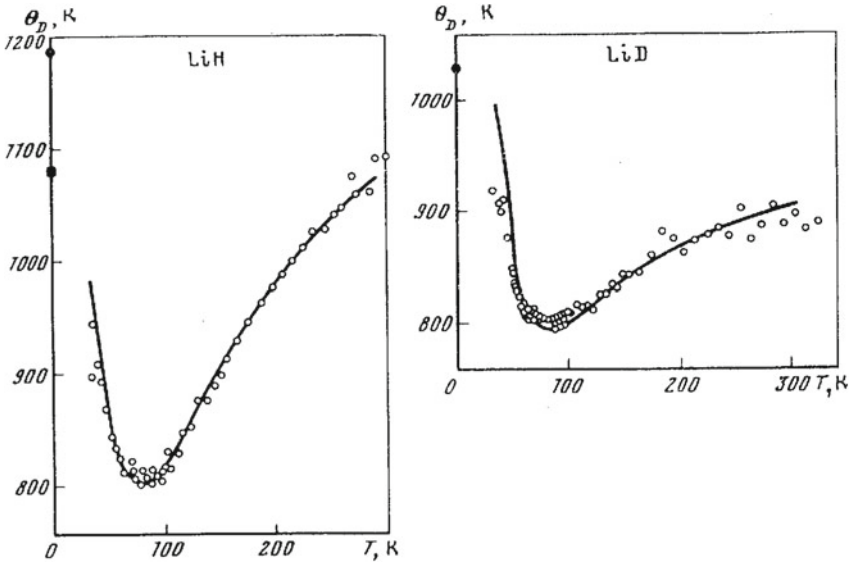

Fig. 4.17 The temperature dependence of the Debye temperature for ^{7}LiH and ^{7}LiD crystals (after [94])

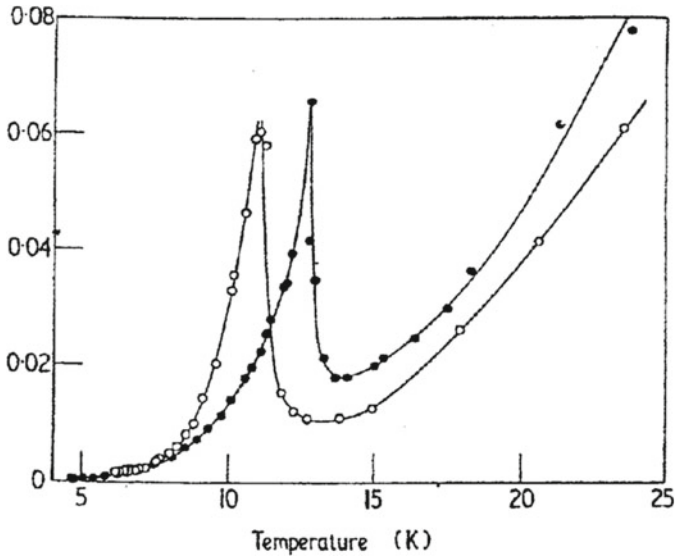

Fig. 4.18 The specific heat C_P of ^{7}LiH (○) and ^{7}LiD (●) crystals at low temperature (after [94])

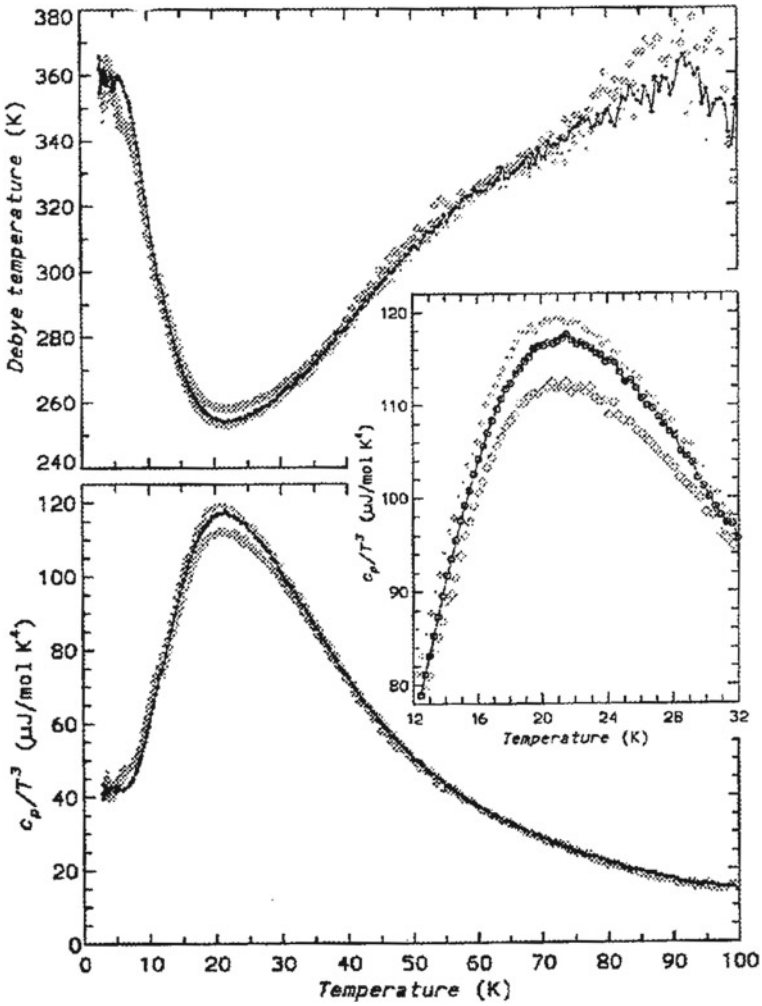

Fig. 4.19 Molar heat capacity C_P(T) of the three measured crystal samples: $^{70/76}$Ge (+), ^{nat}Ge. Circles connected by a thin line and ^{70}Ge (◇): plot of C_P/T^3 against T (lower panel), and (upper panel) corresponding Debye temperature θ_D as a function of temperature T. The inset shows a magnification of the plot in the lower panel (after [102])

4.4.3 Dependence of Thermal Conductivity on the Isotope Composition of Materials

All solids—one better, the other worse—are able to conduct the heat. In isotropic solid, the spreading of heat is obeyed to the Fourier law (discovered in 1882)

$$Q = -k\text{grad}T = -k\left(\frac{\partial T}{\partial n}\right), \tag{4.35}$$

where Q is the surface density of the heat stream, e.g., it is a vector a module of which is equal to the heat flow across the cross section which is perpendicular to Q; T is the temperature; $\frac{\partial T}{\partial n}$ is gradient of the temperature along normal $\boldsymbol{n}$ to isothermic surface and k is the heat conductivity. The sign of minus to the right of the expression (4.35) is connected with the fact that the heat is flowing in the direction opposite gradient of the temperature, e.g., from the hot side to the cold one. In anisotropic solids, the tensor of second rank and its form depend upon the symmetry of the crystals.

In common case, in solids, there are two main mechanisms of the heat transfer: the transfer of the heat energy of free electrons and the transfer of the heat energy by the vibrations of the crystal-forming particles. In metals, the effect of both mechanisms acts simultaneously, while in the insulators, the heat energy transfer is carried out by atomic (ionic) vibrations. The kinetic energy of the vibrations is transferred from the heat strip to the cold one. The beam of the kinetic energy of atoms is macroscopically looked like the heat flow. This process is similar to the process of the spread of elastic sound waves in solids. When explaining the phenomenon of the heat conductivity it is allowed to consider yet that the atoms perform the strong harmonic vibrations diffusing in the crystal lattice like the system not interacting elastic waves. Such waves would spread in the crystal freely without damping and, consequently, they would unlimited mean free path. The heat flow, even at small gradients of the temperature could exist indefinitely long, before the heat equilibrium would set up and the heat conductivity in such case would be endless.

In real solids as it was shown in the experiments [105], the heat conductivity is turned out to be finite. The finite value of the heat conductivity is connected with such circumstance that in real crystal the vibrations of the crystal-forming particles are not pure harmonic. The reason for this circumstance is that the forces interacting between atoms do not depend linear but depend on the displacement of atoms. The anharmonic character of vibrations is taken into account by the expanding of potential energy by the anharmonic term gx^3. Keeping the anharmonic term in the expanding of the potential energy we take into account the presence the interaction between vibration modes in real situation. This interaction is usually described as the mutual scattering of phonons. In the first step, there are considered three-phonon processes: the decay of one phonon into two others, sticking together of two phonons, etc. Mutual scattering of phonons is accompanied by the creation and annihilation of phonons (see also Ashcroft and Mermin [89]).

As it was shown by Peierls in 1929 [107] that the probability of indicated transitions in the case of three phonons processes does not equal to zero, if the next two conditions are fulfilled:

$$\hbar\omega_1 + \hbar\omega_2 = \hbar\omega_3, \tag{4.36}$$

$$\hbar\boldsymbol{k}_1 + \hbar\boldsymbol{k}_2 = \hbar\boldsymbol{k}_3 + \boldsymbol{G}. \tag{4.37}$$

Here, $\boldsymbol{G} = 2\pi\boldsymbol{H}$, and $\boldsymbol{H} = \boldsymbol{h}a + \boldsymbol{k}b + \boldsymbol{l}c$ is the vector of the reciprocal lattice. The expression (4.36) is the energy conservation law for the three-phonon processes. The phonon with quasi-impulse $\boldsymbol{k}$ and frequency ω, commonly speaking, does not possess impulse as the ordinary material particle. However, the value of $\hbar\boldsymbol{k}$, called the quasi-impulse (wave vector) in common case, is equivalent to pulse. The expression (4.37) at $\boldsymbol{G} = 0$ corresponds to the wave vector conservation law. The interaction at which the condition $\boldsymbol{G} = 0$ is fulfilled is called normal or N-process. This term is originated from the analogy of the interaction of elementary particles (e.g., electrons) for which the law of conservation of energy and momentum is fulfilled. In distinction from ordinary particles, at the phonons interactions, the number of phonons does not conserved. Moreover, at the phonons collisions, the wave vector could be conserved with the precision equal to the vector of reciprocal lattice. This means that the crystal lattice in which the phonons move also takes part in the collisions, taking away part of momentum equal to $\boldsymbol{G} = 2\pi\boldsymbol{H}$.

The interaction at which in the expression (4.37) $\boldsymbol{G} \neq 0$, Peierls called the process of throw over (of the transfer) or U-process, which is derived from the German word Umklapprozesse—the process of transfer. In the U-process, the energy must conserve as in normal process. The difference between N- and U-processes is determined if $\boldsymbol{G}$ is larger or smaller than the value of wave vector of the third phonon ($\boldsymbol{k}_3$) performed at the collision of the two phonons with the wave vectors $\boldsymbol{k}_2$ and $\boldsymbol{k}_1$. If $\boldsymbol{k}_3 = \boldsymbol{k}_2 + \boldsymbol{k}_1 < \boldsymbol{G}$, e.g., $\boldsymbol{k}_3$ does not leave the border of the first Brillouin zone, in such case all three vectors have positive direction relating to k_x and for them is justified the relations (4.36) and (4.37) at $\boldsymbol{G} = 0$. This picture is in accordance with N-process. So far in this situation, $\boldsymbol{k}_3$ coincides with the direction, in which the energy is effectively transferred by phonon modes with $\boldsymbol{k}_1$ and $\boldsymbol{k}_2$, so in this case, as was shown by Peierls, the N-processes by themselves do not lead to the reconstruction of the equilibrium distribution of phonons. The latter means that the finished transfer of the energy can be conserved and at the absence of gradient of the temperature, e.g., the heat conductivity is infinitely large. However, after U-process the heat energy is transferred in the direction, which does not coincide with the direction of group velocities in the modes of $\boldsymbol{k}_1$ and $\boldsymbol{k}_2$. Such essential changes $\boldsymbol{k}$ always lead to the reconstruction of equilibrium distribution of phonons, and consequently to the finite value of the heat conductivity.

In insulators and semiconductors (at $T < \theta_D$), the thermal conduction is effected by phonons, predominantly acoustic ones [62, 105]. Thermal conductivity of crystals has been subject of many experimental theoretical studies (see, e.g., reviews and monographs [65, 76, 86, 104, 107–111]). The first experimental results (see, e.g., [111]) have already pointed out the existence of maximum of the thermal conductivity coefficient k_{m} at about $T \approx 0.05\theta_D$, where θ_D is the Debye temperature. The growth of k at low temperatures has been related to phonon scattering due to Umklapp (U)-type processes [107]. In the vicinity of k_{m} thermal conductivity is quite sensitive to impurities and defects in the specimen. The scattering of phonons dynamic isotope disorder is independent of temperature and lattice anharmonicity. The role of isotopes as an additional channel of phonon scattering and their influence on thermal conductivity was first theoretically studied by Pomeranchuk [108] in 1942

and was experimentally studied using Ge in 1958 [76]. According to the results of the latter reference, for a Ge specimen (having 95.8% ^{74}Ge), a threefold growth of the thermal conductivity coefficient as compared to the specimen of germanium with natural isotope composition was observed. Later, the influence of isotopes on diamond thermal conductivity was studied many times [14, 86, 87, 109, 110, 112].

It is generally assumed (see, e.g., [30]) that at not too high temperatures, the dominant interacting among phonons involve three phonons. In a "normal" (N-) process, the wave vectors $\boldsymbol{q}$ of the phonons are conserved and such process tend to restore a disturbed phonon distribution to one which can be described as a displaced Planck distribution (see, e.g., Fig. 5.2 in [7]) which is unaffected by N-processes and corresponds to a heat flow. By themselves, therefore, N-processes would not lead to a thermal resistance.

In U-process [109], the wave vectors are not conserved and, as in other resistive processes, they tend to restore a disturbed phonon distribution to the equilibrium Planck distribution which corresponds to zero heat flow, and thus lead to a finite conductivity (for more details, see review [30]). The Debye expression [65] for the conductivity $k(T)$ is derived from an adoptions of the simple kinetic theory

$$k(T) = \frac{1}{3}\langle v_{\mathrm{ph}}\rangle \ell_{\mathrm{ph}}(T) C_p(T), \tag{4.38}$$

where $\langle v_{\mathrm{ph}}\rangle$ is an average phonon velocity, $\ell_{\mathrm{ph}}(T)$ their mean free path and $C_p(T)$ the corresponding specific heat (for diamond see [86, 109, 110]). A theory of $k(T)$ requires basically the calculation of

$$\ell_{\mathrm{ph}}(T) = \tau_{\mathrm{ph}}(T)\langle v_{\mathrm{ph}}\rangle \tag{4.39}$$

a rather formidable task since several scattering mechanisms (normal-, u-processes, boundary of sample, and isotope scattering) [1] contribute to determining the mean free path. In formula (4.39) $\tau_{\mathrm{ph}}(T)$ is the phonon relaxation time. The simplest of these mechanisms, and the one that can be varied for a given material of the acoustic phonons by isotopic mass fluctuations. This scattering is equivalent to Rayleigh scattering (of photons) at point defect. Within Debye approximation, we will have

$$k(T) = \frac{k_{\mathrm{B}}}{2\pi\nu}\left(\frac{k_{\mathrm{B}}}{\hbar}\right)^3 T^3 \int_0^{\frac{\theta_{\mathrm{D}}}{T}} \tau(x)\frac{x^4 e^{\mathrm{x}}}{(e^{\mathrm{x}}-1)^2}\mathrm{d}x. \tag{4.40}$$

In last expression, k_{B} is the Boltzmann constant. Klemens [59] was the first to try to take the role of N-processes into account. Using perturbation theory, Klemens [59] developed the following expression for the scattering rate $\tau_{\mathrm{isotope}}^{-1}$:

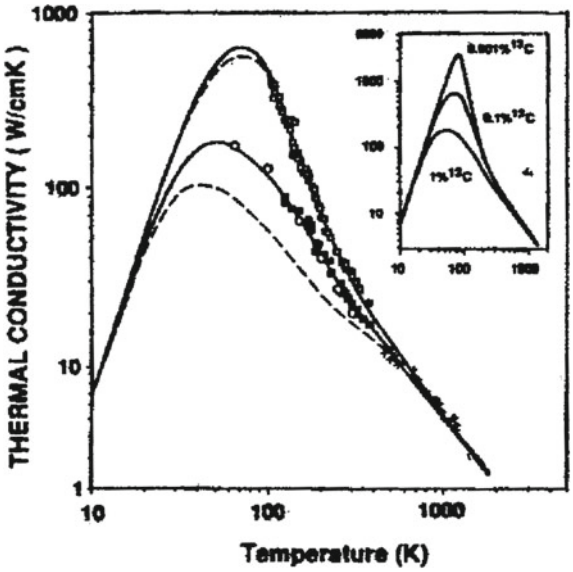

Fig. 4.20 Thermal conductivity of natural abundance (1.1% of ^{13}C) diamonds (lower squares), isotopically enriched (0.1% ^{13}C) diamond (upper squares), together with the low-temperature data (circles) and high-temperature data. The solid curves are the result of fitting the Callaway theory [112] to the data, using the same set fitting parameters. The inset shows the calculated thermal conductivity corresponding to 1, 0.1 and 0.001% ^{13}C concentration according to Callaway theory (after [86])

$$\tau_{\text{isotope}}^{-1} = \frac{x(x-1)V_0}{4\pi\langle v_{\text{ph}}\rangle^3}\left(\frac{\Delta M}{M}\right)^2 \omega^2, \tag{4.41}$$

where V_0 is a volume per atom (for diamond $5.7 \cdot 10^{-24}\,\text{cm}^3$) and ω is phonon frequency. Callaway approach [87] successfully introduces normal phonon scattering (τ_{N}^{-1}) and resistive scattering (τ_{R}^{-1}) (see formula (4.51) in [30]).

In Fig. 4.20, we present the results of Wei et al. [86]. The solid curves are the results of fitting the Callaway theory [87], using a single set of fitting parameter. In this paper, Wei et al. have measured a record thermal conductivity of $410\,\text{Wcm}^{-1}\text{K}^{-1}$ at 104 K for a 99.9% ^{12}C enriched diamond. These authors predict that a 99.999% ^{12}C diamond should have a peak value of thermal conductivity exceeding $2000\,\text{Wcm}^{-1}\text{K}^{-1}$, at about 80 K, assuming, of course, that is not limited by point defect scattering mechanisms other than minority isotopes. Similar results have very recently been reported by Olson et al. [110]. We should stress that none of the currently existing theories accurately takes into account all the possible scattering processes.

Thermal conductivity studies have also performed on very highly enriched, ultra-pure ^{70}Ge (see reviews [30, 31]). The maximum value of $k_{\text{m}} = 10.5\,\text{kWm}^{-1}\text{K}^{-1}$ was observed, in the vicinity of $T = 16.5\,\text{K}$, for the ^{70}Ge specimen of 99.99% purity, which is significantly higher than the value for sapphire ($6\,\text{kWm}^{-1}\text{K}^{-1}$

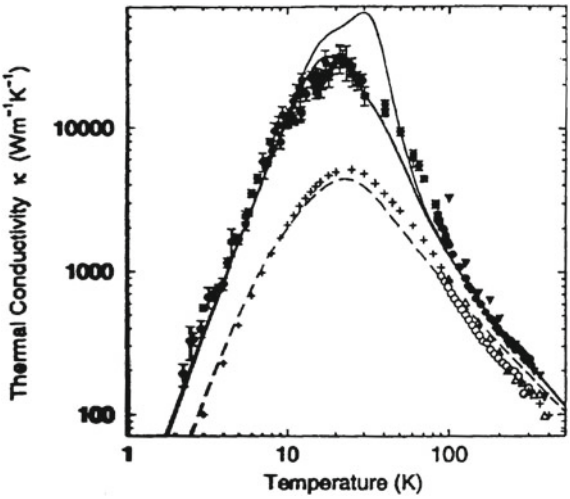

Fig. 4.21 Thermal conductivity of the highly isotopically enriched ^{28}Si sample SI284 (filled circles) and the natural Si reference SINI (open circles). The filled and open triangles are other measurements for highly isotopically enriched ^{28}Si and natural Si, respectively (from [113]); "plus" symbols denote the "standard" curve for natural Si. The thin solid and dashed lines are the theoretical results of [88] for ^{28}Si and natural Si, respectively. The thick solid line has been calculated with the same theory using the actual mass variance g_2 of sample SI284 (see also Table 4.6) (after [88])

around $T_m = 35$ K) and comparable to the value for silver (11 kWm^{-1}K^{-1} near $T_m = 15.4$ K). Comparison of experimental results shows [5] that, at its maximum (see, e.g., Fig. 6a [94]), the thermal conductivity of the $^{70/76}$Ge (91.91%) specimen is 14 times less than that of ^{70}Ge (91.91%). An increase in k reaches, however, only 30% at $T = 300$ K (see also [30, 31]).

The thermal conductivity of monoisotopic and isotopically mixed specimens of silicon crystals has been studied in following papers [88, 113–115]. Since the most detailed results have been obtained by the authors of [88], we restrict ourselves to their consideration. It is well known that natural silicon consists of three isotopes: ^{28}Si (∼92%), ^{29}Si (∼5%), and ^{30}Si (∼3%). The use of monoisotopic silicon (for example, ^{28}Si) can substantially reduce the value of dissipated energy scattered in electronic elements made of silicon (e.g., in the memory of electronic computers [116]). The results studies of the thermal conductivity of monoisotopic and isotopically mixed crystals are shown in Fig. 4.21. According to the results presented in this Fig. 4.21, for SI284 specimen $k = 237(8)$ Wm^{-1}K^{-1} at 300 K, whereas for the SINI (natural Si) specimen, it is equal to 150 Wm^{-1}K^{-1}. This means that at 300 K the thermal conductivity of a monoisotopic ^{28}Si specimen grows, as compared to the natural silicon, by 60% (later - 10%, see erratum). At the same time, at about 20 K (in the vicinity of the maximum of the silicon thermal conductivity curve) k reaches the value of 30,000 ± 5,000 Wm^{-1}K^{-1}, which is six times higher the value $k =$ 5,140 Wm^{-1}K^{-1} for natural specimen (see also [117]).

The thin solid and dashed lines in Fig. 4.21 correspond to the results of theoretical computations of thermal conductivity for monoisotopic specimen SI284 and for a specimen with natural silicon isotope composition. In these calculations, the model of the Ge thermal conductivity developed in [116] with modified Debye temperature and phonon mean free path has been used. For fitting, the authors have used the low-temperature results, where the thermal conductivity is described by the T^3 law. Calculations presented in Fig. 4.21 were performed, for the natural specimen, for free mean path equals 5.0 mm (dashed line). For comparison, let us point out that in [88] the analogous quantity was equal to 5.7 mm, and for isotopically pure SI284 specimen the corresponding value was 14.0 mm (thin solid line). As seen from Fig. 4.21, there is an agreement between theory and experiment, which has also been mentioned by the authors of [88] themselves. They have also pointed out a good agreement between their experimental results and calculations made in [114, 115], except for the domain of U-processes. Besides that, Ruf and co-authors have mentioned an unsatisfactory agreement between theory and experiment in the domain of high temperatures (300–400 K), especially for the specimen with natural isotope composition. They think that this disagreement can occur due to fundamental reasons that require further study. In particular, taking into account the fine structure of the nonequilibrium phonon distribution function could bring theoretical and experimental results much closer. A qualitative comparison of the influence of the isotope effect on the thermal of germanium, silicon, and diamond is given in Table 4.6.

In conclusion, we should remark that until recently, all theories on thermal conductivity had a strongly phenomenological flavor, making use of the relaxation time approximation. In recent years, considerable progress toward an ab initio theory has been made [114, 115]. These authors used two- and three-body potentials obtained by fitting phonon dispersion relations and related the anharmonic properties with a single average Grüneisen parameter. In this manner, they determined the third-order coupling coefficients for all possible three-phonon combinations. They then solved iteratively the Boltzmann equation for phonon transport without using the relaxation-time approximation. A scattering time must, however, still be used to describe boundary scattering in the lowest temperature region. In this manner, they reproduced rather well the thermal conductivities of Ge, Si, and diamond and the observed isotope effects (for details see [114, 115]).

Improvement in the thermal conductivity of silicon is important because as the feature size continuously decreases, the current density increases and more heat is generated per unit volume, causing device operating temperatures to rise. The integrated circuit industry (AMD and other companies) is moving toward lower operating voltages and sophisticated mechanical means to minimize this heat build up, but greater heat dissipation on the microscale is becoming essential to improve device performance and ability.

Other, more subtle benefits may also be available with isotopically pure silicon. As device dimensions, the gate oxide thickness in CMOS devices also must decrease. As the transistor size approaches 0.1 micron, the gate oxide thickness will be about 2 nm (0.002 microns). This is equivalent to five atomic layers of silicon dioxide. The gate oxide integrity or breakdown voltage of oxides of this thickness is a key

stumbling block to making smaller devices. The more perfect crystal structure of isotopically pure silicon and silicon dioxide may lead to improved gate oxide integrity and fewer surface traps at the silicon–silicon dioxide interface. It has already been shown that the use of deuterium, an isotope of hydrogen (see also above) instead of a normal hydrogen during the processing of CMOS (complementary metal-oxide-semiconductor) devices has lead to reduced "hot electron" damage and 50–100 times longer lifetimes before oxide wear-out (for details see Lyding et al. [118]).

Isonics Corporation (Colorado, USA) is a world leader in isotopically engineering material, who has taken the concept of isotopically pure silicon and made it a reality. The first product to be offered for sale is an epitaxial silicon wafer, which is the starting wafer for all advanced microprocessors. This wafer has a thin layer of isotopically pure silicon-28 grown on the surface of prime quality, natural silicon wafer. Epitaxial wafers made to custom specifications are currently available in of sizes to integrated circuit manufactures. Many of the advantages of isotopically pure silicon can be obtained with this type of wafer, while keeping costs down.

By the way, it should be mentioned that in short communication of Capinski et al. [88] it was shown that at the isotopical substitution in Si the thermal conductivity was increased by a factor $\approx$7 in the k (at $T \approx 25$ K) (more details see also Capinski et al. [88]) with respect natural Si (see also Table 4.6).

Thus, the analysis of the thermal conductivity of Ge and Si samples as well as diamond with several isotopic composition, using a modified Callaway–Holland formalism, works well below 200 K. To conclude this part, we should mention that the crystals of diamond and Ge (Si) at present time few unique samples where much detail investigation of the influence the isotope effects on the thermal conductivity was done. In this connection, we must add that analogous investigation of the isotope effects of the thermal conductivity in LiH_xD_{1-x} crystals will be very intriguing taking into account the presence of the local vibrations at low concentration x and two-mode behavior of LO phonons at large concentrations [119].

4.4.4 Influence of the Isotope Composition Materials on the Lattice Constant

4.4.4.1 Background

It is widely known that the lattice parameter is, at any temperature, determined by three factors. The first and the most important are the atomic radius and the nature of the chemical bond between the atoms. The latter determines not only the interatomic spacing but also the crystal structure. The second contribution to a is due to the influence of temperature on the interatomic distance. As a rule, an increase in temperature leads to the expansion of the crystalline lattice due to increased amplitudes of the atoms oscillations around their equilibrium position. The third contribution is related to atomic displacement due to zero vibrations—a purely quantum-mechanical effect.

As the latter contribution is usually small at $T = 0\,\mathrm{K}$, it is often neglected (see, however, [7]). The fact that this contribution is difficult to detect experimentally is also of importance. There is, however, an important exception to this rule. It is related to isotope substitution. Inasmuch as, in this case, the chemical substances are identical (this practically is the same substance, the first contribution (atomic size) is constant for substances containing different isotopes. A difference in the lattice constant will, therefore, be fully determined by the difference in thermal expansion and displacements due to zero vibrations. The differences mentioned are indeed great for lithium hydride and its isotopic analogs, lithium deuteride, and lithium tritide. This follows mainly from big change in the mass at isotope substitution and, therefore, from a big change in the reduced mass of the unit cell [30].

The first paper devoted to the calculation of a change in the molecular volume upon isotopic substitution was the paper of London [120], which is now become classic. He started with an expression for the free energy using the Einstein free energy function to reach the expression

$$\frac{M}{V}\frac{\mathrm{d}V}{\mathrm{d}M} = \frac{\gamma\beta}{V}[U - E_0 - TC_v]\left[\frac{\mathrm{d}\ln\nu}{\mathrm{d}\ln M}\right], \tag{4.42}$$

where V is molecular volume, M is the atomic mass, γ is Grüneisen constant $\gamma = \frac{\alpha V}{\beta C_v}$, α is the volume expansion coefficient, β is compressibility, C_v is the molar specific heat, E_0 is the potential energy, ν is the phonon frequency, and U is the total energy.

For monoatomic solids

$$\mathrm{d}ln\nu/\mathrm{d}lnM = -1/2 \tag{4.43}$$

and $\mathrm{d}V/\mathrm{d}M$ can be expressed through a Debye function with characteristic temperature θ_D. At high temperatures, one can express Debye function by a power series in $(\theta_D/T)^2$. Then, (4.42) becomes

$$\frac{M}{V}\frac{\mathrm{d}V}{\mathrm{d}M} = -\frac{1}{20}\alpha T(\theta_D/T)\left[1 + \frac{11}{420}(\theta_D/T)^2 + \cdots\right] \tag{4.44}$$

and at absolute zero

$$\frac{M}{V}\frac{\mathrm{d}V}{\mathrm{d}M} = -\frac{9}{16}\frac{\gamma\beta}{V}R\theta_D. \tag{4.45}$$

Here, R is the gas constant.

For diatomic cubic crystal with atomic masses M and m, we have (see also Born and Huang [90])

$$\nu^2 \sim \left(\frac{1}{M} + \frac{1}{m}\right). \tag{4.46}$$

Therefore

$$\frac{\mathrm{d}\ln\nu}{\mathrm{d}\ln M} = -\frac{1}{2}\frac{1}{\left(1 + \frac{M}{m}\right)} \tag{4.47}$$

which leads to

$$\frac{M}{V}\frac{\mathrm{d}V}{\mathrm{d}M} = -\frac{1}{20}\alpha T(\theta_D/T)^2\frac{1}{1+\frac{M}{m}}. \tag{4.48}$$

As pointed out by London, in order to obtain more accurate results one should have a detailed knowledge of the frequency spectrum since ν not depend on M in a simple fashion. The values predicted by London's analysis are in reasonable agreement with the experimental findings (for details see London [119]).

4.4.4.2 Lithium Hydride

Various investigators [81, 84, 92, 119] experimentally and theoretically examined the effect of isotope substitution on the lattice parameter of the LiH crystals (see also reviews by Shpil'rain et al. [123]; Berezin and Ibrahim [121]). These investigations demonstrate that the isotope effect on the lattice parameter and coefficient of thermal expansion shows a definite trend in which the lighter isotopes produce larger lattice parameters and smaller coefficients of thermal expansion than the heavier isotopes. The effects are more pronounced when a lighter element is substituted at low temperatures.

Closely related to the molar volume is the thermal expansion (see, e.g., Kogan [84]). Table 4.7 gives values of lattice constants and thermal expansion coefficients for isotopic LiH [71, 81]. The data indicate that the isotope effect, e.g., lighter isotopes having larger lattice constants, is reduced at higher temperatures. Heavier isotopes have larger thermal expansion coefficients. Similar findings were reported also by other workers (see, e.g., [96, 123]). These findings are expected since Debye theory predicts a larger heat capacity (see also above) for heavier isotopes, and then from the Grüneisen relation,

$$\alpha = \gamma C_v/3\beta V, \tag{4.49}$$

one can obtain $\alpha_{\text{heavy}} > \alpha_{\text{light}}$.

After classical London's paper [119], later in Anderson et al. [81], a simple empirical expression that related changes in the reduced mass μ of the unit cell and in the lattice constant upon isotopic substitution was suggested:

$$a = A\mu + B, \tag{4.50}$$

where A and B are constants, which are, however, dependent on temperature. This relation can be readily obtained taking into account a linear temperature dependence of the lattice constant, which is typical for high temperatures. The nonlinear temperature dependence of the lattice constant of LiH and LiD crystals [71, 82] observed in experiments (Fig. 4.22) can be described by the second-degree polynomial

$$\frac{\Delta a}{a} = \frac{\sqrt{\mu_{\text{LiD}}} - \sqrt{\mu_{\text{LiH}}}}{\sqrt{\mu_{\text{LiH}}\mu_{\text{LiD}}}}\left[A + B(T-T_0) + C(T-T_0)^2\right], \tag{4.51}$$

Table 4.7 Lattice constants and thermal coefficients for isotopic LiH (after Anderson et al. [81])

	−190 °C	25 °C	140 °C	240 °C
^{6}LiH	4.066	4.0851	4.1013	4.1218
^{7}LiH	4.0657	4.0829	4.1005	4.1224
^{6}LiD	4.0499	4.0708	4.0888	4.1110
^{7}LiD	4.0477	4.0693	4.0893	4.1119
^{7}LiT	4.0403	4.0633	–	–
Material thermal expansion coefficient $\alpha \cdot 10^6$				
	−190–25 °C		25–140 °C	140–240 °C
^{6}LiH	21 ± 0.3		34.3 ± 0.8	50 ± 1.0
^{7}LiH	19.8 ± 0.4		37.4 ± 0.4	53.3 ± 0.6
^{6}LiD	24.0 ± 1.0		38.4 ± 1.8	54.3 ± 1.0
^{7}LiD	24.8 ± 0.4		42.9 ± 1.0	55.0 ± 1.4
^{7}LiT	26.4 ± 0.5		–	–

where $\Delta a = a_{\mathrm{LiH}} - a_{\mathrm{LiD}}$, $I/\mu_{\mathrm{LiH}} = 1/M_{\mathrm{H}} + 1/M_{\mathrm{Li}}$, $T = 25\,°\mathrm{C}$, and $\theta = 1080\,\mathrm{K}$ is the Debye temperature of a LiH crystal. The values of constants A, B, and C, determined by the method of least squares, are presented in Table 4.8. For comparison, the values of these constants, calculated in a similar way for diamond, silicon, and germanium [124], are also given. The value of temperature $T = 810\,\mathrm{K}$, at which the lattice constant is the same for LiH and LiD crystals, was found from theoretical calculations. The lattice constant is equal to 4.165 Å. This means that the temperature dependence $a(T)$ in LiD crystals (a heavy isotope), which have a smaller Debye temperature, is stronger than in LiH crystals. This general conclusion is valid for a broad class of compounds, from an ionic LiH crystal to a covalent germanium crystal. It follows from theoretical calculations (Fig. 4.22) that for $T > 810$, the lattice constant of LiD crystals is larger than that of LiH crystals. This agrees qualitatively with the results of microscopic calculations of the temperature dependence of a change in the unit cell upon isotopic substitution, according to which $\mathrm{a}_{\mathrm{LiH}} = a_{\mathrm{LiD}}$ at 900–950 K [30]. The change in the lattice constant upon isotopic substitution is mainly determined by the anharmonicity of vibrations, which results in the dependence of the distance between atoms on the vibration amplitude, i.e., on the mean vibrational energy. It is well known that the vibrational energy depends not only on temperature but also on the isotopic composition as well. Therefore, to take into account the thermal expansion of a crystal lattice, one should consider the effect of anharmonic terms in the expression for potential energy of pair interaction between atoms at temperature T.

4.4.4.3 Germanium and Silicon

Among semiconducting crystals, the Ge crystal was the first for which the dependence of the lattice constant on an isotope effect was investigated both theoretically

Table 4.8 Values of coefficients of polynomial (4.62) describing the temperature dependence of the lattice constant upon isotopic substitution of a mass (after Plekhanov [93])

Substance	A $\cdot 10^3$	B $\cdot 10^6$	C $\cdot 10^9$
LiH	55.4	–55.54	–102.8
C	–5.48	3.55	8.21
Si	–1.60	3.94	–6.90
Ge	–0.72	2.27	–6.40

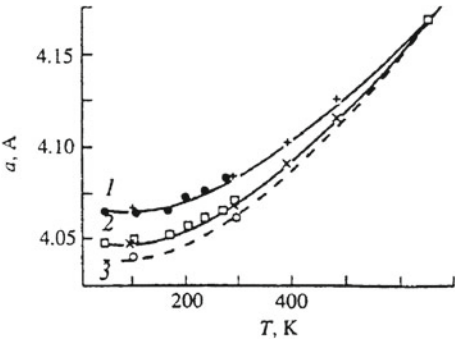

Fig. 4.22 Temperature dependence of the lattice constant of 1—LIH, 2—LiD, and 3—LiT crystals. Experimental data are taken from Smith and Leider [71] and Anderson and co-workers [81]. The solid line is theoretically calculated (after [96])

and experimentally [124, 125]. In the very first paper [122], this dependence was experimentally studied a highly perfect crystal of natural isotopic composition (average $M = 72.59$) and the second crystal was isotopically enriched, containing 95.8% of ^{74}Ge (average $M = 73.93$). Using the following equation, analogous (4.62), for the relative changes in the lattice constant a with isotopic mass at low temperature ($e^{-\frac{\hbar\omega}{k_B T}} \ll 1$):

$$\frac{\Delta a}{a} = -\frac{C}{a^3}\frac{\Delta M}{M}\left(\gamma_0 \hbar\omega_0 + \frac{3}{4}\gamma_a k_B \theta_D\right), \tag{4.52}$$

where $\gamma_0 = 1.12$ and $\gamma_a = 0.40$ are the Grüneisen parameters for optical and acoustical phonon modes in Ge, $\theta_D = 374$ K is the Debye temperature and $\hbar\omega_0 = 37.3$ meV. Buschert et al. evaluated the equation (4.63) for a 95.8% enriched ^{74}Ge crystal in comparison with a natural crystal. Equation (4.52) predicts $12 \cdot 10^{-6}$ and $6 \cdot 10^{-6}$ reduction in a for $T = 0$ and $T = 300$ K, respectively. Buschert et al. [122] experimentally found reductions of 14.9 and 6.3 ppm at 77 K and $T = 300$ K, respectively. The agreement between calculated and measured values is very good considering the uncertainties of the Grüneisen parameter values used in the theory. After this paper [125], they published two theoretical papers [124, 126] in which the isotope effect and its temperature dependence were studied. In the paper of Pavone and Baroni [129], the dependence of the lattice constant of C, Si, and Ge upon their isotopic

purity using the first-principles calculations, performed by treating nuclear vibrations by density-functional perturbation theory. The main results of this paper were depicted in Fig. 4.23. The values of the constant A, B, and C, see (4.51) as fitted to theoretical data for the three materials studied in the paper of Pavone and Baroni [129] as well as for LiH [92], are reported in Table 4.8. Noya et al. [124] studied the dependence of the lattice parameter upon the isotope mass for five isotopically pure Ge crystals by quantum path-integral Monte Carlo simulations. The interatomic interactions in the solid were described by an empirical of the Stillinger–Weber type. At 50 K, the isotopic effect leads to an increase of $2.3 \cdot 10^{-4}$ Å in the lattice parameter of ^{70}Ge with respect ^{76}Ge. Comparison of the simulation results with available experimental data for ^{74}Ge (see also Buschert et al. [122]) shows that the employed model provides a realistic description of this anharmonic effect. It was shown by Noya et al. that the calculated fractional change of the lattice parameter of ^{74}Ge with respect to a crystal whose atoms have the average mass of natural Ge amounts to $\frac{\Delta a}{a} = -9.2 \cdot 10^{-6}$ at $T = 0$ K is in agreement with the results of Buschert et al. (see also [122]). More detailed investigations of the crystal lattice constant of Ge were performed by Ma and Tse [126]. The temperature dependence of the equilibrium lattice constants for five isotopically pure Ge crystals and naturally occurring Ge were calculated from ab initio electronic theory within quasi-harmonic approximation (Figs. 4.24 and 4.25). At very low temperature (close to 0 K), the inclusion of zero-point motion is shown to account quantitatively for observed differences in the lattice constants between the isotopes (see Fig. 4.25). The discrepancy between the theoretical and experimental thermal expansion on ^{73}Ge isotope alone is unlikely to provide a satisfactory explanation of this discrepancy. The cited authors thought that perhaps the nuclear spin (for $^{73}\mathrm{Ge} - I = 9/2$) may have a subtle effect on the phonon property of this crystal affecting the thermal expansion [126]. In conclusion of this part, we should mention the paper by Herrero [128] which studied the dependence of the silicon lattice constant on isotopic mass.

4.4.4.4 Diamond

The isotopic dependence of the lattice constant of diamond has also attracted interest in connection with the above thermal properties (see above part of thermal conductivity). Banholzer et al. [127] reported the lattice constant of natural and ^{13}C diamond by X-ray diffraction using the powder samples and single crystals. Holloway and coworkers [130, 132] examined the influence of the isotope ratio on the lattice constant of mixed crystals of $^{13}\mathrm{C}_x^{12}\mathrm{C}_{1-x}$ by single-crystal X-ray diffractometry. According their results, the lattice constant, as in case of LiH [131], decreased linearly with ^{13}C content according to the expression

$$a(x) = 3.56714 - 5.4 \cdot 10^{-4} x. \tag{4.53}$$

The fractional difference $\Delta a/a$ between both end compositions is $1.5 \cdot 10^{-4}$. The lattice constants of the five samples of the mixed-diamond with different isotopic

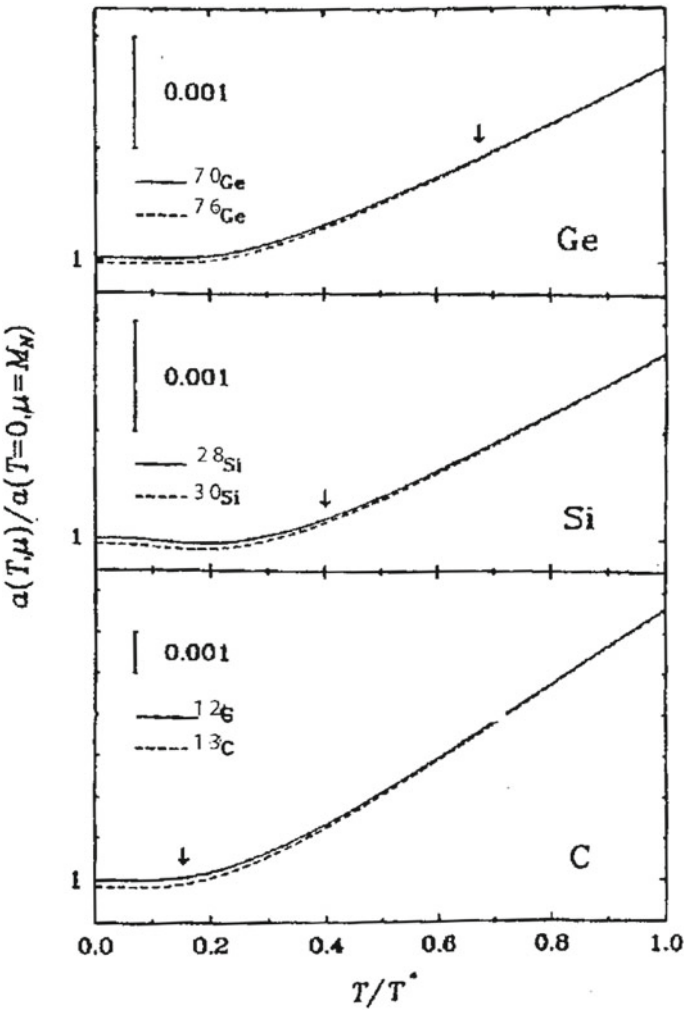

Fig. 4.23 Dependence of the equilibrium lattice constant of C, Si, and Ge upon temperature for different isotopic masses. The temperature is given in units of T* [T*(C) = 1941 K, T*(Si) = 744 K, T*(Ge) = 440]. The arrows indicate the room temperature (25 °C). The lattice constants are in units of the zero-temperature lattice constants at the natural isotopic compositions ($a_C = 6.71$; $a_{Si} = 10.23$; and $a_{Ge} = 10.61$ a.u.). Note the different units in three panels, which are indicated by the vertical bars (after Pavone et al. [129])

compositions were studied in the paper of Yamanaka et al. [132]. In this paper, it was shown that the standard deviations of the lattice constant were in the range of $5 \div 9 \cdot 10^{-5}$ Å. The lattice constant is varied (see also Fig. 4.26) with the isotope ratio and it can be expressed in quadratic form as

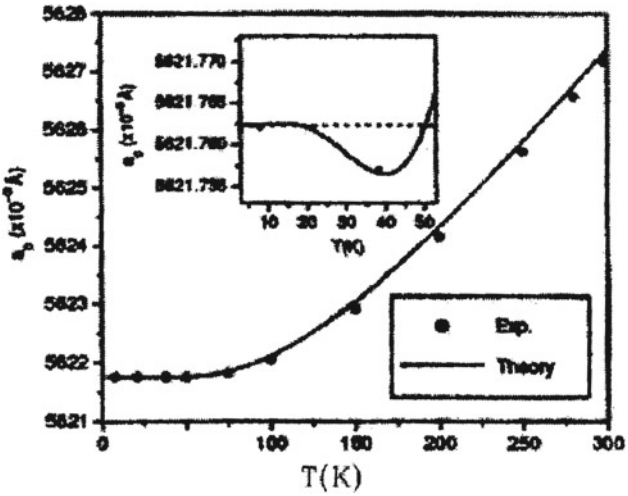

Fig. 4.24 Temperature dependence of the calculated lattice parameter for ^{70}Ge. The inset shows the details at low temperature below 53 K. The solid line is the calculated (after [126])

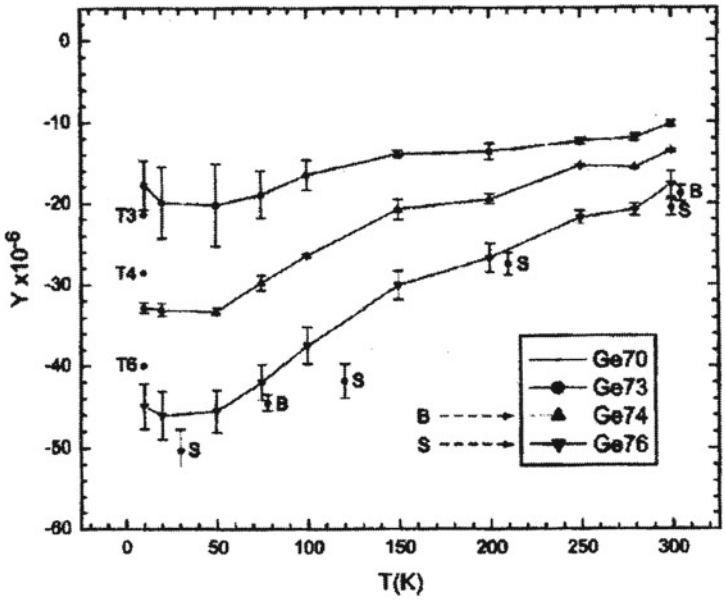

Fig. 4.25 Plots of $Y = [a(M) - a(70)]/a(70)]$ with temperature (after [126])

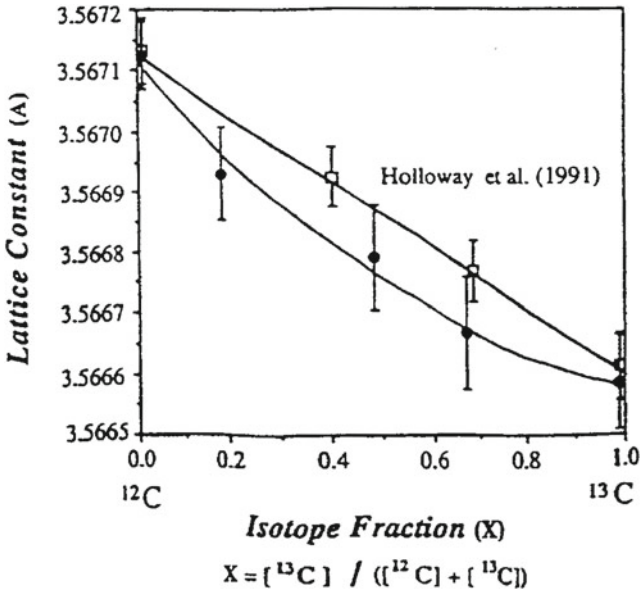

Fig. 4.26 Isotope dependence of the lattice constant of diamond. The curved line shows the quadratic (4.65), which fits the solid circles obtained by Yamanaka et al. The straight line fits to open squares those obtained by Holloway et al. [128, 130] (after Yamanaka et al. [132])

$$a(x) = 3.56712 - 9.0 \cdot 10^{-4}x + 3.7 \cdot 10^{-4}x^2, \tag{4.54}$$

where $x = [\frac{^{13}C}{^{12}C+^{13}C}]$. This expression is in contrast to linear relation reported by Holloway and coworkers [130]. A linear relation between the lattice constant and isotope ratio would be somewhat puzzling, because compressibility and Grüneisen parameter are not the same for different isotopes (see also [92]).

In conclusion of this section, we should stress the premier role of the anharmonic effect in the dependence of a on the isotopic effect. Really, as was pointed out by Vogelgesang and coworkers [133] the concentration-dependent lattice parameter incorporating zero-point motion in combination with anharmonicity, deduced in Chap. 2:

$$a(x) = a_{12} - \frac{\hbar g_1}{(6k_1^3 M_{12})^{\frac{1}{2}}}\left[1 - \left(\frac{M_{12}}{M_x}\right)^{1/2}\right] \tag{4.55}$$

with $M_x = (1-x)M_{12} + xM_{13}$. A comparison of (4.66) with the data of Holloway et al. for $a(x)$ and $k_1 = 3B_s a = 4.76 \cdot 10^5$dyn/cm for natural diamond yields $g_1 = (4.5 \pm 0.4) \cdot 10^{14}$erg/cm^3. The results of Yamanaka et al. are analyzed in the same manner, which yield $g_1 = (4.7 \pm 0.4) \cdot 10^{14}$erg/cm^3, i.e., very close to the Holloway's data.

4.4.4.5 Compound Semiconductors: GaAs and ZnSe

These compounds were studied in the papers of Garro et al. [134] and Debernardi and Cardona [135]. In binary semiconductors, the calculations of the dependence of volume (or lattice parameter) on isotopic masses are more complicated. It is not possible to write the relative variation of the crystal volume as a simple function of the relative variation of the mass. Phonon frequency depends differently on the two masses, and this dependence has to be known, together with the corresponding Grüneisen parameter for all phonon modes, in order to calculate the dependence of the lattice constant on the isotopic masses. For ZnSe Garro et al. have employed an 11-parameter rigid-ion model (RIM, [97, 136]) at two different unit cell volumes to obtain the Grüneisen parameters. Due to the absence of a similar dynamic model for GaAs (note that the only stable As isotope is ^{75}As), an estimation of the variation of its lattice parameter with Ga and As masses has been performed by interpolating of ZnSe and Ge results.

In order to connect the change in volume with phonon parameters Garro and coworkers used the Helmholtz free energy F, which is related for a system of independent oscillators (phonons) through a partition function [124]. In terms of the energy of individual oscillators, F can be written as

$$F = \sum_{\nu,\boldsymbol{q}} \left\{ \frac{1}{2}\hbar\omega_\nu(\boldsymbol{q}) + kTln\left[1 - \exp(-\hbar\omega_\nu(\boldsymbol{q})/kT)\right] \right\}. \tag{4.56}$$

The volume of a sample is related to the bulk modulus through $(\frac{\Delta V}{V})_{\mathrm{T}} = -\frac{\Delta p}{B_{\mathrm{s}}}$, while p can be written as $p = (\frac{\Delta F}{\Delta V})_{\mathrm{T}}$. Using these expressions, we can write

$$V = V_0 + \frac{1}{B_{\mathrm{s}}} \sum_{v,\boldsymbol{q}} \hbar\omega_\nu(\boldsymbol{q})\gamma_\nu(\boldsymbol{q}) \left[n_{\mathrm{B}}(\omega_\nu(\boldsymbol{q})) + \frac{1}{2} \right], \tag{4.57}$$

where it has introduced the mode Grüneisen parameters $\gamma_\nu(\boldsymbol{q})$ defined as $\gamma_\nu(\boldsymbol{q}) = -\frac{\partial \ln \omega_\nu}{\partial \ln V}$ and $n_{\mathrm{B}}(\omega_\nu(\boldsymbol{q}))$ is the Bose–Einstein factor. In the last equation, V_0 represents the crystal in the limit of infinitive masses. In terms of the lattice constant of the conventional unit cell (a_0 in the limit of infinitive masses) for zinc-blende-type materials last equation can be written as

$$\frac{a(M_1, M_2) - a_0}{a_0} = \frac{4\hbar}{3B_{\mathrm{s}}a_0^3} \sum_{v,\boldsymbol{q}} \left[\omega_\nu(\vec{\boldsymbol{q}})\gamma_\nu(\vec{\boldsymbol{q}}) \left[n_{\mathrm{B}}(\omega_\nu(\vec{\boldsymbol{q}})) + \frac{1}{2} \right] \right], \tag{4.58}$$

where $a(M_1, M_2)$ is the lattice constant for a finite mass of atoms 1 and 2 in the primitive cell at a given temperature. Here, we are interested in the change of the lattice parameter when one of the atomic masses changes $(\frac{\partial \ln a}{\partial M_k})$ and in the low-temperature limit in which $n_{\mathrm{B}} \approx 0$. If we change the mass of atom k ($k = 1; 2$) from M_k to $M_k + \Delta M_k$, the relative change in the lattice parameter is

$$\frac{a(M_k + \Delta M_k) - a(M_k)}{a(M_k)} \simeq \frac{[a(M_k + \Delta M_k) - a_0] - [a(M_k) - a_0]}{a_0}$$
$$\simeq \frac{2\hbar}{3B_s a_0^3} \sum_{v,\boldsymbol{q}} \Delta_{\mathrm{k}}[\omega_\nu(\boldsymbol{q})\gamma_\nu(\boldsymbol{q})]. \tag{4.59}$$

$\Delta_{\mathrm{k}}[\omega_\nu(\boldsymbol{q})\gamma_\nu(\boldsymbol{q})]$ is mean the difference of the quantity in brackets evaluated at two different isotopic masses. As was shown by Garro et al., this term is usually negative for an increase in either of the masses. Thus, it can be understood as an "isotopic contraction" of the lattice parameter.

The calculation of (4.59) requires an integration over the whole Brillouin zone. For this reason, it is convenient to define the "lattice spectral function".

$$\Phi(M_1, M_2; \Omega) = \frac{2\hbar}{3B_s a_0^3} \sum_{v,\boldsymbol{q}} \Omega\gamma_\nu(\boldsymbol{q})\delta[\Omega - \omega_\nu(\boldsymbol{q})], \tag{4.60}$$

which represents the spectral dependence of the changes in lattice parameter induced by a mass configuration M_1 and M_2. In terms (4.59), (4.60) becomes

$$\frac{\Delta_{\mathrm{k}} a}{a} = \int_0^{\Omega_{\max}} \mathrm{d}\Omega\, \Delta_{\mathrm{k}} \Phi(M_1, M_2; \Omega). \tag{4.61}$$

Garro et al. calculated the spectral functions to two different isotopic masses of Zn. These authors were compared the results for ZnSe with those for Ge obtained by Pavone and Baroni [129], it was note that the effect of changing both masses in the unit cell is nearly the same for both materials. However, whereas for Ge the two atoms contribute equally, and for ZnSe, the contributions of the anion and the cation are rather asymmetric. The dependence of the GaAs lattice parameter on the Ga and As masses has been obtained by linear interpolation the values found for Ge and ZnSe because of the less extensive knowledge of Grüneisen parameters for GaAs than for ZnSe. Debernardi and Cardona [135] have described an efficient way to compute the derivatives of the lattice constant with respect to the mass in polar semiconductors. It is necessary to point out at the absence of the isotopic effect for the lattice constant in KCN crystals [82, 96].

4.4.5 Isotopic Fiber Optics

The current rapid progress in the technology of high-density optical storage makes the mere announcing of any other thinkable alternatives a rather unthankful task. An obvious query "who needs it and what for?" has, nevertheless, served very little purpose in the past and should not be used to veto the discussion of nonorthodox technological possibilities. One such possibility, namely, the technology of isotopic information storage (IIS) is discussed in this paragraph. Isotopic information storage

may consist in assigning the information "zero" or "one" to monoisotopic microislands (or even to a single atom) within a bulk crystalline (or thin film) structure. This technique could lead to a very high density of ROM-type (read-only memory or permanent storage) information storage [23], probably up to 10^{18} bits per cm^3. The details are discussed by Berezin et al. [2, 6, 121] and Haller [3]: here it notes only that the use of tri-isotopic systems (e.g., ^{28}Si; ^{29}Si; ^{30}Si) rather than di-isotopic (e.g., ^{12}C; ^{13}C) could naturally lead to direct three-dimensional color imaging without the need for complicated redigitizing (it is known that any visible color can be simulated by a properly weighted combination of three prime colors, but not of two). Indeed, let us assume that the characteristic size of one information-bearing isotopic unit (several atoms) is 100 Å. Then, 1 cm^3 of crystalline structure, e.g., diamond, is able to store roughly $(10^8)^3/100 = 10^{18}$ bits of information [23]. This capacity greatly exceeds that need to store the information content of all literature ever published ($\cong 10^{17}$ bits), including all newspapers (see, e.g. [138]).

The main potential advantage of isotope-mixed crystals lies in the fact that the information is incorporated in the chemically homogeneous matrix. There are no chemically different impurities (like in optical storage with color centers) or grain boundaries between islands of different magnetization (like in common magnetic storage). The information in isotope-mixed crystals exists as a part of the regular crystals lattice. Therefore, the stored information in isotope-mixed crystals is protected by the rigidity of the crystal itself. There are no "weak points" in the structure (impurities, domain wells, lattice strain, etc.) which can lead to the information loss due to bond strains, enhanced diffusion, remagnetization, etc. Differences in the bond lengths between different isotopes (e.g., ^{28}Si–^{29}Si or ^{29}Si–^{30}Si, H–D, and so on) are due to the anharmonicity of zero-point vibrations (see, e.g., [7]). This is not enough for the development of any noticeable lattice strains although these differences are sufficiently large to be distinguishably detected in IIS reading).

Optical communication using fibers is a major new technology which will profoundly impact telephone systems, computer interconnections, and instrumentation (Internet). Fiber links provide several major advantages over conventional electronic communications systems. These include immunity to electromagnetic interference, thinner and lighter cables, lower transmission losses (especially for very data rates), and potential kilometer-long-link capabilities extending to the gigahertz region. An optical waveguide is a dielectric structure that transports energy at wavelengths in the infrared or visible ranges [139, 140] of the electromagnetic spectrum. In practice, waveguides used for optical communications are highly flexible fibers composed of nearly transparent dielectric materials. The cross section of these fibers is small comparable to the thickness of a human hair and generally is divisible into three layers as shown in Fig. 4.27. The central region is the core, which is surrounded by the cladding, which in turn is surrounded by a protective jacket. Within the core, the refractive-index profile n can be uniform or graded, while the cladding index is typically uniform [141, 142]. The two situations correspond to the step-index and graded-index profiles shown in the insets in Fig. 4.27. It is necessary that the core index be greater than the cladding index [143], at least in some region of the cross section, if guidance is to take place. For the majority of applications, most of the

light energy propagates in the core and only a small fraction travels in the cladding. The jacket is almost optically isolated from the core, so for this reason we usually ignore its effect and assume an unbounded cladding for simplicity in the analysis. As usual optical waveguides can be conveniently divided into two subclasses called multimode waveguides (with comparatively large cores) and single-mode waveguides (with comparatively small cores). The demarcation between the two is below. Multimode waveguides obey the condition (see, e.g., [144]) $(2\pi\rho/\lambda)(n_{\mathrm{co}}^2 - n_{\mathrm{cl}}^2)^{1/2} \gg 1$, where ρ is a linear dimension in the core, e.g., the radius of the fiber core, λ is the wavelength of light in free space, n_{co} is the maximum refractive index in the core and n_{cl} is the uniform refractive index in the cladding. As will be shown below, electromagnetic propagation along optical waveguides is described exactly by Maxwell's equations. However, it is well known that classical geometric optics provides an approximate description of light propagation in regions where the refractive index varies only slightly over a distance comparable to the wavelength of light. This is typical of multimode optical waveguides used for communication. Thus, the most direct and conceptually simple way to describe light propagation in multimode waveguides is by tracing rays along the core (see also [145], [146, 147]). By using classical geometric optics, we should ignore all wave effects. In multimode waveguides, wave effects are usually negligible [141], but there are exceptional situations when such effects accumulate exponentially with the distance light travels. Naturally in this case, wave effects must be retained, since they can have a significant influence on long waveguides. In each such situation, we modify the classical geometric optics description by taking into account the local plane wave number of light. The phenomenon of greatest practical interest in fibers used for long distance communications is the spread of pulses as they propagate along the fiber. For idealized multimode fibers, pulse spreading is easily described by classical geometric optics. But since propagation in multimode guides is so complex, simple models and physical understanding are generally of much greater assistance than a precise, exact analysis [148].

The reflection and transmission of a plane wave, or ray, which is incident on a planar interface between two semi-infinite, uniform media is determined by Snell's laws (see, e.g., [5, 143]). In Fig. 4.27, the refractive indices of the medium of incidence and the second medium are n_{co} (core) and n_{cl} (cladding) $< n_{\mathrm{co}}$, respectively, and the critical angle $\alpha_{\mathrm{c}} = \sin^{-1}(n_{\mathrm{cl}}/n_{\mathrm{co}})$. Further, we denote the angles of incidence, reflection, and transmission, or refraction, relative to the normal QN (see Fig. 4.28) by α_i, α_r, and α_t, respectively. The incident, reflection and transmitted, or refracted, rays and the normal QN are coplanar. If $\alpha_i > \alpha_c$, the incident ray in Fig. 4.28a undergoes total internal reflection and $\alpha_r = \alpha_i$, but if $\alpha_i < \alpha_c$ there is partial transmission, or refraction, as shown in Fig. 4.28b and the angles satisfy

$$\alpha_i = \alpha_r \tag{4.62}$$

$$\text{and} \quad n_{\mathrm{co}} \sin\alpha_i = n_{\mathrm{cl}} \sin\alpha_t. \tag{4.63}$$

Usually for the planar waveguides, it is convenient to express these laws in terms of the complementary angles of incidence, reflection, and transmission, i.e.,

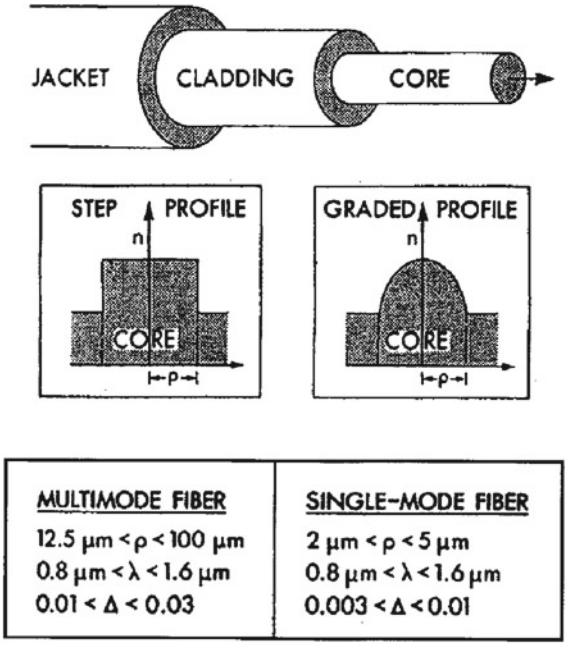

Fig. 4.27 Nomenclature, profiles band ranges of dimensions for typical optical fibers, where ρ is the core radius, λ is the free-space wavelength of light, and $\Delta = (1 - n_{\mathrm{cl}}^2/n_{\mathrm{co}}^2)/2$ (after [139])

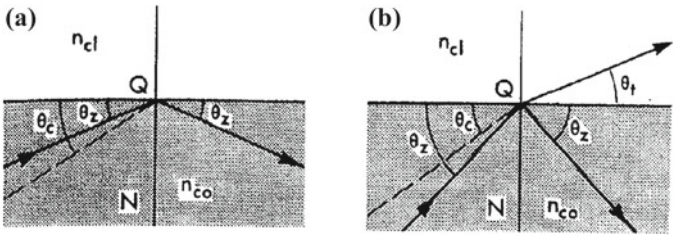

Fig. 4.28 Reflection at a planar interface between unbounded regions of refractive indices n_{co} and $n_{\mathrm{cl}} < n_{\mathrm{co}}$ showing **a** total internal reflection and **b** partial reflection and refraction (after [5])

$\theta z = \pi/2 - \alpha_i = \pi/2 - \alpha_r$ and $\theta_t = \pi/2 - \alpha_t$ and the complementary critical angle $\theta_c = \pi/2 - \alpha_c$.

One of the possible major applications of isotopic engineering are considered in isotopic fiber optics and isotopic optoelectronics at large (see also [146, 147]). It is known that for typical solids the lattice constant variations of isotopically different samples are usually within the limits

$$\Delta \mathrm{d}/\mathrm{d} \sim 10^{-3} - 10^{-4}. \tag{4.64}$$

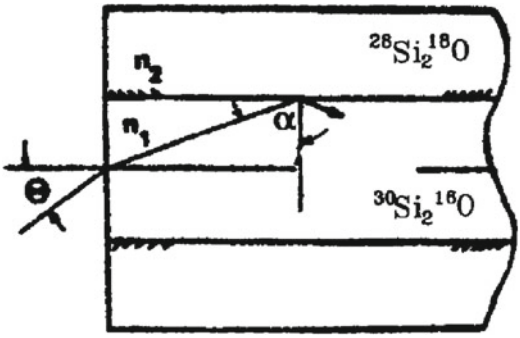

Fig. 4.29 Isotopic fiber in which the core and cladding are both pure SiO_2, but with a different isotopic composition (after [7])

Let us define an isotopic fiber as a structure in which core and cladding have the same chemical content but different isotopic compositions (see Fig. 4.29). The boundary between different isotopic regions forms an isotopic interface. The difference in the refractive index on both sides of the isotopic interface could lead to the possibility of total internal reflection of light and, consequently, could provide an alternative route to the confinement of light. For a quantitative estimate, let us consider a boundary between SiO_2 (the main component of silica) where body sides are identical chemically and structurally but have a different isotopic content, e.g., $^{28}Si^{16}O_2$ and $^{30}Si^{18}O_2$, respectively (Fig. 4.29). In the first approximation the refractive index n is proportional to the number of light scatterers in the unit volume. From the Clausius–Mossotti relation

$$\frac{\varepsilon - 1}{\varepsilon + 2} = \frac{N_A \rho \alpha}{3M}, \tag{4.65}$$

where ρ is the mass density, N_A is Avogadro's number, M is the molecular weight, and α is molecular polarizability (see, e.g., [146]); for the refractive index, one can deduce the following proportion (at $\Delta n \ll n$).

$$\Delta n/n \simeq 3c\Delta \mathrm{d}/\mathrm{d}, \tag{4.66}$$

where c is a dimensionless adjustment factor of the order of unity. Substituting (4.64) into (4.66), we can obtain

$$\Delta n/n \sim 3x10^{-3} - 10^{-4}. \tag{4.67}$$

Using the Snell law of light refraction, we obtain the following expression for the ray bending angle θ when light travels through the refractive boundary (see also Fig. 4.28):

$$\theta \simeq \alpha_0 - \arcsin[(n_1/n_2)\sin\alpha_0], \tag{4.68}$$

where α_0 is the angle between the falling ray and the direction normal to the interface. For a sliding ray ($\alpha_0 \simeq 90°$), which is the control case for light confinement in fibers, the combining of (4.67) and (4.68) leads to an estimate

$$\theta \sim 1.5\text{–}4.5^\circ. \tag{4.69}$$

Thus, the isotopic fibers in which core and cladding are made of different isotopes the half-angle of the acceptance-cone could be up to several degrees [147]. The resulting lattice mismatch and strains at the isotopic boundaries are correspondingly one part per few thousand [5] and, therefore, could be tolerated. Further advancement of this "isotopic option" could open the way for an essentially monolithic optical chip with built-in isotopic channels inside the fully integrated and chemically uniform structure. Besides that, we should pay attention to the fact that composition (different isotopes) fluctuation is subject to the restoring force of the total free energy of the glass system which will also seek to minimize itself. Using isotope pure materials for core and cladding, we should receive significant less Rayleigh scattering (for details see [5, 146]). This is the first application of isotope technology on the optical fiber. The modern point-to-point optical-fiber communication may have the electrical input signals which are converted to optical signals using an optical source (LED or laser—see below). The optical signals are coupled into the fiber and transmitted to the photodetector, where they are converted back to electrical signals.

4.5 Isotope-Mixed Graphene and Its Application

The richness of optical and electronic properties of graphene attracts enormous interest [149]. Carbon atom is built from six protons, A neutrons, and six electrons, where $A = 6$ or 7 yields the stable isotopes ^{12}C and ^{13}C, respectively, and $A = 8$ characterizes the radioactive isotope ^{14}C. The isotope ^{12}C, with nuclear spin $I = 0$, is the most common one in nature with 99% of all carbon atoms, whereas only ~1% are ^{13}C with nuclear spin $I = 1/2$. There are only traces of ^{14}C (10^{-12} of all carbon atoms) which transforms into nitrogen ^{14}N by β-decays. Although ^{14}C only occurs rarely, it is important isotope used for historical dating (see, e.g., [7]).

Carbon, which is one of the most basic elements in nature, still gives a lot of surprises. It is found in many different forms—allotropes—from zero-dimensional fullerene, one-dimensional carbon nanotubes, two-dimensional graphene and graphite, to three-dimensional diamond (Fig. 4.30), and the properties of the various carbon allotropes can vary widely [149, 150]. For instance, diamond is the hardest material, while graphite is one of the softest: diamond is transparent to the visible part of spectrum, while graphite is opaque; diamond is an electrical insulator, while graphite is a conductor. Very important is that all these different properties originate from the same carbon atoms, simply with different arrangements of the atomic structure.

In two-dimensional graphene, carbon atoms are periodically arranged in an infinite honeycomb lattice (Fig. 1a in [151]). Such an atomic structure is defined by two types of bonds within the sp^2 hybridization. From the four valence orbitals of the carbon atom (the 2s, 2p$_x$, 2p$_y$, and 2p$_z$ orbitals, where z is the direction perpendicular to the sheet), the (s, p$_x$, p$_y$) orbitals combine to form the in-plane σ (bonding or occupied)

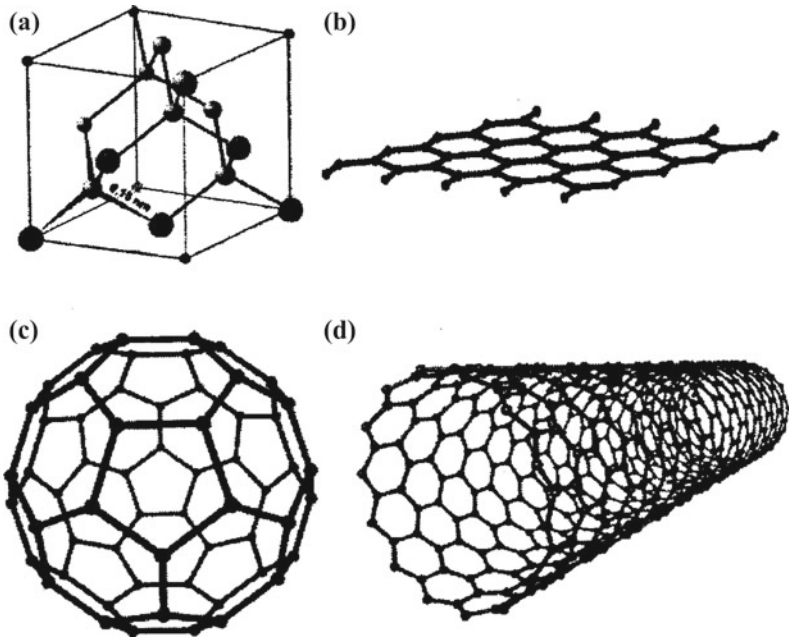

Fig. 4.30 Structure of some representative carbon allotropes: **a** diamond, **b** graphene, **c** fullerene, **d** SWCNT

and σ^* (antibonding or unoccupied) orbitals. Three σ-bonds join a C atom to its three neighbors. They are quite strong, leading to optical-phonon frequencies much higher than observed in diamond (see below). Such orbitals are even with respect to the planar symmetry. The σ bonds are strongly covalent bonds determining the energetic stability and the elastic properties of graphene. The remaining p_z orbital, pointing out of the graphene sheet is odd with respect to the planar symmetry and decoupled from the σ states. From the lateral interaction with neighboring p_z orbitals (called the $pp\pi$ interaction), localized π (bonding) and π^* (antibonding) orbitals are formed [150]. Graphite consists of a stack of many graphene layers. The unit cell in graphite can be primarily defined using two graphene layers translated from each other by a C–C distance ($a_{c-c} = 1.42$ Å). The three-dimensional structure of graphite is maintained by the weak interlayer van der Waals interaction between π bonds of adjacent layers, which generate a weak but finite out-of-plane delocalization [147]. The bonding and antibonding σ bands are actually strongly separated in energy >12 eV at, and therefore, their contribution to electronic properties is commonly disregarded, while the bonding and antibonding π states lie in the vicinity of the Fermi level (Fig. 4.31). The two remaining π bands completely describe the low-energy electronic excitations in both graphene and graphite (see [157] and references therein). The bonding π and antibonding π^* orbitals produce valence and conduction bands (Fig. 4.31) which cross at the charge neutrality point (Fermi level of undoped

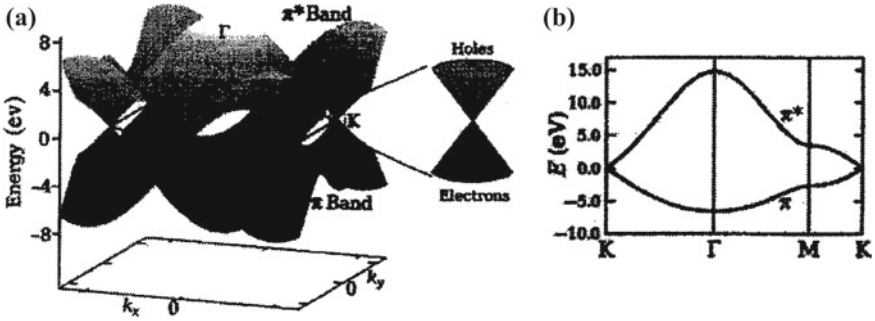

Fig. 4.31 Energy dispersion of graphene obtained within the tight-binding approximation. **a** Energy dispersion relation for graphene, drawn in the entire region of the Brillouin zone. Since in this approximation to ignore the coupling between the graphene sheets, the bands depend only on k_x and k_y. The π band is completely filled and meets the totally empty π^* band at the K points. Near these points both bands linear dispersion as described in the literature. **b** The dispersion along the high symmetry points ΓMK

graphene) at vertices of the hexagonal Brillouin zone. Carbon atoms in a graphene plane are located at the vertices of a hexagonal lattice.

This graphene network can be regarded as a triangular Braves lattice with two atoms per unit cell (A and B). Each A- or B-type atom is surrounded by three atoms of the opposite type. In a simple neighbor model, graphene is a semimetal with zero overlap between valence and conduction bands. The energy dispersion of π electrons in graphene was first derived in 1947 by Wallace [162] within the tight-binding approximation. In this case, the wavefunction of graphene is a linear combination of Bloch function for sublattice A

$$\Phi_{\mathrm{A}} = \frac{1}{\sqrt{N}} \sum_{\boldsymbol{R}_{\mathrm{A}}} e^{\mathrm{i}\boldsymbol{k}\boldsymbol{R}_{\mathrm{A}}} \varphi(\boldsymbol{r} - \boldsymbol{R}_{\mathrm{A}}), \tag{4.70}$$

and equilibrium function Φ_{B} for the B sublattice. Here, N is the number of unit cells, $\boldsymbol{R}_{\mathrm{A}}$ are the position of the atom A and $\varphi(\boldsymbol{r} - \boldsymbol{R}_{\mathrm{A}})$ is the $2p_{\mathrm{z}}$ orbital of the atom at $\boldsymbol{R}_{\mathrm{A}}$. The sum runs over all unit cells, i.e., all possible lattice vectors. in the nearest neighbor approximation (every A site has three nearest B sites, and vice versa), the energy eigenvalues can be obtained in a closed form [147, 151]

$$\varepsilon(k_x, k_y) = \pm\gamma_0 \left[1 + 4\cos\frac{\sqrt{3}k_x a}{2} \cos\frac{k_y a}{2} + 4\cos^2\frac{k_y a}{2} \right]^{1/2}, \tag{4.71}$$

where γ_0 is the transfer integral between the nearest neighbors. The energy dispersion of two-dimensional graphene according to this formula is plotted in Fig. 4.31a as a function of the wave vector $\boldsymbol{k}$. The upper half of the curves is called the π^* or the anti-bonding band while the lower one is π or the bonding band. The two bands degenerate

at the two K points given by the reciprocal space vectors $\boldsymbol{K} = (2\pi/a)(1/3, 1/\sqrt{3})$ and $\boldsymbol{K}' = (2\pi/a)(-1/3, 1/\sqrt{3})$ points where the dispersion vanishes (see above).

Basically, graphene has redefined the limits of what a material can do: it boasts record thermal conductivity and the highest current density at room temperature ever measured (a million times that of copper!); it is the strongest material known (a hundred times stronger than steel!) yet is highly mechanically flexible; it is the least permeable material known (not even helium atoms can pass through it!); the best transparent conductive film; the thinnest material known; and the list goes on ... [151]. In the vicinity of K-points (as it can be seen from Fig. 4.31), the low-energy electron/hole dispersion relation is proportional to momentum, rather than its square. This is analogous to the energy dispersion relation of massless relativistic electrons, so the electrons/holes of graphene are described as Dirac fermions having no mass. In a simple neighbor model graphene is a semimetal with zero overlap between valence and conduction bands. In order to make graphene a real technology, a special issue must be solved: creating an energy gap at K-points in the Brillouin zone. Different attempts have been made by researches, such as patterning graphene into nanoribbon [152], forming graphene quantum dots [153–157], making use of multilayer graphene sheets [158, 159] and applying an external electric field [160]. It was shown that the uniaxial strain can open a bandgap in a metallic carbon nanotubes as well as carbon nanoribbon [161]. Very shortly the isotopically bandgap opening in graphene was described in [162]. The present paragraph is a more systematic analysis than our previous publication [163].

Further, we will briefly discuss the dependence of the electronic gap (E_g) as well as phonon states of diamond with its isotopic composition. Figure 4.32 compares the edge luminescence for a natural diamond with that for a synthetic (^{13}C) diamond. The peaks are labeled A, B, and C due, respectively, to the recombination of a free exciton with emission of transverse-acoustic, transverse-optic, and longitudinal-optic phonons having wave vector $\pm k_{\min}$ [31, 164].

As it can be seen from Fig. 4.32, the bandgap of ^{13}C has increased by 13.6 meV. Numerous examples of bandgap increment at hard isotope substitution were collected in the papers [31, 164]. The effect of the isotopic ^{12}C to ^{13}C ratio on the first- and second-order Raman scattering of light in the diamond has been investigated in [164]. As the ^{13}C content is increased from the natural ratio ($^{12}C/^{13}C = (1-x)/x$, where $x = 0.011$), to the almost pure ^{13}C ($x = 0.987$), the whole spectrum has shifted toward longer wavelengths (see Fig. 4.33) in good agreement with the expected $\mathrm{M}^{-0.5}$ frequency dependence on the reduced mass M. For an approximately equal mix of the two isotopes, the authors reported that the features seen in the above two-phonon spectra were either broadened or unresolvable. We should stress that the main line in the first-order Raman scattering spectrum of light at $\omega = 1332\,\mathrm{cm}^{-1}$ also shifts to the long-wavelength side on the $52.3\,\mathrm{cm}^{-1}$ [163, 164].

Elastic and inelastic light scattering are powerful tools for investigating graphene [164–170]. Mandelstam–Landsberg–Raman spectroscopy allows monitoring of doping, defects, disorder, chemical and isotope [30, 163] modifications, as well as edges and uniaxial strain. All sp^2-bonded carbons show common features in their Raman spectra, the so-called G and D peaks (see, e.g., Fig. 8 in [149]), around 1580 and

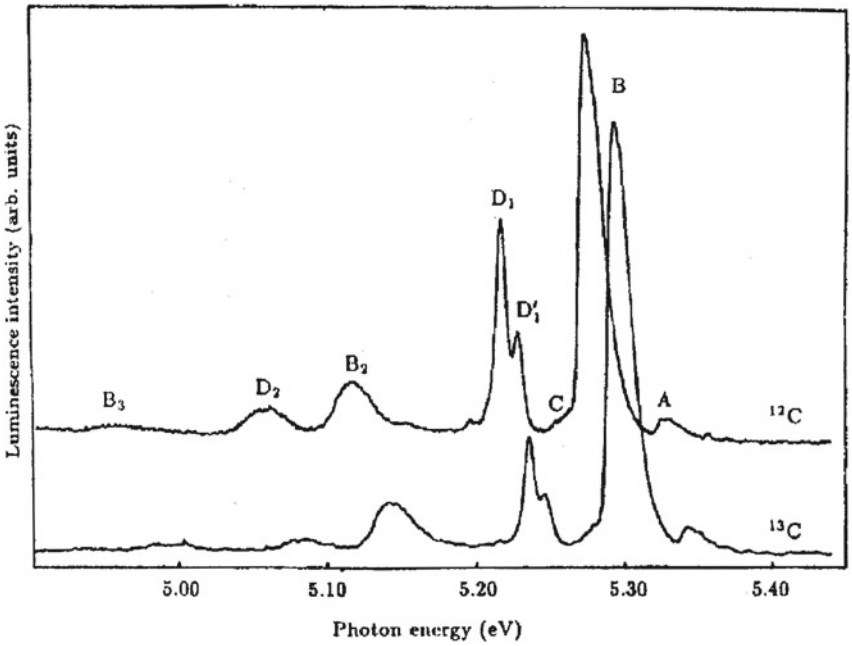

Fig. 4.32 Cathodoluminescence spectra of ^{12}C and ^{13}C at 77 K [163]

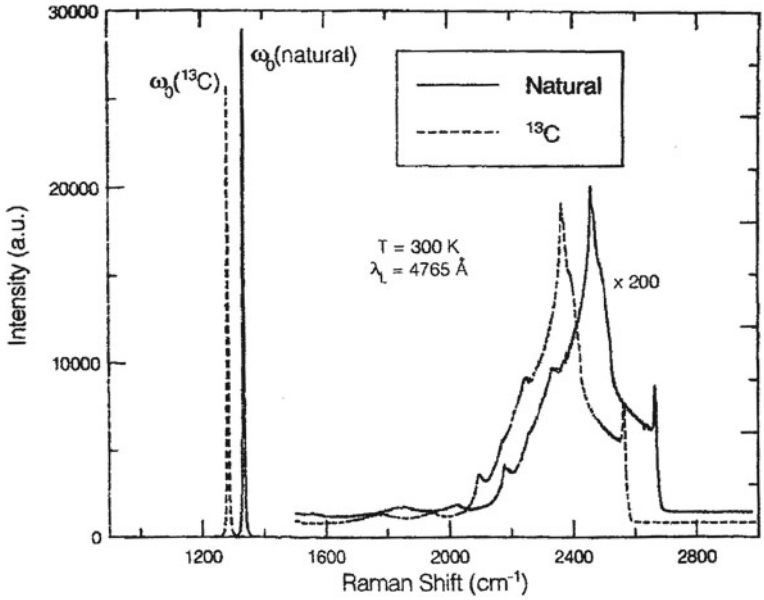

Fig. 4.33 The Raman spectrum of a natural and a ^{13}C diamond. The spectra show the dominant first-order, Raman-active F_{2g} line and the significantly weaker, quasi-continuous multi-phonon features [164]

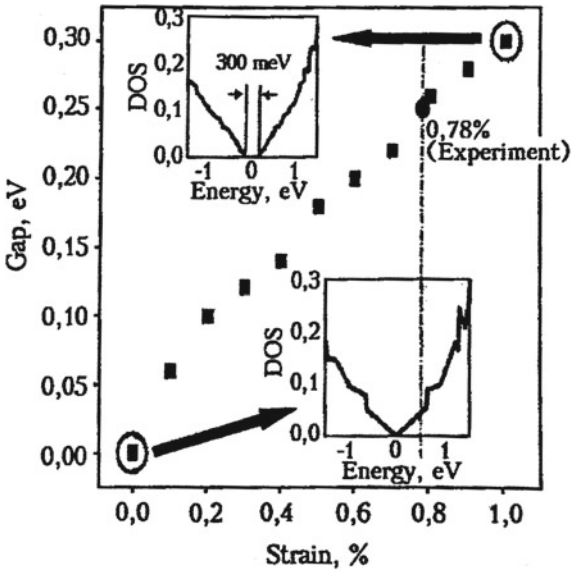

Fig. 4.34 The bandgap of strained graphene with the increase of uniaxial tensile strain on graphene. The magnitude of gap is determined by the gap opening of density of states. The insets show the calculated density of states of unstrained and 1% tensile strained graphene. The dashed line and solid dot indicate the calculated bandgap of graphene under the highest strain (0.78%) [161]

$1360\,\mathrm{cm}^{-1}$ (see, e.g., [166, 167]). The G peak (see also below Fig. 4.35) corresponds to the E_{2g} phonon at the Brillouin zone center (Γ-point). The D peak is due to the breathing modes of six-atom rings and requires a defect for its activation. It comes from TO phonons around the Brillouin zone K point, and it is activated by an intravalley scattering process [166]. The $2D$ peak is the second order of the D peak. This is a single peak in monolayer graphene, whereas it splits into four bands in bilayer graphene, reflecting the evolution of the band structure [151]. The Raman spectrum of graphene also shows significantly less intensive defect-activated peaks such as the D' peak, which lies at $\sim 1620\,\mathrm{cm}^{-1}$. This is activated by an intravalley process, i.e., connecting two points belonging to the same cone around K (see Fig. 4.31) [163]. The second order of the D' peak is called $2D'$ peak. Since $2D$ and $2D'$ peaks originate from a Raman scattering process where momentum conservation is obtained by the participation of two phonons with opposite wave vector ($\boldsymbol{q}$ and $-\boldsymbol{q}$), they do not require the presence of defects. Thus, they are always visible in the Raman spectrum (see cited papers [164, 165, 165–170] and references therein).

Graphene is a unique material which shows properties which are not found in other materials. One of these unique features of graphene is the influence of long-range strains on the electronic properties. The possibility of tuning the dynamics of carriers as well as phonons by appropriately designed strain patterns opens the way for novel applications of graphene, not possible with any other materials (see, e.g., [171] and references therein). At present time, we have several reports, which have examined graphene properties under uniaxial deformation [161, 170–172].

Strain can be very efficiently studied by Raman spectroscopy since this modifies the crystal phonon frequency, depending on the anharmonicity of the interatomic

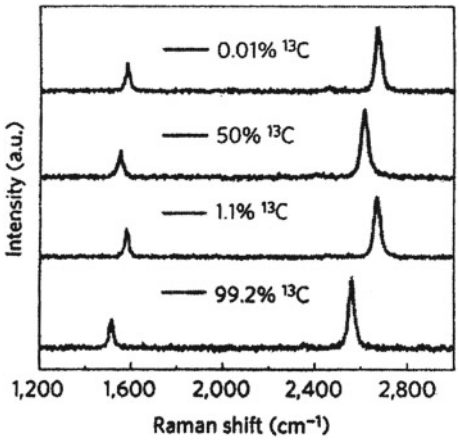

Fig. 4.35 Raman spectra of graphene with different isotope concentration at room temperature [168]

potentials of the atoms. Raman spectra of strained graphene show significant red-shifts of $2D$ and G band (see Table 4.9) because of the elongated of the carbon–carbon bonds. The authors of the paper [161] have proposed that by applying uniaxial strain on graphene, tunable bandgap at K-point can be realized. First-principle calculations predicted a bandgap opening of $\simeq$300 meV for graphene under 1% uniaxial tensile strain (Fig. 4.34). Thus, the strained graphene provides an alternative way to experimentally tune the bandgap of graphene, which would be more efficient and more controllable than other methods (see above) that are used to open bandgap in graphene.

The method of the isotope renormalization of the energy of elementary excitations in solid is often used in the last five decades and is well described in the scientific literature (see, for example, reviews [30, 31]). Nowadays, there is a large list of the paper devoted to the investigation of the isotope-mixed graphene [157, 162, 169, 173–177]. Chen and coworkers [168] have reported the first experimental study of the isotope effect on the thermal properties of graphene. The thermal conductivity K, of isotopically pure ^{12}C (0.01^{13}C) graphene determined was higher than 4000 W/mK (approximately two times more than it in diamond [160]) at the measured temperature $T_m \sim 320$ K, and more than a factor of two higher than the value of K in a graphene sheets composed of a 50–50% mixture of ^{12}C and ^{13}C. Raman spectroscopy transferred to the 285 nm SiO_2/Si wafer was performed under 532 nm laser excitation [168]. The G peak and $2D$ band positions in Raman spectra of graphene with 0.01, 1.1 , 50 and 99.2% ^{13}C-isotope are presented in Fig. 4.35. Isotope shift of the G and $2D$ bands in the Raman spectra is depicted in Fig. 4.36 [177].

As in the case of isotope-mixed diamond [30, 31] the Brillouin zone-center optical-phonon frequency ω varies with the atomic mass M as $\omega \sim M^{-1/2}$ making the Raman shift for ^{13}C approximately $(12/13)^{-1/2}$ times smaller than that for ^{12}C. The experimental difference between the lowest 99.2% ^{13}C and the highest 0.01% ^{13}C peak is $\sim$64 cm^{-1} which is according [168] in agreement with the theory, and attests for the high quality of isotopically modified graphene. By the way, we

Table 4.9 Red shift of the G and $2D$ bands in the Raman spectra in graphene monolayers under uniaxial tensile stress

Ref.	Shift of G (G^+ and G^-) band $cm^{-1}/\%$	Shift of $2D$ band $cm^{-1}/\%$	E_g,meV
15	14.2	27.8	300
25	5.6; 12.5	21	
27	10.8; 31.7	64	
26			
Theory			$\simeq$500

should indicate that in the Raman spectra in diamond (with sp^3-bond) analogous shift of first-order line in Raman spectrum is equal to 52.3 cm^{-1} [178], which is consistent with the isotope mass ratio. Substituting a light isotope (^{12}C, H) with a heavy one increases the interband transition energy in the case $^{12}C_x^{13}C_{1-x}$ on 14.7 meV and LiH_xD_{1-x} on 103 meV [163]. Taking into account a more soft bond (sp^2-bond instead sp^3-bond in diamond) isotope-induced bandgap opening in graphene of some hundreds meV (up to E_g of Si) was predicted in paper [152]. Such estimation of the value of isotopic bandgap opening in graphene agrees with not only the results of paper [178] but with very small value $C_{44} = 0.5 \cdot 10^{10}$dyn/cm^2. Such small value indicates the strong electron–phonon interaction—which is the main reason for renormalization of electron excitation energy (for the details, see, e.g., [179]). Very close to isotopically renormalization of electronic excitation energy is the hydrogenation of graphene [152, 154]. In the last mechanism, there is observable bandgap opening in graphene. We should add that use deuterium instead of hydrogen we may increase the value of E_g [163]. Thus, isotope substitution will be a very useful method for renormalization of the bandgap in graphene—future semiconducting material. Moreover, this method not only allows to control the strong nuclear interaction (quantum chromodynamics) but also takes into account the renormalization of the electromagnetic interaction (quantum electrodynamics) [163]. Adding ^{13}C makes magnetic materials isotope out of graphene. Thus, the use of the method of isotope effect in graphene may throw light on the renormalization of the mass of massless fermion in graphene.

Graphene and its derivatives are being studied in nearly every field of science and engineering. Recent progress has shown that the graphene-based materials can have a profound impact on electronic (see below) and optoelectronic devices: chemical sensors, photodetectors, touch screens, light-emitting devices, photovoltaics, transparent conductors, terahertz devices, and optical limiters. Many reports [159, 180, 181] confirmed that single-layer graphene absorbs 2.3% of incident light over a broad wavelength range in spite of being just monolayer (see Fig. 4.37). Graphene transmittance can be well described in terms of fine structure constants [181, 182]. The adsorption of light was found to be increasing with the addition of a number of layers linearly, each layer absorption $A = 1 - T = \pi\alpha 2.3\ \%$, where $\alpha \simeq 1/137$ is the fine structure constant. The graphene can be imaged by optical contrast on Si/SiO_2 substrate due to interference, and the contrast increases with the number of

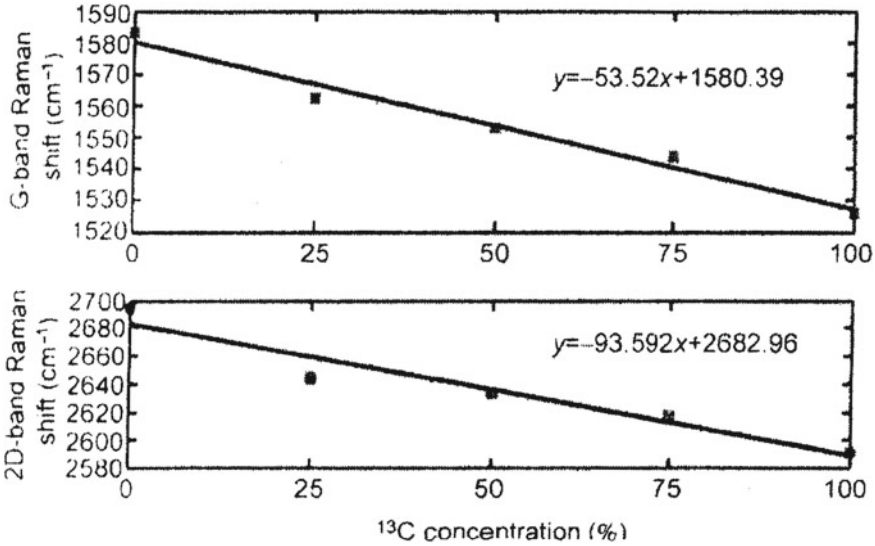

Fig. 4.36 Peak position of G and $2D$ bands in Raman spectra as a function of the concentration of ^{13}C [177]

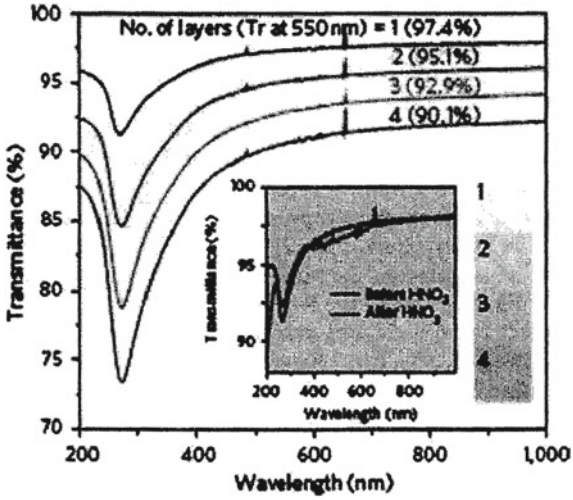

Fig. 4.37 Representative of transmittance of different graphene layers. UV-visible spectra roll-to-roll layer by layer transferred graphene films on quartz substrates. The inset shows the UV spectra of graphene films with and without HNO_3 doping. The right inset shows optical images for the corresponding number of transferred layers ($1 \times 1\,cm^2$) (after [180])

layers. The absorption for monolayer graphene is flat from 300 to 2500 nm, the peak at ~250 nm (4.6 eV) in UV region is attributed to the interband electronic transition from unoccupied π^* states [181, 182].

It was demonstrated that thin film (⟨30 nm) is semitransparent to visible and near IR region while thick films are opaque. The transmittance and conductivity of the graphene oxide/ reduced graphene oxide (RGO) film can be tuned by tuning the

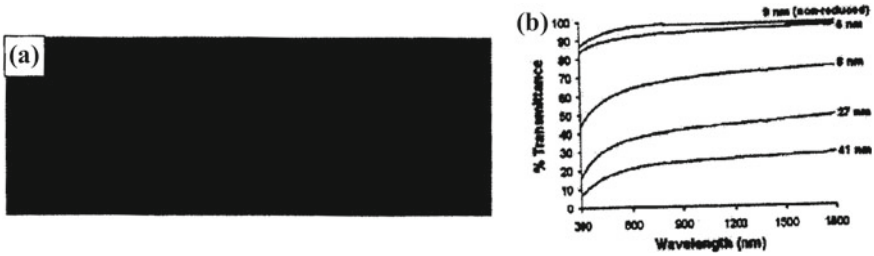

Fig. 4.38 Optical and electrical characterization of spin coated graphene oxide films on quartz. **a** photograph of an unreduced (leftmost) and series of high-temperature reduced graphene oxide films of increasing thickness. Black scale bar is 1 cm. **b** optical transmittance spectra of the films in **a** with the film thickness indicated (after [183])

thickness of the film and the degree of reduction [183]. Figure 4.38 shows how the transparency of RGO varies with film thickness. The leftmost film is 9 nm thick graphene oxide while the rest of the films are RGO (annealed in 1100 °C for 3 h) with thickness 6, 8, 27, and 41 nm (from left to right). As it can be seen that, as the film gets thicker, the transmittance gets reduced, while the conductivity of the RGO thin film increases with the degree of reduction and transmittance decrease. Therefore, the optimization of film thickness and reduction parameters is the key for achieving high-performance transparency and conducting RGO thin film.

Due to their transparency, conducting, and flexible nature, RGO thin film is considered to be a promising electrode material for organic electronic and optoelectronic applications Presently, indium-doped tin oxide (ITO) is widely used as transparent and conducting electrodes in optoelectronic applications. However, the ITO-based materials are expensive [184] and their limitation of mechanical flexibility [185] makes them unattractive for flexible display and solar cell applications. In this respect, RGO electrodes provide several advantages:

1. possibilities on one phase reaction without additional surfactant due to water-soluble properties,
2. the homogeneity and composition of the films are simply determined by the composition of the parent suspension and surface modification of the substrate,
3. relatively inexpensive starting materials, and
4. low-temperature and high-throughput processing.

In addition, the work function of RGO (4.2–4.6 eV) matches with HOMO level of most of the organic materials, and π–π interaction exists between RGO and organic material (see, e.g., [186, 187]). Wang et al. reported that RGO films can be employed for fabrication of dye-sensitized solar cells [188].

As indicated above, RGO transparent electrodes can be used for solar cell electrodes. Several studies suggest that graphene oxide/RGO can also be used as hole transport layer as well as a part of active material. The polymeric donor and acceptor materials often result in recombination of carriers and current leakage. Figure 4.39 shows a schematic diagram of a solar cell using RGO as an active material.

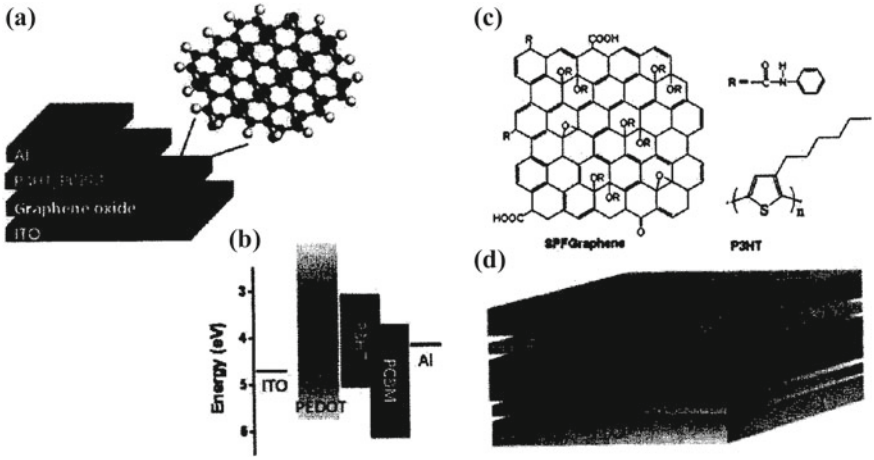

Fig. 4.39 **a** Schematic of the photovoltaic device consisting of the following: ITO/graphene oxide/P3HT:PCBM/Al. **b** Energy-level diagrams of the bottom electrode ITO, interlayer materials IPEDOT:PSS, graphene oxide), P3HT (donor), and PCBM (acceptor), and the top electrode Al. **c** The schematic chemical structure of SPF graphene and P3HT. **d** Schematic structure of the devices with the P3HT/SPF graphene thin film as the active layer; ITO ($\sim 17\Omega q^{-1}$)/PEDOT:PSS (40 nm)/P3HT:SPF graphene (100 nm)/LIF (1 nm)/Al (70 nm) (after [192])

RGO is highly promising for electrochemical and biological sensors due to their different functionalists on the edge [189–191], which are very sensitive to change in chemical and biological environment. The responses have been analyzed by changes in conductivities, capacitances, and doping effects field-effect transistors made with RGO. By the way, graphene-based composite materials have been studied for gas sensor (see also [189–191] and references therein).

Increasing energy demands have motivated researches to look for the alternative energy resources. Among various alternatives, a considerable attention has been given to the lithium-ion batteries due to its rechargeable characteristics, higher specific energy and longer cycle life. The unique properties of graphene including superior electrical conductivity, high surface to volume ratio, ultrathin flexible nature, and chemical stability make it ideal candidate to build the composites with metal and metal oxide nanoparticle for energy storage applications. In such composites, graphene provides support for nanoparticles and prevent the volume expansion–contraction of nanoparticles during charge and discharge process. Currently used graphitize carbon anode material shows low capacity (372 mAh/g) because of limited Li-ion storage sites within sp^2 carbon hexahedrons. One possibility to increase the Li intercalation in the charge/discharge process is using the layered structure of graphene sheets. Yoo et al. [194] reported the enhanced specific capacity of these carbon-based electrodes through the interaction of graphene nanosheets with C60 and CNT, which facilitates the nanospace size for lithium-ion ($r \sim 0.06$ nm) intercalation. Higher reversible capacity (794–1054 mAh/g) and cyclic stability were also

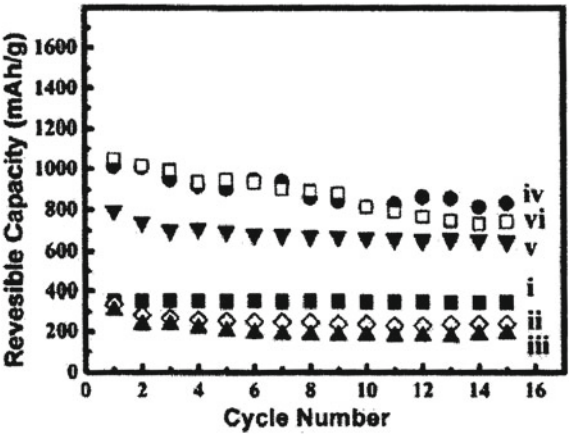

Fig. 4.40 Reversible (charge) capacity verse cycle numbers at a current density of 0.05 A/g, for natural graphite (i), pristine graphene oxide (ii), hydrazine reduced graphene oxide (iii), 300 °C pyrolytic graphene oxide (iv), 600 °C pyrolytic graphene oxide (v), and electron-beam reduced graphene oxide (vi) (after [193])

demonstrated in disordered graphene nanosheets, as the presence of edge and vacancies defects in graphene sheets provides [193, 195] additional reversible storage sites for Li-ions (see Fig. 4.40).

4.6 Chemical Mechanisms Bandgap Engineering in Graphene

Advances in synthesizing graphene offer opportunities for making novel materials for nonelectronics and many other applications. The first challenge for nanoelectronics (optoelectronics) graphene devices is the absence of a bandgap in this material. Such an insulating energy region allows us to control current flow by gating, which is at heart of every digital transistor, and predominantly used to electrostatically define tunable quantum dots (see next paragraph) in semiconductor nanostructures. Several mechanisms to open a bandgap in graphene have been suggested (see also above). As is well known, in typical semiconductor, electrons and holes occupy the conduction and valence energy bands, respectively. A finite energy called the energy gap must be added to a particle to move it from the valence band to the conduction band. Electrons and holes move like regular particles (see, e.g., [89]). They have a mass, their speed increases from zero as they are accelerated, and their kinetic energy is proportional to the square of their speed. In graphene [196], the behavior of electrons and holes, as we can see above, is very different. The particles move with a constant speed v_F that does not depend on their kinetic energy E. This is similar to the behavior of photons, which always travel at the speed of light c. In graphene, the speed of electrons and holes is slower than light by a factor 300 [197]. Graphene also differs because there is no energy gap [196]. As we can see from Fig. 4.30 the conduction and valence bands are shaped like an inverted pair of cones that meet in a single point at $E = 0$ in

momentum space. The relativistic form of the energy bands is new for solids, and it changes the tunes that govern how electrons move through a graphene-based device.

Novoselov et al. [198] found that one could control the carrier density in graphene in an unusual way. A positive gate voltage attracts electrons, so the Fermi energy lies at positive energies $E\rangle 0$ in the cone-shaped conduction band. As the gate voltage made less positive, the density of electrons decreases, but the conductance G does not fall to zero at $E = 0$, as it would in a normal semiconductor. Instead, it reaches a minimum value comparable to the quantum conductance $G_Q = e^2/\hbar$, where e is the electron charge, and $\hbar$ is Planck constant. As the gate voltage is moved to negative values, the conductance increases again, because holes are attracted. Because there is no energy gap, it is not possible to deplete the carriers completely and drive the conductance to zero [197].

Below we will consider two chemical mechanisms of bandgap engineering in graphene. Graphene oxide (GO) is usually synthesized through the oxidation of graphite using oxidants including concentrated sulfuric acid, nitric acid, and potassium permanganate based on Hummers method [199]. Compared to pristine graphite, GO is heavily oxygenated bearing hydroxyl and epoxy groups on sp^3 hybridized carbon on the basal plane, in addition to carbonyl and carboxyl groups located at the sheet edges on sp^2 hybridized carbon. Hence, GO is highly hydrophilic and readily exfoliated in water, yielding stable dispersion consisting mostly of single-layered sheets (graphene oxide). It is important to note that although graphite oxide and graphene oxide share similar chemical properties (i.e., surface functional group), their structure is different. Graphene oxide is a monolayer material produced by the exfoliation of GO. Sufficiently dilute colloidal suspension of graphene oxide prepared by sonication are clear homogeneous and state indefinitely. The chemical structure of graphene oxide such as the type and distribution of oxygen-containing functional groups have been studied using NMR ^{13}C-labeled graphene oxide [200, 201] suggesting that the basal plane of the sheet is decorated with hydroxyl and epoxy (1, 2-ether) functional groups with small amount of lactol, ester, acid, and ketone carbonyl groups at the edge. These functional groups provide reactive sites for a variety of surface-modification reactions to develop functionalized graphene oxide- and graphene-based materials. The thermal reduction is an approach to reduce GO to reduction graphene oxide that utilizes the heat treatment to remove the oxide functional groups from graphene oxide surfaces. For example, the electron mean free path is limited by the distance between two defective sites either by C–O or vacancy [202].

A fully comprehensive, systematic study of the impact of plasma oxidation on graphene was done in papers [203–205]. To study the relationship between oxidation density and the optical gap, cited authors have performed the Raman scattering of light and photoluminescence measurement the samples with different oxidation densities. The structure and density of states (DOS) of GO are depicted in Fig. 4.41. As we can see, the oxygen atoms displace between carbon atoms (see also [206]). As was shown above, the Raman spectroscopy is a valuable source of information when performed on carbon materials, providing insight into the structural as wells electronic properties of the material. Carbon allotropes show their fingerprints under a

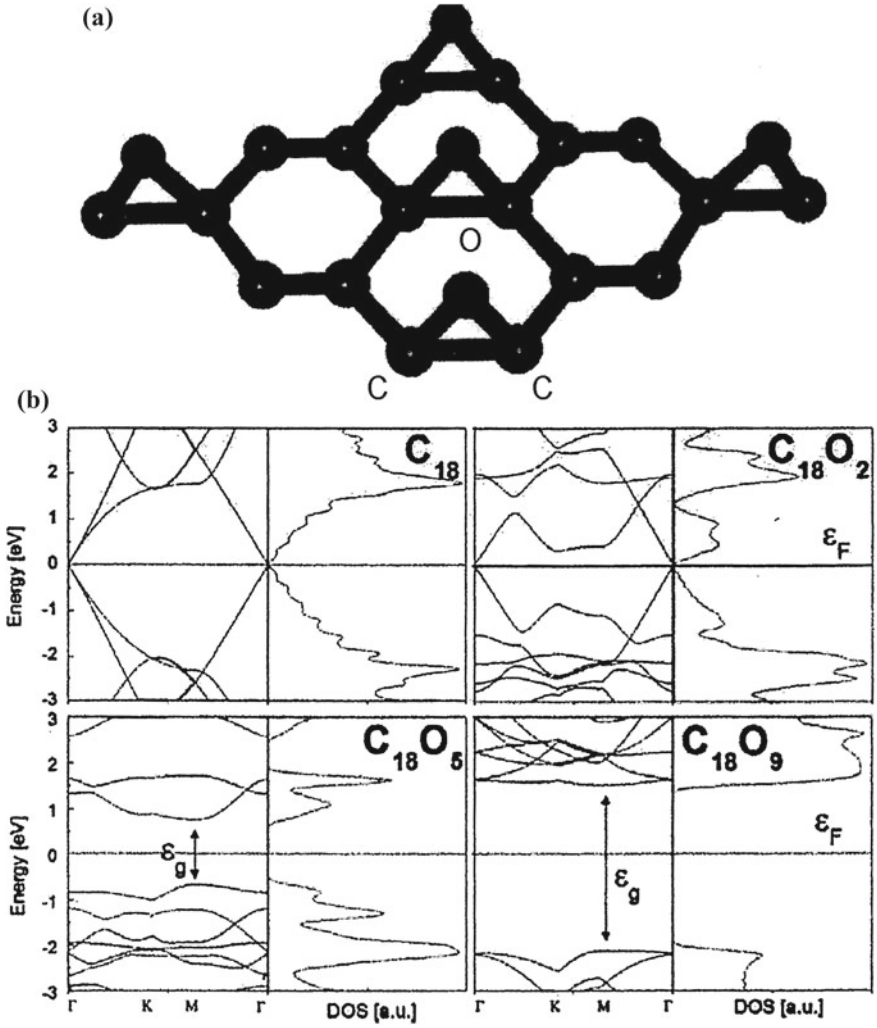

Fig. 4.41 **a** Atomic structure of the graphene supercell employed for the DFT calculations presented in [204], corresponding to the structure $C_{18}O_5$. **b** Electronic band structure and electronic density of states (DOS) calculated for different oxygen densities. The electronic states are calculated along the $\Gamma - K - M - \Gamma$ direction of the supercell Brillouin zone. The Fermi energy ε_F is set to zero (after [204])

man spectroscopy mostly in D, G, and $2D$ peaks around $1350\,cm^{-1}$, $1580\,cm^{-1}$, and $2700\,cm^{-1}$, respectively, due to the change in electron band. Identification of these features allows the characterization of graphene layers in terms of number of layers present and their effect of strain, doping concentration, and effect of temperature and presence of defects [207]. The G band is associated with the doubly degenerated E_{2g} phonon mode at the Brillouin zone center. This band (near $1580\,cm^{-1}$) arises

due to the in-plane vibration of the sp^2 carbon atoms, whereas the $2D$ band is almost double the frequency of the D band and originates from the second-order Raman scattering of graphene, ripples, and puddles [169]. Figure 4.42 compares the Raman specter of pristine (curve 1) and O_2 plasma-treated (curve 2) single-layer graphene (SLG) (15 W, 3 s). The shape and position ($\sim$2640 cm^{-1}) and FWHM ($\sim$25 cm^{-1}) of $2D$ peak [204] of the pristine sample confirm the SLG. The absence of a significant D peak is evidence of the good crystalline quality of the SLG sample [169]. As was shown above, the D peak requires either a defect for its activation or a break of the plane sp^2 symmetry in the graphene lattice, such a the graphene edges [167]. Consequently, the D peak is allowed in small and isolated domains and its intensity I_D is associated with the amount of non-sp^2 bonding [208, 209].

After exposed to an O_2 plasma for 3 s., the Raman spectrum (curve 1, a) shows significant changes. The D peak appears at 1318 cm^{-1}, indicating a deviation from pristine SLG character ($\sim$1350 cm^{-1}). The G peak downshifts ($\sim$1590 cm^{-1}) and appears structured when compared the pristine SLG spectrum, exhibiting a "shoulder" D' peak (at $\sim$1615 cm^{-1}). Moreover, the $2D$ peak broadens ($\sim$130 cm^{-1}), downshifts ($\sim$2617 cm^{-1}) and appearance of new broad peak at $\sim$2900 cm^{-1}. The last one has been referred to as combination $G + D$ peaks, or another origin. Authors of paper [204] have calculated the electronic band structures and density of states (DOS) of pristine and oxygen-decorated SLG (see Fig. 4.41). They use the configuration shown in Fig. 4.41a whereby a single oxygen atom lies midway above the C bond, denoted as epoxide, because it is the most energetically favorable chemisorption configuration (see also [206, 210] and reference therein). The assumption is only valid as long as SLG lattice retains its structural integrity upon oxygen functionalization. Experimentally [203–206], this condition implies that the O_2 plasma treatment does not affect the structural crystallinity of the SLG lattice. The calculated results are demonstrated in Fig. 4.42b. Progressively, denser oxygen contents functionalization strong affects the electronic structure of SLG. The band structure calculated in the C_{18} configuration (on oxygen atoms) correctly shows the features of pristine SLG with linear bands interesting at ε_F. The $C_{18}O_2$ configuration shows the appearance of a 0.2 eV bandgap. The bandgap value increases monotonically with the oxygen density. For an oxygen density as high as 50%, the bandgap calculations are thus in agreement with the experimental data, as well as theoretical calculations of the paper [205]. The results of this paper are demonstrated in Fig. 4.44. According to cited authors, the highest calculated value of E_g at the ratio O/C equals 50% is 3.004 eV. This value is very close to $E_g = 3.6$ eV at 50% oxygen density of [204]. Figure 4.43 shows the optimized lattice constants of the three most stable configurations as a function of O/C ratio. The calculated lattice constant of $a = 2.47$ Å for pristine graphene agrees well with the experimental value for bulk graphite, 2.46 Å. The optimal lattice constant increases with the O coverage monotonously, which is similar to the result of [211]. The lattice constant for O/C = 50 5 is 7.4% greater than that of pristine graphene. Furthermore, the authors of paper [205] found that the lattice constant can be fitted very well with quadratic function (see Fig. 4.43). The results of the paper [205] are summarized in Fig. 4.45. Notably, the bandgap is not monotonic function of oxygen density but exhibits multipeaks and valleys.

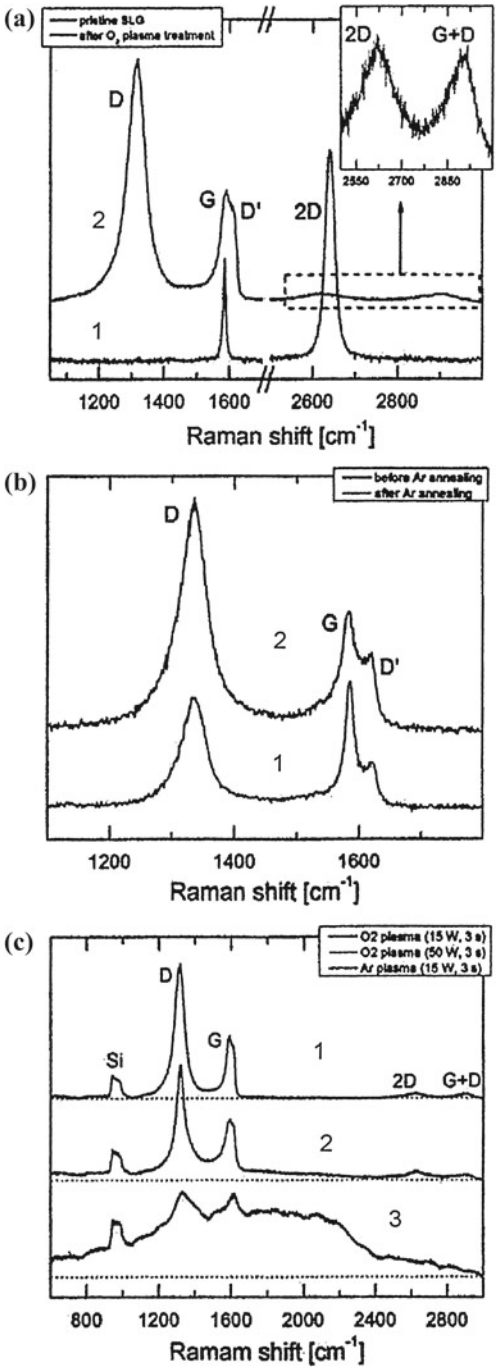

Fig. 4.42 **a** Raman spectra collected on a pristine before (1) and after (2) exposure to O_2 plasma (15 W, 3 s). The inset shows a detail of higher Raman shifts (>2500 cm^{-1}) for the plasma-treated SLG sample. **b** Raman spectra collected on an O_2 plasma-treated SLG sample before (2) and after (1) annealing in inert Ar atmosphere (250 °C). **c** Raman spectra of pristine SLG samples subjected to different plasma conditions. All the relevant Raman peaks are indexed. The spectra are rescaled to the intensity of the G peak (~1580 cm^{-1})in **a** and **b** and to that of the second-order of the Si transverse-optical peak (~970 cm^{-1}) in **c** (after [204])

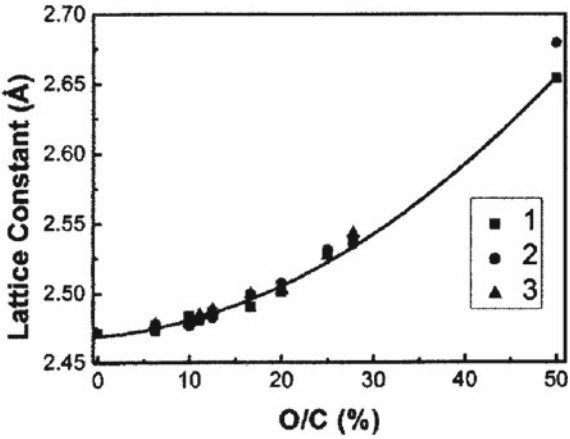

Fig. 4.43 Optimal lattice constant a of RGO as a function of O/C ratio. Squares, circles, and triangles represent the most, the second most, and the third most stable oxygen configurations, respectively. The quadratic function fit for the most stable configuration is shown in the black solid line, and described by the following expression: $a = 6.351 \cdot 10^{-5}x^2 + 5.378 \cdot 10^{-4} + 2.469$, where x is the O/C ratio (%) (after [205])

It is important results of [205] that the effect of lattice relaxation on the electronic properties of RGO is found to be negligible for low O density and crucial for higher O density, respectively.

In a recent theoretical study, Sofo et al. predicted that hydrogenation of the graphane surface should create a stable material, graphane, with a large energy band. Cited authors have found that graphane has two favorable conformations: a chair-like conformer with the hydrogen atoms alternating on both sides of the plane and boatlike conformer with the hydrogen atoms alternating in pairs. A perspective view of chair conformer is shown in Fig. 4.46. In the chair conformer, every C–C bond connects carbon atoms with hydrogen attached at opposite sides of the plane. The calculated C–C bond length of 1.52 Å is similar to the sp^3 bond length of 1.53 Å in diamond and is much greater than 1.42 Å characteristic of sp^2 carbon in graphene. The boat conformer has two different types of C–C bonds: those connecting carbons bonded to hydrogen atoms on opposite sides of the plane (see also [156]) with a bond length of 1.52 Å and those connecting carbon atoms bonded to hydrogen atoms on the same side of the plane with a bond length of 1.56 Å, slightly longer due to H–H repulsion. The C–H bond length of 1.1 Å is similar in both conformers and is typical of hydrocarbon compounds [210].

Hydrogenation is a process in which an added hydrogen atom bonds to another atom by sharing its only electron with this atom. Recently, Elias et al. [156, 157] have presented the first experimental demonstration that graphene is chemically active and that the energy gap can be produced without cutting graphene into a ribbon (see also [157]). Adding atomic hydrogen to graphene is not a simple task: hydrogenation first requires breaking apart the diatomic molecules of hydrogen gas; this is why hydrogenation in chemistry is usually performed with a hot catalyst (see, e.g., [213]). Elias et al. exposed the graphene samples to a hydrogen plasma discharge, in which the hydrogen gas is dissociated into hydrogen ions. The sample has to be placed some distance from the plasma discharge to avoid mechanical damage of graphene by energetic ions. The emergence of the energy gap manifests

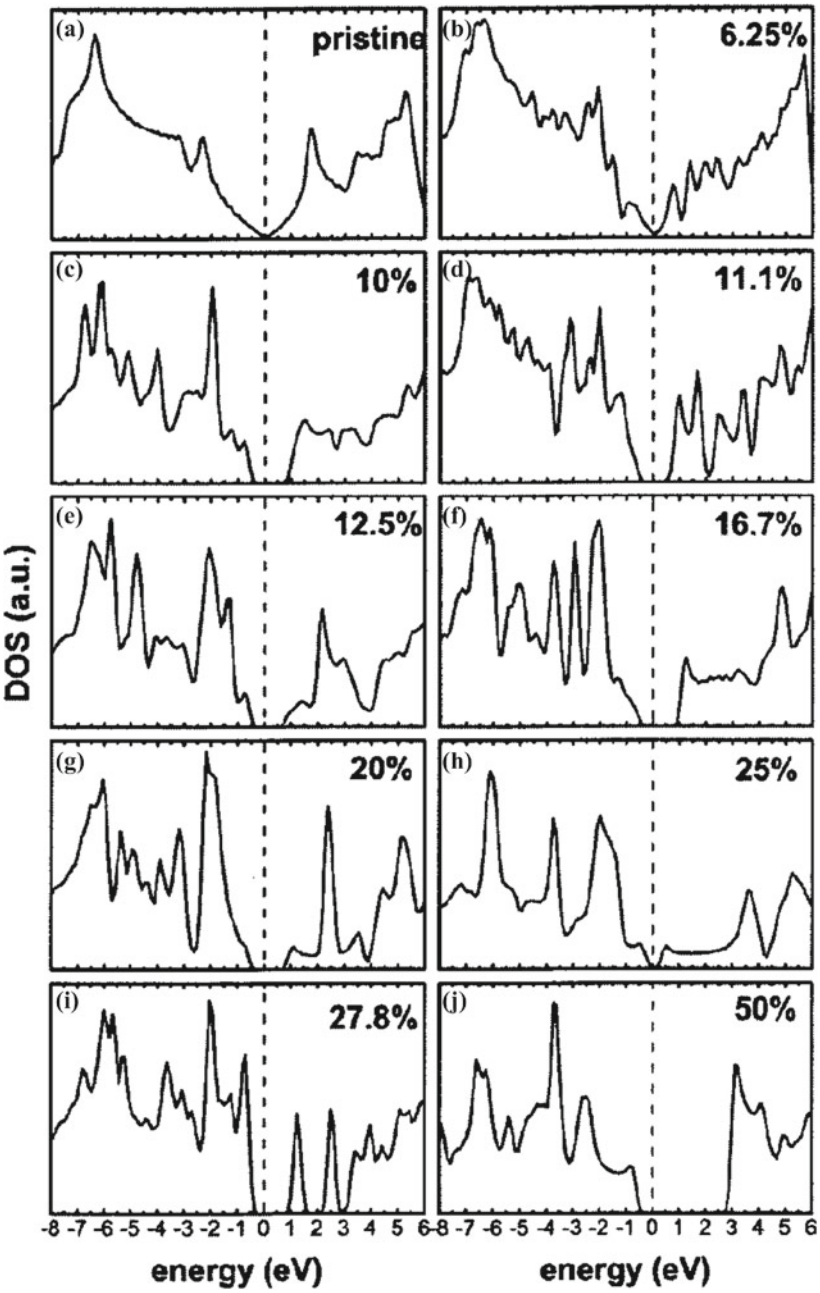

Fig. 4.44 Total density of states (arbitrary units) of the most stable configuration of RGO with the oxygen coverage of **a** 0% (pristine), **b** 6.25% ($C_{64}O_4$), **c** 10% ($C_{30}O_3$), **d** 11.1% ($C_{18}O_2$), **e** 12.5% ($C_{32}O_4$), **f** 16.7% ($C_{24}O_4$), **g** 20% ($C_{30}O_6$), **h** 25% (C_8O_2), **i** 27.8% ($C_{18}O_5$), and **j** 50% (C_4O_2). The Fermi level (indicated via dashed lines) has been set to zero for each configuration (after [205])

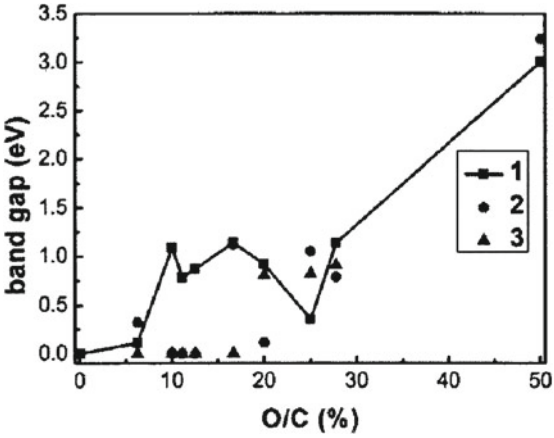

Fig. 4.45 The bandgap of the reduced graphene oxide vs. the O/C ratio. The squares correspond to the most stable configurations of each O/C ratio, and the circles and triangles correspond to the second most and the third most stable configurations, respectively. The solid line is to guide the eyes (after [205])

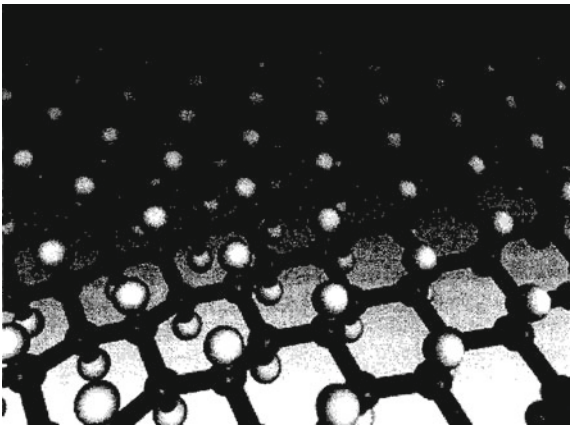

Fig. 4.46 Structure of graphane in the chair conformation. The carbon atoms are shown in gray, and the hydrogen atoms are white. The figure shows the hexagonal network with carbon in the sp^3 hybridization (after [212])

itself in the electrical conductance which becomes, as was shown by Mott (see, e.g., [214]), strongly temperature. Mott described that at very low temperature, there is not enough thermal energy for the charge to go from valence band to conduction band via hopping among the localized states. According to Mott [214], the conductivity of such system can be described as

$$\sigma = A \exp\left(-\frac{T_0}{T^{1/(d+1)}}\right), \tag{4.72}$$

where A is constant, T_0 is critical temperature, and d is the dimensionality of the system. So for a $2D$ system, the relation (4.72) became $\sigma \sim T^{-1/3}$ (the more details see [206]). Although in pristine graphene, electrons are free to move across the crystal, the presence of the gap after hydrogenation forces them to "hop" from one site to another and this conduction mechanism is much more efficient at higher

temperature, see (4.72). In the paper [156], the changes by hydrogenation have been corroborated by Raman spectroscopy. Figure 4.47 shows the evolution of Raman spectra for graphene crystals that are hydrogenated and annealed simultaneously. As it can see hydrogenation resulted in the appearance of sharp D and D' peaks, slight broadening and a decrease of the high of the $2D$ peak relative to the G peak, and the onset of a combination mode $(D + D')$ around $2950\,\mathrm{cm}^{-1}$ (compare to Fig. 4.42), which unlike the $2D$ and $2D'$ bands, requires a defect for its activation because it is a combination of two phonons with different momentum. The D peak in hydrogenated graphene is observed at $1342\,\mathrm{cm}^{-1}$ (instead $1350\,\mathrm{cm}^{-1}$ in pristine graphene) and is very sharp, as compared with that in disordered or nanostructured carbon-based materials [206, 208]. Cited authors attribute the activation of this sharp D peak in hydrogenated samples to breaking of the translational symmetry of C–C sp^2 bonds after formation of C–H sp^3 bonds. Although the majority of carbon bonds in hydrogenated graphene are expected to acquire sp^3 hybridization in [156] authors are not see any Raman signature of C–C sp^3 bonds because their cross section at visible light excitation is negligible as compared with that of resonant C–C sp^2 bonds, and therefore even a small residual sp^2 phase should generally dominate Raman spectra, as happens in other diamondlike compounds [208]. After annealing, the Raman spectrum recovered to almost its original shape, and all of the defect-related peaks (D, D' and $D + D'$) were strongly suppressed (the more details see [156]).

According to the results of paper [212], the electronic band structure of the two conformers is very similar. They have a direct bandgap at the Γ point with $E_g = 3.5\,\mathrm{eV}$ for the chair conformer and $E_g = 3.7\,\mathrm{eV}$ for the boat conformer. The band structure and corresponding density of states (DOS) for the chair conformer are displayed in Fig. 4.48. The top of the valence band is doubly degenerate, with two different effective masses, and decomposition of the DOS shows that these states are mainly of p symmetry. On the contrary, the bottom of the conduction band exhibits mainly s-characterized has a larger effective mass. Graphene shows a moderate charge transfer from hydrogen to carbon (of the same order magnitude as other hydrocarbons [213] as well as lithium hydride [30]). By the way, we should remind the results of paper [157] where it was indicated that deuteration of the graphene increases the bandgap [30]. The demonstration in [156] of reversible hydrogenation of graphene is an important step in expanding the device application for this exciting material. This extremely thin material with an energy gap is also likely to find use in nonelectronics (optoelectronics). Naturally, research will probably not be limited only oxygen and hydrogen to graphene, very perspective in this direction deuteration of the graphene. With an energy gap, one can then deplete the carrier concentration with a barrier or gate, as with conventional device.

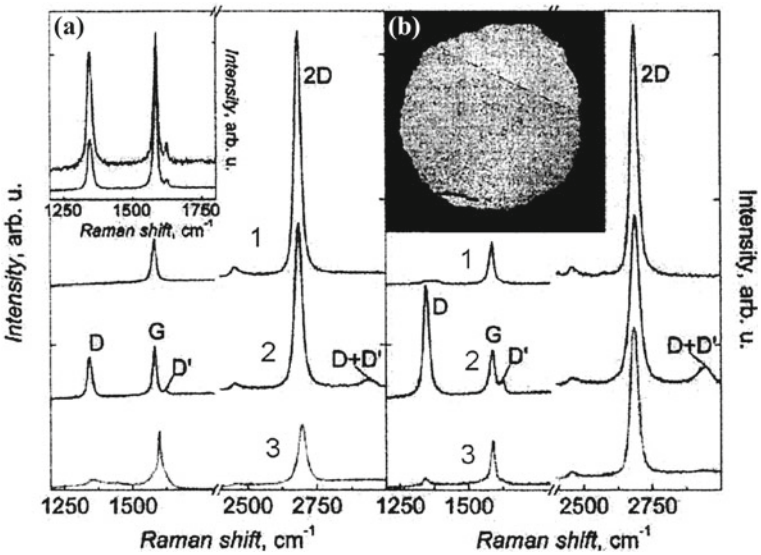

Fig. 4.47 Changes in Raman spectra of graphene caused by hydrogenation. The spectra are normalized to have a similar intensity of the *G* peak. **a** Graphene on SiO_2. **b** Freestanding graphene. 1, 2, 3 curves (top to bottom correspond to pristine, hydrogenated, and annealing samples, respectively (after [163])

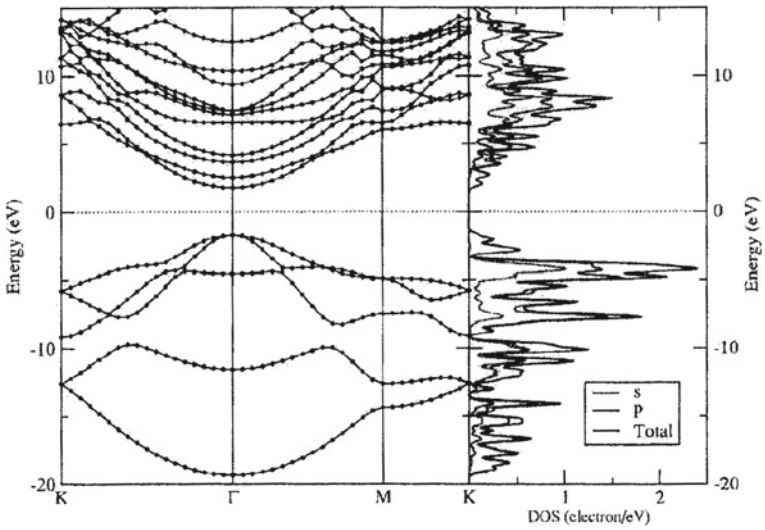

Fig. 4.48 Band structure (left and density of states (right)) of the chair conformer. The states at the top of the valence band are mainly of p symmetry, while the states at the bottom of the conduction band have s symmetry (after [212])

4.7 Low-Dimensional Devices

4.7.1 Background

Low-dimensional structures have become one of the most active researches in nanoscience and nanotechnology. Nanoscience is nor physics, chemistry, engineering, or biology—it is all of them. It is naturally to remark: why has nanoscience attracted such intense global interest? To answer this, a broad definition and brief description of the field required. Nanoscale science, engineering, and technology are concerned with the manipulation of matter on the nanometer scale, which is now generally taken as the 1 to 100 nm range (see, e.g., [215]). Although nanoscience might simply be seen as a natural and necessary progression from the (sub)micron-scale engineering that has driven the microelectronics and computing industries thus far, it is not merely the trend toward higher levels of miniaturization but the wealth of novel physical, chemical and biological behavior that occurs on the nanometer scale that makes nanoscience such a fundamentally exciting and technologically relevant area of research (see also [12–14]). The length scales appropriate to nanoscience are such that the field might be thought of as "straddling" solid-state and atomic/molecular physics and chemistry. That is, instead of dealing with an infinitely extended solid or individual atoms and molecules, nanoscience is concerned with the properties, interactions, and processing of units containing a countable number of atoms. These units—whether they are, for example, clusters of atoms (quantum dots), fullerenes, carbon nanotubes, and bimolecules—have novel electronic, optical, and chemical properties by virtue of their nanometer dimensions. Furthermore, by varying the size of the units and—equally importantly—controlling their interactions, the fundamental properties of nanostructured materials synthesized from these building blocks may be tuned. The synthesis of a material from nanoscale building blocks—building from the bottom up—differs radically from the top-down, lithographic approach conventionally used to fabricate submicron devices both industrially and in the majority of experimental solid-state and low-dimensional physics [10–12]. In "There is Plenty of Room at the Bottom" [216], Feynman noted that nanometer-scale engineering would require the development of complex instrumentation that could act as researcher eyes and fingers in the nanoworld. This vision was realized in the early 1980s by the invention of the scanning tunneling microscope(STM) [217, 218], an instrument that exploits the quantum-mechanical tunnel current flowing between a sharp metal tip and a conducting substrate to generate atomically resolved surface images [14]. A family of related scanning probe instruments (including the atomic force microscope (AFM) [20]), magnetic force microscope (MFM) and scanning near-field optical microscope (SNOM) were developed in the decade following the invention of the STM (see also [219, 220]). With each new scanning probe instrument came a new method of investigating material properties at the nanometer level.

The STM-based atomic manipulation described above as a rule was carried out on metal surfaces at cryogenic temperatures. Low temperatures are necessary to inhibit atomic diffusion of metals where surface diffusion barriers are small. It is

only within the last few years that it has become possible to manipulate adsorbates at room temperature using STM. The difficulty in achieving controlled positioning at room temperature arise from the relatively small number of adsorbate–substrate systems where the diffusion barrier for the adsorbate is large enough that diffusion at room temperature is inhibited yet the adsorbate–substrate bond is sufficiently weak that the STM tip can controllably move the adsorbate.

On the first consideration, one might imagine that prototypical nanoclusters should consist of a size-selected collection of atoms, isolated in the gas phase and synthesized under (ultra)high-vacuum conditions (to ensure the absence of foreign chemical species either in the cluster volume or at its surface). Indeed, this is generally the case in fundamental cluster science where dedicated cluster sources are used to provide beams of nanoclusters of almost any element with sizes ranging from several atoms to several tens of thousands of atoms.

The high level of circuit integration in today's silicon technology could not have been achieved with III–V semiconductors. However, from point of view of operating speed, III–V devices show many advantages (see below), mainly due to the high carrier mobility, μ, and lower effective mass of electrons in III–V compounds [221]. As is well known, carrier mobility in GaAs is about one order of magnitude higher than that of silicon [221]. In fact, the electron velocity in a semiconductor under the effect of an applied external file is probably the most representative parameter for the design of high-speed advanced electronic circuits. Figure 4.49 shows the maximum operation frequency (in GHz) of different modulation-doped field-effect transistors (MODFETs) as a function of gate length (in microns) [222]. Due to their particular characteristics, these transistors are also called high-electron mobility transistors (HENTs) [223]. For comparison purpose, Fig. 4.49 also includes typical parameters of silicon metal-oxide-semiconductor field-effect transistors (MOSFETs) as well as GaAs MESFETs. On this picture frequency values are given at room temperature (300 K) although these frequencies are much higher for operation temperature close to 0 K, as a consequence of the increase in mobility at low temperature (see also [223, 224]). At present, MODFET devices with gate lengths of about 100 nm and maximum operating frequencies at room temperature of several hundreds of GHz are available.

The knowledge gained in the previous discussion makes it possible to consider and analyze a variety of different nanostructure devices. In this chapter as a first step, we consider electronic and optical devices. Some of these mimic the well-known microelectronic devices but with small-dimensional scales. This approach finds application in devices with shorter response times and higher operational frequencies that operate at lower working currents, dissipate less power, and exhibit other useful properties and enhanced characteristics. Such examples include, in the first step, the field-effect transistors considered below. On the other hand, new generations of the devices are based on new physical principles, which cannot be realized in microscale devices. Among these novel devices are the resonant-tunneling devices described in the following section, and single-electron transistor as well as optoelectronic devices (light-emitting diodes and lasers).

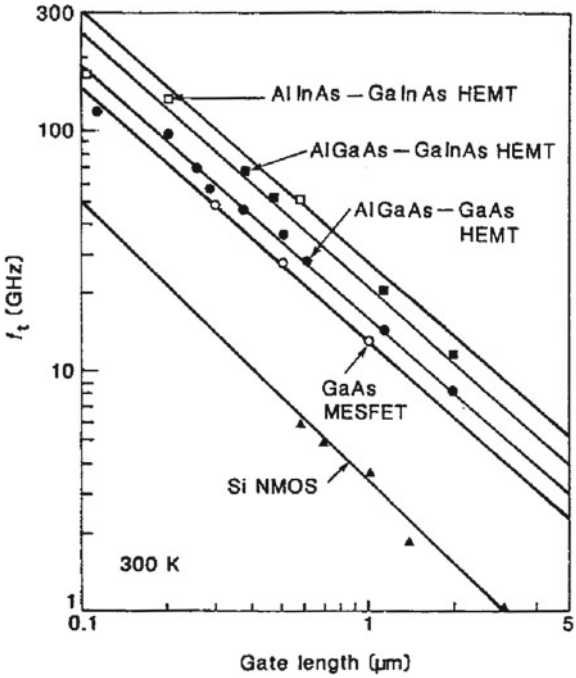

Fig. 4.49 Maximum operation frequencies reached by MODFET, MESFET, and MOSFETs as function of gate length (after [222])

4.7.2 Resonant-Tunneling Diodes

Another very interesting quantum effect to take into account for the development of advanced transistors is the so-called resonant-tunneling effect [225]. Resonant-tunneling diodes (RTD), based on that effect, basically consist of a quantum well surrounded by two potential barriers thin enough to allow electron tunneling. Due to the extremely low electron transit time through these semiconductors structures, electronic devices based on RTDs can operate at extremely high frequencies, in the range of 1 THz. By the addition of an RTD to a bipolar transistor or to an FET, it is possible to build resonant-tunneling transistor (RTT). In these transistors, the resonant-tunnel structure injects very hot electrons (i.e., electrons of very high kinetic energy) into the transistor active region. The reduction of the characteristic device size to the nanometric range leads to a notable reduction in the number of electrons contained in the electric signals transferred through electronic devices. This tendency has led to the development of the so-called single-electron transistor (SET) [226]. As will be seen below, the performance of SETs is based on the Coulomb blockade effect, which is manifested in zero-dimensional semiconductor structures—QDs (see [14]).

As shown above electrons in heterojunctions and in QWs can respond with very high mobility to applied electric fields parallel to the interfaces (see also [227]). In this paragraph, the response to an electrical field perpendicular to the potential barriers at the interfaces will be considered. Under certain circumstances, electrons

can tunnel through these potential barriers, constituting the so-called perpendicular transport (see also [228, 229]). Tunneling currents through heterostructures can show zones of negative differential resistance (NDR) (see Fig. 4.50), which arise when the current level decreases for increasing voltage (see also [13]). The operation of NDR QW electronic devices is based on the so-called resonant-tunnel effect (RTE), which takes place when the current travels through a structure formed by two thin barriers with a QW between them. The I–V characteristics of RTE devices are depicted in Fig. 4.50. This figure also shows the representation of the conduction band of a double heterojunction with a QW between the junctions. The thickness of the QW is supposed to be small enough (5–10 nm) as to have only one allowed energy-level E_1 (resonant level). The well region is made from lightly doped GaAs surrounded by higher gap AlGaAs (see, e.g., [10, 226]). The outer layers are made from heavily doped n-type GaAs (n^+ GaAs) to facilitate the electrical contacts. The Fermi level of the n^+ GaAs is represented within the conduction band, since it can be considered a degenerated semiconductor [230]. Let us suppose that an external voltage, V, is applied, starting from 0 V. It can be expected that some electrons tunnel from the n^+ GaAs conduction band through the potential barrier, thus resulting in increasing current for increasing voltage (region 1–2 in the I–V curve of Fig. 4.50c). When the voltage increases, the electron energy in n^+ GaAs increases until the value $2E_1/e$ is reached, for which the energy of the electrons located in the neighborhood of the Fermi level coincides with that of level E_1 of the electrons in the well (see Fig. 4.50b). In this case, resonance occurs and the coefficient of quantum transmission through the barriers rises very sharply. In effect, when the resonant condition is reached, the electron wave corresponding to the electrons in the well is coherently (see, e.g., Fig. 10.18 in [227]) reflected between two barriers. In this case, the electron wave incident from the left excites the resonant level of the electron in the well, thus increasing the transmission coefficient (and thus the current through the potential barrier (region 2 in Fig. 4.50c). If the voltage further increased (region 2–3), the resonant energy level of the well is located below the cathode lead Fermi level and the current decreases, thus leading to the so-called negative differential resistance (NDR) region (region 2–3 of Fig. 4.50). Finally, for even higher applied voltage, Fig. 4.50d, the current again rises due to the thermo-ionic emission over the barrier (region 4). RTD used in microwave applications are based on this effect. A figure of merit used for RTD is the peak-to-valley current ratio of their I–V characteristic, given by the ratio between the maximum current (point 2) and the minimum current in the valley (point 3). Although the normal values of the figure of merit are about five for AlGaAs–GaAs structures at room temperature, values up to ten can be reached in devices fabricated from strained InAs layers, surrounded by AlAs barriers and operating at liquid nitrogen temperature [13]. If RTD are simulated by a negative resistance in parallel with a diode capacitance C and a series resistance RS, as is the case of normal diodes, it is relatively easy to demonstrate that the maximum operation frequency increases as C decreases. The resonant-tunnel diode is fabricated from relatively low-doped semiconductors, which results in wide depletion regions between the barriers and the collector region, and accordingly, small equivalent capacity. For this reason, RTDs can operate at frequencies up to several THz, much higher than those

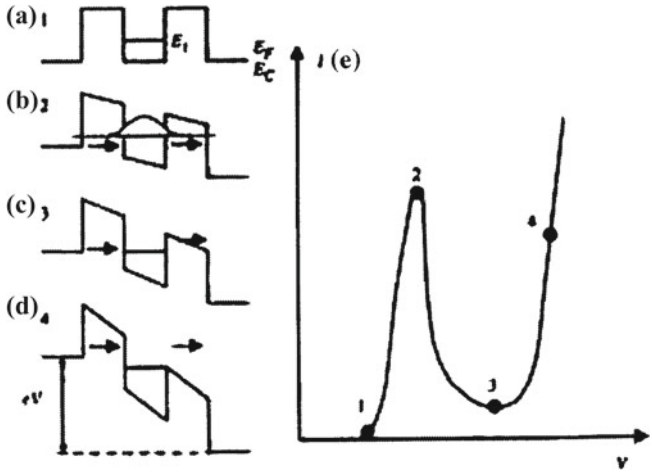

Fig. 4.50 Schematic representation of the conduction band of a resonant-tunnel diode: **a** with no voltage, **b**–**d** for increasing applied voltage, **c** current–voltage characteristic

corresponding earlier tunnel diodes which just reach about 100 GHz, with response time under 10^{-13}s. Small values of the NDR, i.e., an abrupt fall after the maximum on the I–V curve result in high cutoff frequencies of operation. In fact, RTDs are the only purely electronic devices that can operate up to frequencies close to 1 THz, the highest of any electron transit time device (see also [14, 231]).

4.7.3 Field-Effect Transistor

It will become apparent that new generations of devices result from the use of heterojunctions as a feature in device design. High-speed semiconductor devices are key elements in the development of electronic systems for data processing or analog signal handling at ever-higher frequencies (the state of the art is currently in excess of 100 GHz, a detailed discussion of a wide range of devices is given in [222]). Most of these systems use circuits based on Si devices prepared by implantation or diffusion, but these fabrication processes are limited in their ability to produce the small-scale device structures required or high-speed operation. This section describes the variations of the field-effect transistor (FET) principle, using vertical transport, i.e., perpendicular to the sheets. It is interesting to note that, with the exception of resonant-tunneling and superlattice structures, the performance characteristics of these devices are not primarily due to quantum confinement effects associated with their two-dimensional nature, although these may play a secondary role in some instances. The previously analyzed diodes are the simplest electronic devices, for which the current is controlled by the diode bias and vice versa. A useful function

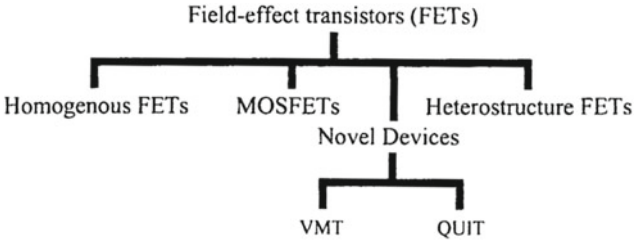

Fig. 4.51 The family tree of FETs consists of thee groups of conventional FETs that have much in common in their technologies, properties, and application and new groups of novel devices. The abbreviations used in this chart are defined as follows: MOSFET—metal-oxide-semiconductor FET, VMT—velocity modulation transistor, and QUI—quantum interference transistor

can be performed mainly due to the nonlinearity of current–voltage dependences. In contrast, in three-terminal devices known as transistors, there exists the possibility of controlling the current through two electrodes by varying the voltage or the current through the third electrode. The field-effect transistors (FET) family can be classified as shown in Fig. 4.51, where the short explanation for the abbreviation used to denote these FETs was also given. The basic principle of the FET is illustrated in Fig. 4.52. The flow of charge carriers between two ohmic contacts, the source and drain, is controlled, as indicated above, by the voltage applied to the third electrode, the gate, isolated from the conducting region either by a layer of insulator, as in a metal–insulator–semiconductor–FET (MISFET, or if the insulator is an oxide, MOSFET), or by the depletion region of a Schottky barrier, as in the metal–semiconductor–FET (MESFET). The gate, insulator/depletion region and conducting channel form a parallel-plate capacitor structure, so that application of a voltage across this structure will determine the number of charge carriers in the conducting channel, and hence the magnitude of the current flowing between the source and drain.

Below, we briefly describe the field-effect transistors (FETs) on the base of the nanowires. Nanowire FETs can be configured by depositing the nanomaterial onto an insulating substrate surface and make source and drain on the nanowire ends. Figure 4.53 illustrates this approach, where we show a schematic diagram of a Si-nanowire FET with the nanowire, the metal source, and drain electrodes on the surface of the SiO_2/Si substrate (see also [232]). This approach may serve as the basis for hybrid electronic systems consisting of nanoscale building blocks integrated with more complex planar silicon circuitry [13]. We should note that an extremely small FET may be built on the basis of carbon nanotube [148, 233]. In conclusion, we have noted that the nanowire devices discussed here have great potential for applications in nano- and optoelectronics.

Note that so far we have made no reference to the wavelike properties of electrons nor to the fact that the channel is made from individual atoms. The only quantum property that has had a role in our explanation is the Pauli principle, which dictates that each possible state for an electron in the channel can be occupied at most only one electron. This means that only a certain number of electrons can accumulate in

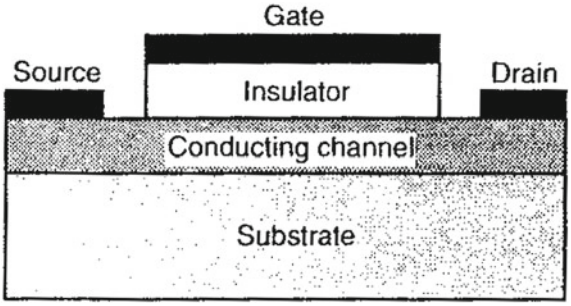

Fig. 4.52 Schematic structure of a basic FET

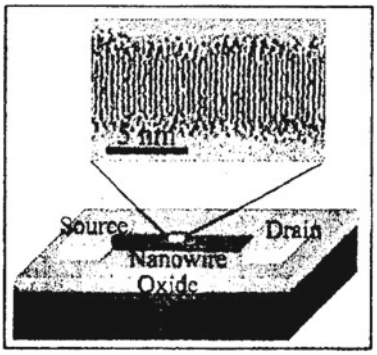

Fig. 4.53 A schematic diagram of a Si-FET with nanowire, the metal source, and drain electrodes on the surface of a SiO_2/Si substrate (after [232])

the channel, setting a limit on the current flow. However, the quantum properties of electrons and atoms will be increasingly important as FETs are made smaller. For example, the wave nature of electrons will influence the way they travel through the channel. When the transverse dimension of the channel becomes comparable to the wavelength of electrons (around 100 nm [226]), electron propagation becomes more sensitive to the atomic disorder in the device, which is inherent in the present fabrication process. The disorder makes the channel remain insulating even when the density of electrons is high. In an ideal situation, we might want electrons to be scattered only by the gate-dependent potential, with of the scattering mechanisms always being determinal to amplification. But the confinement of electrons in the channel by tunnel barriers, in the source–drain direction, can also lead to a new kind of amplification principle. This is the basis of the single-electron transistor (SET).

4.7.4 Single-Electron Transistor

If electron motion is quantized in all three possible directions, we obtain a new physical object, a macroatom. Questions concerning the usefulness of such objects for applications naturally arise from the point of view of their electronic applications. A fundamental question is the following: what is the current through a macroatom?

A valid answer is that there exists the possibility of passing an electric current through an artificial atom due to tunneling of electrons through quantum levels of the macroatom (see, e.g., [85, 89]). The field of single-electron tunneling (SET) comprises phenomena where the tunneling of a microscopic charge, usually carried by an electron or a Cooper pair, leads to microscopically observable effects (see also [96, 106, 234]). The basic principles governing single charge tunneling through QD are briefly outlined in this paragraph.

Below we will show that even change of one elementary charge (electron) in such small systems has a measurable effect in the electrical and transport properties of the dot [14]. This phenomenon is known as Coulomb blockade, which we will discuss in the simplest possible terms (see also [232]). Let us imagine a semiconductor dot structure, connected to electron reservoirs (e.g., drain and source) of each side by potential barriers or tunnel junctions (see Fig. 3.3 in [14]). In order to allow the transport of electrons to or from reservoirs, the barriers will have to be sufficiently thin, so that the electrons can cross them by the tunnel effect. Further suppose that we wish to change the number N of electrons in the dot by adding just one electron, which will have to tunnel, for instance, from left reservoir into the dot. For this to happen, we will provide the potential energy eV to the electron by means of a voltage source. If the charge in the QD is Q and its capacitance C, the potential energy is $Q^2/2C$. Therefore, an energy of at least $e^2/2C$ will have to be provided to the electron, which means that for the electron to enter the dot, the voltage will have to be raised to at least $e^2/2C$. Since the electron can either enter the dot or leave (this process is equivalent to a hole entering the dot), we see that electrons cannot tunnel if

$$| V | < e/2C. \tag{4.73}$$

Therefore, there this is a voltage range, between $-e/2C$ and $e/2C$, represented in Fig. 3.3 in [14], in which current cannot go through the dot; hence, the name Coulomb blockade is given to this phenomenon (see also [226] and references therein). Evidently, if the above process is continued and we keep adding more electrons, we will have the situation represented in Fig. 3.4 in [14], in which we will observe discontinuities in the current through the QD whenever the voltage acquires the values expressed by

$$V = \left(\frac{1}{2C}\right)(2n+1)e, \quad n = 0, 1, 2, 3, \ldots \tag{4.74}$$

Observe that in Fig. 3.4 in [14] we have made use of normalized coordinates, both in horizontal and vertical axes, to better appreciate the effect of the quantification in current and voltage.

It is also interesting to observe from the above equations that as the size of the QD is reduced, and therefore C gets smaller, the value of the energy necessary to change the number of electrons in the dot increases. In this case, it will be easier to observe the Coulomb blockade, since the changes in voltage and electric energy have to be much larger than the thermal energy kT at the working temperature,

in order to observe measurable Coulomb blockade effects. Therefore, we should have for the capacitance:

$$C \ll \frac{e^2}{kT}. \tag{4.75}$$

For this condition to be fulfilled, either the capacitance of the dot should be very small (values less than 10^{-16}F are very difficult to get) or we should work at very low temperatures, usually smaller than 1 K.

Another condition to observe SET is that the number of electrons in the dot should not fluctuate in equilibrium. Let us assume that the time taken for an electron to be transferred in or out of dot is of the order of $R_T C$, where R_T is the equivalent resistance of the tunnel barrier and C the capacitance of the dot. Fluctuations in the number of electrons in the dot induce changes in potential energy of the order of e^2/C. Therefore, we should have, according to the uncertainty principle

$$\Delta E \cdot \Delta t = \frac{e^2}{C} R_T C > h \tag{4.76}$$

and consequently for Coulomb blockade effects to be clearly observed we should have

$$R_T \gg \frac{h}{e^2} = 25.8 k\Omega. \tag{4.77}$$

In single-electron transport experiments, usually the current is measured, which is proportional to the conductance. In terms of the conductance, the above condition can be written as (for details see also [226, 232])

$$G \ll \frac{e^2}{h}. \tag{4.78}$$

In reality, electrical methods applied to QDs to realize useful devices are not the only method possible. The control of the electric current through the dots can also be realized by means of light, sound, etc. (see, e.g., [12, 13]). Consider here optical control of the dots and optoelectronic functions of zero-dimensional devices. The main peculiarities of the optical properties of QDs arise due to electron and hole quantization (see also [235]).

The so-called single electronics [225, 226, 232, 236] that appeared in the late 1980s, is at present a tremendously expanded research field covering future digital and analog circuits, metrological standards, sensors, and quantum information processing and transfer [23, 237]. Unlike the FET, whose principle does not require the motion of electrons to be quantum mechanical, the SET is based on an intrinsically quantum phenomenon: the tunnel effect through a metal–insulator–metal junction. When two metallic electrodes are separated by an insulating barrier whose thickness is only ~1 nm, electrons at the Fermi energy can traverse the insulator even though their energy is too low to overcome, in classical motion, the large potential barrier of the insulating region. The tunnel effect manifests itself by a finite resistance R_T of the

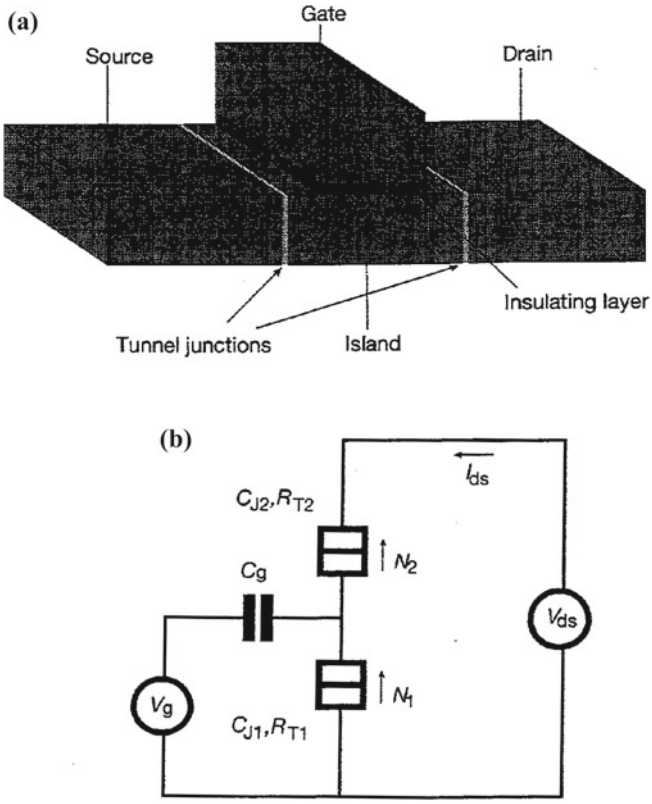

Fig. 4.54 The single-electron tunneling transistor (SET). **a** Simplified three-dimensional structure of the SET. The channel of the FET is replaced here by a sandwich consisting of a nanoscale metal electrode (island), which is connected to the drain and the source by tunnel junctions. As in FET, a gate electrode influences the island electrostatically. **b** Circuit diagram of the SET. The square box symbol represents a tunnel junction, and integers N_1 and N_2 denote the numbers of electrons having through the two junctions. Each junction is characterized by its capacitance and its tunnel resistance (after [226])

insulating barrier. This resistance depends both on the transmission coefficient $\check{T}$ of the barrier to electron waves (which is exponentially decreasing function of its thickness) and on the number M of independent electron wave modes impinging on the barrier (this number is equal to the area of the junction divided by the square of the electron wavelength). The SET uses a key property of the tunnel effect in a many-electron system: for barriers such that $\check{T}M \ll 1$, the charge Q transferred through the barrier becomes quantized with $q = \mathrm{Ne}$, where N is an integer [226]. In other words, for N not to be subject to quantum fluctuations, the resistance of the junction must be large compared with the resistance quantum $R_T \gg h/e^2 = R_k = 25.8\,\mathrm{k}\Omega$ [238, 239]. The SET consists of two such tunnel junctions placed in series (Fig. 4.54). An "island" is thus formed between the two junctions. A gate electrode is coupled electrostatistically to the island. The SET can thus be described as an FET in which the

semiconducting channel has been replaced by a metallic island sandwiched between two tunnel barriers [239]. The island has a total capacitance $C_{\sum}$, which the sum of the gate and junction capacitances

$$C_{\sum} = C_g + C_{j1} + C_{j2}. \tag{4.79}$$

The basic device, called a single-electron device (SED), literally enables the control of electrons on the level of an elementary charge (see also [13, 232]). Because electrons interact strongly via the Coulomb interaction when they pass through the island, the analysis of the SET differs fundamentally from that of the FET. In the FET, electrons go from source to drain independently, and in such numbers that one can consider that the potential seen by one is an average which does not depend on the configuration adopted by all of the others. Electrical transport results from a simple addition of the motion of each electron. In the SET, by contrast, transport results from transitions between collective charge states of the system. These charge states are described by the two numbers N_1 and N_2 of electrons having traversed the junction (Fig. 4.54b).

The basic devices, called a single-electron device, literally enable, as was shown, the control of electrons on the level of an elementary charge. There are rich varieties of SEDs (see, e.g., [223–226]), but the operation principle of all SEDs is basically the same. SEDs rely on a phenomenon that occurs when electrons are to enter a tiny conducting material. When the tiny conducting material, or metallic "island", is extremely small, the electrostatic potential of the island significantly increases even when only one electron enters it (see Fig. 4.54). For example, for a nanometer-scale island having a capacitance C of, say, 1 aF (10^{-18}F), the increase in the voltage, which is e/C with $e = 1.6 \cdot 10^{-19}$C, reaches 160 mV. This is much larger than the thermal noise voltage at room temperature, 25.9 mV. Coulomb repulsion prevents additional electrons from entering the island unless the island potential is intentionally lowered by an external bias. If the island potential is lowered gradually, the other electrons can enter the island one by one with negligibly small power dissipation (for details see [224, 240] and references therein). The single-electron transistor works as follows. The electron transfer is determined by two factors: the Coulomb charging of the dot and the quantized energy levels in the dot (see above). If the drain is biased with respect to the source, an electric current occurs in the regime of single-electron transfer. By applying the voltage to the gate and changing the QD parameters, one can change the conditions of electron tunneling and affect the source–drain current. Examples of modulation of the conductance in single-electron transistors by the gate voltage are presented in Figs. 4.55, 4.56. The devices have almost the same geometry (see also Fig. 6 in [239]). Their dimensions are large enough to have a number of quantized levels. In Fig. 4.56, each peak in the conductance corresponds to transfer of one electron, when an energy level enters into resonance with the electron states in the contacts. Although the conductance versus gate voltage dependencies are different, i.e., not reproducible, the peak spacing is the same for both devices. It is determined by the change in the gate voltage required to change the charging energy of the QDs by one electron. Figure 4.56 shows clearly that the electric current is modulated

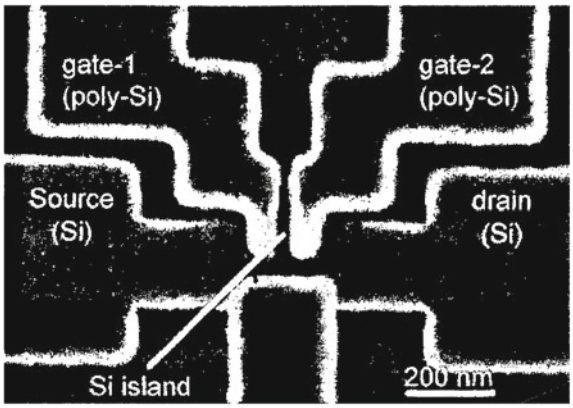

Fig. 4.55 A scanning electron microscope image of a single-electron transistor (after [224])

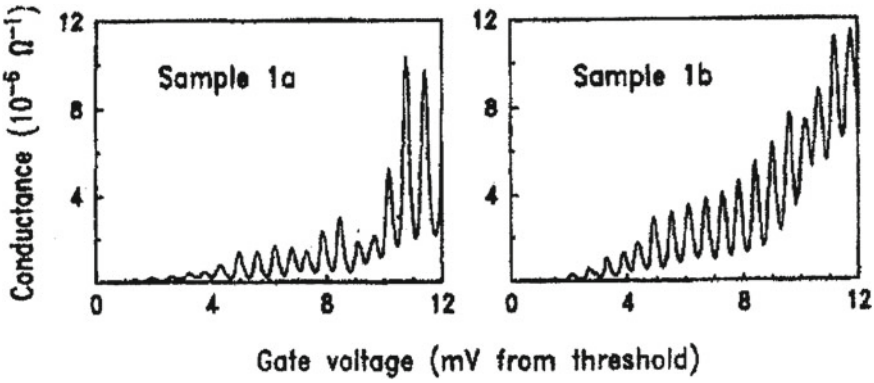

Fig. 4.56 Conductance as a function of V_g for two samples with the same geometry (after [223])

significantly by the gate voltage. Thus, for transistors with single-electron transport, strong control of very small electric current may be possible.

4.7.5 Graphene Quantum Dots Electronics

Quantum dots formed in semiconductor heterostructures have been studied extensively because they are considered promising candidates for applications in optoelectronics on the nanometer scale [24, 241, 242]. For instance, dots might be used in detectors, diodes, memory, and laser devices. Furthermore, single-electron transport devices which make use of quantum dots could be employed as transistors, and spin-based devices might be useful for quantum logic gates (see, e.g., [237]). Electrons confined in usual semiconductor dots, with a typical size of a few hundreds

of nanometers, are described by the Schrödinger equation and most of their electronic properties are now well understood and have been experimentally studied by many research groups (see [24] and references therein).

The physics of graphene quantum dots is very different from that in usual semiconductor dots [155, 157, 243–246]. The reason is twofold:

1. Charge carriers are massless and obey the relativistic $2D$ Weyl–Dirac equation

$$H\Psi_{1,2} = E\Psi_{1,2}, \tag{4.80}$$

$$H = -i\hbar v_{\mathrm{F}}(\sigma_y\sigma_x \mp \sigma_x\sigma_y) = \hbar v_{\mathrm{F}} \begin{pmatrix} 0 & -\partial_x \pm i\partial \\ \partial_x \pm i\partial_y & 0 \end{pmatrix}, \tag{4.81}$$

   which have dispersion as $\varepsilon_{k\pm} \propto \pm \mid \boldsymbol{k} - \boldsymbol{K}_i \mid$. These equations become invalid away from the cones [196]. The spinor wavefunction $\Psi_1(\Psi_2)$ corresponds to the electron states near the cone K(K'). The upper (lower) sign in (4.81) corresponds to $K(k')$. The low-energy physics of electrons in graphene is equivalent to four species of two-dimensional massless Dirac electrons: two different spin directions and two cones, K and k', giving overall fourfold degeneracy.
2. The different configurations of the carbon atoms at the boundaries of the dot affect significantly the dot properties.

There are two basic methods of defining a graphene quantum dot. In the first method, the dots are defined by the actual geometry of the graphene layer and they are usually referred to as graphene islands. In the second method, the dots are defined through the application of electric and magnetic fields. Of course, quantum dots can also be defined by combining these two methods and recently some other ideas have been put forward for dot formation, which, for example, include the application of strain to the graphene sheet, a spectral gap opening, and even chemical techniques [153–157, 206].

Before describing transport in graphene nanostructures we will briefly discuss Coulomb blockade in graphene. Early measurements of Coulomb resonances in thin graphitic flakes have been performed using highly resistive contacts such as tunneling barriers [247]. However, such devices are limited in terms of island size and barrier controllability. Using narrow graphene constrictions as tunneling barriers, some of these limitations can be overcome [155, 248, 249]. An example of a large graphene quantum-dot device (single-electron transistor (SET)) is shown in Fig. 4.57a. The island is connected to source and drain contacts via two narrow graphene constrictions. In addition to the silicon back gate (bg), in-plane graphene gates are used to locally tune the potential of the tunneling barriers (lg, rg) and the island plunger gate (pg). The current through the device as a function of bg is plotted in Fg. 4–57^{B} for low source–drain bias ($V_b = 250\,\mu\mathrm{V}$) and has been recorded at a temperature of $T = 1.7\,\mathrm{K}$. The measurement is dominated by the transport gaps of the two constrictions, separating hole—from electron transport (see also Fig. 4.57b).

Pronounced Coulomb blockade peaks are observed by changing the pg which acts mainly on the island potential Fig. 4.58a. By varying the bias voltage in addition to gate voltage and measuring the differential conductance, the charging energy

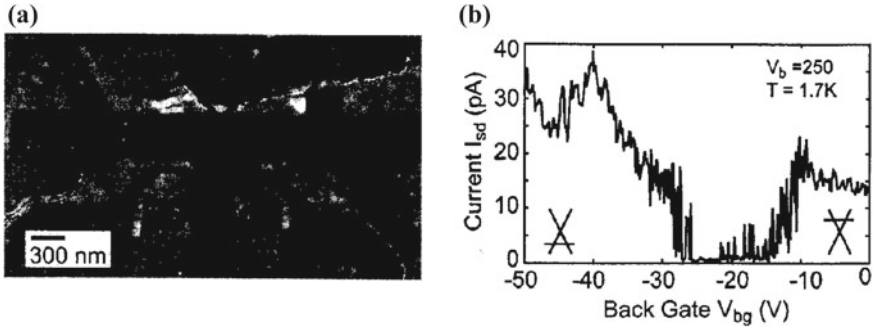

Fig. 4.57 **a** Graphene SET etched from a graphene sheet. The island is connected to source (s) and drain (d) over two narrow graphene constrictions tunable by the side gates lg and rg. The plunger gate (pg) is used to tune the dot and with the bg (not shown) the global potential is adjusted. **b** Source–drain current as a function of bg voltage. In between the hole and the electron transport, the barriers are closed due to the transport gaps in the constrictions (after [245])

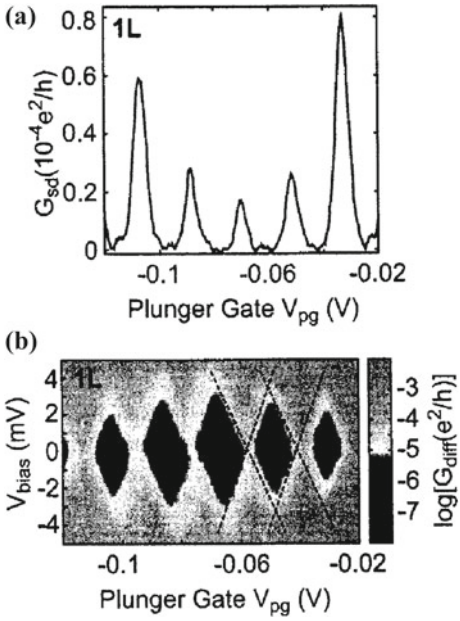

Fig. 4.58 **a** SET conductance as a function of pg voltage at low bias for the single-layer device. **b** Differential SET conductance as a function of pg and symmetrically applied bias voltage. In the diamond-shaped regions, the conductance is suppressed due to Coulomb blockade (after [248])

of the island can be estimated. The measurement is in Fig. 4.58b demonstrating so-called Coulomb diamonds of blocked conductance with a constant number of electrons on the dot. From the size of the diamonds a charging energy of $E_c \simeq 3.4\,\text{meV}$ is extracted which is in reasonable agreement with the size of the island and the electrostatic environment (for details see [248]). In summary, the possibility to tune the different parts of the device with side gates is important not only to adjust the barrier transmission but also for being able to separate parasitic effects

in the construction from Coulomb blockade on the dot. The separate identification is increasingly more difficult for smaller devices as the gates generally tune less selectively and the size and energy difference between the island and the localizations in the constrictions is reduced.

An all-graphene single transistor, exhibiting Coulomb blockade behavior, was operating well above liquid helium temperature [155]. The Coulomb blockade peaks are (nearly periodic as a function of gate voltage for large islands (>100 nm), and nonperiodic for small ones (<100 nm). The distance between the peaks is proportional to the sum of charging and confinement energies. The former, being typically constant for a specific dot geometry, dominates for large islands [155]. For small islands, the size quantization becomes important, and the confinement energy prevails, leading to nonperiodic peaks (see, e.g., Fig. 1 in [155]). The energy-level statistics of graphene islands was also probed, and it was shown to agree well with the theory of chaotic Dirac billiards [155]. In conclusion of this part, we should underline the new mechanism creation of quantum dots in graphene. As was shown early [157], very effective mechanism creation quantum dots in graphene is usage the mechanism of the neutron transmutation graphene. Thus, isotope creation of the quantum dots in graphene may throw light on the renormalization of the mass of massless fermion in graphene.

4.7.6 Light-Emitting Diodes and Lasers

Photonic devices are devices in which the basic particle of light—photon—plays a major role. In this section, we consider some photonic devices: light-emitting diodes (LEDs) and lasers (light amplification by stimulated emission of radiation) which convert electrical energy into photon energy. The dominant operating process of LEDs is spontaneous emission, for the laser diodes (LDs) it is stimulated emission, and for the photodetectors (see next paragraph) and the solar cells it is absorption. The recombination of electron and hole produces a photon with energy $\hbar\omega$ nearly equal to the bandgap energy (see below). The electrical input signal is generally modulated at high frequencies. This signal causes the direct modulation of the injected current in an LED. In recent years, certain organic semiconductors have been studied for electroluminescence applications. The organic light-emitting diode (OLED) is particularly for a multicolor. Various kinds of organic semiconductors have various bandgaps. Naturally, the optical emission and absorption of an OLED depend on its bandgap. The high-performance OLED was developed using the concept of multilayer structures.

So far, we have studied electronic nanoscale devices, i.e., a class of devices that exploit the electrical properties of nanostructures and operate with electric input and output signals. Another class is composed of optoelectronic devices, which are based on both electrical and optical properties of materials and work with optical and electric signals. In this paragraph, we will analyze two very important classes of optoelectronic devices: light-emitting diodes and lasers (diodes as well as photodetectors

—see below). These optoelectronic devices have a huge number of applications and deserve consideration in detail (see also [250–255]).

A light-emitting diode (LED) is an optoelectronic device which generates light via electroluminescence. It contains a p–n junction, through which an electric current is sent. In the heterojunction, the current generates electrons and holes, which release their energy portions as photons when they radiative recombine—the Lossev effect. Although the fundamental process of light generation is the same as in laser diodes, light-emitting diodes do not exhibit laser action, i.e., they usually do not exploit stimulated emission. Their optical spectrum is substantially wider (see Fig. 4.59). The color of the emission light (corresponding to the energy of the photon) is determined by the energy bandgap of the material (semiconductors, insulators, etc.). An LED is often small in area less than 1 mm^2. As in other diodes, current flows easily from the p-side, or anode, to the n-side, or cathode, but not in the reverse direction. Charge carriers–electrons and holes flow into the junction from electrodes with different voltages. The materials used for the LED have a direct bandgap with energies corresponding to near-infrared, visible, or near-UV light.

To produce light which can be seen the junction must be optimized and the correct materials must be chosen. Pure gallium arsenide releases in the infrared (IR) portion of the spectrum (see Fig. 4.59). To bring the light emission into the visible red end of the spectrum aluminum is added to the semiconductor to give aluminum gallium arsenide (AlGaAs). Phosphorus can also be added to give red light. For other colors, other materials are used. For example, GaP gives green light and aluminum indium gallium phosphide is used for yellow and orange light. Most LEDs are based on gallium semiconductor.

Although stimulated emission from the injection laser diode is very important (see below), practically, subthreshold operation of the diode—when only spontaneous light is emitted—is in many cases advantageous and has a number of applications. The important characteristic of the LED is the spectral distribution of emission The spectrum of emission is determined, primarily, by the electron/hole distributions. Thus, the ambient temperature, T, defines both spectral maximum and the spectral width of emission. The peak value of the spectral distribution can be estimated as [10, 227]

$$\hbar\omega = E_g + \frac{k_B T}{2}. \tag{4.82}$$

The full width at half-maximum of the distribution is $\Delta\omega \approx 2k_B T/\hbar$ and is independent of ω. In terms of the wavelength, λ, we obtain

$$\begin{aligned} \Delta\lambda &= \left[\lambda_m^2/(2\pi c)\Delta\omega\right] \\ \text{or} \quad \Delta\lambda &= 1.45\lambda^2 k_B T, \end{aligned} \tag{4.83}$$

where λ_m corresponds to the maximum of the spectral distribution, $\Delta\lambda$ and λ_m are expressed in micrometers, and k_BT is expressed in eV. Figure 4.60 shows the spectral density as a function of the wavelength for light-emitting diodes based on various materials. For these different materials, the spectral line width increase in proportion

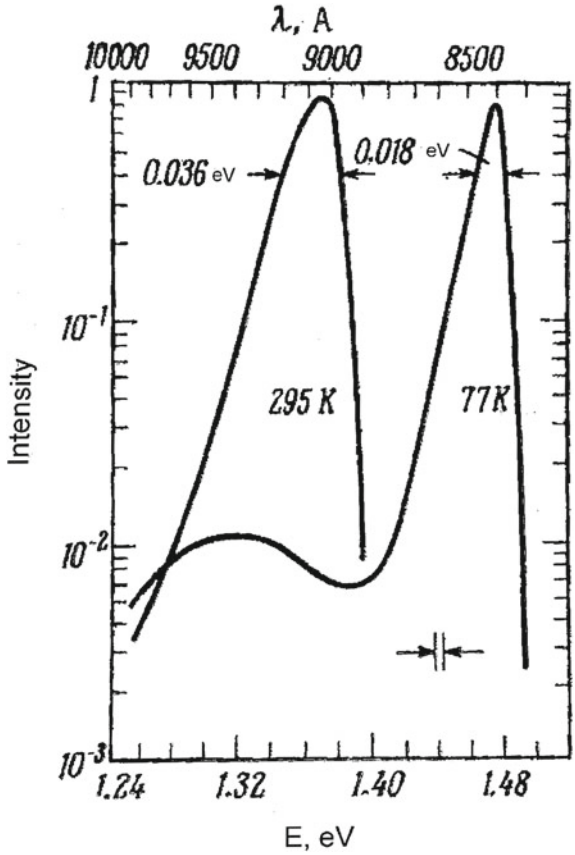

Fig. 4.59 Spontaneous emission spectra of GaAs LED at two temperatures (after [250])

to λ^2, in accordance with (4.83). From Fig. 4.60, one can see that light-emitting diodes cover a wide spectral region from the infrared—about 8 μm for InGaAsP alloys—to the near ultraviolet −0.4 μm for GaN, and to UV ∼5.47 eV from isotope-based diamond LED [34, 36]. Light-emitting diodes are, indeed very universal light sources [24].

Powerful and easy-to-use lasers operating in the mid-IR range, 2–5 μm, are very important for a variety of military, biomedical, environmental, and industrial applications including range-finding, laser surgery, and remote trace gas sensing. The first successful mid-IR (2–5 μm) laser was with double-heterojunction structure active region (Fig. 4.61). But poor performance, such as high threshold current, low output power, and low maximum operating temperature, of such lasers restricted their applications [251]. However, using quantum well (QW) in the active region of the laser enhanced the devices performance [252–255]. Nevertheless, semiconductor lasers based on interband transition of QW active region structure are difficult to achieve long-wavelength lasing 3.5 μm$\leq \lambda \leq$ 5.0 μm. So, mid-IR emission quantum cascade (QC) structure was proposed [256, 257] for developing wavelength

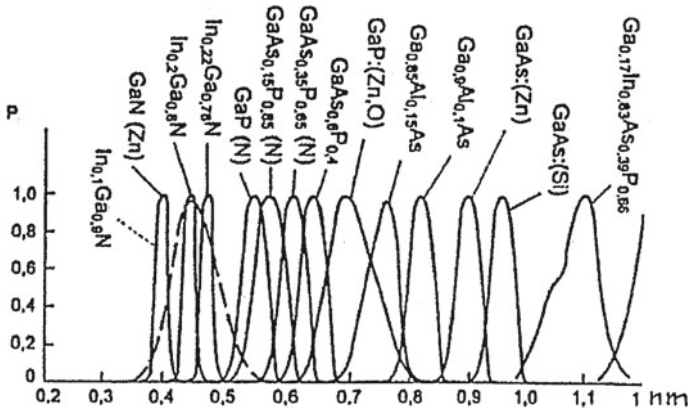

Fig. 4.60 The spectra of light-emitting semiconductor diode with different bandgaps (after [222])

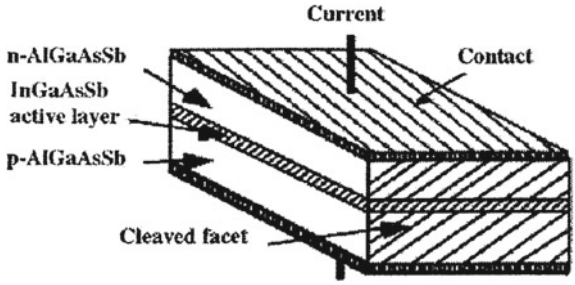

Fig. 4.61 Schematic diagram of double-heterojunction laser diode

mid-IR lasers. Semiconductor QC structure opens the new quantum structure engineering for designing mid-IR lasers emitting at longer wavelength region $3.5\,\mu m \leq \lambda \leq 5.0\,\mu m$. QC lasers rely on the electrical injection due to the large mobility of electrons. Repeated QC structures allow recycling of the electrons to increase the optical gain, which makes these lasers reach the quantum efficiency above 100% [258].

Semiconductor lasers are similar to the solid-state ruby laser and helium–neon gas laser in that the emitted radiation is highly monochromatic and produces a highly directional beam of light. However, laser differs from other lasers in that it is easily modulated at high frequencies simply by modulating the biasing current. Because of these unique properties, the semiconductor lasers is one of the most important light sources for optical-fiber communication. It is also used in video recording, optical reading, and high-speed laser printing. All lasing semiconductors have a direct bandgap. At the present, the laser emission wavelength covers the range from 0.3 to over $30\,\mu m$. In the double heterostructure laser, the carriers are confined on both sides of the active region by the heterojunction barriers, whereas in the homojunction laser the carriers can move away from the active region, where radiative recombination occurs. We should remind that a homojunction laser has the same semiconductor material (e.g., GaAs on both sides of the junction. The structure of a QW laser is

similar to that a double heterostructure laser except that the thickness of the active layer in a QW laser is very small, about 10–20 nm [251, 252]. In quantum-wire and quantum-dot lasers, the active regions are reduced to the de Broglie wavelength regime, into 1D (one dimension) (wire) or D (zero dimension) (island) formation. These wires and dots are placed between a p–n junction.

At present time, semiconductor lasers incorporating low-dimensional heterostructures, quantum wires (QWr) and quantum dots (QDs), are attracting considerable interest of their potential for improved performance over QW lasers (see, e.g., [254, 255, 259]). This prediction is based, in the single-particle picture, on the sharper density of states resulting from the confinement of the charge carriers in two or three directions. Among other advantages, the ideal QD and QWr lasers would exhibit higher and narrower gain spectrum, low threshold currents, better stability with temperature, lower diffusion of carriers to the device surfaces, and a narrower emission line than double heterostructure or QW lasers (see also [260]). The observation of lasing from excitons in optically excited V-groove GaAs/AlGaAs QWr laser structures was described in detail [261]. The observable emission is attributed to the recombinations of excitons associated with the lowest energy electron—and hole—subbands of the QWr. Moreover, these authors show that the emission energy remains nearly constant within the inhomogeneously broadened photoluminescence line of the QWrs for both continuous wave (CW) and pulsed optical excitation over a wide range of power densities. These results corroborate the important role played by electron–hole Coulomb correlations [262] in the optical emission from quasi-1D QWrs in the density regime of the Mott transition.

Optical emission of the QWr laser structure are displayed in Fig. 4.62 for different values of the optical power density below, at and above the threshold for lasing in the QWr. Upon increasing the pump power, these authors observe a nearly constant energy of the peak at 1.581 eV that corresponds to the optical transition $e_1 - h_1$ associated with the ground electron–hole–subband of the QWrs. A significant spectral narrowing is also found as the power density is increased and crosses the lasing threshold. This evidences the existence of amplified spontaneous emission within this inhomogeneously broadened PL line in this density regime. The observable emission intensity varies linearly at low excitation power over three orders of magnitude (from 0.1 to 100 mW) [263]). Above the lasing threshold (at 350 mW) the intensity variation is again linear (see Fig. 4.62b), indicating that the modal gain is saturated. In Fig. 4.62c, a high-resolution emission spectrum obtained above threshold features well-resolved Fabry–Perot modes that correspond to different longitudinal optical modes within the inhomogeneous line of the QWr-PL. Detailed investigations of PL and PLE spectra (see Fig. 4.63) of the QWr allowed the indicated authors to conclude that the lasing emission originates from the recombination of excitons as it is the case for the QWr-peak of the cw-PL spectrum (for details see [263]).

In QDs, as indicated above, carriers are confined in the three directions in a very small region of space, producing quantum effects in the electronic properties. As we can see in Chap. 2, the electronic joint density of states for QD shows sharp peaks corresponding to transitions between discrete energy levels of electrons and holes. Outside of these levels, the DOS vanishes. In many ways, the electronic structure of

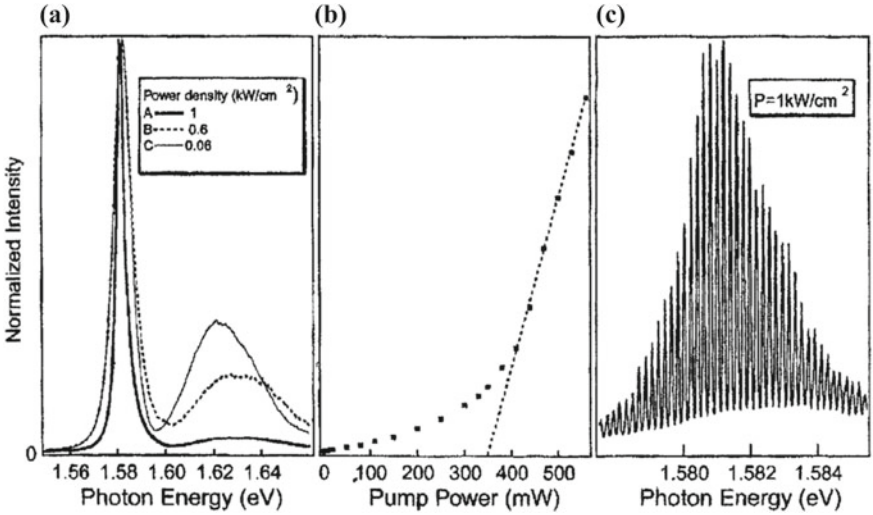

Fig. 4.62 **a** Photoluminescence spectra at 10 K of the QWr laser sample above, below, and near the lasing threshold in TE-polarization. **b** Dependence on input excitation power of the PL output power; arrows indicate the excitation powers used for the optical spectra depicted in **a**. **c** High-resolution emission spectrum above the lasing threshold showing the Fabri–Perrot modes of the optical cavity (after [263])

a QD resembles that a single atom [235]. Lasers based on QDs could have properties similar to those of conventional ion gas lasers, with the advantage that the electronic structure of a QD can be engineered by changing the base material, size and shape. In the next, we assume that the QDs are small enough so that the separation between the first two electron energy levels for both electrons and holes is much larger than the thermal energy KT. Then, for an undoped system, injected electrons and holes will occupy only the lowest level. Therefore, all injected electrons will contribute to the lasing transitions from the E_{1e} to the E_{1hh} levels, reducing the threshold current with respect to other systems with lower confinement. Emission spectra from nanowire arrays of ZnO below and above the lasing threshold are demonstrated in Fig. 4.64. It is clear seen UV stimulated emission. Isotope substitution in ZnO will done more wide lasing spectrum [30]. The evolution of the threshold current density obtained along the years for various laser structures is shown in Fig. 4.65. The lowest threshold currents have already been reached for QD lasers [7]. As long as the thermal energy is lower than the separation between the first and second levels, the emission band in an ideal QD laser is very sharp and does not depend on temperature (see also [255, 259]). Therefore, QD lasers should have a better stability with temperature without the need for cooling. We should add that QDs have the narrowest spectrum and the highest gain (for details see also [10, 227, 255]).

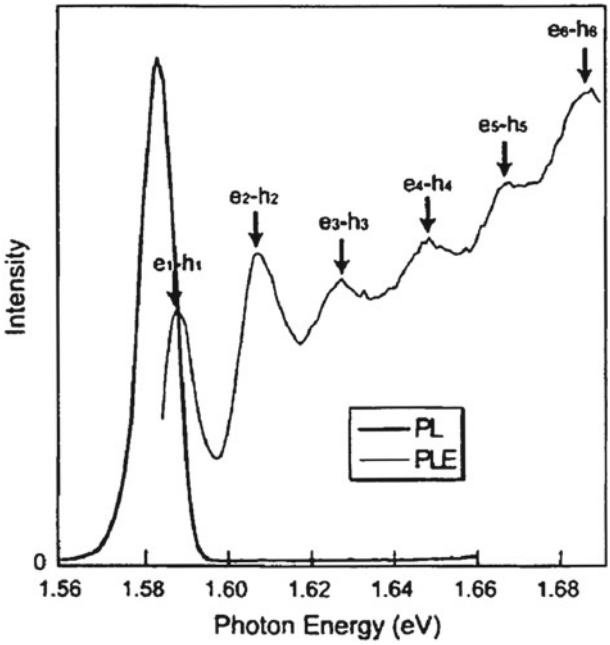

Fig. 4.63 Linearly polarized PLE spectrum and the corresponding PL spectrum of an etched QWr laser sample at 10 K. The polarization of the excitation is parallel to the wire axis. The different optical transition e_n - h_n are marked by arrows (after [263])

4.7.7 Radiation Detectors

Photodiode is a semiconductor diode that produces a significant photocurrent when illuminated. Photodetectors with sufficiently fast response that provides a measurable output for a small amount of light are easily reproducible and are economical, which are worth investigating for applications in high-speed optical communications. This category includes avalanche photodiodes (APDs) and positive intrinsic negative photodiodes (PINs). The PIN photodiode includes an intrinsic layer in between the P- and N-type materials. The PIN must be reverse bias due to the high resistivity of the intrinsic layer; the PIN has a larger depletion region which allows more electron–hole pairs to develop at a lower capacitance. The illumination window for a PIN is on the P-side of the diode because the mobility of electrons is greater than holes which results in better frequency response.

An avalanche photodiode is operated at reverse bias close to the breakdown, which causes photoexcited charge carriers to accelerate in the depletion region and produce additional carriers by avalanching (see Fig. 4.66). The avalanche photodiodes are good for fiber-optic systems that require low light levels with quantum efficiency larger than 100%. The APD is a semiconductor device that, when reverse-biased, creates strong fields in the junction region. When a photon causes an electron–hole

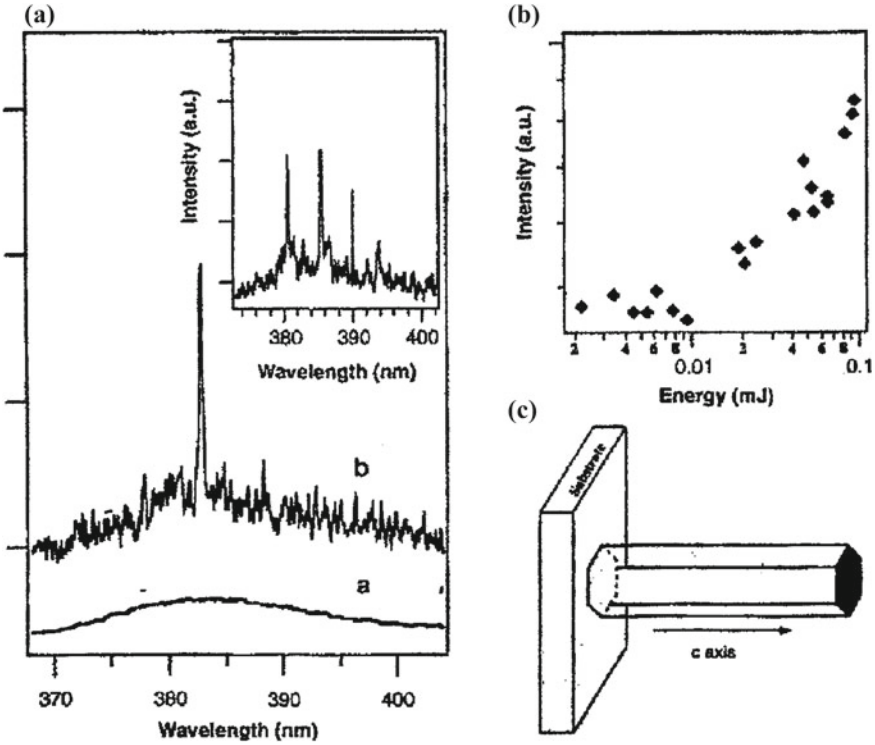

Fig. 4.64 **a** Emission spectra from nanowire arrays below (line a) and above (line b and inset) the lasing threshold. The pump power for these spectra is 20, 100, and 150 kW/cm, respectively. The spectra are offset for easy comparison. **b** Integrated emission intensity from nanowires as a function of optical pumping intensity. **c** Schematic illustration of a nanowire as a resonance cavity with two naturally faceted hexagonal end faces acting as reflecting mirror. Stimulated emission from the nanowires was collected in the direction along the nanowire's end-plane normal (the symmetric axis) with a monochromator combined with a Peltier-cooled charge-coupled device. The 226-nm pump beam was focused to the nanowire array at an angle 10° to the end-plane normal. All experiments were carried at room temperature (after [264])

pair, the pair flows through the junction. Because of the strong fields in the junction, the electron gains enough energy to cause secondary electron–hole pairs, which in turn cause more. Thus, a multiplication (or avalanche) process takes place (hence the name), and a substantial current is generated from few initial photons. The gain M of an APD is expressed by

$$M = I_{\mathrm{APD}}/I_{\mathrm{primary}}, \tag{4.84}$$

where I_{APD} is the APD output current and I_{primary} is the current due to photon–electrons conversion (see, e.g., [265–267]). However, during this multiplication

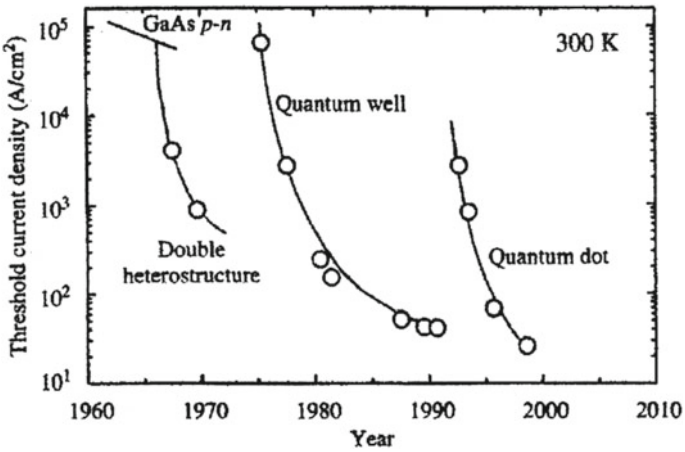

Fig. 4.65 Evolution of threshold current density for lasers based on different confinement structures (after [7])

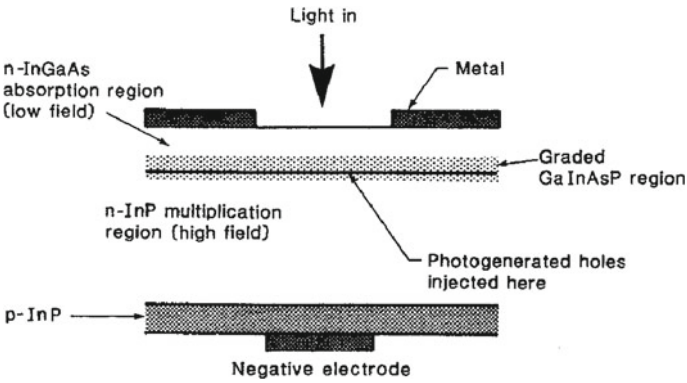

Fig. 4.66 Schematic diagram of the separate absorption and multiplication avalanche photodiode for 1.3–1.6 μm operation (after [267])

process, shot noise is multiplied as well and is estimated as 2eIM2p, where P is the APD noise factor.

If $\tau^{\sim}$ is the effective transit time through the avalanche region, the APD bandwidth is approximated as

$$B_{\mathrm{APD}} = \frac{1}{2pM\tau}.$$

Photodiodes are mainly made from gallium arsenide (see Table 4.10) instead of silicon because silicon creates crystal lattice vibrations called phonons when photons are absorbed in order to create electron–hole pairs. Gallium arsenide can produce

Table 4.10 Operating wavelength ranges for several different photodetector materials

Material	Energy gap, eV	λ_{cutoff}, nm	Wavelength range, nm
Si	1.17	1060	400–1060
Ge	0.775	1600	600–1600
GaAs	1.424	0.870	650–870
InGaAs	0.73	1700	900–1700
InGaAsP	0.75–1.35	1650–920	800–1650

electron–hole pairs without the slowly moving phonons; this allows faster switching between on and off states and GaAs also is more sensitive to the light intensity. Once charge carriers are produced in the diode material, the carriers reach the junction by diffusion. Important parameters for the photodiode include quantum efficiency, current, and capacitance which will be covered in the equations section.

In principle, QWs can be used for the detection of light in any spectral region. As we all know the optical properties to interband transitions in QWs are quite different than those corresponding to bulk materials, since one has to consider both the $2D$ optical density of states (see Chap. 2) and the fact that excitonic absorption is much stronger in $2D$ systems. With respect to intraband transitions, in contrast to the $3D$ situation, $2D$ systems can show transitions without the necessity of involving phonons. Intraband transitions can be among electrons (or holes) in confined states in wells, or between confined states and the continuum (see Fig. 4.67). These transition can be tailored for detection of light (IR photodetectors [10, 139, 140]. Thus, it is in the IR region between 2 and 20 microns that QW photodetectors are preferably used, for example, in applications of night and thermal imaging (see also [139, 266, 268]). The problem with photodiodes based on band-to-band transitions across the bandgap E_g in p–n homojunctions is that they require materials with very low values of E_g, which makes it necessary to work at cryogenic temperatures. For instance, in the case of III–V compounds, this leaves us with $InAs_{1-x}Sb_x$ with $x \approx 0.5$. Some A_2B_6 compounds like HgCdTe can also be used in the IR, but these materials are quite soft, difficult to process, and have large dark currents. Very perspective as QW photodetectors is isotope-mixed germanium as well as other isotope-mixed materials. In QWs, wavelength tunability is easily implemented since the energies of the levels in a QW can be adjusted by the fabrication parameters, in particular its width. Figure 4.67 shows the absorption transitions suitable for IR detection for a single QW under the action of an applied electric field, although practical devices are made with MQWs. In Fig. 4.67a, there are two energy levels in each well, the second level being located close to the top of the barriers. The separation between levels should be in the range 0.1–0.2 eV, which for III–V compounds implies a width of the wells about 10 nm [10, 268]. Sometimes, it is more effective to make use of absorption transitions between a single level in the well and the first continuum narrow band outside it (Fig. 4.67b). In the case of the system AlGaAs–GaAs–lGaAs, this energy is about 0.12 eV, and therefore, the spectral response is around 10 μm

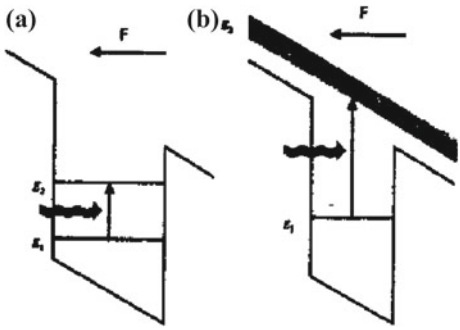

Fig. 4.67 Optical absorption transition for IR detection in a QW: **a** intersubband transitions; **b** transition from a bound state to the continuum narrow band outside the potential wells. F is the applied electric field (after [215])

[139]. The advantage of using this scheme is that the photodetector dark current is smaller than for the previous case in which the carriers had to leave the walls by tunneling (for details see [10]).

It is known [268] that avalanche photodetectors based on semiconductors can present a high level of noise if precaution is not taken. The noise can be gradually reduced if the avalanche multiplication coefficient, M, is much larger for one of the carriers, for instance, electrons, in comparison to the other carrier (hole) multiplication coefficient. In this sense, silicon is a very appropriate semiconductor for avalanche photodetectors, since the ratio M_e/M_h has a value of about 30 [140]. For a given material, the ratio M_e/M_h is practically fused by the semiconductor band structure [268]. QW, on the other hand, allow a design control M_e/M_h. For example, a superlattice or MQW structure can be designed such that the conduction band discontinuities ΔE_c are much larger than the ΔE_v ones corresponding to the valence band. In this way, the electrons gain much more kinetic energy than the holes when they cross the band discontinuity. The same objective can be achieved by design of a staircase profile superlattice for which the bandgap is graded in each well. In this case, the electrons have an extra kinetic energy ΔE_c when they enter the next quantum well. This extra energy makes the impact ionization phenomenon very efficient so that electron avalanche is easily generated under the action of an electric field F. Most superlattice APDs with very low noise figures are based on III–V compounds such as GaAs or InP.

4.8 Isotope-Based Quantum Computers

4.8.1 General Remarks

Within the past three decades, the focus of the research on the fundamental aspects of quantum theory has been shifted from esoteric and philosophical to more "down to earth" as a result of the understand the nature of the quantum information [23]. Therefore, quantum mechanics has had an enormous technological and social impact. To appreciate this point, it is sufficient to consider the invention of the transistor,

perhaps the most remarkable among the countless other application of quantum mechanics. On the other hand, it is easy to see the enormous impact of computers on every life. The importance of computers is such that it is appropriate to say that we are now living in the information age. This information revolution became possible thanks to the invention of the transistor, that is, thanks to the synergy between computer science and quantum physics. Today, this synergy offers completely new opportunities and promises exciting advances in both fundamental science and technological application. We are referring here to the fact that quantum mechanics can be used to process and transmit information. Information is quantized in classical digital information processing as well as in quantum information processing. As is well known [269, 270] in analogy to the classical bit, the elementary quantum information processing is called a qubit [271]. Any two distinct states of a quantum system can be used as qubit (see Fig. 3.4 in Chap. 3 [237]). The two main concepts in quantum computing are the qubit and the unitary logic gate (see also [272]). The main insight into quantum computing is to represent numbers in a register consisting of a row of cells where each cell, instead of strong a 0 or 1 as in a classical computer, is represented by a two-level quantum system in a superposition state. We will see how in this way a quantum register can hold a superposition of all numbers from $0...2^n - 1$, where n is the number of cells in the register.

A register consisting of n qubits can store numbers from 0 to $2^n - 1$. To specify this state requires 2^n complex numbers or 2^{n+1} real numbers. To store them with a precision of one byte on a classical computer would require the same number of bytes. So the state of a 50-bit quantum computer would require $2^{51} = 2.25 \cdot 10^{15}$ bits ($\sim$2 million gigabytes) of memory on a classical computer. Since the evolution of quantum systems is determined by unitary transformation [269, 270] any set of operations carried out on a quantum computer will have to be reversible (see, e.g., [273]). That means we will have to redesign many classical logic gates to perform the logical operations reversibly. For example, a classical AND gate is irreversible (it is in general impossible to reconstruct the input from the output) so one needs to find a reversible system that is logically equivalent. What is called a logic gate in quantum computing is just a series of rotations of the spin 1/2 system representing a qubit [237]. The power of quantum computers is due to typical quantum phenomena, such as the superposition of quantum state and entanglement [237]. There is quantum parallelism associated with the superposition principle. In simple terms, a quantum computer can process a large number of classical inputs in a single run. On the other hand, this implies a large number of possible output. In short, to be useful, quantum computers require the development of appropriate quantum software, that is, of efficient quantum algorithms.

4.8.2 Current Status: The Di Vincenzo Criteria

In this part, we consider the five criteria of Di Vincenzo [274] checklist, which must all be satisfied for any physical implementation of a quantum computer. We have

written about these five criteria of the Di Vincenzo before [23, 237] but they are worth considering in detail here again, since we have found that these criteria provide a unifying framework for these investigations which encompass in astonishingly broad and rich range of fundamental physics.

1. A scalable physical system with well-characterized qubits that means a well-defined Hilbert space [269, 270] within which to represent quantum information.

To start with, a scalable physical system with well-characterized qubits is needed. In order to build a quantum computer with many qubits, we need some physical system that:

(a) allows us to implement such qubits, and

(b) accommodates a sufficiently large number of them. Actually, point a) is not quite that obvious. After all, we know that quantum computers rely on quantum effects, and in everyday life, such effects are almost always negligible. So we already know that the system we are looking for must allow us to tap into the quantum world, and that means our candidates for qubits presumably have to be very small, possibly on the scale of individual particles that obey the rules of quantum physics, such as photons, electrons, excitons, atoms (ions), and so forth.

As for point (b), we will see that in some cases, one can find systems that can very successfully hold a handful of qubits but can not be extended to accommodate tens or even hundreds of them. Scalability is, therefore, one of the major obstacles in many realizations of quantum computation.

2. Initialization of the qubits to a known (pure) state.

The second of the Di Vincenzo criteria looks even more obvious, but in fact is very subtle. Clearly, in order to perform a calculation, we must first have a "blank state" to write our input on, such as a number we want to factorize. In classical computers, this simply means flushing the memory and writing a "0" in each memory element. In the quantum world, however, things are not quite that simple, and we really have to make sure that each qubit is in the quantum state $|0\rangle$, which can involve rather complicated manipulations [269, 270].

3. Qubit readout. It means a performing arbitrary unitary transformation on the state of the qubits (typically by implementing arbitrary single-qubit operations and at least one nontrivial two-qubit operation).

(3) One way to classifying the range of systems involved is to consider the range of timescales available for manipulation of quantum computation, corresponding to the range of excitation energies ΔE and corresponding timescales $\hbar/\Delta E$. So what exactly is a long decoherence time? Seconds, minutes? Or might millisecond already be enough? The answer is it depends. And what it depends on is, not surprisingly, the times it takes to complete a calculation, or a part of it. Since quantum calculations are made up of lots of quantum logic gates, it all boils to a simple equation. If we call $t_{\text{decoherence}}$ the time in which a quantum state is destroyed due to decoherence and t_{gate} the time it takes to run the state through a quantum logic gate, then quantum computation is possible if

$$t_{\text{decoherence}} > t_{\text{gate}}. \tag{4.85}$$

It is a bit like in a battle: nobody will ever be strong enough to fight forever—it is enough to last just a little longer than the enemy. As will be shown below, the long decoherence time (of the order of a second) of liquid state NMR is one of its biggest advantages. However, typical gate times are at least several milliseconds, so the number of gates that can be applied is limited to approximately 100 (for details see [269, 270] and Table 4.11).

4. Long coherence time, in other words, avoiding decoherence for long enough to compute.

5. Some means of reading out the state of the qubits at the end of the calculation.

(4, 5) The fourth and last of Di Vincenzo's criteria states that it is necessary to be able to perform high quantum efficiency, qubit-specific measurements. "High quantum efficiency" means that when one makes a measurement, one is very likely to actually get an answer. Similar requirements apply, for instance, to quantum cryptography (see above). There it is necessary to have photodetectors that register an arriving photon with a high probability. Likewise, in quantum computing the end result is read out from the qubit by a quantum measurement, and if such a measurement fails to give a result, that is bad news. Finally, qubit-specific means that if one has a quantum computer with, say, ten qubits and one wants to read out the state of qubit number 5, then one should actually read out the state of that specific qubit and not of qubit number 4 or 6. Again, this may sound pretty obvious, but practice this can be a big obstacle.

According to the modern definition, quantum computer is the device if it obeys the following criteria: any quantum computer must consist of a quantum memory, with additional structure that

1. facilitates a controlled quantum evolution of the quantum memory;
2. includes a method for information theoretic cooling of the memory; and
3. provides a readout mechanism for subsets of the quantum memory. The criteria are met when the device is scalable and operates fault tolerantly (for details see [275]).

4.8.3 Elementary Gates for Quantum Computation

The field of quantum information science is a juxtaposition of two great scientific advents of the twentieth century: quantum mechanics and information theory. The evolution of nano- and optoelectronic devices [13, 139] and the associated digitization of information has relied on improvements in the fabrication of materials that have led to ever smaller and faster components. Then, the size, in particular, has allowed more components to be packed onto a chip, thus making them more powerful by integrating more functions. Simultaneously, the decrease in size is a prerequisite for making faster devices, as long as they rely on a fixed, system-wide clock. As early as 1965, Moore [276] noticed that the number of components that could be placed on a chip had grown exponentially over many years, while the feature size had shrunk

Table 4.11 Important times for various two-level systems in quantum mechanics that might be used as quantum bits, including prospective qubits ranging from nuclear physics, through atomic, electronic, and photonic systems to electron and nuclear spin. The time t_{switch} is the minimum time required to execute one quantum gate; it is estimate as $\hbar/\Delta E$, where ΔE is the typical energy splitting in the two-level system; the duration of a π tipping pulse cannot be shorter than this uncertainty time for each system. The phase coherence time as seen experimentally, t_Φ, is the upper bond on the length of time over which a complete quantum computation can be executed accurately. The ratio of these two times gives the largest number of steps permitted in a quantum computation using these quantum bits (after [274])

Quantum system	t_{switch} (s)	t_Φ (s)	Ratio
Mössbauer nucleus	10^{-19}	10^{-10}	10^9
Electrons: GaAs	10^{-13}	10^{-10}	10^3
Electrons: Au	10^{-14}	10^{-8}	10^6
Trapped ions: In	10^{-14}	10^{-1}	10^{13}
Optical microcavity	10^{-14}	10^{-5}	10^9
Electron spin	10^{-7}	10^{-3}	10^4
Electron quantum dot	10^{-6}	10^{-3}	10^3
Nuclear spin	10^{-3}	10^4	10^7

at a similar rate. This trend continued over the next 40 years and is expected to do so for the foreseeable future.

Figure 4.68 shows the current expectation: it represents the projections that the semiconducting industry association makes for the coming decade. As shown in Fig. 4.68 the feature size of electronic devices is now less than 100 nm and decreasing at a rate of some 12% per year [13]. This trend could in principle continue for another forty years before the ultimate limit is reached, which corresponds to the size of atom. Much before this ultimate limit, however, the feature size will become smaller than some less well-defined limit, where the electrons that do the work in the modern devices, will start to show that their behavior is governed by quantum mechanics, rather than the classical physical laws that are currently to describe their behavior (see also [277]).

In quantum mechanics, there are some basic principles: such as the correspondence principle, Heisenberg's uncertainty principle, or Pauli's principle that encode the fundamentals of that theory. The knowledge of those principles provides us with the essential understanding of a quantum mechanics at a glance, without going into the complete formalism of that subject (see, e.g., [278]). A similar thing happens either other areas in physics. In *computer science*, there are guiding principles for the architecture of a computer (hardware) and the programs to be run (software) [269, 270]. Likewise, in quantum computing we have seen that there are basic principles associated with the ideas of quantum parallelism (superposition principle) and quantum programming (constructive interference). By principles of quantum computation, we mean those rules that are specific to the act of computing according to the laws of quantum mechanics. As was mentioned above, that the quantum version

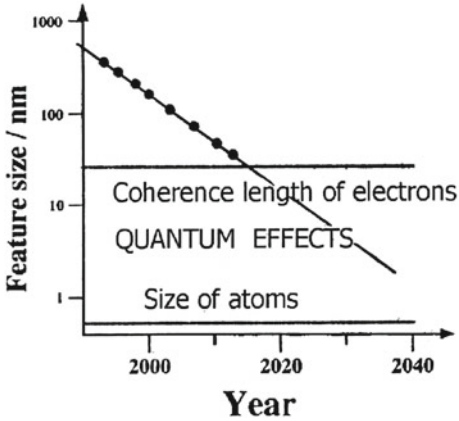

Fig. 4.68 Prospective evolution of feature size in microelectronic (nanoelectronics) circuits (after international semiconductor association roadmap)

of parallelism is realized through the superposition principle of quantum-mechanical amplitudes, likewise the act of programming a quantum computer should be closely related to a constructive interference of those amplitudes involved in the superposition of quantum states in the register of the computer (for details see [279, 280]).

It is well known that a small set of elementary logic gates allows the implementation of any complex computation on a classical computer. This is very important: it means that, when we change the problem, we do not need to modify our computer hardware. Fortunately, the same property remains valid for a quantum computer. It turns out that, in the quantum circuit model, each unitary transformation acting on a many-qubit system can be decomposed into gates acting on a single qubit and a single gate acting on two qubits, for instance, the CNOT gate (see below). We should stress that a key step toward the realization of the practical quantum computer is to decompose its functioning into the simplest possible primitive operations or gates (see also [279, 280]). In any computation, we must provide an n-bit input to recover an l-bit output. Namely, we must compute logical function of the next form: f: $\{0, 1\}^n \longrightarrow \{0, 1\}^l$. As we shall show in this section, the evaluation of any such function may be decomposed into a sequence of elementary logical operations. First of all, we introduce a few logic gates that are useful for computation. In order to encode a message written in binary code using a one-time pad, we saw that it was sufficient to perform an addition modulo 2 on each pair of digits in the message and in the key. Equivalently, we could apply the logic function XOR on these pairs [279]. Apart from XOR, there are a number of other such functions like NOT, OR, AND, and NAND that act on one or two bits and return one bit as an output. The action of these functions can be summarized in truth tables in which the possible combinations of inputs and outputs are listed. Obviously, one can build more complicated combined gates by applying, for instance, an AND operation to two bits, then another logic gate to the result of that operation, and so forth. In that way, large inputs can be processed step-by-step to produce an output. Such successions of logic gates are called logic circuits.

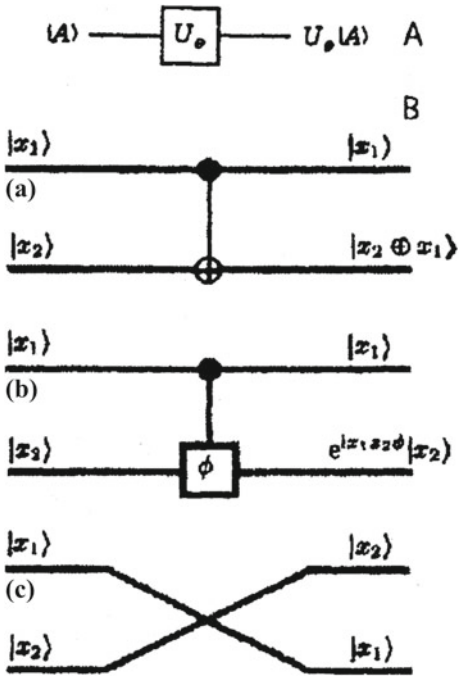

Fig. 4.69 A—Example of a unitary gate; B—quantum binary *gates*: **a** CNOT gate, **b** CPHASE gate, and **c** SWAP gate (after [272])

A universal gate such as NAND (in classical computers) operates locally on a very reduced number of bits (actually two). However, by combining NAND gates in the appropriate number sequence, we can carry out arbitrary computations on arbitrary many bits. This was very useful in practice for it allowed device, leaving the rest to the circuit designer. The same rationale applies to quantum circuits. When a quantum computer is working it is a unitary evolution operator that is effecting a predetermined action on a series of qubits. These qubits form the memory register of the machine, or a quantum register. A quantum register is a string of qubits with a predetermined finite length. The space of all the possible register states makes up the Hilbert space of states associates with the quantum computer. A quantum memory register can store multiple sequences of classical bits in superposition. This is a manifestation of quantum parallelism. A quantum logic gate is a unitary operator acting on the states of a certain set of qubits (see also Fig. 4.69a). If the number of such qubits is n, the quantum gate is represented by a $2^n \times 2^n$ matrix in the unitary group $U(2^n)$. It is thus a reversible gate: we can reverse the action, thereby receiving the initial quantum state from final one. One qubits are the simplest possible gates because they take one input qubit and transform it into one output qubit. The quantum NOT gate is a one-qubit *gate* (Fig. 4.69a). Its unitary evolution operator U_{NOT} is [280]

$$U_{\text{NOT}} = \begin{bmatrix} 0 & 1 \\ 1 & 0 \end{bmatrix}. \tag{4.86}$$

a	$\overline{a}$
0	1
1	0

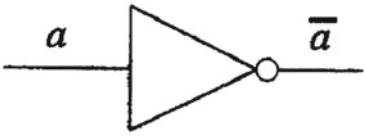

Fig. 4.70 The truth table and circuit representation for the identity gate

The action of a unitary operator U_{NOT}on a quantum state $|\Psi\rangle = a\,|0\rangle + b\,|1\rangle$ or write in matrix notation as $|\Psi\rangle = \begin{bmatrix} a \\ b \end{bmatrix}$ (see also [237, 281])

$$|\Psi\rangle_{\text{final}} = U\,|\Psi\rangle_{\text{initial}} \tag{4.87}$$

can be calculated by standard matrix multiplication. For example, the output state obtained after applying U_{NOT} to $|\Psi\rangle = .\begin{bmatrix} a \\ b \end{bmatrix}$ is

$$U_{\text{NOT}}\,|\Psi\rangle = \begin{bmatrix} 0 & 1 \\ 1 & 0 \end{bmatrix} \cdot \begin{bmatrix} a \\ b \end{bmatrix} = \begin{bmatrix} b \\ a \end{bmatrix}, \tag{4.88}$$

which is state vector corresponding to the state a$|\,1\rangle + b\,|\,0\rangle$ (for details see [272, 281]).

Another one-qubit gate without analog in classical circuity and heavily used in quantum computers is the so-called Hadamard (H) gate [279, 280]. This gate is defined as

$$U_{\text{H}} = \frac{1}{\sqrt{2}} \begin{bmatrix} 1 & 1 \\ 1 & -1 \end{bmatrix}. \tag{4.89}$$

This gate transforms the computational basis states into the equal superposition states, and back

$$|\,0\rangle \leftrightarrow^{\text{H}}\leftrightarrow \frac{|\,0\rangle + |\,1\rangle}{\sqrt{2}} \quad \text{and} \quad |\,1\rangle \leftrightarrow^{\text{H}}\leftrightarrow \frac{|\,0\rangle - |\,1\rangle}{\sqrt{2}}. \tag{4.90}$$

The Hadamard gate corresponds to a rotation over 180° about an axis halfway between the $\widehat{x}$ and the $\widehat{z}$ axes. The NOT corresponds to a 180° rotation about the $\widehat{x}$ axis, up to an overall phase factor, which is irrelevant (see also Figs. 4.70, 4.71, 4.72, 4.73, 4.74 and 4.75).

The XOR (exclusive OR), or CNOT (controlled NOT) gate is an example of a quantum logic gate on two qubits (see also [282–287]). It is instructive to give the unitary action $U_{XOR,\ CNOT}$ of this gate in several forms [288]. Its action on the two-qubit basis states is

a	b	$a \wedge b$
0	0	0
0	1	0
1	0	0
1	1	1

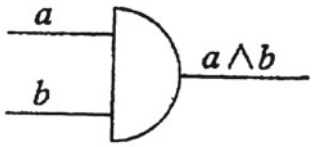

Fig. 4.71 The truth table and circuit representation for the NOT gate

a	b	$a \vee b$
0	0	0
0	1	1
1	0	1
1	1	1

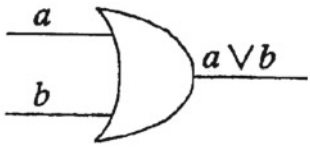

Fig. 4.72 The truth table and circuit representation for the AND gate

a	b	$a \oplus b$
0	0	0
0	1	1
1	0	1
1	1	0

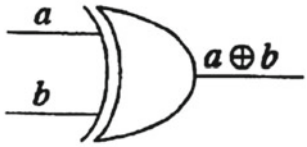

Fig. 4.73 The truth table and circuit representation for the OR gate

$$U_{\text{CNOT}} \mid 00\rangle = \mid 00\rangle; \quad U_{\text{CNOT}} \mid 10\rangle = \mid 11\rangle;$$
$$U_{\text{CNOT}} \mid 01\rangle = \mid 01\rangle; \quad U_{\text{CNOT}} \mid 11\rangle = \mid 10\rangle; \tag{4.91}$$

From this definition, we can see that the name of this gate is quite apparent, for it means that it executes a NOT operation on the second qubit conditioned to have the first qubit in the state $\mid 1\rangle$. Its matrix representation is

a	b	$a \uparrow b$
0	0	1
0	1	1
1	0	1
1	1	0

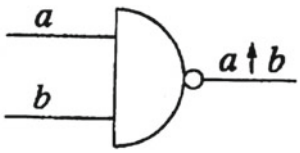

Fig. 4.74 The truth table and circuit representation for the XOR gate

a	b	$a \downarrow b$
0	0	1
0	1	0
1	0	0
1	1	0

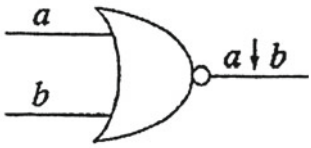

Fig. 4.75 The truth table and circuit representation for the NAND gate

$$U_{\text{CNOT}} = U_{\text{XOR}} = \begin{vmatrix} 1 & 0 & 0 & 0 \\ 0 & 1 & 0 & 0 \\ 0 & 0 & 0 & 1 \\ 0 & 0 & 1 & 0 \end{vmatrix} = \begin{vmatrix} I & 0 \\ 0 & \sigma_x \end{vmatrix}. \tag{4.92}$$

The action of the CNOT operator (4.92) immediately translates into a corresponding truth table. The diagrammatic representation of the CNOT gate is shown in Fig. 4.69b. We shall see how this quantum CNOT gate plays a paramount role in both the theory and experimental realization of quantum computers. It allows the implementation of conditional logic at a quantum level. The generalization of the CNOT gate is the control-U (CU) gate, where the Pauli matrix σ_x is replaced by a 2×2 unitary matrix U:

$$CU = \begin{vmatrix} I & 0 \\ 0 & U \end{vmatrix}. \tag{4.93}$$

The CU gate leaves the target bit unchanged if $x = 0$ and modify it as $|y\rangle \longrightarrow U|y\rangle$ if $x = 1$. The CU gate can be constructed starting from the CNOT gate. It is necessary to find three unitary operators A, B, and C such that

$$CBA = I, \quad C\sigma_x B\sigma_x A = U. \tag{4.94}$$

In quantum physics, the Toffoli gate may be constructed from CU gates and CNOT gates (with $U = \sqrt{\sigma_x}$) and the equation

$$\sqrt{\sigma_x} = \frac{1}{1+i}\begin{vmatrix} 1 & i \\ i & 1 \end{vmatrix}, \tag{4.95}$$

which is not possible in classical physics where the operation $\sqrt{\sigma_x}$ does not exist. In contrast to the classical case, it is not necessary to introduce the Toffoli gate explicitly to construct the ensemble of reversible logic circuit (for details see [269, 270, 289, 290]).

Unlike the CNOT gate, there two-qubit gates with no classical analog (see also [291]). One example is the controlled-phase gate or CPHASE:

$$U_{\text{CPHASE}} = \begin{bmatrix} 1 & 0 & 0 & 0 \\ 0 & 1 & 0 & 0 \\ 0 & 0 & 1 & 0 \\ 0 & 0 & 0 & e^{\mathrm{i}}\Phi \end{bmatrix}. \tag{4.96}$$

It implements a conditional phase shift on the second qubit [280]. Other interesting two-qubit gates are the SWAP gate, which interchanges the states of the two qubits, and the $\sqrt{SWAP}$ gate, whose matrix representation are

$$U_{\text{SWAP}} = \begin{bmatrix} 1 & 0 & 0 & 0 \\ 0 & 1 & 0 & 0 \\ 0 & 0 & 1 & 0 \\ 0 & 0 & 0 & 1 \end{bmatrix}, \tag{4.97}$$

$$U_{\sqrt{SWAP}} = \begin{bmatrix} 1 & 0 & 0 & 0 \\ 0 & \frac{1+i}{2} & \frac{1-i}{2} & 0 \\ 0 & \frac{1-i}{2} & \frac{1+i}{2} & 0 \\ 0 & 0 & 0 & 0 \end{bmatrix}. \tag{4.98}$$

An immediate extension of the CNOT construction to three qubits yields the CCNOT gate (or C^2 NOT-controlled-controlled-not gate) which is also called Toffoli gate [289, 290] (see also [292]). The Deutsch gate $D(\theta)$ is also an important three-qubit gate [293]. It is a controlled-controlled- S or C^2S operation, where

$$U_{\mathrm{D}(\theta)} = ie^{-\frac{\theta\sigma_{\mathrm{x}}}{2}} = i\cos\frac{\theta}{2} + \sigma_{\mathrm{x}}\sin\frac{\theta}{2} \tag{4.99}$$

is a unitary operation that rotates a qubit about the x axis by an angle θ and then multiplies it by a factor i and σ_x. Here, σ_x is the Pauli matrix

$$\sigma_x = \begin{bmatrix} 0 & 1 \\ 1 & 0 \end{bmatrix}. \tag{4.100}$$

and other Pauli matrixes are

$$\sigma_y = \begin{bmatrix} 0 & -i \\ i & 0 \end{bmatrix}, \quad \sigma_z = \begin{bmatrix} 1 & 0 \\ 0 & -1 \end{bmatrix}, \tag{4.101}$$

which obey the relations

$$\sigma_x\sigma_y = i\sigma_z, \quad \sigma_x\sigma_z = -i\sigma_y, \quad \sigma_y\sigma_z = i\sigma_x \tag{4.102}$$

$$\sigma_x^2 = \sigma_y^2 = \sigma_z^2 = \sigma_{\mathrm{I}}, \tag{4.103}$$

where

$$\sigma_{\mathrm{I}} = \begin{bmatrix} 1 & 0 \\ 0 & 1 \end{bmatrix}. \tag{4.104}$$

The rest of the discussion of one-qubit gates expands on the following notion: any one-qubit unitary operation can be written in the form (see, e.g., [269, 270])

$$U = e^{\mathrm{i}} R_{\widehat{n}}(\theta), \tag{4.105}$$

where $\mathrm{R}_{\widehat{n}}(\theta)$ corresponds to a rotation in the Bloch sphere about the $\widehat{n} = (n_x, n_y, n_z)$ axis and over an angle θ. With $\boldsymbol{\sigma} = (\sigma_x, \sigma_y, \sigma_z)$ we can construct $\mathrm{R}_{\widehat{n}}(\theta)$ by exponentiating the Pauli operators as follows:

$$R_{\widehat{n}}(\theta) \equiv \exp\left(-i\frac{\theta\widehat{n}\boldsymbol{\sigma}}{2}\right) = \cos(\theta/2)\sigma_{\mathrm{I}} - \mathrm{i}\sin(\theta/2)\left[n_x\sigma_x + n_y\sigma_y + n_z\sigma_z\right]. \tag{4.106}$$

Rotations about $\widehat{x}$, $\widehat{y}$ and $\widehat{z}$ axis, respectively, are thus given by

$$\begin{aligned} R_x(\theta) &= \exp\left(\frac{-i\theta\sigma_x}{2}\right) \\ &= \cos(\theta/2)\sigma_{\mathrm{I}} - i\sin(\theta/2)\sigma_x = \begin{bmatrix} \cos\frac{\theta}{2} & -isin\frac{\theta}{2} \\ -i\sin\frac{\theta}{2} & \cos\frac{\theta}{2} \end{bmatrix}, \end{aligned} \tag{4.107}$$

$$\begin{aligned} R_y(\theta) &= \exp\left(\frac{-i\theta\sigma_y}{2}\right) \\ &= \cos(\theta/2)\sigma_{\mathrm{I}} - i\sin(\theta/2)\sigma_y = \begin{bmatrix} \cos\frac{\theta}{2} & -\sin\frac{\theta}{2} \\ -\sin\frac{\theta}{2} & \cos\frac{\theta}{2} \end{bmatrix}, \end{aligned} \tag{4.108}$$

$$\begin{aligned} R_z(\theta) &= \exp\left(\frac{-i\theta\sigma_z}{2}\right) \\ &= \cos(\theta/2)\sigma_{\mathrm{I}} - i\sin(\theta/2)\sigma_z = \begin{bmatrix} e^{-\mathrm{i}`/2} & 0 \\ 0 & e^{-\mathrm{i}`/2} \end{bmatrix}. \end{aligned} \tag{4.109}$$

Examples of multi-qubit gates can be found in the references [288–293]. Thus, any function $f: \{0, 1\}^n \longrightarrow \{0, 1\}^m$ can be constructed from elementary gates AND, OR, NOT, and FANOUT. Therefore, we say that these constitute a universal set of gates for classical computation. To solve any problem, a certain amount of resources is necessary; for instance, to run an algorithm on a computer, we need space (that is memory), time, and energy (see above). Computational complexity is the study of the resources required to solve computational problems. Sometimes it is immediately obvious if one problem is easier to solve than another. For instance, we know that it is easier to add two numbers than multiply them.

4.8.4 A Physical Models for a Quantum Computer

Today's classical computers do not operate in a reversible manner. Note, for example, that my computer generates heat. Also, note that is not possible to reconstruct the input of a traditional AND gate from its output (see above the table of truth). This is obvious since the AND gate has two input bite and only one output bit; it is never possible to reconstruct the value of two bits starting from only one bit. But even if we introduce a second output bit, it is not possible to make the AND gate reversible. This is because the AND gate is not single-valued. If the output is 00, we cannot know whether the input was 00 or 01. It is thus natural to ask whether universal computation can be done reversibly. Rolf Landauer and Charles Bennet showed that indeed any computation can be performed in a completely reversible manner, that is without (or with infinitesimal) energy dissipation (see, e.g., [294] and references quoted therein). The only time must be dissipated is in the process of resetting a bit, which irreversibly erases the information contained in the bit and thus necessarily increases the entropy [295]. Any multivalued function $f, x \longrightarrow f(x)$ can be made reversible by introducing a second input bit string y of the same length as $f(x)$, i.e., $(x, y) \longrightarrow (x, y \oplus (x)$. We can thus construct a reversible version of the AND gate, for example, by using an additional input bit (more details see [269]).

4.8.4.1 Liquid State NMR Quantum Computer

We begin with a description of the NMR system, based on its system Hamiltonian and the control Hamiltonian. The system Hamiltonian gives the energy of single and coupled spins in a static magnetic field, and the control Hamiltonian arise from the application of radio frequency pulses to the system at, or near, its resonant frequencies. A rotating reference frame is employed, providing a very convenient description (see below). The time evolution of a spin $-1/2$ (we shall not consider higher order spins in this section) in a magnetic field of strength B_0 along the z axis is [294, 296] governed by the Hamiltonian:

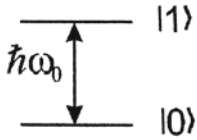

Fig. 4.76 Energy diagram for a single spin −1/2

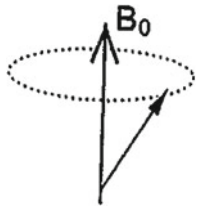

Fig. 4.77 Precession of a spin about the axis of a static magnetic field

$$H_0 = -\hbar\gamma B_0 I_z = -\hbar\omega_0 I_z = \begin{bmatrix} -\hbar\omega_0/2 & 0 \\ 0 & \hbar\omega_0/2 \end{bmatrix}, \tag{4.110}$$

where γ is the gyromagnetic ratio of the nucleus and $\omega_0/2\pi$ is the Larmor frequency of the spin (often call ω_0 simply the Larmor frequency). I_z is the angular momentum operator in the z direction, which relates to the well-known Pauli matrix as $2I_z = \sigma_z$ ($2I_x = \sigma_x$ and $2I_y = \sigma_y$). The interpretation of (4.110) is that the energy of the $|\,0\rangle$ or $|\uparrow\rangle$ state (given by $\langle 0 \mid H \mid 0\rangle$ the upper left element of H) is lower than the energy of $|\,1\rangle$ or $|\downarrow\rangle(\langle 1 \mid H \mid 1\rangle)$ by an amount $\hbar\omega_0$, as illustrated in the energy diagram in Fig. 4.76. The energy splitting is known as the Zeeman splitting. The time evolution $e^{-iHt/\hbar}$ of the spin state under the Hamiltonian of (4.110) corresponds to a precession motion in the Bloch sphere (see Fig. 3.4 [237]) about the axis of the static magnetic field, similar to the precession of a spinning top about the ais of gravitation, as shown in Fig. 4.77. The B_0 field is typically on the order of 10 Tesla, resulting in precession frequencies ω_0 of a few hundred MHz, which is in the radio frequency range. In the field of nuclear magnetic resonance (NMR) over the last few decades, sophisticated techniques have been developed to manipulate and detect nuclear spin states using both static and oscillating magnetic fields simultaneously [296]. These techniques have been used, for instance, to study structural properties of molecules and even biological samples [294, 297, 298]. The qubits in NMR quantum computing are given by the spins of suitable atomic nuclei [299], placed in a static magnetic field $\boldsymbol{B}_0$. Therefore, we shall here be exclusively interested in spin −1/2 nuclei, such as ^{1}H, ^{13}C, ^{15}N, ^{19}F as well as ^{31}P, as they have two discrete eigenstates (see Fig. 4.76). Spin −0 nuclei, for example, ^{12}C and ^{16}O, are not magnetic and therefore not detectable with NMR. Nuclei with spin quantum number greater than 1/2, such as ^{2}H, ^{14}N, ^{35}Cl, ^{79}Br, don't make for good qubits, either, mapping the larger number of states (e.g., the spin quantum number of a spin −3/2 particle can be −3/2, −1/2, 1/2 or 3/2) onto qubit states, and performing quantum logic gates on them, introduces additional complications. More significantly, nuclear spins with spin >1/2 tend to have very short coherence time.

The magnetic signal of a single nuclear spin is too weak to be directly detected. Therefore, NMR experiments are done using a large ensemble of identical molecules, typically on the order of 10^{18}, dissolved in a liquid solvent. The same operations are applied to all the molecules in the ensemble, so the final state of the spins is the same in all molecules.

NMR quantum computation is based on the same principle that is used in magnetic resonance imaging for medical diagnosis (see above). As the name suggests, this technique involves atomic nuclei, or more precisely, their spins. Nuclear spins give rise to magnetic moment, meaning that the nuclei behave like little compass needles when exposed to magnetic fields. Spins are quantized and can only take on specific values (contrary to compass needles, which can point in any direction, i.e., take any desired value. One can switch between these values (see Fig. 4.76) by irradiating the nucleus with microwave at a particular frequency, the so-called resonance frequency of the nuclear spin. Since inside a molecule a particular atomic nucleus has a couple of neighbors that slightly change the resonance frequency of its spin, one can address a specific nucleus by tuning to its precise resonance frequency. The switching between spin states and the coupling between neighboring nuclear spins are good starting points for quantum computation. The spins can act as qubits, and the coupling makes it possible to realize two-qubit gates [300]. In 1998, Chuang and his colleagues manage [301, 302] to run Deutsch's algorithm on a chloroform molecule (see also [269, 270]). By sending carefully tailored microwave pulses to the molecules, they could perform the quantum logic gates necessary to implemented the algorithm and read out the final answer. In 2001, a more complex molecule was used to realize Shor's algorithm [296, 303] on the number 15.

That NMR quantum computation will one day lead to a commercially available quantum computer is rather unlikely. Although the demonstration of Shor's algorithm using NMR was an important step and stimulated research efforts in quantum computation, there are obvious reasons why this approach is not the way for the future. The most obvious of those reasons is the lack of scalability. In Chuang's experiment, Shor's algorithm was essentially carried out on billions of identical copies of the same computer, a molecule containing a handful of atoms. Therefore, the power of an NMR quantum computer is fundamentally limited by what a single molecule can do. That, in turn, will depend on the number and kind of atoms the molecule contains, how they are arranged in the molecule, and so forth. Thus, NMR method has been the workhorse or the experimental implementation of quantum protocols, allowing exquisite control of systems to seven qubits in size. We should stress the useful this method or the implementation of quantum information processing task.

4.8.4.2 Trapped Ions and Atoms

Before discussing future prospects, we will highlight in this part the strength of current ion-trap technology. We consider the three requirements for quantum information processing, which are quantum memory, quantum logic gates, and measurement of quantum states. The primary consideration for all of these is precision and

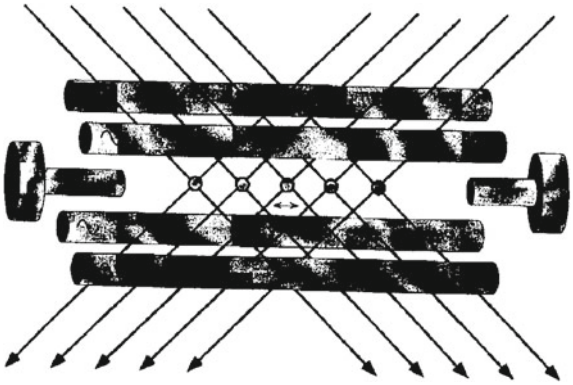

Fig. 4.78 Ion-trap quantum information processor. A string of singly charged atoms is stored in a linear ion trap. The ions are separated by ~20 μm by their mutual repulsion. Each ion is addressed by a pair of laser beams which coherently drive both Raman transitions in the ions, and also transitions in the state of motion of the string. The motional degree of freedom serves as a single-qubit "bus" to transport quantum information among the ions. State preparation is by optical pumping and laser cooling; readout is by electron shelving and resonance fluorescence, which enables the state of each ion to be measured with high signal-to-noise ratio

reliability, simply because we need the computer to work; we are willing to sacrifice both speed of operation and ease of construction, if it makes the difference between a computer which works and one which does not. Note that all the three requirements are equally significant. On the experimental side, implementing quantum processors is a formidable task, and no realistic scalable design presently exists. The activity has been focused on the operation of simple systems, with at most a few qubits [304]. First, microscopic quantum systems like atoms [304–306] and ions [307] has been considered (see also [308]). Their main advantage is their excellent quantum, but their scalability is questionable. The most advanced qubit implementation is based on ions in linear traps, coupled to their longitudinal motion [307] and addressed optically. Although the trend is to develop atom chips, these implementations based on microscopic quantum object still lack the flexibility of microfabricated electronic circuits, which constitute the second main road investigated. Here, quantumness is limited by the complexity of the circuits that always involve a macroscopic number of atoms and electrons.

The ion-trap method is illustrated in Fig. 4.78, and described in detail in literature [307, 308]. A string of ions is confined by a combination of oscillating and static electric fields in a linear "Paul trap" [309] in high vacuum (10^{-8} Pa). A single laser beam is split by beam splitters and acousto-optic modulators into many beam pairs, one pair illuminating each ion. Each ion has two long-lived state, for example, different levels of the ground-state hyperfine structure (the lifetime of such states against spontaneous decay can exceed thousands of years). Following [308], let us refer to these two states as $|g\rangle$ and $|e\rangle$; they are orthogonal and so together represent one qubit. Each laser beam pair can drive coherent Raman transitions between the

internal states of the relevant ion. This allows any single-qubit quantum gate to be applied to any ion, but not two-qubit gates. The latter requires an interaction between ions, and this is provided by their Coulomb repulsion. However, exactly how to use this interaction is far from obvious; it required the important insight by the authors of ion-trap quantum processor [310, 311].

Light carries not only energy but also momentum, so whenever a laser beam pair interacts with an ion, it exchanges momentum with the ion. In fact, the mutual repulsion of the ions means that the whole string of ions moves end mass when the motion is quantized (analog Mössbauer effect) [295, 312]. The motion of the ion string is quantized because the ion string is confined in the potential provided by the Paul trap [309]. The quantum states of motion correspond to the different degrees of excitation (phonons) of the normal modes of vibration of the string. In particular we focus on the ground state of motion $|\, n = 0\rangle$ and the lowest excited state $|\, n = 1\rangle$ of the fundamental mode. To achieve, for example, CNOT between ion x and ion y, we start with the motion in the ground state $|\, n = 0\rangle$. A pulse of the laser beams on ion x drives the transitions $|\, n = 0\rangle\, |\, g\rangle_x \longrightarrow |\, n = 0\rangle\, |\, g\rangle_x$, $|\, n = 0\rangle\, |\, e\rangle_x \longrightarrow |\, n = 1\rangle\, |\, g\rangle_x$, so the ion finishes in the ground state, and the motion finishes in the initial state of the ion: this is an SWAP operation. Next a pulse of the laser beams on ion y drives the transitions

$$\begin{aligned}
|\, n = 0\rangle\, |\, g\rangle_y &\longrightarrow |\, n = 0\rangle\, |\, g\rangle_y \\
|\, n = 0\rangle\, |\, e\rangle_y &\longrightarrow |\, n = 0\rangle\, |\, e\rangle_y \\
|\, n = 1\rangle\, |\, g\rangle_y &\longrightarrow |\, n = 1\rangle\, |\, g\rangle_y \\
|\, n = 1\rangle\, |\, e\rangle_y &\longrightarrow |\, n = 1\rangle\, |\, e\rangle_y .
\end{aligned} \tag{4.111}$$

Finally, we repeat the initial pulse on ion x. The overall effect of three pulses is

$$\begin{aligned}
|\, n = 0\rangle\, |\, g\rangle_x\, |\, g\rangle_y &\longrightarrow |\, n = 0\rangle\, |\, g\rangle_x\, |\, g\rangle_y \\
|\, n = 0\rangle\, |\, g\rangle_x\, |\, e\rangle_y &\longrightarrow |\, n = 0\rangle\, |\, g\rangle_x\, |\, e\rangle_y \\
|\, n = 0\rangle\, |\, e\rangle_x\, |\, g\rangle_y &\longrightarrow |\, n = 0\rangle\, |\, e\rangle_x\, |\, g\rangle_y \\
|\, n = 0\rangle\, |\, e\rangle_x\, |\, e\rangle_y &\longrightarrow -\, |\, n = 0\rangle\, |\, e\rangle_x\, |\, e\rangle_y ,
\end{aligned} \tag{4.112}$$

which is exactly a CNOT between x and y. Each laser pulse must have a precisely controlled frequency and duration (see, e.g., [310, 311]). The CNOT gate and the single-qubit gates together provide a universal set, so we can perform arbitrary transformations of the joint state of all the ions. To complete the description of this method, we must be able to prepare the initial state and measure the final state. The first is possible through the methods of optical pumping and laser cooling, the second through the quantum jump or electron shelving measurement technique. All these are powerful techniques developed in the atomic physics community over the last three decades. In concluding, the basic requirements for a general purpose quantum computing device with trapped ions have been demonstrated and no fundamental road block is in sight. However, building such a device is extremely challenging.

Especially, the stringed requirements for fault tolerance and for scalability to many thousands of qubits pose huge difficulties (for details see [308] and references therein). Ion-trap methods currently offer the only way to achieve multiparticle entangled states in a controllable way. They offer the prospect in the fairly near term of achieving various fundamental principles of quantum information physics, such as entanglement-enhanced communication and repeatable error correction. It is clear that the controlled coupling of a trapped ion or neutral atom to a single-photon field in a high-finesse cavity also merits investigation for both quantum communication and quantum computing experiments.

4.8.4.3 Solid-State Quantum Processors

There have been almost as many proposals for solid-state implementations of quantum computers as all the other proposals put together. We believe that solid-state physics is the most versatile branch of physics, in that almost any phenomenon possible in physics can be embodied in a correctly designed condensed matter system. Even rather esoteric properties of field theories which are of interest in high-energy physics have useful realizations, for example, in the fractional Hall effect [313]. A related reason is that solid-state physics, being so closely allied with computer technology, has exhibited great versatility over the years in the creation of artificial structures and devices which are tailored to show a great variety of desired physical effects. This has been exploited very powerfully to produce ever more capable computational devices. It would be natural to extrapolate to say that this versatility will extend to the creation of solid-state quantum computers as well [272]; the plethora of proposals would indicate that this is indeed true, although time will tell whether of these proposals will actually provide a successful route to a quantum computer. At first sight, it might appear crazy for solid-state physicists to enter the field of quantum information processing. After all, the entities with which they deal are typically much more strongly interacting than the atomic components used in atom-trap or ion-trap approaches (see also [313]), and this would seem to make them much less suitable for the coherent manipulation of quantum information. But this has not prevented the appearance of a number of very imaginative proposals for using the numerous excitations in condensed matter for quantum information processing. At the moment these are just proposals. But very significant progress is being made toward surmounting the technological challenges required to turn the proposals into reality. Our brief consideration will no means be comprehensive, but it will serve to illustrate something of the tremendous range of possible condensed-matter approaches to quantum information processing including isotope-mixed crystals processors.

A. Superconducting qubits.

We will not review the superconducting proposals in detail, but we will give a brief description of how it is satisfied and indicate the reader where he/she can find more information on these developments. In two preceding examples, the qubits were carried by individual quantum objects, nuclear spins in the NMR case, and ions

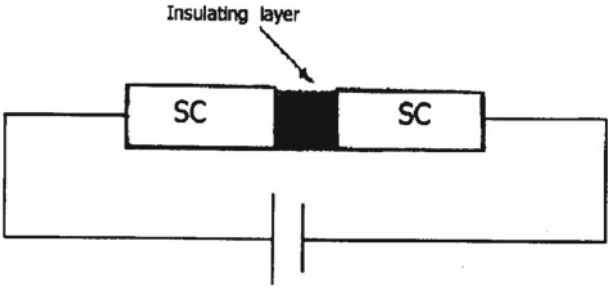

Fig. 4.79 Schematic depiction of a Josephson junction: a thin insulating layer is sandwiched between two superconducting (SC) wires

(atoms) in the case of trapped ions. The superconducting qubit proposals differ from all other proposals discussed here in the qubit is represented by two quantum states which are collective states are macroscopic number of particles: flux states resulting from the motion of millions to billions Cooper pairs through an SQUID or charge states produced by millions of Cooper pairs in box. Several schemes have been proposed for logic gates. One-qubit rotations involve the application of local magnetic fields which change the environment of a specific qubit. Below we turn to a system where the qubits are carried by a macroscopic degree of freedom, the current in a superconducting circuit containing one or several Josephson junction (Fig. 4.79). As we all know, low temperatures of the order of tens of millikelvins are required for these circuits to exhibit quantum behavior. These circuits are small by everyday standards (a few micrometers), but very large compared to atomic sizes. Still more remarkable is the fact that the parameters of these quantum systems are fixed by fabrication and not by nature as is the case for individual quantum system like electrons or ions (see also [314]). They are engineered quantities which can be modified by changing the dimensions of the circuits, and in this sense, they are unambiguously macroscopic quantities. It has been known for about a century that at low temperatures, the electrical resistance of most metals and alloys drops abruptly to zero below a transition temperature T_C of order 1 K, and the metal becomes a superconductor. Superconductors also exhibit a remarkable feature called Meissner effect: magnetic fields are expelled from the bulk of a superconductor: they cannot penetrate deeper than a distance known as the London penetration length, which is of order 0.1 μm (for details see, e.g., [315]).

Although the currents that flow in superconductors consist of millions of electrons, they can be viewed as a single huge quantum state. Consequently, it is also possible for the current to exist in a superposition of two or more quantum states; for example, in a superposition of flowing at the same time clockwise and counterclockwise inside a metal ring. Also, a current swinging back and forth in an oscillator circuit can exist in a superposition of several harmonic oscillator states (which are very familiar to those of ions oscillating in a trap). It is tempting, therefore, to use such states of superconductors as qubits for quantum computation [316].

There are several advantages of such an approach compared to ion traps and optical lattices. First, superconducting circuits are man-made objects, and hence, it is possible to adjust the properties of the circuit (almost) at will. Ions and atoms, by contrast, are provided by nature and can only be taken as they come. Second, superconducting circuits can be fabricated using the well-known techniques that are also used for making integrated circuits and microchips. And finally, we know a lot about controlling currents and electrons in circuits, so it will be easy to control qubits in superconductors.

In spite of these advantages, using superconductors for quantum computation is not quite as straightforward as it may seem at first sight. One fundamental reason for why one cannot simply use the quantized states of a superconducting oscillator circuit is that these quantum states all are the same distance from each other. This makes it impossible to single out exactly two states that will be $|0\rangle$ and $|1\rangle$ of potential qubit. But there is a remedy, the so-called Josephson junction. Such a junction consists, basically, of a tiny slab of insulating material between two superconductor wires (see Fig. 4.79). Classically no current flow through an insulator, but in quantum mechanics, the Cooper pairs in the superconductors can bridge the gap by tunneling. In a Josephson junction, it is possible to single out two quantized states that can be used as $|0\rangle$ and $|1\rangle$ states of a qubit [278]. The first realization of CNOT gate in superconductor was recently described in [317].

B. Kane's model.

As was shown above the crystal lattice quantum computer has the potential for scaling up to several hundred qubits. The development of efficient quantum algorithms for classically hard problems has generated interest in the construction of a quantum computer. A quantum computer uses superpositions of all possible input states. By exploiting this quantum parallelism, certain algorithms allow one to factorize [7, 318, 319] large integers with astounding speed, and rapidly search through large databases [320–323], and efficiently simulate quantum systems [324–326]. In the nearer term, such devices could facilitate secure communication and distributed computing. In any physical system, bit errors will occur during the computation. In quantum computing, this is particularly catastrophic because the errors cause decoherence [272] and can destroy the delicate superposition that needs to be preserved throughout the computation. With the discovery of quantum error correction [7, 318, 319, 327, 328] and fault-tolerant computing, in which these errors are continuously corrected without destroying the quantum information, the construction of a real computer has become a distinct possibility. The task that lies ahead to create an actual quantum computer is formidable: Preskill [329] has estimated that a quantum computer operating on 10^6 qubits with a 10^{-6} probability of error in each operation would exceed the capabilities of contemporary conventional computers on the prime factorization problem. To make use of error-correcting codes, logical operations and measurement must be able to proceed in parallel on qubits throughout the computer (for details see [237]).

Phosphorous donors in silicon present a unique opportunity for solid-state quantum computation [320, 330, 331]. Kane proposed an approach which integrates

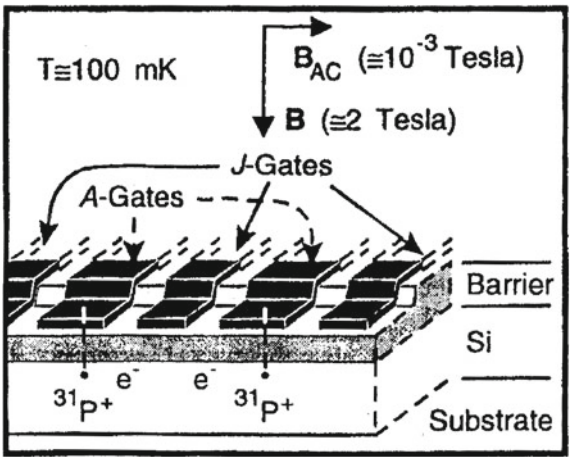

Fig. 4.80 Model of a Kane-type quantum computer (after [330])

solid-state NMR on donor atoms with semiconductor electronics. The quantum bits are embodied by the spin $-1/2$ nucleus of ^{31}P dopants arranged in a regular array below the surface in a spinless I = 0 ^{28}Si lattice (Fig. 4.80), placed in a static magnetic field perpendicular to the surface. Electrons spins on isolated Si:P donors have very long decoherence times of ~60 ms in isotopically purified ^{28}Si at 7 K [332]. By contrast, electron spin dephasing times in GaAs (for example) are orders of magnitude shorter due to spin–orbit interaction, and the background nuclear spins of the III–V host lattice cannot be eliminated by isotope selection. Finally, the Si:P donor is a self-confined, perfectly uniform single-electron quantum dot with a nondegenerate ground state. A strong Coulomb potential breaks the 6-valley degeneracy of the silicon conduction band near donor site, yielding a substantial energy gap of ~15 meV to the lowest excited [333] as needed for quantum computation. As we all know, the Si:^{31}P system was exhaustively studied more than 40 years ago in the first electron-nuclear double-resonance experiments. At sufficiently low ^{31}P concentrations at temperature $T = 1.5$ K, the electron spin relaxation time is thousands of seconds and the ^{31}P nuclear spin relaxation time exceeds 10 hours. It is likely that at millikelvin temperatures the phonon limited ^{31}P relaxation time is of the order of 10^{18} seconds [237], making, as we said above, this system ideal for quantum computation. Two-bit gates between adjacent phosphorus nuclei coupling mechanism mediated by their respective electrons.

The Kane architecture employs an array of top gates (see Fig. 4.80) to manipulate the ground-state wavefunctions of the spin-polarized electrons at each donor site in a high magnetic field B ~2 T, at very low temperature ($T \simeq 100$ mK). "A-gates" above each donor turn single-qubit NMR rotations via the contact hyperfine interaction, and "J-gates" between them induce an indirect two-qubit nuclear exchange interaction via overlap of the spin-polarized electron wavefunctions (see also [96]). In other words, spin $-1/2$ ^{31}P donor nuclei are qubits, while donor electrons together with external A-gates provide single-qubit (using external magnetic field) and two-qubit

operations (using hyperfine and electron exchange interactions). Specifically, the single donor nuclear spin splitting is given by [330–335]

$$\hbar\omega_{\mathrm{A}} = 2g_n\mu_n B + 2A + \frac{2A^2}{\mu_{\mathrm{B}} B}, \tag{4.113}$$

where g_n is the nuclear spin g-factor (= 1.13 for ^{31}P [329]), μ_n is the nuclear magneton, A is the strength of the hyperfine coupling between the ^{31}P nucleus and the donor electron spin, and B is the applied magnetic field. It's clear that by changing A one can effectively change the nuclear spin splitting, thus allow resonant manipulations of individual nuclear spins. If the donor electrons of two nearby donors are allowed to overlap, the interaction part of the spin Hamiltonian for the two electrons and the two *nuclei* include electron-nuclear hyperfine coupling and electron–electron exchange coupling [330, 331] (see also [334, 335])

$$H = H_{\mathrm{Zeeman}} + H_{\mathrm{int}} = H_{\mathrm{Zeeman}} + A_1\boldsymbol{S}_1 \cdot \boldsymbol{I}_1 + A_2\boldsymbol{S}_2 \cdot \boldsymbol{I}_2 + J\boldsymbol{S}_1\boldsymbol{S}_2, \tag{4.114}$$

where $\boldsymbol{S}_1$ and $\boldsymbol{S}_2$ represent the two electron spins, $\boldsymbol{I}_1$ and $\boldsymbol{I}_2$ are the two nuclear spins, A_1 and A_2 represent the hyperfine coupling strength at the two donor sites, and J is the exchange coupling strength between the two donor electrons, which is determined by the overlap of the donor electron wavefunctions. The lowest order perturbation calculation (assuming $A_1 = A_2 = A$ and J is much smaller than the electron Zeeman splitting) results in an effective exchange coupling between the two nuclei and the coupling strength is (see [320, 331])

$$J_{\mathrm{nn}} = \frac{4A^2 J}{\mu_{\mathrm{B}} B(\mu_{\mathrm{B}} B - 2J)}. \tag{4.115}$$

Now, the two donor electrons are essentially shuttled different nuclear spin qubits and are controlled by external gate voltages. The final measurement is done by first transferring nuclear spin information into electron spins using hyperfine interaction, then converting electron spin information into charge states such as charge locations [334]. A significant advantage of silicon is that its most abundant isotope ^{28}Si is spinless, thus providing a "quiet" environment for the donor nuclear spin qubits. In addition, Si has also smaller intrinsic spin–orbit coupling than other popular semiconductors such as GaAs. In general, nuclear spins have very long coherence times because they do not strongly couple with their environment, and are thus good candidates for qubits (see also [281, 335]).

Although the nuclear spin offers unlimited decoherence times for quantum information processing, the technical problems of dealing with nuclear spins through the electrons are exceedingly difficult. A modified version of the Kane architecture was soon proposed using the spin of the donor electron as the qubit [336–338]. In the first scheme [336], A-gates would modulate the electron g-factor by polarizing its ground state into Ge-rich regions of a SiGe heterostructure for selective ESR rotations, while two-qubit electron exchange is induced through wavefunction

overlap. In the studies of Shlimak et al. [337–339], they used a new technology to grow Si/Ge heterostructures. Recent achievement in Si/Ge technology allows one to obtain high-quality heterojunctions with a mobility of about $(1-5)\cdot 10^5\,\mathrm{cm}^2\mathrm{V}^{-1}\mathrm{s}^{-1}$ [337–340]. Using Si/Ge heterostructures has several advantages concerning semiconductor based nuclear spin quantum computers (S-NSQCs). First, the concentration of nuclear spins in Ge and Si crystals is much lower, because only one isotope (^{73}Ge and ^{29}Si [341]) has a nuclear spin, and the natural abundance of this isotope is small (see also [342]). Second, the variation of isotopic composition for Ge and Si will lead to the creation of a material with a controlled concentration of nuclear spin, and even without nuclear spins. Utilization of isotopically engineered Ge and Si elements in the growth of the active Si/Ge layers could help realize an almost zero nuclear spin layer that is coplanar with the 2DEG. Then, one might deliberately vary the isotopic composition to produce layers, wires, and dots that could serve as nuclear spin qubits with a controlled number of nuclear spins (see also [281]).

The key point of a novel technology is the growth of the central Si and barrier $Si_{0.85}Ge_{0.15}$ layers from different isotopes: the $Si_{0.85}Ge_{0.15}$ layers from isotope ^{28}Si and ^{72}Ge and the central Si layer from isotope ^{28}Si with ^{30}Si spots introduced by means of the nanolithography (see Fig. 4.22 in [237]) [343]. The formation of quasi-one-dimensional Si wires will be achieved in a subsequent operation by the etching of Si layer between wires and the filling of the resulting gaps by the $Si_{0.85}Ge_{0.15}$ barrier composed from isotopes ^{28}Si and ^{72}Ge. Because different isotopes of Si and Ge are chemically identical, this technology guarantees the high quality of the grown structures [235]. After preparation, these structures will be irradiated with a neutron flux in a nuclear reactor by the fast annealing of radiation damage (see [281] and references cited therein).

All the charged-based schemes mentioned so far use single charged semiconductor quantum dot. The associated strong Coulomb interaction provides a convenient means for fast qubit manipulation, but can also lead to fast decoherence. One way to alleviate this problem is to use neutral excitations such as excitons as qubits, where there is the added benefit that excitons can be precisely controlled optically (see, e.g., [344]). Indeed, uncharged quantum dots have been proposed as possible candidates for quantum information processing [345, 346] and many experiments have been done to demonstrate exciton coherence and control in single quantum dot [24, 229]. Here, single excitons are optically excited in individual quantum dots and can be coherently manipulated optically. The presence and absence of an *exciton* in a quantum dot provide two states of a qubit. Again, entanglement between different qubits is based on Coulomb renormalization of the energy levels. The exciton-based quantum computer in isotope-mixed crystals [215] proposals clearly illustrate the dichotomy faced by all quantum computer architectures: excitons are neutral and therefore are more insulated from their environment and decohere more slowly than the single charge-based schemes. However, the charge neutrality also strongly reduces the interaction between spatially separated excitons, thus rendering it more difficult to perform entangling operation. We should add that an optically controlled exciton transfer process was shown to lead to the generation of Bell and Greenberger–Horne–Zeilinger state in systems comprising two and three couple dots, respectively [347].

C. Color centers processors

Silicon

Several other proposals exist for the implementation of quantum computers, in addition to those we have discussed in the preceding sections. Below we will briefly describe of them (see also [237]). The authors of the paper [348] have proposed a new approach to constructing gates for quantum information processing, exploiting the properties of deep impurities in silicon (color centers). Localized spins in solids have properties suitable for representing quantum information. Quantum gates require mutual coherent evolution of such states, necessitating interactions between them. Indicated schemes (see above) to control interactions required gate electrodes positioned near to specific highly polarizable defects which would be readily ionized except at low temperatures. The formidable fabrication (see Fig. 4.80) requirements may introduce further significant sources of decoherence. Novel control, proposed in paper [349] avoids electrodes. According to the results of this paper, interactions are controlled by electronic excitations [341]. One implementation embodies qubits in electron spins of deep donors (A, B), not ionized at working temperature. Typical A, B spacings should be large enough for ground-state interactions between donor spins to be small, perhaps 7–10 nm for a deep donor like Si:Bi [348]. Controlled optical excitation of a charge-transfer transition [104] from a nearby control impurity C, possibly Er, promotes a control electron from C into a molecular state of A and B, analogous to the hydrogen molecular ion H_2^- . In this excited state, there is an effective exchange interaction between the qubit spins. Qubit-qubit interactions are switched on by optical excitation and off by stimulated de-excitation of the control electron (see Fig. 4.81). The sup[posed approach has two key feature. Clearly, the spins encoding the quantum information must have an acceptable time. Further, there must be an electronically excited state in which the entanglement is changed significantly. This scheme has two major advantages. First, ground-state quantum information storage is largely separated from excited-state informational control. Second, no small energy scale is involved in the gate operation: it might operate at liquid nitrogen temperatures or even near room temperature. Cited authors indicate that processors following their approach might be made in near-future semiconductor fabrication plants.

Another promising semiconductor qubit system uses the electron and/or nuclear spins of neutral shallow donor impurities (D^0) such as ^{31}P in Si [348, 350]. The nuclear spin of neutral ^{31}P in isotopically purified ^{28}Si can reach a coherence time of 180 s; however, like all shallow D^0, this is an inherently low-temperature system, and in addition, the donors begin to thermally ionize above ~30 K (Fig. 4.82). Thewalt and coworkers [350] show that the nuclear spin of ionized donor (D^+) has important advantages over that of D^0 and is not limited to operation at cryogenic temperatures. The optical transitions between D^0 and the donor bound exciton (D^0X) used for hyperpolarization, readout, and donor ionization are shown in Fig. 4.82. The cited authors used optical methods and dynamic decoupling and observed a room-temperature coherence time of over 39 minutes of an ensemble phosphorus-31 in isotopically purified silicon-28. To conclude the authors of paper [350] have underlined

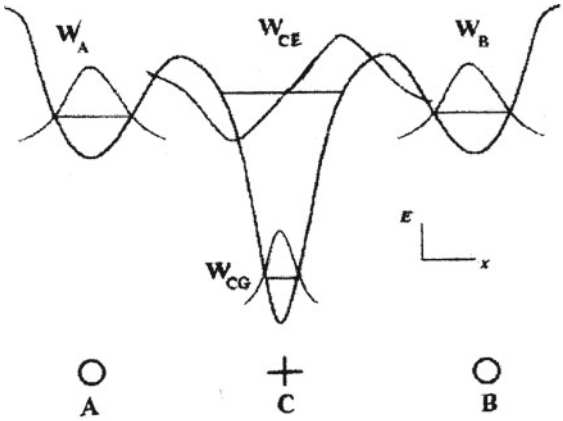

Fig. 4.81 A schematic diagram of the quantum gate. The qubit spins are on deep donors A and B (◯) with wavefunctions W_A and W_B. The control atom, C(+), is the source of a control electron. In the ground state, the control electron is in the state W_{CG}, whose wavefunction and potential well are shown schematically. In the excited state, the control electron is in a charge-transfer, molecular-like, state, W_{CE}, which overlaps both qubit electrons. Neither the qubits nor the control electron interacts significantly in the ground state, but interact causing entanglement in the excited state (after [349])

that another promising possibility would be deep defects in wider-gap materials such as diamond [351] and SiC [352], which also be isotopically purified to remove background spins and where the method of charge-state control could be combined with initialization and readout at room temperature.

Isotope-based Diamond

Since the nitrogen–vacancy (N–V) center in diamond (see Fig. 4.83) has been detected at a single site level, the center has attracted attention for various quantum information processing applications [351, 353–357]. The N–V center occurs in diamond containing single substitutional nitrogen when irradiated and annealed [358]. Electron irradiation with energies greater than 200 keV creates vacancies [359]. The vacancies are mobile at 800 °C and can become trapped adjacent to the nitrogen impurities. The nitrogen–vacancy complex formed a strong optical transitions with zero-phonon line at 1.945 eV (637 nm) accompanied by a vibronic band at higher energy in absorption and lower energy in emission (see, e.g., [351, 354]). The origin of zero-phonon line due the optical transitions $^3A-^3E$ (see Fig. 4.84) between ground ^3A and excited ^3E electronic states which are both the spin triplet ($S = 1$). The ground ^3A state is split by 2.88 GHz into the lower $m_s = 0$ and the upper $m_s = \pm 1$ levels. The center can be individually isolated and optically detected [354, 355], thus opening the excess to long-lived single spin $S = 1$ in the ground ^3a state which can be physical carrier of qubit. The first step for coherent single spin manipulation is to prepare a pure state of the internal spin structure. For the $[N–V]^-$ center, spin state

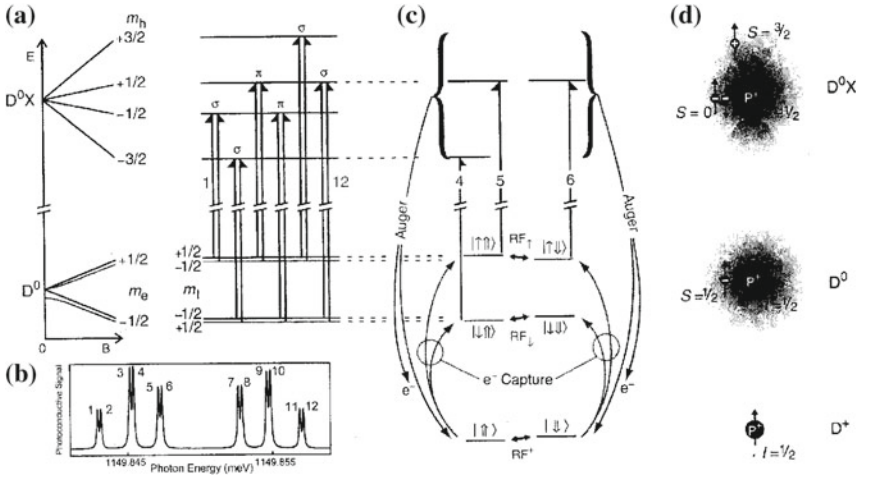

Fig. 4.82 Energy levels and transitions of the P neutral donor (D^0), donor bonds exciton (D^0X), and ionized donor (D^+). **a** The Zeeman splittings of the D^0 and D^0X states are shown from $B_0 = 0$ to $B_0 = 845.3$ G, along with the dipole-allowed optical transitions. **b** Photoconductive readout spectrum without any D^0 hyperpolarization. **c** The specific optical transitions (lines 4, 5, and 6) and nuclear magnetic resonance transitions ($RF_\uparrow$, $RF_\downarrow$ and RF^+) used here to hyperpolarize, manipulate, and read out the nuclear spins. The magnitude of the D^+ Zeeman splitting (RF^+) has been exaggerated to show the ordering of the D^+ state, and the small nuclear Zeeman energy is ignored for the D^0X states. although the energy difference between the D^0 and D^0X levels are precisely fixed in ^{28}Si, the D^+ energy is not well defined because of the kinetic energy of the e^-. **d** Scethees of the spins and charge densities of D^+, D^0 and D^0X (after [352])

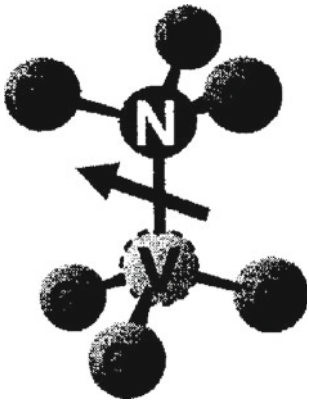

Fig. 4.83 Structure of the nitrogen–vacancy (NV) center. The single substitutional nitrogen atom (N) is accompanied by a vacancy (V) at a nearest neighbor lattice position

preparation can be achieved by optical pumping with a polarized laser beam tuned above the absorption band [356]. Decay from the ^3E level via optical emission dominates but conserve spin. On the other hand, decay via the metastable singlet level ^1A is slower since it does not conserve spin. Competition between those two processes leads to a spin polarization of the ^3A ground level [351]. Once polarized, the electron spin can be manipulated using microwave resonant fields and spin echo techniques.

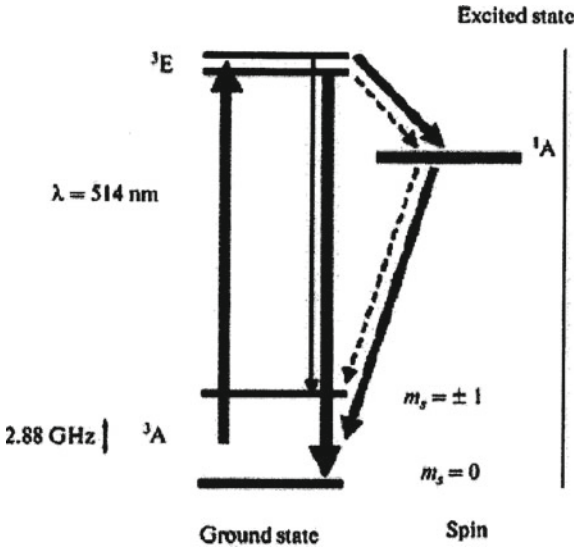

Fig. 4.84 Energy levels of the N–V center. The excited state is split by spin–orbit interaction whereas the ground state is split by spin–spin interaction (not shown to scale). The solid arrows indicated the spin-allowed optical transitions. The diagonal arrows give inter-system crossing allowed by spin–orbit interaction

Such experiments have been performed both on $[N–V]^-$ ensembles and at the single color center [354]. Readout of the spin state is achieved optically because the fluorescence occurs predominantly when the spin state is $m_s = 0$ for both ^3A ground and ^3E excited energy levels [351]. The electron spin of the center exhibited coherence time of about few μs, measured at room temperature in relatively impure diamond with large nitrogen content. In that material, limitation of coherence time arises from local magnetic field fluctuation induced by nearby defects (mostly, by flipping nitrogen electron spin $S = 1/2$). The need for ultrapure diamond samples was highlighted and it was demonstrated that in pure diamond samples the coherence time has been increased up to few hundreds of μs, respectively. A two-qubit conditional quantum gate with fidelity of nearly 90% was demonstrated using a single isolated $[N–V]^-$ color center coupled to a ^{13}C nucleus disposed in the first coordination sphere near the vacancy of the center. Recently, spin-entanglement was generated for two electron spins belonging to closely spaced pairs of $[N–V]^-$ ($S = 1$) and substitutional nitrogen defects ($S = 1/2$) [360, 361] these realizations of two-qubit entangled states were an important next step toward realistic quantum processors on a long spin chain or 2D arrays. Thus, accessibility of single spins for a manipulation even at room temperature, coherent control and readout, demonstrated by the investigations of the $[N–V]^-$ color centers, together with the proposal of application of these centers for room-temperature quantum computer. During last 10 years, there was an impressive progress in understanding of its nontrivial photophysics based on both experimental and theoretical activities (Table 4.12).

Table 4.12 Larmor frequency ω_0 some nuclei in magnetic field H = 11.7 Tl (after [299])

Nuclear	^{1}H	^{2}H	^{13}C	^{15}N	^{19}F	^{31}P
MHz	0	500	77	126–51	470	202

Although many challenges remain on the road to constructing a useful quantum computer, the pace of discovery seems to be accelerating, and spins in semiconductors are poised to play a major role. Several materials systems and architectures have already come to fruition, but others waiting in the wings might prove to be even better for some application. For example, the remarkable properties of the diamond N–V center motivate the search for other impurity-based spin systems with similar properties, possibly in more versatile host materials. Indeed, optically addressable defect spins with room-temperature coherence have recently been discovered in silicon carbide [352], which boast well-developed techniques for heteroepitaxy and fabrication of complex structures (see also [361]).

References

1. V.Ju. Baranov (ed.), *Isotopes*, vols. 1, 2 (Fizmatlit, Moscow, 2005). (in Russian)
2. A.A. Berezin, Isotopic engineering (perspectives). J. Phys. Chem. Solids **50**, 5–8 (1989)
3. E.E. Haller, Isotopically engineered semiconductors. J. Appl. Phys. **77**, 2857–2878 (1995)
4. V.G. Plekhanov, Isotope engineering. Uspekhi - Phys. **170**, 1245–1252 (2000). (in Russian)
5. V.G. Plekhanov, *Applications of the Isotopic Effect in Solids* (Springer, Heidelberg, 2004)
6. A.A. Berezin, Stable isotopes in nanotechnology. Nanotechn. Percept. **5**, 27–36 (2009)
7. V.G. Plekhanov, *Isotopes in Condensed Matter* (Springer, Heidelberg, 2013)
8. A. Sudbery, *Quantum Mechanics and the Particles of Nature* (Cambridge University Press, Cambridge, 1986)
9. J.W. Gibbs, One of the equilibrium of heterogeneous substances, in *The Scientific Papers of J.W. Gibbs* (Dover, New York, 1961)
10. M.J. Kelly, *Low-Dimensional Semiconductors* (Clarendon Press, Oxford, 1995)
11. J.H. Davis, *The Physics of Low-Dimensional Semiconductors* (Cambridge University Press, Cambridge, 1998)
12. P. Harrison, *Qquantum Wells, Wires and Dots* (Wiley, New York, 2001)
13. K. Goser, P. Glösekötter, J. Dienstuhl, *Nanoelectronics and Nanosystems* (Springer, Berlin, 2004)
14. V.G. Plekhanov, *Isotope Low-Dimensional Structures* (Heidelberg, Springer, 2012)
15. A. Cho (ed.), *Molecular Beam Epitaxy* (Springer, Berlin, 1997)
16. G.B. Stringfellow, *Organometallic Vapor-Phase Epitaxy: Theory and Practice*, 2nd edn. (Academic Press, London, 1999)
17. A. Rastelli, S. Kiravittaya, O.G, Schmidt, Growth and control of optically active quantum dots, in *Nanoscience and Technology*, ed. by P. Mihler (Springer, Berlin, 2009)
18. V.A. Shchukin, D. Bimberg, Spontaneous ordering of nanostructures on crystal surfaces. Rev. Mod. Phys. **71**, 1125–1171 (1999)
19. J. Strangl, V. Holy, G. Bauer, Structural properties of self-organized semiconductor nanostructures. ibid **76**, 725–783 (2004)
20. C.J. Chen, *Introduction to Scanning Tunneling Microscoppy* (Oxford University Press, New York, 1993)

21. L. Esaki, R. Tsu, Supelattice and negative differential conductivity in semiconductors. IBM J. Res. Develop. **14**, 61 (1970)
22. V.G. Plekhanov, *Isotope Effects in Solid State Physics* (Academic Press, San Diego, 2001)
23. V.G. Plekhanov, *Isotope-Based Quantum Information* (2009), arXiv: quant-ph/0909.0820
24. P. Michler (ed.) *Single Semiconductor Quantum Dots* (Springer, Berlin, 2009)
25. G. Bastard, *Wave Mechanics Applied to Semiconductor Heterostructures* (Halsted Press, New York, 1988)
26. C. Weisbuch, B. Vinter, *Quantum Semiconductor Structures* (Academic Press, San Diego, 1991)
27. K. Thyagarajan, A.K. Ghatak (eds.), *Lasers Theory and Applications* (Plenum Press, New York, 1982)
28. C. Klingshirn, Lasers processes in semiconductors, in *Spectr. Solid-State Laser Type Matter, Proceedings of Course Enrico Fermi, Erice* (New York, London, 1989)
29. C. Klingshirn, H. Haug, Optical properties of highly excited direct gap semiconductors. Phys. Rep. **70**, 315–398 (1981)
30. V.G. Plekhanov, Elementary excitations in isotope-mixed crystals. Phys. Rep. **410**, 1–235 (2005)
31. M. Cardona, M.L.W. Thewalt, Isotope effect on optical spectra of semiconductors. Rev. Mod. Phys. **77**, 1173–1224 (2005)
32. K. Takiyama, M.I. Abd-Elrahman, T. Fujita et al., Photoluminescence and decay kinetics of indirect free excitons in diamonds under near-resonant laser excitation. Solid State Commun. **99**, 793–796 (1996)
33. K. Horiuchi, K. Nakamura, S. Yamashita, Current injection free-exciton recombination emission from synthesized diamond. Jpn. J. Appl. Phys. **39**, L604–L608 (2000)
34. S. Koizumi, K. Watanabe, M. Hasegawa et al., Ultraviolet emission from a diamond pn junction. Science **292**, 1899–1901 (2001)
35. B.E. Kane, A silicon-based nuclear spin quantum computer. Nature **393**, 133–137 (1998)
36. H. Watanabe, C.E. Nebel, S. Shikata, Isotopic homojunction band engineering from diamond. Science **324**, 1425–1428 (2009)
37. V.F. Agekyan, B.G. Alexandrov, Yu.A. Stepanov, Spectral and time domain characteristics of thermal localized excitons in solid solutions $CdS_1 - xSe_x$. Phys. Techn. Semicond. (St.-Petrsburg) **22**, 1221 (1988). (in Ruasian)
38. H. Haug, Ultrafast physical processes in semiconductors, in *Semiconductor and Semimetalls*, vol. 67, ed. by K.T. Tsen, R.K. Willardson, K. Weber (San Diego, Academic Press, 2001) p. 201
39. K.C. Liu, R. Liboff, Criterion for exciton lasing in pure crystals. J. Appl. Phys. **54**, 5633–5637 (1983)
40. C.A. Benoit la Guilaume, A. Bonnot, J.M. Debever, Luminescence from polaritons. Phys. Rev. Lett. **24**, 1235–1238 (1970)
41. B. Honerlage, R. Levy, J.R. Grun, The dispersion of excitons, polaritons and biexcitons in direct-gap semiconductors. Phys. Rep. **124**, 161–253 (1985)
42. V.G. Plekhanov, Comparative study of isotope and chemical effects on the exciton states in LiH crystals. Prog. Solid State Chem. **29**, 71–177 (2001)
43. H. Haug, S.W. Koch, *Quantum Theory of Optical and Electronic Properties of Semiconductors* (World Scientific, London, 1993)
44. S.I. Pekar, *Crystal Optics and Additional Light Waves* (Menlo Park, Benjamin/Cummings, San Francisco, 1983)
45. Y. Toyozawa, On dynamical behavior of excitons. Prog. Theor. Phys. (Kyoto) **12** (Suppl.) 111–140 (1959)
46. N.G. Basov, O.V. Bogdankevich, A.G. Devyatkov, Cadmium sulfide laser excited by fast electrons. Sov. Phys. JETP **20**, 1067–1068 (1964)
47. L.A. Kulevsky, A.M. Prokhorov, The nature of the laser emission in CdS crystal at 90 K with two-photon excitation. IEEE QE **2**, 584–586 (1966)

48. V.G. Plekhanov, Resonant secondary emission spectra, in *Proceedings of the International Conference on LASERS'80* (STS Press, McClean, 1981), pp. 91–99
49. V.G. Plekhanov, V.I. Altukhov, Free exciton luminescence and exciton - phonon interaction parameters of wide-gap insulators, in *Proceedings of the International Conference on LASER-S'82* (STS Press, McClean, 1983), pp. 292–299
50. V.G. Plekhanov, Wannier-Mott excitons in isotope disordered crystals. Rep. Prog. Phys. **61**, 1045–1097 (1998)
51. V.G. Plekhanov, Changes in spectra of luminescence and Raman scattering in lithium hydride under growth in the excitation intensity. Quantum Electron. (Moscow) **16**, 2156–2159 (1989)
52. R.S. Knox, *Theory of Excitons* (Academic Press, New York, 1963)
53. E.F. Gross, *Selected Papers* (Leningrad, Science, 1976). (in Russian)
54. G. Leifried, W. Ludwig, *Theory of Anharmonic Effect in Crystals* (Academic Press, New York, 1961)
55. W. Cochran, R.A. Cowley, Phonons in perfect crystals, in *Encyclopedia of Physics*, ed. by S. Flügge (ed), vol. 25/2 (Light and Matter) (Springer, Berlin, 1967)
56. G.P. Srivastawa, *The Physics of Phonons* (Hilger, Bristol, 1990)
57. I.E. Tamm, Eine Bemerkung zur Diracschen Theorie der Lichtenstroung und Dispersion. Zs. Phys. **62**, 705–708 (1930)
58. M. Blackman, The specific heat of solids, in *Handbuch der Physik*, vol. 7, Pt. 1, ed. by S. Flüge (Springer, Berlin, 1955), pp. 325–367
59. P. Klemens, Thermal conductivity and lattice vibrational modes, in *Solid State Physics*, vol. 7, ed. by F. Seitz, D. Turnbull (Academic Press, New York, 1959), pp. 1–98
60. P. Debye, The Debye theory of specific heat. Ann. Phys. (Leipzig) **4**(39), 789–803 (1912)
61. L.D. Landau, E.M. Lifshitz, *Statistical Physics* (Pergamon Press, New York, 1968)
62. V.A. Krymov, D.L. Fukc, Transactions of the Universities of USSR. Phys. **30**, 39–51 (1987). (in Russian)
63. E. Grüneisen, Theorie des festen Zustandes einatomiger Elemente. Ann. Phys. **4**(39), 257–306 (1912)
64. E. Grüneisen, Zustand des festen Körpers. Handbuch der Physik **10**, 1–59 (1926)
65. P. Debye, Zur Theorie der spezifischen Wärmen. Ann. Phys. **4**(39), 789–807 (1912)
66. G. Dolling, R.A. Cowley, The thermodynamic and optical properties of germanium, silicon, diamond and gallium arsenide. Proc. Phys. Soc. **88**, 463–494 (1966)
67. T.H. Baron, J.G. Collins, G.K. White, Thermal expansion of solids at low temperatures. Adv. Phys. **29**, 609–730 (1980)
68. V.I. Ozhogin, A.V. Inyushkin, A.N. Taldenkov, Isotope effect for thermal expansion coefficient of germanium. JETP Lett. (Moscow) **63**, 463–466 (1996)
69. D.F. Gibbons, Thermal expansion of some crystals with the diamond structure. Phys. Rev. **112**, 136–140 (1958)
70. S.I. Novikova, *Thermal Expansion of Solids* (Science, Moscow, 1974) (in Russian)
71. D.K. Smith, H.R. Leider, Low-temperature thermal expansion of LiH, MgO and CaO. J. Appl. Cryst. **1**, 246–249 (1968)
72. H. Jex, Thermal expansion and mode Grüneisen parameters of LiH and LiD. J. Phys. Chem. Solids **35**, 1221–1223 (1974)
73. B.W. James, H. Kherandish, The low temperature variation of the elastic constants of LiH and LiD. J. Phys. C: Solid State Phys. **15**, 6321–6339 (1982)
74. D. Gerlich, C.S. Smith, The pressure and temperature derivatives of the elastic module of lithium hydride. J. Phys. Chem Solids **35**, 1587–1592 (1974)
75. Q. Johnson, A.C. Mitchel, Search for the NaCl and CsCl transition in LiH by flash X-ray diffraction. Acta Cryst. **A31**, S241–S245 (1975)
76. T.H. Geballe, G.W. Hull, Isotopic and other types of thermal resistance in germanium. Phys. Rev. **110**, 773–775 (1958)
77. J.J. Fontanella, D.E. Schuele, Low temperature Grüneisen parameter of RbI from elasticity data. J. Phys. Chem. Solids **31**, 647–654 (1970)

78. S. Haussuhl, I. Skorczyk, Elastische und thermoelastische Eigenschaften von LiH und LiD einkristallen. Zs. Krist. **130**, 340–345 (1969)
79. A.R. Ubellohde, *The Molten State of Substances* (Metallurgy, Moscow, 1982). (in Russian)
80. H. Dammak, E. Antonshchenkova, M. Hayoun et al., Isotope effect in lithium hydride and lithium deuteride by molecular dynamics simulations. J. Phys. Condens. Matt. **24**, 435402–6 (2012)
81. G.L. Anderson, G. Nasise, K. Phillipson et al., Isotopic effects on the thermal expansion of lithium hydride. J. Phys. Chem. Solids **31**, 613–618 (1970)
82. R.B. Von Dreele, J.G. Morgan, S.M. Stishov, Thermal expansion and equation of state of KCN of different isotopic composition. JETP (Moscow) **114**, 2182–2186 (1998). (in Russian)
83. V.I. Tyutyunnik, Effect of isotope substitution on thermal expansion of LiH crystal. Phys. Status Solidi (b) **172**, 539–543 (1992)
84. V.S. Kogan, Isotope effect in structuring properties. Sov. Phys. Uspekhi **5**, 579–618 (1963)
85. V.I. Ozhogin, A.V. Inyushkin, A.N. Taldenkov et al., Isotope effect for thermal expansion coefficient of germanium. JETP (Moscow) **115**, 243–248 (1999). (in Russian)
86. L. Wei, P.K. Kuo, R.L. Thomas, Thermal conductivity of isotopically modified single crystal diamond. Phys. Rev. Lett. **79**, 3764–3767 (1993)
87. M. Asen-Palmer, K. Bartkowsky, E. Gmelin et al., Thermal conductivity of germanium crystals with different isotopic composition. Phys. Rev. B **56**, 9431–9447 (1997)
88. T. Ruf, R.W. Henn, M. Asen-Palmer et al., Thermal conductivity of isotopically enriched silicon. Solid State Commun. **115**, 243–247 (2000); Erratum **127**, 257 (2003)
89. N.W. Aschcroft, N. David Mermin, *Solid State Physics* (Harcourt Brace College Publishers, New York, 1975)
90. M. Born, K. Huang, *Dynamical Theory of Crystal Lattice* (Oxford University Press, Oxford, 1988)
91. V.N. Kostryukov, The capacity of LiH between 3.7 and 295K. Zh. Fiz. Khim. (Moscow) **35**, 1759–1762 (1961) (in Russian)
92. D.N. Batchelor, R.O. Simons, Lattice constants and thermal expansivities of silicon and calcium fluoride between 6 and 322K. J. Chem. Phys. **41**, 2324–2330 (1964)
93. V.G. Plekhanov, Isotope effect in lattice dynamics. Physics - Uspekhi (Moscow) **46**, 689–717 (2003)
94. G. Yates, G.H. Wostenholm, J.K. Bingham, The specific heat of ^{7}LiH and ^{7}LiD at low temperature. J. Phys. C: Solid state Phys. **7**, 1769–1778 (1974)
95. F.F. Voronov, V.A. Goncharov, Compressions of lithium hydride. Fiz. Tverd. Tela (St. Petersburg) **8**, 1643–1645 (1966). (in Russian)
96. V.G. Plekhanov, Lattice dynamics of isotopically mixed crystals. Opt. Spectr. (St. Petersburg) **82**, 95–124 (1997)
97. V.G. Plekhanov, Isotope effect on the lattice dynamics of crystals. Mater. Sci. Eng. **R35**, 139–237 (2001)
98. D.P. Schumacher, Polymorphies transition of LiH. Phys. Rev. **126**, 1679–1684 (1962)
99. D.R. Stephens, E.M. Lilley, Compressions of isotopes lithium hydride. J. Appl. Phys. **39**, 177–180 (1968)
100. Y. Kondo, K.J. Asaumi, Effect of pressure on the direct gap of LiH. J. Phys. Soc. Jpn. **57**, 367–371 (1988)
101. K. Chandehari, A. Ruoff, Band gap and index refraction of CsH to 25 GPa. Solid State Commun. **95**, 385–388 (1995)
102. W. Schnelle, E. Gmelin, Heat capacity of germanium crystals with different isotopic composition. J. Phys: Condens. Matter **13**, 6087–6094 (2001)
103. M. Sanati, S.K. Estreicher, Specific heat and entropy of GaN. ibid **16**, L327–L331 (2004)
104. J.M. Ziman, *Models of Disorder* (Cambridge University Press, Cambridge, 1979)
105. R. Berman, *Thermal Conductions of Solids* (Clarendon Press, Oxford, 1976)
106. M. Planck, Zur Theorie der Wärmestrahlung. Ann. Phys. **336**, 758–768 (1910)
107. R.E. Peierls, *Quantum Theory of Solids* (Clarendon Press, Oxford, 1955)

108. I.Ya. Pomeranchuk, About thermal conductivity of dielectrics. J. Phys. (USSR) **6**, 237–246 (1942)
109. D.G. Onn, A. Witek, Y.Z. Qiu et al., Some aspect of the thermal conductivity of isotopically enriched diamond single crystals. Phys. Rev. Lett. **68**, 2806–2809 (1992)
110. J.R. Olson, R.O. Pohl, J.W. Vandersande et al., Thermal conductivity of diamond between 170 and 1200K and the isotopic effect. Phys. Rev. **B47**, 14850–14856 (1993)
111. M. Cardona, R.K. Kremer, M. Sanati et al., Measurements of the heat capacity of diamond with different isotopic composition. Solid State Commun. **133**, 465–468 (2005)
112. J. Callaway, Model for lattice thermal conductivity at low temperatures. Phys. Rev. **113**, 1046–1051 (1959)
113. A.P. Zhernov, A.V. Inyushkin, Kinetic coefficients in isotopically disordered crystals. Physics - Uspekhi (Moscow) **45**, 573–599 (2002)
114. M. Omini, A. Sparavigna, Heat transport in dielectric solids with diamond structure. Nuovo Cimento **D19**, 1537–1563 (1997)
115. A. Sparavigna, Influence of isotope scattering on the thermal conductivity of diamond. Phys. Rev. **B65**, 064305-5 (2002), ibid, **B67**, 144305-4 (2003)
116. W.C. Capinski, H.J. Maris, S. Tamura, Analysis of the effect of isotope scattering on the thermal conductivity of crystalline silicon. Phys. Rev. B **59**, 10105–10110 (1999)
117. M.G. Holland, Thermal conductivity, in *Physics of III–V Compounds, in: Semiconductor and Semimetal*, vol. 2, ed. by R.K. Willardson, A.C. Beer (Academic Press, New York, 1966), p. 3
118. J.W. Lyding, K. Hess, I.C. Kizilyalli, Reduction of hot electron degradation in metal oxide semiconductor transistors by deuterium processing. Apll. Phys. Lett. **68**, 2526–2529 (1996)
119. G. London, The difference in molecular volume of isotopes. Z. Phys. Chem. Neue Folge **16**, 3021–3029 (1958)
120. A.R. Ruffa, Thermal expansion and zer point displacement in isotopic lithium hydride. Phys. Rev. B **27**, 1321–1325 (1983)
121. A.A. Berezin, A.M. Ibrahim, Effects of the diversity of stable isotopes on properties of materials. Mater. Chem. Phys. **19**, 420–437 (1988)
122. R.C. Bushert, A.E. Merlin, S. Pace et al., Effect of isotope concentration on the lattice parameter of germanium perfect crystals. Phys. Rev. B **38**, 5219–5221 (1988)
123. E.E. Shpilrain, K.A. Yakimovich, T.N. Mel'nikova, *Thermal Properties of Lithium Hydride-Deuteride and their Solutions with Lithium* (Energoatomizdat, Moscow, 1983). (in Russian)
124. J.C. Noya, C.P. Hrrero, R. Ramirez, Isotope dependence of the lattice parameter of germanium from path-integral Monte Carlo simulations. Phys. Rev. B **56**, 237–243 (1997)
125. A. Kazimirov, J. Zegenhagen, M. Cardona, Isotopic mass and lattice constant X-ray standing wave measurements. Science **282**, 930–932 (1998)
126. Y. Ma, J.S. Tse, Ab initio detrmination of crystal lattice constant and thermal expansion for germanium isotopes. Solid State Commun. **143**, 161–165 (2007)
127. W. Banholzer, T. Anthony, Diamond properties as a function of isotopic composition. Thin Solid Films **212**, 1–10 (1992)
128. H. Holloway, K.C. Hass, M.A. Tamor et al., Isotopic dependence of lattice constants of diamond. Phys. Rev. B **44**, 7123–7126 (1991)
129. P. Pavone, S. Baroni, Dependence of the crystal lattice constant on isotopic composition. Solid State Commun. **90**, 295–297 (1994)
130. H. Holloway, K.C. Hass, M.A. Tamor et al., Isotopic dependence of lattice constants of diamond. ibid, B **45**, 6353E (1992)
131. W.B. Zimmerman, Lattice constant dependence on isotopic composition in the ^{7}Li(H, D) system. Phys. Rev. B **5**, 4704–4707 (1972)
132. T. Yamanaka, S. Morimoto, H. Kanda, Influence of the isotope ratio on the lattice constant of diamond. ibid **B49**, 9341–9343 (1994)
133. R. Vogelgesang, A.K. Ramdas, S. Rodriguez et al., Brillouin and Raman in natural and isotopically controlled diamond. Phys. Rev. B **54**, 3989–3999 (1996)

134. N. Garo, A. Cantarero, T. Ruf et al., Dependence of the lattice parameters and energy gap of zinc-blende-type semiconductors on isotopic mass. Phys. Rev. B **54**, 4732–7440 (1996)
135. A. Debernardi, M. Cardona, Isotopic effect on the lattice constant in compound semiconductors by perturbation theory: An ab initio calculation. Phys. Rev. B **54**, 11305–11310 (1996)
136. H. Bilz, W. Kress, *Phonon Dispersion Relations in Insulators* (Springer, Berlin, 1979)
137. H. Kressel (ed.), *Semiconductor Devices for Optical Communications: Topics in Applied Physics*, vol. 39 (Springer, Berlin, 1982)
138. P.C. Becker, M.R.X. de Barras, in *Materials for Optoelectronics*, ed. by M. Quilec (Kluver Academic Publishers, Boston, 1996)
139. A.W. Snyder, J.D. Love, *Optical Waveguide Theory* (Chapman and Hall Medical, London, 1996)
140. D. Marcuse, *Light Transmission Optics* (Van Nostrand, New York, 1972)
141. W.B. Allan, *Fibre Optics Theory and Practice* (Plenum Press, New York, 1973)
142. N.S. Kapany, *Fiber Optics* (Academic Press, New York, 1967)
143. J.A. Arnaud, *Beam and Fibre Optics* (Academic Press, New York, 1976)
144. D. Marcuse, *Theory of Dielectric Optical Waveguides* (Academic Press, New York, 1974)
145. J.E. Midwinter, *Optical Fibers for Transmission* (Wiley, New York, 1979)
146. R.W. Pohl, *Introduction into Optics* (Science, Moscow, 1947). (in Russian)
147. L.M. Zhuravleva, V.G. Plekhanov, Method of Fiber's Manufacture. Patent of Russian Federation N **2302381**, 10 (2007)
148. V.G. Plekhanov, Applications of isotope effects in solids. J. Mater. Sci. **38**, 3341–3429 (2003)
149. A. Jorio, G. Dresselhaus, M.S. Dresselhaus (eds.), *Carbon Nanotubes*. Topics Applied Physics, vol. 111 (Springer, Heidelberg, 2008)
150. M.S. Dresselhaus, P.C. Eklund, Phonons in carbon nanotubes. Adv. Phys. **49**, 705–814 (2000)
151. J.C. Charlier, P.C. Eklund, A.C. Ferrari, Electron and phonon properties of graphene: their relationship with carbon nanotubes, in *[157]*, pp. 673–709
152. S. Reich, C. Thomsen, J. Maultzsch, *Carbon Nanotubes: Basic Concepts and Physics Properties* (Imperial College Press, London, 2004)
153. V.G. Plekhanov, Manifestation of the strong nuclear interactions in the isotope-induced band-gap-opening of graphene, in *Horizons in World Physics*, vol. 281 (Nova Science Publishers, Inc., New York, 2013), pp. 197–202
154. M.Y. Han, B. Ozyilmaz, Y. Zhang, Energy band-gap engineering of graphene nanoribbons. Phys. Rev. Lett. **98**, 206805-4 (2007)
155. L.A. Ponomarenko, F. Schedin, M. Katsnelson et al., Chaotic Dirac billiard in graphene quantum dots. Science **320**, 356–358 (2008)
156. A. Savchenko, Transforming graphene. Science **323**, 589–590 (2009)
157. V.G. Plekhanov, Nuclear technology creation the quantum dots in graphene, in *Transactions Humanitar Institute, Tallinn, 2011*, pp. 66–70 (in Russian); V.G. Plekhanov, 2015 (unpublished results)
158. See Special Issue Nature (2009)
159. K.F. Mak, C.H. Lui, T.F. Heinz, Observation of an electric-field-induced band gap in bilayer graphene by infrared spectroscopy. Phys. Rev. Lett. **102**, 256405-4 (2009)
160. E.V. Castro, K.S. Novoselov, S.V. Morozov, et al., Biased bilayer graphene: semiconductor with a gap tunable by the electric field effect. ibid **99** 216802-4 (2007)
161. ZhH Ni, T. Yu, Y.H. Lu, Uniaxial strain on graphene: Raman spectroscopy study and band-gap opening. ACS Nano **3**, 483–492 (2009)
162. P.R. Wallace, The band theory of graphite. Phys. Rev. **71**, 622–629 (1947)
163. V.G. Plekhanov, Isotopical band-gap opening in graphene. Universal J. Phys. Appl. **10**, 16–21 (2016)
164. A.K. Ramdas, S. Rodriguez, Lattice vibrations and electronic excitations in isotopically controlled diamonds. Phys. Stat. Sol. (b) **215**, 71–80 (1999)
165. S. Prawer, R.J. Nemanich, Raman spectroscopy of diamond and doped diamond. Phil. Transac. R. Soc. (Lond.) **362**, 2537–2565 (2004)

166. M.S. Dresselhaus, G. Dresselhaus, M. Hofman, Raman spectroscopy as a probe of graphene and carbon nanotubes. ibid, **366**, 231–236 (2008)
167. C. Casiraghi, A. Hartschuh, H. Qian et al., Raman spectroscopy of graphene edges. Nano Lett. **9**, 1433–1441 (2009)
168. Sh Chen, Q. Wu, C. Mishra, Thermal properties of isotopically engineered graphene. Nat. Mater. **11**, 203–207 (2012)
169. A. Ferrari, Raman spectroscopy of graphene and graphite: disorder, electron-phonon coupling, doping and nonadiabatic effects. Solid State Commun. **143**, 47–57 (2007)
170. M. Huang, H. Yan, C. Chen et al., Raman spectroscopy of graphene under uniaxial stress: phonon softening and determination of crystallographic orientation. Proc. Natl. Acad. Sci. USA **106**, 7304–7315 (2009)
171. M. Farjam, H. Rafii-Tabar, Comment on "Band structure engineering of graphene by strain: First-principles calculations". Phys. Rev. B **80**, 167401-3 (2009)
172. T.M. Mohiuddin, A. Lombarto, R.R. Nair et al., Uniaxial strain in graphene by Raman spectroscopy: G peak splitting. Grűneisen parameter and sample orientation. ibid, B **79**, 205433-8 (2009)
173. S.D. Costa, C. Fantini, A. Righi et al., Resonant Raman spectroscopy on enriched ^{13}C carbon nanotubes. Carbon **49**, 4919–4723 (20011)
174. J.F. Rodriguez-Nieva, R. Saito, S.D. Costa et al., Effect of ^{13}C doping on the optical phonon modes in graphene: localization and Raman spectroscopy. Phys. Rev. B **85**, 245406-8 (2012)
175. S. Bernard, E. Whiteway, V. Yu et al., Probing the experimental phonon dispersion of graphene using ^{12}C and ^{13}C isotopes. ibid, B **86**, 085409-5 (2012)
176. E. del Corro, M. Kolbac, C. Fantini et al., Isotopic ^{12}C/^{13}C effect on the resonant Raman spectrum of twisted bilayer graphene. ibid, B **88**, 155436-5 (2013)
177. Z.C. Kun, L.Q. YU, T. Bo, et al., Isotope effect of the phonons mean free path in graphene by micro - Raman measurement, Science China. Phys. Mech. Astro. **57**, 1817–1821 (2014)
178. K.C. Hass, M.A. Tamor, T.R. Anthony, W.F. Banholzer, Lattice dynamics and Raman spectra of isotopically mixed diamons. Phys. Rev. B **45**, 7171–7182 (1992)
179. E.G. Browman, Y.M. Kagan, Phonons in non-transition metals, in *Dynamical Properties of Solids*, vol. 1, ed. by G.K. Horton, A.A. Maradudin (North-Holland Publishing Company, 1974), Chapter 4
180. S. Bae, H. Kim, Y. Lee, Roll-to-roll production of 30-inch graphene films for transparent electrodes. Nat. Nanotechnol. **5**, 574–578 (2010)
181. K.F. Mak, L. Ju, T.F. Heinz, Optical spectroscopy of graphene: from the far infrared to the ultraviolet. Solid State Commun. **152**, 1341–1349 (2012)
182. V.G. Kravets, A.N. Grigorenko, R.R. Nair, Spectroscopic ellipsometry of graphene and exciton-shifted in a graphene transistor. Phys. Rev. B **81**, 155413–7 (2010)
183. H.A. Becerril, J. Man, Z. Liu, Evaluation of selection-processed reduced graphene oxide films as transparent conductors. ACS Nano **2**, 463–469 (2008)
184. S.R. Forrest, The path to ubiquitous and low-cost organic electronic appliances on plastic. Nature **428**, 911–915 (2004)
185. Z. Chen, B. Cotterell, W. Wang et al., A mechanical assestment of flexible optoelectronic devices. Thin Solid Films **394**, 201–206 (2001)
186. Z.Y. Yin, S.X. Wu, X.Z. Zhou et al., Electrochemical deposition of ZnO nanorods on transparent reduced graphene oxide electrodes for hybrid solar sells. Small **6**, 307–310 (2010)
187. Z.Y. Yin, S.Y. Sun, T. Salim et al., Organic photovoltaic devices using highly flexible reduced graphene oxide films as transparent electrodes. ACS Nano **4**, 5263–5267 (2010)
188. X. Wang, L.J. Zhi, K. Mullen, Transparent, conductive graphene electrodes for dye-sensitized solar cells. Nano Lett. **8**, 323–329 (2008)
189. I. Jung, D. Dikin, S. Park et al., Effect of water vapor on electrical properties of individual reduced graphene oxide sheets. J. Phys. Chem. **112**, 20264–20268 (2008)
190. J.D. Fowler, M.J. Allen, V.C. Tung et al., Practical chemical sensors from chemically derived graphene. ACS Nano **3**, 301–305 (2008)

191. G. Lu, L.E. Ocola, J. Chen, Gas detection using low-temperature reduced graphene oxide sheets. Appl. Phys. Lett. **94**, 083111–4 (2009)
192. Q. Liu, Z.F. Liu, X.Y. Zhong, Polymer photovoltaic cells based on solution-processable graphene and P3HT. Adv. Funct. Mater. **19**, 894–900 (2009)
193. D. Pan, S. Wang, B. Zhoo et al., Li storage properties of disordered graphene nanosheets. Chem. Mater. **21**, 3136–3141 (2009)
194. E. Yoo, J. Kim, H.-s. Zhou et al., Large reversible Li storage of graphene nanosheet families for use in rechargeable lithium ion batteries. Nano Lett. **8**, 2277–2281 (2008)
195. L.E.F. Foa Torres, S. Roche, J.-C. Charlier, *Introduction to Graphene-Based Nanomaterials* (Cambridge, Cambridge University Press, 2014)
196. Ah Castro Net, F. Guinea, N.M.R. Peres et al., The electronic properties of graphene. Rev. Mod. Phys. **81**, 109–162 (2009)
197. X. Du, I. Sachko, A. Barker et al., Approaching dallistic transport in suspended graphene. Nat. Nanotechnol. **3**, 491–497 (2008)
198. K. Novoselov, A. Geim, S. Morozov et al., Electric field effect in atomically thin carbon films. Science **306**, 666–670 (2004)
199. W.S. Hummers, R.E. Offeman, Preparation of graphite oxide. J. Am. Chem. Soc. **80**, 1339–1343 (1958)
200. W.W. Cai, R.D. Piner, F.J. Stademann et al., Synthesis and solid state NMR structural characterization of ^{13}C labelled graphite oxide. Science **321**, 1815–1816 (2008)
201. W. Gao, L.B. Alemany, L. Ci et al., New insights into the structure and reduction of graphite oxide. Nat. Chem. **1**, 403–405 (2009)
202. J.H. Chen, W.G. Cullen, C. Jang et al., Defect scattering in graphene. Phys. Rev. Lett. **102**, 236805–4 (2009)
203. Z. Luo, P.M. Vora, E.J. Mele et al., Photoluminescence and band gap modulation in graphene oxide. Appl. Phys. Lett. **94**, 111909–3 (2009)
204. A. Nourbaksch, M. Cantoro, T. Vosch et al., Band gap opening in oxygen plasma treated graphene. Nanotechnol. **21**, 435203 (2010)
205. H. Huang, Z. Li, J. She et al., Oxygen density dependent band gap of reduced graphene oxide. J. Appl. Phys. **111**, 054317–4 (2012)
206. V. Singh, D. Joung, L. Zhai, Graphene based materials: past, present and future. Prog. Mat. Sci. **56**, 1178–1271 (2011)
207. A.C. Ferrari, J.C. Meyer, V. Scardaci et al., Raman spectrum of graphene and graphene layers. Phys. Rev. Lett. **97**, 187401–4 (2006)
208. A.C. Ferrari, J. Robertson, Interpretation of Raman spectra of disordered and amorphous carbon. Phys. Rev. B **61**, 14095 (2000)
209. A.C. Ferrari, J. Robertson, Resonant Raman spectroscopy of disordered, amorphous and diamondlike carbon. Phys. Rev. B **64**, 075414–7 (2001)
210. T. Nakajima, N. Watanabe, *Graphite Fluorides and Carbon-Fluorine Compounds* (CRC, Roca Baton, 1991)
211. J. Ito, J. Nakamura, A. Natori, Semiconducting nature of the oxygen-adsorbed graphene sheet. J. Appl. Phys. **103**, 113712–5 (2008)
212. J.O. Sofo, A.S. Chauhari, Grpaphane Barber, A two-dimensional hydrocarbon. Phys. Rev. B **75**, 153401–4 (2007)
213. G.A. Olah, A. Molnar, *Hydrocarbon Chemistry* (Wiley-Inerscience, Hoboken, 2003)
214. N.F. Mott, E.A. Davis, *Electronic Processes in Non-crystalline Materials* (Clarendon Press, Oxford, 1979)
215. V.G. Plekhanov, Isotope-based materials science. Universal J. Mat. Sci. **1**, 87–147 (2013)
216. R.P. Feynman (1959), http://www.zyvex.com/nanotech/feynman.html
217. G. Binning, H. Rohrer, Ch. Gerber et al., Surface studies by scanning tunneling microscopy. Phys. Rev. Lett. **49**, 57–60 (1982)
218. G. Binning, H. Rohrer, Ch. Gerber et al., Tunneling through a controllable vacuum gap. Appl. Phys. Lett. **40**, 178–181 (1982)

219. J.A. Stroscio, W.J. Kaiser (eds.), *Scanning Tunneling Microscopy* (Academic Press, Boston, 1993)
220. R. Wiesendanger, *Scanning Probe Microscopy and Spectroscopy* (Cambridge University Press, Cambridge, 1994)
221. J.S. Blakemore, Semiconducting and other major properties of gallium arsenide. J. Appl. Phys. **53**, R123–R181 (1982)
222. S.M. Sze (ed.), *High-Speed Semiconductor Devices* (Wiley, New York, 1990)
223. M.A. Kastner, The single electron transistor. Rev. Mod. Phys. **64**, 849–858 (1992)
224. Y. Ono, A. Fujiwara, K. Nishiguchi et al., Manipulation and detection of single electrons for future information processing. J. Appl. Phys. **97**, 031101–19 (2005)
225. K.K. Likharev, T. Claeson, Single electronics. Sci. Am. (1991). (S.M)
226. H. Grabert, M.H. Devored (eds.), *Single Charge Tunneling: Coulomb Blackade Phenomena in Nanostructures, NATO ASI Series B* (Plenum Press, New York, 1992)
227. K. Barnham, D. Vvedensky (eds.), *Low-Dimensional Semiconductor Structures* (Cambridge University Press, Cambridge, 2009)
228. M.A. Storcio, M. Dutta, *Phonons in Nanostructures* (Cambridge University Press, Cambridge, 2005)
229. A. Kiravittaya, Rastelli, O.G. Schmidt, Advances quantum dot configurations. Rep. Prog. Phys. **72**, 046502–046534 (2009)
230. K. Seeger, *Semiconductor Physics* (Springer, New York, 1973)
231. I.I. Abramov, E.G. Novik, Phys. Tech. Semic **33**, 1388–1394 (1999). (in Russian)
232. N. Gerasimenko, Ju. Parhomenko, *Silicon-Material of Nanoelectronics* (Moscow, Technosphera, 2007). (in Russian)
233. A.V. Eletskii, Mechanical properties of carbon nanostructures and related materialls. Uspekhi Fiz. Nauk **177**, 233–274 (2007). (in Russian)
234. Ch. Kittel, *Thermal Physics* (Wiley, New York, 1969)
235. D. Bimberg, M. Grundman, N.N. Ledentsov, *Quantum Dot Heterostructures* (Wiley, Chichester, 1999)
236. J. Bylander, T. Duty, P. Delsing, Current measurement by real time counting of single electrons. Nature **434**, 6199–6211 (2005)
237. V.G. Plekhanov, *Isotope-Based Quantum Information* (Springer, Heidelberg, 2012)
238. H. Schoeller, G. Schoen, Mesoscopic quantum transport: resonant tunneling in the presence strong Coulomb interaction. Phys. Rev. B **50**, 18436–18442 (1994)
239. L.M. Zhuravleva, V.G. Plekhanov, Isotopetronics: fundamentals and applications, in *Proceedings of the International Conference* (Sophia, Bulgaria, 2012), pp. 23–36
240. D.V. Averin, A.A. Odintsov, S.A. Vyshenskii, Ultimate accuracy of single-electron dc current standards. J. Appl. Phys. **73**, 1297 (1993)
241. W.G. van der Wiel, S. De Franceschi, J.M. Elzerman et al., Electron transport through double quantum dots. Rev. Mod. Phys. **75**, 1–23 (2003)
242. S.M. Reiman, M. Manninen, Electronic structure of quantum dots. ibid **74**, 1283-1342 (2002)
243. P. Recher, B. Trauzel, Quantum dots and spin qubits in graphene. Nanotechnology **21**, 302001–19 (2010)
244. A.V. Rozhkov, G. Giavaras, Y.P. Bliokh, Electronic properties of mesoscopic graphene structures: charge confinement and control of spin and charge transport. Phys. Rep. **503**, 77–114 (2011)
245. J. Güttinger, F. Molitor, C. Stampfer et al., Transport through graphene quantum dots. Rep. Prog. Phys. **75**, 126502–24 (2012)
246. S. Das Sarma, S. Adam, E.H. Hwang et al., Electronic properties in two dimensional graphene. Rev. Mod. Phys. **83**, 407–470 (2011)
247. J.S. Buch, Y. Yaish, M. Brink et al., Coulomb oscillations and Hall effect in quasi-2D graphite quantum dots. Nano Lett. **5**, 287–290 (2005)
248. C. Stampfer, J. Güttinger, F. Molitor et al., Tunable Coulomb blockade in nanostructured graphene. Appl. Phys. Lett. **92**, 012102 (2008)

249. S. Schnez, F. Molitor, C. Stampfer et al., Observation of excited states in graphene quantum dot. ibid **94**, 012107-5 (2009)
250. W.N. Carr, Characteristics of a GaAs spontaneous infrared source with 40 percent efficience. IEEE Electron Dev. **ED-12**, 531–535 (1965)
251. H.C. Casey, M.B. Panish, *Heterostructure Lasers* (Academic, New York, 1978)
252. P.S. Zoty, *Quantum Well Lasers* (Academic, Boston, 1993)
253. Y. Arakawa, in *Confined Electrons and Photons: New Physics and Applications, Semiconductor Nano-Structure Lasers: Fundamentals and Applications*. NATO Series B: Physics, vol. 340, ed. by E. Burstein, C. Weisbuch (New York, Plenum Press, 1995), pp. 647–673
254. L.A. Colderen, S.W. Corzine, *Diode Lasers and Photonic Integrated Cicuits* (Wiley, New York, 1995)
255. N.N. Ledentsov, V.M. Ustinov, V.A. Shchukin et al., Quantum dot heterostructures: Fabrication, properties, lasers. Fiz. and Teh. Polup. (Physics and Technics of Semicond.) **32**, 385–410 (1998). (in Russian)
256. J. Faist, F. Capasso, D.L. Sivco et al., Quantum cascade laser. Science **264**, 553–556 (1994)
257. M. Beck, D. Hofstetter, T. Allen, Continuous wave operation of a mid-infrared semiconductor laser at room temperature. Science **295**, 301–305 (2002)
258. Z. Yin, X. Tang, A review of energy band gap engineering in III–V semiconductor alloys for mid-infrared laser applications. Solid St. Electron. **51**, 6–15 (2005)
259. V.M. Ustinov, A.E. Zukov, AYu. Egorov, N.A. Maleen, *Quantum Dot Lasers* (Oxford University Press, Oxford, 2003)
260. J.M. Martinez-Duart, R.J. Martin-Palme, F. Aguello-Rueda, *Nanotechnology for Microelectronics and Optoelectronics* (Amsterdam, Elsevier, 2006)
261. E. Burstein, C. Weisbuch, *Confined Electrons and Phonons: New Physics and Applications* (Plenum Press, New York, 1995)
262. F. Rossi, E. Molinari, The dominant role of Coulomb correlation. Phys. Rev. B **53**, 16462–16473 (1996)
263. L. Sirgu, Y. Oberli, L. Deriorgi et al., Excitonic lasing in semiconductor quantum wires. Phys. Rev. B **61**, R10575–10584 (2000)
264. M.H. Huang, S. Mao, H. Feick et al., Room temperature ultraviolet nanowire nanolasers. Science **292**, 1897–1899 (2000)
265. Y. Matsishima, S. Akiba, K. Sakaki, High-speed-response InGaAs/InP heterostructure avalanche photodiode with InGaAsP buffer layers. Electron. Lett. **18**, 945–946 (1982)
266. J.C. Campbell, W.T. Tsang, G.J. Qua, High-speed InP/InGaAsP/InGaAs avalanche photodiode grown by chemical beam epitaxy. IEEE QE **24**, 496–500 (1988)
267. L.E. Tarof, D.G. Knight, K.E. Fox et al., Planar InP/InGaAs avalanche photodetectors with partial charge sheet in device periphery. Appl. Phys. Lett. **57**, 670–672 (1990)
268. S. Lindsay, *Introduction to Nanoscience* (Oxford University Press, New York, 2009)
269. M.A. Nielsen, I.L. Chuang, *Quantum Computation and Quantum Information* (Cambridge University Press, New York, 2000)
270. O. Morsch, *Quantum Bits and Quantum Secrets: How Quantum Physics Revolutionizing Codes and Computers* (Wiley, Weinham, 2008)
271. B. Schumacher, Quantum coding. Phys. Rev. A **51**, 2738–2747 (1995)
272. V.G. Plekhanov, Quantum information and quantum computation, in *Transaction of Computer Science College* (Tallinn, 2004), pp. 161–282. (in Russian)
273. B.B. Kadomtsev, *Dynamics and Information* (UFN, Moscow, 1997). (in Russian)
274. D.P. DiVincenzo, The physical implementation of quantum computation. Fortschr. der Physik (Prog. Phys.) **48**, 771–783 (2000)
275. C.A. Perez-Delgado, P. Kok, Quantum computers: definition and implementation. Phys. Rev. A **83**, 012303–012315 (2011)
276. G.E. Moore, Cramming more components onto integrated circuits. Electronics **38**, 114–117 (1965)
277. M. Lacham, M.E. Newman, C. Moore, Why any sufficiently advanced technology is indistinguishable from noise. Am. J. Phys. **72**, 1290–1293 (2004)

278. P.A.M. Dirac, *The Principles of Quantum Mechanics* (OxfordUniversity Press, Oxford, 1958)
279. A. Barenco, C.H. Bennett, R. Cleve et al., Elementary gates for quantum computation. Phys. Rev. A **52**, 3457–3467 (1995)
280. S.L. Braunstein, *Quantum Computations, Encyclopedia of Applied Physics, Update* (Wiley, New York, 1999), pp. 239–256
281. V.G. Plekhanov, Fundamentals and applications of isotope effect in solids. Prog. Mat. Sci. **51**, 287–426 (2006)
282. D. Aharonov, Quantum Computation, in *Annual Reviews of Computational Physics VI*, ed. by D. Stauffer (World Scientific, Singapore, 1998), pp. 143–184
283. D. Aharonov, Adiabatic quantum computer. SIAM J. Comput. **37**, 166–194 (2007)
284. D. Aharonov, Adiabatic Quantum Computer, Lanl arXiv:quant-ph/0405098
285. D. DiVincenzo, Topics in quantum computers, in *Mesoscopic Electron Transport*. NATO ASI Series E, vol. 345, ed. by L. Sohn, L. Kouwenhoven, G. Schon, (Dordrecht, Kluwer, 1997), p. 657
286. D. DiVincenzo, *Topics in Quantum Computers*, vol. 1 (1996), p. 12, arXiv:cond-mat/9612125
287. D. DiVincenzo, Quantum computers and quantum coherence. J. Magn. Magn. Mats. **200**, 202–216 (1999)
288. H.-K. Lo, T. Spiller, S. Popescu (eds.), *Introduction to Quantum Computation and Quantum Information* (World Scientific, London, 1998)
289. T. Toffoli, Reversible computing, in *Automata, Languages and Programming, Seventh Colloqium*, vol. 84, Lecture Notes in Computer Science, ed. by J. de Bakker, J. van Leeuven (Springer, Berlin, 1980), pp. 632–644
290. T. Toffoli, Bicontinuous extensions of invertible combinatorial functions. Math. Syst. Theory **14**, 13–23 (1981)
291. Pellizari T., Quantum computers, error-correction and networking: quantum optical approaches, in *[297]*, pp. 270–311
292. J. Grashka, *Quantum Computing* (McGraw-Hill, New York, 1999)
293. D. Deutsch, Quantum computational networks. Proc. R. Soc. (Lond.) A **425**, 73–90 (1989)
294. J.W. Emsley, J.C. Lindon, *NMR Spectroscopy Using Liquid Crystals Solvents* (Pergamon Press, Oxford, 1975)
295. J. Stolze, D. Suter, *Quantum Computing (A Short Course from Theory to Experiment)* (Wiley, Weiheim, 2008)
296. L.M.K. Vandersypen, I.L. Chuang, NMR techniques for quantum control and computation. Rev. Mod. Phys. **76**, 1037–1069 (2004)
297. M. Levitt, *Spin Dynamics (Basics of Nuclear Magnetic Resonance* (Wiley, New York, 2001)
298. R.R. Ernst, G. Bodenhausen, A. Wokaun, *Principles of Nuclear Magnetic Resonance in One and Two Dimensions* (Oxford University Press, Oxford, 1987)
299. V.G. Plekhanov, *Isotopes in Quantum Information* (Palmarium Academic Publishing, Saarbrücken, 2013). (in Russian)
300. A. Ekert, P. Hayden, H. Inamori, *Basic Concepts in Quantum Computation*, Lanl, arXiv:quant.ph/0011013
301. I.L. Chuang, N. Gershenfeld, M. Kubinec, Experimental implementation of fast quantum searching. Phys. Rev. Lett. **80**, 3408–3411 (1998)
302. I.L. Chuang, N. Gershenfeld, M. Kubinec, Bulk quantum computation with NMR: theory and experiment. Proc. R. Soc. (Lond.) A **454**, 447–467 (1998)
303. L. Vandersypen, M. Steffen, G. Breita et al., Experimental realization of Shor's quantum factoring algorithm using NMR. Nature **414**, 883–887 (2001)
304. D. Esteve, J.M. Raimond, J. Dalibard (eds.), *QuantumCoherence and Information Processing* (Elsevier, London, 2004)
305. I. Bloch, Ultracold quantum gases in optical lattices. Nat. Phys. **1**, 23–27 (2005)
306. T.C. Ralph, Quantum optical systems for the implementation of quantum information processing. Rep. Prog. Phys. **69**, 853–898 (2006)
307. A.M. Steane, The ion trap quantum information processor. Appl. Phys. B **64**, 623–642 (1997)

308. H. Häffner, C.F. Roos, R. Blatt, Quantum computing with trapped ions. Phys. Rep. **469**, 155–203 (2008)
309. W. Paul, Electromagnetic traps for a charged and neutral particles. Rev. Mod. Phys. **62**, 531–540 (1990)
310. J.I. Cirac, P. Zoller, Quantum computations with cold trapped ions. Phys. Rev. Lett. **74**, 4091–4094 (1995)
311. C. Monroe, D.M. Meekhof, B.E. King et al., Demonstration of a universal quantum logic gate. Phys. Rev. Lett. **75**, 4714–4717 (1995)
312. N. Yanofsky, M. Manucci, *Quantum Computing for Computer Scientists* (Cambridge University Press, Cambridge, 2008)
313. D.J. Wineland, M. Barret, J. Britton et al., Quantum information processing with trapped ions. Phil. Trans. R. Soc. (Lond.) A **361**, 1349–1362 (2003)
314. T. Spiller, Quantum information processing: cryptography, computation, and teleportation. Proc. IEEE **84**, 1719–1746 (1996)
315. V.V. Schmidt, *Introduction in Physics of Superconductors* (Science, Moscow, 1982). (in Russian)
316. Yu. Makhlin, G. Schön, A. Shnirman, Quantum-state engineering with Josephson-junction devices. Rev. Mod. Phys. **73**, 357–400 (2001)
317. J.H. Platenberg, P.C. de Groot, C.J.P.M. Harmands, Demonstration of controlled-NOT quantum gates on a pair of superconducting quantum bits. Nature (London) **447**, 836–839 (2007)
318. P. Shor, Polynomial-time algorithms for prime factorization and discrete logarithms on a quantum computer, Lanl, arXiv:quant-ph/9508027
319. P. Shor, Polynomial-time algorithms for prime factorization and dicrete logarithms on a quantum computer. IEEE Press SIAM J. Comput. **26**, 1484–1509 (1997)
320. K.A. Valiev, A.A. Kokin, *Quantum Computers: Hopes and Reality* (RC Dynamics, Moscow, 2001). (in Russian)
321. L.K. Grover, A fast quantum mechanical algorithm for database search, in *Proceedings of the 28th ACM Symposium on Theory of Computation* (Association for Computing, Machinery, New York, 1999), pp. 212–219
322. L.K. Grover, Quantum mechanics helps in searching for a needle in a haystack, Lanl, arXiv:quant-ph/9605043
323. L.K. Grover, Quantum mechanics helps in searching for a needle in a haystack. Phys. Rev. Lett. **79**, 325–328 (1997)
324. P. Benioff, The computer as a physical system: a microscopic quantum mechanical Hamiltonian model of computers as represented by turing machine. J. Stat. Phys. **22**, 563–591 (1980)
325. P. Benioff, Quantum mechanical Hamiltonian models of Turing machine. ibid **29**, 515–546 (1982)
326. P. Benioff, Quantum mechanical models of turing machines that dissipate no energy. Phys. Rev. Lett. **48**, 1681–1684 (1982)
327. P. Shor, Polynomial-time algorithms for prime factorization and discrete logarithms on a quantum computer, in *Proceedings of the 35th Annual Symposium on Foundations of Computer Science* (IEEE Computer Society Press, Los Alamitos, 1994), pp. 124–134
328. A.M. Steane, Error correcting codes in quantum theory. Phys. Rev. Lett. **77**, 793–797 (1996)
329. J. Preskill, Reliable quantum computers. Proc. R. Soc. (Lond.) A **454**, 385–410 (1998)
330. B.E. Kane, Silicon-based quantum computation, Lanl, arXiv:quant-ph/0003031
331. B.E. Kane, Silicon-based quantum computation. Fortschr. Phys. **48**, 1023–1041 (2000)
332. A.M. Tyryshkin, S.A. Lyon, A.V. Astashkin, A.M. Raitsining, Electron spin relaxation times of phosphorus donors in silicon. Phys. Rev. B **68**, 193207–4 (2003)
333. D.K. Wilson, G. Feher, Electron spin resonance on donors in silicon. Phys. Rev. **124**, 1068–1083 (1961)
334. B.E. Kane, N.S. McAlpine, A.S. Dzurak, B.G. Clark, Single spin measurement using single electron transistors to probe two-electron systems. Phys. Rev. B **61**, 2961–2972 (2000)

335. A.J. Skinner, M.E. Davenport, B.E. Kane, Hydrogenic spin quantum computing in silicon. Phys. Rev. Lett. **90**, 087901–087904 (2003)
336. R. Vrijen, E. Yablonovich, K. Wang, Electron spin resonance transistors for quantum computing in Silicon-Germanium heterostructures. Phys. Rev. A **62**, 12306–12309 (2000)
337. I. Shlimak, V.I. Safarov, I. Vagner, Isotopically engineered Si/SiGe nanostructures as basic elements for a nuclear spin quantum computer. J. Phys. Condens. Matter **13**, 6059–6065 (2001)
338. I. Shlimak, V. Ginodman, A. Butenko et al., Electron transport in a slot-gate Si MOSFET, Lanl, arXiv:cond-mat./0803.4432
339. I. Shlimak, I. Vagner, Quantum information processing based on ^{31}P nuclear spin qubits in a qusi-one-dimensional ^{28}Si nanowire. Phys. Rev. B **75**, 045336–6 (2007)
340. F. Schäffler, High-electron-mobility Si/SiGe heterostructures: influence of the relaxed buffer layer. Semicond. Sci. Technol. **7**, 260–267 (1992)
341. V.G. Plekhanov, *Isotopes in Quantum Information*, Preprint N 2 of Computer Science College (Tallinn, 2007). (in Russian)
342. V.G. Plekhanov, Manifestation and origin of the isotope effect, Lanl, arXiv:gen.phys.0907.2024
343. V.G. Plekhanov, *Isotope Effect: Physics and Applications* (Palmarium Academic Publishing, Saarbrücken, 2014). (in Russian)
344. Special issue of Solid State Communications, **149** (2009)
345. A. Olaya-Castro, N.F. Johnson, Quantum information processing in nanostructures, Lanl, arXiv/quant-ph/0406133
346. D. Gammon, D.G. Steel, Optical studies of single quantum dots. Phys. Today **55**, 36–41 (2002)
347. L. Quiroga, N.F. Johnson, Entangled Bell and Greenberg-Horne-Zeilinger state of excitons in coupled quantum dots. Phys. Rev. **83**, 2270–2273 (1999)
348. D.D. Awschalom, L.C. Dassett, A.S. Dzurak, Quantum spintronics: engineering and manipulation atom-like spins in semiconductors. Science **339**, 1174–1179 (2013)
349. A.M. Stoneham, A.J. Fisher, P.T. Greenland, Optically driven silicon-based quantum gates with potential for high-temperature operation. J. Phys. Condens. Matter **15**, L447–L451 (2003)
350. K. Saeedi, S. Simmons, J.Z. Salvail, Room temperature quantum bit storage exceeding 39 minutes using ionized donors in silicon-28. Science **342**, 830–833 (2013)
351. S.Y. Kilin, Diamond-based quantum information technologies, in *Physics, Chemistry and Applications of Nanostructure* (World Scientific, Singapore, 2007), pp. 3–14
352. W.F. Koehl, B.B. Buckley, F.J. Ytrtnans et al., Room temperature coherent control of defect spin qubits in silicon carbide. Nature **479**, 84–87 (2011)
353. D.D. Awschalom, R. Epstein, R. Hanson, The diamond age spintronics. Sci. Am. **84** (2007)
354. J. Wrachtrup, F. Jelezko, Processing quantum information in diamond. J. Phys.: Condens. Matter **18**, S807–S824 (2006)
355. M.V. Guruder Dutt, L. Childress, L. Jiang et al., Quantum register based on individual electronic and nuclear spin qubits in diamond. Science **316**, 1312–1316 (2007)
356. N.B. Manson, J.P. Harrison, M.J. Sellars, The nitrogen-vacancy center in diamond re-visited (2008), arXiv:cond-mat/0601360
357. M. Chen, M. Hirose, P. Cappelaro, Measurement of transverse hyperfine interaction by forbiden transitions. Phys. Rev. B **92**, 020101-9 (2015)
358. L. du Preez, *Thesis* (University of the Witwatersrand, Johannesburg, 1965)
359. J.W. Steeds, S. Charles, T.J. Davis, Creation and mobility of self-interstitials in diamond. Diamond Rel. Mater. **8**, 94–100 (1999)
360. T. Gaebel, M. Domhan, I. Popa, Room temperature coherent control of coupled single spins in solid. Nat. Phys. **2**, 408–413 (2006)
361. E. Rej, T. Gaebel, T. Boele et al., Hyperpolarized nanodiamond with long relaxation time, arXiv:cond-mat/1502.06214

Index

A
Absorption, 19
Acoustical branch of vibrations, 71
Acoustic modes, 71
Acoustic phonons, 119
Adiabatic approximation, 54, 55
Allotropes, 194
AND gate, 240
Angular distribution, 75
Anharmonic broadening, 96
Anharmonic decay, 63
Anharmonic effects, 58
Anharmonic processes, 58, 59
Anharmonic properties, 53
Annihilation operators, 60
Artificial atoms, 2
Atomic Force Microscope (AFM), 215
Atomic Layer Epitaxy (ALE), 140
Avalanche photodiode, 235
Avogadro's number, 193

B
Bandgap engineering, 206
Bell, 261
Biexciton binding energies, 44
Biexciton emission, 47
Biexciton recombination, 44
Biexcitons, 42
Bilayer graphene, 199
Binary semiconductors, 188
Bloch function, 196
Bloch sphere, 250, 252
Bloch's theorem, 103
Bloch wave, 16
Bohr exciton radius, 123
Bohr radius, 40
Boltzmann equation, 178
Bond-charge model, 112
Born approximation, 76
Bose–Einstein factor, 188
Bose factor, 91
Braves crystal, 84
Brillouin zone, 8, 74, 78, 103, 196
Bulk phonons, 119

C
Callaway approach, 176
Callaway–Holland formalism, 179
Carbon, 194
Carbon-based electrodes, 204
Carbon nanotubes, 197
Cauchy principal part, 63
Chemical Beam Epitaxy (CBE), 140
Chemical potential, 143
Cladding, 190
Classical degree of freedom, 33
Classical logic gates, 240
Clausius–Mossotti relation, 193
CNOT gate, 248
Coherent cross section, 73
Coherent Potential Approximation (CPA), 66
Color centers, 262
Compressibility, 180
Confined modes, 101
Confined phonons, 110
Conformer, 213
Constructive interference, 244
Cooper pairs, 258
Copper halides, 18
Core, 190
Coulomb blockade, 217, 222, 227, 228

© Springer Nature Switzerland AG 2018

V. G. Plekhanov, *Introduction to Isotopic Materials Science*,
Springer Series in Materials Science 248, https://doi.org/10.1007/978-3-319-42261-9

Coulomb blockade effects, 223
Coulomb charging, 225
Coulomb forces, 54, 57, 64, 100
Coulombic bound states, 39
Coulombic interaction, 41
Coulomb potential, 38
Coulomb potential breaks, 259
Covalent crystals, 55
Criteria of Di Vincenzo, 240
Cross section, 71, 75
CVD diamond, 148
Cyclic boundary conditions, 168

D
Dark exciton states, 47
De Broglie, 31
De Broglie wavelength, 74, 141
Debye approximation, 170, 171
Debye frequency, 168
Debye function, 180
Debye spectrum, 169
Debye temperature, 168, 169
Debye theory, 164, 165, 167, 168, 181
Debye–Waller factor, 84
Deformable dipoles, 92
Deformation potential, 105, 125
Delta function, 35
Dense excitonic systems, 149
Density of States (DOS), 12, 32, 208
Deuteride, 16
Deuterium, 16
Deutsch gate, 249
Deutsch's algorithm, 253
2D excitons, 124
2D, 1D, and 0D excitons, 123
Diamond, 10, 18, 21
Diamond light-emitting diode (LED), 148
Diamond p–n junction, 146
Dimensional confinement, 100
Dimensional confinement of phonons, 105
Dirac fermions, 197
Disorder activated ≡ DA,DATA,DALA, DATO, and DALO bands, 107
Disorder-induced scattering, 95
Dispersion relation, 70, 74, 78
Donor spins, 262
Drain, 222
Dualism, 29
Dulong and Petit's law, 168
Dynamic isotope disorder, 174

E
Effective mass, 213
Eigenvalues, 92
Eigenvectors, 92
Elastic, 169
Elastically isotropic continuum, 120
Elastic continuum model, 101, 103
Elastic moduli, 160, 161
Elastic stiffness, 161, 162
Electromagnetic field, 31
Electromagnetic spectrum, 190
Electron excitations, 26
Electronic disorder, 65
Electronic polarizability, 87
Electronic quasi-particles, 42
Electron–phonon coupling, 112
Electron–phonon interaction, 7, 16
Electron–phonon rates, 119
Electrons(holes), excitons(polaritons), 6
Electron spin, 265
Elemental semiconductors, 1
Elementary excitations, 6
Elementary particles, 2
Empirical Nonlocal Pseudopotential Method, 8
EmptyQD, 47
Energy states, 33
Enriched crystal, 81
Envelope function, 39, 123
Epitaxial growth techniques, 140
Equilibrium separation, 156
Error-correcting codes, 258
Excited state, 255
Exciton binding energy, 40, 42
Excitonic bandgap, 114
Excitonic ionization, 38
Excitonic luminescence, 149
Excitonic molecules, 42
Exciton–phonon interactions, 123
Exciton–phonon scattering, 124
Exciton–photon interaction, 124
Exciton relaxation, 128
Excitons, 16, 42

F
Fermi energy, 206, 223
Fermi Golden Rule, 15
Fermi level, 218
Fermi's golden rule, 94
Feynman diagrams, 62
Field-Effect Transistor (FET), 219
Folded acoustic phonons, 107

Force constants, 64, 106
Forward currents, 147
Fourier analyzed, 89
Fourier law, 171, 172
Free-electron mass, 32
Free-exciton emission, 114
Free excitons, 23
Fröhlich, 105
Fröhlich interaction, 125
Full Width at Half Maximum (FWHM), 63
Fundamental absorption, 153
Fundamental properties, 12

G
Geometric optics, 191
Germanium, 18, 21
Gibbs paradox, 140
Gigabytes, 240
Graphene, 194
Graphene-based device, 206
Graphene-based materials, 201
Great discrepancy, 86
Greenberger–Horne–Zeilinger state, 261
Green's functions, 65
Grüneisen approximation, 159
Grüneisen constant, 160, 180
Grüneisen parameter, 62, 161, 162, 183, 187, 189
Grüneisen relation, 164, 165, 181

H
Hadamard (H) gate, 246
Harmonic approximation, 54, 94, 157
Harmonic Hamiltonian, 58
Haynes' rule, 144
Heat capacity, 165
Heat conductivity, 173, 174
Heisenberg's uncertainty principle, 243
Helmholtz equation, 102
Helmholtz free energy, 188
Heterointerfaces, 108
Heterojunction, 25
Heterostructures, 39
High-Electron Mobility Transistors (HENTs), 140, 216
Highly excited semiconductors, 142
Hilbert space, 241, 245
Hilbert transform, 63
Homojunctions, 238
Hook's law, 58, 101
Hopfield coefficients, 151
Hopfield transformation, 150
Human knowledge, 139
Hybridization, 9
Hydride, 16
Hydrogenation of graphene, 201
Hyperfine, 3
Hyperpolarization, 262

I
Ideal electron gases, 32
Incoherent cross section, 73
Indirect free exciton, 144
Inelastic neutron scattering, 77, 81
Information technology, 1
Internal energy, 167
Intravalley scattering process, 199
Intrinsic electronic excitation, 152, 153
Inversion symmetry, 87
Ionic, 53
Ion-trap method, 254
Ion-trap quantum processor, 255
IR photodetectors, 238
Isotope-based superlattice, 26
Isotope composition-controlled, 24
Isotope disorder, 58
Isotope-disorder crystals, 107
Isotope effect, 2, 163, 164, 181–183
Isotope-engineered materials, 141
Isotope mass, 18, 23
Isotope-mixed crystals, 45, 65, 115
Isotope-mixed crystals processors, 256
Isotope-mixed diamond, 200
Isotope physics, 2
Isotope ratio, 185
Isotope renormalization, 200
Isotopes, 17
Isotopetronics, 140
Isotopic abundance, 65
Isotopically disordered crystals, 65
Isotopically engineering material, 179
Isotopically enriched, 21
Isotopically enriched samples, 94
Isotopically mixed crystals, 177
Isotopically modified graphene, 200
Isotopically pure silicon, 179
Isotopic broadening, 96
Isotopic channels, 194
Isotopic composition, 1, 11, 162, 163, 165, 179, 182
Isotopic dependence, 20
Isotopic disorder, 97
Isotopic engineering, 139, 192
Isotopic fiber, 193

Isotopic fiber optics, 192
Isotopic Ge superlattices, 109
Isotopic interface, 193
Isotopic low-dimensional structure, 110
Isotopic mass, 112
Isotopic mass disorder, 65
Isotopic materials science, 141
Isotopic optoelectronics, 192
Isotopic purity, 184
Isotopic substitution, 16, 18, 180
Isotopic superlattices, 109, 115

J
Josephson junction, 258

K
Kane architecture, 259, 260
Kinetic energy, 173

L
Langevin equation, 150
Laplace equation, 103
Large-radius excitons, 23, 26
Larmor frequency, 252
Laser action, 149
Laser diodes, 229
Lattice constant, 71, 189
Lattice dynamics, 57, 58
Lattice parameter, 181
Lattice vibrations, 87
LCAO method, 11
Length scale, 141
Light-Emitting Diodes (LED), 229, 231
Light generation, 152
Linear thermal expansion coefficient, 62
Liquid helium, 26
Liquid helium temperature, 229
Liquid Nitrogen Temperature(LNT), 92
Lithium deuteride, 85, 180
Lithium hydride, 26, 85, 180
Lithium-ion batteries, 204
Lithium tritide, 180
Local-Density-Approximation(LDA) plane-wave pseudopotential method, 92
Localized mode, 98
Local modes, 59
Local vibrations, 179
London penetration length, 257
Longitudinal-optical, 121
Longitudinal-transverse splitting, 27
Long-range Coulomb potentials, 55
LO phonon dispersion, 81
Lorentzian, 63
Low-dimensional, 32
Low-dimensional structures, 2, 215
Low-energy thresholds, 25
Luminescence, 125

M
Macroatom, 35, 221
Macroscopic analog, 2
Macroscopic approach, 105
Macroscopic degree of freedom, 257
Macroscopic potential, 103
Magnetic Force Microscope (MFM), 215
Mandelstam–Landsberg–Raman spectra, 170
Mandelstam–Landsberg–Raman spectroscopy, 197
Mass disorder broadening, 95
Massless fermion, 201
Mass, spin, 2
Materials science, 1
Matrix element, 151
Maxwell's equations, 28, 191
MBE method, 127
Mean free paths, 157
Meissner effect, 257
Mesoscopic, 115
Mesoscopic physics, 141
Metal-Organic Chemical Vapor Deposition (MOCVD), 2, 140
Microscopic model, 105
Microstructures, 106
Modern quantum theory, 165
Molecular Beam Epitaxy (MBE), 2, 140
Molecular insulators, 53
Molecular polarizability, 193
Molecules, 16
Monte Carlo simulations, 184
Mössbauer effect, 255
MQWs, 238
Multimode waveguides, 191

N
NAND gates, 244, 245
Nanoelectronic, 31
Nanometer, 2
Nanoscale science, 215
Nanoscale thickness control, 112
Nanoscience, 1, 140, 215
Nanostructured carbon-based materials, 213
Nanostructures, 101, 103

Nanotechnology, 1
Natural isotope composition, 178
Nearly free-electron model, 15
Negative Differential Resistance(NDR), 218
Neutron irradiation, 141
Neutron radiation, 54
Neutrons, 2
Neutron spectroscopy, 68
Newton's second law, 101
Nitrogen–Vacancy (N–V) center, 263
NMR quantum computation, 253
Nonequilibrium phonon distribution function, 178
Normal coordinate, 69
Nuclear magnetic moment, 2
Nuclear Magnetic Resonance (NMR), 252
Nuclear spin, 184, 261
Nuclear technology, 141
Nucleus, 55
Numerically, 39

O
One-dimensional motion, 34
One-mode behavior, 98
Optical branch of vibrations, 71
Optical communication, 190, 235
Optical-fiber communication, 232
Optical modes, 71
Optical spectroscopy, 43
Optical transitions, 124
Optical waveguides, 191
Optic phonon energy, 118

P
11-parameter rigid-ion model, 188
Partition function, 188
Pauli matrix, 248, 249, 252
Pauli operators, 250
Pauli's principle, 243
Paul trap, 254, 255
Peierls, 174
Phase transition, 170
Phonon, 6, 54, 58, 77, 157
Phonon deformation potentials, 101
Phonon density of states, 86, 99
Phonon displacement operator, 59
Phonon frequency, 59, 188
Phonon interaction, 100
Phononless, 27
Phonon mean free path, 178
Phonon parameters, 188
Phonon–phonon interaction, 59
Phonon relaxation time, 175
Phonon spectrum, 68
Photodetectors, 229, 235
Photodiodes, 237
Photoluminescence, 19, 123
Photoluminescence spectra, 144
Photonlike polariton, 150
Piezoelectric interactions, 105
Piezoelectric(PE) coupling, 125
Planck distribution, 174, 175
Planck's constant, 31
Polariton effects, 124
Polarizability tensor, 87, 89
Polyatomic crystals, 99
Positive Intrinsic Negative photodiodes (PINs), 235
Primitive operations or gates, 244
Pristine graphene, 212
Protective jacket, 190
Protons, 2

Q
QD parameters, 225
Quanta, 31
Quantum chromodynamics, 201
Quantum computation, 241
Quantum computer, 240, 248
Quantum computing, 3, 252, 258
Quantum cryptography, 242
Quantum Dots (QDs), 35, 36, 38, 44, 105, 115, 118, 121, 140, 141, 223, 226, 234
Quantum electrodynamics, 201
Quantum heterostructures, 3
Quantum information, 3, 258
Quantum information processing, 256
Quantum information storage, 262
Quantum isotopic effect, 162, 163
Quantum mechanical, 2
Quantum mechanics, 30, 31
Quantum memory, 242
Quantum nanostructures, 3
Quantum nature of matter, 162, 163
Quantum parallelism, 258
Quantum physics, 139
Quantum processors, 265
Quantum size, 1
Quantum theory, 54
Quantum Wells (QWs), 38, 99, 105, 108, 115, 119, 120, 140, 141, 238
Quantum Wires (QWRs), 2, 38, 105, 115, 118, 120, 140, 141

Quantum yield, 153
Quantum-mechanical amplitudes, 243, 244
Quasi-harmonic approximation, 184
Quasi-one-dimensional slab, 101
Qubit, 3, 240, 252
QW lasers, 233
QWr laser structure, 233

R
Radiative annihilation, 26
Raleigh scattering, 89
Raman effect, 7
Rayleigh scattering, 175, 194
Reduced Brillouin zone, 105
Reduced Graphene Oxide (RGO), 202
Reduced mass, 181
Reflection spectra, 16, 170
Reflectivity spectroscopy, 19
Relaxation time approximation, 178
Repetitions, 27
Resonance emission line, 27
Resonant-Tunnel Effect (RTE), 218
Resonant-tunneling devices, 216
Resonant-Tunneling Diodes (RTD), 217
Resonant-tunneling effect, 217
Resonant-Tunneling Transistor (RTT), 217
Right-hand side(rhs), 62
Rydberg, 39

S
Scalability, 241
Scalar potential, 102
Scanning Near-field Optical Microscope (SNOM), 215
Scanning Tunneling Microscope (STM), 215
Scattering cross section, 77
Scattering of thermal neutrons, 77
Scattering spectrum, 77
Schrödinger equation, 54, 56, 227
Second-degree polynomial, 181
Semiconducting industry, 243
Semiconductor lasers, 233
Semiconductor nanostructures, 205
Semiconductor superlattice, 105, 140
Shor's algorithm, 253
Silicon, 18, 21
Silicon metal-oxide-semiconductor field-effect transistors (MOSFETs), 216
Si-nanowire FET, 220
Single-Electron Device (SED), 225
Single electronics, 223
Single-Electron Transistor (SET), 216, 217, 223, 227, 228
Single Electron Tunneling (SET), 35, 222
Single SQDs, 43
Snell's laws, 191
Solid-source MBE technique, 111
Source, 222
Specific heat, 68, 163, 165
Spin-entanglement, 265
Spin–orbit coupling, 8
Spin quadruplet, 44
Spins, 252
Spintronics, 3
Stark effect, 36
Stillinger–Weber type, 184
Stokes–Raman line, 60
Superconductor, 257
Superlattice, 25, 103
Superlattice linear chain model, 100
Superlattice unit cell, 106
Superposition, 245, 258
SWAP gate, 249
Synthetic, 24
Synthetic diamond, 24

T
Tetrahedrally coordinated semiconductors, 66, 86
Thermal conductivity, 157, 174, 177
Thermal expansion, 62, 79, 156, 181
Thermal expansion contribution, 60
Thermal neutron, 71, 74
Thermal properties, 184
Thermal resistance, 175
Thermodynamical potential, 159
Toffoli gate, 249
Total angular momentum, 44
Two-body interactions, 57
Two-dimensional (2D) systems, 2
Two-dimensional graphene, 194
Two-dimensional ground state, 38
Two-oscillator model, 18
Two-phonon DOS, 91
Two-photon absorption coefficient, 142
Two-qubit gates, 249

U
Uncertainty principle, 31, 54
Uniaxial strain, 197
Uniaxial tensile strain, 200
Unit cell, 69, 181
Unitary logic gate, 240

U-process, 174

V
Van der Waals interaction, 195
Variables, 33
Various isotopes, 65
Vibrational properties, 54
Virtual Crystal Approximation (VCA), 11, 65
Virtual crystal model, 18
Volume, 2

W
Wannier–Mott excitons, 149
Wave particle, 29
Wave–particle duality, 31
Wavevector, 30
Wave vector conservation, 21
Weyl–Dirac equation, 227
Wide-gap insulators, 152
Wider-gap materials, 263
Wires, 119
Wurtzite structure, 99

X
X-rays, 54

Y
Young's modulus, 101

Z
Zeeman splitting, 252
Zero-dimensional devices, 223
Zero-phonon line, 263
Zero-point energy, 64
Zero-point motion, 187
Zerotemperature, 54
Zero vibrations, 179
Zinc-blende semiconductors, 9
Zinc-blende-type materials, 188